Thermoelectric Materials 1998— The Next Generation Materials for Small-Scale Refrigeration and Power Generation Applications

19990827 027

DISTRIBUTION STATEMENT A
Approved for Public Release
Distribution Unlimited

MATERIALS RESEARCH SOCIETY
SYMPOSIUM PROCEEDINGS VOLUME 545

Thermoelectric Materials 1998— The Next Generation Materials for Small-Scale Refrigeration and Power Generation Applications

Symposium held November 30–December 3, 1998, Boston, Massachusetts, U.S.A.

EDITORS:

Terry M. Tritt
Clemson University
Clemson, South Carolina, U.S.A.

Mercouri G. Kanatzidis
Michigan State University
East Lansing, Michigan, U.S.A.

Gerald D. Mahan
University of Tennessee
Knoxville, Tennessee, U.S.A.

Hylan B. Lyon, Jr.
Marlow Industries
Dallas, Texas, U.S.A.

Materials Research Society
Warrendale, Pennsylvania

This work was supported in part by the Office of Naval Research under Grant Number N00014-99-1-0169. The United States Government has a royalty-free license throughout the world in all copyrightable material contained herein.

Single article reprints from this publication are available through University Microfilms Inc., 300 North Zeeb Road, Ann Arbor, Michigan 48106

CODEN: MRSPDH

Copyright 1999 by Materials Research Society.
All rights reserved.

This book has been registered with Copyright Clearance Center, Inc. For further information, please contact the Copyright Clearance Center, Salem, Massachusetts.

Published by:

Materials Research Society
506 Keystone Drive
Warrendale, PA 15086
Telephone (724) 779-3003
Fax (724) 779-8313
Website: http://www.mrs.org/

Library of Congress Cataloging in Publication Data

Thermoelectric materials 1998—the next generation materials for small-scale refrigeration and power generation applications : symposium held November 30–December 3, 1998, Boston, Massachusetts, U.S.A. / editors, Terry M. Tritt, Mercouri G. Kanatzidis, Gerald D. Mahan, Hylan B. Lyon Jr.
p.cm.—(Materials Research Society symposium proceedings ; ISSN 0272-9172 ; 545)
Includes bibliographical references and index.
ISBN 1-55899-451-3
1. Thermoelectric materials—Congresses. 2. Thermoelectric apparatus and appliances—Congresses. 3. Refrigeration and refrigerating machinery—Materials—Congresses. 4. Electric power production—Materials—Congresses. I. Tritt, Terry M. II. Kanatzidis, Mercouri G. III. Mahan, Gerald D. IV. Lyon Jr., Hylan B. V. Series: Materials Research Society symposium proceedings ; v. 545.
TK2950.T48 1999 99-18446
620.1'1297—dc21 CIP

Manufactured in the United States of America

CONTENTS

Preface xi

Acknowledgments xiii

Materials Research Society Symposium Proceedings xiv

*Properties of Novel Thermoelectrics From First Principles Calculations 3
D.J. Singh, I.I. Mazin, J.L. Feldman, and M. Fornari

*Atomic Displacement Parameters: A Useful Tool in the Search for New Thermoelectric Materials? 13
B.C. Sales, B.C. Chakoumakos, D. Mandrus, J.W. Sharp, N.R. Dilley, and M.B. Maple

*Electronic Structure of Complex Bismuth Chalcogenides and Other Narrow-Gap Thermoelectric Materials 23
S.D. Mahanti, P. Larson, D-Y. Chung, S. Sportouch, and M.G. Kanatzidis

*The Synthesis of Metastable Skutterudites Using Superlattice Reactants 37
H. Sellinschegg, J.R. Williams, J. Casperson, G. Nolas, and D.C. Johnson

Analysis of Antimony-Tin-Based Skutterudites 47
S.B. Schujman, G.A. Slack, H.C. Nguyen, G.S. Nolas, R.A. Young, F. Mohammed, and T. Tritt

Synthesis of New Thermoelectric Materials Using Modulated Elementary Reactants 53
H. Sellinschegg, J.R. Williams, S.P. Maxwell, D. Sillars, and D.C. Johnson

LnPdSb and $Ln_3Au_3Sb_4$: New Thermoelectric Materials 59
K. Mastronardi, D. Young, C-C. Wang, A.P. Ramirez, P. Khalifah, and R.J. Cava

Flux Synthesis of New Multinary Bismuth Chalcogenides and Their Thermoelectric Properties 65
D-Y. Chung, K-S. Choi, P.W. Brazis, C.R. Kannewurf, and M.G. Kanatzidis

Transport Properties of Doped $CsBi_4Te_6$ Thermoelectric Materials 75
P.W. Brazis, M. Rocci, D-Y. Chung, M.G. Kanatzidis, and C.R. Kannewurf

*Invited Paper

Chevrel Phases as Good Thermoelectric Materials 81
C. Roche, P. Pecheur, M. Riffel, A. Jenny, H. Scherrer, and S. Scherrer

Theoretical Modelling of Thermoelectricity in Bi Nanowires 87
X. Sun, Z. Zhang, G. Dresselhaus, M.S. Dresselhaus, J.Y. Ying, and G. Chen

Growth of Bismuth Telluride Thin Films by Hot Wall Epitaxy, Thermoelectric Properties 93
J.C. Tedenac, S. Dal Corso, A. Haidoux, S. Charar, and B. Liautard

Thermoelectric Properties of $PbTe/Pb_{1-x}Eu_xTe$ Quantum Wells 99
H. Scherrer, Z. Dashevsky, V. Kantser, A. Casian, I. Sur, and A. Sandu

Thermoelectric Properties of $AgBiTe_2$-Ag_2Te Composite 105
Y. Takigawa, T. Imoto, T. Sakakibara, and K. Kurosawa

Experimental Study of Phonon-Folding in Si/Ge and Si/SiGe Structures Designed for Thermoelectric Applications 111
J. Liu, A. Balandin, T. Borca-Tasciuc, Y.S. Tang, K.L. Wang, and G. Chen

Structure and Thermoelectric Properties of $SrBiTe_3$; 12-Fold Superstructure Caused by Distortion of the Two-Dimensional Te-Nets 117
K-S. Choi, D-Y. Chung, J. Heising, P.W. Brazis, C.R. Kannewurf, and M.G. Kanatzidis

Thermoelectric Properties of the Cubic Family of Compounds $AgPbBiQ_3$ (Q = S, Se, Te). Very Low Thermal Conductivity Materials 123
S. Sportouch, M. Bastea, P. Brazis, J. Ireland, C.R. Kannewurf, C. Uher, and M.G. Kanatzidis

The Influence of Silicon Dopant and Processing on Thermoelectric Properties of B_4C Ceramics 131
K-F. Cai, C-W. Nan, and X-M. Min

High-Temperature Transport Probe for Thermopower and Resistivity Measurements 137
R.T. Littleton IV, J. Jeffries, M.A. Kaeser, M. Long, and T.M. Tritt

Fabrication of Thermoelectric Modules Using Thermoelectric Pastes and an Additive Technology 143
X. Xi, G. Matijasevic, L. Ha, and D. Baxter

Modification of Thermoelectric Properties Using Insertion Techniques 149
E. Hatzikraniotis, Th. Kyratsi, K. Chrissafis, and K.M. Paraskevopoulos

Iron Disilicide as a Base for New Improved Thermoelectrics Creation 155
M.I. Fedorov, Yu.V. Ivanov, M.V. Vedernikov, and V.K. Zaitsev

Electrical Properties of Orthorhombic Iron Disilicide 161
J-I. Tani and H. Kido

Thermoelectric Transport Properties of $ReSi_{1.75}$ Thin Films 165
C.A. Kleint, A. Heinrich, H. Griessmann, D. Hofmann, H. Vinzelberg, J. Schumann, D. Schlaefer, G. Behr, and L. Ivanenko

Single Crystal Growth and Thermoelectric Properties of $Ce_5Cu_{19}P_{12}$ 171
K.J. Proctor and F.J. DiSalvo

Thermoelectric and Structural Properties of $Bi_{1-x}Be_{1+x}$ Thin Films on CdTe(111) 177
Y. Kim, S. Cho, A. DiVenere, G.K. Wong, J.R. Meyer, and J.B. Ketterson

MBE Growth and Thermoelectric Properties of Bi_2Te_3 Thin Films 183
S. Cho, Y. Kim, A. DiVenere, G.K.L. Wong, J.R. Meyer, and J.B. Ketterson

Synthesis and Thermoelectric Properties of $Cs_2Bi_{7.33}Se_{12}$, $A_2Bi_8Se_{13}$ (A = Rb, Cs), $Ba_{4-x}Bi_{6+2/3x}Se_{13}$, and $Ba_{3\pm x}Pb_{3\pm x}Bi_6Se_{15}$ 189
L. Iordanidis, P.W. Brazis, C.R. Kannewurf, and M.G. Kanatzidis

Thermoelectric Properties of Mixed Rhenium Chalcogenides $Re_6Te_{15-x}Se_x$ ($0 \le x \le 8$) 197
S. Kilibarda Dalafave, J. Ziegler, and H. McAllister

Thermoelectric Properties of Doped Rhenium Chalcogenides $Re_6Mn_xTe_{15}$ (x = 0, 1, 2; M = Ga, In, Ag) 203
S. Kilibarda Dalafave, H. Barcena, and D. Henningsen

The Nanofabrication of Quantum Wires for the Next Generation of Thermoelectrics 209
D.L. Demske, J.L. Price, N.A. Guardala, N. Lindsey, J.H. Barkyoumb, J. Sharma, H.H. Kang, and L. Salamanca-Riba

*Prospects for Bismuth Nanowires as Thermoelectrics 215
M.S. Dresselhaus, Z. Zhang, X. Sun, J.Y. Ying, J. Heremans, G. Dresselhaus, and G. Chen

Thermoelectric Bismuth Wire Array Composites 227
T.E. Huber, M.J. Graf, and C.A. Foss

*Solid-State Chemistry Approach to Advanced Thermoelectrics. Ternary and Quaternary Alkali Metal Bismuth Chalcogenides as Thermoelectric Materials 233
M.G. Kanatzidis, D-Y. Chung, L. Iordanidis, K-S. Choi, P. Brazis, M. Rocci, T. Hogan, and C. Kannewurf

*Materials With Open Crystal Structure as Prospective Novel Thermoelectrics 247
C. Uher, J. Yang, and S. Hu

*Invited Paper

*Pressure-Tuning in the Search for Improved Thermoelectric Materials 259
D.A. Polvani, J.F. Meng, C.D.W. Jones, F.J. DiSalvo, and J.V. Badding

Boundary Effects in Thin-Film Thermoelectrics 265
M. Bartkowiak and G.D. Mahan

*Preparation and Properties of Porous Bismuth Films 273
W-N. Shen, B. Dunn, F. Ragot, M.S. Goorsky, C.D. Moore, G. Chen, R. Gronsky, W.W. Fuller-Mora, D.J. Gillespie, and A.C. Ehrlich

*$Bi_{1-x}Sb_x$ Alloy Thin Film and Superlattice Thermoelectrics 283
S. Cho, I. Vurgaftman, A.B. Shick, A. DiVenere, Y. Kim, S.J. Youn, C.A. Hoffman, G.K.L. Wong, A.J. Freeman, J.R. Meyer, and J.B. Ketterson

*Materials Development for Thermomagnetic Cooling 295
F. Freibert, A. Migliori, T.W. Darling, and S.A. Trugman

*Thermoelectric Properties of Single-Wall Carbon Nanotubes 303
L. Grigorian, G. Sumanasekera, and P.C. Eklund

Electronic Structure and Transport Properties of $CoSb_3$: A Narrow Bandgap Semiconductor 315
J.O. Sofo and G.D. Mahan

Nickel Substituted Skutterudites: Synthesis and Physical Properties 321
L. Chapon, D. Ravot, and J.C. Tedenac

Physical Properties of Single-Phase Skutterudite Thin Films ($CoSb_3$ and $IrSb_3$) 327
J.C. Caylor, A.M. Stacy, T. Sands, and R. Gronsky

Thermoelectric Properties of Cr_3S_4-Type Selenides 333
G.J. Snyder, T. Caillat, and J-P. Fleurial

Thermal Conductivity of Fe-Doped $CoSb_3$ Skutterudites 339
K.L. Stokes, A.C. Ehrlich, and G.S. Nolas

Imaging of the Carrier Density of States in Low-Dimensional Structures Using Electrostatic Force Microscopy 345
D. Gekhtman, Z.B. Zhang, D. Adderton, M.S. Dresselhaus, and G. Dresselhaus

Fabrication, Characterization and Electronic Properties of Bismuth Nanowire Systems 351
Z.B. Zhang, M.S. Dresselhaus, and J.Y. Ying

*Thermal Conductivity and Phonon Engineering in Low-Dimensional Structures 357
G. Chen, S.G. Volz, T. Borca-Tasciuc, T. Zeng, D. Song, K.L. Wang, and M.S. Dresselhaus

*Invited Paper

Experimental Study of the Effect of the Quantum Well Structures on the Thermoelectric Figure of Merit in $Si/Si_{1-x}Ge_x$ System 369
X. Sun, J. Liu, S.B. Cronin, K.L. Wang, G. Chen, T. Koga, and M.S. Dresselhaus

Carrier Pocket Engineering to Design Superior Thermoelectric Materials Using GaAs/AlAs Superlattices 375
T. Koga, X. Sun, S.B. Cronin, and M.S. Dresselhaus

Substitutional Effects on the Thermoelectric Properties of Transition Metal Pentatellurides 381
R.T. Littleton IV, J.W. Kolis, C.R. Feger, and T.M. Tritt

Thermoelectric Properties of Two Ternary Tellurides 391
J.W. Sharp, B.C. Sales, D.G. Mandrus, and B.C. Chakoumakos

Approaches Toward Chemically Prepared Multiple Quantum Well Structures 397
S.B. Cronin, T. Koga, X. Sun, Z. Ding, S-C. Huang, R.B. Kaner, and M.S. Dresselhaus

*Thermoelectric Properties of the Half-Heusler Compound (Zr,Hf)(Ni,Pd)Sn 403
V.M. Browning, S.J. Poon, T.M. Tritt, A.L. Pope, S. Bhattacharya, P. Volkov, J.G. Song, V. Ponnambalam, and A.C. Ehrlich

Thermoelectric Properties of the AlPdMn Quasicrystalline System 413
A.L. Pope, T.M. Tritt, M. Chernikov, M. Feuerbacher, S. Legault, R. Gagnon, and J. Strom-Olsen

Observed Properties and Electronic Structure of RNiSb Compounds (R = Ho, Er, Tm, Yb and Y). Potential Thermoelectric Materials 421
S. Sportouch, P. Larson, M. Bastea, P. Brazis, J. Ireland, C.R. Kannewurf, S.D. Mahanti, C. Uher, and M.G. Kanatzidis

*Semiconductor Clathrates: A PGEC System With Potential for Thermoelectric Applications 435
G.S. Nolas

Theoretical Calculation of the Vibrational Modes in Ge_{46} Clathrate and Related $M_xGa_yGe_{46-y}$ Type Clathrates 443
J. Dong, O.F. Sankey, A.A. Demkov, G.K. Ramachandran, J. Gryko, P. McMillan, and W. Windl

*Enhanced Thermionic Emission Cooling in High Barrier Superlattice Heterostructures 449
A. Shakouri, C. LaBounty, P. Abraham, J. Piprek, and J.E. Bowers

*Thermionic Refrigeration 459
G.D. Mahan

*Invited Paper

Hot Electron Effects on Thermionic Emission Cooling in Heterostructures 467
T. Zeng and G. Chen

Anisotropic Thermal Conductivity of a Si/Ge Superlattice 473
T. Borca-Tasciuc, D. Song, J.L. Liu, G. Chen, K.L. Wang, X. Sun, M.S. Dresselhaus, T. Radetic, and R. Gronsky

Investigation of the Mechanism of the Enhanced $Z_{3D}T$ in PbTe Based Superlattices 479
T. Koga, T.C. Harman, X. Sun, S.B. Cronin, and M.S. Dresselhaus

***Thermoelectric Transport in Superlattices** 485
D.A. Broido and T.L. Reinecke

Development of Thick-Film Thermoelectric Microcoolers Using Electrochemical Deposition 493
J-P. Fleurial, A. Borshchevsky, M.A. Ryan, W.M. Phillips, J.G. Snyder, T. Caillat, E.A. Kolawa, J.A. Herman, P. Mueller, and M. Nicolet

Reliability of Thermal Conductivity Measured by Harman Method 501
Y. Shinohara, Y. Imai, Y. Isoda, and I.A. Nishida

Microstructure and Thermoelectric Properties of Thin Foils of Bismuth Telluride Alloys 507
E. Koukharenko, N. Frety, V.G. Shepelevich, and J.C. Tedenac

The Effect of a Graded in Profile on the Figure of Merit PbTe 513
Z. Dashevsky, S. Shusterman, A. Horowitz, and M.P. Dariel

Author Index 519

Subject Index 523

PREFACE

This proceedings volume from Symposium Z at the 1998 MRS Fall Meeting in Boston, Massachusetts, is the third in a series of MRS proceedings related to research in new thermoelectric materials (see MRS Proceedings Vol. 234 (1991) and Vol. 478 (1997)). Thermoelectric materials are used in a wide variety of applications related to small-scale solid-state refrigeration or power generation. Over the past 30 years, alloys based on the Bi-Te compounds (refrigeration) $[(Bi_{1-x}Sb_x)_2 (Te_{1-x}Se_x)_3]$ and $Si_{1-x}Ge_x$ compounds (power generation) have been extensively studied and optimized for their use as thermoelectric materials. Thermoelectric cooling is an environmentally "friendly" method of small-scale cooling in specific applications such as cooling computer chips and laser diodes. Currently, one of the most common uses of thermoelectric refrigeration materials is in small beverage coolers. Another very important application of thermoelectric materials is in power generation for deep-space probes such as in the Voyager and Cassini missions. Despite the extensive investigation of these traditional thermoelectric materials, there is still substantial room for improvement, and thus, entirely new classes of compounds will have to be investigated. Therefore, the focus of this symposium centers around the development of "The Next Generation Materials for Small-Scale Refrigeration and Power Generation Applications."

The essence of a good thermoelectric is given by the determination of the material's dimensionless figure of merit, $ZT = (\alpha^2\sigma/\lambda)T$, where α is the Seebeck coefficient, σ is the electrical conductivity, and λ is the total thermal conductivity. The thermal conductivity consists of two parts: the electronic and lattice thermal conductivity. Many of the papers presented in this proceedings revolve around either maximizing the numerator of ZT, called the power factor, $PF = \alpha^2\sigma/\lambda$, or by minimizing the lattice thermal conductivity. As previously described by Glen Slack, a promising thermoelectric material should possess the thermal properties of a glass and the electronic properties of a crystal, i.e., a phonon-glass and electron-crystal (PGEC). This theme is quite prevalent in the many papers presented in this symposium.

The best thermoelectric materials have a value of $ZT \approx 1$. This $ZT \approx 1$ has been an upper limit for more than 30 years, yet no theoretical or thermodynamic reason exists why it cannot be larger. We believe that future advances in thermoelectric applications will come through research in new materials, and that is why we have focused the symposium on exploratory research in such materials. There are currently many new methods of materials synthesis, and much more rapid characterization of thermoelectric materials than were available 20 to 30 years ago. Many new researchers and new ideas are appearing in this field, giving us much anticipation about future advances. These new concepts and capabilities are coupled with new funding opportunities, and together should forward advances in a timely manner. It is the hope of the organizers of this symposium that these proceedings will provide a benchmark for the current state of new thermoelectric materials and should also provide the background for new

people in the field. We hope that this proceedings volume and the papers within will inspire additional new directions and approaches for research than are presented here.

Terry M. Tritt
Mercouri G. Kanatzidis
Gerald D. Mahan
Hylan B. Lyon, Jr.

January 1999

ACKNOWLEDGMENTS

The organizers of Symposium Z, "Thermoelectric Materials 1998—The Next Generation Materials for Small-Scale Refrigeration and Power Generation Applications," would like to acknowledge those who made the symposium and this proceedings possible. First, we acknowledge financial support for the symposium from the Office of Naval Research, DARPA, the Naval Research Laboratory, Keithley Instruments, Quantum Design Inc., MMR Technology, General Motors Research, and the Materials Research Society. We especially wish to acknowledge the administrative support of Miss Marian Walker in all phases of assistance concerning the symposium organization and subsequent proceedings. Her diligence and hard work both before and after the symposium allowed for the timely progress of the manuscripts and preparation for publication. Much of the research and results presented in this proceedings were supported by DARPA, the Office of Naval Research, and the Army Research Office. Their financial support is greatly appreciated and acknowledged. There are many other individuals who had a part in the success of this symposium, and their contributions are very much appreciated.

MATERIALS RESEARCH SOCIETY SYMPOSIUM PROCEEDINGS

Volume 507— Amorphous and Microcrystalline Silicon Technology—1998, R. Schropp, H.M. Branz, M. Hack, I. Shimizu, S. Wagner, 1999, ISBN: 1-55899-413-0
Volume 508— Flat-Panel Display Materials—1998, G. Parsons, C-C. Tsai, T.S. Fahlen, C. Seager, 1998, ISBN: 1-55899-414-9
Volume 509— Materials Issues in Vacuum Microelectronics, W. Zhu, L.S. Pan, T.E. Felter, C. Holland, 1998, ISBN: 1-55899-415-7
Volume 510— Defect and Impurity Engineered Semiconductors and Devices II, S. Ashok, J. Chevallier, K. Sumino, B.L. Sopori, W. Götz, 1998, ISBN: 1-55899-416-5
Volume 511— Low-Dielectric Constant Materials IV, C. Chiang, P.S. Ho, T-M. Lu, J.T. Wetzel, 1998, ISBN: 1-55899-417-3
Volume 512— Wide-Bandgap Semiconductors for High Power, High Frequency and High Temperature, S. DenBaars, J. Palmour, M.S. Shur, M. Spencer, 1998, ISBN: 1-55899-418-1
Volume 513— Hydrogen in Semiconductors and Metals, N.H. Nickel, W.B. Jackson, R.C. Bowman, R.G. Leisure, 1998, ISBN: 1-55899-419-X
Volume 514— Advanced Interconnects and Contact Materials and Processes for Future Integrated Circuits, S.P. Murarka, M. Eizenberg, D.B. Fraser, R. Madar, R. Tung, 1998, ISBN: 1-55899-420-3
Volume 515— Electronic Packaging Materials Science X, D.J. Belton, M. Gaynes, E.G. Jacobs, R. Pearson, T. Wu, 1998, ISBN: 1-55899-421-1
Volume 516— Materials Reliability in Microelectronics VIII, J.C. Bravman, T.N. Marieb, J.R. Lloyd, M.A. Korhonen, 1998, ISBN: 1-55899-422-X
Volume 517— High-Density Magnetic Recording and Integrated Magneto-Optics: Materials and Devices, J. Bain, M. Levy, J. Lorenzo, T. Nolan, Y. Okamura, K. Rubin, B. Stadler, R. Wolfe, 1998, ISBN: 1-55899-423-8
Volume 518— Microelectromechanical Structures for Materials Research, S. Brown, J. Gilbert, H. Guckel, R. Howe, G. Johnston, P. Krulevitch, C. Muhlstein, 1998, ISBN: 1-55899-424-6
Volume 519— Organic/Inorganic Hybrid Materials, R.M. Laine, C. Sanchez, C.J. Brinker, E. Giannelis, 1998, ISBN: 1-55899-425-4
Volume 520— Nanostructured Powders and Their Industrial Application, G. Beaucage, J.E. Mark, G.T. Burns, D-W. Hua, 1998, ISBN: 1-55899-426-2
Volume 521— Porous and Cellular Materials for Structural Applications, D.S. Schwartz, D.S. Shih, A.G. Evans, H.N.G. Wadley, 1998, ISBN: 1-55899-427-0
Volume 522— Fundamentals of Nanoindentation and Nanotribology, N.R. Moody, W.W. Gerberich, N. Burnham, S.P. Baker, 1998, ISBN: 1-55899-428-9
Volume 523— Electron Microscopy of Semiconducting Materials and ULSI Devices, C. Hayzelden, C. Hetherington, F. Ross, 1998, ISBN: 1-55899-429-7
Volume 524— Applications of Synchrotron Radiation Techniques to Materials Science IV, S.M. Mini, S.R. Stock, D.L. Perry, L.J. Terminello, 1998, ISBN: 1-55899-430-0
Volume 525— Rapid Thermal and Integrated Processing VII, M.C. Öztürk, F. Roozeboom, P.J. Timans, S.H. Pas, 1998, ISBN: 1-55899-431-9
Volume 526— Advances in Laser Ablation of Materials, R.K. Singh, D.H. Lowndes, D.B. Chrisey, E. Fogarassy, J. Narayan, 1998, ISBN: 1-55899-432-7
Volume 527— Diffusion Mechanisms in Crystalline Materials, Y. Mishin, G. Vogl, N. Cowern, R. Catlow, D. Farkas, 1998, ISBN: 1-55899-433-5
Volume 528— Mechanisms and Principles of Epitaxial Growth in Metallic Systems, L.T. Wille, C.P. Burmester, K. Terakura, G. Comsa, E.D. Williams, 1998, ISBN: 1-55899-434-3
Volume 529— Computational and Mathematical Models of Microstructural Evolution, J.W. Bullard, L-Q. Chen, R.K. Kalia, A.M. Stoneham, 1998, ISBN: 1-55899-435-1
Volume 530— Biomaterials Regulating Cell Function and Tissue Development, R.C. Thomson, D.J. Mooney, K.E. Healy, Y. Ikada, A.G. Mikos, 1998, ISBN: 1-55899-436-X
Volume 531— Reliability of Photonics Materials and Structures, E. Suhir, M. Fukuda, C.R. Kurkjian, 1998, ISBN: 1-55899-437-8

MATERIALS RESEARCH SOCIETY SYMPOSIUM PROCEEDINGS

Volume 532— Silicon Front-End Technology—Materials Processing and Modelling, N.E.B. Cowern, D.C. Jacobson, P.B. Griffin, P.A. Packan, R.P. Webb, 1998, ISBN: 1-55899-438-6

Volume 533— Epitaxy and Applications of Si-Based Heterostructures, E.A. Fitzgerald, D.C. Houghton, P.M. Mooney, 1998, ISBN: 1-55899-439-4

Volume 535— III-V and IV-IV Materials and Processing Challenges for Highly Integrated Microelectonics and Optoelectronics, S.A. Ringel, E.A. Fitzgerald, I. Adesida, D. Houghton, 1999, ISBN: 1-55899-441-6

Volume 536— Microcrystalline and Nanocrystalline Semiconductors—1998, L.T. Canham, M.J. Sailor, K. Tanaka, C-C. Tsai, 1999, ISBN: 1-55899-442-4

Volume 537— GaN and Related Alloys, S.J. Pearton, C. Kuo, T. Uenoyama, A.F. Wright, 1999, ISBN: 1-55899-443-2

Volume 538— Multiscale Modelling of Materials, V.V. Bulatov, T. Diaz de la Rubia, R. Phillips, E. Kaxiras, N. Ghoniem, 1999, ISBN: 1-55899-444-0

Volume 539— Fracture and Ductile vs. Brittle Behavior—Theory, Modelling and Experiment, G.E. Beltz, R.L. Blumberg Selinger, K-S. Kim, M.P. Marder, 1999, ISBN: 1-55899-445-9

Volume 540— Microstructural Processes in Irradiated Materials, S.J. Zinkle, G. Lucas, R. Ewing, J. Williams, 1999, ISBN: 1-55899-446-7

Volume 541— Ferroelectric Thin Films VII, R.E. Jones, R.W. Schwartz, S. Summerfelt, I.K. Yoo, 1999, ISBN: 1-55899-447-5

Volume 542— Solid Freeform and Additive Fabrication, D. Dimos, S.C. Danforth, M.J. Cima, 1999, ISBN: 1-55899-448-3

Volume 543— Dynamics in Small Confining Systems IV, J.M. Drake, G.S. Grest, J. Klafter, R. Kopelman, 1999, ISBN: 1-55899-449-1

Volume 544— Plasma Deposition and Treatment of Polymers, W.W. Lee, R. d'Agostino, M.R. Wertheimer, B.D. Ratner, 1999, ISBN: 1-55899-450-5

Volume 545— Thermoelectric Materials 1998—The Next Generation Materials for Small-Scale Refrigeration and Power Generation Applications, T.M. Tritt, M.G. Kanatzidis, G.D. Mahan, H.B. Lyon, Jr., 1999, ISBN: 1-55899-451-3

Volume 546— Materials Science of Microelectromechanical Systems (MEMS) Devices, A.H. Heuer, S.J. Jacobs, 1999, ISBN: 1-55899-452-1

Volume 547— Solid-State Chemistry of Inorganic Materials II, S.M. Kauzlarich, E.M. McCarron III, A.W. Sleight, H-C. zur Loye, 1999, ISBN: 1-55899-453-X

Volume 548— Solid-State Ionics V, G-A. Nazri, C. Julien, A. Rougier, 1999, ISBN: 1-55899-454-8

Volume 549— Advanced Catalytic Materials—1998, P.W. Lednor, D.A. Nagaki, L.T. Thompson, 1999, ISBN: 1-55899-455-6

Volume 550— Biomedical Materials—Drug Delivery, Implants and Tissue Engineering, T. Neenan, M. Marcolongo, R.F. Valentini, 1999, ISBN: 1-55899-456-4

Volume 551— Materials in Space—Science, Technology and Exploration, A.F. Hepp, J.M. Prahl, T.G. Keith, S.G. Bailey, J.R. Fowler, 1999, ISBN: 1-55899-457-2

Volume 552— High-Temperature Ordered Intermetallic Alloys VIII, E.P. George, M. Yamaguchi, M.J. Mills, 1999, ISBN: 1-55899-458-0

Volume 553— Quasicrystals, J-M. Dubois, P.A. Thiel, A-P. Tsai, K. Urban, 1999, ISBN: 1-55899-459-9

Volume 554— Bulk Metallic Glasses, W.L. Johnson, C.T. Liu, A. Inoue, 1999, ISBN: 1-55899-460-2

Volume 555— Properties and Processing of Vapor-Deposited Coatings, M. Pickering, B.W. Sheldon, W.Y. Lee, R.N. Johnson, 1999, ISBN: 1-55899-461-0

Volume 556— Scientific Basis for Nuclear Waste Management XXII, D.J. Wronkiewicz, J.H. Lee, 1999, ISBN: 1-55899-462-9

Prior Materials Research Society Symposium Proceedings available by contacting Materials Research Society

Thermoelectric Materials 1998—The Next Generation Materials for Small-Scale Refrigeration and Power Generation Applications

PROPERTIES OF NOVEL THERMOELECTRICS FROM FIRST PRINCIPLES CALCULATIONS

D.J. Singh *, I.I. Mazin *, J.L. Feldman *, M. Fornari **
*Complex Systems Theory Branch, Naval Research Laboratory, Washington, DC 20375
**Computational Sciences and Informatics, George Mason University, Fairfax, VA 22030

ABSTRACT

The use of first principles methods based on density functional theory to investigate novel thermoelectric materials is illustrated for several empty and filled skutterudite compounds, including $CoSb_3$, CoP_3, $La(Fe,Co)_4Sb_{12}$ and $La(Fe,Co)P_{12}$. Band structures and their relationship to transport properties especially as regards optimization of thermoelectric properties is discussed. Phonon models constructed from calculations and existing experimental data for $CoSb_3$ are presented. These have been extended to the filled skutterudites, particularly $LaFe_4Sb_{12}$ using additional first principles calculations to fix the La related parameters in the model. This model allows an interpretation of neutron scattering data as well as an understanding of the low frequency phonon modes that transport heat in these compounds.

INTRODUCTION

The search for new high performance thermoelectric (TE) materials is greatly complicated by the apparently contradictory requirements. TE performance [1] is characterized by a dimensionless figure of merit, $ZT = \sigma S^2 T/\kappa$ where σ is the electrical conductivity, S is the thermopower or Seebeck coefficient and the thermal conductivity, $\kappa = \kappa_e + \kappa_l$ is the sum of an electronic and a lattice contribution. Thus a high ZT material should have a high electrical conductivity (like a metal), a high thermopower (like a lightly doped semiconductor) and a low thermal conductivity (like a glass). The requirement for low thermal conductivity implies a bias towards complex materials characterized by large unit cells. This and the fact that the electronic transport coefficients, σ and S, are strong functions of the doping level in semiconductors further complicate the search. Within this context, it is expected that knowledge of the microscopic origins of the transport properties should be helpful in finding favorable TE compositions, and optimizing these materials for high ZT.

In this paper we discuss the electronic and vibrational properties of skutterudites in relation to their TE properties using first principles calculations, based on density functional theory. Electronic transport (σ and S) is related to the electronic band structure through kinetic transport theory, while the lattice thermal conductivity, κ_l is related to the phonon spectrum. The band structure is obtained directly from the density functional calculations; the phonon spectrum may be determined by fitting force constant models to density functional calculations of the energies and atomic forces as a function of the atomic coordinates, or to a combination of these and experimentally known phonon frequencies.

There has been considerable interest in the TE properties of binary (unfilled) and filled-skutterudites. This has been driven in part by expectations [2] that these compounds may be particularly favorable for TE application and partly by the discovery of two high ZT compositions: $CeFe_4Sb_{12}$ and $La(Fe,Co)_4Sb_{12}$ within this family [3-5]. Attempts to obtain still higher performance by various alloyings and substitutions on the three sites have thus far been unsuccessful, although there are still many possibilities remaining to be explored. Such efforts are complicated by the large variety of realizable modifications of these skutterudites, and the

Mat. Res. Soc. Symp. Proc. Vol. 545 © 1999 Materials Research Society

fact that TE performance is typically a strong function of the doping level. The high ZT values in the two known high ZT skutterudite compounds derive from two things: high power factors, σS^2, which relate to the electronic structures, and a strong suppression of the thermal conductivity of the binaries upon rare earth filling.

Much of the interest has focused on the antimonides, based on expectations of higher mobility due to the chemistry of Sb as compared to, say, P and of lower thermal conductivity due to the heavier mass Sb atoms. There is, however, growing interest in skutterudite arsenides and phosphides. This recognizes both the complex origin of the high values of ZT in the antimonides, which raises doubts about simple arguments that the other pnictides should be less favorable, and the need to better understand the physics of transport in skutterudites and establish trends.

APPROACH

As mentioned the first principles results discussed here were obtained using density functional calculations. These were done using the general potential linearized augmented planewave (LAPW) method [6] within the local density approximation. This method is well suited to materials with open crystal structures and low site symmetries, like skutterudites, because it makes no shape approximations to the density or potential and because it uses a flexible basis in all regions of space. The convergence parameters used in the skutterudite calculations have been discussed in detail elsewhere [7-10] and are not repeated here.

BINARY SKUTTERUDITES

The skutterudite structure consists of a simple cubic transition metal sub-lattice partially filled by almost square four membered pnictogen rings. Three quarters of the sites are filled with rings oriented alternately along the [100], [010] and [001] directions as required by cubic symmetry, while one quarter remain empty. The filled skutterudite structure differs in that this empty site is filled by an ion such as a rare earth or Ba, Th, U or Pb, which modifies both the electronic and thermal properties. We begin therefore with the electronic and vibrational properties of the binary skutterudites, focussing on $CoSb_3$, $CoAs_3$ and CoP_3.

Previous calculations for $CoSb_3$ and $CoAs_3$ show generally similar electronic structures [7], but with differences that are particularly significant in the region near the Fermi energy, E_F, that dominates transport. Both materials have a prominent pseudogap around the Fermi energy that is crossed by a single relatively light band associated with the pnictogen rings. In the antimonides, $CoSb_3$ (and also $IrSb_3$) this band, which disperses upwards from the bottom of the pseudogap to a maximum at Γ has a highly non-parabolic, effectively linear shape. In $CoSb_3$ it just fails to reach the conduction band minimum leading to a narrow direct gap. In stoichiometric material, the Fermi energy lies in this gap. The quasi-linear dispersion, while consistent with high p-type power factors for moderate doping levels, as observed in $IrSb_3$ [2], is not favorable for p-type TE performance. This is because S depends more weakly on the band filling, n, than in the conventional parabolic case [7]. Therefore high enough values of S cannot be obtained for reasonable n. The conduction band structure is parabolic with reasonably heavy masses ($m^* \sim 0.5$). Thus the n-type case would seem more favorable but high quality n-type skutterudite samples are difficult to prepare. In contrast, $CoAs_3$ is found to be a zero gap semiconductor with nearly parabolic valence and conduction bands touching at Γ. Although this appears to be more favorable for a p-type TE, little is known about the arsenides experimentally.

Zhukov [11] has reported a first principles band structure for CoP_3 showing the material to be a narrow indirect gap semiconductor. The conduction bands with their heavy mass, multi-valley character would seem favorable for TE. However, the calculations were performed using the linear muffin-tin orbital atomic sphere approximation (LMTO-ASA) method, which can have errors in band positions of several tenths of an eV in materials with open crystal structures and low site symmetries, as is the case in CoP_3. Because of the small indirect gap, such shifts, if present, could substantially change the picture from a transport point of view. Accordingly, we have performed new calculations with the general potential LAPW method. As noted above, this method has both a flexible basis and freedom from shape approximations. The calculated band structure for CoP_3 in its experimental crystal structure is shown in Fig. 1.

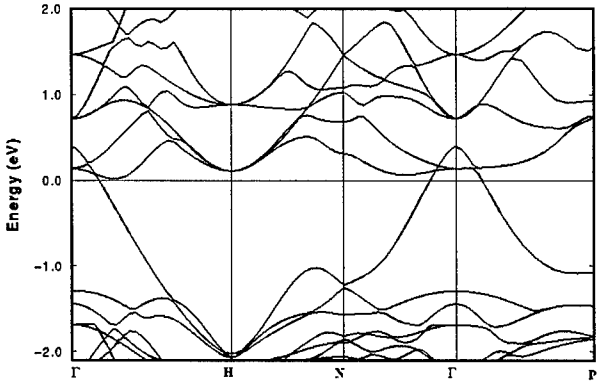

FIG. 1. Calculated LAPW band structure of CoP_3 near the Fermi energy, E_F. The horizontal line indicates the position of E_F that would be required to achieve single sign p-type transport. Note the large carrier concentration.

Our band structure for CoP_3 is globally similar to that of Zhukov, but with small changes near E_F that alter the picture greatly in an unfavorable direction from the point of view of TE. In particular, the pseudogap crossing band enters the conduction bands at Γ so that CoP_3 becomes a low carrier density metal, rather than a semiconductor. Thus, if CoP_3 is to form the basis of a high performance TE material, it will be necessary not only to control its thermal conductivity, but also to considerably modify its band structure.

High TE performance requires not only high S and σS^2 but a low lattice thermal conductivity, κ_l. While the minimum thermal conductivity theory of Slack shows that skutterudites have the potential for very low thermal conductivities this is not realized in the unfilled materials. For example, room temperature thermal conductivities of 100 mW/cmK are reported in $CoSb_3$ samples [4]. While rare earth filling can drastically lower the thermal conductivity to 15 – 25 mW/cmK this is still substantially higher than the theoretical minimum, suggesting that further improvements may be possible. Although the thermal conductivity in skutterudites is still not well understood, there are recent experimental and theoretical investigations that help elucidate the character of the phonon modes involved in heat transport and the effect of filling on them [8,12-14]. Feldman and Singh [8] calculated the phonon spectrum of $CoSb_3$ by using a force constant model that was fixed by frozen phonon calculations and experimental infrared phonon frequencies. The calculated phonon density of states from this model is shown in Fig. 2. The modes below ~50 cm^{-1} are acoustic in character. The phonon modes from 50 cm^{-1} to 175 cm^{-1} are dominated by Sb character. The lower energy

Sb modes have mainly rigid librational Sb_4 ring character, while in order of increasing energy, the modes change to twisting (bond angle changing) motions in the rings, rigid translational motions of the Sb_4, and finally bond stretching motions in the rings. The Co dominated modes are separated from these primarily Sb modes by a gap and occur above 230 cm^{-1}.

Within kinetic transport theory, phonon contributions to the thermal conductivity are related to $v_G^2 G\tau$, where $v_G^2 G$ is the phonon density of states weighted by the squared group velocity and τ is a scattering time. The $v_G^2 G$ factor heavily weights the low frequency part of the spectrum below ~100 cm^{-1} and effectively suppresses any contribution from modes above 200 cm^{-1}. This is illustrated in Fig. 3, where the high temperature transport function (no occupation factor and with constant τ) is given for $CoSb_3$ and $LaFe_4Sb_{12}$.

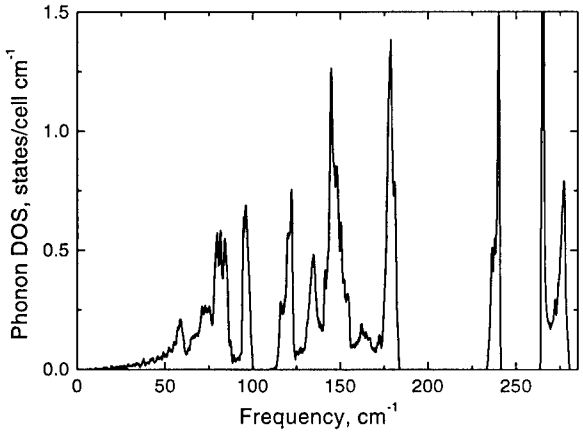

FIG. 2. Phonon density of states of $CoSb_3$ based on the model of Feldman and Singh.

As such, the thermal conductivity of $CoSb_3$ is derived almost entirely from acoustic modes and low-lying optical modes, both of which have strong Sb character. Thus the key to controlling the thermal conductivity in $CoSb_3$ is to scatter Sb related phonons. This in fact occurs upon rare earth filling as discussed below using calculations for $LaFe_4Sb_{12}$ and by interpretation of recent neutron scattering data based on our force constant model.

FILLED SKUTTERUDITES

As mentioned, without modification the unfilled skutterudites, $IrSb_3$, $CoSb_3$ and CoP_3 are unfavorable for TE application because of their high thermal conductivities, and their unfavorable band structures (though in the antimonides the n-type band structure is better). The changes in electronic structure upon La filling of $CoSb_3$ or Ce filling have been discussed in detail elsewhere [9,10] and are not repeated here except to mention the key points. In particular, the band structures are strongly modified due to the interaction of the host $CoSb_3$ derived bands, especially the pseudogap crossing band (which has f-like symmetry about the filling site), with rare earth f states. In the Ce filled skutterudites, this leads to the formation of hybridization gaps at E_F, while in $La(Fe,Co)_4Sb_{12}$ this light crossing band is pushed down to near the bottom of the pseudogap by repulsion from the La f-resonance above E_F. The implication is that La vacancies are strong hole scatters and therefore that both optimizing the

doping level and maximizing the La filling will be important to obtain the highest ZT in $La(Fe,Co)_4Sb_{12}$. Further, the electronic properties underlying the high ZT in La and Ce filled antimonides derive from the details of the interaction between the host lattice band structure and the rare earth f-levels. This means that heavier rare earths, with their inert f-shells, should have electronic structures closer to those of the unfilled skutterudites and different TE performance.

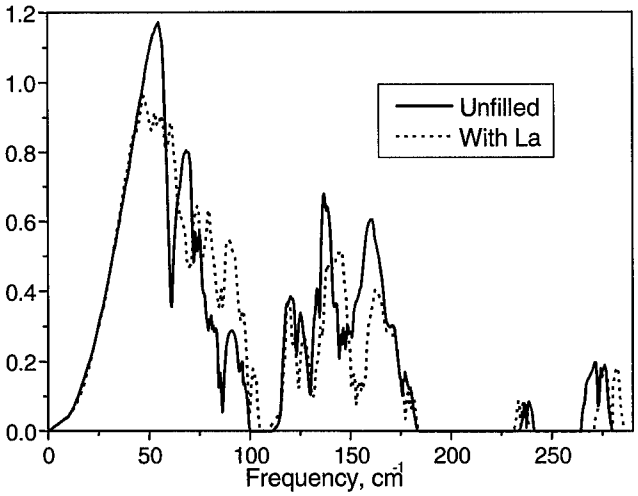

FIG. 3. Calculated phonon transport functions (arbitrary units, see text) for $LaFe_4Sb_{12}$ and $CoSb_3$.

These earlier calculations raise the question as to whether a more favorable electronic structure for TE application can be had by La filling of CoP_3 to make e.g. $La(Fe,Co)_4P_{12}$. We have performed LAPW calculations for $LaFe_4P_{12}$ to address this question. The band structure, calculated at the experimental crystal structure is shown in Fig. 4.

The band structure of $LaFe_4P_{12}$ relative to that of CoP_3 shows qualitatively the same effect as was found in the corresponding antimonides, i.e. the pseudogap crossing band is pushed down via repulsion between it and the La f-resonance 3 eV above. As a result, a gap of 0.10 eV is opened; so that with proper doping semiconducting compositions should be realizable. Along with the lowering of the valence band, there is a related distortion of the conduction bands, since anti-crossing effects between the valence and conduction bands are removed. This distortion shifts the conduction band minimum to Γ. Unlike $LaFe_4Sb_{12}$, however, the valence band maximum is not shifted down far enough to be in proximity to the heavy bands making up the edge of the pseudogap. The implication is that the p-type thermopower will not be high enough with reasonable band filling in $La(Fe,Co)_4P_{12}$ assuming rigid band behavior upon alloying with Co as was found in $La(Fe,Co)_4Sb_{12}$ (n.b. strong non-rigid band behavior, which we do not expect, would also be detrimental to TE performance as it would indicate strong alloy scattering and low carrier mobility). On the other hand the conduction band has a two fold degenerate minimum with a high effective mass $m^* \sim 0.8$. Thus $La(Fe,Co)_4P_{12}$ may be more interesting as an n-type TE material, provided that the thermal

conductivity can be effectively reduced and well-filled n-type material with low defect concentrations and high mobility can be produced.

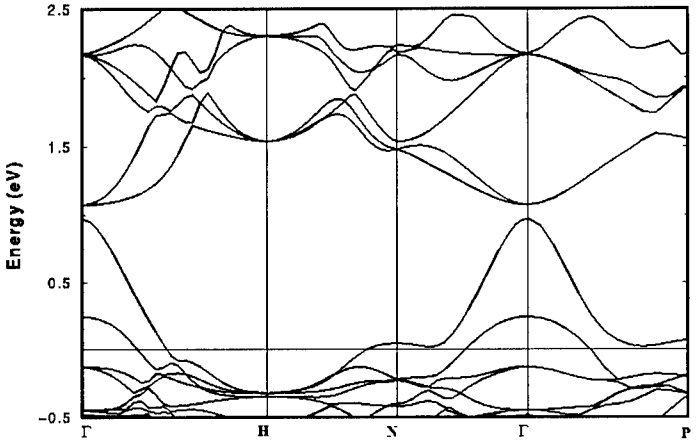

FIG. 4. Calculated band structure of $LaFe_4P_{12}$ in a window near the Fermi energy.

Returning to the question of thermal conductivity, scattering Sb related phonons is key to suppressing κ_l in skutterudite antimonides, and apparently rare earth filling is effective in doing this. Understanding this from a microscopic point of view requires addressing the issue of how the filling atoms interact with the host lattice vibrational modes. To begin, we used LAPW frozen phonon calculations of the energy of $LaFe_4Sb_{12}$ and $CeFe_4Sb_{12}$ as a function of the rare earth position, holding fixed at the experimental geometry all the other structural degrees of freedom (Fig. 5). The bare Einstein frequency corresponding to this distortion (this is not an observable quantity, as the rare earth motion needs to be coupled to the rest of the lattice) was calculated to be 68 cm^{-1} for Ce and 74 cm^{-1} for La. This is squarely in the frequency range of Sb_4 motions that contribute strongly to the thermal conductivity. The harmonic shape of energy vs. rare earth displacement apparent in Fig. 5 deserves comment. In particular, it should be noted that this shape is inconsistent with mechanisms that rely on interactions with strongly anharmonic soft modes or double well type vibrations to incoherently scatter phonons and suppress κ_l. On the other hand, the harmonic shape of the "bare modes" of Fig. 5 should not be interpreted as meaning that the dressed phonons in filled skutterudites involving La or Ce are harmonic. There may well be substantial anharmonicity from e.g. the rare-earth Sb interactions that do not appear in the energy vs. displacement curve of Fig. 5 due to the high symmetry (e.g. cubic anharmonic La-Sb interactions will cancel for this particular distortion).

Having established the character of the vibrational modes of the unfilled skutterudite and the "bare" vibrations of rare earth ions in this lattice, we turn to the interactions between these. Our approach was to construct a force constant model for $LaFe_4Sb_{12}$ starting with that for $CoSb_3$ (model B of Ref. 8) but with additional force constants. The parameters corresponding to these were determined from frozen phonon density functional results with force calculations at approximately 40 distortions of the lattice including small La, Fe and Sb shifts in a variety of patterns.

We find that there are strong force constants between the La and near neighbor Sb atoms and between the La and the near neighbor Fe atoms, and that the two are of opposite

sign. The La-Sb force is a restoring force, whereas the La-Fe force constant, which is about half in magnitude as large (note the number of Sb vs. Fe neighbors), is non-restoring. Using this model, we have calculated the phonon spectrum and transport function of $LaFe_4Sb_{12}$. The resulting transport function is compared with that for $CoSb_3$ in Fig. 3. There are strong changes in the 50 – 175 cm^{-1} range dominated by Sb motions. This reflects the fact that the La and Sb motions are strongly coupled in the filled skutterudites. It is also notable that there is little change in the lower frequency acoustic part of the spectrum.

Keppens and co-workers [12,13] have reported extensive neutron scattering investigations of the vibrational properties of La and Ce filled skutterudite antimonides. In their analysis, they make the important observation that because the La neutron scattering cross-section is much larger than that of Ce, the difference between $LaFe_4Sb_{12}$ and $CeFe_4Sb_{12}$ spectra may be dominated by modes involving rare earth motions. One of the key observations they made was that this difference spectrum has a pronounced two-peak structure. Although their analysis rests on the assumption that the lattice dynamics of the two materials are essentially the same, and we do find differences between La and Ce force constants based on frozen phonon calculation, these differences of ~13% are too small to alter their conclusion. In order to analyze their result in the context of the harmonic "bare modes", revealed by our calculations, we constructed a force constant phonon model for $CeFe_4Sb_{12}$. This was done using the model for $LaFe_4Sb_{12}$ but with the softer rare earth force constants obtained from the frozen phonon calculations for the Ce filled material.

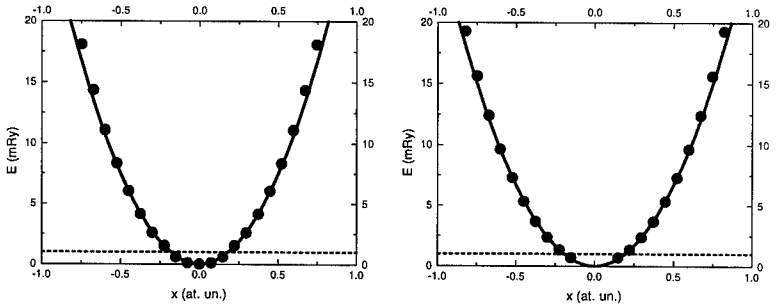

FIG. 5. Total energy as a function of rare earth displacement in $CeFe_4Sb_{12}$ (left) and $LaFe_4Sb_{12}$ (right). The points are the calculated energies while the solid line is the harmonic contribution from the curvature around 0. The dashed horizontal line indicates an energy corresponding to 300 K.

Calculations of the neutron scattering functions were done using only the self-term in the coherent scattering expression for a polycrystalline material at T=20K (the experimental condition). The calculated difference spectrum is compared with experiment in Fig. 6. The two peaks are found in just the same place in both the experimental and calculated spectra. The first peak in the difference spectrum is indeed due to phonon modes that are strongly La derived. The lowering of the "bare mode" Einstein frequency is, however, evidence of the importance of La-Sb interactions.

Besides the strong La component, measured by the experiment, we find that the second peak has a strong Sb character as well. Two additional points about the modes comprising the second peak should be mentioned. First of all, the magnitudes of the displacements of atoms for the modes in this peak are roughly the same for Sb and La and negligible for Fe. Secondly, in the unfilled case ($CoSb_3$) there is an analogous Sb peak in the phonon density of states,

which is at a slightly lower frequency; in our model the frequency difference is related to the La-Sb interaction. Therefore, roughly speaking, for the modes in this second peak the La atoms are being driven by the natural vibrations of the Sb atoms.

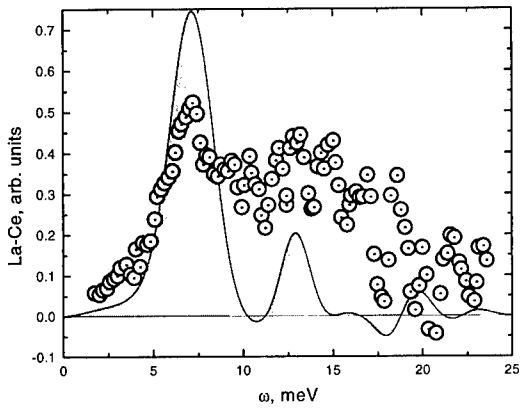

FIG 6. Calculated difference spectrum for $LaFe_4Sb_{12}$ and $CeFe_4Sb_{12}$ (see text) Solid curve is the calculated result, while the points denote experimental data (Ref. 12).

SUMMARY AND CONCLUSIONS

We have discussed the physics of skutterudite TE materials from a microscopic point of view, based on first principles density functional calculations. While there is much that remains to be understood about the physics of these materials, some insights have emerged. Those that we emphasize here are: (1) The electronic properties of La and Ce filled skutterudites are related to interactions between the framework, unfilled skutterudite electronic structure and rare earth f-levels. As such heavier rare earth filling atoms should yield different TE properties. (2) Stoichiometric CoP_3 is a metal, but $La(Fe,Co)_4P_{12}$ is predicted to have a gap, with a light valence band and heavier conduction bands; n-type doping is more likely to form the basis of a TE material in this system. (3) The lattice thermal conductivity in skutterudite antimonides is dominated by Sb related phonons. (4) La and Sb related modes are in the same frequency range and are strongly coupled in $LaFe_4Sb_{12}$ providing a mechanism for the two-peak structure observed in neutron the experiments. This is likely an essential feature of the thermal conductivity suppression upon La filling.

ACKNOWLEDGEMENTS

We are grateful for helpful discussions with T. Caillat, R.S. Feigelson, J.P. Fleurial, D. Mandrus, D. Morelli, L. Nordstrom and W.E. Pickett. We thank ONR and DARPA for supporting this work.

REFERENCES

1. D.M. Rowe, *Handbook of Thermoelectrics*, CRC Press, Boca Raton, 1995.
2. G.A. Slack and V.G. Tsoukala, J. Appl. Phys. **76**, 1665 (1994).

3. J.P. Fleurial, A. Borshchevsky, T. Caillat, D. Morelli and G.P. Meisner, *Proc. 15th Int. Conf. on Thermoelectrics*, p. 91 (IEEE Press, Piscataway, 1996).
4. T. Caillat, J.P. Fleurial and A. Borshchevsky, *Proc. 15th Int. Conf. on Thermoelectrics*, p. 100 (IEEE Press, Piscataway, 1996).
5. B.C. Sales, D. Mandrus and R.K. Williams, Science **272**, 1325 (1996).
6. D.J. Singh, *Planewaves, Pseudopotentials and the LAPW Method*, Kluwer, Boston, 1994.
7. D.J. Singh and W.E. Pickett, Phys. Rev. B **50**, 11235 (1994).
8. J.L. Feldman and D.J. Singh, Phys. Rev. B **53**, 6273 (1996); **54**, 712 (1996).
9. L. Nordstrom and D.J. Singh, Phys. Rev. B **53**, 1103 (1996).
10. D.J. Singh and I.I. Mazin, Phys. Rev. B **56**, R1650 (1997).
11. V.P. Zhukov, Phys. Stat. Solidi **38**, 90 (1996).
12. V. Keppens, D. Mandrus, B.C. Sales, B.C. Chakoumakos, P. Dai, R. Coldea, M.B. Maple, D.A. Gajewski, E.J. Freeman and S. Bennington, Nature **395**, 876 (1998).
13. D. Mandrus, B.C. Sales, V. Keppens, B.C. Chakoumakos, P. Dai, L.A. Boatner, R.K. Williams, J.R. Thompson, T.W. Darling, A. Migliori, M.B. Maple, D.A. Gajewski and E.J. Freeman, MRS Symp. Proc. **478**, 199 (1997).
14. G.S. Nolas, J.L. Cohn and G.A. Slack, Phys. Rev. B **58**, 164 (1998).

ATOMIC DISPLACEMENT PARAMETERS : A USEFUL TOOL IN THE SEARCH FOR NEW THERMOELECTRIC MATERIALS?

B. C. SALES*, B. C. CHAKOUMAKOS*, D. MANDRUS*, J.W. SHARP**, N. R. DILLEY*** AND M. B. MAPLE***
*Solid State Division, Oak Ridge National Laboratory, Oak Ridge , TN 37831
**Research and Development Division, Marlow Industries, Dallas, Texas 75238
***Department of Physics, University of California San Diego 92093

ABSTRACT

The atomic displacement parameters (ADPs) measure the mean-square displacement amplitude of an atom about its equilibrium position in a crystal. It is demonstrated that the ADPs can be used to identify crystalline solids with unusually low lattice thermal conductivties. A low lattice thermal conductivity is essential in the design of thermoelectric materials with improved efficiencies.The atomic displacement parameters (ADPs) have been measured using powder neutron diffraction as a function of temperature for several clathrate-like compounds ($R_xCo_{4-y}Fe_ySb_{12}$, where R= La, Ce, Yb or Tl, x=0.22, 0.8, 1, y=0, 1 ;Tl_2SnTe_5 and Tl_2GeTe_5). The ADP data show that in each of the compounds one of the atoms is weakly bound and "rattles" within its atomic cage. This atomic "rattling" severely reduces the ability of these crystals to conduct heat and in some cases the lattice thermal conductivity approaches the theoretical minimum value. In many clathrate-like compounds, the ADP can also be used to estimate the Einstein frequency of the "rattler", and to predict the existence of localized vibrational modes.

INTRODUCTION

In the description of a new crystalline compound, crystallographers normally tabulate the room temperature ADP values for each distinct atomic site in the structure.[1-4] The various ADP values thus comprise some of the first information that is known about a new crystalline compound. The value of the mean square atomic displacement can be due to the vibration of the atom or to static disorder. The effects that this parameter can have on various physical properties, however, have not been widely recognized. In particular, the ADPs are not normally used by solid state physicists or chemists as a guide in the search for new compounds with specific properties. ADP's are regarded by many scientists as unreliable since in many of the earliest structure determinations, the ADP's were often used as repositories for much of the error in the structure refinement. In addition, crystallographers have not always reported ADP information using a consistent definition,[1] adding further confusion as to the usefulness of ADPs. The purpose of this article is to illustrate that when properly determined, the ADP parameters can be used as a guide in the search for crystalline materials with unusually low lattice thermal conductivities. These materials are of particular interest in the design of thermoelectric compounds with improved efficiencies.[5-8] Furthermore, the variation of the ADP with temperature can be used to estimate the amount of static versus dynamic disorder, and in some cases can be used to determine a characteristic localized vibration frequency for a weakly bound atom that "rattles" within its atomic cage.[2,4]

EXPERIMENT

The compounds investigated here are the filled skutterudites ($R_xCo_{4-y}Fe_ySb_{12}$, where R= La,Ce,Yb or Tl , x=0.22, 0.8, 1, y=0, 1) and two new promising thermoelectric compounds Tl_2SnTe_5 and Tl_2GeTe_5.[9] The filled skutterudites have been studied extensively for the past few years and exhibit excellent thermoelectric properties at elevated temperatures.[10-15] In this structure, the "rattling" of the R atom in an oversized atomic cage is believed to be responsible for its low thermal conductivity. This is illustrated in Figure 1, which shows the large reduction in thermal conductivity that results as Tl is added to Co_4Sb_{12}. In the compound shown ,$Tl_{0.22}Co_4Sb_{12}$, Tl fills 22% of the available cages in the structure. Tl_2SnTe_5 and Tl_2GeTe_5

Mat. Res. Soc. Symp. Proc. Vol. 545 © 1999 Materials Research Society

exhibit a more complicated crystal structure, relative to the cubic filled skutterudites, but have the common features of weakly bound Tl atoms that reside at the center of a distorted, oversized

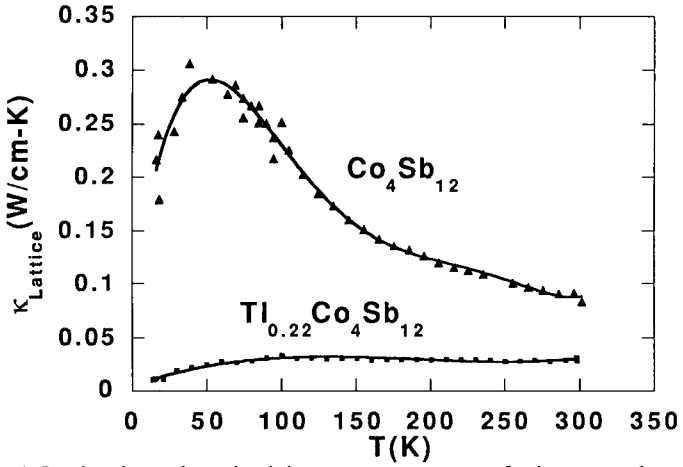

Fig. 1 Lattice thermal conductivity versus temperature for hot-pressed ceramics of Co_4Sb_{12} and $Tl_{0.22}Co_4Sb_{12}$ .The Wiedemann-Franz law has been used to estimate and subtract the electronic portion of the thermal conductivity. The lines through the data are guides to the eye.

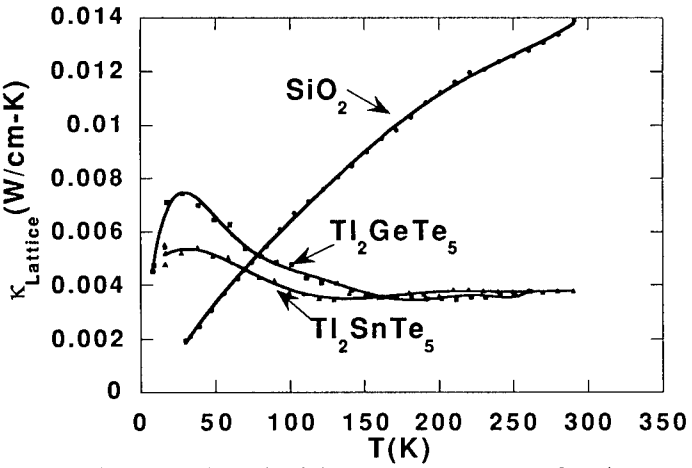

Fig. 2 Lattice thermal conductivity versus temperature for vitreous silica, Tl_2SnTe_5 and Tl_2GeTe_5. The Wiedemann-Franz law has been used to estimate and subtract the electronic portion of the thermal conductivity. The lines through the data are guides to the eye.

cubic site. As can be seen from Figure 2, this results in a remarkably low thermal conductivity, much lower at room temperature than that of vitreous silica. Synthesis of the compounds is similar to that described in Ref. 14, as are the details of the thermal conductivity measurements.

The ADP values were determined by powder neutron diffraction using ORNL's High Flux Isotope Reactor, and a neutron powder diffractometer equipped with a closed cycle liquid helium refrigerator. For each sample the powder pattern was collected at several selected temperatures and refined using GSAS (General Structure Analysis System) software developed by Larson and von Dreele at the Los Alamos National Laboratory. As an additional check of the refinement methods, ADP values were also determined on single crystals of the filled skutterudites using a four-circle neutron diffractometer. Details of the refinement methods are described in Ref. 16. All of the ADP data have been converted to an isotropic, U_{iso}, value that has the dimensions of $Å^2$. U_{iso} measures the mean square displacement amplitude of the atom averaged over all directions.

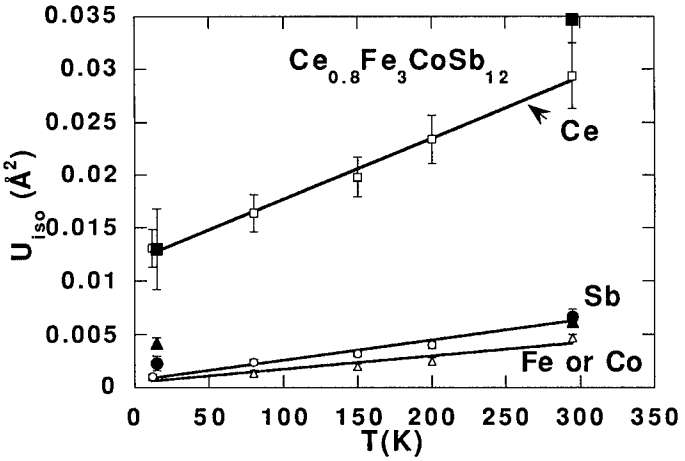

Fig. 3 Atomic displacement parameters versus temperature for $Ce_{0.8}Fe_3CoSb_{12}$ powder (open symbols) and a single crystal (filled symbols). The lines represent least squares fits to the data.

RESULTS AND DISCUSSION

Figure 3 shows the ADP values versus temperature for $Ce_{0.8}Fe_3CoSb_{12}$ powder and a single crystal with the same composition. Within the error bars of the refinement, both the powder and the single crystal data yield the same ADP values. The ADP data for the Ce can be roughly divided into two parts[1,4]. The large ADP value at low temperatures is indicative of static disorder of the Ce caused by a random distribution of iron on the cobalt site and the incomplete filling of the Ce site. The temperature dependent portion of the ADP can be attributed to the dynamic "rattling" of the Ce about its equilibrium position. Evidence for this interpretation is given in Fig. 4 which shows the ADP values for three stochiometric filled skutterudite compounds $LaFe_4Sb_{12}$, $CeFe_4Sb_{12}$, and $YbFe_4Sb_{12}$.[17] For clarity, only the large ADP values for the rare earth atoms are shown. The low temperature ADP values for La, Ce and Yb approach zero. This indicates the absence of significant static disorder and a low value for the zero-point motion of the rare earth atoms. The ADP value for La in a small $LaFe_4Sb_{12}$ single crystal was first measured at room temperature using x-rays by Braun and Jeitschko[18],

the discoverers of the filled skutterudite structure type. Using the same definition for the isotropic U_{iso}, they reported an La ADP value of 0.016 $Å^2$ at room temperature in good agreement with values found in the present work using powder neutron diffraction. The slopes

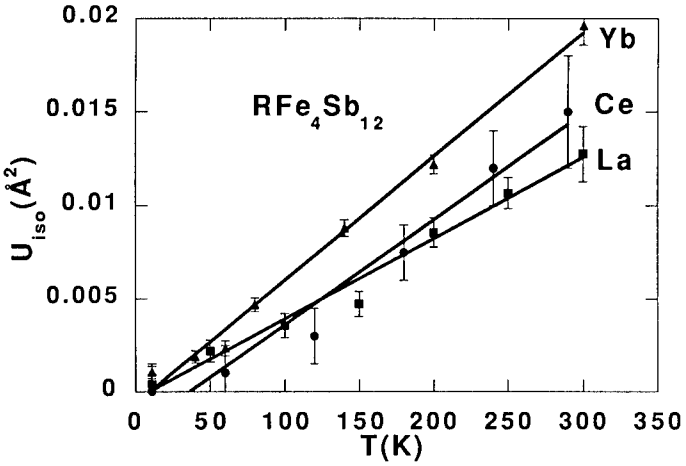

Fig. 4 Atomic displacement parameters versus temperature for $LaFe_4Sb_{12}$, $CeFe_4Sb_{12}$ and $YbFe_4Sb_{12}$ powder. For clarity only the rare earth ADP values are shown in . The lines shown are least squares fits to the data.

of the La,Ce, and Yb ADP data shown in figures 3 and 4 are all comparable with the following values : La : 4.4 $x10^{-5}$ $Å^2$/K, Ce: 5.75 x 10^{-5} $Å^2$/K, and Yb: 6.6 x 10^{-5} $Å^2$/K . Shown in Fig. 5 is the ADP data from the Tl doped skutterudite discussed in Fig 1. The small concentration of Tl in the alloy results in larger error bars for the Tl ADP values. The slope of the Tl ADP data vs temperature is 8.4 x 10^{-5} $Å^2$/K; 1.5 to 2 times as large as that measured for the rare earth atoms in the same structure. As discussed below, a larger ADP vs temperature slope for the "rattler" is indicative of weaker bonding within the cage. In figure 1, and in previous data reported in the literature[10-13], the presence of the rattling rare earth or Tl atoms severely reduces the lattice thermal conductivity of these compounds.

Tl_2SnTe_5 and Tl_2GeTe_5 crystallize in similar tetragonal structures with 32 atoms in the unit cell and are promising candidates for room temperature thermoelectric refrigeration applications.[9] The original room temperature crystallographic data[19] for these compounds reported large ADP values particularly for one of the Tl sites in each crystal structure. The combination of a large number of heavy atoms in the unit cell[6] plus unusually large ADP values at one of the Tl sites, suggest that these materials should have low lattice thermal conductivities. This is indeed the case as is shown in Fig. 2. The room temperature values of the lattice thermal conductivity (0.004 W/cm-K) are close to the minimum thermal conductivity estimated for an amorphous solid of the same average atomic weight.[20,21] The ADP data versus temperature for these two compounds are shown in Figs 6 and 7. Once again there is good agreement between the room temperature ADP values determined using powder neutron diffraction (Figs 6,7) and the ADP values determined with single crystal x-ray diffraction.[19]

Interpreting the meaning of the ADP information requires a model.[2,4] For clathrate-type compounds in which one of the atoms is poorly bonded and rattles in an oversized cage, the simplest model for the "rattler" is that of a harmonic oscillator. How far this model can be

applied to the averaged motion of an averaged atom in a crystal structure is an open question. Clearly the ADP values provide no information about correlations with the motion of other atoms (i.e. lattice dynamics). This local approach, however appears to work quite well for the

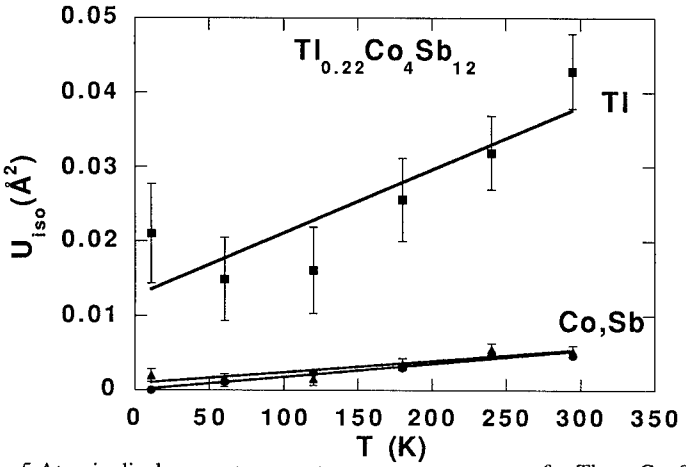

Fig. 5 Atomic displacement parameters versus temperature for $Tl_{0.22}Co_4Sb_{12}$. The lines shown are a least squares fit to the data.

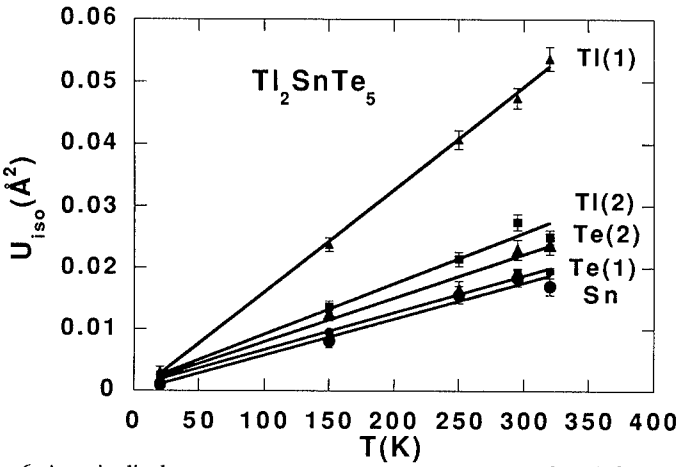

Fig. 6. Atomic displacement parameters versus temperature for Tl_2SnTe_5. The lines shown are a least squares fit to the data.

filled skutterudites, as discussed below. The mean square displacement amplitude, $\langle u^2 \rangle$ of a quantized harmonic oscillator[2] is given by:

$$U_{iso} = \langle u^2 \rangle = h/(8\pi^2 m\nu) \cdot \coth(h\nu/2k_BT) \qquad (1)$$

where ν is the frequency of vibration, m is the reduced mass, and h and k_B are Planck's and Boltzmann's constants, respectively. At high temperatures, where $h\nu << 2k_BT$, Eq.(1) reduces to the classical expression:

$$U_{iso} = k_BT/K \qquad (2)$$

where K is the spring constant of the oscillator. The reduced mass can be replaced by the mass of the La, Ce, Yb or Tl atoms if it is assumed that the atoms vibrate within a rigid cage. Therefore, in the classical limit this model predicts that the slope of ADP parameter (U_{iso}) is given by k_B/K, where $K = (2\pi\nu)^2$ m. Using the data shown in Figs. 3-5, this simple model predicts characteristic temperatures of vibration, $T_{Rattle} = h\nu/k_B$ of 88 K, 77 K, 64 K and 53 K for La, Ce, Yb, and Tl , respectively. With these values, Eq. (1) predicts that the zero point motion should be of the order of 0.002 $Å^2$ and hence can be neglected relative to the measured ADP values.

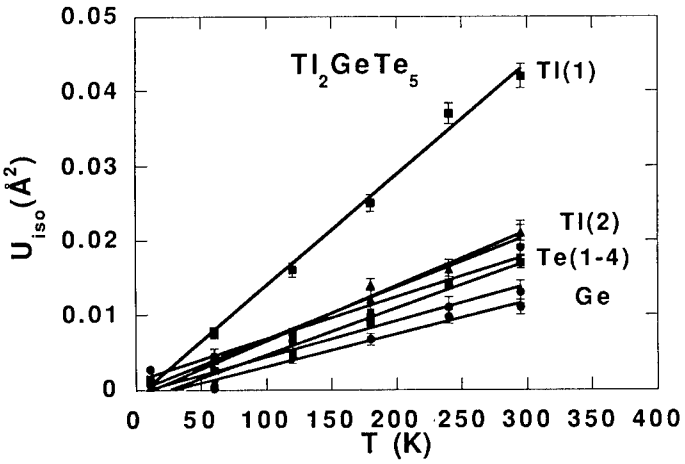

Fig. 7. Atomic displacement parameters versus temperature for Tl_2GeTe_5. The lines shown are a least squares fit to the data.

Keppens et al.[22] recently determined the local vibration temperature, T_{Rattle}, of La in the filled skutterudite structure using inelastic neutron scattering, heat capacity and elastic constant data. Two vibrational modes were attributed to the La; a localized mode with T_{Rattle}= 80 K and a somewhat hybridized La-Sb vibrational mode with a characteristic temperature of 160 K. The T_{Rattle} for the localized mode is in excellent agreement with the T_{Rattle} (88 K) determined from the ADP data. T_{Rattle} has not been measured for the Yb compound. However, heat

capacity measurements on $Tl_{0.22}Co_4Sb_{12}$ and Co_4Sb_{12} were made using a commercial instrument from Quantum Design. The heat capacity difference between these two compounds gives the contribution due to the Tl atoms. The Tl contribution is accurately described by a simple quantized harmonic oscillator (Einstein model) with a characteristic temperature of 55±2 K (Fig. 8), in excellent agreement with the value of 53 K predicted by an analysis of the ADP data in Fig 5.

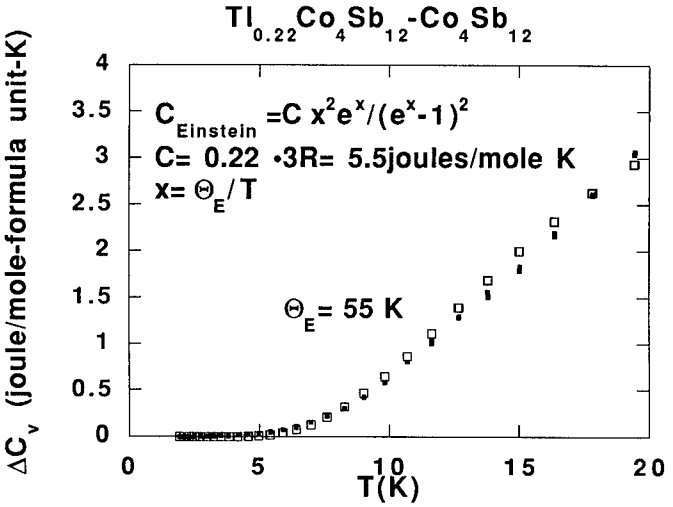

Fig. 8 Difference in heat capacity between $Tl_{0.22}Co_4Sb_{12}$ and Co_4Sb_{12}. The data is accurately described by quantized harmonic oscillator (Einstein model) with an Einstein temperature of 55 K. A small electronic heat capacity contribution was measured and subtracted from the $Tl_{0.22}Co_4Sb_{12}$ data.

For the Tl_2SnTe_5 and Tl_2GeTe_5 compounds, much less information is available and it is not clear how decoupled the Tl(1) vibrations are from the rest of the structure. If a local Tl mode exists in these compounds, T_{Rattle} = 38 K. A good place to test the validity of this simple relationship between the ADP data and local vibrational modes would be with Si and Ge clathrate compounds, such as recently reported by Nolas et al.[23,24] The large cages in these compounds should result in more localized vibrational modes for a variety of filling atoms.

Several groups[6,21,25,26] have shown that localized vibrations of atoms (or molecules) can lower the lattice thermal conductivity of a crystalline solid to values comparable to the heat conducted by a glass of the same composition. Slack[20], as well as Cahill and Pohl[21] have proposed that the thermal conductivity of a crystal cannot be less than a minimum value k_{min}. k_{min} is attained when the mean free path of the heat carrying phonons becomes the order of the phonon wavelength. It has also been shown that the "normal" ways in which the thermal conductivity of a crystal can be lowered, such as mass fluctuation scattering, are not adequate to explain the rapid decrease in the thermal conductivity of the skutterudites as "rattlers" are added to the voids[27,28]. A resonant scattering model , similar to the model proposed by Grannan et al.[29] appears to be needed to explain the rapid decrease in thermal conductivity in these clathrate-like materials. Currently no general theoretical model is available, but some simple observations can be made. Most discussions of the lattice thermal conductivity use an expression adapted from the kinetic theory of gases:

$$\kappa_{Lattice} = 1/3\ C_V\ v_S\ d \qquad (3)$$

where C_V is the heat capacity per unit volume, v_S is the velocity of sound and d is the mean free path of the phonons. The phonon mean free path is determined by the various scattering mechanisms in the crystal, such as grain boundaries, static defects, voids and "rattlers". Phonon scattering in these materials appears to be dominated by the "rattlers"[27]. If the "rattlers" are truly localized vibrations, as suggested by Keppens et al.[22], then the heat carrying phonon mean free path should depend on the distance between the "rattlers" in the crystal. At room temperature, this argument works well for the filled skutterudites such as $LaFe_4Sb_{12}$.[14] Using the measured thermal conductivity, heat capacity and an average value for the velocity of sound[14] yields a mean free path of d= 9 Å. The nearest neighbor distance of the La atoms in $LaFe_4Sb_{12}$ is 8 Å. If other scattering mechanisms can be minimized[30], this simple model would suggest that the thermal resistivity should vary as $x^{1/3}$, where x is the concentration of rattlers. This behavior is observed in $Tl_xCo_4Sb_{11-y}Sn_y$ compounds.[31]

CONCLUSIONS

ADPs can be used to identify new crystalline compounds with unusually low lattice thermal conductivities. In many clathrate-like compounds, the ADP data can also be used to estimate the Einstein frequency of the "rattler", and to predict the existence of localized vibrational modes.

ACKNOWLEDGMENTS

Research was sponsored in part by a Cooperative Research and Development Agreement with Marlow Industries and in part by the Division of Materials Sciences, U.S. Department of Energy Contract No. De-ACO5-96OR22464. Research at U.C.S.D. was supported by the U.S. Department of Energy under grant No. DE-FG03-86ER-45230 and the National Science Foundation under grant No. DMR-97-05454. Oak Ridge National Laboratory is managed by the Lockheed Martin Energy Research Corporation for the U.S. Department of Energy.

REFERENCES

1. W. F. Kuhs, Acta Cryst. **A48**,80 (1992).
2. J.D. Dunitz, V. Schomaker, and K. N. Trueblood, J. Phys. Chem. **92**, 856 (1988).
3. C. Kittel, *Introduction to Solid State Physics, Third Edition* (John Wiley and Sons, New York 1968), pp. 69-70.
4. B. T. M. Willis and A. W. Pryor, *Thermal Vibrations in Crystallography* (Cambridge University Press, London 1975)
5. G. D. Mahan, B. C. Sales and J. W. Sharp, *Physics Today*, **50**, No. 3, 42 (1997).
6. G. A. Slack in *CRC Handbook of Thermoelectrics,* edited by D. M. Rowe (Chemical Rubber, Boca Ratan, FL, 1997) pp. 407-440.
7. H. J. Goldsmid, *Electronic Refrigeration* (Pion Limited, London 1986).
8. B. C. Sales, *MRS Bulletin* **23** , 15 (1998).
9. J. W. Sharp, B. C. Sales, B. C. Chakoumakos and D. Mandrus, to appear in *Appl. Phys. Lett.*
10. D. T. Morelli and G. P. Meisner, J. Appl. Phys. **77**, 3777 (1995).
11. B. C. Sales, D. Mandrus, and R. K. Williams, Science **272**, 1325 (1996).
12. J. -P. Fleurial, A. Borshchevsky, T. Caillat, D. T. Morelli, and G. P. Meisner, in *Proceedings of the Fifteenth Conference on Thermoelectrics, Pasadena CA* (IEEE Piscataway, NJ, 1996) p. 91.
13. G. S. Nolas, G. A. Slack, D. T. Morelli, T. M. Tritt, A. C. Ehrlich, J. Appl. Phys. **79**, 4002 (1996).

14. B. C. Sales, D. Mandrus, B. C. Chakoumakos, V. Keppens and J. R. Thompson, Phys. Rev. B. **56**, 15081.
15. B. Chen, J. X. Xu, C. Uher, D. T. Morelli, G. P. Meisner, J. P. Fleurial , T. Caillat, and A. Borshchevshy, Phys. Rev. B **55**, 1476 (1997).
16. B. C. Chakoumakos, B. C. Sales, D. Mandrus and V. Keppens, *Acta. Cryst.* in press
17. N. R. Dilley, E. J. Freeman, E. D. Bauer, and M. B. Maple, Phys. Rev. B. **58**, 6287 (1998).
18. D. J. Braun and W. Jeitschko, J. Less Common Metals **72**, 147 (1988).
19. V. Agafonov, B. Legendre, N. Rodier, J. M. Cense, E. Dichi, and G. Kra, Acta. Cryst. C**47**. 850 (1991).
20. G. A.Slack, Solid *State Physics*, *Vol. 34* edited by H. Ehrenreich, F. Seitz and D.Turnbull (Academic Press Inc. ,New York, 1979) pp. 1-73.
21. D. G. Cahill, S. K. Watson, and R. O. Pohl, Phys. Rev. B **46**, 6131 (1992).
22. V. Keppens, D. Mandrus, B. C. Sales, B. C. Chakoumakos, P. Dai, R. Coldea, M. B. Maple, D. A. Gajewski, E. J. Freeman, and S. Bennington, Nature **395** , (1998).
23. G. S. Nolas, J. L. Cohn, G. A. Slack, and S. B. Schujman, Appl. Phys. Lett. **73**, 178 (1998).
24. B. Eisenmann, H. Schafer, and R. Zagler J. Less. Common Metals **118**, 43 (1986).
25. M. Zakrzewski and M. A. White, Phys. Rev. B **45** 2809 (1992),
26. D. Michalski and M. A. White, J. Chem. Phys. **106**, 6202 (1997).
27. G. S. Nolas, J. L. Cohn, G. A. Slack, Phys. Rev. B. **58** , 164 (1998).
28. D. T. Morelli, G. P. Meisner, B. Chen, S. Hu, and Citrad Uher, Phys. Rev. B. **56**, 7376 (1997).
29. E. R. Grannan, M. Randeria and J. P. Sethna, Phys. Rev. Lett. **60**, 1402 (1988).
30. G. P. Meisner, D. T. Morelli, S. Hu, J. Jong, and C. Uher, Phys. Rev. Lett. **80**, 3551 (1998).
31. B. C. Sales, unpublished data.

ELECTRONIC STRUCTURE OF COMPLEX BISMUTH CHALCOGENIDES AND OTHER NARROW-GAP THERMOELECTRIC MATERIALS

S. D. Mahanti*, P. Larson*, Duck-Young Chung**, S. Sportouch**, and M. G. Kanatzidis**
*Department of Physics and Astronomy, ** Department of Chemistry, and Center for Fundamental Materials Research, Michigan State University, East Lansing, MI 48824,

ABSTRACT

There is considerable current effort to discover new thermoelectric materials with a high figure of merit Z. Some of these new materials are narrow-gap semiconductors with rather complex crystal structures. In this paper we discuss the results of electronic structure calculations in two classes of such systems. The first class consists of $BaBiTe_3$, a structural and chemical derivative of the well-studied Bi_2Te_3. Similarities and differences in the band structures of these two systems are discussed. The second class consists of half-Heusler or "stuffed"-NaCl compounds MNiX, where M is Y, La, Lu, Yb, and X is a pnictogen; As, Sb, Bi. To understand the physical reason behind the energy gap formation, we compare the electronic structure of YNiSb with that of an isoelectronic system ZrNiSn, another isostructural compound of thermoelectric interest. These calculations were carried out within density functional theory (in generalized gradient approximation) using self-consistent full-potential LAPW method. Energy gaps and effective masses associated with the conduction band minimum and valence band maximum have been calculated and these quantities have been used to estimate transport properties. Large room temperature thermopower values in Bi_2Te_3 and BaB_iTe_3 can be understood in terms of multiple conduction and valence band extrema whereas similar large values in ZrNiSn and other half-Heusler compounds can be ascribed to large electron and hole effective mass.

INTRODUCTION

Binary semiconducting systems based on Bi_2Te_3-based alloys, PbTe-based alloys, and SiGe alloys, with properly optimized carrier concentrations via n-type or p-type doping, are the best thermoelectrics currently available.[1] They have the highest figure of merit (Z) values at their optimum operation temperatures. *Ternary* compounds with complex crystal structures are being synthesized with a view to discover new thermoelectric materials with higher Z values. Since transport properties of these systems depend sensitively on the multiplicity of band extrema, band structure parameters such as the band gap and effective masses associated with conduction and valence band extrema, a careful study of the electronic structure of these systems has become important. Furthermore, electronic structure calculations based on density functional theory and self-consistent methods such as FLAPW (full linearized augmented plane wave method)[2] and potential (linearized muffin tin orbitals-atomic sphere approximation)[3] have been quite successful in giving quantitative information about these band structure parameters in solids where the electron-electron interactions are not very strong (such as in Mott insulators).

In this paper we discuss the electronic structures of two classes of ternary systems of potential thermoelectric interest. The first one is $BaBiTe_3$, a ternary compound which can be

Mat. Res. Soc. Symp. Proc. Vol. 545 © 1999 Materials Research Society

perceived as a structural and chemical derivative of Bi_2Te_3. This compound was first synthesized by Kanatzidis and collaborators and showed promising thermoelectric features.[4] An important property of this material is that it has one of the lowest κ_{latt} (lattice thermal conductivity) values known for chalcogenides and for thermoelectric materials. This is significant because Z is inversely proportional to κ_{latt} which dominates the thermal conductivity in semiconductors.[5] The second class consists of half-Heusler compounds MNiPn, where M is a trivalent ion (Y, La, Lu, Yb) and Pn is a pnictogen (As, Sb, Bi).[6,7] We have also investigated the electronic structure of ZrNiSn which is isostructural and isoelectronic to YNiSb, a compound of considerable recent interest[8,9] for its large thermoelectric power factor ($S^2\sigma$) where S is the thermoelectric coefficient (Seebeck coefficient) and σ is the electrical conductivity.

CRYSTAL STRUCTURE

$BaBiTe_3$

$BaBiTe_3$ crystallizes in the orthorhombic space group $P2_12_12_1$ (no.19) with a = 4.6077A°, b = 17.0437A°, c = 18.2997A°. The crystal structure is given in Fig.1. The unit cell contains 40 atoms (8 formula units).[4] Note that although the unit cell contains 40 atoms, there are only 10 inequivalent atoms. These are denoted as Ba1, Ba2, Bi1, Bi2, Te1, Te2, Te3, Te4, Te5, and Te6 respectively in Fig.1. The structure of $BaBiTe_3$ is layered with $[BiTe_3]$ slabs sandwiching Ba ions in pseudo-trigonal prismatic sites. As was pointed out by Chung et. al.[4], looking down the a-axis (defined as the x direction), one can see $[Bi_4Te_{10}]_n$ "rods" and $[Te_2]_n$ chains linked via Te5 - Te6 interactions.[4] Like $BaBiTe_3$, Bi_2Te_3 is also known to have a quasi two-dimensional structure. Although it can be described as a rhombohedral system (space group R3m)[10], it is easier to visualize its structure as a hexagonal cell which is formed by stacking of layers, perpendicular to the c-axis, of like atoms following the sequence Te1-Bi-Te2-Bi-Te1.[11] Thus there are similarities

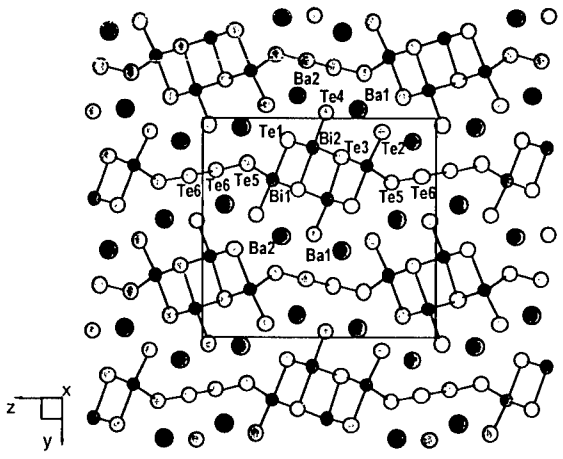

Figure 1. The layered $BaBiTe_3$ structure viewed down the a-axis (x-axis). Inequivalent atoms have been identified with numbers such as Ba1, Ba2 etc.

and yet important differences in the local bonding characteristics of Bi_2Te_3 and $BaBiTe_3$. Investigating the implications of these differences on their band structure is one of our major interests.

MNiPn Compounds

MNiPn compounds formed with light rare earth elements (M) crystallize with a hexagonal ZrBeSi structure (Space group: P 6_3/mmc) whereas those with Ytrium and heavy rare earths crystallize in the cubic MgAgAs structure (Space group: F 43m). In this paper we deal with a few representative members of the latter system. In Table I, we give the experimental values of the lattice constants used in the present study for several compounds. The non-centrosymmetric crystal structure of MNiPn(M =Y and Pn = Sb)

Table 1. Lattice constants and band gap

System	Lattice Constant a (a.u.)	Band Gap (eV)*
YNiSb	11.928	0.28
LuNiSb	11.752	0.19
YNiAs	11.662	0.53
YNiBi	12.115	0.13
ZrNiSn	11.727	0.50

* Band gaps have been calculated within density functional theory (DFT)[12] using Full potential-LAPW method[2] and generalized gradient approximation[13]

is shown in Fig.2. This system can be viewed as a rock-salt structure arrangement of M and Pn atoms with Ni atoms occupying the center of cubes formed by four M and four Pn atoms. There are two such cube-center positions which the Ni atoms can occupy, but in the MNiPn compounds

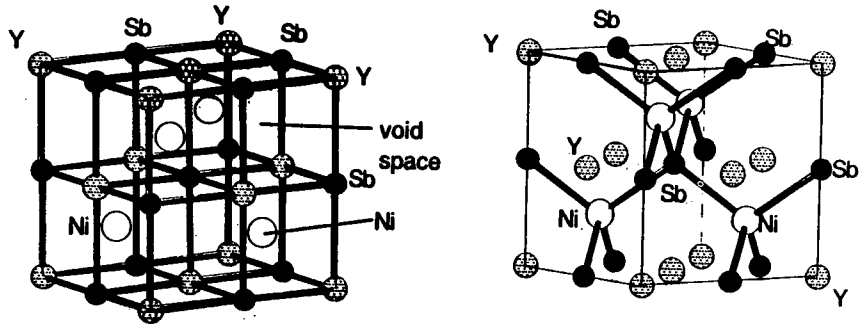

Figure 2. Two different perspectives of the cubic structure of YNiSb. Left: Ni atoms inserted in a YSb NaCl-type lattice. Right: Y atoms inserted in a ZnS-type NiSb lattice.

only one of the cube-center positions is occupied by the Ni atoms. The Ni atoms form a fcc lattice. An alternate description of MNiPn is as a ZnS zinc-blend type lattice formed out of NiPn in which the M atoms occupy octahedral holes in a diamond lattice. As can be seen in the figure, each Ni atom bonds with four M and four Pn nearest neighbor atoms.

METHOD OF ELECTRONIC STRUCTURE CALCULATIONS

Electronic structure calculations were carried out using the self-consistent full-potential linearized augmented plane-wave (LAPW) method[2] within density functional theory (DFT)[12] using the generalized gradient approximation (GGA) of Perdew, Burke, and Ernzerhof[13] for the exchange and correlation potential. The calculations were performed using the WIEN97 package.[14] The values of atomic radii were taken from Pauling's table.[15] They are 2.18 a.u. for Ni and are 2.36 a.u.. for As, Sb, and Bi, with the atomic radii of the rare earths kept constant at 2.46 a.u., close to the value for Y. Adjustment of these radii within a reasonable range showed little dependence of the final band structure on these variations. Convergence of the self-consistent iterations was performed with 22 **k**-points in the reduced Brillouin zone to within 0.0001 Ry with a cutoff between valence and core states of -6.0 Ry.

Scalar relativistic corrections were added for all the systems studied. Spin-orbit (SO) interaction was included using a second variational procedure.[16] SO interaction is very important for systems containing Bi, Te, and rare earth atoms (for f-electrons). All the results reported in this paper include SO interaction. In some cases we give the results without this interaction to emphasize the significance of SO effects.

RESULTS

A. $BaBiTe_3$ and comparison with Bi_2Te_3

Before giving the results of LAPW calculations, let us briefly review some of the earlier calculations in $BaBiTe_3$ done in extended Huckel approximation (EHA) and local density approximation (LDA).[4] The LDA calculations were carried out using LMTO-ASA method[3] and did not include spin-orbit interaction. The EHA calculation also did not include the Ba^{+2} ions and assumed the system to be two-dimensional, i.e. no coupling between $[Bi_4Te_{12}]_n$-layers along the

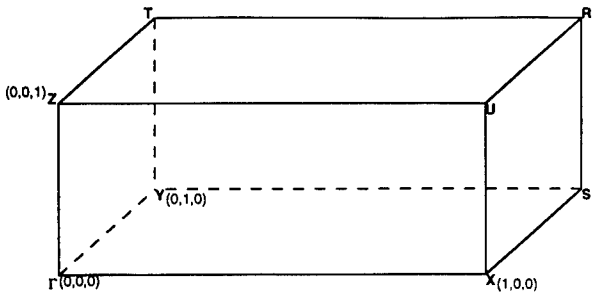

Figure 3 The Brillouin Zone for $BaBiTe_3$

y-direction was included (see Figure 1). The EHA calculation gave several interesting results: (i) the system was metallic (ii) the active bands near the Fermi energy were antibonding $2\sigma^*$ Te5-Te6 states and lone pair Bi orbitals. In contrast, the LDA band structure calculation, which treated the system as three-dimensional, showed that $BaBiTe_3$ was an indirect gap semiconductor with the valence band maximum at the Γ point and the conduction band minimum at the Z point; see Figure 3 for the Brillouin Zone. The band gap was found to be about 0.3 eV, consistent with experiment[4]. Furthermore, the largest dispersion in the highest valence band (HVB) and the lowest conduction band (LCB) were along ΓZ and ΓX directions of the Brillouin zone justifying the quasi two-dimensional character of this compound. However, the angular characters of the HVB and LCB were not analyzed to test the point (ii) above.

The results of our GGA calculation *without* SO interaction is given in Figure 4 and it can be directly compared to the LDA results *without* SO We also find the conduction band minimum to be at the Z point and the valence band maximum to be at the Γ point, but the energy gap is 0.45 eV, about 1.5 times larger than the LDA value. This is consistent with the observation that LDA usually underestimates the gap in semiconductors.[17]

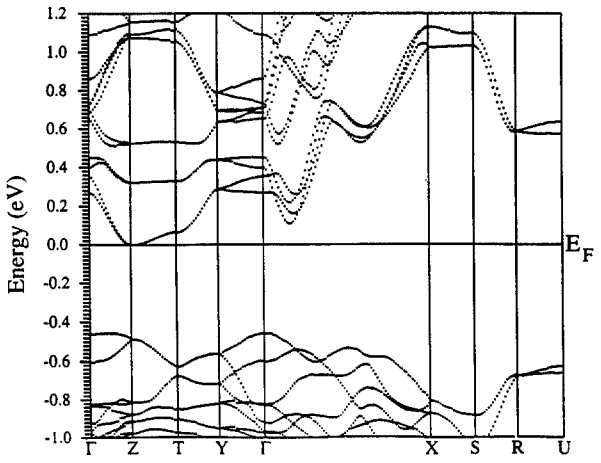

Figure 4 Band structure of $BaBiTe_3$ along symmetry directions (without spin-orbit interaction)

Since it is known that in Bi and Te systems (for example in Bi_2Te_3)[18,19], inclusion of SO interaction dramatically alters the band structure near the Fermi energy and usually reduces the band gap, we suspect that the above value of 0.45 eV is an overestimate. In Fig. 5, we give the band structures both without and with SO interaction over a smaller energy range. Since the conduction band energies are quite high along Γ-X- S-R-U (see Figure 4), we give the band structure for half the ΓX distance (denoted as ΓΔ in Fig. 5). As can be seen, SO interaction dramatically alters the band structure near the gap region. The conduction band minimum shifts away from the symmetry point Z and the valence band maximum appears to shift away from the Γ point to a general point along the ΓZ direction, although it is extremely flat along that

direction. The gap becomes direct and is about 0.22 eV. The direct gap at the Γ point is 0.48 eV. Infrared measurements by Chung et.al.[4] gave two gaps, one at 0.28 eV (weak absorption) and the other at 0.42 (strong absorption). Our theoretical results are consistent with this observation, but a careful calculation of the optical matrix elements has to be done to pin this down.

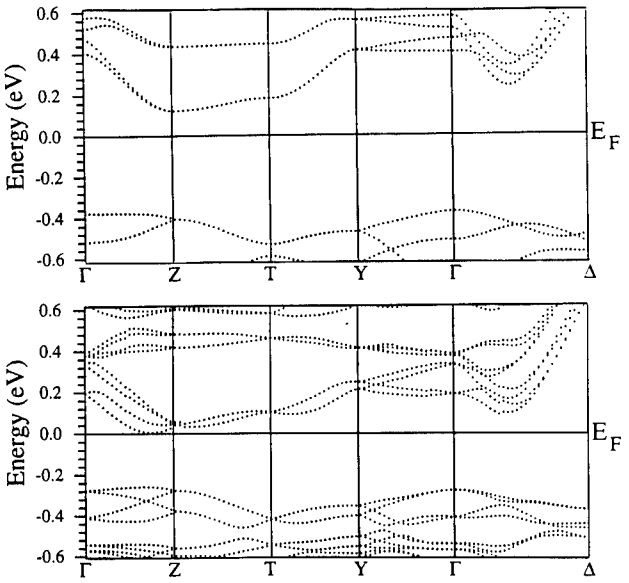

Figure 5 Band structure of $BaBiTe_3$ with (bottom figure) and without (top figure) spin-orbit interaction

In order to see which atomic orbitals contribute dominantly to the HVB and LCB, we have carried out a detailed analysis of the angular characters and atomic parentages of these bands. We find the LCB is predominantly a mixture of Bi1 p,Te5 p, and Te6 p orbitals. (See Figure 1 to identify the different types of atoms). This is consistent with the conjecture of Chung et. al.[4] who suggested that the LCB might be a $2\sigma^*$ Te5-Te6 state. The present calculation however gives a strong Bi1 p admixture. The HVB consists of Te1, Te2 and Te4 p characters and a very tiny amount of Bi2 p. There is hardly any contribution from Bi1 and the other three Te atoms. It is therefore clear that the origin of the gap formation in this system with complex crystal structure is quite subtle. We can say with certainty is that Ba is in 2^+ state and Bi is predominantly in a 3^+ state.

It is worthwhile comparing the band structures and bonding characteristics of Bi_2Te_3 and $BaBiTe_3$. The former is also known to be an indirect narrow gap semiconductor. The LDA calculations within SO interaction showed that neither the valence band maxima nor the conduction band minima were at the symmetry point and the indirect band gap was 0.11 eV.[18] In contrast, in Bi_2Se_3 the valence band maxima and the conduction band minima were at the Γ point both with and without SO interaction (i.e. a direct gap).[18] We have also calculated the electronic

structures for both Bi_2Te_3 and Bi_2Se_3 using GGA. We find the gap in Bi_2Te_3 to be indirect and 0.14 eV, again larger than the LDA value. Our calculated energy gap compares favorably with the experimental value which is about 0.13-0.15 eV. [20] In Bi_2Se_3, we also find a direct band gap at the Γ point without SO interaction, and this is still true when SO interaction is included. One might suspect that relativistic effects associated with the Bi p orbitals are responsible for the indirect gap formation in Bi_2Te_3, but comparison with Bi_2Se_3 results suggests that it is the Te p orbital and its mixing with Bi p which are responsible for the formation of indirect band gap in Bi_2Te_3. It turns out that in this compound which has one type of Bi and two types of Te, namely Te1 and Te2, the HVB is predominantly Te1, whereas the conduction band is a strongly hybridized Bi p- and Te1 p- bands. In this regard Bi_2Te_3 and $BaBiTe_3$ are quite similar.

The effective masses were calculated near the valence band maximum and the conduction band minimum. In $BaBiTe_3$ we find that the effective masses (expressed in units of free electron mass) associated the conduction band minimum are 0.08 (along x), 0.09 (along z), and 0.36 (along y), again confirming the quasi two-dimensionality of the system. However, the corresponding masses associated with the valence band maximum show a different feature: they are 0.13 (along x), 0.35 (along z), and 0.18 (along y). The high effective mass along the z axis is due to a relatively flat valence band along the ΓZ direction (see Fig.5), a consequence of hybridization and relativistic effects. A direct measurement of these effective masses will test the accuracy of the currently available state of the art first-principle DFT calculations. We have also made preliminary calculations of the effective masses for Bi_2Te_3. For the conduction band minimum we find the effective masses along three orthogonal directions as 0.14, 0.15, 0.34 (geometrical mean 0.20 compared to experimental value 0.32[20]). Those associated with the valence band maxima are respectively 0.33, 0.05, 0.18. Thus the effective masses in both these systems are rather low. The large room temperature thermopower values seen in both n- and p-doped Bi_2Te_3 are most likely due to the degeneracies of the conduction and valence band extrema. Similar reasoning should also apply to $BaBiTe_3$. In contrast, we will argue that in half-Heusler ternaries (discussed below), large effective masses rather than multiple degeneracy of the band extrema give rise to large thermopower at room temperature.

B. MNiPn

Before discussing the band structures of systems containing Ni, let us first look at the band structures of MSb (M = Y, Lu) which have the NaCl structure and then see how the insertion of Ni atoms alters this band structure. In Figure 6(a,b) we give the band structures for both these systems which we find to be metals. Our results[7] for YSb agrees qualitatively with an earlier calculation (LDA and no SO interaction) using the APW procedure by Hasegawa[21]. In YSb, the lowest three bands are weakly hybridized Sb-p and Y-d bands , although they have predominantly Sb p-character. (In LuSb, there are two additional flat f-bands below the Fermi energy.) For the sake of argument we will refer to these three bands as the 'valence' bands. Both in our and Hasegawa's calculations, an important feature is the existence of a band which lies just above these `valence' bands. In YSb for example, it starts from the Γ point (has Γ_{25}' symmetry), drops dramatically as one moves towards the X point (X_3 symmetry) and then rises along XW. A detailed analysis of the orbital character reveals that this band is primarily of Y 4d-character. Because this band comes down appreciably and falls below the top of the valence band which is at the Γ point, the system behaves like a semi-metal with pockets of holes around the Γ

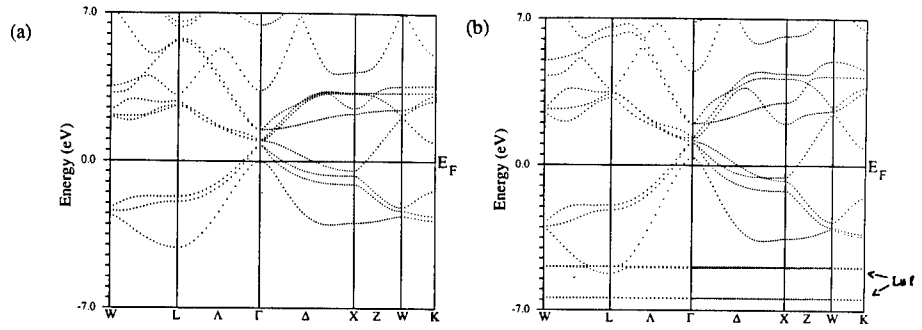

Fig. 6a,b Band structures of YSb (left) and LuSb (right)

point and pockets of electrons around the X point. In LuSb, the presence of *filled* f-levels below the Fermi energy does not change this basic semi-metallic behavior. However, there is some reordering of energy levels near the X point resulting from weak f-p and f-d hybridization.

Let us now analyze the effect of inserting Ni atoms into the MSb systems. As discussed before, MNiSb compounds have the MgAgAs-type structure with M in 4a: (0,0,0), Ni in 4d: (3/4,3/4,3/4), and Sb in 4b: (1/2,1/2,1/2) Wycoff positions, see Figure 2. The position of 4c: (1/4,1/4,1/4) is empty. The band structures for YNiSb and LuNiSb are given in Figure 7(a,b)

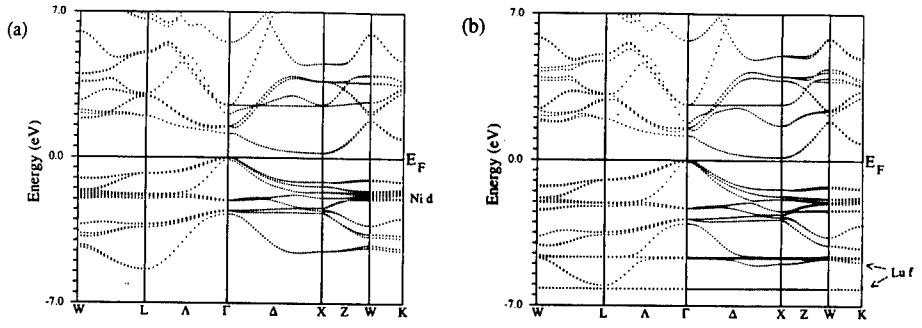

Figure 7a,b Band structures of YNiSb (left) and LuNiSb (right) along symmetry directions. The rare earth f-levels are marked Lu f

respectively. As can be seen in both the cases, most of the Ni d-bands lie below the Fermi level (about 1 to 3 ev below) and above the f-levels in the Lu compound. However the lowest conduction band along Γ-X-W has appreciable Ni d-character. The Ni 4s bands are found considerably above the Fermi level, making Ni an almost d^{10} system. In addition the Ni d-orbitals

interact strongly with the Y and Lu d-orbitals. In particular the X_3 state at the X point in YSb gets pushed sufficiently up and now lies above the valence band maximum at the Γ point. This opens up an energy gap and makes this systems an indirect narrow gap semiconductor. A similar situation also occurs in the Lu system. This gap formation was also seen in the related MNiSn systems by Ogut and Rabe[22] which contain no f electrons. Since the f-levels in the Lu system lie more than 5 eV below the Fermi level, the f-p hybridization does not significantly affect the band structure in the neighborhood of the Fermi level. Thus the origin of the gap formation in these MNiSb compounds must be due to the insertion of Ni d-orbitals, as is in the case of MNiSn.

Comparison of band structures of the isoelectronic compounds YNiSb and ZrNiSn

We now discuss the similarities and differences in the origin of the energy gap formation between ZrNiSn and YNiSb. These two systems are indeed ideal for comparison because (Zr,Y) and (Sn,Sb) are neighboring pairs in the periodic table. The band structure of ZrNiSn was

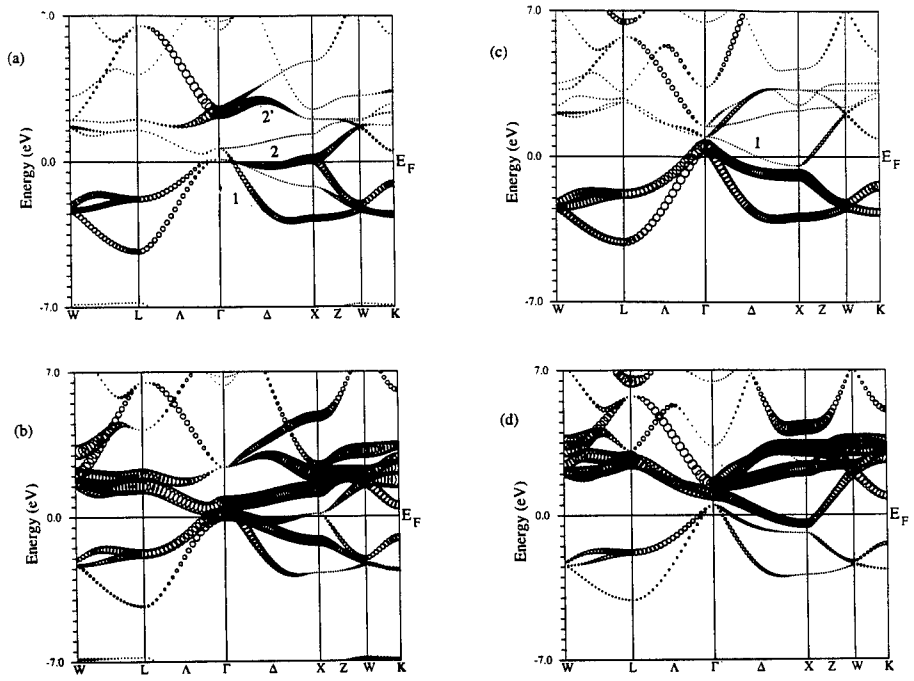

Figure 8 a,b,c,d Comparison of orbital characters and p-d hybridization between the parent compounds ZrSn (a,b) and YSb (c,d). The size of the circles indicates the strength of the particular orbital character. Fig. 8a,c give p-character of Sn and Sb and Fig. 8b,d give d-characters of Zr and Y respectively.

obtained[22] using pseudo-potential method. We have also calculated the band structure of this compound using our procedure. In particular, we are interested in exploring the importance of (i) Zr (Y) d- and Sn (Sb) p- hybridization, and (ii) the Ni d-orbitals on the electronic structure near the Fermi energy. Ogut and Rabe[22] have pointed out the important role played by p-d hybridization (along the ΓX direction) on the energy gap formation in ZrNiSn. In Fig. 8(a,b) we give the results of our FLAPW-GGA calculations for the host system ZrSn. They show the Sn p- (a) and Zr d- characters (b), the strengths of the orbital character being proportional to the size of the circles. Clearly there is evidence of strong k-dependent p-d hybridization (the bands labeled 2 and 2' in Fig.8a and the corresponding bands in Fig.8b) as pointed out by Ogut and Rabe. In contrast, in YSb (see Fig.8c,d) this p-d hybridization is very weak. Thus a strong p-d hybridization does not appear to be a prerequisite for the energy gap formation in these ternary systems. In fact as discussed below, Ni d-orbitals play a crucial role. The orbital characters of the bands in YNiSb and ZrNiSn are shown in Figure 9a,b,c,d,e,f .

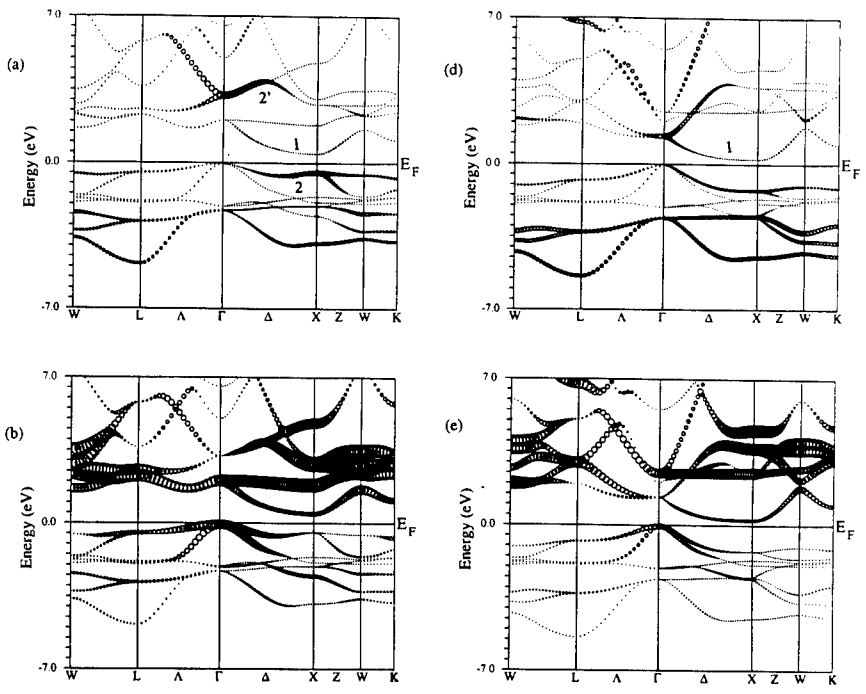

ZrNiSn YNiSb

Figure 9 a,b,d,e Comparison of different orbital characters between ZrNiSn (a,b) and YNiSb (d,e). The size of the circles gives the strength of the particular orbital character. Figure 9 a,d give p-characters of Sn and Sb, and (b,e) give d-characters of Zr and Y respectively.

In ZrNiSn, the Ni d-orbitals do two things. The hybridized Sn p-Y d band with a large dispersion (band labeled 1 in Fig.8a which starts from the Γ point at ~0.5 eV and goes to ~ -2.5 eV at the X point) in ZrSn hybridizes strongly with Ni d orbitals and becomes the lowest conduction band (along ΓX) in ZrNiSn (band labeled 1 in Fig. 9a). In addition, the strongly hybridized Sn p - Y d band (band labeled 2 in Fig.8a which starts from ~0.0 eV at Γ and goes to ~0.1 eV at X) gets slightly modified. The energy of this band at the X point drops below that at the Γ point by about ~ 0.5 eV (band labeled 2 in Fig. 9a). The net effect is the formation of an indirect energy gap semiconductor with a gap of 0.50 eV which agrees well with the previous

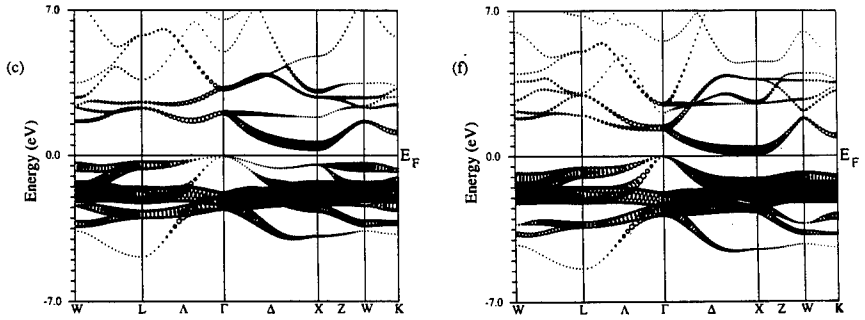

Figure 9 c,f Comparison of Ni d character between ZrNiSn (c) and YNiSb (f). The size of the circles is a measure of the strength of the angular character.

calculation.[22] The situation is completely different in YNiSb. The lowest Y d-band which has a large downward dispersion going from Γ to X (band labeled 1 in Fig. 8c) strongly hybridizes with a Ni d band and somewhat weakly with Sb p-band. This hybridization pushes the conduction band bottom at the X point above the valence band top at the Γ point (see band labeled 1 in Fig. 9d). The net result is a formation of an indirect narrow gap semiconductor, but in this case the gap is 0.28 eV, about a factor of two smaller than that in the isoelectronic compound ZrNiSn. In spite of the basic differences in the nature of bonding, the energy band structure in the neighborhood of the Fermi energy is remarkably similar in ZrNiSn and YNiSb. The LCB has strong Ni d-character along the ΓX direction in both the systems. There are, however, quantitative differences in the dispersion of the top of the valence band along the ΓX and ΓL directions between these two systems which should reflect in their effective masses and transport properties (discussed below).

Comparison of the band gaps in YNiAs, YNiSb, YNiBi

We have calculated the band gaps in YNiM (M=As, Sb, Bi) to see the effect of changing the pnictogen atom on the energy gap. Clearly, relativistic effects increase in going from As to Bi. In addition to the increase in spin orbit splitting of the various Bi p-derived bands, we find that the Pn valence s-band comes down towards the Fermi energy and in Bi compounds it

strongly perturbs the lowest conduction band (along the ΓX direction). The net effect is a decrease in the indirect band gap in going from As to Bi. The calculated band gaps are 0.53, 0.28, and 0.13 eV respectively (see Table I where the band gaps for all the systems studied in this paper are given).

Effective mass and transport properties

Recently Uher et.al.[9] have extensively investigated the transport properties of ZrNiSn and related compounds. They have estimated the average effective mass associated with the states near the bottom of the conduction band from their transport measurements, and find that it is about 2-3 times m_e, the free electron mass. They have suggested that this large effective mass was perhaps the reason behind observed large negative (electron-like) room temperature thermo pawer ($\approx$ - 200μV/K). We have calculated the effective masses associated with the conduction band minimum (at the X point) and find it to be highly anisotropic. Along the XΓ direction the effective mass is about $10m_e$, where as along the two other orthogonal directions, it is nearly m_e. Thus we expect that the average transport mass will be about $(10)^{1/3}$ m_e, which is consistent with Uher et.al.'s finding.[9] A similar situation also occurs in YNiSb in which the heavy electron mass along the XΓ direction is a factor of two larger than that in ZrNiSn. If YNiSb can be doped n-type, it should also show a large negative thermopower at room temperature. We also find that the effective hole masses in ZrNiSn are large ($\approx 1.5m_e$) which suggests that p-doped ZrNiSn should also show large positive thermopower at room temperature. In contrast, the hole effective masses in YNiSb are not as large ($\approx 0.5m_e$) and therefore p-doped YNiSb is expected to show smaller thermopower at room temperature than n-doped material. This observation is consistent with experiment.[23]

SUMMARY

We have carried out self-consistent full potential LAPW calculations within DFT using generalized gradient approximation in several ternary systems which have shown promising thermoelectric behavior. We find that $BaBiTe_3$, inspite of its complex crystal structure, has many features similar to Bi_2Te_3. The effective masses are rather small. Spin orbit interaction is extremely important and it's inclusion gives rise to conduction and valence band extrema away from the symmetry points. The resulting multiplicity of the band extrema is most likely the reason for observed[4] large room temperature thermoelectric coefficient. This, along with the fact that it has a very low lattice thermal conductivity[4], strongly argue in favor of optimizing this system to get high ZT values.

The half-Heusler compounds, on the other hand, exhibit a different characteristics. The band extrema are found to occur at the symmetry points. The origin of the indirect gap in these systems is quite subtle. In ZrNiSn, k-dependent hybridization between Zr d-band and Sn p-band plays a crucial role in the gap formation. This is not so in YNiSb, where Ni d-orbitals play a pivotal role. The lowest conduction band picks up large amount of Ni d-character and the effective masses associated with the conduction band minimum are quite large in both YNiSb and ZrNiSn. Thus these systems when n-doped should show large thermopower as seen in

ZrNiSn[9]. The valence band effective masses are large for ZrNiSn, but not so for YNiSb. Thus in the hole doped regime the former should show large thermopower values.

ACKNOWLEDGMENTS

This work was partially supported by DARPA grant #DAAG55-97-1-0184. We acknowledge C. Uher for sending a preprint of the reference 9 before publication, and for helpful discussions.

REFERENCES

1. C. B. Vining, Mat. Res. Symp. Proc. Vol **478**, 3 (1997), see Figure 4.
2. D. Singh, *Plane waves, pseudopotentials and the LAPW method*, Kluwer Academic, , 1994.
3. H. L. Skriver, *The LMTO Method,* Springer, New York, 1983.
4. D. Y. Chung, S. Jobic, T. Hogan, C. R. Kannewurf, R. Brec, J. Rouxel, and M. G. Kanatzidis, Jour. Am. Chem. Soc. **119**, 2505, (1997).
5. $Z=S^2\sigma/[\kappa_{latt}+\kappa_{el}]\approx S^2\sigma/\kappa_{latt}$, *when* $\kappa_{latt}>>\kappa_{el}$
6. I. Karla, J. Pierre, and R. V. Skolozdra, Jour. of Alloys and Compounds **265**, 42 (1998); S. K. Dhar et. al. , Phys. Rev. B **49**, 641 (1994).
7. P. Larson, S. D. Mahanti, S. Sportouch, and M. G. Kanatzidis (submitted to Physical Review)
8. H. Hohl, A. P. Ramirez, W. K. Fess, Ch. Thurner, Ch. Kloc, and E. Bucher, Mat. Res. Soc. Symp. Proceedings Vol **478**, 109 (1997).
9. C. Uher, J. Yang, S. Hu, D. T. Morelli. and G. P. Meisner (submitted to Phys. Rev. B).
10. R. W. G. Wycoff, Crystal Structure **Vol 2** (Malabar, FL: Kreiger) and reference therein; J. R. Wiese and L. Muldawer, J. Phys. Chem. Solids **15**, 13 (1960).
11. H. Scherrer and S. Scherrer, CRC Handbook of Thermoelectrics, edited by D. M. Rowe , CRC Press (1995). pp 211
12. P. Hohenberg and W. Kohn, Phys. Rev. **136**, B864 (1964); W. Kohn and L. Sham, Phys. Rev. **140**, A1133 (1965).
13. J. P. Perdew, Burke, and Ernzerhof, Phys. Rev. Letters **77**, 3865 (1996).
14. P. Blaha, K. Schwarz, and J. Luitz, WIEN97, Vienna University of Technology 1997.
15. L. Pauling, J. Am. Chem. Soc. , **69**, 542 (1947).
16. D. D. Koelling and B. Harmon, J. Physics C: Sol. St. Phys. **10**, 3107 (1977); P.Novak (1997) to be published.
17. LDA calculations are known to underestimate enrage gaps in semiconductors.
18. S. K. Mishra, S. Satpathy, and O. Jepsen, J. Phys.: Condens. Matters **9**, 461 (1997); G. A. Thomas, D. H. Rapkine, R. B. van Dover, L. F. Matheiss, W. A. Saunder, L. F. Schneemeyer, and J. V. Waszczak, Phys. Rev. B **46**, 1553 (1992).
19. P. Larson and S. D. Mahanti (unpublished)

20. B. M. Gol'tsman, V. A. Kudinov, and I. A. Smirnov, *Semiconductor Thermoelectric Materials Based on Bi_2Te_3 (Moscow: Nauka) (in Russian)* ; S. A. Aliev, Sh. S. Ismailov, and I. G. Tagiev, Phys. Sol. State **37**, 1573 (1995).
21. A. Hasegawa, Jour. Phys. C: Solid State Physics **13**, 6147 (1980).
22. S. Ogut and K. M. Rabe, Phys. Rev. **B51**, 10443 (1995).
23. S. Sportouch, P. Larson, S. D. Mahanti, P. Brazis, C. R. Kannewurf, M. Bastea, C. Uher, M. G. Kanatzidis (this volume)

THE SYNTHESIS OF METASTABLE SKUTTERUDITES USING SUPERLATTICE REACTANTS

HEIKE SELLINSCHEGG*, JOSHUA R. WILLIAMS*, JULIE CASPERSON*, GEORGE NOLAS** AND DAVID C. JOHNSON*
*Materials Science Institute and Department of Chemistry, University of Oregon, Eugene, OR;
**Research and Development Division, Marlow Industries, Dallas, TX

ABSTRACT

The synthesis by controlled crystallization of elementally modulated reactants of a series of kinetically stable, crystalline skutterudites ($M'_{1-x}M_4Sb_{12}$ where M' = vacancy, RE, Hf, Al, Sn, Pb, Bi, In, Ga, Al and Y; M = Fe, Co) is discussed. Low angle diffraction data demonstrates that the elemental layers interdiffuse at temperatures below 150°C. Nucleation of the skutterudite structure occurs exothermically on annealing at temperatures near 200°C regardless of the ternary metal. The metastable ternary compounds and the new binary compound were found to decompose exothermically on higher temperature annealing. The decomposition temperature ranged from 300°C for the binary compound $FeSb_3$ to 550°C for $Eu'_{1-x}Fe_4Sb_{12}$ to higher temperatures for the filled cobalt end members. The occupation of the lattice site for the ternary cation was found to depend on the composition of the initial reactant. Samples up to a half gram in size have been synthesized and hot-pressed into pellets for measurement of both electrical properties and thermal conductivity. Preliminary evidence is presented for the formation of skutterudite superlattices, again synthesized by the controlled crystallization of elementally modulated reactants.

INTRODUCTION

Research aimed at improving thermoelectric performance presents opportunities which span several different research communities. Much of the current materials research has focused on either quantum confinement enhancement as proposed by Dresselhaus[1] or the concept of "electron crystal-phonon glass" proposed by Slack.[2] In both areas, the synthesis of the targeted materials presents considerable difficulties. In the proposal by Dresselhaus, one must prepare crystalline superlattices which maintain high electron mobilities. These non-equilibrium structures are typically prepared by molecular beam epitaxy – a difficult and expensive growth technique to apply to new materials systems. The second approach, the idea of electron crystals- phonon glasses, requires one atom or element in a crystal structure to be weakly bound in a site which is considerably larger than the radius of the respective atom. This results in low frequency vibrations associated with this atom leading to a large phonon scattering cross section. These structures present synthetic difficulties because the "rattling" atom would typically be more stable in another phase in which it is more tightly bound. In the skutterudite based structures, for example, the "rattling" atom must be a large rare earth or alkaline earth cation for the compound to be made from a conventional bulk synthesis. If skutterudites filled with lighter rare earth or other elements are attempted to be prepared using conventional synthesis approaches, mixtures of binary compounds are formed.

Mat. Res. Soc. Symp. Proc. Vol. 545 © 1999 Materials Research Society

In conventional solid state synthesis methods, there is no control of the reaction intermediates. Binary compounds form as reaction intermediates. If these are more stable than the desired compound under the reaction conditions, it is not possible to access the desired product even though it is more stable than the reactants. To circumvent this problem, one needs to control the kinetics of the reaction. We have gained control of the kinetics of solid state reactions by preparing modulated elemental reactants. A modulated elemental reactant consists of repeating alternating layers of the elements in the correct ratio to form the desired product. By controlling the layer thickness we are able to directly control the diffusion length. By reducing the diffusion length we can reduce the diffusion time to the point where interdiffusion is complete before interfacial nucleation occurs. This results in the formation of an amorphous reaction intermediate. We have found that composition of the amorphous reaction intermediate controls what crystallizes. By adjusting the composition, compounds thermodynamically unstable with respect to disproportionation can be preferentially crystallized. We will illustrate this point in this manuscript by discussing the formation of the metastable binary skutterudite $FeSb_3$ and several metastable ternary skutterudites.

The well defined starting structures of modulated elemental reactants make them ideal starting points for controlling reaction kinetics. Analysis of the low angle diffraction pattern of a modulated reactant yields the repeat layer spacing of the reactant as well as the roughness of the film. This allows quantitative comparison between reactants prepared at different times or under different deposition conditions. Low angle diffraction also permits one to follow the interdiffusion of the layers by measuring the decay of the diffraction intensities as a function of annealing time and temperature. Differential scanning calorimetry is also a useful probe, permitting the enthalpies of mixing and crystallization to be measured as well as the temperature at which the amorphous intermediate crystallizes.

Crystalline superlattices can also be prepared using elementally modulated reactants by designing an initial superlattice containing two diffusion lengths as shown in figure 1. Annealing the sample at low temperatures interdiffuses the short lengthscale layers without significant mixing of the long lengthscale composition modulation. Raising the temperature results in nucleation and the rapid growth of the crystallites prevents significant diffusion at the growth fronts. This results in the kinetic trapping of the desired superlattice structure. We will illustrate the formation of crystalline superlattices from elementally modulated reactants with an example of a skutterudite based superlattice.

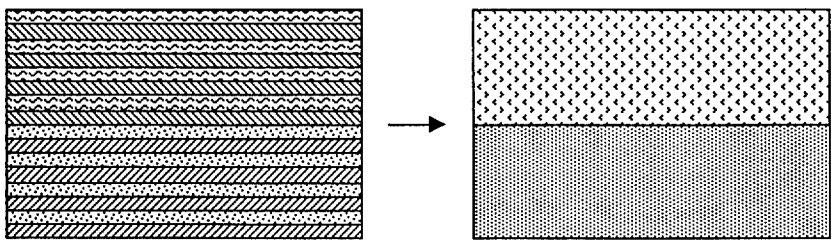

Figure 1: Schematic of the initial modulated reactant designed to yield a superlattice product and the amorphous intermediate formed after annealing but before crystallization.

EXPERIMENT

Elementally modulated reactants prepared in a high-vacuum evaporation system which has been described in detail elsewhere.[3] Briefly, the elements were sequentially deposited in high vacuum (less than. 5×10^{-7} torr) under the control of a personal computer. The gas pressure during deposition was usually limited by the outgassing of the deposition sources. The elements were deposited from electron beam evaporation sources at a rate of 0.5 Å/sec. Each source was independently monitored by a quartz crystal thickness monitor. The thickness of each elemental layer was controlled to the nearest Ångstrom. The repeat thickness (sum of the individual elemental thicknesses) for all of the samples in this study was kept below 25Å to ensure that the films interdiffused at low temperatures without nucleating binary compounds at the reacting interfaces. The elemental composition of the samples were found to be repeatable to within about 5%. The films are simultaneously deposited on silicon, off-cut quartz and photoresist-coated silicon wafers. The silicon substrates are used for low angle diffraction studies. Low angle X-ray diffraction is used to characterize the multilayer periodicity and to study the interdiffusion of the elements. The repeat thickness is determined from the position of the Bragg diffraction maxima. The total film thickness is determined from the higher frequency oscillations resulting from interference of the x-rays between the front and back of the films. The films on the off-cut quartz are annealed and used to collect diffraction data for structural refinement. Free standing films are prepared from the coated substrates by soaking them in acetone which dissolves the photoresist. The elementally modulated film particles are collected from the acetone by filtration with teflon filters. Substrate-free samples were annealed in a differential scanning calorimeter cell. Measured exotherms were correlated with X-ray results to identify and track the interdiffusion of the elements and the crystallization of any compounds.

High angle X-ray diffraction is used to identify crystalline compounds. Copper $K\alpha$ radiation is used in both the low and high angle diffraction studies which are done on a Scintag XDS 2000 θ–θ diffractometer. Samples were annealed in a nitrogen atmosphere or in a dynamic vacuum better than 10^{-5} torr The average composition of the multilayer films are determined by electron microprobe analysis using an energy dispersive X-ray detector.

RESULTS

Preparation of $CoSb_3$ and $FeSb_3$

$CoSb_3$ is one of three thermodynamically stable binary cobalt-antimony compounds at low temperatures. It decomposes peritectically at approximately 770°C.[4] It is typically made by extended annealing of the elements in a sealed ampoule at 700°C or by crystallization from a tin flux. We prepared several Co-Sb modulated elemental reactants with compositions near the 1:3 stoichiometry of $CoSb_3$. Figure 2 shows the DSC trace from a representative free standing film which shows a large exotherm at 148°C. Diffraction data collected before and after the exotherm, shown in Figure 3, shows that the sample was amorphous with respect to x-ray diffraction before the exotherm and crystalline $CoSb_3$ after the exotherm. The low temperature of the crystallization exotherm is somewhat surprising, suggesting that the skutterudite structure

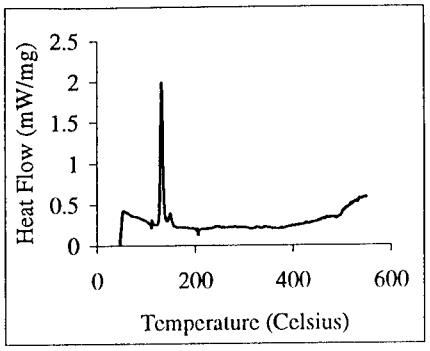

Figure 2: Differential scanning calorimetry trace from a $CoSb_3$ sample.

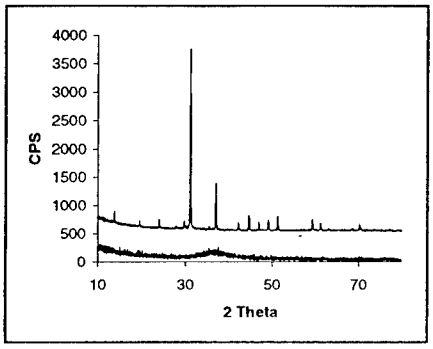

Figure 3: Diffraction data obtained on the $CoSb_3$ sample used to obtain Figure 2.

forms easily. In hindsight, it is reasonable to speculate that the structure of the amorphous precursor also contains cobalt octahedrally coordinated by antimony. If this is true, only local rotations about corner shared antimony atoms are required for crystallization to occur. This may also explain the remarkably well crystallized product obtained from the low temperature nucleation. The unit cell size obtained from the diffraction pattern is consistent with that reported previously in the literature.

Given the ease of $CoSb_3$ formation, we attempted the synthesis of many metastable skutterudites using modulated elemental reactants. One of our first targets was the unknown binary compound $FeSb_3$. The accepted iron - antimony phase diagram, shown in figure 4, contains two compounds - a defect -NiAs phase with a broad composition range labeled ε and $FeSb_2$ with a narrow stoichiometry range.[4] This phase diagram states that at equilibrium, a 1 to 3 mix of iron and antimony consists of a mixture of $FeSb_2$ and elemental antimony. In other words, the targeted binary compound $FeSb_3$ with the skutterudite structure is unstable with respect to disproportionation into a mixture of $FeSb_2$ and Sb. We prepared a series

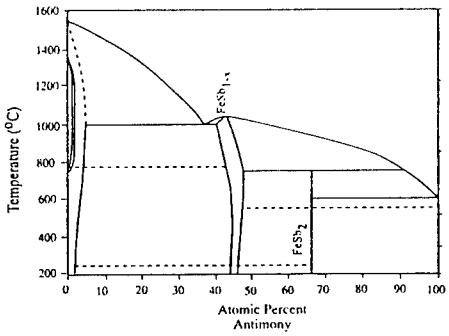

Figure 4: A schematic of the Fe-Sb phase diagram.

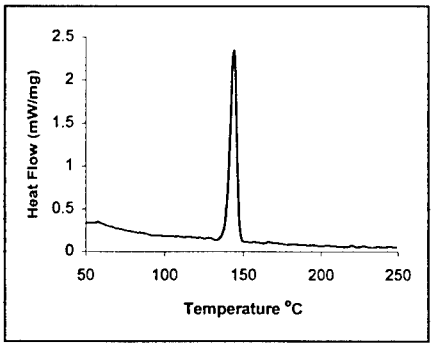

Figure 5: Differential scanning calorimetry trace from a $FeSb_3$ sample.

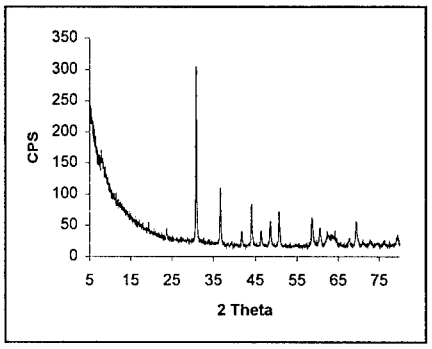

Figure 6: Diffraction data obtained on the $FeSb_3$ sample used to obtain Figure 5.

of binary elementally modulated reactants with compositions near one part iron to three parts antimony was prepared with modulation thickness less than 25Å to attempt the synthesis of $FeSb_3$. Figure 5 contains the DSC trace from a representative free standing film which shows an irreversible exotherm on heating at 145°C. Diffraction data collected after the initial exotherm (Figure 6) showed the quantitative formation of the desired skutterudite compound.

A more detailed investigation of the evolution of the modulated reactant to the desired skutterudite shows that the most stable binary compound, $FeSb_2$, does not form on low temperature annealing. The low angle diffraction pattern of the binary samples on deposition shows diffraction maxima resulting from front surface - back surface interference of the Cu-Kα x-rays used as well as a first order Bragg diffraction maxima from the repeating unit of the multilayer. After annealing at 100°C, the intensity of the Bragg diffraction maxima is significantly reduced as a result of interdiffusion of the deposited layers. Annealing the film has also made it smoother; the front surface - back surface interference pattern continues out to significantly higher diffraction angles. High angle diffraction studies indicate that the film is still amorphous after this 100°C anneal. The compound $FeSb_3$ nucleates soon after the elements interdiffuse, which supports our observation from the Co-Sb studies that this structure nucleates easily from an amorphous mixture of the elements. Annealing a film at higher temperatures, 250°C for 7 hours, resulted in a film suitable for Rietveld structural refinement. The resulting structural parameters are summarized in Table 1. The structure of this new binary skutterudite is very similar to that previously determined for $CoSb_3$.[5, 6] Annealing the sample beyond the second exotherm observed in the DSC results in the formation of a mixture of $FeSb_2$ and Sb expected from the equilibrium phase diagram.

These diffraction results support our proposed reaction pathway summarized in Figure 8. We believe that the initially modulated elemental reactant interdiffuses at low temperatures to form an amorphous intermixed reaction intermediate. Further heating results in the nucleation and growth of the binary skutterudite. The activation energy for the process, determined using a Kissinger analysis of DSC data, is 2 eV per nucleation event. The iron antimony skutterudite formed is kinetically stable below 360°C. Heating above this temperature exothermically decomposes the compound.

Table 1

Positional and Thermal Parameters for $FeSb_3$. Unit cell size is a=9.1762(3)Å R_{wp} = 9.3, R_p=7.1
Deviations given in parentheses for refined parameters.

Im$\bar{3}$	Fe 9(c)	Sb 24(g)
x	1/4	0
y	1/4	0.3400(2)
z	1/4	0.1618(2)
B	0.21(17)	0.95(7)

Preparation of bulk samples of $Lu_yFe_4Sb_{12}$

Literature reports of the synthesis of ternary iron antimony skutterudites via conventional synthesis approaches have been limited to ternary compounds containing large cations from the lower left hand corner of the periodic table such as barium, lanthanum, cerium, praseodymium, neodymium, samarium and europium.[5, 6] In 1997, we reported the synthesis and preparation of ternary iron antimony skutterudites containing all of the rare earth atoms from lanthanum to lutetium using modulated elemental reactants.[7] In early 1998, we reported the synthesis of ternary iron antimonide skutterudites containing post-transition metals as the ternary atom.[8] These ternary compounds we prepared by depositing a number of modulated reactants with compositions in a range around the desired stoichiometries of the ternary skutterudites. DSC data was used to determine crystallization and decomposition temperatures. For the heavier rare earth containing skutterudites, crystallization occurred near 200°C while decomposition occurred between 450 and 500°C depending on the size and occupancy of the ternary cation.

For the synthetic and mechanistic studies described above, small samples of several mg were sufficient for characterization of the intermediates and final products. While the geometry of the films produced is also ideal for measurement of the electrical conductivity and Seebeck coefficient, it is difficult to measure thermal conductivity on thin films. Techniques to

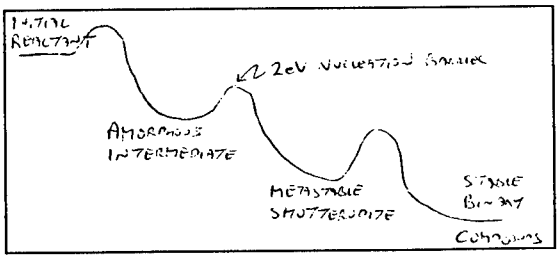

Figure 7: Energy diagram showing enthalpy changes of an iron-antimony sample during heating from room temperature.

measure thermal conductivity on thin film samples have been developed, however bulk measurement of bar samples is the most accepted measurement technique and would more closely approximate the morphology of any initial commercial application of these materials. The key to the preparation of larger samples is increasing the area of the substrate. We modified our sample stage to permit the use of a 20cm by 12cm float glass substrate. This substrate is moved directly above each source in a normal geometry. Because the geometry is the same for each source, the composition thus remains uniform across the substrate even though the layer thickness changes across the substrate. If we keep the repeat thickness in the center of the substrate below that required for the samples to interdiffuse without crystallization, the rest of the sample on the substrate also has repeat layer thicknesses less than this critical value. The entire substrate can then be immersed in a suitable solvent to dissolve the photoresist, removing the modulated elemental precursor from the substrate. The precursor is collected on a teflon filter. On annealing the entire sample interdiffuses and subsequently nucleates the desired ternary skutterudite.

Figure 8 shows the DSC data for a bulk sample of $Lu_xCo_4Sb_{12}$ prepared using the techniques described above. A sharp low temperature exotherm is observed at a similar temperature to that observed for the crystallization of rare earth containing iron-antimony skutterudites. The diffraction data for this sample, shown in figure 9, confirms that the cubic skutterudite structure forms. Scanning electron microscopy data confirms the uniform distribution of lutetium in the sample and Reitveld analysis of the diffraction data requires substantial electron density at the lutetium site to model the data.

To prepare a bulk sample for thermal conductivity measurements, one could either hot press the precursor to form a pellet of the skutterudite or anneal the precursor to form the skutterudite and then hot press to form a pellet. Preliminary investigation of the pathway which hot presses the precursor has clearly shown that the precursor readily forms a significant oxide coating on annealing in air. The preformed skutterudite, however, is much less air sensitive and hot presses well to form a dense (greater than 90% theoretical density) pellet. Figure 10 contains the measured lattice thermal conductivity from a hot pressed lutetium skutterudite sample. The lattice thermal conductivity was obtained from the measured total thermal conductivity by subtracting the contribution from the electrons using the Wiederman-Franz relationship. The resulting thermal conductivity for the lutetium sample is significantly lower than that of the lanthanum analog. Duplicate measurements on additional samples are underway to confirm this result.

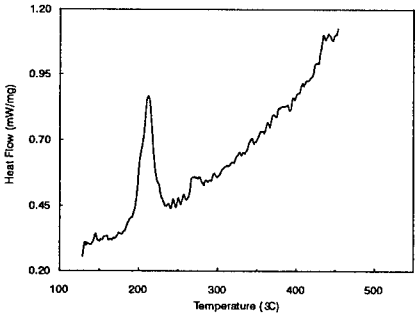

Figure 8: Differential scanning calorimetry trace from a bulk sample of $Lu_xCo_4Sb_{12}$.

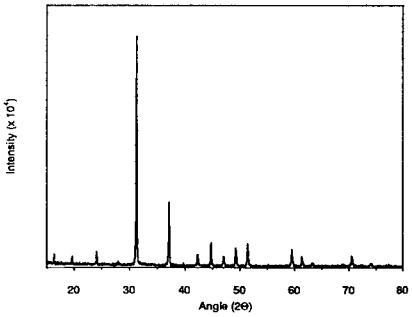

Figure 9: Diffraction data obtained on the $Lu_xCo_4Sb_{12}$ sample used in Figure 9.

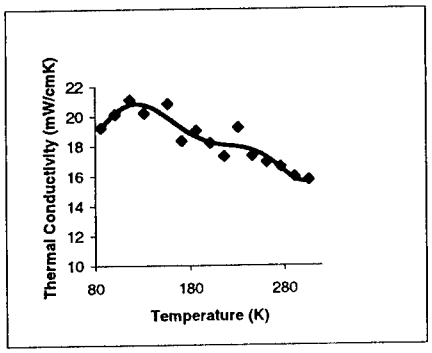

Figure 10: Lattice thermal conductivity of $Lu_xCo_4Sb_{12}$ measured on a pressed pellet.

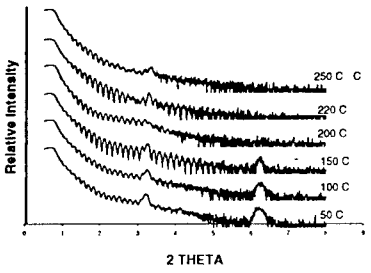

Figure 11: Low angle diffraction data on the $(Y_xCo_4Sb_{12})_m(La_xCo_4Sb_{12})_n$ superlattice sample.

Preparation of skutterudite superlattices

The facile interdiffusion observed for the modulated precursors combined with the low temperature nucleation of the skutterudite structure lead us to attempt the synthesis of a superlattice containing two different skutterudites. Our initial target compound was a $(Y_xCo_4Sb_{12})_m(La_xCo_4Sb_{12})_n$ superlattice. We layered sequentially deposited Y, Co, and Sb at the correct composition ratio for the desired skutterudite until enough material was deposited for m unit cells followed by La, Co and Sb at the correct composition ratio until enough material was deposited for n unit cells. At short interdiffusion times we knew from our studies of simpler reactants that the Y, Co and Sb layers and the La, Co and Sb layers would interdiffuse forming amorphous intermediates. Due to the longer interdiffusion lengths, however, we expected a much slower mixing of the Y-Co-Sb amorphous layer with the La-Co-Sb amorphous layer. This was confirmed by low angle diffraction studies as a function of annealing temperature and time, shown in Figure 11. The high frequency Fourier components, corresponding to the lengthscale of the individual Y-Co-Sb and La-Co-Sb repeat layer spacing, disappear on annealing at low temperature. The first order Fourier component corresponding to the sum of the total Y-Co-Sb plus the total La-Co-Sb layer thickness decreases in intensity much slower. Calorimetry studies of this sample show a sharp exotherm at 200°C as expected for the formation of a crystalline skutterudite. After this exotherm the low angle diffraction data still contains a first order Bragg diffraction maximum indicating that the sample remains compositionally modulated on the expected superlattice lengthscale after crystallization.

The high angle diffraction data for the $(Y_xCo_4Sb_{12})_m(La_xCo_4Sb_{12})_n$ superlattice is shown in Figure 12. The diffraction pattern is that expected for a randomly orientated crystalline skutterudite. There is no evidence of separate diffraction maxima which would be expected for independent crystallites of $Y_xCo_4Sb_{12}$ and $La_xCo_4Sb_{12}$. There is also no evidence of shoulders on the diffraction maxima of the skutterudite which would be expected for a sample containing a supercell. This was surprising in light of the low angle diffraction maxima observed in the low angle diffraction data shown in Figure 11. Figure 13 contains the results of a scan obtained about the most intense skutterudite diffraction peak after a significantly long counting time to improve the statistics. On each side of the main diffraction maxima very weak shoulders are observable at the positions expected from the repeat spacing obtained from the low angle diffraction maxima.

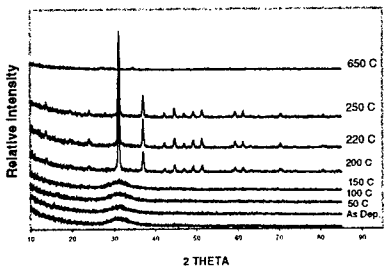

Figure 12: Diffraction intensity as a function of annealing temperature for skutterudite superlattice sample.

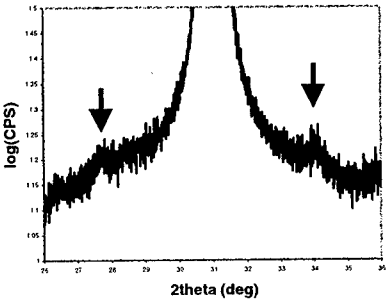

Figure 13: An expansion of the scale about the 310 Bragg diffraction maxima of the superlattice sample. The arrows indicate the expected positions of the superlattice diffraction peaks.

The weak intensity of the diffraction shoulders results in part from the small electron density differences between the two layers (only 18 electrons out of a total of 759). The low and high angle diffraction data suggests that the film consists of randomly orientated crystallites each containing a superlattice periodicity perpendicular to the substrate. Further experiments are underway to prepare skutterudite superlattices with a larger electron density difference between the components of the superlattice.

CONCLUSIONS

Modulated elemental reactants provide access to compounds which are metastable with respect to disproportionation. The $FeSb_3$, $Lu_xFe_4Sb_{12}$ and $(Y_xCo_4Sb_{12})_m(La_xCo_4Sb_{12})_n$ superlattices are all examples of such metastable compounds. While much has been accomplished synthetically in terms of preparing new skutterudites, the challenge remains to optimize their physical properties. The ability to prepare bulk samples, shown here for $Lu_xFe_4Sb_{12}$, is very important. This will permit all of the relevant materials properties (conductivity, Seebeck coefficient, and thermal conductivity) to be measured on the same sample in geometry similar to that which may be used in a thermoelectric device.

From the results presented, it is possible to point to a number of research directions for searching for improved thermoelectric materials. The disorder on the cation site is credited with reducing the phonon thermal conductivity. However, it is not obvious whether the static disorder of the late rare earths or the dynamic disorder of the early rare earths would be superior in this regard. In addition, the partial occupancy of the metastable compounds presents an opportunity to tune the electronic properties by controlling that occupancy. Finally, the ability to prepare superlattices of the skutterudites opens up a wide range of possible compounds to test for optimal thermoelectric properties. Questions remaining include whether the lattice thermal conductivity is reduced due to the superlattice modulation, whether doping by random substitution, for example $LaFe_{4-x}Co_xSb_{12}$ versus doping by layers in a superlattice, $(LaCo_4Sb_{12})_x(LaFe_4Sb_{12})_{4-x}$, is equivalent, and whether organization of dopants into superlattice layers can enhance the mobility of the carriers. We believe such studies are now possible because

the multilayer precursor method allows the rapid synthesis of large families of structurally related metastable compounds.

REFERENCES

1. L. D. Hicks, T.C. Harmon, and M.S. Dresselhaus, Appl. Phys. Lett., **63**: pp. 3230-3232 (1993).
2. G.A. Slack, in *Handbook of Thermoelectrics*, edited by D.M. Rowe, 1995, Chemical Rubber: Boca Raton Fl. p. 407.
3. L. Fister, , X. M. Li, T. Novet, J. McConnell, and D. C. Johnson,. J. Vac. Sci. & Technol. A, **11**: p. 3014–3019 (1993).
4. T. B. Massalski, H. Okamoto, P. R. Subramanian, and L. Kacprzak, eds. *Binary Alloy Phase Diagrams*. 2 ed. . Vol. 3. 1990, ASM International. 2664–2665.
5. A. Kjekshus and T. Rakke, Acta Chemica Scandinavica A, **28**: p. 99-103 (1974).
6. W. Jeitschko and D. Braun, Acta Cryst., **B33**: p. 3401-3406 (1977).
7. H. D. Hornbostel, E. J. Hyer, J. H. Edvalson, and D. C. Johnson, Inorganic Chemistry, **36**: p. 4270-4274 (1997).
8. H. Sellinschegg, S. L. Stuckmeyer, M. D. Hornbostel and D. C. Johnson, Chem. Mater., **10**: p. 1096-1101 (1998).

ANALYSIS OF ANTIMONY-TIN-BASED SKUTTERUDITES

S.B. SCHUJMAN[*], G.A. SLACK[*], H.C. NGUYEN[*], G.S. NOLAS[#], R.A. YOUNG[**], F. MOHAMMED[+]and T. TRITT[+]
[*] Department of Physics, Applied Physics and Astronomy, Rensselaer Polytechnic Institute, Troy, NY 12180
[#] R&D Division, Marlow Industries, Dallas, TX 75238
[**] School of Physics, Georgia Institute of Technology, Atlanta, GA 30332
[+] Department of Physics, Clemson University, Clemson, SC 29634

ABSTRACT

Since the proposal of skutterudites as possible Phonon-Glass, Electron-Crystal materials, a lot of work has been done trying to fill the structural voids with foreign "rattling" atoms. In order to keep the electronic count per unit cell constant (and thus, the semiconducting properties of most of the compounds under study) partial replacement of either the cation or the anion in the original formula by an appropriate neighbor in the periodic table is an option. In the case of antimonides, replacing part of the Sb with Ge or Sn in order to compensate the extra charge introduced by void fillers has proved useful for compounds based on rare-earth filled $IrSb_3$. In the case of $RhSb_3$, we found that large quantities of Sn can be incorporated into the skutterudite structure of $RhSb_3$ without either filling the voids or producing charge carriers.
We have analyzed the stability of several cross-sections of the Rh-Sb-Sn ternary system and have found a wide range of compositions with the basic skutterudite structure as we vary the Sn content. In all the cases, the tin goes substitutionally into the antimony sites. The voids remain empty. Density measurements suggest the existence of metal vacancies, confirmed by Rietveld refinement of the powder X-ray diffraction patterns. The possibility of Sn-induced mixed-valence of Rh on the anion sites is being investigated.

INTRODUCTION

Since the proposal[1] of the "Phonon-Glass; Electron-Crystal" model as a way to get low thermal conductivity and good electrical properties of materials for thermoelectric applications, and the realization that semiconducting skutterudites can be a good example of this type of material, efforts to fill the skutterudite's voids with different atoms that can "rattle" and scatter phonons have been successfully made[2]. In order to maintain the semiconducting properties of these materials during synthesis and doping, the electron count per unit cell must be conserved, and so, the extra charge produced by electrons donated by the void-filling atom must be compensated by counter-doping. This is generally done by replacing part of either the cations or the anions in the skutterudite frame with atoms that donate or absorb the appropriate number of electrons. The cubic unit cell in the semiconducting region should contain 144 electrons.

We have been working mostly with antimony-based skutterudites ($IrSb_3$ and $RhSb_3$), and have been replacing part of the antimony atoms by tin (which should work as an acceptor in the skutterudite frame) in order to compensate the extra charge added by the possible filler atom. We have found that even in the case of non-filled skutterudites, the semiconducting framework can accept considerable amounts of excess Sn, without losing the semiconducting properties. Our results and a possible model to explain them are presented.

Mat. Res. Soc. Symp. Proc. Vol. 545 © 1999 Materials Research Society

EXPERIMENT

In all the cases, the samples were prepared by solid-state diffusion of stoichiometric quantities of the corresponding elements in a chemically-vapor-deposited BN crucible enclosed in a sealed and partially Ar-filled quartz ampoule. The temperature of diffusion was chosen based on the phase-diagrams for the different systems. The general procedure consisted of a three-day long annealing, cooling down and then grinding of the sample followed by another three-day annealing period.

The characterization of the final powders was done by X-ray diffraction (XRD) in a SCINTAG X1 diffractometer with a Peltier cooled solid state detector and a sealed copper X-ray tube. The structures refined by the Rietveld method using DBWS-9411 software[3]. Solid samples were obtained by hot-pressing during two hours at 700 °C and pressures between 2 and 4 kbars, depending on the sample. Chemical characterization on these samples was carried out with a JEOL 733 Electron-beam Microprobe. We were able to measure composition with a precision of 1 atom/%. In the case of single-phase materials, the powder density was measured by determining the N_2 volume necessary to fully fill a cell of known volume that contains the powder in a B.E.T. machine made by Quantachrome.

The electrical resistivity and Seebeck coefficient as a function of temperature were determined for some of the samples. The ends of the samples (the typical samples sizes for these measurements is about 10 mm x 2 mm x 3 mm) were Ni plated and then were soldered to Cu blocks which had 0.003" Au-Fe (0.07at%) vs. chromel thermocouples embedded in the Cu blocks to make the ΔT measurements. Cu lead wires were also soldered to these Cu blocks with one pair to serve as the current leads for the resistance measurements and another pair to serve as voltage leads (V_{TEP}) for the thermopower measurements. A pair of Au leads (V_R) were attached to the sample inside the current leads to measure the sample voltage for the resistance measurements.

RESULTS

Samples with nominal compositions $RhSb_3$, $Rh_4Sb_{12}Sn$, $Rh_4Sb_{12}Sn_2$ and $Rh_4Sb_{11}Sn$ were prepared.

The XRD for all the cases show a skutterudite structure, with lattice parameters increasing as the Sn concentration increases, being 9.229 Å for pure $RhSb_3$, 9.249Å for $Rh_4Sb_{12}Sn$, 9.284Å for $Rh_4Sb_{12}Sn_2$ and 9.2470 Å for $Rh_4Sb_{11}Sn$, see Table I.

The measured powder densities for both Sn-doped samples with excess Sn ($Rh_4Sb_{12}Sn$ and $Rh_4Sb_{12}Sn_2$) are lower than the theoretical value for pure $RhSb_3$, indicating not only that the Sn is going to the antimony sites of the skutterudite frame and not into the voids, but probably that there is a simultaneous generation of metal-atom vacancies due to the introduction of the Sn. In the case of $Rh_4Sb_{11}Sn$, the value of the measured powder density is very similar to the calculated X-ray density, which means that no vacancies are generated. Given the size and the covalent bonding tendency of the Sn, we conclude that it goes into the Sb sites. Rietveld refinement of the structures assuming the Sn is randomly located on the Sb sites results in occupation numbers for both Rh, Sn and Sb that agree very well with the microprobe results and, for the samples with excess Sn, also with the hypothesis of vacancies on the Rh sites.

The resistivity and Seebeck coefficient measurements as a function of temperature for the $Rh_4Sb_{12}Sn$ and $Rh_4Sb_{12}Sn_2$ samples are shown in Figures 1a and 1b.

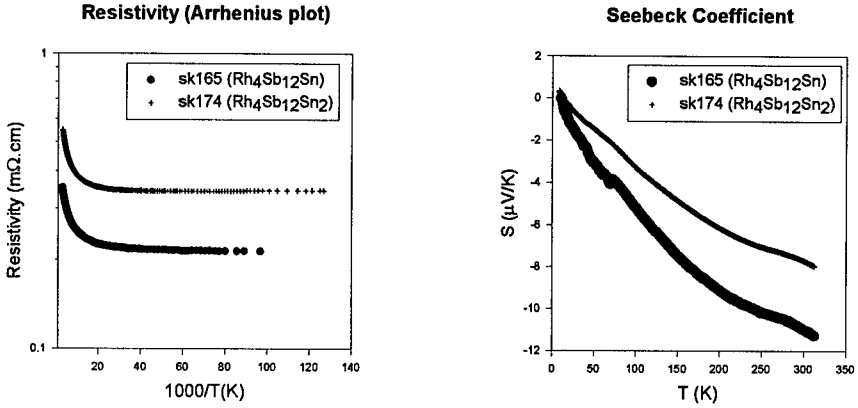

Figure 1:a) Resistivity and b) Seebeck coefficient vs. temperature for $Rh_4Sb_{12}Sn$ (circles) and $Rh_4Sb_{12}Sn_2$ (crosses)

The main feature of these samples is the fact that they can incorporate a substantial amount of Sn without any apparent charge compensation. We think that the charge deficit in the antimony lattice introduced by the Sn is being compensated by a change in the valence state of the transition-metal atoms. This effect has been seen[4] in other skutterudites, particularly in $Ru_{0.5}Pd_{0.5}Sb_3$, where the Ru takes on charge states of +2 and +4. In the case of $Rh_4Sb_{12}Sn$ and $Rh_4Sb_{12}Sn_2$, if all the Rh remains in a +3 charge state, then the the resulting structures should show a defficit in the number of electrons and thus, they should be p-type. This contradicts the Seebeck coefficient measurements (Figure 1b), that shows that the samples are n-type. If we assume such a model for the Sn-doped $RhSb_3$ samples, then we would have a general formula of:

$$\left(Rh_a^{5+} Rh_b^{3+} \square_y\right) Sb_{12-x} Sn_x \qquad (1)$$

We assume that the vacancy concentration, y, adjusts itself to try to maintain:

$$a + b + y = 4 \qquad (2)$$

and 72 electrons per formula unit. This means:

$$5a + 3b + 5(12\text{-}x) + 4x = 72 \qquad (3)$$

In the table I we show the calculated composition for each analyzed sample, the measured lattice parameter and the theoretical and measured powder density. The theoretical powder density was calculated using the measured lattice parameter and Equation (2) to give y.

One interesting feature is the fact that in the cases of $Rh_4Sb_{12}Sn$ and $Rh_4Sb_{11}Sn$, both the ratio of Sn to Sb atoms and the lattice parameter are almost identical. The main difference is the fact that, due to the different initial ratio between metal and non-metal atoms in the composition

with a Sn excess, there is a generation of vacancies (that is reflected in the calculated and measured value of the density) that does not happen in the second compound.

Table I: Comparison between the measured and calculated (according to our model) powder densities for $RhSb_3$ with different Sn-doping levels

Nominal Composition	Modeled Composition	Lattice Parameter (Å)	Calculated Density (g/cm^3)	Powder Density (g/cm^3)
$RhSb_3$	$RhSb_3$	9.229	7.910	
$Rh_4Sb_{12}Sn$	$Rh^{+5}_{.92}Rh^{+3}_{2.77}\square_{.31}Sb_{11.08}Sn_{.92}$	9.249	7.715	7.71 ± 0.05
$Rh_4Sb_{12}Sn_2$	$Rh^{+5}_{1.71}Rh^{+3}_{1.71}\square_{.57}Sb_{10.29}Sn_{1.71}$	9.284	7.505	7.49 ± 0.05
$Rh_4Sb_{11}Sn$	$Rh^{+5}_{0.5}Rh^{+3}_{3.5}Sb_{11}Sn$	9.247	7.852	7.82 ± 0.05

We have carried out similar experiments with $IrSb_3$ doped with excess Sn and have found that up to 22% of the Sb can be replaced by Sn in the skutterudite structure. In $RhSb_3$, we believe the limit is about 14% excess Sn. In $CoSb_3$, Koyanagi *et al.*[5] have found that only 2.4% of the Sb can be replaced by Sn. Thus, the generation of Co^{5+} appears to be much more difficult than that of a +5 valence in Rh or Ir.

Note that in $RhSb_3$ the nominal valence of Rh is +3, while in $RhSb_2$ the nominal valence is +5. Thus, the Sn doping produces mixtures of these two valences.

This result shows why it is difficult to control the carrier concentration and resistivity in $RhSb_3$ or $IrSb_3$ samples when rare earth atoms are added to the voids. However, some control of the carrier concentration in the $(Fe\text{-}Co)Sb_3$ system is possible[6] because Co^{5+} generation is much more difficult.

CONCLUSIONS

In this work there are two separate but related issues: one is the generation of vacancies on the transition-metal sites of the skutterudite structure to accommodate an excess of non-metal atoms and the other one is the change in the valence state of a certain amount of metal atoms in order to compensate the charge deficit introduced by doping with excess tin. We have proof of the first statement by our powder-density measurements and by the agreement between our calculated compositions and the occupation numbers we get when refining these structures based on the powder x-ray diffraction patterns. The second hypothesis, though likely according to our model and the electrical measurements, needs a direct measurement of the valence state of the metal atoms in order to be validated. This can be done, for example, with techniques that allow the determination of chemical state of elements, such as Ultraviolet Photoelectron Spectroscopy (UPS) or Near-Edge X-ray Absorption Fine Structure (NEXAFS) on the compounds. In the case this hypothesis is verified, we should rethink the way we control (or at least try to control) the carrier concentration in filled skutterudites. A different possibility is the utilization of materials with known stable valence behavior of the transition metal, such as Pt in $PtSb_2Sn$ or Ru in $RuSb_2Te$. Although Ru shows mixed-valence behavior in $Ru_{0.5}Pd_{0.5}Sb_3$, its valence state in

$RuSb_2Te$ is 2+, and it is very unlikely to go to 4+, especially when prepared with a small excess Te in order to make n-type samples.

ACKNOWLEDGMENTS

This work was supported in part by ONR on grant No. 00014-94-1-0341

REFERENCES

1. Glen A. Slack, *CRC Handbook of Thermoelectrics,* Chapter 34, edited by D. M. Rowe, Chemical Rubber, Boca Raton, FL, 1995, p. 407
2. G. S. Nolas, G. A. Slack, T. M. Tritt, D. T. Morelli and A. C. Ehrlich, J. Appl. Phys.,**79**, 1996, p. 4002
3. R. A. Young, A. Sakthivel, T. S. Moss and C. O. Paiva-Santos, J. Appl. Cryst. **28**, 1955, pp. 366-367
4. G. S. Nolas, V. G. Harris, G. A. Slack, D. T. Morelli and T. M. Tritt, J. Appl. Phys., **80,** 1996, pp. 6304-6308.
5. T. Koyanagi, T. Tsubouchi, M. Ohtani, K. Kishimoto, H. Anno and K. Matsubara, *Proc. 15th. International Conference on Thermoelectrics*, 1996, p. 107
6. B. C. Sales, D. Mandrus, B. C. Chakoumakos, V. Keppens and J. R.. Thompson, Phys. Rev. B, **56**, 1997, pp. 15081-15089

SYNTHESIS OF NEW THERMOELECTRIC MATERIALS USING MODULATED ELEMENTARY REACTANTS

HEIKE SELLINSCHEGG, JOSHUA R. WILLIAMS, STEVEN P. MAXWELL, DOUGLAS SILLARS and DAVID C. JOHNSON *
*Department of Chemistry and Materials Science Institute
University of Oregon, Eugene, OR, 97403, davej@oregon.uoregon.edu

ABSTRACT

Modulated elemental reactants have been used to synthesize metastable ternary compounds with the skutterudite crystal structure. The initial reactants are made up of multiple repeats of a unit containing elemental layers of a ternary metal, iron or cobalt (or a combination of these two) and antimony. The elemental layers interdiffuse upon low temperature annealing and form amorphous reaction intermediates. In this paper we target the compounds $Pb_xFe_{4-y}Co_ySb_{12}$. On annealing at temperatures between 120° and 150° C (depending on the composition) crystallization of the skutterudite structure occurs. The compounds are only kinetically stable, decomposing into a mixture of binary compounds upon annealing past a temperature of about 600°C. Preliminary data for the Seebeck coefficient and the electrical conductivity was collected The thermoelectric properties of the lead cobalt antimony skutterudite - films were measured as a function of lead occupancy.

INTRODUCTION

The literature discussing potential applications of filled skutterudites as thermoelectric materials has focused on the early rare earth filled skutterudites. These compounds are among the few filled skutterudites which can be readily synthesized by direct reaction of the elements at high temperatures as originally reported by Jeitschko.[1] Attempts to prepare filled iron or cobalt skutterudites with later rare earth elements such as lutetium or transition metal elements such as hafnium have failed. In 1997,Hornbostel reported on the successful synthesis of several filled skutterudites[2], including those just mentioned, by using modulated elemental reactants as precursors. This synthetic approach was shown to be the key to successful preparation of these compounds because it avoided thermodynamically more stable binary compounds as reaction intermediates. Ternary skutterudites readily crystallize from the amorphous reaction intermediate. Sellinschegg[3] followed up on these reports to prepare several filled skutterdites containing post transition elements as the fillingcations. The ability to prepare new filled skutterudite compounds was clearly demonstrated, but there was no discussion of their physical properties. Many questions regarding these properties and the preparation of an optimized thermoelectric material prepared via this synthetic approach remain to be answered.

In this paper we report on the synthesis of another series of filled skutterudites, $Pb_xFe_{4-y}Co_ySb_{12}$, and on our initial measurements of the electrical transport properties of these new compounds.

EXPERIMENT

The elementally modulated reactants were prepared in a high-vacuum evaporation system which has been described in detail elsewhere[4]. Briefly, the elements were sequentially deposited

Mat. Res. Soc. Symp. Proc. Vol. 545 © 1999 Materials Research Society

under high vacuum (10^{-7} torr). A personal computer controls the deposition. The metallic elements were deposited from electron beam evaporation sources at a rate of 0.5 Å/sec. Antimony was deposited by an effusion cell at approximately the same rate. Each source was independently monitored by quartz crystal thickness monitors. This allows the thickness of each elemental layer to be controlled to the nearest Ångstrom. The multilayer repeat thickness (sum of the individual elemental thicknesses) for all of the samples was kept below 25Å to ensure interdiffusion of the elements at low temperatures without nucleating binary compounds at the reacting interfaces. Elemental composition of the samples was found to be repeatable to within about 5%. The films were simultaneously deposited on silicon, off-cut quartz, float glass and photoresist-coated silicon wafers.

Free standing films were prepared from the coated substrates by soaking them in acetone. This dissolves the photoresist and allows for the elementally modulated film particles to be collected on teflon filters. These free standing films were used for differential scanning calorimetry (DSC) experiments. The evolution of the samples as they were exposed to increasing temperature was monitored using a TA9000 calorimeter. The heat flow associated with irreversible changes occurring in the sample during the heating is used in correlation with x-ray results to identify and track the interdiffusion of the elements and the crystallization of the skutterudite compounds.

The silicon substrates were used for low angle diffraction studies, the films on the off-cut quartz were annealed and used to collect diffraction data for structural refinement. Low angle x-ray diffraction was employed to characterize the multilayer periodicity and to study the interdiffusion of the elements. The repeat thickness was determined from the position of the Bragg diffraction maxima, total film thickness was determined from the higher frequency oscillations resulting from interference of the x-rays between the front and back of the films. Crystalline compounds were identified by high angle x-ray diffraction. All x-ray data was collected with a Scintag XDS 2000 θ–θ diffractometer.

The float glass samples served as substrates for measurement of electrical properties. They were annealed at a temperature past the formation exotherm of the skutterudite phase as determined by DSC. A mask was then used to deposit four thin silver lines across the rectangular sample for electrical contacts. The measurement of the electrical properties used a standard four-probe configuration. Two current leads and two copper-constantan thermocouples were attached to the silver lines on the thin film sample with indium solder. The sample was mounted on a He closed cycle refrigerator. An Oxford instruments temperature controller was used to control the temperature of the sample. After the sample reached the desired set point temperature, increasing current was passed through the sample using a Keithley constant current source. The voltage drop between the two inner contacts was measured using a digital voltmeter connected to the copper legs of the thermocouples. The resistance of the sample was calculated from the slope of the resulting I-V line and converted to conductance using the known dimensions of the sample. To measure the Seebeck coefficient, current was passed through a resistor mounted on one end of the sample using a HP constant current source. The resulting temperature gradient across the sample was measured using the two copper constantan thermocouples. The induced voltage difference was again measured by the voltmeter connected across the two copper legs of the thermocouples. The necessary switching was accomplished using a Keithley scanner equipped with a matrix card. The Seebeck coefficient was calculated by plotting the resulting induced voltage versus the temperature gradient. Linear plots were obtained and the resulting slope is reported as the Seebeck coefficient.

Finally, the average composition of the multilayer films was determined by electron microprobe analysis using an energydispersive X-ray detector.

RESULTS

A series of samples with both variable lead occupancy as well as varying iron to cobalt ratios in the solid solution $Pb_xFe_{4-y}Co_ySb_{12}$ was prepared. Data for the intended composition and the formation exotherm temperature as determined by DSC is summarized in Table I.

Table I. Crystallization exotherms and composition (intended) of successfully synthesized skutterudite compounds.

Sample ID	*Exotherm Temperature*	*Intended Composition Pb : Fe : Co : Sb*
Pb-Fe-Co-Sb 01	125°C	1 : 2 : 2 : 12
Pb-Fe-Co-Sb 02	126°C	0.8 : 2 : 2 : 12
Pb-Fe-Co-Sb 03	126°C	0.5 : 2 : 2 : 12
Pb-Fe-Co-Sb 04	128°C	0.2 : 2 : 2 : 12
Pb-Fe-Co-Sb 05	126°C	1.1 : 2 : 2 : 12
Pb-Fe-Co-Sb 06	132°C	1.2 : 2 : 2 : 12
Pb-Fe-Co-Sb 07	126°C	1 : 3 : 1 : 12
Pb-Fe-Co-Sb 08	137°C	1 : 1 : 3 : 12
Pb-Fe-Co-Sb 09	134°C	1 : 1.5 : 2.5 : 12
Pb-Fe-Co-Sb 10	141°C	1 : 2.5 : 1.5 : 12
Pb-Fe-Co-Sb 11	136°C	1 : 3.5 : 0.5 : 12
Pb – Co – Sb 01	134°C	0.25 : 0 : 4 : 12
Pb – Co – Sb 02	152°C	0.5 : 0 : 4 : 12
Pb – Co – Sb 03	132°C	0.75 : 0 : 4 : 12
Pb – Co – Sb 04	133°C	1 : 0 : 4 : 12
Pb – Co – Sb 05	132°C	1 : 0 : 4 : 12
Co – Sb 01	148°C	0 : 0 : 4 : 12

Figure 1 contains a typical calorimetry trace of a lead filled skutterudite. It shows a sharp exotherm at 132°C. Diffraction data was collected as a function of annealing temperature to trace the development of crystalline structure. Figure 2 contains the low angle diffraction data for a representative sample as deposited on the silicon substrate. This data shows a Bragg peak at 5.7° which corresponds to repeat layer thickness of about 15.4Å. Figure 3 contains a diffraction pattern collected after the 132°C exotherm showing the characteristic skutterudite structure. This confirms that the initial sharp exotherm results from crystallization of the sample to form the desired skutterudite compound.

The above results demonstrate that the skutterudite structure is easily formed using modulated elemental reactants. This powerful synthetic technique greatly enhances our ability to search for efficient thermoelectric materials based on the skutterudite structure. It will hopefully allow us to study the variation of properties as a function of composition.

The first aim of this study was to demonstrate that the lead occupancy can be synthetically controlled. Ideally, the initial film composition will correspond to the composition of the crystalline skutterudite. A series of cobalt-antimonides with varying amounts of lead (see Table II) was prepared to determine if we can assume this ideal situation. The low angle diffraction patterns in Figure 4 show that the total repeat spacing becomes larger for samples with higher lead content (the thickness of the antimony and cobalt layers was held constant as the lead content was incremented).

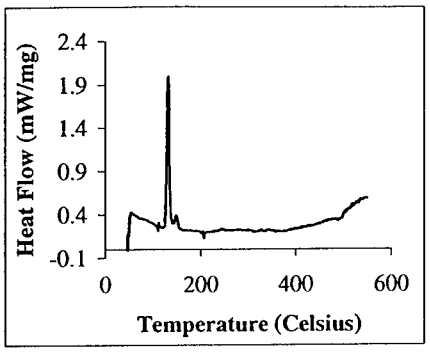

Figure 1. DSC scan of sample Pb-Co-Sb 03 showing and exotherm at 132°C.

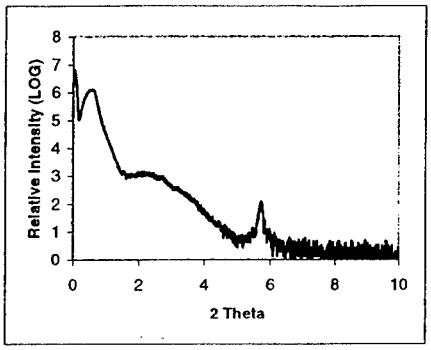

Figure 2. Low angle x-ray pattern of sample Pb-Co-Sb 03 showing a Bragg peak at $2\theta = 5.73°$

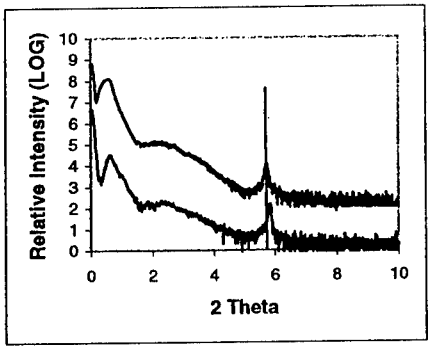

Figure 3. High angle diffraction pattern of Pb-Co-Sb 03 after annealing at 220°C for two hours.

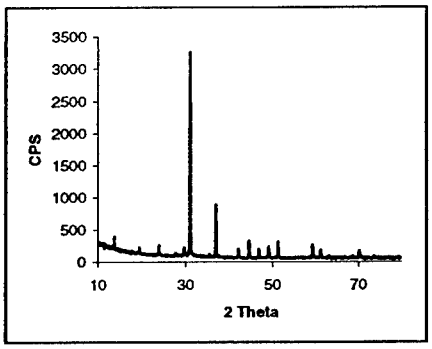

Figure 4. Low angle diffraction patterns of Pb-Co-Sb 03 (top) and Co-Sb 01 (bottom). Note that the Bragg peak for the filled skutterudite occurs at a lower value of 2θ, indicating an increased multilayer repeat distance.

The high angle diffraction data of the films annealed for 2 hours at 220°C is shown in Figure 5. This data demonstrates two important points. First, it is evident from the shifted diffraction peaks that the size of the unit cell becomes larger as the amount of lead in the initial

precursor is increased. This leads to the conclusion that the lead cations are indeed incorporated into the skutterudite structure. Second, simulated x-ray patterns for filled and unfilled cobalt antimonides clearly show decreased intensity of the 110, 200 and 211 Bragg peaks with increased lead filling. The data collected from our samples follow this trend.

Table II. Unit cell sizes and measured repeat thicknesses for selected samples.

Sample ID	*Cell size*	*Measured Repeat Thickness*
Pb – Co – Sb 01	9.061 ± Å	-
Pb – Co – Sb 02	9.057 ± Å	15.4 Å
Pb – Co – Sb 03	9.085 ± Å	16.1 Å
Pb – Co – Sb 05	9.067 ± Å	15.1 Å
Co – Sb 01	9.045 ± Å	15.1 Å

This provides strong evidence that the initial composition of the precursor does control the composition of the final product.

The first measurements of the electrical properties of lead filled skutterudite films have recently been conducted. The pure cobalt antimony skutterudite measured on film has more metallic character than reported previously. This is most likely due to a large number of defects resulting from a very short annealing time. Additional measurements on a film that is annealed for a more extended period of time are underway. The electrical conductivity of the lead-containing sample is considerably higher – as expected. The Seebeck coefficient for the lead filled sample is notably lower, as an expected result of the increased carrier concentration. Preliminary results show that a sample with very high lead content has a negative Seebeck coefficient indicating that electrons, not holes are carrying the current. This is of particular importance since it signifies the first time an n-type cobalt antimonide has successfully been synthesized. We are in the process of confirming the data for our electrical transport properties.

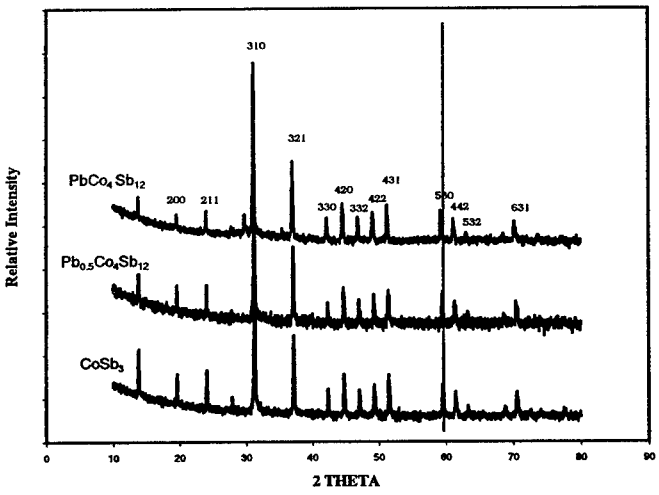

Figure 5. High angle diffraction patterns of skutterudite compounds with various degrees of lead filling. Note that the size of the unit cell increases with increasing lead content.

investigation of skutterudite compounds for thermoelectric applications are presented. The multilayer synthesis approach gives control over thestochiometry of the target compound so that it becomes an easy task to dope the compound and to optimize its thermoelectric properties.

REFERENCES

1. W. Jeitschko, and D. Braun, Acta Cryst. **B33**, p. 3401-3406 (1977).

2. M. D. Hornbostel, E. J. Hyer, et al., Inorganic Chemistry **36**, p. 4270-4274 (1997).

3. H. Sellinschegg, S. L. Stuckmeyer, Chemistry of Materials **10**, p. 1096-1101 (1998).

4. L. Fister, X. M. Li, et al., J. Vac. Sci. & Technol. A **11** p. 3014–3019 (1993).

LnPdSb AND $Ln_3Au_3Sb_4$: NEW THERMOELECTRIC MATERIALS

K. MASTRONARDI*, D. YOUNG*, C.-C. WANG*, A.P. RAMIREZ#, P. KHALIFAH* AND R.J. CAVA*
*Department of Chemistry and Princeton Materials Institute, Princeton University, Princeton NJ 08540
#Bell Laboratories, Lucent Technologies, Murray Hill NJ 07974

ABSTRACT

The thermoelectric properties near ambient temperature of half-Heusler alloys based on HoPdSb, DyPdSb, and ErPdSb are reported. The Seebeck coefficients are between 60 and 250 μV/K. The resistivities range between 0.6 and 20 mΩcm, and the majority carriers are p-type. Thermal conductivities are smallest in intentionally disordered materials. The highest ambient temperature ZT obtained is 0.06. Band structure calculations are presented, and are compared to those for ZrNiSn. It is suggested that half-Heusler alloys with 18 electrons per formula unit may represent a large class of thermoelectric materials. The thermoelectric properties of another family of cubic symmetry antimonides, based on $Ho_3Au_3Sb_4$ and $Sm_3Au_3Sb_4$, are also reported.

INTRODUCTION

Recently, a family of complex materials, the ternary Skutterudites (1), has been found to display potentially interesting thermoelectric properties. Here we describe a new family of thermoelectrics, whose ambient temperature properties are similar to those of the Skutterudites, in some detail. The materials are ternary lanthanide antimonides of formula *Ln*PdSb. We present, in addition, an analysis of their electronic structure. Considering electronic structure calculations for different half-Heusler alloys (2-4), we suggest that good thermoelectric behavior may occur in general for materials with this structure type at an electron count of 18 per formula unit. Initial reports on the thermoelectric properties of stannides with the same structure type have also recently appeared (5,6). We also report our preliminary results on another new family of thermoelectric antimonides, of formula $Ln_3Au_3Sb_4$.

The Heusler phase crystal structure, of formula AT_2X, is a stuffed version of sodium chloride type, with the larger (A) atom and the metalloid (X) in the NaCl arrangement, and the transition metal (T) filling all 8 of the eight-coordinated interstitial positions per cell. In the half-Heusler alloys, only half of those interstitial positions are filled with transition metals, in an ordered array. This structure type is found for many ternary transition metal compounds. Solid solutions are expected in many cases between the half-Heusler and Heusler phases, yielding materials of stoichiometry $AT_{1+y}X$, with $0 \le y \le 1$. This characteristic, along with the large number of A, T, and X atoms which form the phase, and also the possibility of T-X mixing, make a very wide range of chemical manipulations possible for property optimization. The $Ln_3Au_3Sb_4$ structure type is also cubic, but is more complex. Though known for a much more limited number of materials, a wide range of chemical manipulation is also expected to be possible.

EXPERIMENT

We have studied the thermoelectric properties of the half-Heusler phases *Ln*PdSb for the heavy lanthanides Ho, Er and Dy. Samples were made by arc melting (3X, under Ar) mixtures of

Mat. Res. Soc. Symp. Proc. Vol. 545 © 1999 Materials Research Society

the elements of total weight 0.75 grams, wrapping the resulting buttons in Ta foil, and then sealing in an evacuated quartz tubes. Annealing was carried out at 800-900 C for three days, followed by a quench to room temperature. Small variations in the amounts of Pd and Sb (LnPd$_{1.02}$Sb, LnPdSb$_{1.05}$, and LnPd$_{1.02}$Sb$_{1.05}$) were made to broadly test the effect of stoichiometry on the electronic properties. Samples with mixed lanthanides, of the type $Ln(I)_{1-x}Ln(II)_xPd_{1+y}Sb_{1+z}$ were also made. The same procedure was employed to synthesize materials based on $Ln_3Au_3Sb_4$, for Ln=Nd, Gd, Ho, Sm and Ho.

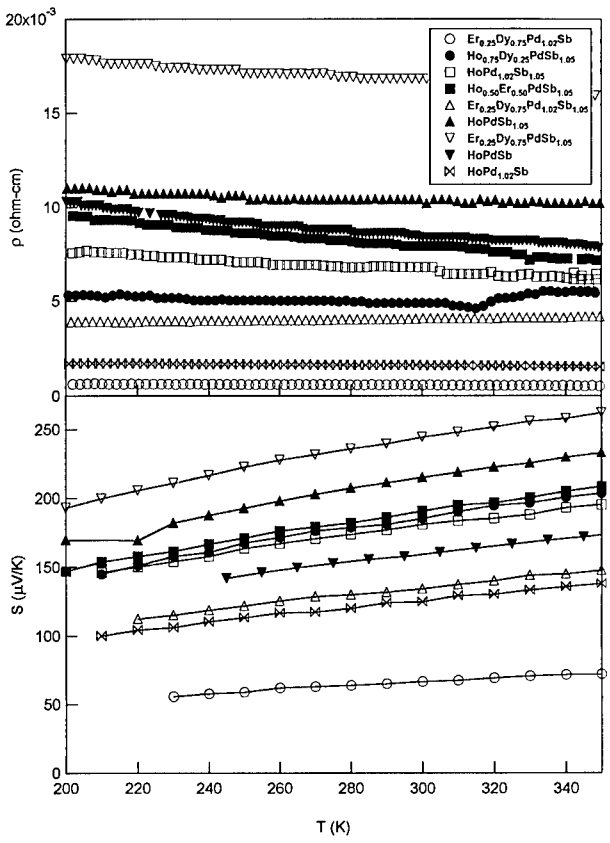

Fig. 1 Electrical resistivities (upper panel) and Seebeck coefficients (lower panel) for selected members of the half-Heusler LnPdSb series.

The post-annealed buttons were employed in the resistivity, Seebeck coefficient and thermal conductivity measurements. The phase purity of the samples was tested by powder X-ray diffraction. The Seebeck coefficient was measured with a commercial apparatus (MMR Technologies) and calibrated by comparison to a constantan standard. Resistivities were measured by a standard 4-point AC method. Thermal conductivities were measured by the longitudinal steady-state method. Band structure calculations were carried out with the program developed by Anderson and others (7,8). The calculations employ the local density approximation (LDA) in the LMTO method, with the atomic sphere approximation, and include relativistic effects but not spin-orbit coupling. Approximately 245 irreducible k-points were used within the Brillouin zone.

RESULTS AND CONCLUSIONS

The electrical characterization of selected materials in the vicinity of ambient temperature is summarized in figure 1. The upper panel shows the measured resistivities, which range between 0.6 and 20 mΩcm. The resistivities are only weakly temperature dependent, consistent

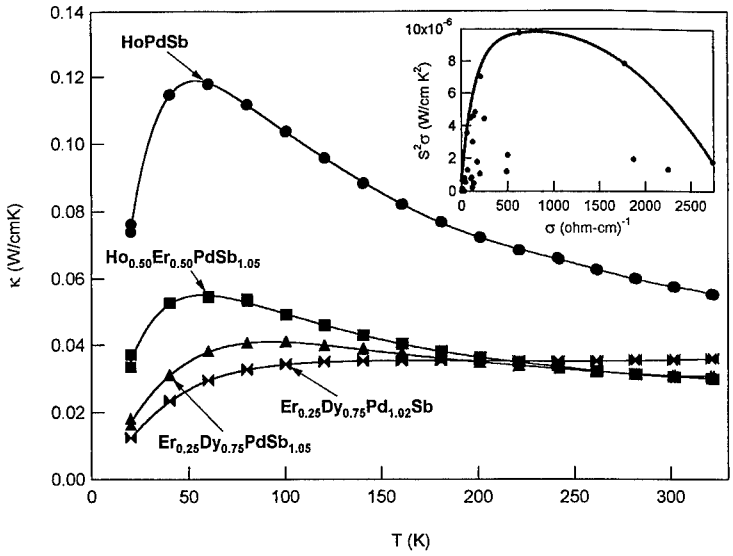

Fig. 2 Main panel - The temperature dependence of the thermal conductivity for three of the half-Heusler antimonides. Insert - The power factor, $S^2\sigma$, as a function of σ for all the *Ln*PdSb alloys studied.

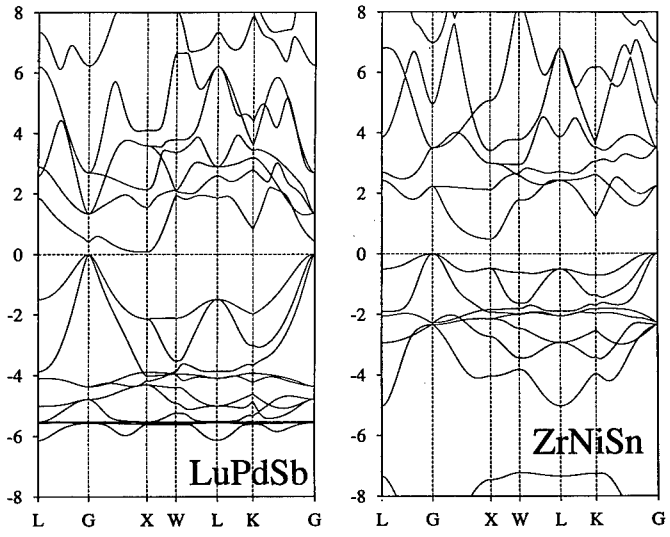

Fig. 3 The calculated band structures of LuPdSb and ZrNiSn. The horizontal axis is labeled with the standard designations for the FCC Brillouin zone. Energies in eV.

with the behavior expected for doped small band gap semiconductors. The general effects of nonstoichiometry can be seen for the materials based on HoPdSb. Increase of the relative Sb content raises the resistivity. An increase in the Pd content, which drives the composition towards that of the full Heusler alloys, decreases the resistivity significantly. The multiple non-stoichiometry has an intermediate effect. Some of the best resistivities are observed for the mixed lanthanide samples, indicating that disorder scattering on the *Ln* sublattice does not significantly effect the electrical resistivity in this temperature range. The resistivities for the *Ln*PdSb phases are very similar to those found for the filled Skutterudites at ambient temperature (1).

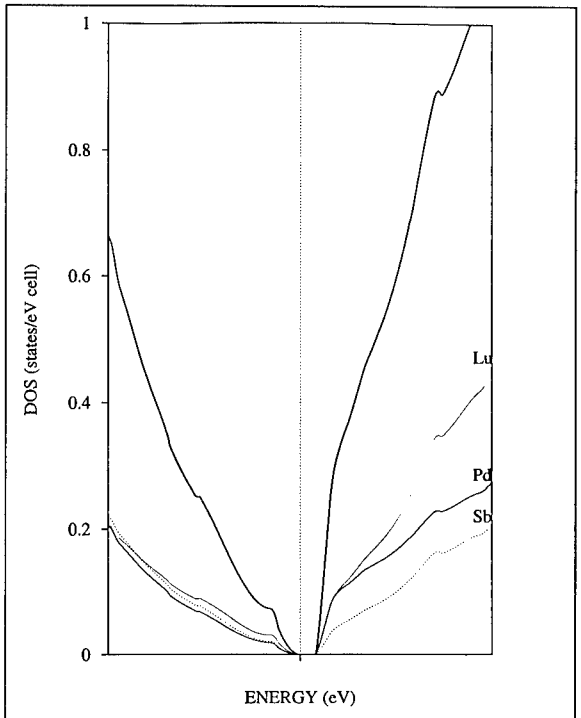

Fig. 4 The density of electronic states (DOS) for LuPdSb in the vicinity (± 1eV) of E_F (dotted line), total (bold line) and partial contributions as shown.

The Seebeck coefficients in the same temperature range are presented in the lower panel of figure 1. They are seen to be large, between 60 and 250 μV/K, predominantly falling in the range of 150-200 μV/K. They increase in magnitude with increasing temperature. The positive Seebeck coefficients indicate that the dominant carriers in the electrical conduction are holes. The higher Seebeck coefficients are found for the materials with the higher resistivities, as expected. We have not yet explored chemical substitutions which might result in n-type conductivity. The Seebeck coefficients for the present materials are comparable to those found for the Skutterudites in the same temperature range (1).

We have not measured the mobilities or carrier concentrations of the present materials, but show, as an insert to figure 2, a plot of $S^2\sigma$ (the thermoelectric power factor) vs. σ for all the materials synthesized in this study, including those not shown in figure 1. The line drawn in the figure is an envelope suggesting optimized thermoelectric behavior at an intermediate carrier concentration (σ is proportional to carrier concentration), which we postulate represents the behavior of materials with the best mobilities at any carrier concentration. The materials whose power factors fall below the line may have lower carrier mobilities due to crystalline defects, impurities or disorder. Further study would be necessary to clarify the behavior suggested by the figure.

The thermal conductivities of a selection of the antimonide based half-Heusler alloys is presented in the main panel to figure 2. For pure HoPdSb, the thermal conductivity is 5W/mK at ambient temperature and increases with decreasing temperature. The peak observed near 50 K occurs at the temperature where the mean free path of the phonons is approximately equal to the

crystallite size. The thermal conductivities of three of the lanthanide disordered phases are also shown in the figure. These are lower than that seen for the pure material, approximately 3.5W/mK at 300K, consistent with the limitation of the phonon mean free path by disorder scattering. The thermal conductivities of the half-Heusler phases are low, but still relatively high compared to those of the Skutterudites and Bi_2Te_3 (1,9), which are approximately 1.6-1.8 W/mK. As a result, the thermoelectric figure of merit for the current materials is about half that for the Skutterudites at ambient temperature.

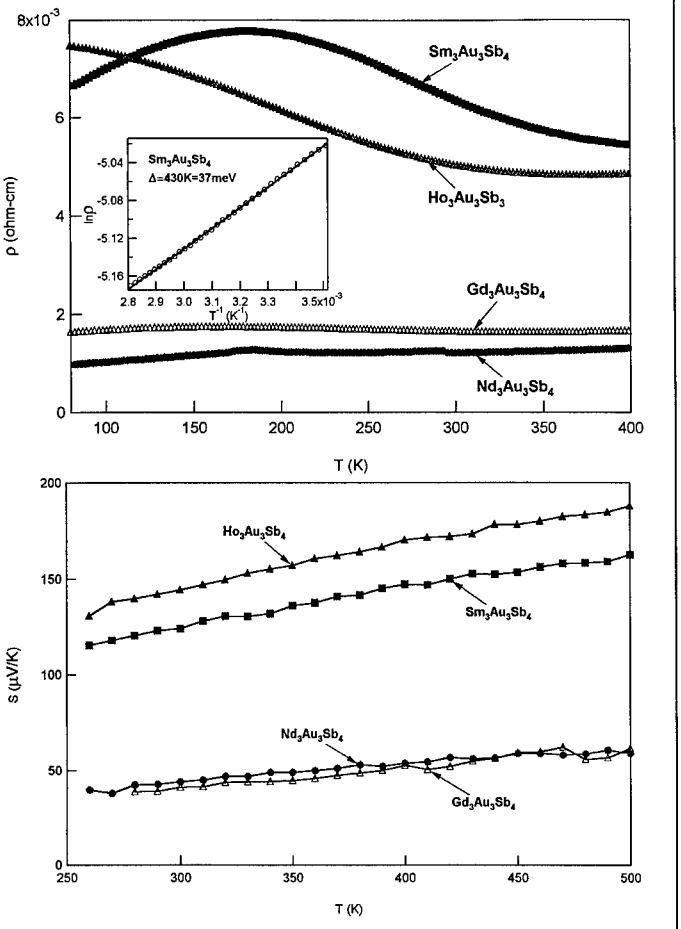

Fig. 5 Electrical resistivities (upper panel) and Seebeck coefficients (lower panel) for selected members of the $Ln_3Au_3Sb_4$ series.

We have performed band structure calculations for LuPdSb and ZrNiSn to provide a basis for the discussion of the electronic properties. The calculated band structures are shown in figure 3. The band structures are seen to be very similar in overall nature, with the most significant differences occurring near the Γ point in the conduction band. For both, the maximum in the valence band is at the Γ point (0,0,0) due to the presence of parabolic-like bands of different curvature rising in energy towards E_F from the general manifold of occupied states. Both heavy and light holes will be present, therefore, in p-type material. The conduction band minimum for both materials, at the X point (1/2,0,1/2), is distinctly non-parabolic in character. Doped electrons and doped holes can therefore be expected to have quite different effective masses. The figure shows that the band gaps are indirect. Analysis of the orbital contributions to the bands indicates the presence of strong hybridization

of the Pd, Sb, and Lu states in both the valence and conduction bands closest to E_F, with a smaller contribution of the Sb states in the conduction band, as shown in figure 4. The band gap occurs at an electron count of 18 valence electrons per formula unit in both materials, and semiconductors are therefore expected for a wide range of combinations of chemical constituents at this electron count. The best ZT so far observed in the *Ln*PdSb half-Heusler series is approximately 0.06 at ambient temperature. The Seebeck coefficients in the tin based half-Heusler phases, HfNiSn and ZrNiSn, are very similar to those reported here, and indicate them to be n-type (5,6). These higher ZT values reported for the stannides at ambient temperature suggest that the mobilities of electrons in the half-Heusler phases may be larger than those of the holes.

Finally, we show in figure 5, the electrical characterization of the stoichiometric alloys of the $Ln_3Au_3Sb_4$ type. The figure shows that high Seebeck coefficients and small bandgap electrical behavior are also found in this class of materials, with especially promising behavior for the materials based on the smaller rare earths. Further optimization of these materials is presently underway.

The properties of both these materials families suggests that good thermoelectric properties may be a general characteristic of the large class of semiconducting materials with the half-Heusler structure and other cubic intermetallic structure types with significant metalloid content, and that related compounds yet to be tested may also be excellent thermoelectrics.

ACKNOWLEDGMENT

We gratefully acknowledge the support of the Seaver Foundation for this research. We also thank C. Felser for the band structure program and helpful conversations.

REFERENCES

1. B.C. Sales, D. Mandrus, and R.K. Williams, Science **272** 1325 (1996)
2. S. Ishida, T. Masaki, J. Fujii and S. Asano, Physica B **237-238** 363 (1997)
3. J. Tobola, J. Pierre, S. Kaprzyk, R.V. Skolozdra, and M. Kouacou, J. Phys: Condens. Matter **10** 1013 (1998)
4. S. Ogut and K.M. Rabe, Phys. Rev. **B51** 10,443 (1995)
5. W. Kafer, K. Fess, C. Kloc, K. Freimelt, E. Bucher, Proceedings ICT'97: 16th International Conference on Thermoelectrics, p. 489
6. C. Uher, H. Siqing, J. Yang, G.P. Meisner, D.T. Morelli, Proceedings ICT'97: 16th International Conference on Thermoelectrics, p. 485
7. O.K. Andersen and O. Jepsen, Phys. Rev. Lett. **53** 2571 (1984)
8. O.K. Andersen, Z. Pawlowska, and O. Jepsen, Phys. Rev. **B34** 5253 (1986)
9. see, e.g., H. Scherrer and S. Scherrer, in *CRC Handbook of Thermoelectrics*, D.M. Rowe, ed., CRC Press Inc., Boca Raton, FL, 1995, pp. 211-237

FLUX SYNTHESIS OF NEW MULTINARY BISMUTH CHALCOGENIDES AND THEIR THERMOELECTRIC PROPERTIES

DUCK-YOUNG CHUNG[1], KYOUNG-SHIN CHOI[1], PAUL W. BRAZIS[2], CARL R. KANNEWURF[2] AND MERCOURI G. KANATZIDIS[1*]

[1]*Department of Chemistry and Center for Fundamental Materials Research, Michigan State University, East Lansing, MI 48824.* [2]*Department of Electrical and Computer Engineering, Northwestern University, Evanston, IL 60208*

ABSTRACT

We present the synthesis and structure of the new chalcogenide compounds, $Rb_{0.5}Bi_{1.83}Te_3$, $APb_2Bi_3Te_7$ (A = Cs, Rb), $K_{1.25}Pb_{3.50}Bi_{7.25}Se_{15}$ and $A_{1+x}Pb_{4-2x}Sb_{7+x}Se_{15}$ (A = K, Rb). The layered structures of the first two telluride compounds are related to each other in a very interesting fashion. These compounds are n-type metallic conductors and solid solutions with Se and Sb have also been synthesized. $K_{1.25}Pb_{3.50}Bi_{7.25}Se_{15}$ and its Sb analogs have a complex three-dimensional structure composed of NaCl- and Bi_2Te_3-type building units. The thermal stability, melting behavior, electrical conductivity and thermopower of these compounds are reported.

INTRODUCTION

Although binary bismuth and lead chalcogenides such as Bi_2Te_3 and PbTe and their solid solutions[1,2] have been intensively studied for thermoelectric applications, the origin of their high thermoelectric figure of merits[3] of these compounds remains ill understood at the fundamental level. Furthermore, not until recently has serious attention been devoted to explore a new class of chemical system other than M_2Q_3 (M = Bi, Sb; Q = Se, Te).

The most distinguished electronic feature of Bi and Pb is the $6s^2$ lone pair electrons. The stereochemical expression of the $6s^2$ lone pair electrons influences the structure type and electronic structure, and consequently the electrical properties of Bi and Pb compounds. Because they exhibit very similar coordination geometry and crystallographic behavior, this chemistry produces diverse combinations of fragments which are essentially "excised" out of the structures of PbQ and Bi_2Q_3 (Q = S, Se, Te), as shown in the widely known mineral sulfo-, seleno-, and tellurosalts; $PbBi_2Q_4$ (Q = S[4], Se[5], Te[6]), $Pb_2Bi_2Q_5$ (Q = S[7], Se[8], Te[9]), $PbBi_4Q_7$ (Q = S[10], Se[11], Te[12]), $PbBi_6S_{10}$[13], $Pb_2Bi_6S_{11}$[14], $Pb_3Bi_2S_6$[15], $Pb_6Bi_2S_9$[16], $PbBiSe_2$[17], and $PbBi_6Se_7Te_2$[18].

In an effort to expand the Pb/Bi/Q chemistry and obtain thermoelectrically interesting materials, we added alkali metals in the system through the alkali metal polychalcogenide flux.[19] Introduction of alkali metal into the structure is expected to yield materials with more ionic character and greater structural and compositional complexity. This may lead to more complex electronic structure and higher thermoelectric power according to the Mott formula.[20] Our work with ternary A/Bi/Q (A = alkali metal; Q = S, Se, Te) systems[21] has shown that the alkali metals in the structure reside in the cages or tunnels of the covalent metal-chalcogenide framework. The phonon modes associated with the "rattling" of the alkali ions in these spaces are very soft and produce a phonon damping effect which results in dramatic reduction of the solid's lattice thermal conductivity.[22] A certain degree of disorder between alkali atoms and Bi atoms in the structure can also generate "mass fluctuation" scattering of the lattice phonons, which results in low thermal conductivity. This is consistent with the concept of "phonon glass electron crystal"[23] introduced by Slack as the limiting characteristic for a superior thermoelectric. Therefore, the role of alkali metals in a Pb/Bi/Q framework is expected to be similar to that in the A/Bi/Q system and it would be interesting to see how it affects the electrical properties of the resulting compounds.

Mat. Res. Soc. Symp. Proc. Vol. 545 © 1999 Materials Research Society

Here we describe two classes of new compounds, 1) two-dimensional telluride compounds, $Rb_{0.5}Bi_{1.83}Te_3$ and $APb_2Bi_3Te_7$ (A = Cs, Rb), and 2) three-dimensional selenide compounds, $K_{1.25}Pb_{3.5}Bi_{7.25}Se_{15}$ and $A_{1+x}Pb_{4-x}Sb_{7+x}Se_{15}$ (A = K, Rb). We report the synthesis, physicochemical, spectroscopic, structural, and charge transport characterization of these materials.

RESULTS AND DISCUSSION

The compound, $Rb_{0.5}Bi_{1.83}Te_3$, was synthesized in two different ways, a vapor transport of Rb metal to Bi_2Te_3 at 580 °C and a reaction of Bi_2Te_3 with an excess amount of Rb_2Te at 650 °C for 4 days. The summarized crystallographic data of $Rb_{0.5}Bi_{1.83}Te_3$ are shown in Table 1.

Table 1. Summary of Crystallographic Data for the Telluride Compounds

Formula	$Rb_{0.5}Bi_{1.83}Te_3$	$CsPb_2Bi_3Te_7$	$RbPb_2Bi_3Te_7$
Crystal habit	silvery needle	silvery needle	silvery needle
a (Å)	6.329(1)	4.4053(9)	4.4351(9)
b (Å)	28.216(4)	32.799(7)	32.710(7)
c (Å)	4.386(1)	12.667(3)	12.673(3)
Z, V (Å^3)	4, 783.2(3)	4, 1830.3(6)	4, 1838.5(6)
Space Group	Cmcm	Cmcm	Cmcm
Temperature (K)[1]	151	170	295
R/R_w (%)	5.4 / 6.7	5.9 / 6.6	5.1 / 10.8[2]

[1] the data collection temperature ; [2] R_1/wR_2 for all data

The structure of $Rb_{0.5}Bi_{1.83}Te_3$ is composed of $[Rb_{0.17}Bi_{1.83}Te_3]$ layers separated by Rb atoms, see Figure 1(a). The Rb and Bi atoms in this layer are statistically disordered (i.e. mixed occupancy). The $[Rb_{0.17}Bi_{1.83}Te_3]$ layer has a similar array of $[MTe_6]$ octahedra to that of Bi_2Te_3 and can be considered a fragment excised out of the NaCl structure. The excision is cut along the (110) plane of the NaCl-type lattice, while the Bi_2Te_3 layer is formed by excising along the (111) plane. As shown in Figure 1, these two types of layers have the same thickness of $[BiTe_6]$ octahedra and thus both have the same stoichiometry of $[M_2Te_3]$. Between the $[Rb_{0.17}Bi_{1.83}Te_3]$ layers, Rb atoms are sandwiched whose sites are filled only at the 0.667 level occupancy. Therefore, this compound can be formulated as $Rb_{0.33}[Rb_{0.17}Bi_{1.83}Te_3]$.

The statistical disorder of Rb and Bi atoms inside the $[Rb_{0.17}Bi_{1.83}Te_3]$ layer and Rb site vacancies in the interlayer space are the novel structural features of this compound. The Rb atoms between the layers display some mobility due to the available vacant space, which is responsible for the high thermal parameter of 4.0. This situation indicates that Rb atoms indeed "rattle" between the layers and may favorably impact the thermal conductivity of $Rb_{0.5}Bi_{1.83}Te_3$. On the other hand, Rb atoms in the layers are expected to create the discontinuity of the covalent bonding in the $[Rb_{0.17}Bi_{1.83}Te_3]$ framework. The presence of these ionic species, therefore, may give rise to low symmetry of the $[Rb_{0.17}Bi_{1.83}Te_3]$ band structure compared to that of Bi_2Te_3.

The "as made" single crystals of $Rb_{0.5}Bi_{1.83}Te_3$ show n-type metallic behavior with conductivity of 925 S/cm and thermopower of -41 μV/K at room temperature, see Figure 2(a). Because the compound is valence precise, it is likely to be a narrow-gap material or a semimetal. A semimetal could result from near contact or even partial overlap of conduction and valence bands at the Fermi level. The exact nature of the electronic structure near the Fermi level will not be known until further experiments and an electronic band structure calculation are performed.

To examine whether the band-gap width responds to the partial substitution of Sb atoms in the Bi sites or Se atoms in the Te sites, we prepared solid solutions of Sb and Se with 5 and 10

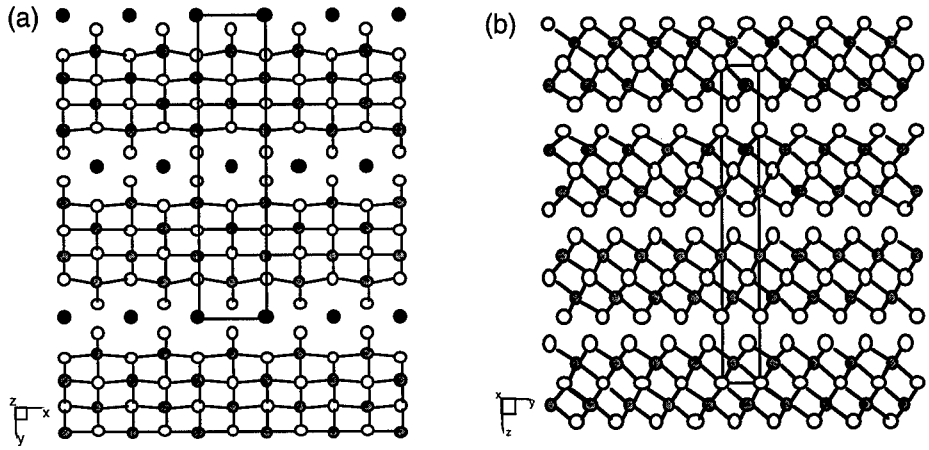

Figure 1. The structure of $Rb_{0.5}Bi_{1.83}Te_3$ viewed down c-axis and (b) Bi_2Te_3 viewed down a-axis. Open circles are Te atoms, light gray circles Bi atoms.

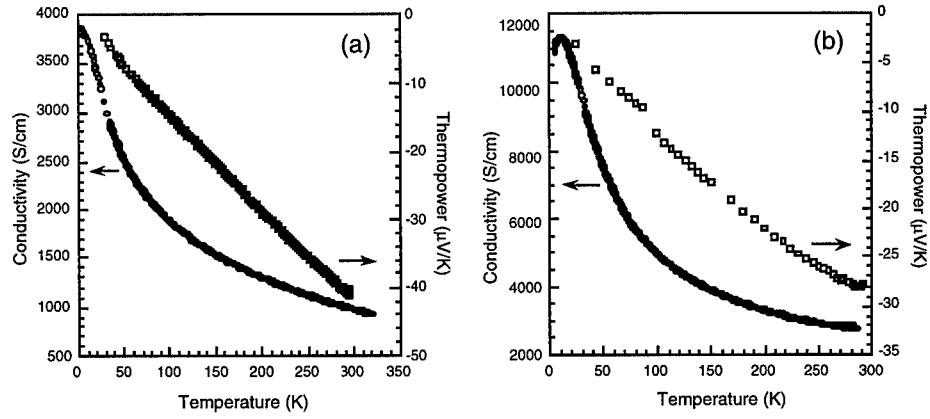

Figure 2. Variable temperature electrical conductivity and thermopower data for a single crystal of (a) $Rb_{0.5}Bi_{1.83}Te_3$ and (b) $Rb_{0.5}Bi_{1.65}Sb_{0.18}Te_3$.

mol %, respectively, which correspond to $Rb_{0.5}Bi_{1.74}Sb_{0.09}Te_3$, $Rb_{0.5}Bi_{1.65}Sb_{0.18}Te_3$, $Rb_{0.5}Bi_{1.83}Te_{2.85}Se_{0.15}$, and $Rb_{0.5}Bi_{1.83}Te_{2.70}Se_{0.30}$. The room temperature conductivities of these solid solutions are 738, 2950, 1872, and 1106 S/cm, and thermopowers -41, -28, -31, -31 μV/K, respectively, see Figure 2(b). Although the thermopower values of the solid solutions are still low and remain almost unchanged, this manipulation of the composition gives rise to a significant change in the electrical conductivity which are attributed to the change of the bands near the Fermi level and the number of carriers. The substitution of Se for Te is expected to increase the band gap of the compound and result in lower electrical conductivity. The fact that this is not observed suggests that either there is no significant band gap in the compound (i.e. a semimetal) or the amount of Se added is not enough yet to bring about significant changes in the charge transport properties. We will test the latter hypothesis by attempting to increase the Se/Te ratio in the compound. The extension of this type of substitution is known, but it is noteworthy that the $Rb_{0.33}[Rb_{0.17}Bi_{1.83}Se_3]$ compound has not been observed thus far.

The compounds $APb_2Bi_3Te_7$ (A = Cs, Rb) were prepared by a stoichiometric reaction of a corresponding mixture of Pb/Bi/Te/A_2Te at 720 °C. The crystallographic data of $APb_2Bi_3Te_7$ (A = Cs, Rb) are summarized in Table 1. These two compounds are isostructural and possess a very similar type layer to that observed in the structure of $Rb_{0.5}Bi_{1.83}Te_3$. In the $APb_2Bi_3Te_7$, the alkali metal atoms reside only between the layers. The $[Pb_2Bi_3Te_7]$ (M_5Te_7; M = Bi, Pb) layer consists of $[2M_2Te_3]$ (M_4Te_6) layer, which is the exactly same structural framework as $[Rb_{0.17}Bi_{1.83}Te_3]$ (M_2Te_3) in $Rb_{0.5}Bi_{1.83}Te_3$, with an additional [MTe] monolayer attached. Therefore, the $[Pb_2Bi_3Te_7]$ layer is one [BiTe] unit thicker than $[Rb_{0.17}Bi_{1.83}Te_3]$, as shown in Figure 1(a) and 3(a). The distinction between Pb and Bi atoms in Pb/Bi mixed structures was not possible due to almost identical X-ray scattering power (Z_{Bi} = 83, Z_{Pb} = 82). In $APb_2Bi_3Te_7$, we tentatively assume that the Pb atoms are disordered over all Bi atom sites.

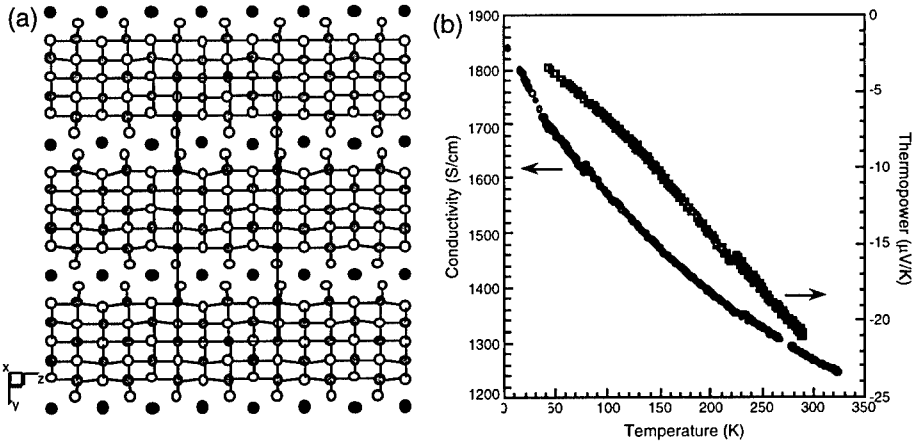

Figure 3. (a) The structure of $CsPb_2Bi_3Te_7$ viewed down a-axis and (b) variable temperature electrical conductivity and thermopower data for a single crystal of $RbPb_2Bi_3Te_7$.

The temperature dependence of conductivity and thermopower of $RbPb_2Bi_3Te_7$ is shown in Figure 3(b). The compound $CsPb_2Bi_3Te_7$ has a similar behavior in both conductivity and thermopower, which reveal n-type conductor. The room temperature conductivity and

thermopower are 970 S/cm and -20 μV/K for $CsPb_2Bi_3Te_7$, and 1270 S/cm and -20 μV/K for $RbPb_2Bi_3Te_7$. Interestingly, the values and behavior over the temperature change are very similar to those of $Rb_{0.5}Bi_{1.83}Te_3$. First attempts to prepare solid solutions were also carried out for $APb_2Bi_3Te_7$ (A = Cs, Rb) with Se of 10 mol %. Both the electrical conductivity and thermopower remained essentially unaffected in this system (at room temperature, 520 S/cm and -18 μV/K for $CsPb_2Bi_3Te_{6.3}Se_{0.7}$, and 1100 S/cm and -25 μV/K for $RbPb_2Bi_3Te_{6.3}Se_{0.7}$). This indicates that thicker layer may give rise to the wider band which is less affected by a small scale of compositional modification. The substitution with larger quantities of Se will be tried.

Materials with metallic properties have been ruled out in the field of thermoelectrics because they typically possess low thermopower and high thermal conductivity. However, the alkali metals in these compounds are likely to lead to intrinsically low lattice thermal conductivity due to the rattling effect of the alkali atoms inside the structural framework. This suggests that the challenge in achieving high figure of merit in this system is only the improvement of thermopower. We plan to carry out more extensive studies including the band structure calculations on $Rb_{0.5}Bi_{1.83}Te_3$ and $APb_2Bi_3Te_7$ to get a better idea, which suggest the correct type of compositional changes needed for optimization.

When the Te was replaced by Se a completely different type of compound was discovered. The isostructural compounds, $K_{1.25}Pb_{3.50}Bi_{7.25}Se_{15}$ and $A_{1+x}Pb_{4-2x}Sb_{7+x}Se_{15}$ (A = K, Rb), were obtained in pure form as silvery needles by reactions of A_2Se, Pb, Bi_2Se_3/Sb_2Se_3, and Se at 540 °C for 5 days. The crystallographic data of these compounds are summarized in Table 2.

Table 2. Summary of Crystallographic Data for the Selenide Compounds.

Formula	$K_{1.25}Pb_{3.50}Bi_{7.25}Se_{15}$	$K_{1+x}Pb_{4-x}Sb_{7+x}Se_{15}$(I)	$K_{1+x}Pb_{4-x}Sb_{7+x}Se_{15}$(II)	$Rb_{1+x}Pb_{4-x}Sb_{7+x}Se_{15}$
Crystal habit	black needle	black needle	black needle	black needle
a (Å)	17.4481(8)	17.1204(6)	17.167(4)	17.3160(7)
b (Å)	4.1964(2)	4.1568(2)	4.1494(9)	4.1406(2)
c (Å)	21.695(1)	21.6362(8)	21.684(5)	21.6401(8)
β (deg)	98.850(1)	98.706(1)	98.664(3)	99.139(1)
Z, V (Å^3)	2, 1569.54(13)	2, 1522.02(11)	2, 1527.0(6)	2, 1531.87(11)
Space Group	$P2_1/m$	$P2_1/m$	$P2_1/m$	$P2_1/m$
Temperature (K) [1]	298	171	298	171
R_1/wR_2 (%) [2]	9.10 / 12.11	8.50 / 12.12	6.05 / 13.64	6.03 / 9.86

[1] the data collection temperature. ; [2] final values for all data.

In the $K_{1+x}Pb_{4-2x}Sb_{7+x}Se_{15}$ system, two different ratios of the starting materials yielded two compounds, $K_{1+x}Pb_{4-2x}Sb_{7+x}Se_{15}$(I) with high Pb content and $K_{1+x}Pb_{4-2x}Sb_{7+x}Se_{15}$(II) with low Pb content. The exact x values could not be determined by X-ray single crystal study due to the disorder and simultaneous occupancy of three different distinguishable species, K^+, Pb^{2+}, and Sb^{3+}, on one crystallographic site. Therefore, we report the compositions of the compounds based on the results of SEM/EDS analysis as $K_{1+x}Pb_{4-2x}Sb_{7+x}Se_{15}$ ($x \approx 0.45$ for (I), 1.15 for (II)) and $Rb_{1+x}Pb_{4-2x}Sb_{7+x}Se_{15}$ ($x \approx 0.45$), respectively. It should be noted that $K_{1+x}Pb_{4-x}Sb_{7+x}Se_{15}$(II) contains only one half of Pb atoms present in $K_{1+x}Pb_{4-x}Sb_{7+x}Se_{15}$(I). In the Bi compound, Bi^{3+} and Pb^{2+} could be regarded as the same species in a crystallographic sense. Therefore, the disorder could be though of as between K^+ and (Pb^{2+}/Bi^{3+}) and the occupancy of the K^+ ions and the combined (Pb^{2+}, Bi^{3+}) ions were able to determined. Then, the occupancies of Pb^{2+} and Bi^{3+} ions were calculated under the assumption that this material is

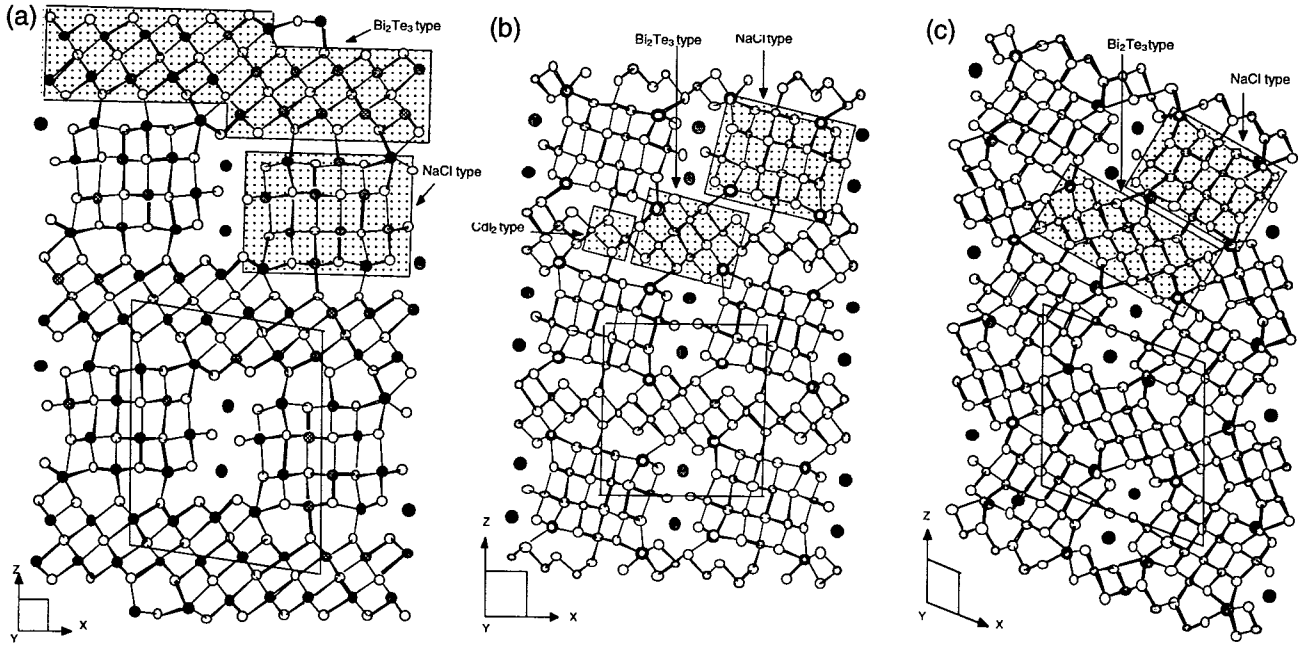

Figure 4. The structures of (a) $K_{1.25}Pb_{3.5}Bi_{7.25}Se_{15}$, (b) β-$K_2Bi_8Se_{13}$, and (c) $K_{2.5}Bi_{8.5}Se_{14}$ viewed down b-axis. In each case, NaCl-, Bi_2Te_3- and CdI_2-type fragments are highlighted by the shaded areas.

valence precise, and the composition proposed is $K_{1.25}Pb_{3.50}Bi_{7.25}Se_{15}$. This reasonably agrees with the composition $K_{1.4}Pb_{3.2}Bi_{7.4}Se_{15}$ obtained from SEM/EDS analysis.

These compounds have a three dimensional framework which contains NaCl- and Bi_2Te_3-type units connecting to each other to form K^+ filled tunnels. Figure 4(a) shows the structure of $K_{1.25}Pb_{3.50}Bi_{7.25}Se_{15}$ viewed down the b-axis. This structure is closely related to those of β-$K_2Bi_8Se_{13}$ and $K_{2.5}Bi_{8.5}Se_{14}$[21]. The local environment of alkali metal ion and the size of the NaCl-type block in $K_{1.25}Pb_{3.50}Bi_{7.25}Se_{15}$ are exactly same as those of β-$K_2Bi_8Se_{13}$ and $K_{2.5}Bi_{8.5}Se_{14}$, see Figure 4(b) and (c). Only the size of the Bi_2Te_3-type unit in each compound is different.

The relationship between these compounds can easily be seen if the composition is broken down into two parts, the anionic framework and the alkali metal in the tunnels. For example, in β-$K_2Bi_8Se_{13}$, one equivalent of K^+ is stabilized in the tunnel and the other equivalent of K^+ is disordered with Bi atoms in the anionic framework. Therefore, the formula can be described as $K^+[KBi_8Se_{13}]^-$ or $K^+[M_9Se_{13}]^-$ (M = K + Bi in the anionic framework). In the same way, $K_{2.5}Bi_{8.5}Se_{14}$ can be described as $K^+[M_{10}Se_{14}]^-$ and $K_{1.25}Pb_{3.5}Bi_{7.25}Se_{15}$ as $K^+[M_{11}Se_{15}]^-$ (M = K + Bi + Pb in the anionic framework). Therefore, $K_{2.5}Bi_{8.5}Se_{14}$ and $K_{1+x}Pb_{4-2x}Bi_{7+x}Se_{15}$ are the results of successively adding of "MSe" units to $K_2Bi_8Se_{13}$ as follows.

$$K^+[KBi_8Se_{13}]^- \xrightarrow{[MSe]} K^+[KBi_9Se_{14}]^- \xrightarrow{[MSe]} K^+[K_{0.25}Pb_{3.5}Bi_{7.25}Se_{15}]^-$$
$$K^+[M_9Se_{13}]^- \qquad\qquad K^+[KM_{10}Se_{14}]^- \qquad\qquad K^+[M_{11}Se_{15}]^-$$

This structure type is flexible enough to preserve the basic framework through successive addition of "MSe" equivalents by adjusting the width of the Bi_2Te_3-type blocks.

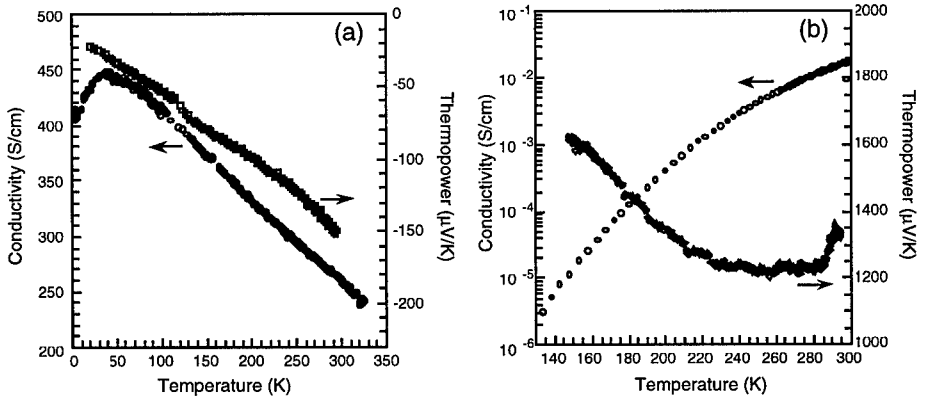

Figure 5. Variable temperature electrical conductivity and thermopower data for a single crystal of (a) $K_{1.25}Pb_{3.5}Bi_{7.25}Se_{15}$ (b) $Rb_{1+x}Pb_{4-x}Sb_{7+x}Se_{15}$.

The electrical properties of these compounds were measured from single crystal samples. The room temperature conductivity of $K_{1.25}Pb_{3.50}Bi_{7.25}Se_{15}$ was obtained around 260 S/cm. The conductivity shows a metallic trend between 300 K and 50 K and it turns semiconducting below 50 K, see Figure 5(a).

$K_{1.25}Pb_{3.50}Bi_{7.25}Se_{15}$ shows quite large negative Seebeck coefficients, -150 μV/K at room temperature. The negative sign indicates that charge carriers are electrons (n-type). The electrical conductivities of Sb compounds are 10^5 times smaller than that of the Bi compound. The conductivity and thermopower data of $Rb_{1+x}Pb_{4-x}Sb_{7+x}Se_{15}$ are shown in Figure 5(b). The compounds, $K_{1+x}Pb_{4-x}Sb_{7+x}Se_{15}$(I), $K_{1+x}Pb_{4-x}Sb_{7+x}Se_{15}$(II), and $Rb_{1+x}Pb_{4-x}Sb_{7+x}Se_{15}$, exhibit a similar semiconducting behavior with room temperature conductivity of 2.6 x 10^{-3}, 1.2 x 10^{-3}, and 1.7 x 10^{-2} S/cm, respectively. $K_{1+x}Pb_{4-x}Sb_{7+x}Se_{15}$(I), which has a higher Pb content, shows higher conductivity than $K_{1+x}Pb_{4-x}Sb_{7+x}Se_{15}$(II). The room temperature Seebeck coefficients of these Sb compounds are 1029, 1071, and 1331 μV/K, respectively. Despite the different electrical conductivities, $K_{1+x}Pb_{4-x}Sb_{7+x}Se_{15}$(I) and $K_{1+x}Pb_{4-x}Sb_{7+x}Se_{15}$(II) exhibit similar thermopower suggesting that the electrical conductivity can be increased by increasing the Pb content in the structure without concomitant loss of thermopower. Unlike $K_{1.25}Pb_{3.50}Bi_{7.25}Se_{15}$, the Sb compounds are p-type conductors.

Diffuse reflectance spectroscopy revealed the presence of band gaps at 0.53, 0.45, 0.60, 0.36 eV at room temperature for $K_{1.25}Pb_{3.50}Bi_{7.25}Se_{15}$, $K_{1+x}Pb_{4-x}Sb_{7+x}Se_{15}$(I), $K_{1+x}Pb_{4-x}Sb_{7+x}Se_{15}$(II), and $Rb_{1+x}Pb_{4-x}Sb_{7+x}Se_{15}$, respectively, see Figure 6. The band gap of $K_{1+x}Pb_{4-x}Sb_{7+x}Se_{15}$(I) is narrower than that of $K_{1+x}Pb_{4-x}Sb_{7+x}Se_{15}$(II), which is consistent with the electrical conductivity data.

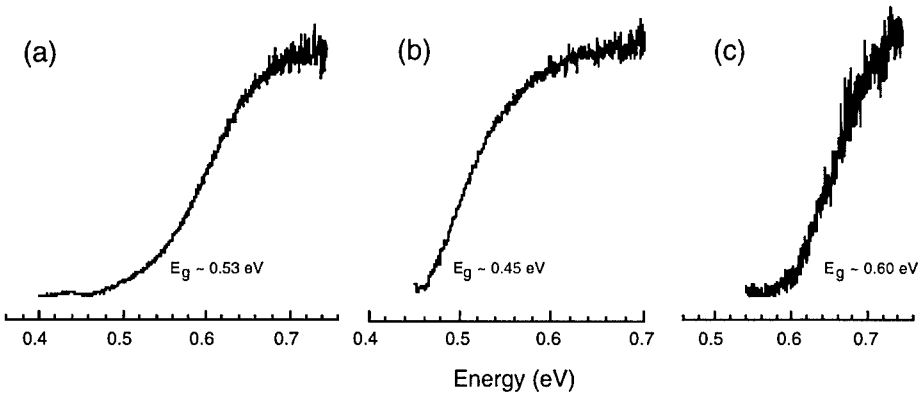

Figure 6. Optical absorption spectra of (a) $K_{1.25}Pb_{3.5}Bi_{7.25}Se_{15}$, (b) $K_{1+x}Pb_{4-x}Sb_{7+x}Se_{15}$(I), and (c) $K_{1+x}Pb_{4-x}Sb_{7+x}Se_{15}$(II). The band gap values, E_g in eV, are shown.

DTA measurements show that $Rb_{0.5}Bi_{1.83}Te_3$, $CsPb_2Bi_3Te_7$, and $RbPb_2Bi_3Te_7$ melt incongruently at 540, 582, 579 °C, respectively, and $K_{1.25}Pb_{3.5}Bi_{7.25}Se_{15}$, $K_{1+x}Pb_{4-x}Sb_{7+x}Se_{15}$(I), $K_{1+x}Pb_{4-x}Sb_{7+x}Se_{15}$(II), and $Rb_{1+x}Pb_{4-x}Sb_{7+x}Se_{15}$ melt congruently at 685, 576, 576, and 578 °C, respectively.

CONCLUDING REMARKS

Synthetic investigations in the multinary bismuth chalcogenide system resulted in several new and interesting compounds. The two-dimensional compounds, $Rb_{0.5}Bi_{1.83}Te_3$ and $APb_2Bi_3Te_7$ (A = Cs, Rb), showed n-type metallic behaviors with relatively high conductivity and low thermopower. These electrical properties are not dependent on the size of alkali atoms and the thickness of the $[MTe]_x$ (M = Bi, Pb) layers. Based on the preliminary results obtained with solid solutions of Sb and Se, large amount of these elements should be added in the compounds to see changes in the properties. Also p-type doping should be pursued. The three-dimensional $K_{1.25}Pb_{3.50}Bi_{7.25}Se_{15}$ and $A_{1+x}Pb_{4-2x}Sb_{7+x}Se_{15}$ (A = K, Rb) have been identified as semiconductors. The study on two members of $K_{1+x}Pb_{4-2x}Sb_{7+x}Se_{15}$ showed that this structure can be formed with various ratios of A/Pb/Sb and that this compositional change seems to affect the electrical conductivity without changing the thermopower. Based on these results, we suggest that $K_{1.25}Pb_{3.50}Bi_{7.25}Se_{15}$, which showed rather promising electrical properties, should be further optimized by tuning the Pb content in the structure.

ACKNOLEDGEMENTS

Financial support from the Office of Naval Research (Contract No. N00014-98-1-0443) is gratefully acknowledged. At NU this work made use of Central Facilities supported by NSF through the Materials Research Center (DMR-96-32472).

REFERENCES

1. (a) Ainsworth, R. S.; Scanlon, W. W. *Phys. Rev.*, **1958**, *111*, 1029. (b) Goldsmid, H. J. *Thermoelectric Refrigeration*; Pion Ltd.: London, 1986. (c) Yim, W.; Rosi, F. D. *Solid State Electron.*, **1972**, *15*, 1121. (d) Rosi, F. D.; Ramberg, F. G. Thermoelectricity, Egli, P. M., Ed.; John Wiley & Sons: New York, 1960. (e) Jeon, H. -H.; Ha, H. -P.; Hyun, D. -B.; Shim, J. -D. *J. Phys. Chem. Solids*, **1991**, *4*, 579-585.
2. (a) Rowe, D. M.; Bhandari, C. M. *Modern thermoelectrics*; Holt, Rinehart, and Winston: London, 1983. (b) Ravich, Y. I.; Efimova, B. A.; Smirnov, I. A. *Semiconducting Lead Chalcogenides*; Stilbans, L. S., Ed.; Plenum Press: New York, 1970. (c) Parker, S. G.; Johnson, R. E. "Preparation and Properties of (Pb,Sn)Te" in *Preparation and Properties of Solid State Materials*, Vol. 6; Wilcok, W. R., Ed.; Dekker: New York, 1981.
3. Thermoelectric figure of merit; $ZT = (\sigma \cdot S^2/\kappa) \cdot T$, where σ is electrical conductivity, S thermoelectric power, κ thermal conductivity, and T temperature.
4. (a) Iitaka, Y.; Nowacki, W. *Acta Cryst.*, **1962**, *15*, 691-698 (b) Takeuchi, Y.; Takagi, J. *Proc. Japan Acad.*, **1974**, *50*, 222-225.
5. Agaev, K. A.; Semiletov, S. A. *Soviet Phys. - Crystallogr.*, **1968**, *13*, 201-203.
6. Zhkova, T. B.; Zaslavskii, A. I. *Soviet Phys. - Crystallogr.*, **1971**, *16*, 796-800.
7. Srikrishnan, T.; Nowacki, W. Z. *Z. Kristallogr.* **1974**, *140*, 114-136.
8. Agaev, K. A.; Talybov, A. G.; Semiletov, S. A. *Kristallografiya*, **1966**, *11*, 736-740.
9. Petrov, I. I.; Imamov, R. M. *Soviet Phys. - Crystallogr.*, **1969**, *14*, 593-596.

10. Takeuchi, Y.; Takagi, J.; Yamanaka T. *Proc. Japan Acad.*, **1974**, *50*, 317-321.

11. Takeuchi, Y.; Takagi, J. *Proc. Japan Acad.*, **1974**, *50*, 76-79.

12. (a) Golovanova, N. S.; Zlomanov, V. P.; Tannaeva, O. I. *Inorg. Mater.*, **1983**, *19*, 669-672. (b) Zhkova, T. B.; Zaslavskii, A. I. *J. Strut. Chem.*, **1970**, *11*, 423-428.

13. Otto, H. H.; Strunz, H. *N. Jb. Miner. Abh.*, **1968**, *108*, 1-9.

14. Tilley, R. J. D.; Wright, A. C. *J. Solid State Chem.*, **1986**, *65*, 45-62.

15. Takagi, J.; Takeuchi, Y. *Acta Cryst.*, B, **1972**, *28*, 649-651.

16. Takeuchi, Y.; Takagi, J. *Proc. Japan Acad.*, **1974**, *50*, 76-79.

17. Palatnik, L. S.; Konovalov, O. M.; Gladkikh, N. T.; Kolesnikov, V. N. *Phys. Metal Metallogr.*, **1961**, *15*, 36-39.

18. Kapinskij, O. G. *Acta Crystallogr. A*, **1978**, *34A*, S80.

19. Kanatzidis, M. G.; Sutorik, A. C. *Prog. Inorg. Chem.*, **1995**, *43*, 151-265.

20. Chung, D.-Y.; Choi, K-.S; Iordanidis, L.; Schindler, J. L.; Brazis, P. W.; Kannewurf, C. R.; Chen, B.; Hu, S.; Uher C.; Kanatzidis, M. G. *Chem. Mater.*, **1997**, *9*, 3060-3071.

21. (a) Kanatzidis, M. G.; DiSalvo, F. J. *Naval Research Reviews*, **1996**, *4*, 14-22. (b) reference 20

22. Kanatzidis, M. G.; McCarthy, T. J.; Tanzer, T. A.; Chen, L. -H.; Iordanidis, L.; Hogan, T.; Kannewurf, C. R.; Uher, C.; Chen, B. *Chem. Mater.*, **1996**, *8*, 1465-1474.

23. (a) Slack, G. A. "New Materials and Performance Limits for Thermoelectric Cooling" in *CRC Handbook of Thermoelectrics*; Rowe, D. M., Ed.; CRC Press: Boca Raton, 1995, pp. 407-440. (b) Slack, G. A. *Solid State Physics*; Ehrenreich, H.; Seitz, F.; Turnbull, D., Ed.; Academic: New York, **1997**, *34*, 1

TRANSPORT PROPERTIES OF DOPED $CsBi_4Te_6$ THERMOELECTRIC MATERIALS

PAUL W. BRAZIS*, MELISSA ROCCI*, DUCK-YOUNG CHUNG**, MERCOURI G. KANATZIDIS**, AND CARL R. KANNEWURF*,

*Department of Electrical and Computer Engineering, Northwestern University, Evanston, IL 60208-3118
**Department of Chemistry and Center for Fundamental Materials Research, Michigan State University, East Lansing, MI 48824-1322

ABSTRACT

In previous investigations we have introduced a variety of new chalcogenide-based materials with promising properties for thermoelectric applications. The chalcogenide $CsBi_4Te_6$ was previously reported to have a high ZT product with a maximum value at 260K. In order to improve this value, a series of doped $CsBi_4Te_6$ samples has been synthesized. Current doping studies have been very encouraging, with one sample found to have a maximum power factor of 51.5 $\mu W/cm \cdot K^2$ at 184 K. This paper reports on material characterization studies through the usual transport measurements to determine optimum doping concentration for various dopants.

INTRODUCTION

Previously reported materials derived chemically and/or structurally from Bi_2Te_3 have shown transport properties favorable for applications such as thermoelectric cooling devices[1-4]. In particular, the material $CsBi_4Te_6$ has exhibited similar electrical properties as Bi_2Te_3, but the lower crystal symmetry acts to reduce the thermal conductivity[5]. The previously reported maximum value of ZT was 0.32 at 260K. This suggested that optimizing the thermoelectric properties of $CsBi_4Te_6$ by the introduction of dopants may result in a composition approaching the performance of Bi_2Te_3. In addition to improving ZT, it was desirable to create both n- and p-type materials, which are necessary for the realization of a practical device. This report describes the thermoelectric properties of $CsBi_4Te_6$ doped with varying concentrations of SbI_3, BiI_3, SnTe, and In_2Te_3 with an emphasis on the data for SbI_3 which gave the highest power factor for these dopants.

EXPERIMENTAL

Single crystal samples of doped $CsBi_4Te_6$ were prepared as described elsewhere[6-8]. Crystals of $CsBi_4Te_6$ doped with varying concentrations of SbI_3, BiI_3, SnTe, and In_2Te_3 were synthesized. Some crystals of doped $CsBi_4Te_6$ were annealed in order to observe the influence on transport properties. The resulting crystals showed a thin, needle-like morphology with a typical cross-sectional area in the range of 10 to 200 square microns. Larger samples generally consisted of fused bundles of smaller crystals, which were not desirable for transport measurements. Single crystals typically exhibited lengths on the order of 1 to 10 mm along the needle axis, which provided an excellent geometry for electrical conductivity and Seebeck measurements. Several samples of each composition were examined in order to ensure that the transport properties were reproducible among the crystals.

The electrical conductivity of the prepared single crystals was measured using a computer-controlled, four-probe technique[9]. Electrical contacts consisted of fine gold wire (25 to 60 μm diameter) attached to the crystals with gold paste. Contacts with gold paste have been found to be superior to those made with silver paste for these materials. Samples were placed under vacuum for at least 24 hours to allow the gold paste to dry completely, which improved contact performance. Excitation currents were kept as low as possible, typically below 1 mA, in order to minimize any non-ohmic voltage response and thermoelectric effects at the contact-sample interface.

Mat. Res. Soc. Symp. Proc. Vol. 545 © 1999 Materials Research Society

Variable-temperature (4.2K to 295K) thermopower data were taken using a slow-ac measurement technique[10]. The measurement apparatus featured Au(0.07% Fe)/Chromel differential thermocouples for monitoring the applied temperature gradients. Samples were mounted on 60 μm gold wire using gold paste. Fine gold wire (10 μm in diameter) was used for sample voltage contacts, which were made as long as possible in order to minimize thermal conduction through the leads. The sample and thermocouple voltages were measured using Keithley Model 181 and Keithley Model 182 nanovoltmeters, respectively. The applied temperature gradient was in the range of 0.1 to 0.4 K. Measurements were taken under a turbopumped vacuum maintained below 10^{-5} Torr. The sample chamber was evacuated for at least one hour prior to cooling to remove any residual water vapor or solvents in the gold paste. Mobility and carrier concentration data were obtained using dc Hall effect measurements. Applied current and magnetic field strength were typically 10 mA and 7 kG, respectively. Electrical conductivity and Hall effect data were taken simultaneously; mobility values were calculated from these data.

RESULTS

The crystal structure of $CsBi_4Te_6$ has been reported previously[7,8]. Like other alkali-metal Bi-Te compounds, these materials display a layered crystal structure that is derived from Bi_2Te_3, exhibiting a structure with the alkali metal atoms between adjacent Bi_2Te_3 layers. Electrical conductivity data for all doped samples exhibited a similar temperature dependence as the undoped $CsBi_4Te_6$ samples. The data generally displayed a weak metallic dependence, with the conductivity decreasing as temperature increased from 4.2 K to 340 K as shown in Figure 1 for the SbI_3 dopant. Room temperature (295 K) electrical conductivities ranged from 417 S/cm (0.3% SbI_3) to 2100 S/cm (1.5% In_2Te_3). These values are generally greater than the conductivity for the undoped $CsBi_4Te_6$, which was found to have an average conductivity of 363 S/cm at room temperature. Annealing of the crystals decreased the measured electrical conductivity by as much as 60%. For example, the room temperature electrical conductivity of the 0.2% BiI_3-doped samples dropped from a range of 859-1110 S/cm to 511-805 S/cm.

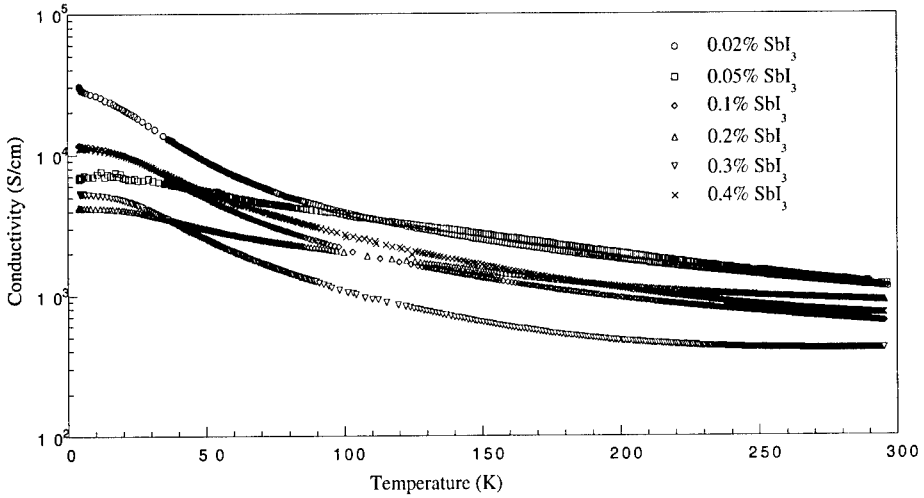

Figure 1. Temperature-dependent conductivity of series of SbI_3-doped $CsBi_4Te_6$ samples.

Thermopower data, shown in Figure 2 for the SbI_3 dopant, exhibited similar behavior as the undoped $CsBi_4Te_6$ material[5]. The p-type thermoelectric response tended toward zero as the

temperature approached 0 K, which is characteristic of metallic materials. However, the range of the thermopower magnitudes above 100 K is more typical of semiconductors. The maximum value of +177 μV/K obtained for the 0.05% doped sample at 238 K is significantly higher than the maximum value of +116 μV/K obtained for undoped $CsBi_4Te_6$ just below 300 K. For the various dopants maximum thermopower values were generally found at or slightly below 300 K depending on dopant type and doping level.

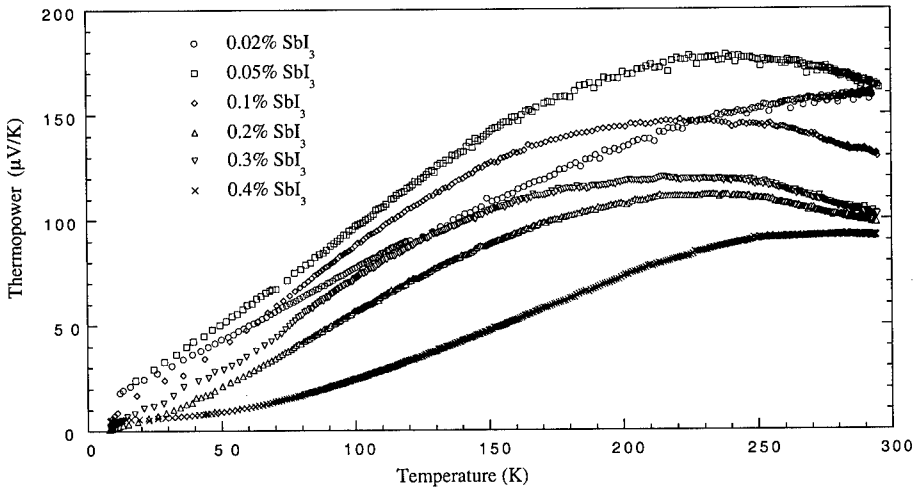

Figure 2. Temperature-dependent thermopower for a series of SbI_3-doped $CsBi_4Te_6$ samples.

Hall effect measurements for SbI_3-doped samples show that carrier concentrations are on the order of 10^{18} to 10^{19} cm^{-3} for samples doped at 0.1% and 0.2% SbI_3 (Figure 3a). Hole mobilities calculated from the electrical conductivity and Hall data show exponentially decreasing mobility as temperature increases. Mobilities show an increase as the carrier concentration increases from 0.1% to 0.2% SbI_3 (Figure 3b).

DISCUSSION

The four dopants were chosen in order to create both n- and p-type materials, which are necessary for the design of a practical thermoelectric device. The In_2Te_3 and SnTe dopants were intended to substitute the bismuth in the Bi_2Te_3 layers of $CsBi_4Te_6$ with indium and tin, respectively. This should introduce holes, resulting in p-type material. Thermopower data confirm that these samples give the expected p-type response. The SbI_3- and the BiI_3-doped materials were expected to show n-type behavior, with the intent that iodine would replace tellurium in the Bi_2Te_3 layers of $CsBi_4Te_6$, introducing one electron per iodine atom. However, these materials showed p-type behavior as well. This is what would be expected if antimony and bismuth replaced tellurium sites. Further work is in progress to explain this behavior in $CsBi_4Te_6$.

The conductivity and thermopower data were used to calculate the power factors, $S^2\sigma$, for each dopant versus temperature and doping concentration. The power factor data were used to determine optimal doping levels for each dopant, as well as the temperature where the power factor was a maximum. From these data, the optimal concentration for each dopant was found. The most promising material was 0.05% SbI_3-doped $CsBi_4Te_6$, which shows a maximum power factor of 51.5 $\mu W/cm \cdot K^2$ at 184 K (Figure 4). This value is 17% higher than the maximum power factor for undoped $CsBi_4Te_6$ which occurs at ≈180 K. It is interesting to compare the maximum power factor for a commercially prepared p-type alloy of Bi_2Te_3 with the SbI_3 doped $CsBi_4Te_6$ data as

shown in Figure 4[14]. The maximum power factor for the Bi_2Te_3 sample is 42.5 $\mu W/cm \cdot K^2$ at ≈225 K which is below the range of maximum values for all 0.05% SbI_3-doped samples examined.

The next highest power factor is 45.0 $\mu W/cm \cdot K^2$ at 147 K for the 0.3% BiI_3-doped samples. Both the maximum and room temperature power factors for all doped materials are shown in Table I.

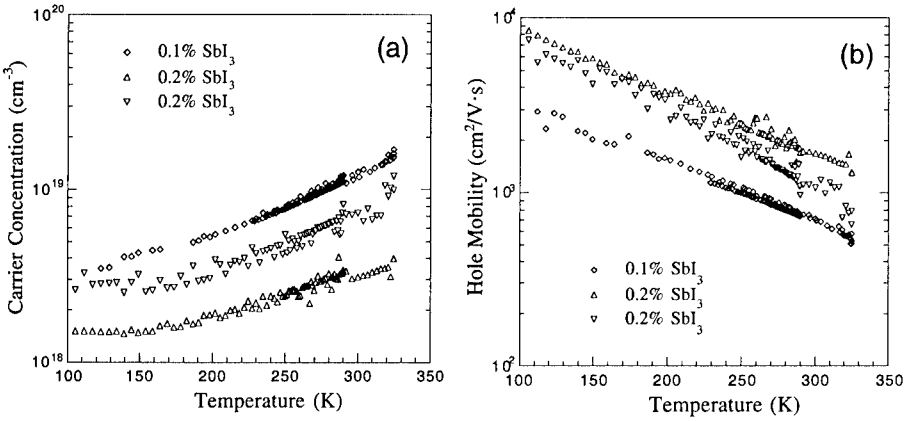

Figure 3. Carrier concentration (a) and mobility (b) for typical samples of the 0.1% and 0.2% SbI_3-doped $CsBi_4Te_6$.

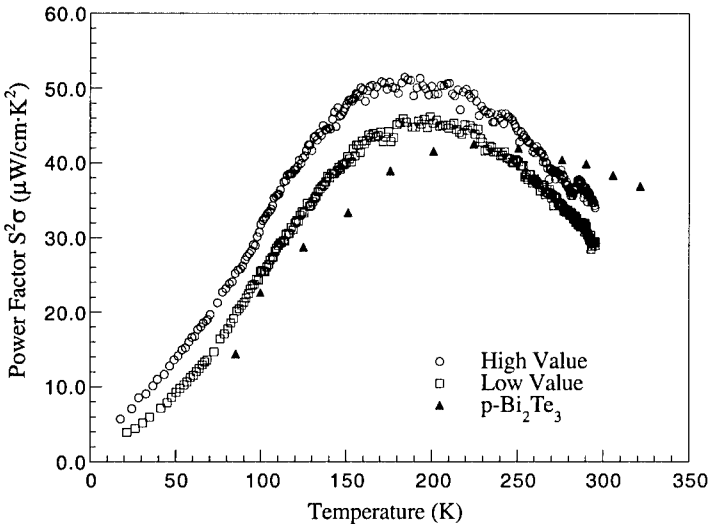

Figure 4. Power factor versus temperature for 0.05% SbI_3-doped $CsBi_4Te_6$. Data for all other samples examined at this doping level fall between these curves. Also shown for comparison are data from a sample of p-type Bi_2Te_3[14].

Table I. Power factor values for each dopant at room temperature and the temperature where the maximum value occurs. Maximum power factor observed for each dopant identified by (*).

Dopant	Concentration, %	$S^2\sigma$ at 295 K, $\mu W/cm \cdot K^2$	Maximum $S^2\sigma$, $\mu W/cm \cdot K^2$	Maximum $S^2\sigma$, Temperature (K)
p-Bi_2Te_3[a]	—	39.9	42.5	225
Undoped[b]	—	31.7	45.4	186
Undoped[c]	—	4.82	6.40	211
SbI_3	0.02	26.7	28.8	235
	0.05*	34.0	51.5	184
	0.1	11.0	22.1	165
	0.2	8.95	13.9	214
	0.3	4.98	7.14	166
	0.4	6.28	7.19	248
BiI_3	0.1	7.62	8.82	235
	0.2	11.2	11.5	270
	0.3*	14.5	45.0	147
	0.4	2.95	2.95	295
SnTe	0.3*	9.45	11.9	229
	0.6	7.82	7.91	272
	1.0	4.94	5.14	258
	1.5	3.43	3.53	282
In_2Te_3	0.6	9.20	10.3	231
	0.9	16.2	22.3	204
	1.5*	22.4	32.1	188
	2.0	1.58	1.58	295
	3.0	0.034	9.55	136
	4.0	1.68	3.44	111

[a] See Ref. 14.

[b] Calculated from sample with highest conductivity (See Ref. 5).

[c] Calculated from sample with lowest conductivity (See Ref. 5).

The room temperature carrier concentration measured for the SbI_3-doped $CsBi_4Te_6$ samples was found to be less than an order of magnitude below the optimal value for thermoelectric applications ($\approx 10^{19}$ cm^{-3} [11,12]). Carrier concentration was found to be weakly dependent on temperature, with values decreasing as the temperature was lowered. The carrier concentration tends to diminish as the doping increases away from 0.05% SbI_3, the material found to have the highest power factor. For these samples, the carrier concentration data could be correlated with the power factor data, showing that the power factor decreased as carrier concentration moved away from 10^{19} cm^{-3}. Additional Hall effect measurements now in progress are expected to help in refining the identification of the optimal doping concentration.

Thermal conductivity measurements on pressed pellets of undoped $CsBi_4Te_6$ have been reported previously[5]. The thermal conductivity was found to vary from 9 to 12 mW/cm·K, with a shallow minimum between 170 and 210 K. The electronic contribution to the thermal conductivity was estimated using the Wiedemann-Franz law for metals as approximately $\kappa_{el} \approx 1.3$ mW/cm·K[5]. This suggests that the measured thermal conductivities are dominated by the lattice contribution. It has been pointed out previously that a small percentage of dopants introduced to a thermoelectric material will not significantly affect the lattice contribution to the thermal

conductivity[13]. This is presently being investigated with thermal conductivity measurements of polycrystalline samples of doped $CsBi_4Te_6$.

CONCLUSIONS

The initial work on undoped $CsBi_4Te_6$ has now been extended to consider the effect of introducing dopants into the basic structure. All dopants examined here show p-type conduction. Power factors have been obtained that exceed those of both undoped $CsBi_4Te_6$ and p-type Bi_2Te_3. Current work is continuing with the more promising dopants reported here as well as with new dopants such as Zn, Mg, and Te to further enhance the power factor values and to obtain n-type samples. The data presented in this paper are all from very small-sized single crystal specimens, which are not satisfactory for thermal conductivity measurements. In order to determine ZT values, polycrystalline ingots are now being synthesized for transport measurements. The studies carried out thus far on the $CsBi_4Te_6$ system suggest that this material may be more suitable than Bi_2Te_3 for applications in the in the temperature range of 50 to 100 K below the region where the maximum ZT occurs for Bi_2Te_3.

ACKNOWLEDGMENTS

This work was supported at NU and MSU by the Office of Naval Research grant no. N00014-98-1-0443. Work at NU made use of the Central Facilities supported by the National Science Foundation through the NU Materials Research Center (DMR-9632472).

REFERENCES

[1] H. Kaibe, Y. Tanaka, M. Sakata, and I. Nishida, *J. Phys. Chem. Solids*, vol. 50, no. 9, pp.945- 950, 1989.
[2] H.-W. Jeon, H.-P. Ha, D.-B. Hyun, and J.-D. Shim, *J. Phys. Chem. Solids*, vol. 52, no. 4, pp. 579 - 585, 1991.
[3] G. A. Slack, in *CRC Handbook of Thermoelectrics*, edited by D. M. Rowe, (CRC Press, Boca Raton, FL, 1995) pp. 408-409.
[4] J. Seo, K. Park, C. Lee, and J. Kim, in *Thermoelectric Materials - New Directions and Approaches*, edited by M. G. Kanatzidis, H. Lyon, G. Mahan, and T. Tritt, (Mater. Res. Soc. Proc. **478**, San Francisco, CA, 1997) pp. 127-132.
[5] J. L. Schindler, T. P. Hogan, P. W. Brazis, C. R. Kannewurf, D.-Y. Chung, and M. G. Kanatzidis, in *Thermoelectric Materials - New Directions and Approaches*, edited by M. G. Kanatzidis, H. Lyon, G. Mahan, and T. Tritt, (Mater. Res. Soc. Proc. **478**, San Francisco, CA, 1997) pp. 327-332.
[6] D.-Y. Chung, T. Hogan, J. Schindler, L. Iordanidis, P. Brazis, C. R. Kannewurf, B. Chen, C. Uher, M. G. Kanatzidis, in *Thermoelectric Materials - New Directions and Approaches*, edited by M. G. Kanatzidis, H. Lyon, G. Mahan, and T. Tritt, (Mater. Res. Soc. Proc. **478**, San Francisco, CA, 1997) pp.333-344.
[7] D.-Y. Chung, P. W. Brazis, C. R. Kannewurf, and M. G. Kanatzidis, to be submitted for publication.
[8] D.-Y. Chung, T. Hogan, J. Schindler, L. Iordanidis, P. Brazis, C. R. Kannewurf, B. Chen, C. Uher, and M. G. Kanatzidis, in *Proceedings, Sixteenth International Conference on Thermoelectrics,* The International Thermoelectric Society (IEEE, Piscataway, N. J., 1998) pp. 459-462.
[9] J. W. Lyding, H. O. Marcy, T. J. Marks, and C. R. Kannewurf, *IEEE Trans. Instrum. Meas.*, vol. 37, no. 1, pp. 76 - 80, 1988.
[10] H. O. Marcy, T. J. Marks, and C. R. Kannewurf, *IEEE Trans. Instrum. Meas.*, vol. 39, no. 5, pp. 756 - 760, 1990.
[11] T. M. Tritt, in *Thermoelectric Materials - New Directions and Approaches*, edited by M. G. Kanatzidis, H. Lyon, G. Mahan, and T. Tritt, (Mater. Res. Soc. Proc. **478**, San Francisco, CA, 1997) pp. 25-35.
[12] C. Wood, in *Report of the Progress in Physics*, vol. 51, pp. 459-539, 1991.
[13] C. M. Bhandari, in *CRC Handbook of Thermoelectrics*, edited by D. M. Rowe, (CRC Press, Boca Raton, FL, 1995) pp. 35, 56.
[14] Bi_2Te_3 p-type samples and data obtained from Marlow Industries, Inc., Dallas, Texas.

Chevrel phases as good thermoelectric materials

C. Roche, P. Pecheur, M. Riffel, A. Jenny, H. Scherrer, S. Scherrer
Laboratoire de Physique des Matériaux, CNRS UMR 7556, Ecole des Mines, 54042 NANCY, FRANCE

Abstract

Chevrel phases have an open lattice with large voids in which cations can be inserted. These cations are good scattering centers for phonons. The thermal conductivity of these compounds must be low. Chevrel phases are generally metallic, but we calculated the density of states of several compounds and we found that $Zn_2Mo_6Se_8$, $Cd_2Mo_6Se_8$, $TiMo_6Se_8$ are semiconducting whereas $SnMo_6Se_8$, $Cu_2Mo_6Se_8$ and $CrMo_6Se_8$ are metallic. We are currently trying to synthesize $Zn_2Mo_6Se_8$ by different ways.

Introduction

Chevrel phases were first synthesized in 1971 by Chevrel [1]. They were especially studied for their superconducting properties, indeed they have a high critical field. They are now studied as new thermoelectric materials, as it is expected that they will have low thermal conductivity.
Slack [2] proposed a model for the ideal thermoelectric material with a high figure of merit. He calls this material a Phonon-Glass and an Electron single Crystal (PGEC). This material has a low lattice thermal conductivity, a narrow band gap and high charge carrier mobility. That means we must study materials with an open lattice and low average electronegativity difference. Following this model Chevrel phases seem to be good candidates for thermoelectric application.
The general formula of Chevrel phases is $M_xMo_6X_8$ where X is a chalcogen (S, Se or Te). First thermoelectric measurements have been made by Caillat [3] on $Mo_2Re_4Se_8$. We present here the crystallography of Chevrel phase compounds and the link with the number of valence electrons. We have made band structure calculations on several compounds [4] in order to find semiconducting ones.

Crystallography and valence electrons

Chevrel phases have a complex crystallographic structure. It consists of a stacking of Mo_6X_8 building blocks where X is a chalcogen [5-6]. Each building block is formed by an octahedron of molybdenum atoms surrounded by 8 chalcogen atoms. The chalcogens atoms form nearly a cube. The stacking of these blocks leads to a rhombohedral structure with an angle close to 90°. The building blocks are turned by an angle of about 27° around the ternary axis of the rhombohedral structure (figure 1). That means that even if the angle of the structure is 90° the symmetric isn't cubic. Two types of chalcogen atoms can therefore be distinguished, peripheral chalcogens, noted X1 and axial chalcogens, noted X2, situated on the ternary axis. Moreover this rotation leads to the formation of Mo-X and Mo-Mo intercluster liaisons (figure 2). The lattice of Chevrel phases compounds can be seen as a superposition of 3 subnetworks, a chalcogen network, a Mo_6 octahedron network and a cation network.
The stacking of the building blocks leaves a certain number of cavities. There are 3 types of cavities (figure 3). The biggest one, called site 1, is almost cubic shaped and formed by 8 chalcogen atoms belonging to 8 different clusters. The second one, site 2, is more irregular and is formed by 8 chalcogen atoms belonging to 4 different clusters. The smallest one, site 3, is formed by 8 chalcogen atoms belonging to 2 different clusters. Inserted cations are located in site 1 and 2 depending on their size. Site 3 isn't occupied because of intercluster liaisons.

Mat. Res. Soc. Symp. Proc. Vol. 545 ©1999 Materials Research Society

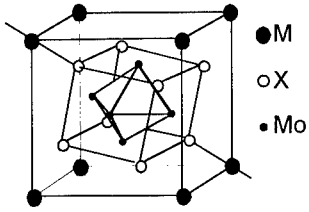

Figure 1 : Elementary cell of rhombohedral structure. Inserted cations are located in position (0,0,0), the building block is turned by an angle of about 27° around the ternary axis

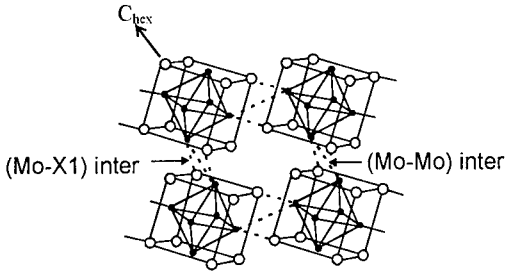

o : X = S, Se, Te

• : Mo

Figure 2 : building block arrangement. (Mo-Mo) intercluster liaisons and (Mo-X1) intercluster liaisons are represented by dashed lines.

We can distinguish 2 types of cations : big and small cations. Big cations (Pb, Sn, ...) are located in the middle of site 1 at the origin of the rhombohedral structure (figure 3). Compounds with big cations are stoichiometric. Small cations (Cu, Zn, Cd, ...) are statistically distributed between 12 positions (figure 4) and lead to a non-stoichiometric compound. Only 6 positions could be occupied simultaneously. But the limit concentration of small cations is determined by electronic factors rather than by geometrical factors.

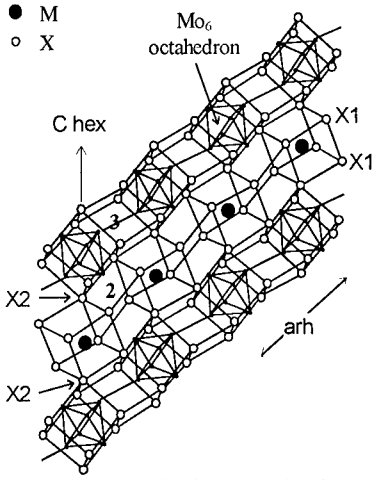

Figure 3 : Projection on the hexagonal $(11\bar{2}0)$ hexagonal plane. The three types of cavities are represented and big cations are located in site 1. We can see the 2 types of chalcogen atoms X1 and X2.

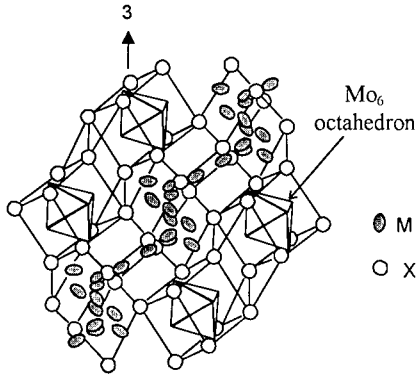

Figure 4 : Distribution of small cations in the lattice

Indeed there is a charge transfer from the cation to the Mo_6 octahedron. Then as the cation concentration increases, the Mo_6 octahedron contracts and becomes more regular. There is then a correlation between the Mo-Mo intracluster distances and the number of valence electrons (figure 5). Yvon [7] introduced a parameter which he calls the Valence Electron Concentration (VEC). It is calculated by adding the number of valence electrons of the cation to the number of valence electrons of molybdenum and by substracting the number of electrons needed to fill the octet of the chalcogen, or in other words the number of electrons needed to fill the empty states below the Fermi level. To obtain the VEC per molybdenum atoms, we must divide this value by the number of molybdenum atoms. It works well for sulfides. In selenides and tellurides, the Se-Se and Te-Te distances are smaller than purely ionic distances, their covalence is then higher and their formal charge decreases. A correction factor must then be introduced when calculating the VEC for selenides and tellurides [8]. Yvon [5] supposes that each Mo atom forms a liaison with Mo atoms of neighboring clusters. The X1-X2 liaisons are supposed to be completely saturated, 4 electrons are then needed to saturate the Mo-Mo liaisons. So when the VEC equals 4, the Mo d-band are saturated and we can expect to have a semiconducting material.
We made band structure calculations on several compounds to find semiconducting ones.

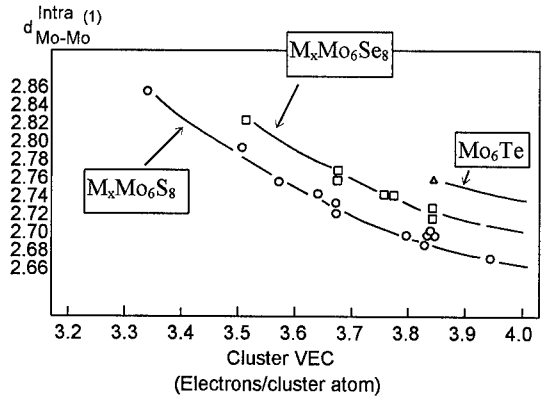

Figure 5 : The shortest Mo-Mo intracluster distance as a function of the cluster valence electrons concentration for sulfides, selenides and tellurides. [5]

Band structure calculations

The calculations were made on selenide compounds. We used the LMTO-TB (Linear muffin-tin orbitals-tight binding) method in the ASA (atomic sphere approximation). We calculated the density of states in direct space using the recursion method. We obtained the Green function for each orbital of the unequivalent atoms. We used the simple square root termination for the continuous fraction so that we obtained a very deep minimum instead of a real gap. This method is best for compact structures. As we saw, Chevrel phases aren't compact, but the building block is almost a FCC structure. Nohl, Klose and Andersen [9] used this method in reciprocal space for some Chevrel phases, choosing the radius of atomic sphere so that the filling rate is greater than 60%.

We performed calculations for $Zn_2Mo_6Se_8$, $Cd_2Mo_6Se_8$, $TiMo_6Se_8$ and $CrMo_6Se_8$. Following Nohl [9] we used the metallic sphere radius for Mo (r = 1.55 Å) and the atomic radius for Se (r = 1.40 Å). We choosed the radius of the inserted cation so that space filling is greater than 60% and the overlap with the nearest Se neighbors is smaller than 20% (or the number of spheres with an overlap over 20% is small comparing to the total number of spheres). Our calculation is not self-consistent, but we adjusted the radius of the cation so that Mo atoms have 6 valence electrons and Se atoms have about 6.1 valence electrons following the results obtained by Freeman and Jarlborg [10]. The choice of the radius is summarized in Table I.

Table I : Value of radius used for calculation

atom	$SnMo_6Se_8$	$Zn_2Mo_6Se_8$	$Cd_2Mo_6Se_8$	$TiMo_6Se_8$	$CrMo_6Se_8$
Mo	1.55	1.55	1.55	1.55	1.55
Se	1.40	1.40	1.40	1.40	1.40
M	1.62	1.39	1.54	1.47	1.41

As we said, big cations have a fixed position whereas small cations are statistically distributed between 12 positions. We chose fixed positions for small cations to obtain a periodic system. The 6 Mo atoms and the 8 Se atoms become then unequivalent and we made the calculation on a 15 or 16 unequivalent atoms unit cell. We used the position of Cu in $Cu_2Mo_6Se_8$ for Zn_2 and $Cd_2Mo_6Se_8$ because the lattice parameters of these compounds are similar. For Ti Mo_6Se_8 we used structural parameters given by Chevrel [11] and for $CrMo_6Se_8$ we used the parameter given by Mançour-Billah [12].

We performed a test calculation on $SnMo_6Se_8$ (figure 6) and obtained results similar to those of Freeman and Jarlborg [10] who used a self-consistent calculation on a simplified structure. We obtain a narrow Sn s-band below the main p-d band (between d orbitals of Mo and p orbitals of Se). This band is filled by 2 electrons and the 2 other valence electrons of Sn are in the valence band so that there is an empty state in the valence band and the compound is metallic. In contrast calculations for $Zn_2Mo_6Se_8$, $Cd_2Mo_6Se_8$, $TiMo_6Se_8$ and $CrMo_6Se_8$ show no distinct s-band for Zn, Cd, Ti, Cr. We only see M (M = Zn, Cd, Ti) d-states which fall within and below the valence band for Zn and Cd respectively (figures 7 and 8), within the conduction band for Ti (figure 9). For Cr the d-states are lower (figure 10) and there is no gap anymore. For Zn and Cd, the d-states are filled anyway, which means that the four valence electrons from the 2 Zn (or Cd) are in the valence band and the Fermi level is in the gap. The four valence electrons of Ti are in the valence band as well and the Fermi level is in the gap too. For $CrMo_6Se_8$, we have a metallic compound since there is no gap anymore.

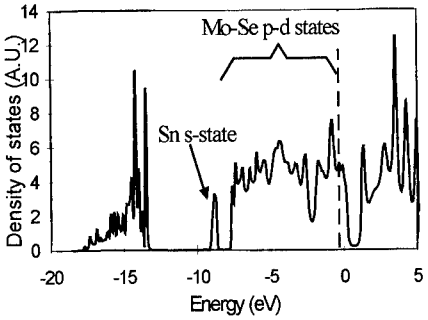

Figure 6 : Density of states of $SnMo_6Se_8$, the Fermi level is indicated by a dashed line.

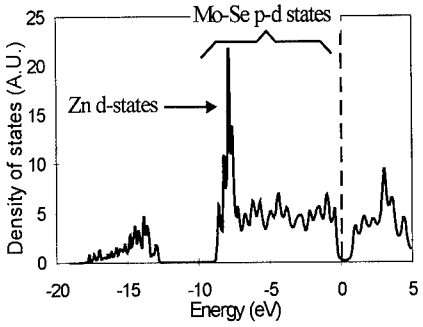

Figure 7 : Density of states of $Zn_2Mo_6Se_8$. The Fermi level is indicated by a dashed line

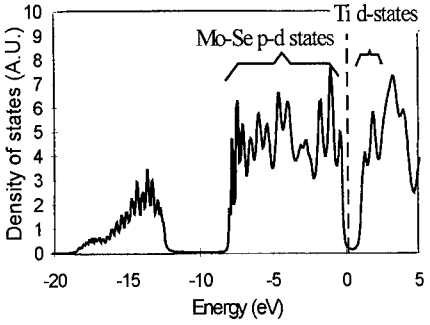

Figure 9 : density of states of $TiMo_6Se_8$, the Fermi level is indicated by a dashed line.

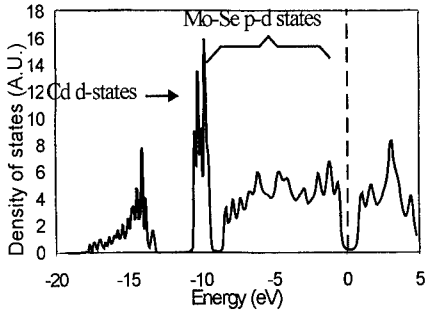

Figure 8 : Density of states of $Cd_2Mo_6Se_8$, the Fermi level is indicated by a dashed line

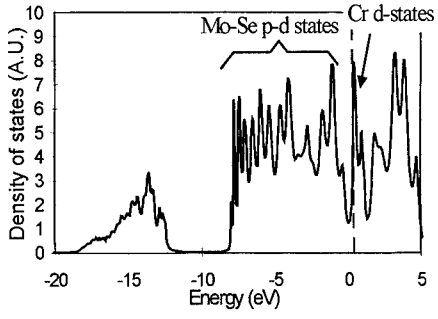

Figure 10 : density of states of $CrMo_6Se_8$, the Fermi level is indicated by a dashed line.

So $Zn_2Mo_6Se_8$, $Cd_2Mo_6Se_8$ and $TiMo_6Se_8$ are semiconducting compounds and appear to be good candidates for thermoelectric applications because of their crystallographic structure.

Conclusion

Chevrel phases have an open lattice with large voids, so that we expect they will have low thermal conductivity, Caillat found a thermal conductivity value of 1 W/m.K [13]. As we saw, the number of valence electrons is correlated with structural and physical properties of the compound.

We have found with band structure calculation that $Zn_2Mo_6Se_8$, $Cd_2Mo_6Se_8$ and $TiMo_6Se_8$ are semiconducting compounds. Other authors also found by theoretical calculations that $Zn_2Mo_6Se_8$ is semiconducting [14] and $TiMo_6Se_8$ was experimentally found semiconducting [13]

We are performing further calculations on sulfides and selenides with transition-metal as inserted cation. And we are trying to elaborate $Zn_2Mo_6Se_8$ by different ways : ceramic synthesis at high temperature starting from the elements (Zn, Mo, Se) or from precursors (ZnSe, $MoSe_2$ and Mo), phase vapor diffusion at low temperature ...

Acknowledgment

We would like to thank Professor Roger Chevrel for fruitful discussion on the synthesis, properties and crystal structure of the material.

References

[1] R. Chevrel, M. Sergent, J. Prigent, Journal of Solid State Chemistry **3**, pp. 515-519, 1971

[2] G.A. Slack, in CRC Handbook of Thermoelectrics, ed. by D.M. Rowe, chap. 34, pp. 407-440, 1995

[3] T. Caillat, J.P. Fleurial, Proceedings of the 16th Conference on Thermoelectrics, Dresden, Germany, 446, 1997

[4] C. Roche, P. Pecheur, G. Toussaint, A. Jenny, H. Scherrer, S. Scherrer, Journal of Physics : Condensed Matter **10**, L333, 1998

[5] K. Yvon, Current Topics in Materials Science vol. **3**, ed. by E. Kaldis, North-Holland publishing company, pp. 53-129, 1979

[6] R. Chevrel, M. Sergent, Topics in Current Physics : Superconductivity in Ternary Compounds vol. **1**, eds. Ø. Fisher and M.B. Maple (Berlin: Springer), pp. 25-86, 1982

[7] K. Yvon, A. Paoli, Solid State Communications **24**, pp. 41-45, 1977

[8] The formal charge of Se decrease by about 1/8 and the one of tellurium by about 0.3 units with respect to the formal charge of sulfur.

[9] H. Nohl, W. Klose, O.K. Andersen, Topics in Current Physics : Superconductivity in Ternary Compounds vol. **1**, eds. Ø. Fisher and M.B. Maple (Berlin: Springer), pp. 165-221, 1982

[10]A.J. Freeman, T. Jarlborg, Topics in Current Physics : Superconductivity in Ternary Compounds vol. **2**, eds. Ø. Fisher and M.B. Maple (Berlin: Springer), pp. 167-200, 1982

[11] R. Chevrel (private communication)

[12] A. Mançour-Billah, P. Gougeon, J.Y. Pivan, M. Sergent, R. Chevrel, Croatica Chemica Acta **68**, pp. 891-899, 1995

[13] T. Caillat, G.J. Snyder, A. Borshchevsky, J.P. Fleurial, Materials Research Society Symposium Proceedings Series, vol **545**, Boston MA, 1998

[14] R.W. Nunes et al, to be published

THEORETICAL MODELING OF THERMOELECTRICITY IN Bi NANOWIRES

X. Sun[a], Z. Zhang[a], G. Dresselhaus[b], M. S. Dresselhaus[c], J. Y. Ying[d], G. Chen[e]
[a]Department of Physics, Massachusetts Institute of Technology, Cambridge, MA 02139
[b]Francis Bitter Magnet Laboratory, Massachusetts Institute of Technology, Cambridge, MA 02139
[c]Department of Electrical Engineering and Computer Science and Department of Physics, Massachusetts Institute of Technology, Cambridge, MA 02139
[d]Department of Chemical Engineering, Massachusetts Institute of Technology, Cambridge, MA 02139
[e]Department of Mechanical and Aerospace Engineering, University of California, Los Angeles, CA 90024

ABSTRACT

Bismuth as a semimetal is not a good thermoelectric material in bulk form because of the approximate cancellation between the electron and hole contributions. However, quantum confinement can be introduced by making Bi nanowires to move the lowest conduction subband edge up and the highest valence subband edge down to get a one-dimensional (1D) semiconductor at some critical wire diameter d_c. A theoretical model based on the basic band structure of bulk Bi is developed to predict the dependence of these quantities on wire diameter and on the crystalline orientation of the bismuth nanowires. Numerical modeling is performed for trigonal, binary and bisectrix crystal orientations. By carefully tailoring the Bi wire diameter and carrier concentration, substantial enhancement in the thermoelectric figure of merit is expected for small nanowire diameters.

INTRODUCTION

Nanowire systems have attracted a great deal of research interest because of their potential applications in thermoelectric devices and their promise for studying 1D transport properties. The quantum confinement of carriers in the two dimensions normal to the wire axis significantly changes their electronic energy states and makes the transport properties of these 1D systems very different from their bulk counterparts.

Bismuth, which is a semimetal and has a very small electron effective mass, is considered as a good candidate to study the quantum confinement effects in a 1D system. By introducing quantum confinement, a semimetal-semiconductor transition can be achieved, thereby, by adjusting the doping level carefully, an enhancement in the thermoelectric figure of merit over its bulk form is expected. The extremely small electron effective mass of Bi, the high anisotropy of its Fermi surface, together its high atomic number make low-dimensional Bi a very promising material for thermoelectric applications [1].

Making nanoscale Bi wires has been challenging in laboratories. One promising approach to fabricate nanowire systems is to fill an array of parallel nano-channels with the media of interest for thermoelectric applications. Porous anodic alumina [2], which has a hexagonal array of nanometer-sized channels, is one such possible host template. Substantial progress in the fabrication techniques has been made recently [3].

Mat. Res. Soc. Symp. Proc. Vol. 545 © 1999 Materials Research Society

ONE-DIMENSIONAL THERMOELECTRICITY OF Bi

The effect on Z of using materials in one-dimensional structures, such as 1D quantum wires, has been studied earlier in the context of a single band structure, and it was shown theoretically that this approach could yield a significant increase in Z over the bulk value and its two-dimensional form [4]. In the framework of semiclassical theory, the electronic transport properties, including the electrical conductivity σ, the Seebeck coefficient S and the electronic part of thermal conductivity κ_e, determine the thermoelectric figure of merit

$$Z = \frac{S^2\sigma}{\kappa_e + \kappa_L}, \tag{1}$$

where κ_L is the lattice thermal conductivity. These transport properties can be found from:

$$\sigma = L^{(0)}, \tag{2}$$

$$S = -\left(\frac{1}{eT}\right)(L^{(0)})^{-1}L^{(1)}, \tag{3}$$

$$\kappa_e = \left(\frac{1}{e^2T}\right)(L^{(2)} - L^{(1)}(L^{(0)})^{-1}L^{(1)}), \tag{4}$$

where

$$L^{(\alpha)} = e^2 \int \frac{dk}{\pi a^2}\left(-\frac{\partial f}{\partial \varepsilon}\right)\tau(k)v(k)v(k)(\varepsilon(k) - \zeta)^{\alpha}, \tag{5}$$

in which f is the Fermi-Dirac distribution function, $\varepsilon(k)$ the energy dispersion relation for electrons, a the size of the quantum wire which is assumed to have a square cross section, $\tau(k)$ the relaxation time for electrons, and ζ the chemical potential in the 1D electronic system.

Bismuth has a rhombohedral lattice, which can be expressed in terms of a hexagonal unit cell with lattice parameters $a_0 = 4.5\,\text{Å}$ and $c_0 = 11.9\,\text{Å}$ [5]. Electrons are distributed in three equivalent ellipsoids at the L-points of the Brillouin zone and the holes in a single ellipsoid at the T-point.

As we introduce quantum confinement into the Bi nanowire system, the extremal conduction subband and valence subband edges will move in opposite directions to eventually form a positive energy band gap, thereby leading to a semimetal-semiconductor transition as the wire diameter is decreased below d_c. Over a large range of wire diameters where quantum confinement becomes important in Bi nanowires, the separation between the lowest L-point conduction subband edge and the highest T-point valence subband edge are so close, even in the semiconductor range, that we need to take into account the contributions to the transport properties from both electrons and holes. In this case, the transport tensor elements shown in Eq. (5) become a summation of terms due to both electrons and holes.* When the nanowires are fabricated so that their wire axes are along a crystalline direction other than the trigonal direction, multiple contributions from the electronic subbands arising from the anisotropy of the carrier pockets must also be considered. Taking all these facts into account, the transport tensor elements are calculated to be

$$L^{(0)} = D_e\left[\frac{1}{2}F^e_{-\frac{1}{2}}\right] + D_h\left[\frac{1}{2}F^h_{-\frac{1}{2}}\right] \tag{6}$$

*Note, however, that $L^{(1)}$ experiences a cancellation from the electron and hole contributions because of the odd charge parity e shown in Eq. (3).

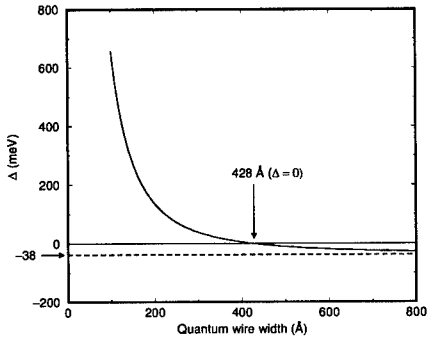

Figure 1: The quantum confinement-induced band gap as a function of Bi quantum wire width at 300 K. The conduction-valence band overlap is 38 meV in bulk form. The semimetal-semiconductor transition occurs at a quantum wire width of 428 Å.

$$L^{(1)} = (k_B T)\left(D_e\left[\frac{3}{2}F^e_{\frac{1}{2}} - \frac{1}{2}\zeta^*_e F^e_{-\frac{1}{2}}\right] - D_h\left[\frac{3}{2}F^h_{\frac{1}{2}} - \frac{1}{2}\zeta^*_h F^h_{-\frac{1}{2}}\right]\right) \tag{7}$$

$$L^{(2)} = (k_B T)^2\left(D_e\left[\frac{5}{2}F^e_{\frac{3}{2}} - 3\zeta^*_e F^e_{\frac{1}{2}} + \frac{1}{2}\zeta^{*2}_e F^e_{-\frac{1}{2}}\right] + D_h\left[\frac{5}{2}F^h_{\frac{3}{2}} - 3\zeta^*_h F^h_{\frac{1}{2}} + \frac{1}{2}\zeta^{*2}_h F^h_{-\frac{1}{2}}\right]\right) \tag{8}$$

where D_e and D_h are given by

$$D_{e,h} = \frac{2e}{\pi a^2}\left(\frac{2k_B T}{\hbar^2}\right)^{\frac{1}{2}}(m^*_{e,h})^{\frac{1}{2}}\mu_{e,h}, \tag{9}$$

and where

$$F^{e,h}_i = \int_0^\infty \frac{x^i dx}{e^{(x-\zeta^*_{e,h})}+1} \tag{10}$$

denote the Fermi-Dirac functions. The reduced chemical potentials $\zeta^*_{e,h} = (\zeta_{e,h} - \varepsilon^{e,h}_0)/k_B T$, where $\varepsilon^{e,h}_0$ denote the subband edges of the conduction and valence bands, respectively, are related to each other through

$$\zeta^*_e + \zeta^*_h = -\Delta \tag{11}$$

where Δ is the energy gap between the L-point conduction band and the T-point valence band.† The chemical potential can be adjusted to set the system into an optimal configuration for thermoelectric application by controlling the doping level. In Eq. (9), $m^*_{e,h}$ and $\mu_{e,h}$ are effective masses and carrier mobilities, respectively, along the transport direction for electrons and holes.

NUMERICAL RESULTS

The effective mass tensors for the L-point electrons and the T-point holes in Bi can be expressed as

$$(m^*_e)_{ij} = \begin{pmatrix} m^e_1 & 0 & 0 \\ 0 & m^e_2 & m^e_4 \\ 0 & m^e_4 & m^e_3 \end{pmatrix}, \qquad (m^*_h)_{ij} = \begin{pmatrix} m^h_1 & 0 & 0 \\ 0 & m^h_1 & 0 \\ 0 & 0 & m^h_3 \end{pmatrix}. \tag{12}$$

†For bulk Bi, $\Delta = -38\,\text{meV}$, whereas $\Delta > 0$ indicates that a semimetal-semiconductor transition has been achieved.

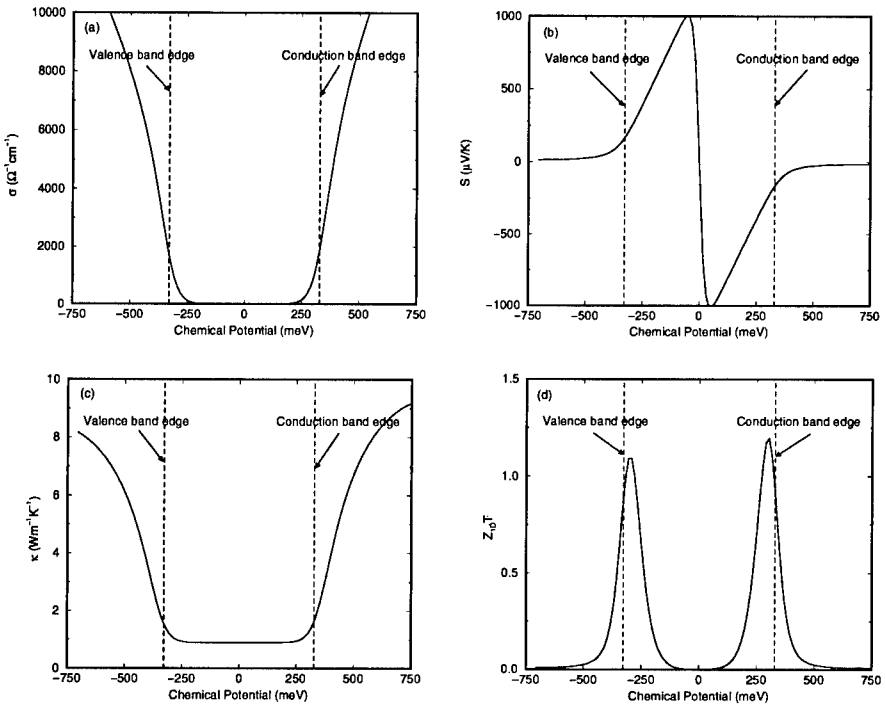

Figure 2: The calculated (a) electrical conductivity, (b) Seebeck coefficient, and (c) thermal conductivity for an 100 Å Bi quantum wire at 300 K using semiclassical theory. The resulting thermoelectric figure of merit is shown in (d). The maximum thermoeletric figure of merit occurs very close to the conduction band edge and valence band edge for n-type and p-type quantum wires, respectively.

As a first approximation, we used a parabolic dispersion relation for both electrons and holes in Bi,[‡]

$$\varepsilon = \varepsilon_0 \pm \frac{\hbar^2}{2} \sum_{i,j} \frac{k_i k_j}{m_{ij}}, \tag{13}$$

where $\pm$ refers to electrons and holes, respectively. The bulk band edge effective mass tensor components are $m_1^e = 0.00651 m_0$, $m_2^e = 1.362 m_0$, $m_3^e = 0.0297 m_0$, $m_4^e = 0.1635 m_0$ for electrons and $m_1^h = 0.0644 m_0$, $m_3^h = 0.696 m_0$ for holes, where m_0 is the free electron mass [6].

The numerically calculated band gap Δ as a function of quantum wire width for the transport direction along the trigonal direction at room temperature is shown in Fig. 1. It is seen that the semimetal-semiconductor transition takes place at a wire width of 428 Å [7]. As

[‡]In fact, the conduction band at L-point is highly non-parabolic. The detailed study of this effect will be discussed elsewhere.

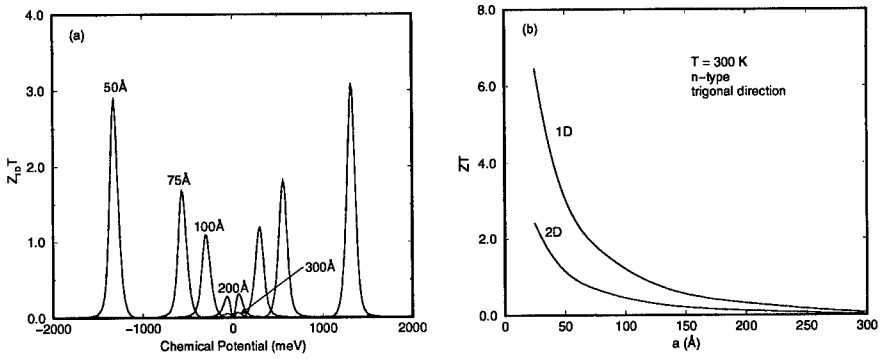

Figure 3: (a) The thermoelectric figure of merit as a function of chemical potential for Bi quantum wires of different sizes at room temperature. (b) The optimal thermoelectric figure of merit as a function of the size of quantum wire at room temperature. For comparison, the optimal figure of merit for two-dimensional (2D) quantum well system is also shown.

the quantum wire width becomes smaller than 200 Å, the conduction and valence extremal subband edges separate quite rapidly. The electronic transport properties for a 100 Å Bi quantum wire at room temperature are calculated using Eqs. (2)–(4) and (6)–(8), and the results are shown in Fig. 2(a)–(c). The thermoeletric figure of merit that is achieved using Eq. (1) is shown in Fig. 2(d). We see that the maximum thermoeletric figure of merit occurs very close to the conduction subband and valence subband edges for n-type and p-type Bi quantum wires, respectively, and the maximum $Z_{1D}T$ for both n-type and p-type Bi quantum wires is over 1.0, which makes this system very interesting even for room temperature thermoelectric applications.

The thermoelectric figure of merit for various Bi nanowires with different wire widths at room temperature is shown in Fig. 3(a). A value of $Z_{2D}T \sim 3.0$ could be achieved in a system with quantum wire width of 50 Å. The optimal $Z_{1D}T$ as a function of quantum wire width is shown in Fig. 3(b). For comparison, the optimal figure of merit for a two-dimensional (2D) quantum well system is also shown. This result shows that a one-dimensional system has a greater potential for the enhancement of thermoelectric performance over bulk than its two-dimensional counterpart.

Bismuth is a highly anisotropic material. It is therefore important to study the transport properties along crystal directions other than the trigonal direction. We therefore calculated the thermoelectric figure of merit for a 100 Å quantum wire with the transport direction along the bisectrix and binary directions, as shown in Fig. 4. We found that the n-type bisectrix nanowire has a slightly better $Z_{1D}T$ than the trigonal wire of the same wire width. However, the $Z_{1D}T$ for the p-type nanowire is much lower than that for the trigonal wire due to the much smaller density of states for the holes arising from the smaller mass component along the bisectrix direction. The binary transport direction is predicted to be less favorable for n-type semiconducting bismuth because only one of the three electron pockets strongly contributes to the power factor. It is interesting to see that a very small second peak in $Z_{1D}T$ appears in the n-type range, which is arises from the other two degenerate electron pockets with a higher subband edge.

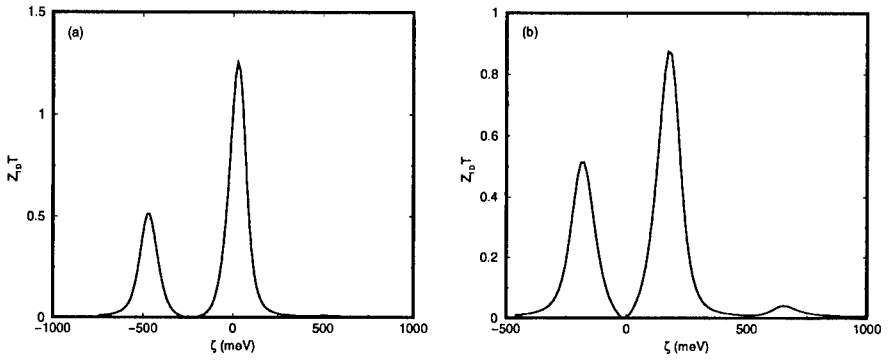

Figure 4: The thermoelectric figure of merit as function of chemical potential for an 100 Å Bi quantum wire with transport direction along (a) bisectrix and (b) binary directions at room temperature. The zero point of chemical potential is arbitrary.

CONCLUSION

A theoretical model based on a parabolic approximation for the basic band structure of bulk Bi, suitably modified for the 1D system, has been developed. Our model calculations show that the Bi nanowire system, when appropriately doped, is potentially an interesting thermoelectric material. More detailed calculations with non-parabolic dispersion relations for the L-point electrons are needed to obtain reliable estimation for the dependence of $Z_{1D}T$ on nanowire size.

ACKNOWLEDGMENTS

The authors gratefully acknowledge support by the US Navy under Contract No. N00167-98-K-0024, and by NSF under grants CTS-9257223 and DMR-9400334, and by the MURI subcontract #0205-G-7A114-01.

REFERENCES

[1] L. D. Hicks, T. C. Harman, and M. S. Dresselhaus, Appl. Phys. Lett. **63**, 3230 (1993).

[2] K. Itaya, S. Sugarwara, K. Arai, and S. Saito, J. Chem. Engr. Jpn. **17**, 514 (1984).

[3] Z. Zhang, J. Y. Ying, and M. S. Dresselhaus, J. Mater. Res. **13**, 1745 (1998).

[4] L. D. Hicks and M. S. Dresselhaus, Phys. Rev. B **47**, 16631 (1993).

[5] D. Schiferl and C. S. Barrett, J. Appl. Crystallogr. **2**, 30 (1969).

[6] R. T. Isaacson and G. A. Williams, Phys. Rev. **185**, 682 (1969).

[7] Z. Zhang, X. Sun, M. S. Dresselhaus, J. Y. Ying, and J. Heremans, Appl. Phys. Lett. **73**(11), 1589 (1998).

GROWTH OF BISMUTH TELLURIDE THIN FILMS BY HOT WALL EPITAXY, THERMOELECTRIC PROPERTIES

J.C.Tedenac*, S. Dal Corso**, A. Haidoux*, S.Charar***, B.Liautard*
*LPMC - UMR5617,***GES – UMR 5650
Université Montpellier II, Place Eugène Bataillon, 34095 Montpellier Cedex 05 Fr.
tedenac@univ-montp2.fr, charar@ges.univ-monpt2.fr
**MEDCOS S.A., Cap Alpha, Av. de l'Europe, Clapiers, 34940 Montpellier Cdex 09 Fr.,
nouaoura@medcos.com, www.medcos.com

ABSTRACT

It is well known that bismuth telluride (Bi_2Te_3), its isomorphs (Bi_2Se_3 and Sb_2Te_3) and their alloys have the optimum bandgap (0.13 eV to 0.21 eV) for efficient solid state cooling applications around 300 K. Recently interesting work argued that the use of quantum well structures can enhance the figure of merit ZT as a result of the improvement of carrier charge density of state and the reduction of the thermal conductivity. However, for the production of such structures it is necessary to establish the optimum growth conditions and the doping levels of thin films based on Bi_2Te_3 and its isomorphs.

In this paper we report on the growth characteristics of Bi_2Te_3 ternary alloys (even quaternary) thin films elaborated by the Hot Wall Epitaxy (HWE) technique. Ternary alloys based on bismuth telluride have been deposited as thin films on silicon and silica substrates. Hot Wall Epitaxy have been demonstrated to be a suitable technique in chalcogenides growth. These films are formed in a closed chamber, that make possible to keep substrates at relatively high temperature T_s without selective loss of individual components from condensate. Experimental procedures, such as substrate and source materials preparations, have been described in our previous publications. Thin films obtained are well oriented (00l) and have block single-crystal structure. These films were studied by microstructural investigations and electrical measurements (electrical conductivity σ, Hall coefficient R_H and Hall mobility μ_h) in the temperature range from liquid nitrogen to 570 K.

INTRODUCTION

The purpose of this paper is to present the growth of layers of both p and n type bismuth telluride alloys by H.W.E. technique on various substrates, to analyse the growth mechanism and the thermoelectric properties. This technique is based on the application of the solid-vapour phase equilibria.

The crystal growth of Bi_2Te_3, Sb_2Te_3 and Bi_2Se_3 layers on Bi_2Te_3 single crystals substrates have been studied previously [1-2-3]. In order to understand the growth mechanism, these thin films were studied by Atomic Force Microscopy (AFM) [4]. The study of the first steps in the growth shows the existence of Volmer-Weber mechanism and we have shown that the H. W. E. technique is convenient for the growth of chalcogenide based materials.

From a thermoelectric point of view our experimental results were very interesting but the problem concerning the integration of the cooler on microelectronic devices is not solved by this way. It is nescessary to study the deposition of thin layers on other types of substrates intending the integration. Thin films of Bi_2Te_3 alloys were grown by HWE technique on SiO_2/Si and Si substrates and studied by mean of electrical measurements such as electrical

Mat. Res. Soc. Symp. Proc. Vol. 545 © 1999 Materials Research Society

conductivity, Hall coefficient (R_H) and Hall mobility (μ_h) in the temperature range from liquid nitrogen to 570 K have been performed.

EXPERIMENT

Optimization of the growth conditions

The H.W.E. technique is a method leading to growth conditions closed to the thermodynamic equilibrium as well in the evaporation process as in the deposition [1-2-3-4].

Pellets of Bi_2Te_3 were used as material source and tellurium as source compensation in order to obtain n-type layers. Films were deposited respectively on kapton, silica, silicon (100) and SiO_2/Si substrates. Three furnaces are used to evaporate different source materials. Two deposition parameters are important in the HWE technique: the source temperatures and the substrate temperature.

Layers were investigated by means of X-ray diffraction method, scanning electron microscopy, atomic force microscopy and by electrical measurements and thermopower measurements.

A systematic study was made to optimize these parameters by studying the morphology, the chemical composition, electrical properties and Seebeck power. The layers were made in the aim of the better mobility with a carriers concentration close to 10^{19} cm^{-3}. The optimisation scheme was :

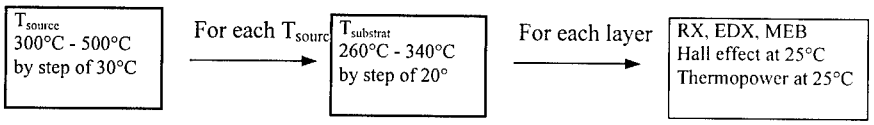

In following sections, results are given for layers deposited in optimal conditions.

RESULTS

Binary material

In the study of the binary materials the correlation between the growth conditions, the carriers mobility and the carriers concentration is shown. Carriers concentration increases with the source temperature and decreases with the substrate temperature. Experimental values from $9{,}6.10^{19}$ to $1{,}77.10^{19}$ cm^{-3} are obtained in optimized samples. The carriers mobilities are closed to the range 100-300 cm^2/Vs. The better results are obtained for the temperatures conditions : for 470°C as source temperature and for 320°C as substrate temperature.

Optimal value of thermoelectric power is 218 $\mu V/K$ for p-type sample and 204 $\mu V/K$ for n-type samples ; these values are closed to those measured on bulk materials (table 1) [5].

T_{source} (°C)	$T_{substrat}$ (°C)	T_{comp} (°C)	Type	ρ ($x10^{-3}$) (Ωcm)	P ($x10^{19}$) (cm^{-3})	μ (cm^2/Vs)	S (μV/K)
470	**320**	**-**	**p**	**2,08**	**1,77**	**169**	**218**
470	**320**	**300**	**n**	**2,22**	**1,13**	**102**	**-204**

Table1 : Electrical characteristics of Bi_2Te_3 /silica

Structure and microstructure analysis were studied by X ray diffraction and scanning electron microscopy. All the diffractions peaks are very weak and correspond to the (000l) crystallographic planes. Surfaces observations by S.E.M. show only one kind of crystallites. They are hexagonal shapes and oriented with their c axis perpendicular to the plane of the films substrate with a size of 6 to 8 μm, only few cristallites are misoriented with respect to the (000l) planes.

A similar study was made on silicon substrates oriented (100) and (111) and showed similar results. Carriers concentrations are close to $10^{20}cm^{-3}$, which is probaly due to a high concentration of tellurium. The sticking coefficient of tellurium is very different tot that to that of metal's one [3].

The X-ray diffraction pattern is different in this case. They evidence the diffraction peaks corresponding to the (0kl) and (h0l) crytallographic plans, proof of misoriented growth. This is confirmed by the existence of a lot of misoriented crystallites.

T_{source} (°C)	$T_{substrate}$ (°C)	T_{comp} (°C)	type	ρ ($x10^{-3}$) (Ωcm)	P ($x10^{19}$) (cm^{-3})	μ (cm^2/Vs)	S (μV/K)
470	420	200	p	2,99	2,99	70	105
470	420	270	p	3,63	3,06	56	-
470	420	300	p	3,22	2,63	74	95

Table 2 : Electrical characteristics of Bi_2Te_3 /silicon samples

Finally the growth conditions have been studied on SiO_2/Si substrates. In this case we have obtained the better results in the same conditions of the previous study (i.e. with T_{source} = 470°C, $T_{substrat}$ = 320°C et $T_{compensation}$ = 300°C.). These layers are oriented with respect to the <000l> direction. Electrical characteristics are shown in figure 1.

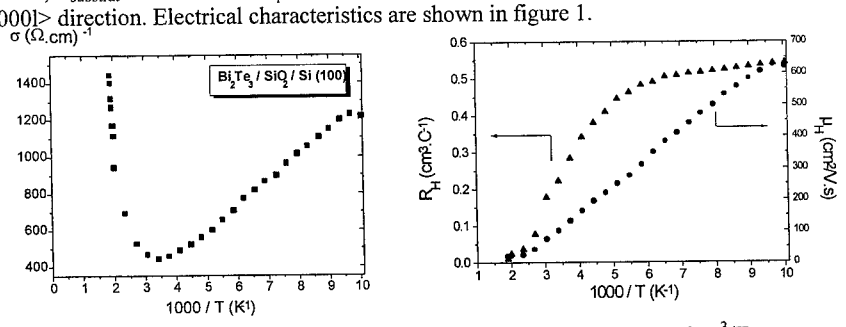

Figure 1: Electrical conductivity and Hall coefficient as a function of $10^3/T$.

Hall coefficient R_H shows a degenerated behaviour of an intrinsec semiconductor at low temperature according to [6] : $R_H = (N_d\, e)^{-1}$ the donors concentration is $N_d = 1{,}18.10^{19}$ cm^{-3}. This variation of the Hall coefficient was previously observed on bulk samples [7,8].

The electrical conductivity is similar to that reported for single crystals [9,10] as well as those from Boikov [11-12-13] in thin films layers. One can observed a maximun on the curve probably due to a change in the carriers scattering mode. In fact we have observed that at low temperatures the behaviour or the carriers concentration is due to the ionized impurities ($T < 320K$).

From the intrinsec part of the electrical conductivity ($T < 320K$), and according to the relation $\sigma = A\exp(-Eg/kT)$ the energy gap is $E_g = 0{,}12$ eV which is similar to that [14-15] measured by IR absorpsion.

The carriers mobility as a function of the temperature shows the law $\mu_h = 2{,}6.10^6\ T^{-1,75}$ $cm^2/V.s$. This is a proof that the lattice scattering is dominant.

Ternary and quaternary alloys based materials

The modification of properties were studied by alloying Bi_2Te_3,Sb_2Te_3 and Bi_2Se_3 in ternary solid solutions; the compositions $Bi_2Te_{2,7}Se_{0,3}$ and $Bi_{0,5}Sb_{1,5}Te_3$ showing actually the better thermoelectric characterics for both n- type and p- type [16].

A systematic study of deposition conditions was made using as materials source an alloy of composition $Bi_{0,5}Sb_{1,5}Te_3$ on silica and silicon substrates. In both cases, the ternary alloy can be obtained in the p-type only. The temperature conditions were : 450°C for source temperature and 260°C for substrate temperature. The layers were characterized and the results are presented in table 3.

By X-Ray two peaks are observed, they correspond to the (0kil) and (h0il) orientations, over the classical(000l) ; this misorientation is confirmed by SEM.

Substrat	**T_{source} (°C)**	**T_{subs} (°C)**	**Comp (300°C)**	**type**	**ρ ($x10^{-3}$) (Ωcm)**	**p ($x10^{18}$) (cm^{-3})**	**μ (cm^2/Vs)**	**S ($\mu V/K$)**
SiO_2	450	240	no	p	5,32	6,08	193	138
SiO_2	450	260	-	p	2,65	10,3	228	140
Si	430	240	-	p	8,94	10,5	77	98
Si	450	260	-	p	8,80	8,83	181	291

Table 3 : Electrical characteristics of $(Bi_{1-x}Sb_x)_2Te_3$ layers.

The ternary layers $Bi_2(Te_{1-x}Se_x)_3$ are of higher quality than those of antimony and they are obtained for both type p or n with the growth conditions: 450° for the source temperature and 280, 250°C for the substrates in both kind of layers but in these experiments it is necessary to use of a compensention source of selenium.

Materials deposited on silicon present the better mobilities: 300 et 400 cm^2/Vs for p and n type respectively. The electrical measurements are given in table 4.

Substrat	T_{source} (°C)	T_{subs} (°C)	Comp (300°C)	type	ρ ($x10^{-3}$) (Ω.cm)	P ($x10^{18}$) (cm^{-3})	μ (cm^2/Vs)	S (μV/K)
Si	450	280	Se	p	1,53	14,1	290	140
Si	450	250	Se	n	22,3	9,23	404	-120

Table 4 : Electrical characteristics of $Bi_2(Te_{1-x}Se_x)_3$ layers.

The quaternary alloys studied were $(Bi_{1-x}Sb_x)_2(Te_{1-y}Se_y)_3$ and particularly the composition $Bi_{0,5}Sb_{1,5}Te_{2,9}Se_{0,1}$.

The results are similar to that of antimony alloys and in our conditions it was impossible to doped the materials.

CONCLUSION

In this paper we have shown the ability of this process for obtaining thin films of multicomponent alloys of bismuth telluride on various substrates as well as their thermoelectric properties.

The films obtained are oriented along the (0001) axis and have block single crystal structures.

The electrical properties of Bi_2 Te_3 based thin films have been studied. Electrical measurements such as electrical conductivity (s), Hall coefficient (R_H) and Hall mobility (μ_H) in the temperature range from liquid nitrogen to 570K were carried out.

It is seen that the behaviour of Hall coefficient R_H, electrical conductivity s and Hall mobility μ_H are similar to the results reported for Bi_2 Te_3 single crystals obtained by solidification process. Thermoelectric measurements show that these layers are optimized and finally this method is a good one to obtain such optimized thermoeletric layers.

Acknowledgement. This work was suported by CNRS (F) and by a grant f rom the DGA/DRET n° 961127.

REFERENCES

[1] B. Gardes, J. Ameziane, G. Brun, J.C. Tedenac, A. Boyer, J. Mater. Sc. 29, p 2751(1994)
[2] A. Mzerd, D. Sayah, J.C. Tedenac, A. Boyer, Int. J. Electronics, 77, p. 291 (1994)
[3] A. Mzerd, D. Sayah, J.C. Tedenac, A. Boyer, J. Cryst. Growth, 140, p. 365 (1994)
[4] F. Marhoun, ThesisMontpellier , p. 20 (1997)
[5] D.M. Rowe, "CRC Handbook of Thermoelectrics", ed. D.M. ROWE, CRC press Inc. (1995).
[6] N.B. Hanney, "Semiconductors", Chapmann & all, London, (1960), p.32.
[7] S. Shigetomi, S. Mori, J. Phys. Soc. Japan, **11**, (1956), p.915.
[8] C.B. Satterthaite, R.W. Ure, Phys. Rev, **108**, (1957), p.108.
[9] R. Mansfield, W. Williams, Proc. Phys. Soc, **72**, (1958), p.733.
[10] C.H. Champness, A.L. Kipling, Canad. J. Phys, **44**, (1966), p.769.
[11] Y.A. Boikov, O.S. Gribanova, V.A. Danilov, I.M. Deryagina, "Proc. 8th Conf; Thermoelec. Energy Conversion", Ed INPL, (1989), p.18.
[12] Y.A. Boikov, O.S. Gribanova, V.A. Danilov, V.A. Kustanov, Sov. Phys. Solid State, **33**, (1991), p.1926.

[13] Y.A. Boikov, O.S. Gribanova, V.A. Danilov, V.A. Kustanov, Sov. Phys. Solid State, **32**, (1990), p.2056.
[14] I.G. Austin, Proc. Phys. Soc, **72**, (1958), p.545.
[15] El Kaddouri, S. Charar, S. Benet, T. Maurice, J.C. Tedenac, Phys. Stat. Solidi, (1998°? to be published.
[16] F.D. Rosi, Solid State Electron, **11**, (1968), p.833.

THERMOELECTRIC PROPERTIES OF $PbTe/Pb_{1-x}Eu_xTe$ QUANTUM WELLS

H. SCHERRER[1], Z. DASHEVSKY[2], V. KANTSER[3], A. CASIAN[4], I. SUR[4], and A. SANDU[4]
[1] Laboratoire de Physique du Solide, F-54042 Ecole des Mines, Nancy, France
[2] Ben-Gurion University of Negev, Beer-Sheva, Israel
[3] Institute of Applied Physics, Academy of Science of Moldova
[4] Technical University of Moldova, MD-2004, Kishinau, Moldova

ABSTRACT

The electrical conductivity, Seebeck coefficient, and thermoelectric power factor of $PbTe/Pb_{1-x}Eu_xTe$ quantum well structures are investigated theoretically. The variational method is employed. The anisotropy of effective masses, the multivalley character of the bulk semiconductors and also the dependence of effective masses in dimensional quantization subbands on the well width are taken into account. The carrier scattering both on optical and acoustical phonons is considered for structures with (111) and (100) crystallographic orientation. It is found that the power factor is larger in (100) oriented quantum wells. The results of recent experiments are discussed.

INTRODUCTION

Since then as in the papers [1, 2] it was shown that one may greatly increase the thermoelectric figure of merit ZT of certain materials by preparing them in quantum-well (QW) two-dimensional (2D) layered structures, the interest for the investigations, both theoretical and experimental, of such structures has grown considerable. It needs to note that these predictions were made on the base of the simplest and idealized well-model when the effects of finite barrier height and of the penetration of carriers into barrier were neglected and the approximation of a constant relaxation time was employed. In the papers [3-6] the effects of finite barrier widths and of finite heights on thermoelectric transport in superlattices systems have been taken into consideration. It was shown that these effects tend to decrease ZT as compared with that for ideal two-dimensional systems.

The role of energy dependence of the carrier-phonon scattering rates on the thermoelectric figure of merit was studied in [7]. This effect leads to decreasing carrier mobility with decreasing well thickness.

Recently we have investigated the electronic states, the electrical conductivity, Seebeck coefficient and the thermoelectric power factor in more realistic model of $PbTe/Pb_{1-x}Eu_xTe$ QW which takes into consideration the anisotropy of effective masses, the multi-valley character of the bulk semiconductors and the coupling between the longitudinal motion of electrons along the QW and transversal motion across the well [7,8]. Moreover, the QWs with (111) and (100) crystallographic orientation were considered. It was shown that the power factor is higher in (100) oriented QW.

In this paper we complete [7,8] by taking into consideration the dependencies of carrier effective masses in dimensional quantization subband for given QW not only on the well height, but also on the well width values. The electrical conductivity and Seebeck coefficient are calculated for the transport in the plane of QW using the variational method. The scattering of carriers both on optical and acoustical phonons is considered. The thermoelectric power factor as a function of the well width is determined and analyzed.

Mat. Res. Soc. Symp. Proc. Vol. 545 © 1999 Materials Research Society

THEORY

Carrier Effective Masses in Dimensional Quantization Subbands

We consider a rectangular quantum well formed of thin PbTe layer of the thickness d (region 2) between two barrier layers of $Pb_{1-x}Eu_x$ Te (regions 1 and 3) [7,8] of the thickness b. The height of potential barrier is U. We choose the axis z in perpendicular to QW plane direction, and axes x, y in plane of well. In order to determine the energetic spectrum of electrons in QW we apply the methods of effective masses and of envelope-wave function. From the boundary conditions for the envelope function at the QW interfaces in direction z the following equation is obtained

$$kd = \alpha\pi - 2\arcsin(k/\sqrt{(m_{z2}/m_{z1})^2\Delta^2 + k^2}), \qquad (1)$$

which determine the energy levels E_α and the dispersion law $E_\alpha(k_x, k_y)$ of electrons on the level α in the QW. Here

$$k^2 = 2m_{z2}\hbar^{-2}E', \quad \Delta^2 = 2m_{z1}\hbar^{-2}(U + \varepsilon_1 - \varepsilon_2 - E'), \qquad (2)$$

$E' < U+\varepsilon_1-\varepsilon_2$, $\varepsilon_l(k_x,k_y)$ is the electron kinetic energy in the corresponding layer l, (l = 1, 2, 3), m_{z1} and m_{z2} are the effective masses in the direction z into barrier and QW, respectively, calculated for structures with different crystallographic orientation through longitudinal $m_\parallel$ and transversal $m_\perp$ bulk effective masses. Full energy of an electron is $E_\alpha(k_x, k_y) = E'_\alpha(k_x, k_y) + \varepsilon_2(k_x, k_y)$ and it forms sets of minisubbands, where E'_α is determined from (1). It needs to note that due to the finite potential barrier and to anisotropy of effective masses the longitudinal motion of electrons is not separated from transversal one. Hence it follows that the electron effective masses in the QW depend not only on crystallographic orientation of the QW and on barrier height, but also on the well width d.

The equation (1) was solved numerically. The approach of Ref. [9] was used to calculate the band offsets for QW and also the band gaps and bulk effective masses for $Pb_{1-x}Eu_xTe$. This gave, $m_\parallel = 0.620m_0$ (m_0 is the free electron mass) and $m_\perp = 0.053m_0$ for PbTe, $m_\parallel = 1.12m_0$ and $m_\perp = 0.076m_0$ for barrier material with x=0.073 (U = 171 meV) and $m_\parallel = 1.4m_0$, $m_\perp = 0.094m_0$ for the material with x = 0.098 (U = 250 meV). The masses m_{x1}, m_{y1}, m_{z1}, m_{x2}, m_{y2}, m_{z2} were then calculated for (100) and (111) oriented structures (in the latter case for the longitudinal and oblique ellipsoids apart) [7]. These masses determine the 2D parabolic dispersion laws $\varepsilon_1(k_x, k_y)$ and $\varepsilon_2(k_x, k_y)$ of electrons in barrier layers and in QW.

In the paper [8] we have used these masses for the investigation of electron transport along the well layer. But this approximation is sufficiently only for large QWs. Really it needs to determine from (1) the dispersion law for each dimensional quantization subband and for each d. It is found that due to the finite barrier and to anisotropy of effective masses the dispersion law is nonparabolic, although in the bulk materials it was considered parabolic.

In this paper we consider the electron dispersion law in each subband parabolic, but unlike the Ref. [8] we calculate from (1) the electron effective masses $m_x(d)$ and $m_y(d)$ at the bottom of the subband which are functions of d. Jast these masses will characterise the electron transport in the subbands. The estimations demonstrate that this is a rather good approximation.

Each valley forms its set of subbands. For (111) oriented QW the valley degeneracy is partially lifted and therefore we have one set of subbands arising from the longitudinal ellipsoid, which is oriented along [111] direction or perpendicular to the QW's plan (longitudinal

subbands), and other set, arising from three oblique to [111] direction ellipsoids (oblique subbands). In the case of (100) oriented QW the valley degeneracy is preserved and as result there is only one set of subbands.

The study of electron population of the subbands has shown that in the case of (100) oriented QWs only the lowest subband from this set is populated for a large interval of well widths $d \leq 100$Å and electron concentrations $n \leq 10^{19}$ cm^{-3}. The situation is more complicated for (111) QW. In this case one must take into consideration at least two subbands: the lowest longitudinal and the lowest oblique subbands.

Fig.1 shows the variation of relative electron effective masses $(m_i(d) - m_i)/m_i$, where $i=x, y$, in dimensional quantization subbands as a function of well width for (100) and (111) oriented QWs. It is seen that the masses $m_x(d)$, $m_y(d)$ in the longitudinal subband of (111) QW grow very weakly with the decease of d. The masses $m_x(d)$, $m_y(d)$ in the oblique subband grow more, and the highest growth occurs for the masses in (100) QW.

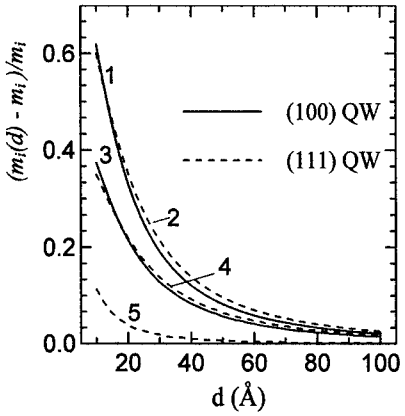

Fig. 1 Variation of the relative electron effective mass in dimensional quantization subbands as a function of the QWs width d. Potential barriers height is U = 171 meV. Curve 1 is for m_y in the lowest subband of (100) well; 2 is for m_y in the oblique subband of (111) well; 3 is for m_x in (100) well; 4 is for m_x in the oblique subband of (111) well; 5 is for m_x and m_y in the longitudinal subband of (111) well.

Elecrical Conductivity and Thermopower

In order to calculate the electrical conductivity we have deduced the system of kinetic equations of Boltzmann for the nonequilibrium distribution functions of electrons in the given 2D subband deriving from the each valley. The scattering both on optical and acoustical phonons was taken into consideration. The kinetic equations were linearized in a weak electric field and then were solved by the variational method using the simplest variational function [10] with one variational parameter.

The total conductivity σ is the sum of conductivity tensors σ_{ij} of all valleys led up to a certain definite coordinate system. One can observe that because of cubic symmetry of initial materials σ is a scalar both for (100) and for (111) oriented QWs. As it was noted above, in the case of (100) QWs for the well widths $d \leq 100$Å and electron concentrations $n \leq 10^{19}$ cm^{-3} one may employ the one-subband approximation. In the case of (111) QWs it needs to take into account two lowest subbands arising from longitudinal and oblique ellipsoids, respectively.

For the calculation of the thermoelectric power tensor S_{ij} it was also employed the variational method, but now the variational function must contain at least two variational parameters. As in the case of σ the total 2D thermoelectric power is a scalar and it is noted by S.

RESULTS AND DISCUSSION

The results of numerical calculation of σ are shown in Fig. 2. The values of parameters were taken from [11]. The potential barrier height was chosen $U = 171$ meV corresponding to Eu content $x = 0.073$ as in experimental work [12]. It is confirmed that the scattering on optical phonons is more important although the scattering on acoustical phonons must also be taken into account.

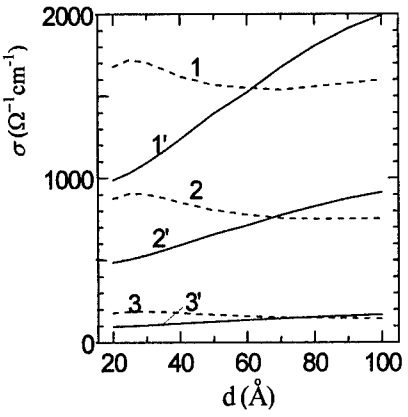

Fig. 2. Calculated electrical conductivity σ of $PbTe/Pb_{1-x}Eu_xTe$ quantum wells as a function of the well width d for (100) oriented QWs, σ_{100}, (solid lines) and for (111) ones, σ_{111}, (dashed lines). Potential barrier height $U = 171$ meV (x = 0.073), T = 300K. Curves 1 and 1′ are for $n = 10^{19}cm^{-3}$; 2 and 2′ for $n = 5 \cdot 10^{18}cm^{-3}$; 3 and 3′ for $n = 10^{18}$ cm^{-3}.

Fig. 2 shows, that σ_{100} decreases when the well width decreases too. This is connected with the increase of the phonon phase-space region involved in scattering processes, and, as a consequence, with the increase of the scattering probability when d decreases. This effect is more pronounced at higher electron concentrations. Another behaviour has σ_{111}. At very small d the main contribution to conductivity is given by the longitudinal subband with small effective masses and high mobilities. Therefore σ_{111} is higher than σ_{100}. When d increases, the electrons pass more and more to oblique subband where the density of states is much greater. But in this subband the effective masses are heavier and carrier mobilities are smaller, and σ_{111} decreases. In all QWs the 2D conductivity is less than in respective bulk material.

The results of numerical calculations of S as a function of d are shown in Fig. 3. It is seen that S reaches the highest values in (100) oriented QWs at small d. In these wells the degree of valley degeneracy is maximum. For increasing well widths, S_{100} decreases as a result of decreasing densities of states. The values of S_{100} at $d = 20$A are only 4 to 6% higher (for diferent concentrations) than in case [8] when the dependence of effective masses on d was neglected.

In (111) QWs the valley degeneracy is partially lifted and there are two subbands. At small d it is populated mainly the longitudinal subband in which the density of states is low. When d increases, S_{111} decreases at small d as S_{100}. With the further increase of d it begins the transfer of electrons from longitudinal to oblique subband where the density of states is much higher, and therefore a weak growth of S_{111} is observed. The values of S_{111} nearly coincide with those obtained when the effective mass dependence on d was negelected.

The above presented data about the conductivity σ and thermopower S permite us now to investigate the power factor $S^2\sigma$ separately for (100) and for (111) oriented QWs.

In Fig. 4 the values of $(S^2\sigma)_{100}$ and $(S^2\sigma)_{111}$ are shown as a function of the well width d for two carrier concentrations. It is seen that the power factor grows with the decrease of d and this effect is more pronounced at very small d. The values of $(S^2\sigma)_{100}$ are higher than those of $(S^2\sigma)_{111}$. The carrier concentrations $n = 10^{19}$ cm^{-3} is near to optimum.

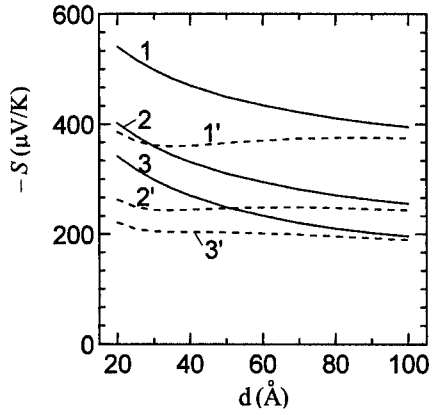

Fig. 3. Calculated thermoelectric power S of PbTe/$Pb_{1-x}Eu_xTe$ quantum wells as a function of the well width d for (100) oriented QWs, S_{100}, (solid lines) and for (111) ones, S_{111}, (dashed lines). Potential barriers height U = 171 meV (x = 0.073), T=300K. Curves 1 and 1′ are for $n = 10^{18}$ cm^{-3}; 2 and 2′ for $n = 5{\cdot}10^{18}$ cm^{-3}; 3 and 3′ for $n = 10^{19}$cm^{-3}.

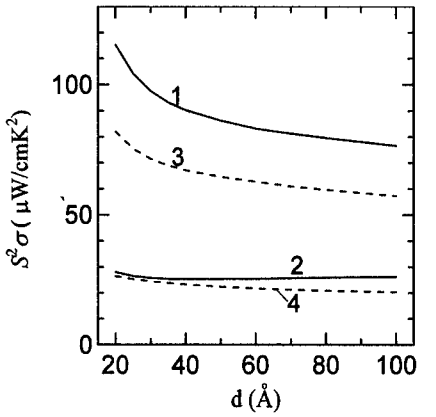

Fig. 4. Thermoelectric power factor $S^2\sigma$ for (100) oriented QWs, $(S^2\sigma)_{100}$ (solid lines) and for (111) ones, $(S^2\sigma)_{111}$, (dashed lines) vs. well width d at T = 300K. Curves 1 and 3 are for $n = 10^{19}$ cm^{-3}; 2 and 4 for $n = 10^{18}$ cm^{-3}.

Thus one may expect that the thermoelectric properties of (100) oriented QWs will be better than of those with (111) orientation, but now the ratio of $(S^2\sigma)_{100}$ to $(S^2\sigma)_{111}$ at d = 20A, $n = 10^{19}$ cm^{-3} and T= 300K is only 1.44 as compared with 1.72 [8] in the case when the effective mass dependence on d was neglected. The expected values of power factor are, respectively, $(S^2\sigma)_{100}$ = 118 μW/cmK^2 and $(S^2\sigma)_{111}$ = 82 μW/cmK^2, which are higher then the best bulk value of 38 μW/cmK^2 [12]. The increase of subband effective masses with decreasing d made worse the thermoelectric properties of QWs.

Finally, it is interesting to compare our results with experimental data for (111) oriented PbTe/$Pb_{1-x}Eu_xTe$ QWs with x = 0.073 presented in the paper [12]. We will not discuss the data for the exceptional sample T-225 with especially high conductivity which is of 47% higher than calculated here. The conductivities of other samples from Table IV in [12] are 13 to 27% lower than calculated values. It is natural because we have naglected some more weak scattering

mechanisms, as scattering on nonpolar optical phonons, intervalley scaterring, intersubband scattering and al. The calculated curves for thermopower and for power factor lie near to measured values. In our opinion, it would be interested to understand the role of interface effects in more narrow than 20 A wells and the role of intersubband scattering in larger ones.

CONCLUSIONS

We have presented the results of a theoretical investigation of the most realistic up today $PbTe/Pb_{1-x}Eu_xTe$ QW model that permits to verify the predicted earlier significant increase of the figure of merit and to determine the expected thermoelectric opportunities of such structures. Calculated values of the conductivity, thermopower (Seebeck coefficient) and power factor are in qualitative agreement with the measured in [12] data for (111) oriented multiple-quantum-well structures with $x = 0.073$. So, the mean of the power factors of four structures with the well widths near 20 A and the carrier concentration near 10^{19} cm^{-3} is 60 $\mu W/cmK^2$, but the calculated values is 82 $\mu W/cmK^2$.

It would be interested to understand the role of interface effects in more narrow than 20 A QWs and the role of intersubband scattering in larger ones.

ACKNOWLEDGEMENT

This work was supported by INTAS under Contract No. 96-0535.

REFERENCES

1. L. D. Hicks and M. S. Dresselhaus, Phys. Rev. **B 47**, 12727 (1993).

2. L. D. Hicks, T. C. Harman and M. S. Dresselhaus, Appl.Phys. Lett. **65**, 3230, (1993).

3. J. O. Sofo and G. D. Mahan, Appl. Phys. Lett. **65**, 2690 (1994).

4. D. A. Broido and T. L. Reinecke, Phys. Rev. **B 51**, 13797 (1995).

5. P. J. Lin –Chung and T.L.Reinecke, Phys. Rev. **B 51**, 13244 (1995).

6. D. A. Broido and T. L. Reinecke, Appl. Phys. Lett. **67**, 1170 (1995).

7. A. Casian, Z. Dashevsky, H. Scherrer, I. Sur and A. Sandu, J. of Thermoel., N3, 29 (1998).

8. A. Casian, Z. Dashevsky, V. Kantser, H. Scherrer, I. Sur and A. Sandu, Proc. of XVII Intern. Conf. on Thermoelectr., Nagoya, 1998 (in press).

9. Shu Yuan, G. Springholz, G. Bauer and M.Kriechbaum, Phys.Rev. **B 49**, 5476 (1994).

10. J. Ziman. *Electrons and Phonons*, Clarendon Press, Oxford, 1960, Chap.10, p. 5.

11. Yu. I. Ravich, B. A. Efimova and I. A. Smirnov, *Methods of investigation of semiconductors applied to lead chalcogenides PbTe, PbSe, PbS*, Nauca Press, Moscow 1968, Annex B.

12. T. C. Harman, D. L. Spears, M. J. Manfra , J. of Electr. Mater., Vol. 25, No 7, 1121 (1996).

THERMOELECTRIC PROPERTIES OF $AgBiTe_2$-Ag_2Te COMPOSITE

Y. TAKIGAWA*, T. IMOTO*, T. SAKAKIBARA*+, K.KUROSAWA**

* Department of Solids State Electronics, Osaka Electro-Communication University, Neyagawa, Osaka 572-8530, Japan, takigawa@isc.osakac.ac.jp
** Department of E&E Eng., University of Miyazaki, Miyazaki 889-2192, Japan
+ Permanent address: Aisin-Cosmos R&D Co., Ltd., Kariya, Aichi 444-0021, Japan

ABSTRACT

We prepared composite materials of $AgBiTe_2$ with several contents of Ag_2Te small-size grains for applications to thermoelectric devices. By enhancing long-wavelength phonon scattering at the grain boundaries, lattice thermal conductivity (thermal conductivity due to lattice vibrations) decreased 30% and thus the thermoelectric characteristics were significantly improved.

INTRODUCTION

Bi_2Te_3 system has been paid much attention for practical thermoelectric devices, because it has been improved significantly by enhancing short-wavelength phonon scattering[1]. In this case, impurity atoms are usually added to a Bi_2Te_3 material and enhance short-wavelength phonon scattering to improve the thermal conductivity. There are a few elements, however, which make solid solutions with Bi_2Te_3. Long-wavelength phonon scattering also contributes to decreases of thermal conductivity [2] and to improve the figure-of-merit for thermoelectric material. For efficient phonon scattering, second-phase grains which have the same order of the dimensions as the phonon wavelength could be incorporated as the phonon wavelength could be incorporated in the matrix. $AgBiTe_2$ [3] and Ag_2Te [4] are thermoelectric semiconductors with relatively low thermal conductivity. Since they have very different melting points for each other [5] [6], Ag_2Te grains would be dispersed in $AgBiTe_2$ matrix by a simple solidification method. In this paper, we prepared a series of $AgBiTe_2$ composite materials dispersed with Ag_2Te grains, and improved thermoelectric properties and also figure-of-merit for thermoelectric materials.

EXPERIMENT

An appropriate ratios of high-purity Ag (above 99.99% purity) wires and Bi (99.999%) and Te (99.999%) lumps were introduced in a silica glass tube. It was evacuated to $\sim 1 \times 10^{-3}$ Pa and then sealed off. The tube was placed in a vertical furnace in which the upper end was kept at 1273 K and the lower end at 1373 K. The raw materials circulated in the tube by convection to be mixed well. The solid solution was cooled down to a temperature below the melting temperature

Mat. Res. Soc. Symp. Proc. Vol. 545 © 1999 Materials Research Society

of Ag_2Te to solidify Ag_2Te but above that of $AgBiTe_2$. In this stage, Ag_2Te grains dispersed in liquid $AgBiTe_2$. Finally, it was quenched to room temperature. The compositions of the final products $(AgBiTe_2)_{1-x}(Ag_2Te)_x$ were varied from x = 0 to1.

Powdered samples were examined with an X-ray diffraction method to clarify the crystal structures. Textures of the composites and sizes of Ag_2Te grains were examined with Electron Probe Micro-Analysis (EPMA: Shimadzu EPMA-850A) . The samples were characterized by measuring electrical conductivity, Seebeck coefficient, Hall mobility, thermal conductivity at room temperature. Electrical conductivity was measured for samples of $2\times2\times12$ mm^3 with a four prove method. Seebeck coefficient was measured for the same size samples by applying 10 K temperature difference in 1×10^{-3} Pa. The Hall mobility was measured with a Van der Pauw method by applying 0.7 T magnetic field. Thermal conductivity was measured for $3.5\times3.5\times4$ mm^3 samples with a absolute method [7] in a vacuum, in which the measured values were calibrated with that of transparent silica glass to be obtained the absolute values. Thermal conductivity consists of phonon and carrier parts. Phonon part is calculated from the measured thermal conductivity by subtracting the calculated carrier part, which are calculated after equation (1) by assuming scattering coefficient (r_n) = 1, because mobility of the composites follow $T^{-1/2}$.

$$\kappa_{car} = (r_n + 5/2)(k_B / e)^2 \qquad (1)$$

RESULTS AND DISCUSSION

In Fig.1 are shown back-scattered electron images taken by an EPMA for $(AgBiTe_2)_{1-x}(Ag_2Te)_x$ with x = 0, 0.15, 0.5, 0.75, and 1. In these figures, the white parts are identified to be $AgBiTe_2$ and the black parts are Ag_2Te with an quantitative analysis by a ZAF method. X-ray diffraction patterns also indicated the samples consisted with $AgBiTe_2$ and Ag_2Te. The images show an important fact that Ag_2Te is not soluble in $AgBiTe_2$ and thus the Ag_2Te grains disperse in the Ag_2Te matrices. The Ag_2Te grain sizes are 200μm for the x = 0.75 sample (d) and 10μm for the x = 0.5 sample (c).

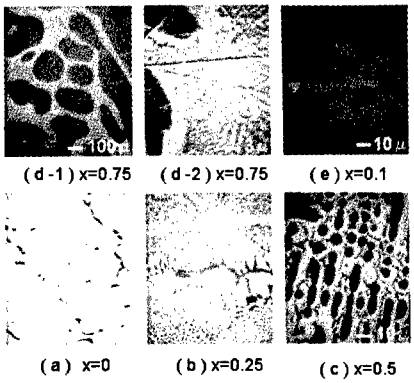

Fig.1. Back scattered electron photographs of $(AgBiTe_2)_{1-x}(Ag_2Te)_x$.

Electrical conductivity and Hall mobility measured for the samples are plotted against the compositions in Fig. 2 and Fig. 3, respectively. Ag_2Te showed the maximum value of 571 S/cm among the samples, and $AgBiTe_2$ did the minimum value of 119 S/cm. The other samples

S/cm among the samples, and $AgBiTe_2$ did the minimum value of 119 S/cm. The other samples had the value between them as expected. The dotted curve showed calculated values according to Maxwell's equation (2) by assuming that $AgBiTe_2$ and Ag_2Te have no interactions. It should be noted here that the value of x = 0.5 sample is on the curve, but the others are not on it.

$$\sigma_m = \sigma_d \frac{\sigma_c + 2\sigma_d - 2(1-V_d)(\sigma_d - \sigma_c)}{\sigma_c + 2\sigma_d + (1-V_d)(\sigma_d - \sigma_c)} \qquad (2)$$

Where σ_m is the electrical conductivity of mixture. σ_c is one of matrix. σ_d is one of dispersoid and V_d is volume percentage of dispersoid.

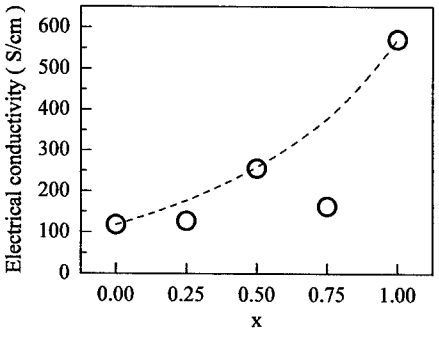

Fig.2. Electrical conductivity of $(AgBiTe_2)_{1-x}(Ag_2Te)_x$ at room temperature.

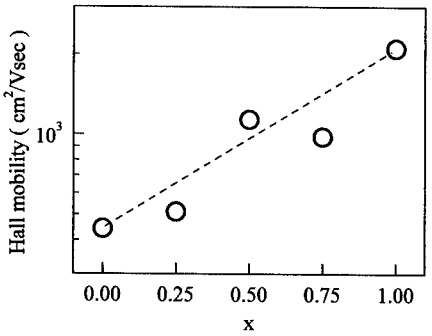

Fig.3. Hall mobility of $(AgBiTe_2)_{1-x}(Ag_2Te)_x$ at room temperature.

Hall mobility data show that the x = 0 sample had the minimum value of 442 cm^2/Vs and the x = 1 sample showed the maximum value of 2099 cm^2/Vs. The dotted line indicates values for the composites ideally insoluble. The x = 0.5 value is on the line, but the others are not. These findings imply that carriers are not scattered at the boundaries between $AgBiTe_2$ matrix and Ag_2TeTe grains in the x = 0.5 sample, but they scattered significantly in the x = 0.25 and 0.75 samples. The carrier scattering induces the electrical conductivity degradation by mixing $AgBiTe_2$ and Ag_2Te with x = 0.25 and 0.75. In this stage we cannot explain why the mixing of $AgBiTe_2$ and Ag_2Te with 50/50 ratio does not affect on the electron scattering.

In Fig. 4 are shown Seebeck coefficient plotted against the composite composition. The negative values indicate they all are electron-carrier type (n-type) semiconductors. Further they are almost the same value.

In Fig. 5 are plotted lattice thermal conductivity against the composition. The values

decrease considerably by mixing Ag_2Te grains in $AgBiTe_2$ matrices. If phonons are not scattered at the grain boundaries, lattice thermal conductivity as shown as dotted line, changes ideally with x after equation (3),

$$\kappa_m = \kappa_c \frac{1-2V_d \dfrac{1-\kappa_d/\kappa_c}{2+\kappa_d/\kappa_c}}{1+V_d \dfrac{1-\kappa_d/\kappa_c}{2+\kappa_d/\kappa_c}} \qquad (3)$$

Where κ_m is the electrical conductivity of mixture. κ_c is one of matrix. κ_d is one of dispersoid .

The composites showed the much smaller values than the ideal ones, which means phonons are effectively scattered at the grain boundaries. We can explain the most effective phonon scattering occurs in the x = 0.5 sample in which the small Ag_2Te grains grew. As the result, the lattice thermal conductivity decreases up to 30 % from the value of dotted line.

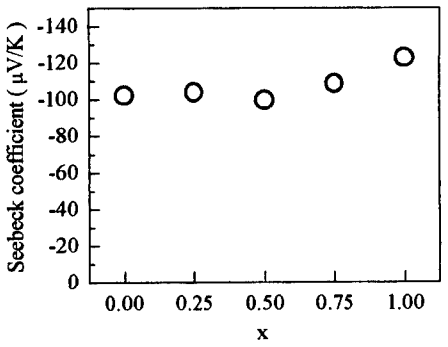

Fig.4. Seebeck coefficient of $(AgBiTe_2)_{1-x}(Ag_2Te)_x$ at room temperature.

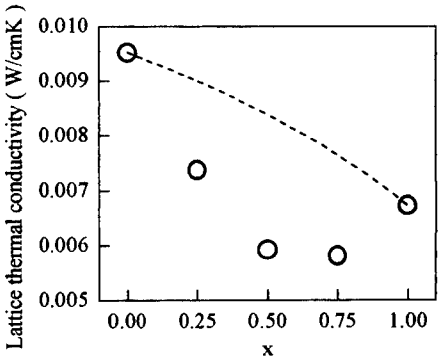

Fig.5. Lattice thermal conductivity of $(AgBiTe_2)_{1-x}(Ag_2Te)_x$ at room temperature.

Figure-of-merit is the most convenient indicator for the practical applications. We estimate the values from equation (4) by using the equation of figure of merit for pai-type module[8].

$$Z_m = \left\{ \frac{\alpha_c(1-V_d)+\alpha_d V_d}{(\kappa_c/\sigma_c)^{1/2}(1-V_d)+(\kappa_d/\sigma_d)^{1/2}V_d} \right\}^2 \qquad (4)$$

Where Z_m is the figure-of-merit of mixture, α_c is Seebeck coefficient of matrix, α_d is one of dispersoid.

In this case, figure-of-merit of the composites are assumed to have the average values with the volume contents. It should be pointed out here that the x = 0.5 sample has the figure-of-merit three times larger than that of $AgBiTe_2$. It means that the thermal conductivity is significantly enhanced by dispersing Ag_2Te grains in $AgBiTe_2$ matrices.

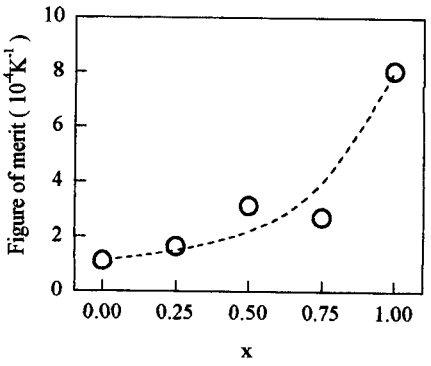

Fig.6. Figure of merit of $(AgBiTe_2)_{1-x}(Ag_2Te)_x$ at room temperature.

CONCLUSIONS

We prepared a series of composite materials of $(AgBiTe_2)_{1-x}(Ag_2Te)_x$ with x = 0, 0.25, 0.5, 0.75 and 1, and examined the effects of long-wavelength phonon scattering at the grain boundaries of Ag_2Te on the thermoelectric properties of $AgBiTe_2$ thermoelectric semiconductors. Ag_2Te was insoluble in $AgBiTe_2$ and deposited as the grains. The enhancement of the phonon scattering resulted in the enhancement of the figure of merit. This leads an alternative way to improve thermoelectric property.

ACKNOWLEDGMENTS

We gratefully acknowledge the financial support of the president, Mr. Hori, in carrying out the research.

REFERENCES

[1] W.M. Yim and F.D. Rosi, Solid-State Electronic **15**, 1121 (1972).

[2] N. Savvides and H.J. Goldsmid, J. Phys. C:Solid St. Phys. **13**, 4657(1980)

[3] A.V. Petrov and E.L. Shtrum, Soviet Physics-Solid state **4**, 1061 (1962).

[4] P. F. Taylor and C. Wood, J. Appl. Phys. **32**, 1 (1961)

[5] A. Stegherr, P. Eckerlin and F. Wald, Z. Metallkde. **54**, 598 (1963)

[6] T.B. Massalski, *Binary alloy phase diagrams,* 2nd ed. (ASM Inter.,1990).,Vol.1,p.102

[7] M.H. Ettenberg, W.A. Jesser and F.D. Rosi, *Proceedings 15th International Conference on Thermoelectrics*, Pasadena, U.S.A.,1996, p.53-56 (IEEE)

[8] P.H. Klein, *Thermoelectric Materials and Devices*, edited by I. B. Cadoff and E. Miller, (Reinhold Publishing Corporation, New York, 1960) p.55

EXPERIMENTAL STUDY OF PHONON-FOLDING IN Si/Ge and Si/SiGe STRUCTURES DESIGNED FOR THERMOELECTRIC APPLICATIONS

J. LIU *, A. BALANDIN *, T. BORCA-TASCIUC**, Y.S. TANG *, K.L. WANG *, G. CHEN **

* Device Research Laboratory, Electrical Engineering Department, University of California - Los Angeles, Los Angeles, CA 90095 USA, alexb@ee.ucla.edu

** Nanoscale Heat Transfer and Termoelectricity Laboratory, Department of Mechanical and Aerospace Engineering, University of California - Los Angeles, Los Angeles, CA 90095 USA

ABSTRACT

We report data of Raman study of Si/Ge and Si/SiGe superlattices designed for thermoelectric applications. The obtained Raman spectra clearly indicate the presence of folded doublets from longitudinal acoustic phonons. Due to the significant difference in the sound velocities for Si and Ge the position of the doublets strongly depends on the superlattice layer thickness and ordering. Comparison of the Raman data for different samples with measured thermal and thermoelectric properties allows us to determine a correlation between the strength of the phonon confinement in these structures and their thermoelectric properties. Our experimental results are consistent with recent theoretical prediction of increased thermoelectric figure of merit in semiconductor quantum wells.

INTRODUCTION

It was recently shown theoretically that confinement of acoustic phonon modes in semiconductor structures may bring about significant modification of their thermoelectric properties [1-3]. The predicted increase of the thermoelectric figure of merit in quantum wells and superlattices with distinct boundaries was a result of a significant drop of the phonon group velocities due to spatial confinement. The latter leads to an increase of the phonon relaxation rates and thus, a strong drop in the lattice thermal conductivity. This modification of the thermoelectric figure of merit ZT comes in addition to earlier predicted increase due to two-dimensional confinement of carriers [4-5], and increased boundary scattering [6].

In this experimental work, we tried to establish the strength of phonon confinement (folding) in Si/SiGe and Si/Ge superlattices and its possible relation to the thermoelectric properties of the samples. Since conduction band discontinuity is not big for such structures, the possible modification of the samples' thermoelectric properties is likely related to their phonon properties and/or boundary scattering. The paper is organized as follows. First we describe sample preparation and Raman spectroscopic measurements. Then, the results of simple theoretic modeling are compared with the folded phonon frequencies extracted from the experiment. Finally we discuss the relevance of the phonon folding to the modification of the thermoelectric properties of the superlattices.

Mat. Res. Soc. Symp. Proc. Vol. 545 © 1999 Materials Research Society

EXPERIMENT

The samples were grown using a solid source molecular beam epitaxy (MBE) system. A bonded SOI wafer with 200 nm Si on 360 nm SiO_2 was cleaned using a standard Shiraki's cleaning method and introduced into the MBE system immediately. The protective oxide layer was removed by subsequent heating of the substrate to 930°C for 15 minutes. Then, the substrate temperature was reduced to 500°C. After that in order to manufacture the sample JL057, a graded $Si_{1-X}Ge_X$ (x from 0 to 0.3) of 200 nm was first grown, followed by a 5 periods $Si_{0.7}Ge_{0.3}$ (30 nm)/Si (5 nm) with n-type δ-doping in the center of $Si_{0.7}Ge_{0.3}$ layer.

For JL092, a p-type Si (100) wafer was selected as substrate. After similar chemical cleaning and thermal cleaning process, the substrate temperature was reduced and kept at 500°C. 1.1μ-thick relaxed $Si_{1-X}Ge_X$ graded buffer was then grown on the substrate. Ge concentration x is ranging from 0 to 1 with a step of 0.1, which means there are 11 layers with each layer thickness of 100 nm in the buffer. On the top of the buffer, there are 150 periods of 33 Å Si /33 Å Ge superlattice with a uniformly heavy n-type doping.

Raman spectra were measured using a Renishaw Raman 2000 microscope at the room temperature. All spectra were excited by the 514-nm line of an Ar ion laser in the back-scattering configuration and recorded by a Si CCD camera. The spectral resolution of the instrument was about 0.1 cm^{-1}.

A typical Raman spectrum of the sample JL057 is shown in Fig. 1. In addition to regular Ge-Ge and Si-Ge Raman peaks, the spectrum clearly displays a vibrational mode of the doublet structure with a midfrequency at $\Delta\omega$ = 129.1 1/cm.. This doublet was attributed (see next section) to the longitudinal acoustic folded phonon mode of the order of 3. Other lower and upper laying folded phonon modes are not clearly seen because they are overshadowed by the laser fundamental peak and Ge-Ge Raman peak, respectively. The assignment of acoustic folded phonon peaks is based on the elastic continuum approximation, and is briefly discussed below.

In Fig. 2 we present a Raman spectrum of the sample JL092. A strong peak is clearly seen at 96.9 1/cm. The peak intensity is rather high at the given incident light and detector polarizations. We attributed this peak to the second order folded acoustic phonon. The first order folded phonon peak is around 54.2 1/cm. The peak is broader than the one in Fig. 1. This is attributed to the difference in sample quality, and confirmed by TEM data.

THEORY AND DISCUSSION

In order to find approximate folded phonon peak positions, we use Rytov's model which describes layered elastic media [8]. Recently, this model was successfully used to describe phonon folding in a number of material systems [9, 10]. The dispersion relation of the longitudinal acoustic phonons in superlattices is given by the following approximate relation

$$\omega(q) \equiv \omega_m(q) = V_{eff}\,(q + 2\pi m / D),$$
$$m = 0;\pm 1;\pm 2;\ldots, \qquad (1)$$
$$\frac{D}{V_{eff}} = \frac{D_1}{V_1} + \frac{D_2}{V_2},$$

where $D=D_1+D_2$ is the period of the superlattice, V_{eff} is the effective sound velocity in the structure, V_1 and V_2 are the longitudinal sound velocities in the material 1 and 2 (Si or SiGe, in our case), ω is the phonon frequency, q is the phonon wave vector, and m is the folding index.

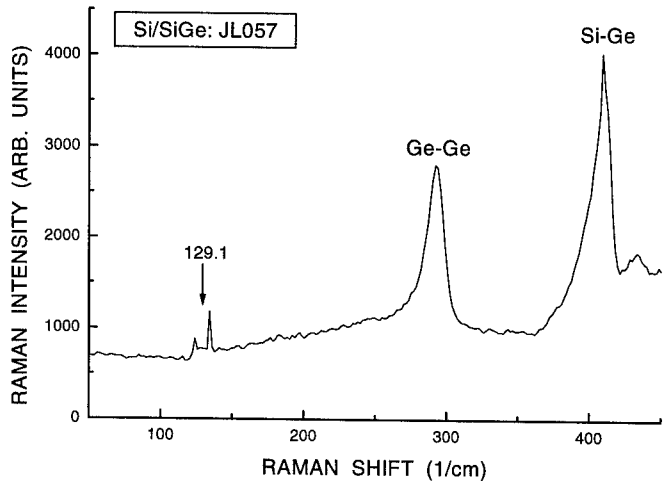

Figure 1. Raman spectrum of sample JL057. A folded peak (note the doublet structure) from the longitudinal acoustic phonon is clearly seen at 129.1 1/cm.

In our numerical simulation for the sample JL057, we have used the following sound velocities for the constituent materials: $V_1 = V_{Si}$=9.1 10^5 cm/sec, V_{Ge}=5.0 10^5 cm/sec. The velocity V_2 of the $Si_{0.7}Ge_{0.3}$ layer was estimated to be 6.96 10^5 cm/sec. The effective velocity for the JL057 sample was calculated using Eq. (1), and is equal to 7.2 10^5 cm/sec. Using Rytov model of Eq. (1) we have evaluated positions of acoustic folded phonon modes. The results are summarized in Table I.

Table I. Theoretical and experimental midfrequencies for JL057

M	1	2	3	4
ω_m^{theory} (1/cm)	43.1	86.2	129.2	172.3
ω_m^{exper} (1/cm)	-	(89.2)	129.1	(175.0)

As one can see from the table the calculated peak positions are close to the experimentally measured ones. These results indicate that acoustic phonon modes in the thermoelectric samples are strongly modified. The later is expected to effect the lattice thermal conductivity of the superlattices, and eventually, the thermoelectric figure of merit. Note that the peaks at 89.2 1/cm and 175.0 1/cm are not as clearly seen in Fig. 1 as the peak at 129.1 1/cm. They were detected only at particular polarization selected by a detector.

We were not able to fit experimentally observed peaks for the sample JL092 using the same procedure as described above. It is possible that due to higher strain in the thin-layer Si/Ge superlattice, the longitudinal sound velocities V_1 and V_2 in the layers of Si and Ge are very much different (smaller) from the bulk. In such a case, the value of the effective velocity calculated using Eq. (1) will be incorrect.

Assuming that the peaks at 56.0 1/cm and 96.9 1/cm are indeed first (m=1) and second (m=2) order folded acoustic phonons, we can evaluate the effective sound velocity in the sample JL092. Since the peak at 96.9 1/cm has the highest intensity we use it as a reference point and calculate the effective velocity from the equation

$$V_{eff} = \omega_m D / (2\pi m). \qquad (2)$$

For the given peak position and m=2, the effective velocity is V_{eff}=1.5 10^5 cm/sec which is much less then expected from the bulk values.

THERMAL CONDUCTIVITY DATA

Thermal conductivity measurements have been carried out for the same samples using the 2 wire-3ω method. The experimental set-up and sample preparation are described elsewhere [11]. Both buffer and superlattice structure of the sample JL092 have anisotropic thermophysical properties. The measured thermal conductivity for the buffer layer is 8.5 W/mK in the in-plane direction and 10.32 W/mK in the cross-plane direction. The thermal conductivity of the superlattice of this sample is 1.7 W/mK in the in-plane direction and 2.78 W/mK for the cross-plane direction, respectively. Obtained thermal conductivities are considerably lower than those determined using the bulk thermal conductivities for Si, Ge, and Si_xGe_{1-x} alloys [11]. This drop in thermal conductivity may be attributed to the strong modification of the phonon modes (and corresponding phonon velocities) which lead to the phonon folding observed in Raman spectra.

Indeed, the band gap offset between $Si_{1-x}Ge_x$ and Si is estimated to be around 127 meV. The first confined level for electrons in a 50 A wide Si quantum well has the energy of about 79 meV. This means that the carrier confinement is not very strong in such structures, and observed decrease of the thermal conductivity of such structures can be

attributed not only to qusi-2D carrier confinement but also to the modification of phonon modes.

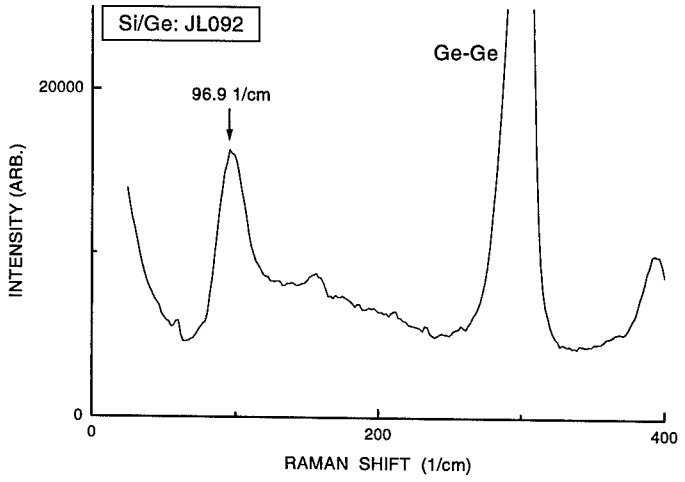

Figure 2. Raman spectrum of sample JL092. A strong folded peak from the longitudinal acoustic phonon is clearly seen at 96.9 1/cm.

CONCLUSIONS

We presented preliminary results of Raman study of Si/Ge and Si/SiGe superlattices designed for thermoelectric applications. The obtained Raman spectra clearly indicate the presence of folded doublets from the longitudinal acoustic phonons. Due to the significant difference in the sound velocities for Si and Ge the position of the doublets strongly depends on the superlattice layer thickness and ordering. We argue that modification of phonon modes affects significantly lattice thermal transport through the sample and, as a result, thermoelectric properties. Experimentally observed drop in the thermal conductivity of Si/Ge sample maybe attributed to the decrease of phonon velocities due to phonon confinement (folding). Further investigation and comparison of the Raman data for different Si/Ge and Si/SiGe samples with measured thermal and thermoelectric properties is needed in order to determine exact correlation between the strength of the phonon confinement in these structures and their thermoelectric properties.

ACKNOWLEDGEMENT

This work was supported by the DoD MURI-ONR program on Thermoelectrics (Dr. John Pazik).

REFERENCES

1. A. Balandin and K.L. Wang, Phys. Rev. B **58**, 1544 (1998).

2. A. Balandin and K.L. Wang, "Giant drop of the lattice thermal conductivity due to confinement of acoustic phonons," in *Nanostructures: Physics and Technology*, edited by Zh. Alferov, L. Esaki (Ioffe Institute, St. Petersburg, 1998), p. 24.

3. A. Balandin and K.L. Wang, J. Appl. Phys., **84**, 6149 (1998).

4. L.D. Hicks, M.S. Dresselhaus, Phys. Rev. B **47**, 12727 (1993).

5. L.D. Hicks, T.C. Harman, X. Sun, and M. Dresselhaus, Phys. Rev. B **53**, R10493 (1996).

6. G. Chen, Trans. Of ASME **119**, 220 (1997); G. Chen, Phys. Rev. B **57**, 14958 (1998).

7. K.L. Wang and X. Zheng, in *Properties of Strained and Relaxed Silicon Germanium*, edited by E. Kasper (INSPEC, the Institution of Electrical Engineers, London, UK, 1995), p. 70-78.

8. S.M. Rytov, Soviet Phys. Acoust. **2**, 67 (1956).

9. C. Colvard, T.A. Gant, M.V. Klein, R. Merlin, R. Fischer, H. Korkoc, and A.C. Gossard, Phys. Rev. B., **31**, 2080 (1985).

10. X.L. Wu, G.G. Siu, M.J. Stokes, S. Tong, F. Yan, X.N. Liu, X.M. Bao, S.S. Jiang, X.K.Zhang, and D. Feng, Appl. Phys. Lett **69**, 1855 (1996).

11. T.Borca-Tasciuc, D. Song, J. L. Liu, G. Chen K. L. Wang, X. Sun, M. S. Dresselhaus, T. Radetic , R.Gronsky, "Anisotropic thermal conducitvity of Si/Ge superlattices," paper presented at the 1998 MRS fall meeting.

Structure and Thermoelectric Properties of $SrBiTe_3$; 12-Fold Superstructure Caused by Distortion of the Two-Dimensional Te-Nets

Kyoung-Shin Choi*, Duck-Young Chung*, Joy Heising*, Paul W. Brazis**, Carl R. Kannewurf** and Mercouri G. Kanatzidis*
*Department of Chemistry and Center for Fundamental Materials Research, Michigan State University, East Lansing, MI, 48824.
**Department of Electrical Engineering and Computer Science, Northwestern University, Evanston, IL 60208.

ABSTRACT

The ternary compound, $SrBiTe_3$, was prepared by the molten flux method. It crystallizes in the orthorhombic space group Pmmn with a=4.665(2)Å, b=4.517(2)Å, c=16.129Å, and Z=2. The compound is composed of a NaCl-type $[Bi_2Te_4]^{2-}$ layer and a flat square $(Te_2)^{2-}$ net with equal Te-Te distances of 3.24Å. The Sr^{2+} ions are stabilized between the layers in monocapped square antiprismatic sites. X-ray and electron diffraction studies reveal a 12-fold superstructure due to subtle distortions within the Te net of the compound. The superstructure was refined in the monoclinic space group C2 with a=27.923(5)Å, b=32.228(6)Å, c=4.5069(9)Å, β=90.000(3)°. The compound is a semiconductor with a band gap value of 0.14 eV. It melts incongruently at 613 °C.

INTRODUCTION

Given that solid solutions of Bi_2Te_3 are currently the leading thermoelectric materials for cooling applications near room temperature, solid state Bi compounds are receiving a great deal of attention. The challenge in finding a superior thermoelectric material lies in simultaneously achieving high electrical conductivity (σ), high thermopower (S), and low thermal conductivity (κ). These properties define the thermoelectric figure of merit $ZT = (\sigma \cdot S^2/\kappa) \cdot T$. Our approach to obtain compounds with a high figure of merit has been to synthesize new bismuth chalcogenide materials with greater compositional and structural complexity. Specifically, we decided to incorporate alkali, alkaline earth, and lanthanide metal ions into the bismuth chalcogenide framework. These ions are stabilized between the layers or in the channels of the anionic framework and act as "rattlers". These rattlers create low frequency vibration modes that scatter acoustic phonons and thus, reduce the thermal conductivity. The complexity in the structure tends to produce a corresponding complexity in the electronic band structure, which according to the Mott formula may give rise to high thermopower as well as high electrical conductivity.[1]

Recently, we have prepared several new compounds, including $BaBiTe_3$[2], β-$K_2Bi_8Se_{13}$[1], $K_{2.5}Bi_{8.5}Se_{14}$[1], $CsBi_4Te_6$[3], $ALn_{1\pm x}Bi_{4\pm x}S_8$ (A = K, Rb; Ln = La, Ce, Pr, Nd)[4], and $K_{1.25}Pb_{3.5}Bi_{7.25}Se_{15}$[5]. These compounds exhibit very promising thermoelectric properties, which warranted a systematic study of this class of compounds. As a subsequent study to $BaBiTe_3$, we became interested in the properties of the Sr analog. The structure of $SrBiTe_3$ was first reported in 1982[6] in the noncentrosymmetric space group, $Pmn2_1$, and it is entirely different from that of $BaBiTe_3$. It is composed of Sr^{2+} ions sandwiched between $[Bi_2Te_4]^{2-}$ layers and flat $(Te_2)^{2-}$ nets. We, however, noticed a center of inversion in the structure and decided to perform a careful structural study as well as physicochemical and charge transport characterization. In doing so, we discovered a 12-fold superstructure caused by the subtle displacement of Te atoms in the net. In addition, we found that Bi sites may be disordered with a considerable amount of Sr atoms, giving the strontium rich formula $Sr_{1+x}Bi_{1-x}Te_3$($0.28<x<0.35$). For simplicity, we refer to this

Mat. Res. Soc. Symp. Proc. Vol. 545 © 1999 Materials Research Society

compound as $SrBiTe_3$ throughout this manuscript. Here, we report a complete structural study, physicochemical, and thermoelectric properties of $SrBiTe_3$.

RESULTS AND DISCUSSION

Synthesis and Physicochemical Characterization

$SrBiTe_3$ was synthesized from a mixture of Sr/Bi/Te in a ratio of 2:1:8 that was sealed in an evacuated carbon-coated quartz ampoule, heated at 800 °C for 6 days, and cooled to room temperature at a rate of -4 °C/h. Square plates of $SrBiTe_3$ were obtained by isolation in water to remove the excess $SrTe_x$ and washing with tri-n-butylphosphine to remove elemental Te present in excess (yield >90 % based on Bi metal). The crystals are stable in air and water. This compound melts incongruently at 613 °C.

The Raman spectrum shows shifts at 161cm^{-1} and 166cm^{-1} due to the stretching vibration of the Te-Te bonds[7]. The optical diffuse reflectance spectrum was obtained from the finely ground sample at room temperature. It shows the presence of an energy gap at 0.14 eV confirming that this compound is a narrow gap semiconductor, see Figure 1. This value is smaller than that of $BaBiTe_3$ which is found around 0.28eV[2].

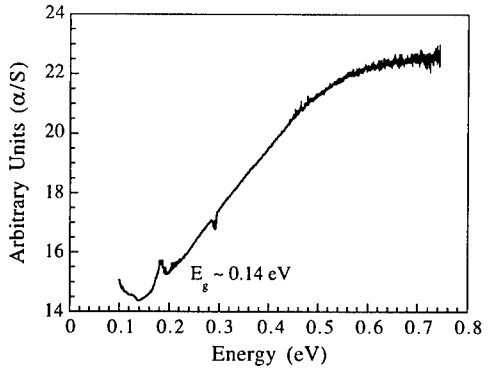

Figure 1. Optical absorption spectra of $SrBiTe_3$.

Structure

Initially, the intensity data for the substructure were collected on a Rigaku AFC6S four-circle automated diffractometer equipped with a graphite-crystal monochromator. The substructure with the unit cell of a = 4.665(2) Å, b = 4.517(2) Å, c = 16.129(5) Å was solved and refined successfully with the centrosymmetric Pmmn space group suggesting that the earlier description in the $Pmn2_1$ space group is incorrect. The overall structure of $SrBiTe_3$, viewed down to the b-axis, is shown in Figure 2. It is composed of two different kind of slabs, $[Bi_2Te_4]^{2-}$ layers and flat $(Te_2)^{2-}$ layers, with Sr^{2+} ions stabilized between them. The $[Bi_2Te_4]^{2-}$ layers are built from edge-shared $BiTe_6$ octahedra. All the $BiTe_6$ octhedra are distorted in such a way that the Bi^{3+} ion has three long bonds and three short bonds mostly due to the stereochemical expression of the $6s^2$ lone pair electrons of Bi^{3+} ions. The local environment of Sr^{2+} ions is best described as 9-coordinate monocapped square antiprismatic. The Sr-Te distance is 3.327(1) Å . The $(Te_2)^{2-}$ layer is composed of square Te nets with equal Te-Te distances of 3.24 Å , which is longer than the normal Te-Te bond distance of 2.78 Å found in Rb_2Te_2 [5]. We observed that one of the anisotropic

temperature factors, U22, of Te atoms in the Te net was unusually high compared to the others indicating that there might exist a supercell due to the positional modulation of Te atoms along the b-axis. The possibility for superstructure was examined by transmission electron microscopy (TEM). Indeed, electron diffraction studies revealed a 6-fold supercell along the a-axis, see Figure 3. We then carefully recollected single crystal X-ray data on a Siemens SMART Platform CCD diffractometer using long exposure time and found an additional two-fold supercell along the c-axis resulting in a 12-fold superstructure (a' = 6a, b' = 2c, c' = b).

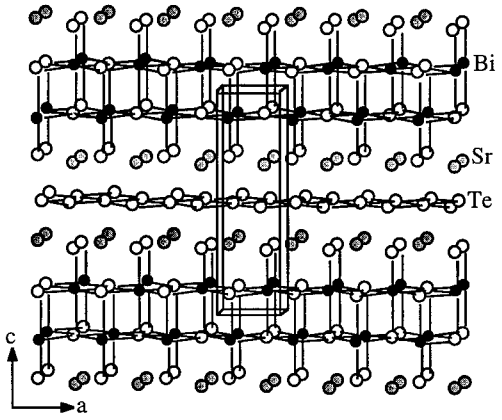

Figure 2. The substructure of $SrBiTe_3$ viewed down to the b-axis.

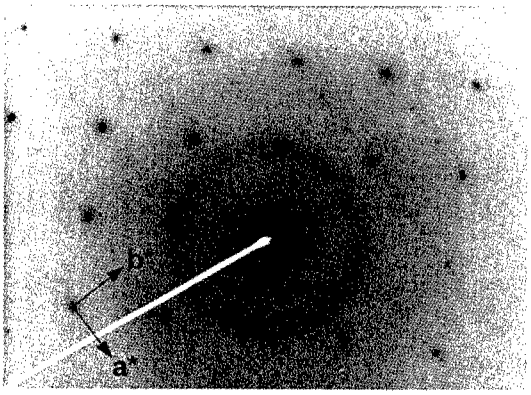

Figure 3. Selected area electron diffraction pattern of $SrBiTe_3$ with the beam parallel to the [001] zone axis showing weak 6-fold supercell reflections along the a-axis.

The superstructure was solved and refined successfully in the monoclinic space group C2 with a'=27.923(5)Å, b'=32.228(6)Å, c'=4.5069(9)Å, β=90.000(3)°. This superstructure shows a clearly distorted Te net, which more accurately presents the

positions of Te atoms in the net. There exist seven crystallographically distinct Te atoms in the superstructure and their positions are slightly moved from those in the substructure along the b-axis (c'-axis in superstructure), resulting in 6-fold supercell along the a-axis. The distance of Te-Te bonds in the net varies from 3.121 Å to 3.359 Å instead of one equal distance of 3.24 Å in the substructure. If a Te-Te bond is drawn between Te atoms which have shorter interatomic distances than 3.2 Å, Te atoms form an infinite zigzag chain, not a Te square net, see Figure 4. The distortion from the ideal square net eliminates all the symmetry elements present in the substructure except the two-fold axis parallel to the c-axis (b'-axis of the superstructure) and lowers the symmetry of the supercell to the noncentrosymmetric C2 space group. The reason why the c-axis of the substructure is doubled in the superstructure is also related with the Te nets. When the Te net stacks along the c-axis, every other layer of Te net is shifted by 1/2 a' along the a'- axis thus doubling the repeating unit along the c-axis. The positional change of Bi, Sr and Te atoms in the $[Bi_2Te_4]^{2-}$ layer with respect to the substructure is negligible.

After successive refinement, the temperature factors of several Bi atoms remained high, suggesting either that these sites are disordered with lighter Sr atoms or that there exist vacancies on these sites. Allowing mixed occupancy between Bi and Sr atoms dropped the temperature factors and R-values significantly (from R1=0.0685 wR2=0.1960 to R1=0.0587 wR2=0.1476). We performed the occupancy refinement on several different crystals and the resulting formula were consistent as $Sr_{1+x}Bi_{1-x}Te_3$ ($0.27<x<0.35$). At this point, the oxidation state of the Te net remains uncertain since we cannot exclude the possibility that these sites contain vacancies instead of disorder. A quantitative analysis such as ICP is need to confirm the formula. In any case, we expect this compound to exhibit substancially low thermal conductivity due to the presence of disorder or vacancies.

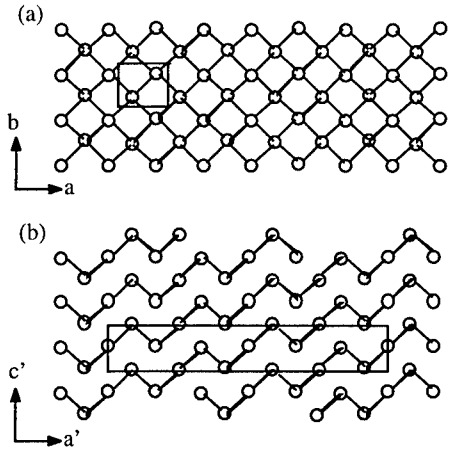

Figure 4. The Te layer as it appears in the substructure is an ideal square net(a) and in the superstructure is a distorted net(b).

Charge Transport Properties

It was very difficult to obtain large single crystals of suitable quality for transport measurement. The electrical properties of $SrBiTe_3$ were measured on small single crystal samples, see Figure 5. The room temperature conductivity of the compound, ~5 S/cm, is

considerably lower than what we expected based on the narrow band gap (0.14 eV) of the material.

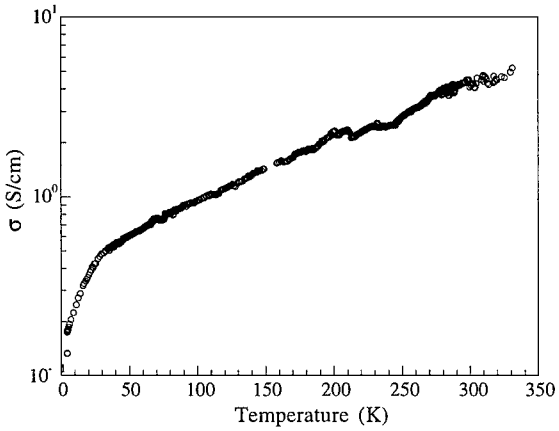

Figure 5. Electrical conductivity as a function of temperature for a crystal of $SrBiTe_3$. The crystal is shown in Figure 6.

To check the quality of the specimens, we performed an SEM microscopic examination on the same crystal used for the measurement. Figure 6 shows that the crystal does not have a high quality due to many cracks on the surface, which most likely interfered with the measurement and substantially decreased the electrical conductivity. Nevertheless, we proceeded to measure thermopower at room temperature just to probe the nature of the charge carriers in the material. The thermopower data shows a positive Seebeck coefficient, 58 μV/K indicating the charge carriers are holes (p-type).

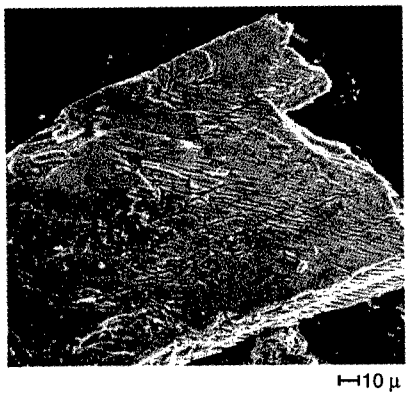

Figure 6. SEM photograph of the small crystal of $SrBiTe_3$ which was used for the electrical conductivity measurements.

We believe that both of the electrical properties were underestimated due to the poor quality of the specimens. The growth of good samples of $SrBiTe_3$ is challenging due to the greater thermodynamic stability of Bi_2Te_3. At this point, we are trying to optimize the synthetic conditions to obtain crystals with better quality, which will allow us to perform better measurements on this compound.

CONCLUSIONS

The ternary compound $SrBiTe_3$ was prepared by the molten flux method and has a very large unit cell due to the subtle distortion of its square Te net. This compound is a p-type semiconductor with a narrow band gap of 0.14 eV. The electrical conductivity measurements, however, were not successful due to the poor quality of the crystals. We are currently optimizing synthetic conditions to produce crystals of higher quality. A possibility of replacing Sr^{2+} with Eu^{2+} atoms is also under investigation to study the difference in structure and properties when a rare earth is substituted for an alkaline earth metal in a similar structural environment[8].

ACKNOWLEDGMENTS

Financial support from the Office of Naval Research (Grant No. N00014-98-1-0443) is gratefully acknowledged. Work at Northwestern University made use of the Center Facilities support by the National Science Foundation though the Northwestern University Materials Research Center (DMR-9632472).

REFERENCES

1. D.-Y. Chung, K.-S. Choi, L. Iordanidis, J. L. Schindler, P. Brazis, C. R. Kannewurf, B. Chen, S. Hu, C. Uher, and M. G. Kanatzidis, Chem. Mater. **9**, 3060 (1997).
2. D.-Y. Chung, S. Jobic, T. Hogan, C. R. Kannewurf, R. Brec, J. Rouxel, and M. G. Kanatzidis, J. Am. Chem. Soc. **119**, 2505 (1997).
3. D.-Y. Chung, T. Hogan, P. Brazis, C. R. Kannewurf, and M. G. Kanatzidis, manuscript in preparation.
4.. L. Iordanidis, J. L. Schindler, C. R. Kannewurf, and M. G. Kanatzidis, J. Solid State Chem., in press.
5. K.-S. Choi, D.-Y. Chung, P. Brazis, C. R. Kannewurf, C. Uher, and M. G. Kanatzidis, manuscript in preparation.
6. R. Cook and H. Schäfer, in *Studies in Inorganic Chemistry* Vol. 3, edited by R. Metselaar, H. J. M. Heijligers and J. Schoonman (Elsevier Scientific Publishing Company, Amsterdam, 1983), p. 757-760.
7. P. Böttcher and J. Getzschmann, R. Keller, Z. anorg. allg. Chem. **619**, 476 (1993).
8. K.-S. Choi, M. G. Kanatzidis, work in progress.

THERMOELECTRIC PROPERTIES OF THE CUBIC FAMILY OF COMPOUNDS $AgPbBiQ_3$ (Q = S, Se, Te). VERY LOW THERMAL CONDUCTIVITY MATERIALS

S. Sportouch*, M. Bastea†, P. Brazis#, J. Ireland#, C.R. Kannewurf#, C. Uher† and M.G. Kanatzidis*

** Department of Chemistry, Michigan State University, East Lansing, MI 48824*
† Department of Physics, University of Michigan, Ann Arbor, MI 48190-1120
 # Department of Electrical Engineering and Computer Science, Northwestern University, Evanston,IL 60208

ABSTRACT

The $AgPbBiQ_3$ class of compounds and their solid solution members are related to the NaCl structure type, where Ag, Pb and Bi atoms are statistically disordered on the Na site and Q atoms occupy the Cl site. These compounds were synthesized by combining the elements in the appropriate ratio and heating under static vacuum at 900° C for 3 days. They are narrow gap semiconductors with band gaps in the range of 0.6 to 0.28 eV. The charge-transport properties were measured on ingots as a function of temperature. The compounds $AgPbBiTe_3$, $AgPbBiSe_3$, $AgPbBiTe_{2.75}Se_{0.25}$ and $AgPbBiTe_2Se$, undoped, possess an electrical conductivity in the range of 70 S/cm to 400 S/cm. These materials exhibit negative thermopower ranging from -40 μV/K to -160 μV/K at room temperature and thermal conductivity less than 1.30 W/mK.

INTRODUCTION

The best thermoelectric cooling and generator devices developed over the past forty years have been made with doped bismuth telluride alloys.[1] The efficiency of these materials at room temperature, however, is only about 10% of the Carnot efficiency. In comparison, a regular freon cooling system achieves about 40% of the Carnot efficiency[2], and some thermodynamic studies have shown that the Carnot efficiency of thermoelectric systems can be improved to 80% or higher.[2] The tremendous possibility for improvement in these materials has been a powerful motivation for the present research.

A thermoelectric material is characterized by, the "so-called" figure of merit,

$$ZT = S^2\sigma T/\kappa$$

where S is the Seebeck coefficient, σ is electrical conductivity ,T is temperature and κ represents thermal conductivity, which is a function of both electron and phonon contributions. Consequently, to improve a material for thermoelectric applications means that one must achieve a high Seebeck coefficient combined with low thermal conductivity and high electrical conductivity. All these parameters are interdependent and are related to the electronic structure and charge carrier scattering of the material. Optimized n or p doped Bi_2Te_3 alloys[3] possess a figure of merit of about 0.9-1.0, with conductivity around 900 S/cm, a Seebeck coefficient of ± 220 μV/K, and thermal conductivity of about 1.5 W/Km. An increase in this figure of merit by more than 100% would already be a significant step forward. A systematic approach is developed in the $AgPbBiQ_3$ system to identify multinary compounds with the cubic NaCl-structure type which may be suitable for thermoelectric applications.

Mat. Res. Soc. Symp. Proc. Vol. 545 © 1999 Materials Research Society

RESULTS-DISCUSSION

The $AgPbBiQ_3$ compounds[4,5], (Q = S, Te) crystallize in the NaCl structure type ($Fm\bar{3}m$). The Ag, Pb and Bi atoms occupy the Na site and are statistically disordered, whereas the chalcogen atoms are found on the Cl site. These compounds can be viewed as derivatives of the cubic (NaCl) $AgBiQ_2$ compounds mixed with PbQ. It has already been shown that high temperature forms of $AgBiS_2$ and $AgBiTe_2$ form a complete series of solid solutions with PbS and PbTe[6]. Surprisingly, the cell parameters of the solid solutions $(AgBiS_2)_{1-x}(PbS)_x$ were reported to have nonlinear dependence on the composition whereas $(AgBiTe_2)_{1-x}(PbTe)_x$ solid solutions exhibit linear dependence (Vegard's law). In addition, no previous work has been reported in the literature on $AgPbBiSe_3$.

It is worthwhile to explore the possibility that $AgPbBiSe_3$ can be obtained with the NaCl structure type and to investigate its charge transport properties; hence, we can compare them with the S and Te members and synthesize corresponding solid solution members.

$AgPbBiQ_3$, (Q=S, Se, Te) synthesis and properties.

All the compounds have been synthesized by combining the elements in stoichiometric amounts and heating under static vacuum at 900° C for 3 days. The $AgPbBiSe_3$ compound was synthesized as well as its homologues with Te and S. The X-ray powder diffraction patterns were in agreement with a NaCl structure type for the three compounds, with no visible impurities, see Figure 1. The position of the powder X-ray diffraction peaks were determined using the program PROLIX[7]. The cell parameters were refined from the experimental powder pattern data with the program U-Fit[8], and found to be 5.865(1) Å, 5.954(1) Å, and 6.290(2) Å respectively for the sulfur, selenium and tellurium compounds. The differential thermal analyses show that $AgPbBiS_3$, $AgPbBiSe_3$ and $AgPbBiTe_3$ do not melt below 900° C; however, a weak phase transformation occurs around 820° C for $AgPbBiSe_3$. Throughout this paper the quoted values of the charge transport properties are for room temperature.

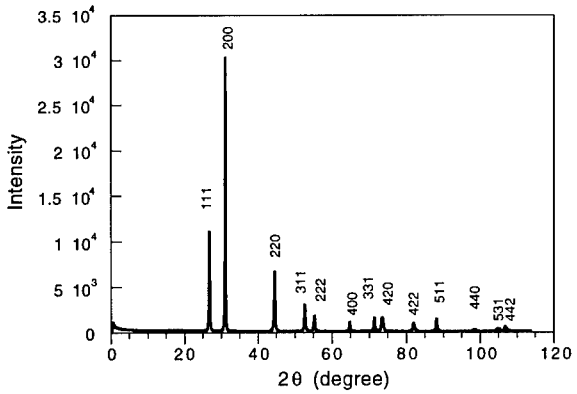

Figure 1 : X-ray powder pattern of $AgPbBiS_3$

The electrical conductivities are shown Figure 2 as a function of temperature. The corresponding room temperature values are 25, 67 and 300 S/cm for $AgPbBiS_3$, $AgPbBiSe_3$ and $AgPbBiTe_3$, respectively. The temperature dependence of the resistivity for $AgPbBiTe_3$ is metallic type while the dependences of the other members are typically semiconducting. In the case of $AgPbBiS_3$, below 100 K this dependence is characteristic of conduction due to impurities. Using diffuse reflectance infrared spectroscopy, the semiconductor energy band gaps are found to be 0.54 eV, 0.48 eV and 0.28 eV respectively for $AgPbBiS_3$, $AgPbBiSe_3$ and $AgPbBiTe_3$. The electrical conductivity of the materials increases as the band gap decreases, which follows the expected trend.

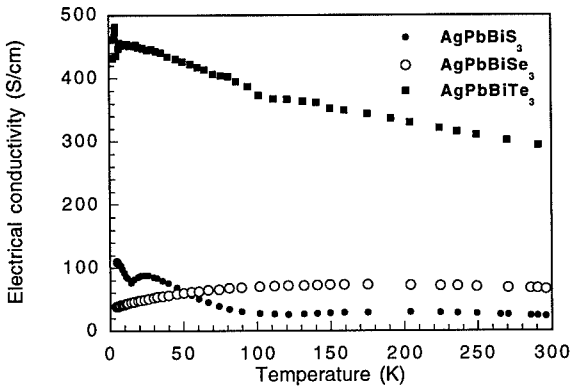

Figure 2 : Electrical conductivity versus temperature for $AgPbBiQ_3$ (Q=S, Se, Te).

The Seebeck coefficient versus temperature, reported in Figure 3, indicates that the

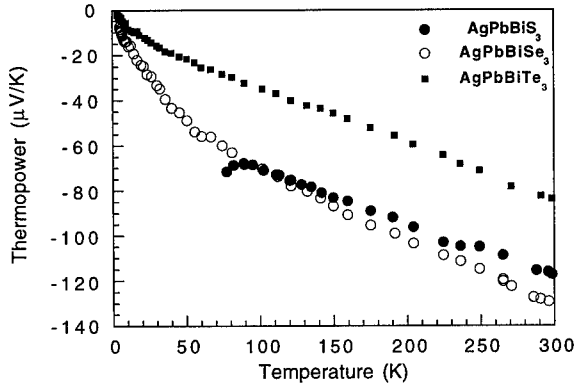

Figure 3 : Thermopower as a function of temperature for $AgPbBiQ_3$ (Q=S, Se, Te).

S, Se and Te members possess negative thermopower which increases as a function of temperature. The S and Se compounds have higher thermopower values, -160 μV/K and -130 μV/K respectively, than the Te compounds, which have thermopower value of -90 μV/K. The power factor ($S^2\sigma$, where S is the thermopower and σ is the electrical conductivity) of these n type semiconducting compounds decreases in the sequence Te, Se, S and the values are 0.064 mW/K^2m, 0.113 mW/K^2m and 0.243 mW/K^2m.

The thermal conductivities of these materials, as shown in Figure 4, are very low for undoped compounds especially ones with a small cubic unit cell. Their values vary from 1.3 W/mK for $AgPbBiS_3$ to 1.0 W/mK for $AgPbBiSe_3$ and 1.20 W/mK for $AgPbBiTe_3$. Above 30 K, the temperature dependence of the thermal conductivity is dominated by the electron and phonon scattering, and the curves are typical of semiconductor materials.

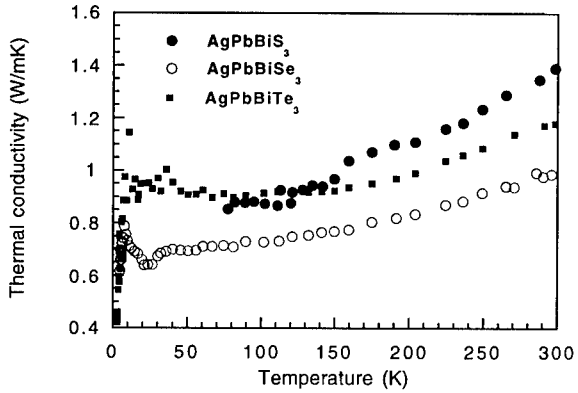

Figure 4 : Thermal conductivity versus temperature in the $AgPbBiQ_3$ (Q=S, Se, Te) system.

The impressively low thermal conductivity in these semiconductor compounds may be due to fact that the contribution of the phonons to the thermal conductivity is minimized in these systems. Several mechanisms are known to reduce the lattice thermal conductivity such as electron-phonon scattering in heavily doped compounds, electron charge transfer scattering in mixed valence systems and mass fluctuation scattering in solid solutions. The only possible mechanism corresponding to the studied compounds is the mass fluctuation scattering. The mass fluctuations in $AgPbBiQ_3$ may be caused by statistical disorder of three different kinds of heavy atoms Ag, Pb and Bi in the structure which eliminates any long range ordering. Similar observations have been made on $Ag_xPb_{1-2x}Sb_xTe$ system[9] where the "rattling" motion of the Ag atoms causes low thermal conductivity. The mass fluctuation statement is limited to short wavelength phonons, unfortunately, because the scattering law is a function of ν^4, where ν is the phonon frequency. Another consequence of the mass fluctuation is to reduce the mobility of the carriers especially those carriers

which move along energy bands composed of the orbitals of the disordered atoms, i.e. Ag, Pb and Bi.

In order to study how these thermoelectric properties can be varied, we first studied the solid solutions between $AgPbBiTe_3$ and $AgPbBiSe_3$.

$AgPbBiTe_{3-x}Se_x$ Solid solutions

Some selected members, $AgPbBiTe_{2.75}Se_{0.25}$, $AgPbBiTe_{2.5}Se_{0.5}$, $AgPbBiTe_{2.25}Se_{0.75}$ and $AgPbBiTe_2Se$, were synthesized using the same procedure described above. The cell parameters of the compounds were determined using the experimental powder diffraction patterns and were refined with the program U-Fit. The lattice parameters are 6.274(1) Å, 6.247(1) Å, 6.191(1) Å and 6.185(2) Å for $AgPbBiTe_{2.75}Se_{0.25}$, $AgPbBiTe_{2.5}Se_{0.5}$, $AgPbBiTe_{2.25}Se_{0.75}$ and $AgPbBiTe_2Se$ respectively, They follow Vegard's law between the end members $AgPbBiTe_3$ and $AgPbBiSe_3$ as shown in Figure 5.

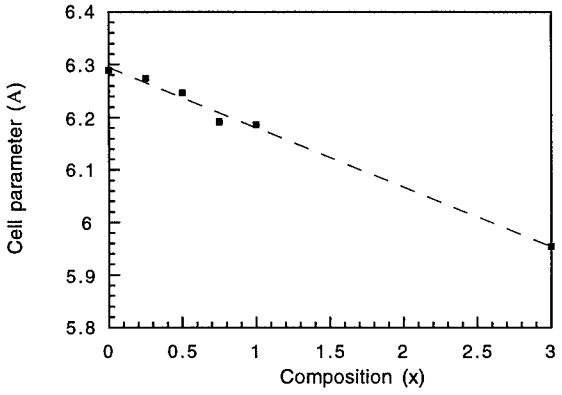

Figure 5 : Relationship between cell parameters and composition.

The temperature dependence of the electrical conductivity (see Figure 6) from 50 to 300K is typical semiconducting type, decreasing as a function of the temperature for $AgPbBiTe_{2.5}Se_{0.5}$, and $AgPbBiTe_{2.25}Se_{0.75}$. The electrical conductivity values are 133 S/cm, 77 S/cm, 150 S/cm and 400 S/cm respectively for $AgPbBiTe_{2.75}Se_{0.25}$, $AgPbBiTe_{2.5}Se_{0.5}$, $AgPbBiTe_{2.25}Se_{0.75}$ and $AgPbBiTe_2Se$. These values lie between the electrical conductivity values of the end members except for the $AgPbBiTe_2Se$ compound. The comparison of this last sample with the end member $AgPbBiTe_3$ corresponds to an improvement of the electrical conductivity by 33%. The corresponding band gaps of these materials are 0.29 eV for both $AgPbBiTe_{2.5}Se_{0.5}$ and $AgPbBiTe_{2.25}Se_{0.75}$ and 0.32 eV for $AgPbBiTe_2Se$, which are in the same range as $AgPbBiTe_3$.

The thermal conductivity versus temperature (see Figure 7) gives low thermal conductivity values of 1.15 W/mK, 1.6 W/mK, 1.1 W/mK, and 1.3 W/mK for

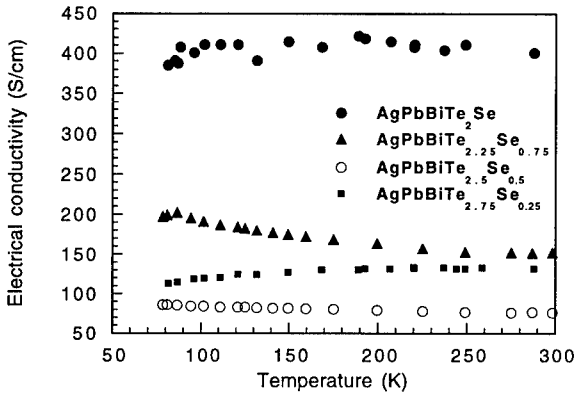

Figure 6 : Electrical conductivity versus temperature in the solid solution $AgPbBiTe_{3-x}Se_x$ (x=0.25, 0.5, 0.75 and 1).

$AgPbBiTe_{2.75}Se_{0.25}$, $AgPbBiTe_{2.5}Se_{0.5}$, $AgPbBiTe_{2.25}Se_{0.75}$ and $AgPbBiTe_2Se$, respectively. However, the thermal conductivity is not significantly decreased compared to the end members. Usually the main effect of a solid solution on the charge transport properties is to reduce the thermal conductivity by increasing the disorder in the lattice and therefore increasing the phonon scattering. Here the pure end members possess already very low thermal conductivity due to the statistical disorder of Ag, Pb and Bi atoms and further disordered between Te and Se seem to have a minimal effect.

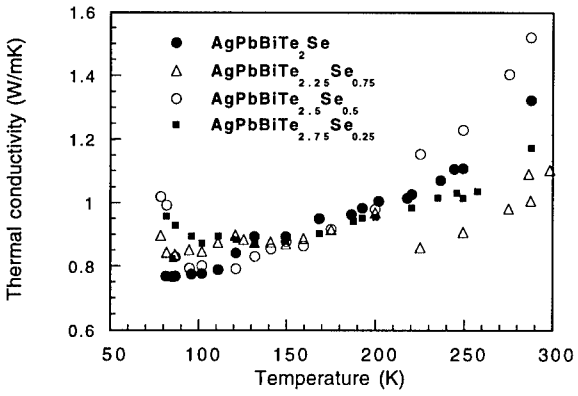

Figure 7 : Thermal conductivity versus temperature in the solid solution $AgPbBiTe_{3-x}Se_x$ (x=0.25, 0.5, 0.75 and 1).

The Seebeck coefficients of these compounds are negative and fall between the end member values, -105 μV/K, -80 μV/K, -40 μV/K and -60 μV/K for $AgPbBiTe_{2.75}Se_{0.25}$, $AgPbBiTe_{2.5}Se_{0.5}$, $AgPbBiTe_{2.25}Se_{0.75}$ and $AgPbBiTe_2Se$ respectively. These negative thermopower values increase as a function of temperature, see Figure 8. A minimum is observed for x=0.75, and the end member, $AgPbBiTe_3$, retains the highest power factor (0.147 mW/K^2m, 0.049 mW/K^2m, 0.024 mW/K^2m and 0.134 mW/K^2m for $AgPbBiTe_{2.75}Se_{0.25}$, $AgPbBiTe_{2.5}Se_{0.5}$, $AgPbBiTe_{2.25}Se_{0.75}$ and $AgPbBiTe_2Se$, respectively). The figures of merit achieved for the solid solution members are below or the same as the values obtained for the pure members. A figure of merit of 0.03 is achieved for $AgPbBiTe_2Se$ and 0.04 for $AgPbBiTe_{2.75}Se_{0.25}$.

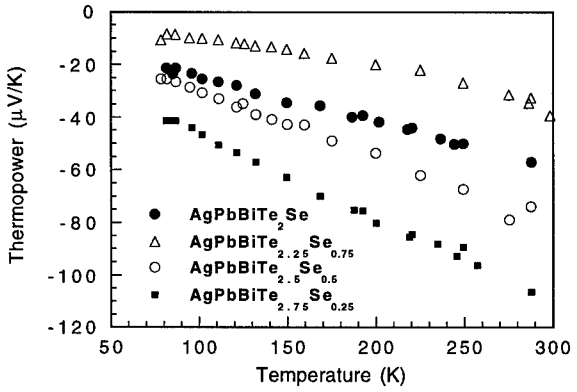

Figure 8 : Thermopower as a function of the temperature in the solid solution $AgPbBiTe_{3-x}Se_x$ (x=0.25, 0.5, 0.75 and 1).

CONCLUSION

We have studied the charge transport properties of the $AgPbBiQ_3$ (Q=S, Se, Te) compounds as well as those of $AgPbBiTe_{3-x}Se_x$ solid solutions. All these compounds are n-type semiconductors with Seebeck coefficients in the range of -40 μV/K to -160 μV/K. Their electrical conductivities are from 25 S/cm to 400 S/cm with the lower values for the solid solution members. Their corresponding semiconductor energy band gaps are narrow (0.28 - 0.54 eV). The thermal conductivities of all these materials are very low, about 1.2 W/Km a value which is even lower than for Bi_2Te_3. Given the relatively low electrical conductivity of the solid solutions, it appears that the introduction of mass fluctuation on both sites of the NaCl lattice substantially reduces the carrier mobilities. An optimum situation would be if p-type materials could be made in which the holes would move predominantly through the Q-based valence bands while the phonons would scatter through the disordered Ag/Pb/Bi sublattice.

Our synthetic investigations reveal that $AgPbBiSe_3$ can be synthesized and this compound forms a series of solid solution members with $AgPbBiTe_3$. Their cell parameters follow a linear function of the composition (Vegard's law). This law is not followed by $AgPbBiS_3$ This work calls attention to a new class of very low thermal conductivity compounds, $AgPbBiTe_3$, $AgPbBiSe_3$, $AgPbBiTe_{2.75}Se_{0.25}$ and $AgPbBiTe_2Se$, as promising candidates for thermoelectric applications. Efforts to dope these compounds are in progress.

ACKNOWLEDGMENTS

This work was supported at NU and MSU by the Office of Naval Research (grant no. N00014-98-1-0443). Work at NU made use of the Central Facilities supported by the National Science Foundation through the NU Materials Research Center (DMR-9632472).

REFERENCES

1. G. Mahan, B. Sales, J. Sharp, *Physics Today* **50**, 3, 42 (1997).
2. M.G. Kanatzidis, F.J. Disalvo, *Naval Research Reviews* **4**, 14 (1996).
3. *CRC Handbook of thermoelectrics*, D.M. Rowe, Eds CRS Press, Inc. Boca Raton, Fl,1995 and references therein.
4. H. Fleischmann, O.G. Folberth, H. Pfister, *Z. Naturforsch.* **14A**, 999 (1959).
5. G.D. Guseinov,E.M. Godzhaev, Kh.Ya.Khalilov, F.M. Seidov, A.M. Pashaev, *Inorg. Mater.* **8**, 9, 1377 (1972).
6. J.H. Wernick, *Am. Mineral.* **45**, 591, (1960).
7. M. Evain, J.M. Barbet, P. Deniard, R. Brec, *Powder Diffraction Meeting*, Toulouse, France (1990).
8. M. Evain, *U-fit : "A cell parameter refinement program"*, Institut des Matériaux de Nantes, France (1992).
9. M.C. Goetz, J.A. Cowen, *Solid State Commum.* **41**, 293 (1982).

THE INFLUENCE OF SILICON DOPANT AND PROCESSING ON THERMOELECTRIC PROPERTIES OF B_4C CERAMICS

Ke-feng CAI, Ce-Wen NAN and Xin-min MIN
State Key Laboratory of Advanced Technology for Materials Synthesis and Processing,
Wuhan University of Technology, Wuhan 430070, China

ABSTRACT

B_4C ceramics doped with various content of Si (0 to 2.03 at%) are prepared via hot pressing. The composition and microstructure of the ceramics are characterized by means of XRD and EPMA. Their electrical conductivity and Seebeck coefficient of the samples are measured from room temperature up to 1500K. The electrical conductivity increases with temperature, and more rapidly after 1300K; the Seebeck coefficient of the ceramics also increases with temperature and rises to a value of about $320\mu VK^{-1}$. The value of the figure of merit of Si-doped B_4C rises to about $4 \times 10^{-4} K^{-1}$ at 1500K.

INTRODUCTION

Boron-rich carbides with anomalously large Seebeck coefficient, surprisingly low thermal conductivity and high-temperature stability indicate a potential use as high-temperature thermoelectric (TE) materials [1-3]. As TE materials, there have recently been many studies on the boron carbides (B_xC) in the literature. Among them, Wood and Emin[4] investigated the effect of carbon concentration on the Seebeck coefficient and electrical conductivity of B_xC (up to 1273 K) and developed a small polaron hopping theory for the electronic transport in B_xC. Wood, Emin and Grey [5] measured the thermal conductivity of B_xC for a series of x values as a function of temperature up to 1300K. Bouchacout and Thevnot [2] also measured TE power, electrical and thermal conductivities of B_xC in the single phase homogeneity range from $B_{10.5}C$ to B_4C, and their results are slightly different from the results given by Wood and co-workers. In the literature, actually, different and even conflicting results have been obtained for these properties of B_xC [2].This might be due to different raw materials and different processing route used to fabricate B_xC. Also there have been a few studies on the structure of B_xC[6,7].

Until recently, most work on the boron carbides has been focused on the effect of the carbon concentration on the TE properties and structure of B_xC. There has been only a little published work on doping effect in the boron carbides on their TE properties. For example, Wood [8] has reported a p-type sample of B_9C doped with 0.5% Mg with value of thermoelectric figure-of-merit (Z) as large as 5×10^{-4} at 1000 ^oC; Aselage[3] has studied P-doped boron carbide. On the other hand, there has been little published work on the effect of microstructure of the boron carbide ceramics on their TE properties. Compared with boron-rich carbides, B_4C has lower figure of merit mainly because of its lower electrical conductivity. A recent calculation by the quantum chemical method (SCC-DV-Xα) shows that doping Si into B_4C will change the electrical structure of B_4C and increase the electrical conductivity of B_4C[9]. In this work, we dope Si into B_4C and investigate the effect of Si dopant in B_4C and the processing on the TE properties and microstructure of B_4C ceramics so as to improve the TE properties of B_4C.

Mat. Res. Soc. Symp. Proc. Vol. 545 © 1999 Materials Research Society

EXPERIMENT

B_4C powder (average particle size 0.5 μm, Moudanjiang boron carbide powder plant, China) was mixed with various content of Si (analysis purity, -400 mesh). The mixture was milled (B_4C:WC-based cement ball=1:10 wt.) for 10 hours in alcohol and then dried in vacuum. Cylindrical samples (10 mm in diameter, 15 mm in height) were prepared by hot-pressing at 1900°C and 25-35 MPa for 30-90min under argon in boron nitride-lined graphite dies. During the hot-pressing, graphite end caps (10 mm in diameter, 1 mm in thickness) were bonded to the cylinders, which facilitated attachment of platinum electrodes (10 mm in diameter, 0.3 mm in thickness) located at the two ends of the sample and prevented the reaction between B and Pt. Thermocouple and electrical leads for Seebeck coefficient and electrical conductivity measurements were soldered on the slices of the platinum electrode. Electrical conductivity and Seebeck coefficient measurements were carried out using a computer control testing system up to 1500 K under argon. Two-probe method with chopped direct current was employed to measure the electrical conductivity. Seebeck coefficient was determined by the slop of the linear relationship between the thermal electromotive force and temperature difference (about 10-15 K) between the two ends of the specimen, which was caused by cooling one end of the sample using cold argon. Thermal conductivity were measured by using the common laser flash method on 2-3 mm thick slices. The density and apparent porosity of the samples were determined by the method given by the American Society of Testing and Materials Criterion(ASTMC375[10]). XRD, EPMA (JXA-8800R type) were used for characterizing the samples.

RESULTS AND DISCUSSION

The density of the samples doped with 0, 1.2, 1.62, 2.03 at% Si and prepared under the same condition (1900 ℃ × 30min × 25MPa) are 1.991,1.6976, 1.6782,1.6686g/cm^3, respectively. The XRD analyses show that undoped sample contains only B_4C and a small amount of W_2B_5, while all the Si-doped samples contain B_4C, W_2B_5, Si and SiC, which implies that the solubility of Si in B_4C under the present sintering condition is smaller than 1.2%. It is considered that W_2B_5 is introduced via ball milling. Because of the high hardness of B_4C, the composition (WC) of the balls is introduced into the B_4C powder by ball wear during the ball-milling, and then W_2B_5 particles are produced via the reaction between WC and B_4C during sintering. During the sintering, beside forming solid solution with B_4C, Si also reacts with the byproduct, C, of the reaction between WC and B_4C to produce SiC. Because SiC is also difficult to be sintered, Si-doped samples have lower density.

The electrical conductivity of all the samples increases with temperature (Fig.1a). As the temperature is below 1100K, the electrical conductivity of Si-doped samples is lower than that of undoped sample, because the former has lower density and contains SiC with lower electrical conductivity than B_4C. As the temperature rises, 1.62% Si-doped sample has higher conductivity. The Seebeck coefficient of all the samples linearly increase with temperature. 1.2% Si doped sample has a little lower Seebeck coefficient and 1.62% Si doped sample has higher Seebeck coefficient (Fig.1b). Relatively speaking, 1.62% Si-doped sample has better thermoelectric properties. Therefore, the influence of sintering condition (pressure and soaked time) on the thermoelectric properties of 1.62% Si-doped sample was studied below.

The density of the samples hot-pressed at 1900 ℃ for 30min but at different pressure, 25, 30 and 35 MPa, are 1.6782, 1.9159 and 1.919 g/cm^3, respectively. The XRD of the samples shows that dissociated Si disappears but the content of SiC increases with increasing pressure.

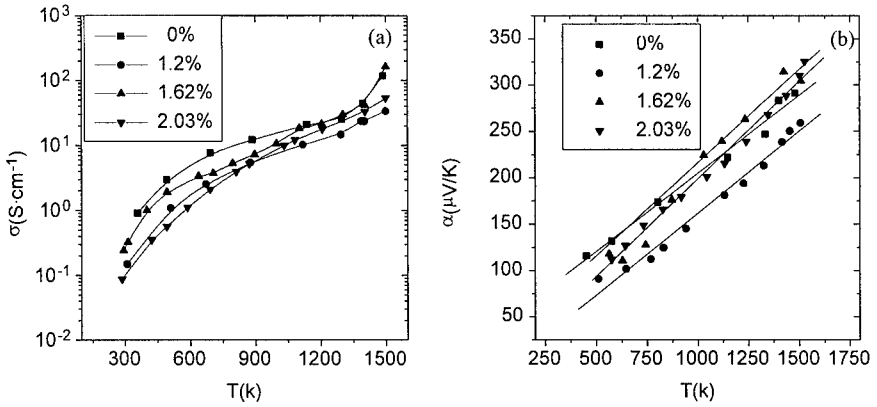

Fig.1 (a) Electrical conductivity and (b) Seebeck coefficient as a function of temperature for Si-doped B_4C samples doped with different Si.

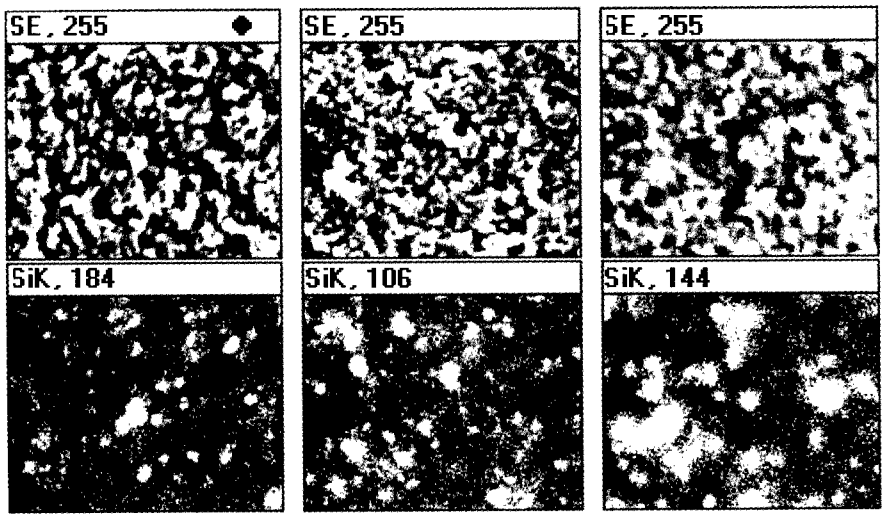

Fig.2. Second electron images and Si images of the samples HPed at 1900℃for 30 min and at various pressure (a) 25MPa, (b) 30MPa and (c) 35MPa.

The EPMA analysis (Fig.2) of the samples more clearly illustrates the change in microstructure with pressure.

The samples hot pressed at three different pressures almost have the same value of electrical conductivity as the temperature is below 1000K, while above 1000K the sample hot pressed under 25MPa has higher electrical conductivity because there is less content of SiC in the sample (Fig.3 a). Fig.3 b also shows that the Seebeck coefficient for all the samples increases monotonicaly with temperature, and the Seebeck coefficient for the sample pressed under 25MPa is higher.

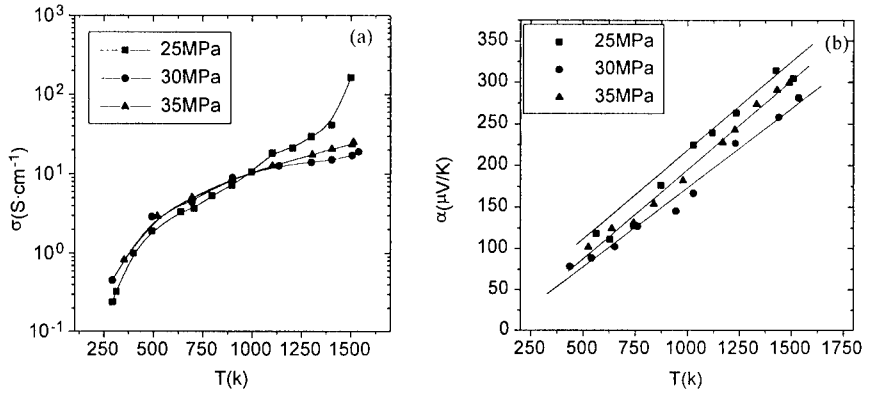

Fig. 3 Temperature dependence of (a) electrical conductivity and (b) Seebeck coefficient for 1.62% Si-doped B_4C hot pressed at three pressures

The density of the samples hot-pressed at the same temperature (1900℃) and pressure (25 MPa) but for different soaked time, 30 45, 90 min, are 1.6782, 1.7466 and 1.7295 g/cm^3, respectively. Their XRD analyses show that as the soaked time increase there is no dissociated Si left and that the sample soaked for 45 min has weak peaks for SiC and the sample soaked for 90 min has strong SiC peaks relatively. That is to say, the content of soild solution of Si in B4C in 45 min soaked sample is more than that in other two samples. It also can be known by comparing their EPMA analyses that the Si distribution in the soaked 45 min sample is more uniform than in the others.(Fig.4).

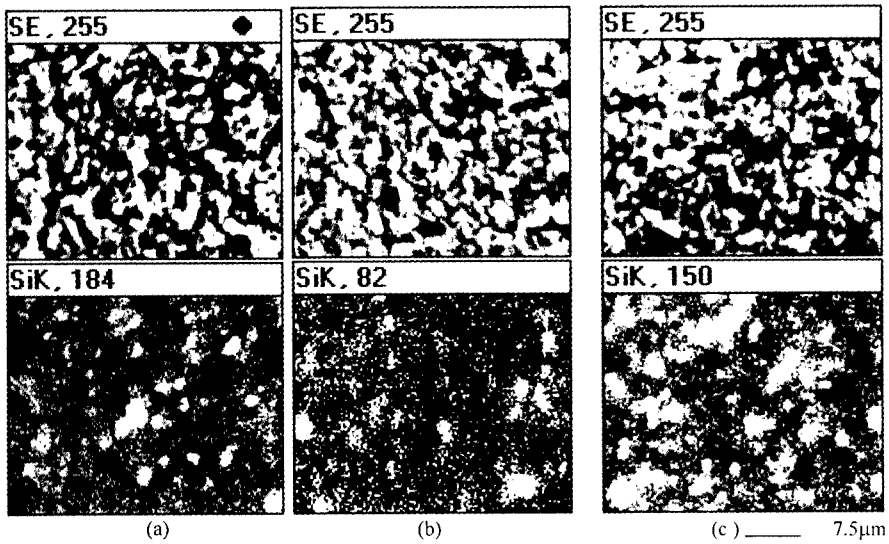

Fig.4. Second electron images and Si images of the samples HPed at 1900℃ and 25 MPa for various soaked time (a) 30min, (b) 45 min and (c) 90min.

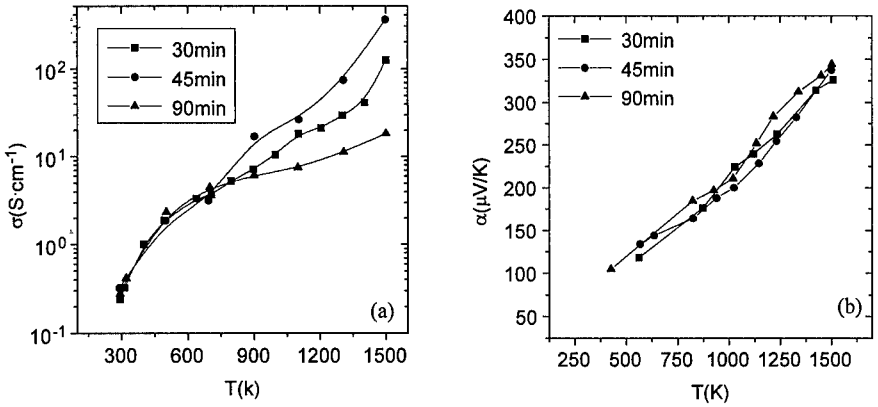

Fig.5 Temperature dependence of (a) electrical conductivity and (b) Seebeck coefficient of the samples soaked for different time.

Fig.5 shows the temperature dependence of electrical conductivity and Seebeck coefficient of these three samples. As the temperature is below 750K, the electrical conductivity of the samples is not sensitive to the sintering temperature, while the electrical conductivity of the 45 min soaked sample is the biggest and that of the 90 min soaked sample smallest, as the temperature is above 750K. It indicates that the electrical conductivity in the high-temperature range of the ceramics is very sensitive to the content of SiC. Similarly, the Seebeck coefficient for these three samples increases linearly with temperature and is nearly independent of soaked time. The power factor (Fig.6) calculated from the measurement of Seebeck coefficient and electrical conductivity of the samples has similar temperature dependence to their electrical conductivity. At 1500K, the power factor of the sample soaked for 45 min is about 40 $\mu W/cm \cdot K^2$, and its thermal conductivity is about 10 $W/m \cdot K$, hence, the figure of merit of the sample is up to $4 \times 10^{-4} K^{-1}$ at 1500K, and seems to increase with temperature in the high temperature range. It indicates that the ceramic has good thermoelectric properties at high temperature.

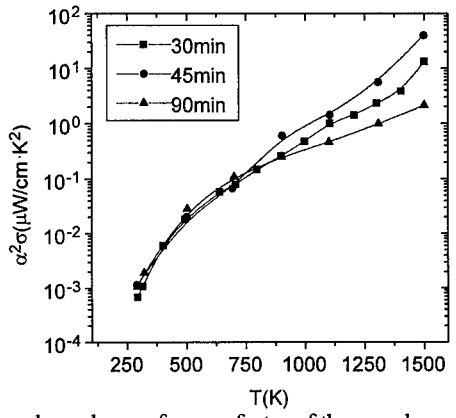

Fig.6. Temperature dependence of power factor of the samples soaked for different time.

CONCLUSION

The results above have shown that the thermoelectric properties at high temperature of the Si-doped B_4C ceramics depends strongly on Si dopant amount and the sintering conditions. Both too high pressure and too long soaked time are unprofitable to improvement in the thermoelectric properties. The lower the content of SiC in a sample, the higher the thermoelectric properties of the ceramics. The amount of Si dopant in B_4C is rather limited, also depending on the sintering conditions. The 1.62 % Si-doped B_4C ceramic hot pressed at 1900 ℃ and 25 MPa for 45min has better thermoelectric properties and its figure of merit at 1500 K is 4×10^{-4} K^{-1}. The thermoelectric properties of the Si-doped B_4C ceramics can be further improved by the optimizing of the amount of dopant and processing routes.

ACKNOWLEDGMENT

This work was supported by the National Natural Science Foundation of China through Outstanding Young Scientist Foundation under Grant No. 59825102.

REFERENCES

1 C. Wood, Rep. Prog. Phys. **51**, 514(1988).
2. Bouchacourt, F. Thevenot, J. Mat.Sci. **20**, 1237(1985).
3. T.L.Aselage, Mat. Res. Soc. Symp. Proc. **234**, 145(1991).
4. C.Wood and D. Emin, Phy. Rev. B **29**(8), 4582 (1984).
5. C. Wood, D. Emin and P. E. Grey, Phy. Rev. B **31**(10), 6811 (1985).
6. D.Emin, Phy. Rev. B **38**(9), 6401 (1988).
7. D.M.Bylander, L. Kleinman, and S. Lee, Phy. Rev. B **42**(2),1394 (1990).
8. C.Wood, in Boron-Rich Solids, AIP Conf. Proc., D. Emin, T.Aselage, C. Beckel, I.Howard, and C. Wood, eds., American Institute of physics, New York,**140**, 362(1986).
9. X. M. Min, K. F. Cai and C. W. Nan, J. Wuhan University of Technology, **20**, 28 (1998).
10. ASTM Specification C373, ASTM Standards part 13, American Society for Testing and Materials, Philadelphia, (1969).

HIGH TEMPERATURE TRANSPORT PROBE FOR THERMOPOWER AND RESISTIVITY MEASUREMENTS

R. T. Littleton IV[1], Jason Jeffries[2], Michael A. Kaeser[2],
Michael Long[2], and Terry M. Tritt[1,2]
1 Materials Science and Engineering Department
2 Department of Physics and Astronomy
Clemson University, Clemson, SC 29634 USA

Abstract:

We have recently developed a device to measure resistivity and Seebeck values of a material as a function of temperature over a range of 80K < T < 700K. These measurements overlap in temperature with our existing apparatus (4K < T < 320K). These measurements are necessary for the investigation of potential thermoelectric materials at elevated temperatures, where power generation applications are important. The probe design allows for various types of samples to be evaluated from needle like samples (L ≈ 2mm, D ≈ 50μm) to larger pressed pellet samples (≈ 2mm x 2mm x 10mm). Separate high temperature cartridge heaters are used to stabilize both the absolute temperature, T, as well as the temperature difference, ΔT. Thermocouples measuring T+ΔT/2 and T-ΔT/2 are also employed to measure sample voltages for resistance and thermoelectric power. Design details and measurement specifics will be discussed. Data taken on standards a well as some research samples will be presented.

Apparatus:

The body of the high temperature probe, shown in Figure 1 and 2, consists of two stainless steel half cylinders which are bolted together and separated by a thin sheet of machinable ceramic, Macor®. A 100 Watt Omegalux® cartridge heater is inserted into each half cylinder. Each heater is independently controlled to establish T+ΔT/2 and T-ΔT/2. On the top faces of the half-cylinders are 0.016" thick quartz substrates which are attached with Dupont® 5007 silver paint. The sample is then secured across the surfaces of the substrates, using Dupont® 5007 silver paint as well. Type K thermocouples (0.002") are attached at each end of the sample. Two platinum wires (0.002") are also attached just inside each of the sample ends.

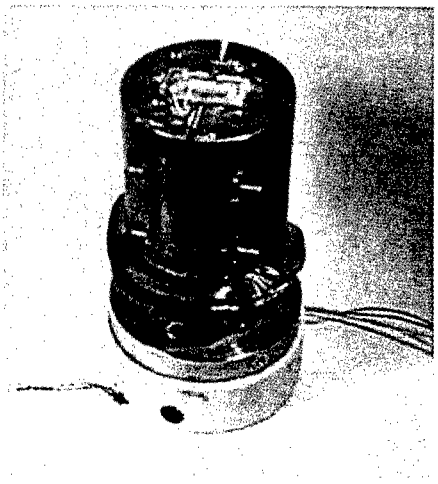

Figure 1. Photograph of the high temperature transport probe head.

Mat. Res. Soc. Symp. Proc. Vol. 545 © 1999 Materials Research Society

These sample wires, as well as the current leads to the cartridge heaters, travel through multi-bore alumina posts to an electrical connector. These posts run through the stainless steel half cylinders, through several thin stainless steel shims, and finally terminate after passing through a 3/4" thick Macor® cylinder. The stainless steel shims help reflect the heat from the half cylinders, while the Macor® cylinder insulates the wire so that shielded wire may be used thereafter. The electrical disconnects enables the high temperature probe head to be dismounted from the rest of the probe. This allows separate probe heads to be exchanged, reducing down time due to the sample mount procedure.

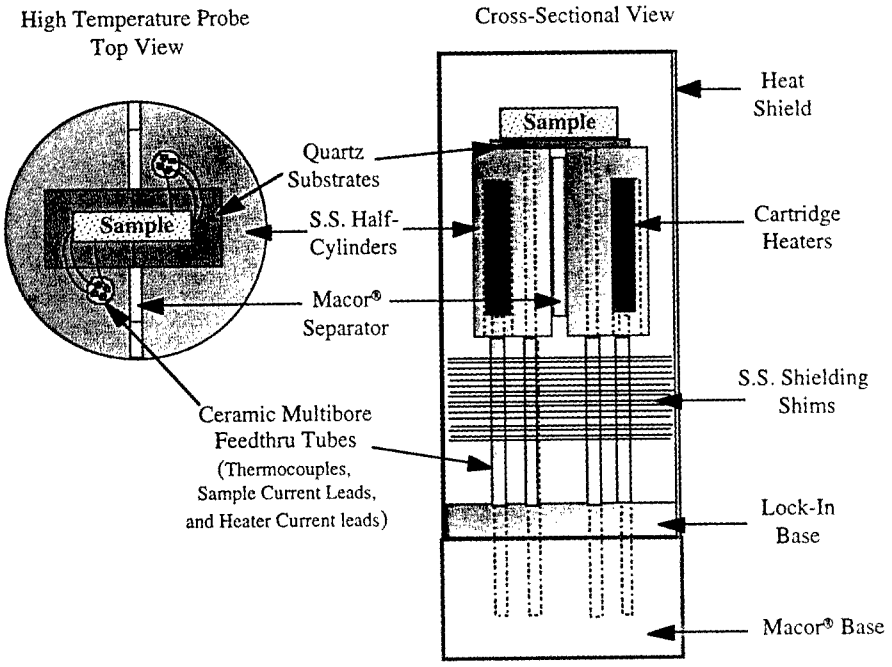

Figure 2. High temperature probe design illustration of top and cross sectional side views. (S.S. = Stainless Steel)

Measurement:

In order to record thermopower and resistivity simultaneously at a certain temperature, several measurements are made in a relatively short period of time. The thermocouples, which are attached to the sample and used to determine T+ΔT/2 and T-ΔT/2, are referenced to a massive copper block external to the system. The temperature of the copper block is measured by a calibrated platinum resistive thermometer. Voltages read from the thermocouples and thermometer are measured by a Keithly 2001 multi-scan meter with 0.1 μVolt resolution, via a scanner card. The sample current is controlled by a 2400 Keithly digital source power supply. Each of the cartridge heaters are regulated by a Kepco ABC 60-2DM power supply. The measurement sequence, at a certain temperature, consists of a series of LabView® controlled commands. The sample voltages are the first set of measurements which consists of reading voltages across the alumel legs, V_{AA}, and the chromel legs, V_{CC}, of the pair of attached thermocouples. The voltage bias is taken as positive when the thermocouple junction with a higher potential is on the hotter end of the sample. A current, +I, is then established across the sample through the Platinum leads and the sample voltages are recorded. The sample current is set back to zero and the voltages reread. The sample current, -I, is then established and the sample voltages measured again. Finally, the sample current is reset to zero and the sample voltages are remeasured.

The absolute Seebeck values are calculated similar to previous methods used by Singh and Ramani[1]. The thermoelectric power of the sample, α_S, is related to the measured sample voltages V_{AA} and V_{CC} by:

$$V_{AA} = (\alpha_S - \alpha_A)\cdot\Delta T \text{ and}$$

$$V_{CC} = (\alpha_S - \alpha_C)\cdot\Delta T,$$

where α_A and α_C are the absolute thermoelectric power of each of the thermocouple legs (alumel and chromel respectively), and ΔT is the temperature difference between the two thermocouple junctions. Eliminating ΔT and solving for α_S gives:

$$\alpha_S = \frac{V_{AA}\alpha_C - V_{CC}\alpha_A}{V_{AA} - V_{CC}}.$$

The resistance of the sample can be determined from the sample voltages, V_{AA} and V_{CC}, measured with the applied currents +I and -I. These voltage difference due to reversed currents are used to factor out any induced thermal emfs to determine the sample resistance, R:

$$R = \frac{V_{AA}(+I) - V_{AA}(-I)}{2|I|} = \frac{V_{CC}(+I) - V_{CC}(-I)}{2|I|}.$$

Results and Discussion:

A 99.999% pure bulk bismuth standard of length and cross sectional area: L ≈ 5.5mm and A ≈ 2.2mm^2, was measured in the high temperature apparatus to determine the resistivity accuracy. Resistance data was recorded and resistivity values were calculated from 80K to 550K (Figure 3). A 273K (0°C) resistivity value of 105 μΩ•cm was measured, which agrees well with the accepted resistivity of 106.8 μΩ•cm at 273K.[2] A well defined transition was recorded at T≈540K. This resistive anomaly is produced by a phase transition which is also well documented.[3-11] The agreement of both the measured resistivity values and the temperature of the transition were in excellent agreement with these published values.

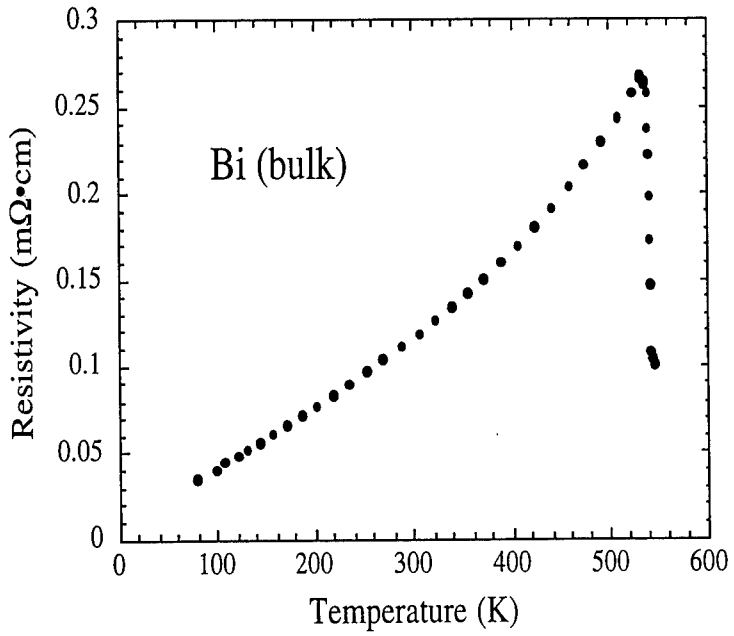

Figure 3. Resistivity as a function of temperature for a 99.999% bulk Bi sample measured on the high temperature probe.

A Skutterudite ($IrSb_3$) sample was used as a standard to test the Seebeck measurement capabilities of the high temperature probe. The thermopower of an $IrSb_3$ pressed pellet, with a length of: $L \approx 6.3$mm, and a cross sectional area of: $A \approx 0.6$mm^2 was measured from $80K < T < 650K$ (Figure 4). The measurements were made, as previously described, while maintaining a regulated constant ΔT. The temperature dependency of the thermopower of the $IrSb_3$ sample was linear-like within the temperature range measured. The room temperature value was ≈ 70 $\mu V/K$, which is in good agreement as is the temperature dependency with previous studies by Slack et. al.[12] and Tritt et. al.[13]

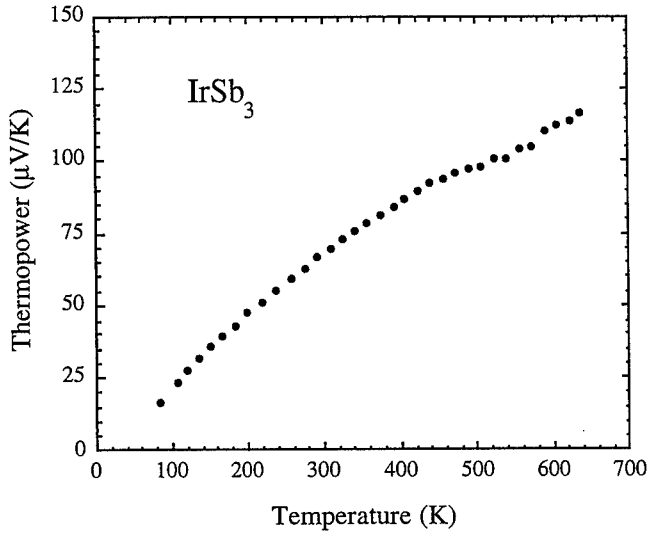

Figure 4. Absolute thermopower as function of temperature for an $IrSb_3$ Skutterudite sample measured on the high temperature probe.

Resistivity and thermopower measurements were also made on single crystal bundles of $HfTe_5$ and $ZrTe_5$ from $80K < T < 500K$ (Figure 5). These samples were approximately 2mm in length and 100μm in diameter. Group IV pentatelluride materials exhibit large thermopowers and exotic electrical transport which are promising characteristics for thermoelectric applications.[14-16] A distinct resistivity peak, representative of an undetermined anomaly, occurs in the parent pentatellurides. These resistive peak temperatures have been determined to be $T_p \approx 80K$ for $HfTe_5$, and $T_p \approx 140K$ for $ZrTe_5$.[14-16]

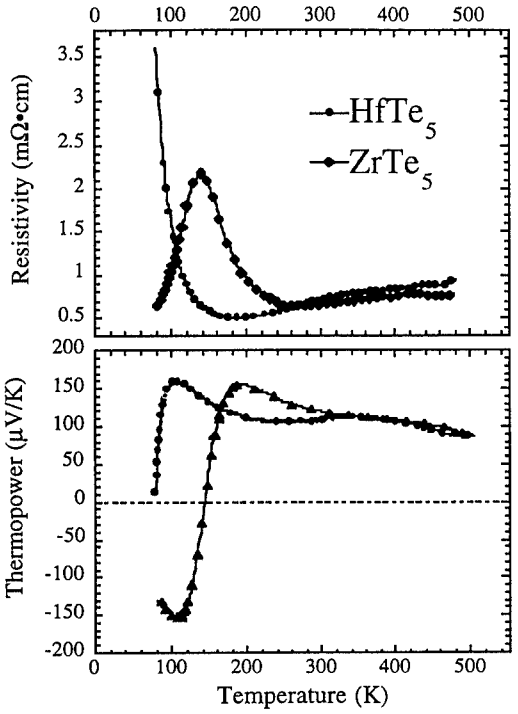

Figure 5. Resistivity and absolute thermopower as function of temperature for single crystals of $HfTe_5$ and $ZrTe_5$ samples measured on the high temperature probe.

Discussion:

An apparatus has been developed to measure sample resistivity and absolute thermopower as a function of temperature from 80K < T < 700K. The device has successfully measured samples of various physical dimensions. Preliminary data on standards are in good agreement with previous results. Second generation probes are underway to increase the capabilities of the basic design. Probe heads with smaller mass should allow a more stable ΔT and T sweep rate as well as minimizing radiating heat. These improvements should also extend the current temperature limitations closer to the desired goal of $T_{max} \approx 1000K$. PID temperature controllers are also being incorporated to assist with temperature stabilization.

The authors would like to acknowledge support from an ARO/DARPA grant (#DAAG55-97-1-0267) and from the research funds provided (TMT) from Clemson University

Refrences

1. A. K. Singh, and Geetha Ramani, Rev. Sci. Instrum. **49**, 1324 (1978)
2. Alfa Aesar, J. Mathey Catalog Co. 669 (1997)
3. *Electrical Resistivity Handbook*, edited by G. T. Dyos and T. Farrell, 95-6, (1992)
4. Von A. Roll, and H. Motz, Z. Metallkd., **48**, 272-80 (1957)
5. G. K. White, and S. B. Woods S. B., Philos. Mag., **3**, 342-59 (1958)
6. 'S. Takeuchi, and H. Endo, Trans. Jpn. Inst. Met., **3**, 30-5 (1962)
7. G. Busch, and Y. Tieche, Phys. Condens. Matter, **1**, 78-104 (1963)
8. Von H. U. Tschirner, Z. Metallkd., **60**, 46-9 (1969)
9. Von A. Roll, H. Felger, and H. Z. Motz, Z. Metallkd., **47**, 707-13 (1956)
10. S. Takeuchi, and H. Endo, Trans. Jpn. Inst. Met., **3**, 30 (1962)
11. G. A. Ivanov, and Yu. T. Levitskiy, Fiz. Met. Metalloved., **24**, 253-9 (1967)
12. Glen A. Slack, and Veneta G. Tsoukala, J. Appl. Phys., **76**, 1665-71 (1994)
13. T. M. Tritt, G. S. Nolas, G. A. Slack, A. C. Ehrlich, D. J. Gillespie, and J. Cohn, J. Appl. Phys., **79**, 8412-8 (1996)
14. R. T. Littleton IV, M.L. Wilson, C. R. Feger, M. J. Marone, J. Kolis, and T. M. Tritt, Proceedings of the XVI International Conference on Thermoelectrics, edited by A. Heinrich (1997)
15. T. M. Tritt et. al., M.R.S. Proc., Thermoelectric Materials: New Directions and Approaches, Spring 97, edited by T. M. Tritt et. al., **478**, 249-54 (1997)
16. R. T. Littleton IV, T. M. Tritt, C. R. Feger, J. Kolis, M. L. Wilson, M. Marone, J. Payne, D. Verebeli, and F. Levy, Appl. Phys. L., **72**, 2056-8, (1998)

FABRICATION OF THERMOELECTRIC MODULES USING THERMOELECTRIC PASTES AND AN ADDITIVE TECHNOLOGY

Xiaomei Xi, Goran Matijasevic, Linh Ha, and Dan Baxter
Ormet Corporation, 2236 Rutherford Rd., Carlsbad, CA 92008

ABSTRACT

Polymer based thermoelectric pastes have been developed by dispersing metal and metal alloy powders into a polymer binder system. Thermoelectric materials and elements are formed by depositing the pastes into a mold or onto a substrate and subsequently sintering them to form a conductive network with thermoelectric properties. A Seebeck coefficient of 65 μV/°K, and a resistivity of 0.05 Ω-cm have been achieved in the early stage of material development. A novel processing method has also been developed for the fabrication of small size thermoelectric elements and thermoelectric modules with a multitude of thermoelectric couples using these pastes. Thermoelectric elements as small as 250 μm in diameter and 25 μm in thickness have been achieved. Thermoelectric modules with 275 couples/in^2 have been fabricated using the thermoelectric pastes and the fabrication technique. Further improvement in the material properties and reduction in the sizes of the thermoelectric elements are underway.

INTRODUCTION

Thermoelectric materials are widely used in thermoelectric coolers (Peltier cooler), thermoelectric power generators, temperature sensors, and the like. The performance of a thermoelectric material is expressed using the figure of merit Z:

$$Z = S^2 \sigma / k \qquad (1)$$

Where S is the Seebeck coefficient (V/°K), k is the thermal conductivity of the material (W/m°K), and σ is the electrical conductivity of the material $(\Omega \cdot m)^{-1}$. From equation (1), one can see that in order for a thermoelectric material to have a high value of Z, it must have a large value of Seebeck coefficient (S), a large value of electrical conductivity σ, and a low value of thermal conductivity (k). In terms of a material's thermoelectric properties, materials with a larger figure of merit are more desirable. However, to be useful as thermoelectric materials, many applications require that the material also has good mechanical properties (i.e. adequate strength and not brittle), chemical stability, temperature stability, and processability.

Thermoelectric materials, such as Bi_2Te_3, PbTe, Bi_2Se_3, $(Bi,Sb)_2Te_3$, Si-Ge, etc. [1-4], usually have a high Seebeck coefficient (S) when in their single and polycrystalline structure. However, the fabrication of these thermoelectric materials is complicated. A high temperature and long treatment time are usually needed and the rate of production is low. In addition, these crystalline thermoelectric materials suffer from poor mechanical properties, and high sensitivity to the raw material properties.

Mat. Res. Soc. Symp. Proc. Vol. 545 © 1999 Materials Research Society

Thermoelectric modules are conventionally fabricated by slicing an ingot thermoelectric material into bulk thermoelectric elements and bonding them onto electrodes through soldering [5-6]. Ingot thermoelectric materials are produced by high temperature alloying, powder sintering, poly-crystallization zone melting, mechanical alloying, etc. However, the conventional production of thermoelectric modules involves the following problems: (1) high process temperature and long processing time are needed; (2) automation of the fabrication is difficult; and (3) small size thermoelectric elements are very hard to produce. This also limits the number of thermoelectric couples that can be fabricated in a thermoelectric module. Thus it is very difficult to produce compact, high performance thermoelectric modules or thermoelectric modules with a multitude of thermoelectric couples using this conventional method.

New low temperature sinterable thermoelectric materials and new processing techniques are needed for cost-effectively producing high performance thermoelectric materials, thermoelectric elements, and thermoelectric modules which contain a multitude of thermoelectric couples.

POLYMER BASED THERMOELECTRIC PASTES

To overcome the disadvantages of the conventional thermoelectric materials, novel polymer based thermoelectric pastes have been developed using a low temperature transient-liquid-phase-sintering (TLPS) technique [7]. The thermoelectric pastes were formed by incorporating metal or metal alloy powders into a polymer binder system. During TLPS process, one or more metal powders melt and react with each other or with the other metal powders in the system to form a conductive composite network with thermoelectric properties. By applying this composition in a mold or on a substrate, thermoelectric elements can be formed simultaneously with the formation of the thermoelectric materials. The formed thermoelectric material exhibits better mechanical properties than their single crystal counterpart due to their composite structure.

A variety of P- and N- type thermoelectric pastes have been developed [7]. The main components of the pastes are solder powders, metal powders, and epoxy resin. As shown in Table 1, pastes with Seebeck coefficient of 60 - 135 $\mu V/^{o}K$, and resistivity of 0.02 to 0.6 Ω-cm (measurement were done in Naval Research Laboratory) have been achieved in our early stage of materials development. Further improvement in the material properties is possible by adjusting the component ratio, type of metal powders, and by using higher purity raw materials.

Table 1. Properties of thermoelectric pastes

Paste No.	Seebeck Coefficient at 20°C ($\mu V/^{o}K$)	Resistivity at 20°C (Ω-cm)	Thermal conductivity (W/m°K)
1A	+ 65	0.05	< 5
1B	~ - 60	0.03	< 5
1C	~ +135	0.6	< 5

The processing of thermoelectric pastes is very simple. Thermoelectric materials and elements have been produced by depositing the pastes into desired positions or molds using screen printing, stencil printing, and subsequently curing or sintering the deposited pastes at low temperatures (≤ 300°C). The curing of the pastes has been accomplished in a convection oven, an inert gas protected oven, and a vapor phase condensation oven. By depositing the pastes into the designed molds, thermoelectric elements can be produced simultaneously with the formation of the thermoelectric materials. With a proper design, a large number of thermoelectric elements can be fabricated with this simple process of depositing and curing.

FABRICATION OF THERMOELECTRIC MODULES

A novel processing technique have been developed for the cost-effective production of thermoelectric modules with a multitude of thermoelectric couples [8]. In this method, thermoelectric pastes instead of ingot thermoelectric materials are used to produce thermoelectric elements. Polymer based conductive pastes are chosen to fabricate composite conductive traces and electrodes. Thermoelectric elements are obtained by depositing the thermoelectric pastes into the designed mold followed by curing or sintering of the deposited pastes. Location, shape and size of the individual thermoelectric elements are thereby determined by the designed mold.

Various substrate materials, such as Al, anodized Al, and polymer/glass composite materials have been evaluated for the fabrication of thermoelectric modules. The conductive traces are first screen printed on the substrate and cured. A layer of dielectric material is then applied on the top of the conductive traces and patterned. P- and N- pastes are deposited into the alternative positions using screen printing, doctor blading, pressure filling, or stencil printing. After the deposited pastes are cured or sintered to form P- and N- thermoelectric elements, another layer of conductive traces are then screen printed on the top of the thermoelectric elements and processed. These conductive traces serve to connect the thermoelectric couples electrically in series and thermally in parallel. The fabrication of thermoelectric module is completed when the top insulating plate is affixed on. The detailed processing procedure is shown in Figure 1.

Step one: Apply Ormet® conductive ink on a substrate and cure.

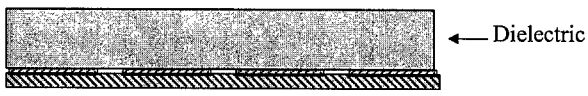

Step two: Apply a dielectric layer.

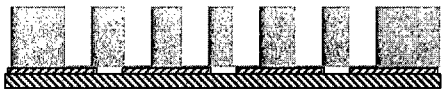

Step three: Produce vias in the dielectric.

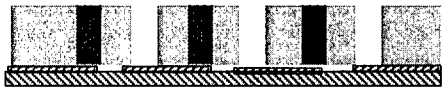

Step four: Apply P-type thermoelectric composite and cure.

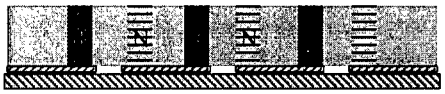

Step five: Apply N-type thermoelectric composite and cure.

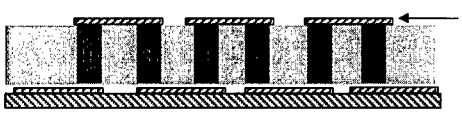

Step Six: Apply Ormet® conductive ink and cure.

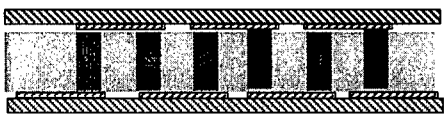

Step seven: Apply top electrical insulation plate.

Figure 1. The processing procedure of thermoelectric modules.

THERMOELECTRIC MODULES

Thermoelectric modules with four different configurations have been designed and fabricated. The four configurations are: 2 mm in element diameter and 4 mm in spacing (40 couples/ in^2); 1 mm in element diameter and 2 mm in spacing (153 couples/in^2); 0.5 mm in elements diameter and 2 mm in spacing (153 couples/in^2); as well as 0.25 mm in elements diameter and 1.5 mm in spacing (275 couples/in^2). Thermoelectric modules were fabricated using the new processing technique and the

polymer based pastes discussed above. The cross section of the thermoelectric modules exhibits the same structure as revealed in Step seven of the Figure 1. Figure 2 shows the cross section of p- and n- thermoelectric elements and their connections with the conductive traces. As expected, the elements formed using above discussed technologies are dense and connected well with the conductive traces.

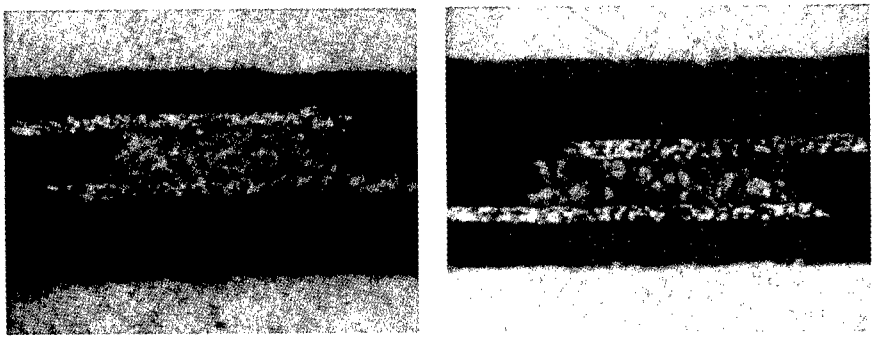

Figure 2. Cross section of p- and n- thermoelectric elements

ONGOING WORK

The next stage of research will be concentrated on further improving the thermoelectric properties and processability of the thermoelectric pastes by reformulation. New designs and fabrication methods will also be developed to achieve a large number of thermoelectric elements in a small area. The goal is to fabricate thermoelectric modules with an element size of ≤ 250 μm in diameter and ≤ 500 μm in spacing.

SUMMARY

Polymer based thermoelectric pastes with useful thermoelectric properties have been developed. With these thermoelectric pastes, fabrication of the thermoelectric materials and elements can be accomplished in a simple process. A novel fabrication technique have been developed for the fabrication of thermoelectric modules using these pastes. Thermoelectric modules with a large number of thermoelectric couples have been fabricated using the thermoelectric pastes and the new fabrication technology. Compact, high performance thermoelectric modules are possible by fabricating compact modules with a multitude of small size thermoelectric elements.

ACKNOWLEDGMENTS

The research described in this paper is supported by BMDO SBIR Phase I contract No. N00014-98-M-0071. We thank technical monitor Dr. John Pazik of ONR for his support. The authors would like to thank Drs. Alexander Ehrlich and Wendy Fuller-Mora of Naval Research Laboratory for the measurements thermoelectric properties.

REFERENCES

1. Marshall Sittig, "Thermoelectric Materials", Noyes Data Corporation, USA (1970).
2. B. Lenoir, M. Cassart, M. Kinany-Alaoui, H. Scherrer, and S. Scherrer, "Thermoelectric Properties of Bi-Sb Alloys Prepared by THM", 13th International Conference On Thermoelectric, P230-235 (1994).
3. S. Sugihara, M. Tizuka, and Y. Katou, " Thermoelectric properties of Sintered n and p type Bi_2Te_3", 13th International Conference On Thermoelectric, P282-285 (1994).
4. C. B. Vining, "Thermoelectric Properties of Pressure-sintered $Si_{0.8}Ge_{0.2}$ Thermoelectric alloy", J. Appl. Phys. 69 (8), 15 April 1991, P 4333-4340.
5. S. Godfrey, "An Introduction to Thermoelectric Coolers", Electric Cooling, Vol.2, no. 3, Sept. 1996, P30-32.
6. T. Ohta, T. Kajikawa, U.S. patent 4,902,648.
7. Patent pending.
8. Patent pending.

MODIFICATION OF THERMOELECTRIC PROPERTIES USING INSERTION TECHNIQUES

E. Hatzikraniotis, Th. Kyratsi, K. Chrissafis and K.M. Paraskevopoulos
Department of Physics - Solid State Physics Section
Aristotle University of Thessaloniki, 54006 Thessaloniki, GREECE

ABSTRACT

In this work is presented the application insertion techniques for the modification of the performance of thermoelectric materials. The results indicate that in cases as in Bi_2Se_3 compounds where insertion of foreign species in the lattice is possible due to its particular crystal structure, the insertion technique could be proved a valuable easy to apply and cost effective, alternative to doping technique. The techniques can produce homogeneous materials with electronic and thermoelectric properties finely tuned.

INTRODUCTION

Materials for use in thermoelectric applications is a «hot» subject of research for both material science and technology, especially for use in thermoelectric modules. As a consequence of the rapid increase of the commercial products in which thermoelectric materials play a key role, industry is focused to the enhancement of the thermoelectric Figure of Merit optimized for cost of production. The «ultimate» material should have a high electric conductivity (σ) and Seebeck coefficient (α) and low thermal conductivity (λ). According to electron transport theory, the Seebeck coefficient and electrical conductivity depend strongly on the Fermi level, which in turn depends upon the carrier concentration, the carrier effective mass and temperature. As the free carrier concentration increases, the electric conductivity will also increase while, the Seebeck coefficient decreases, and this results in a maximum of the *power factor* ($\alpha^2\sigma$)[1]. As the thermal conductivity (λ) depends only weakly on the free carrier concentration, the general effect of an increase in carrier concentration would manifest itself in the figure-of-merit, through the *power factor*.

In last years the trends in applied research can be grouped in two directions: research for novel materials and modification-optimization of known and widely accepted materials for their thermoelectric properties. For applications operating in room temperatures, the materials in commercial use today are narrow gap semiconductors[1,2] like the M_2X_3 (M:Bi,Sb και X:SeTe) family of compounds with free carrier concentration 10^{18}-10^{20} cm^{-3} where the Figure-of-Merit (Z) reaches maximum. Commercial products available today use single crystalline pellets of mixed composition (Bi_2Te_3-Sb_2Te_3) and the optimization of the free carrier concentration is done by conventional doping.

In this work we propose an alternative approach for the modification of the electronic properties, and thus of thermoelectric performance, using insertion techniques instead of conventional doping: The free carrier concentration can be changed due to charge transfer reaction realized by insertion of foreign species to the host[3]. The M_2X_3 family of compounds and solid solutions have a layered structure[4] that is proved by our earlier work to be susceptible to intercalation[5-7]. This approach can be directly applied to industrial technology having a number of advantages vs.

Mat. Res. Soc. Symp. Proc. Vol. 545 © 1999 Materials Research Society

can be directly applied to industrial technology having a number of advantages vs. conventional doping, as it is a simple to use technique that can monitor the modification of the electronic properties of already grown material in desired level.

The aim of this work is to examine the application of insertion technique in Bi_2Se_3 single crystals, having different initial free carrier concentration, check the quality of the intercalated materials in terms of homogeneous distribution of the inserted species in the samples and analyze the modification of the conductivity and the thermopower in terms of electron transport theory.

EXPERIMENTAL RESULTS

The free carrier concentration in stoichiometric Bi_2Se_3[8] is about $2\cdot10^{19}cm^{-3}$. This value places the material just after the expected maximum of the power factor ($\alpha^2\sigma$). Further increase in the free carrier concentration will result in the decrease of the Seebeck term (α^2) not balanced by the increase in conductivity (σ) term, and this would result in materials with a continuous decrease of the ($\alpha^2\sigma$) factor.

The single crystals used in this work were grown by direct fusion of high purity (99.99%) elements using with the Bridgmann method, with slight excess of Se, which results in materials with lower carrier concentration[9] ($n\approx1\div3\cdot10^{18}$ cm^{-3}). The lower free carrier concentration places the grown single crystals closer to the maximum of the thermoelectric performance.

The crystals obtained were of layered structure and high quality, easy to cleave revealing shinny dark gray surfaces. The samples used were cleaved from the single crystal and cut into almost a square shape of lateral dimension of 2-3mm and thickness 50-100 μm and were exposed to intercalation in sealed cells. The Li-intercalation was realized in room temperature direct butyl-litium reaction.

Electron transport due to intercalation of Li

The lithium uptake was monitored by in-situ conductivity and Hall effect measurements using a four probe experimental setup in the van der Pauw configuration[10]. Upon intercalation the electronic conductivity in the samples is smoothly increased due to a considerable increase of the free carrier concentration, up to $\Delta n\approx10^{20}cm^{-3}$. In figure 1, the electron transport properties of several different samples from different grown ingots, having different initial value of conductivity (σ) and free carrier concentration (n) are presented. Despite the difference in initial value of conductivity, all samples as lithiated, follow very well the same σ vs. n dependence, within experimental error.

As expected, the increase upon intercalation of the free carrier concentration results in a decrease (in absolute value) of the Seebeck coefficient (α). The thermoelectric measurements were carried out in room temperature using an automated, computer controlled, setup. The samples were mounted between two mini-heaters with two thermocouples welded on their sides. The two mini-heaters could alternate the temperature gradient along the sample at a maximum $\Delta T=\pm4°C$, and the Seebeck coefficient was the calculated by the measured thermopower vs. ΔT slope[11]. As can be seen in figure 2, the measured Seebeck coefficient smoothly decreases as the free carrier concentration increases upon intercalation.

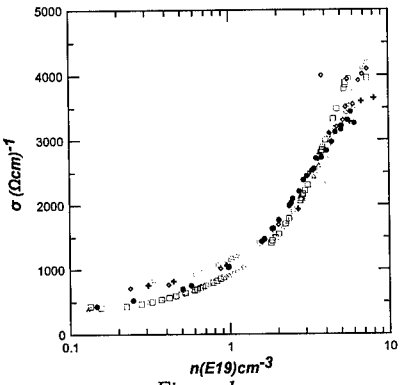

Figure 1

Electron transport properties (σ vs. n) in various lithiated of Bi_2Se_3 samples.

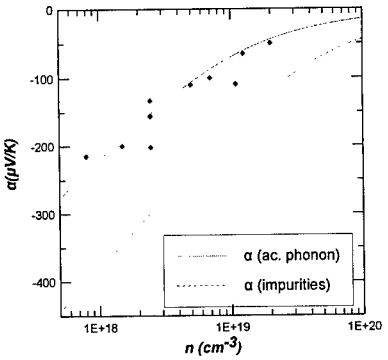

Figure 2

Seebeck coefficient (α) for different Bi_2Se_3 lithiated samples

Material homogeneity

At the end of intercalation we examined the homogeneity of the lithium uptake in the samples by IR reflectivity measurements. The samples were successively cleaved and the IR reflectivity spectra were recorded at room temperature in the spectral region of free carriers plasma, using a Bruker IFS113V spectrophotometer. Drude analysis of the IR spectra enable us to extract the free carrier concentration locally on each successively cleaved surface. According to Drude model, the reflectivity is expressed as[12] :

$$R = \frac{\sqrt{\varepsilon_1^2+\varepsilon_2^2} - \sqrt{2\left(\varepsilon_1 + \sqrt{\varepsilon_1^2+\varepsilon_2^2}\right)+1}}{\sqrt{\varepsilon_1^2+\varepsilon_2^2} + \sqrt{2\left(\varepsilon_1 + \sqrt{\varepsilon_1^2+\varepsilon_2^2}\right)+1}} \qquad (1)$$

$$\varepsilon_1 = \varepsilon_\infty - \frac{\varepsilon_\infty \omega_{pl}^2}{\omega^2+\Gamma^2} \quad , \quad \varepsilon_2 = \frac{\Gamma}{\omega}\cdot\frac{\varepsilon_\infty \omega_{pl}^2}{\omega^2+\Gamma^2}$$

where ε_1 and ε_2 are the real and imaginary parts of the dielectric function, ε_∞ the high frequency dielectric constant, m* is the effective mass of the free carriers, Γ is the dumping factor, related to carrier scattering and ω_{pl} is the free carrier plasma frequency, which is related to the free carrier concentration (n) through the expression:

$$\omega_{pl}^2 = \frac{n\cdot e^2}{m^*\varepsilon_\infty \varepsilon_o} \qquad (2)$$

where m* is the effective mass of the free carriers.

In pristine low carrier concentration Bi_2Se_3 the plasma frequency is about $\omega_{pl}\approx 310cm^{-1}$ which corresponds to $n\approx 3*10^{18}cm^{-3}$. As can be seen in figure 3, in Li intercalated samples, the plasma minimum is significantly shifted to higher wavenumbers. The results of Drude analysis for the successive spectra from outer to

having taken $m^*=0.16m_0$[13]. As can be seen, the calculated free carrier concentration is about $1.12\cdot10^{20}cm^{-3}$ and remains almost constant all over the bulk of the intercalated samples. The variation of the free carrier concentration is less than 3% which indicates that Li is intercalated homogeneously. Furthermore, the similar values in Γ dumping factor reveal that the electron scattering is also of the same origin in all examined layers.

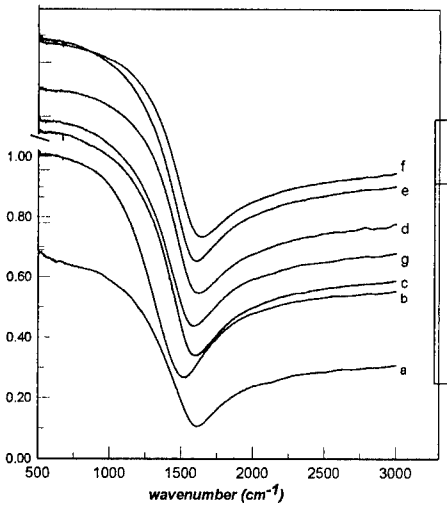

Table I
Results of Drude analysis
d indicates the thickness measured from the bottom surface.

Spectr. d(μm)	ω_{pl} (cm^{-1})	Γ (cm^{-1})	n ($10^{20}cm^{-3}$)
a - top	1497	221	1.21
b - 120	1391	216	1.13
c - 108	1499	210	1.13
d - 99	1526	216	1.22
e - 77	1508	217	1.19
f - 68	1541	221	1.19
g - btm	1485	223	1.16

Figure 3
IR reflectivity spectra of the outer and successive inner layers of fully intercalated Bi_2Se_3, sample.

DISCUSSION

In terms of electron transport theory the electronic conductivity (σ) and the free carrier concentration (n) are expressed as[14] :

$$n=\frac{1}{3\pi^2}\int_0^{\infty}\left(-\frac{\partial f}{\partial\varepsilon}\right)k^3(\varepsilon)d\varepsilon \quad , \quad \sigma=\frac{e^2}{3\pi^2}\int_0^{\infty}\left(-\frac{\partial f}{\partial\varepsilon}\right)\frac{\tau(\varepsilon)}{m^*(\varepsilon)}k^3(\varepsilon)d\varepsilon \qquad (3)$$

where f(ε) is the Fermi distribution function, $m^*=m^*(\varepsilon)$ is the energy dependent effective mass, k(ε) is the band description and $\tau=\tau(\varepsilon)$ is the carrier relaxation time. Adopting the Kane model as being the most appropriate for the description for the electron transport in Bi_2Se_3[15], expressions 4 can be written as:

$$n=\left[\frac{(2m_o^*k_BT)^{3/2}}{3\pi^2\hbar^3}\right]{}^0L_0^{3/2}=N_0\cdot{}^0L_0^{3/2} \quad , \quad \sigma=\left[N_0\cdot\frac{e^2\tau_{0,r}}{m_0^*}\right]{}^0L_{-2}^{r+1}=\sigma_0\cdot{}^0L_{-2}^{r+1} \qquad (4)$$

in terms of the generalized Fermi integrals[16]

$${}^nL_k^m(\eta,\beta)=\int_0^{\infty}\left(-\frac{\partial f}{\partial\varepsilon}\right)z^n\left(z+\beta z^2\right)^m\left(1+2\beta z\right)^k dz \qquad (5)$$

where the term N_0 is the effective density of states at the bottom of the conduction band, m_0^* is the density of states effective mass at the bottom of the conduction band

where the term N_0 is the effective density of states at the bottom of the conduction band, m_0^* is the density of states effective mass at the bottom of the conduction band and β=kT/Eg, the band gap Eg. At a constant temperature the terms N_0 and σ_0 are constant and thus the conductivity (σ) and the free carrier concentration (n) depend only on the Fermi level (η), ie. on band filling. Similarly, the Seebeck coefficient depends on band filling and is expressed as :

$$\alpha = \frac{k_B}{e}\left[\frac{{}^{r+1}\mathbf{L}^{1}_{-2}}{{}^{r}\mathbf{L}^{1}_{-2}} - \eta\right] \qquad (6)$$

In order to analyze the electron transport upon intercalation we evaluated numerically the generalized Fermi integrals in theoretical expressions. As experimentally one measures the Hall coefficient (R_H) and not directly the free carrier concentration (n), our calculations were based on R_H, which in terms of generalized Fermi integrals is expressed as:

$$R_H = \frac{1}{e}\left[\frac{3\pi^2\hbar^3}{(2m_o^* k_B T)^{3/2}}\right]\frac{{}^{0}\mathbf{L}^{2r+1/2}_{-4}}{({}^{0}\mathbf{L}^{r+1}_{-2})^2} \qquad (7)$$

and determined the Hall mobility (μ_H=σ·R_H). The variation of Hall mobility (μ_H) upon intercalation is presented in figure 4. As can be seen, the experimental data for all intercalated samples, despite their initial σ and n values, follow the same pattern of μ_H vs. $(eR_H)^{-1}$ that can be very well represented by the theoretical variation (solid line in figure 4) which was calculated assuming acoustic phonon scattering as the scattering predominant mechanism. Acoustic phonon scattering also describes very well the variation of the Seebeck coefficient (top solid line in figure 2). The thermoelectric performance of the intercalated samples was then estimated by the evaluation of the power factor ($\alpha^2\sigma$) shown in figure 5 for different intercalated samples. The higher the power factor, the better thermoelectric performance is expected. As can be seen in figure 5, there is a very good agreement of the power factor in different samples and the theoretical dependence (solid line) based on electron transport calculations.

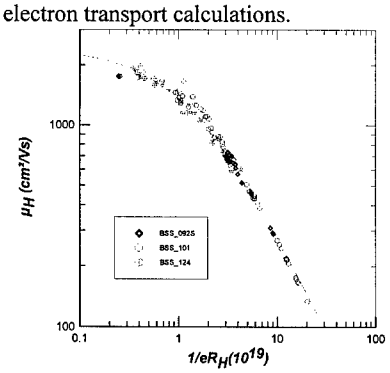

Figure 4
Variation of Hall mobility (μ_H vs. $1/eR_H$) in various lithiated of Bi_2Se_3 samples.

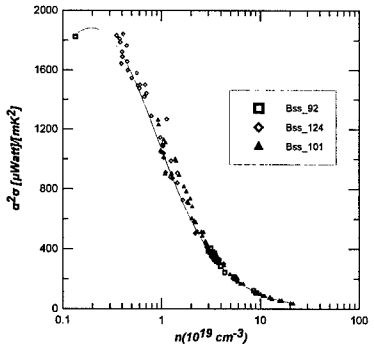

Figure 5
Estimated thermoelectric performance based on ($\alpha^2\sigma$) factor, for different Bi_2Se_3 lithiated samples

CONCLUSION

The feasibility of using insertion techniques in the modification of the performance of thermoelectric materials has been examined, and from the results it is indicated that insertion reaction can produce an homogeneous material and the electronic properties can be changed smoothly in a well defined and predictable way. Electron transport analysis over a very wide range of free carrier variation ($\Delta n \approx 10^{20} cm^{-3}$) is very well described only by acoustic phonon scattering, which indicates that the inserted Li simply shifts the Fermi level upwards through a charge transfer mechanism, without introducing new impurity centers. Our first results, though limited to Li as intercalant clearly indicate that if insertion is possible due to the particular crystal structure, as in the case of Bi_2Se_3 compounds, the insertion technique could be proved a valuable, easy to be applied and cost effective technique, alternative to doping.

RERERENCES

1. C.M.Bhandari and D.M.Rowe in *CRC Handbook of Thermoelectrics*, ed. D.M.Rowe, CRC Press N.Y.1995, pp.43
2. J.O.Sofo and G.D.Mahan, Phys.Rev **B49**, 4565, (1994)
3. Y. Liang in *Intercalation in Layered Materials*, ed. M.S. Dresselhaous, 1986, Plenum Press N.Y.
4. E. Ya. Atabaeva, N.A. Bendeliani and S.V. Popova, Sov. Physics Solid State **V15**, 2345 (1973)
5. K.M. Paraskevopoulos, E. Hatzikraniotis, K. Chrissafis, K. Alexiadis, J. Stoemenos, N.A. Economou and M. Balkanski, Mat.Sci. and Engin.(B) **1**, 147 (1988).
6. Th. Kyratsi, E. Hatzikraniotis, K.M. Paraskevopoulos and K. Chrissafis, Ionics 3, 305 (1997)
7. A. Kalampokis, E. Hatzikraniotis, and K.M. Paraskevopoulos, Mat. Res. Bul., **33** (9), 1356 (1998)
8. A. Krost in *Landolt - Bornstein Neue Serie*, Vol. 17, 1983, pp. 269-271.
9. Gorbecht, H., Seeck, S.,:Z. Phys. **222**, 93 (1969)
10. Van der Pauw, Phillips Res. Repts. **13**, 1 (1958)
11. E. Compans, Rev. Sci. Instrum. **60 (8)**, 2715 (1989)
12. T.S. Moss, *Optical Properties of Semiconductors*, 1959, Butterworths, London
13. L. Tichy and J. Horak, Phys. Rev. **B 19**, 1126 (1979)
14. P.S. Kireev, *Semiconductor Physics*, Mir Publ, Moscow, 1978, p.234
15. E. Hatzikraniotis, K.M. Paraskevopoulos and K. Chrissafis, Proc. 20th ICPS, ed. E.M.Anastassakis and J.D. Johanopoulos, World Scientific, vol.3 p.1799 (1993)
16. W. Zawadski, Adv. Phys.**23**, 435 (1974).

IRON DISILICIDE AS A BASE FOR NEW IMPROVED THERMOELECTRICS CREATION

M.I.FEDOROV, YU.V.IVANOV, M.V.VEDERNIKOV, V.K.ZAITSEV
A.F.Ioffe Physical-Technical Institute, Polytekhnicheskaya ul., 26, St.Petersburg, 194021, Russia, M.Fedorov@shuvpop.ioffe.rssi.ru

ABSTRACT

It is well known that the temperature dependence of Seebeck coefficient of β-iron disilicide has unusual shape that cannot be described by an ordinary theory. A theory describing such a shape is suggested. It is shown this shape can be explained by optical phonon drag effect. Very high value of ZT could be achieved in some material on the base of this effect.

INTRODUCTION

The possibility of increasing the figure of merit of traditional thermoelectrics is practically exhausted. The ways of progress in thermoelectricity lay now among such materials as low-dimensional structures, semimetals (skutterudites) and materials of low current carriers mobility. $\beta - FeSi_2$ is a representative of the later class of materials. The usual undoped $\beta - FeSi_2$ has low enough mobility of current carriers (low than 10 $cm^2V^{-1}c^{-1}$ [1, 2]) and high thermal conductivity of crystal lattice ($\sim 8W \cdot m^{-1}K^{-1}$). Nevertheless doped by cobalt $\beta - FeSi_2$ (n-type) has $Z = 0.5 \cdot 10^{-3}K^{-1}$ at $T = 820K$ [3]. What is the reason of creation so relatively effective material on so poor base?

EXPERIMENTAL BACKGROUND

$\beta - FeSi_2$ has the unusual shape of temperature dependence of Seebeck coefficient. Fig.1 shows the temperature dependence of Seebeck coefficient for various samples of $\beta - FeSi_2$ measured by different investigators on both poly- and single crystals. The most important feature of these dependences is a sharp growth of Seebeck coefficient when temperature increases in the temperature range 100-300 K. This feature cannot be connected with impurities because it is present on both n- and p-type undoped materials and on materials doped by various impurities. Moreover, a special study carried out by A.Heinrich and co-workers [4] showed that the more pure materials have higher peak value of Seebeck coefficient. The shape of this growth can be described as exponential growth. What is the reason of this feature?

PROPOSED THEORY

In 1987 V.Zaitsev et al [6] supposed that such a feature could be explained by optical phonon drag effect. Although acoustic phonon drag effect is well known one the optical phonon drag effect was considered as a negligible one because of small phonon dispersion. Recently Yu.Ivanov [7] et al studied theoretically the optical phonon drag effect in polar semiconductors. The theory was developed in approximation of parabolic character of both electron and phonon spectrum:

$$\epsilon_{\mathbf{k}} = \frac{\hbar^2 k^2}{2m}, \qquad \omega_{\mathbf{q}} = \omega_0 + aq^2. \tag{1}$$

Mat. Res. Soc. Symp. Proc. Vol. 545 © 1999 Materials Research Society

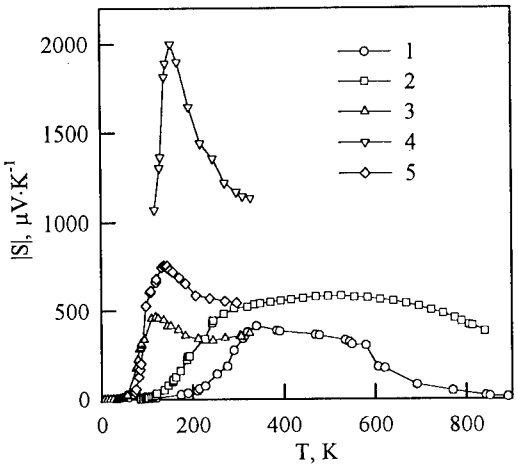

Figure 1: Absolute value of Seebeck coefficient of some $\beta - FeSi_2$ samples:
1: $FeSi_2$, undoped [1]; 2: $FeSi_2$<1%Mn> our data; 3: $FeSi_2$<0.7%Co> [5]; 4: $FeSi_2$, high purity Fe [4]; 5: $FeSi_2$, low purity Fe [4]; samples 1,2 are polycrystals, the other are single crystals.

here m is the effective mass of current carrier, parameter a determines phonon dispersion, ϵ and k are electron energy and quasimomentum, ω and q are phonon frequency and wave vector.

Our calculation showed that in such a case the optical phonon drag contribution in Seebeck coefficient is S_p:

$$S_p = \frac{2k_B\alpha am\omega_0}{e\hbar\nu_{pa}^0} D(\eta, r, s) \ , \tag{2}$$

here k_B is Boltzmann constant, α is a dimensionless electron-phonon coupling constant, ν_{pa}^0 is the constant determining the frequency of long-wavelength optical phonon decay into two acoustic phonons, $\eta = \hbar\omega_0/k_BT$, r - scattering parameter (for example, for scattering from acoustic phonons $r = -1/2$ and for scattering from ionized impurities $r = 3/2$). The dimensionless parameter s determines the relative significance of carrier interactions with optical phonons and "defects": when phonon scattering on defects is strong enough $s \to 0$. The function $D(\eta, r, s)$ determines the temperature dependence of optical phonon drag contribution in Seebeck coefficient. When $s \to 0$ it can be designated as $D(\eta, r)$. It could be calculated through Bessel functions and in limiting cases $\eta \ll 2$ and $\eta \gg 2$ it can be calculated directly:

$$D(\eta, r) \ \to \ \frac{\sqrt{\pi}}{\Gamma(r+5/2)}\eta^{r+2}e^{-\eta}, \qquad \eta \gg 2 \quad \text{(low temperature)} \tag{3}$$

$$D(\eta, r) \ \to \ \frac{\Gamma(r+2)}{2\Gamma(r+5/2)}\eta^{3/2}, \qquad \eta \ll 2 \quad \text{(high temperature)} \tag{4}$$

here $\Gamma(t)$ is gamma-function.

DISCUSSION

Fig.2 shows the comparison of experimentally measured Seebeck coefficient of pure and Mn-doped $\beta - FeSi_2$ with its theoretical value (2) using the approximations (3) and (4). The used formulas were reduced to

$$S_p = S_0(T_0/T)^{(r+2)}e^{-T_0/T}, \quad (5)$$

$$S_p = S_1(T_0/T)^{3/2}. \quad (6)$$

here $T_0 = \hbar\omega_0/k_B$, $S_0 = \sqrt{\pi}/\Gamma(r+5/2)$ and $S_1 = \Gamma(r+2)/(2\Gamma(r+5/2))$ are fitting parameters. The dependence between fitting parameters and the quality of fitting is a weak one. There are many combinations of parameters providing a good fitting. It is necessary to use additional conditions to determine the right parameters. For example the maximum optical phonon frequency for pure $\beta - FeSi_2$ corresponds T_0 less than 700 K. So it is necessary to choice the set of fitting parameters where $T_0 < 700$ K for pure $\beta - FeSi_2$. The parameters used for fitting are shown in the table 1.

Table 1: Parameters of fitting by formula (5).

Parameter	$\beta - FeSi_2$, low purity Fe		$\beta - FeSi_2 <$ 1%Mn >	
r	-0.5	1.5	-0.5	1.5
S_0, μV/K	24000	1200	2100	217
T_0, K	675	850	850	1250

It is seen from the fig.2 that there is a good agreement between experimental and theoretical dependence of the low temperature growth of Seebeck coefficient. It should be mentioned that there is no agreement with T^3 dependence that is characteristic one for acoustic phonon drag. The value of $T_0 = 675$ K for pure $\beta - FeSi_2$ is very close to the frequency of longitudinal optical phonon, that was determined from reflectance spectra of single crystal $\beta - FeSi_2$ (698 K [8] and 674 K [9]). It allows to suppose that the scattering mechanism is mainly the scattering by acoustic phonons ($r = -0.5$).

There is a strong dependence of Seebeck coefficient value on impurity content. Samples prepared of high and low purity iron [4] have the opposite sign and very different absolute value. Nevertheless the low temperature growth of Seebeck coefficient for both samples can be described by the formula (5) with the same parameters. Doping (by manganese, for example) results in large shift of Seebeck coefficient temperature dependence to higher temperature. The existence of the corresponding shift of optical phonon frequency due to manganese doping have not been studied yet.

Fig.3 shows temperature dependences of electrical conductivity of various $\beta - FeSi_2$ samples. It shows poly- and single crystals, doped and undoped samples. One can see that contrary to Seebeck coefficient electrical conductivity has no common feature for various samples. Suggested explanations of temperature dependence for a set of samples cannot be supported by a new measurement of other set of samples and there is no strict theory of electrical conductivity in $\beta - FeSi_2$. The existence of phonon drag influences very weakly on electrical conductivity, but some conductivity mechanisms could strongly influence on phonon drag. So, the study of electrical conductivity mechanism in $\beta - FeSi_2$ should be continued.

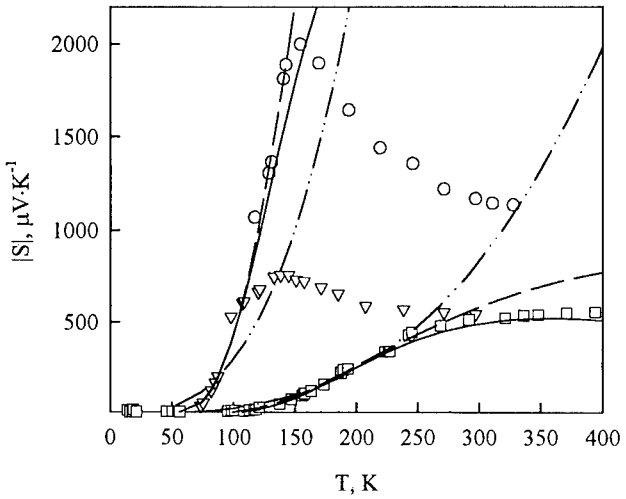

Figure 2: Comparison of temperature dependence of absolute value of Seebeck coefficient with theoretical estimations for some $\beta - FeSi_2$ samples: □ - $FeSi_2$<1%Mn>, ○ - $FeSi_2$, high purity Fe [4], ▽ - $FeSi_2$, low purity Fe [4].
Solid lines are the fitting according to (5) with $r = 3/2$ and dashed is that with $r = -1/2$. Dash-dotted curve shows T^3 dependence.

Let us consider a possibility to use optical phonon drag for creation a high effective thermoelectric. Let us estimate the contribution of optical phonon drag into Seebeck coefficient (2). The typical value for ν^0_{pa} is $\nu^0_{pa} \sim 10^{-3}\omega_0$ (see, for instance [11, 12]). It can be suggested that $\alpha \approx 0.5$ and $am/\hbar \sim 0.1$. Therefore

$$S_p \approx 2\frac{k_B}{e} 0.5 \cdot 0.1 \cdot 10^3 \approx 8\text{mV/K}.$$

This value corresponds to the fitting parameter S_0 twice lower than that shown in Tab.1. If electrical conductivity is about 7 $\Omega^{-1}\text{cm}^{-1}$ and thermal conductivity about 3 $\text{W} \cdot \text{m}^{-1}\text{K}^{-1}$ then

$$Z \sim 1.5 \cdot 10^{-2}\text{K}^{-1}$$

and if $T_{max} \approx 200$ K then

$$ZT \sim 3.$$

So, using the optical phonon drag effect is very perspective way for the creation of more effective thermoelectrics. Even if our estimation is higher than a real possibility to increase the figure of merit it is necessary to search for new materials where optcal phonon drag takes place and to study optical phonon drag in more details.

CONCLUSION

Conductivity mechanism of $\beta - FeSi_2$ is not determined yet notwithstanding the numerous efforts to do it. It is shown that optical phonon drag makes an essential contribution into charge and heat transport. A search for materials with high optical phonon drag could allow to create a thermoelectric of very high figure of merit.

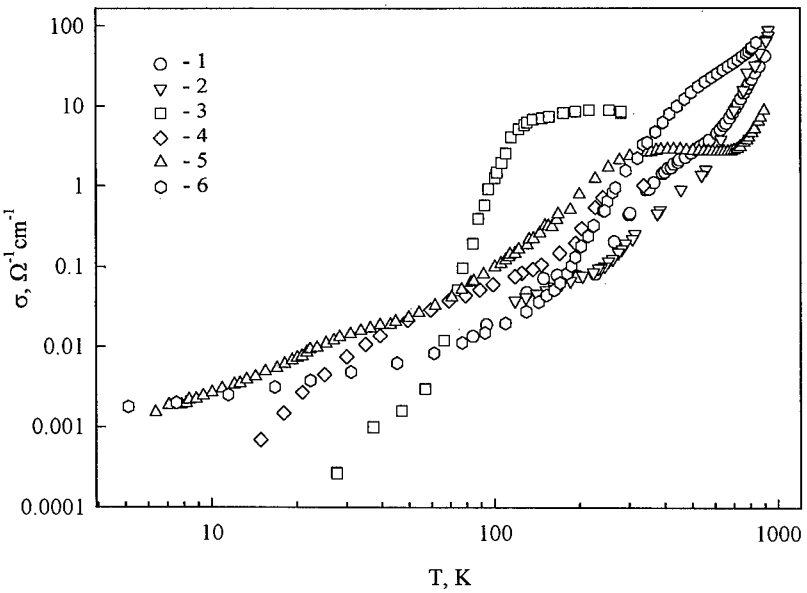

Figure 3: Electrical conductivity of some $\beta - FeSi_2$ samples:
1: polycrystal; 2: polycrystal [1]; 3: single crystal [10]; 4: single crystal [4]; 5: polycrystal, $\beta - FeSi_2 < 0.01\%Co >$; 6: polycrystal, $\beta - FeSi_2 < 1\%Mn >$. 5, 6 - our data.

REFERENCES

[1] U.Birkholz, J.Schelm, Phys. Stat.sol., **27**, p.413-425 (1968).

[2] T.Kojima, Phys. stat. sol. (a), **111**, p.233-242 (1989).

[3] J.Hesse, Zeitschrift fur Angewandte Physik, **28**, p.133-137 (1969).

[4] A.Heinrich, G.Behr, H.Griessmann, in *Sixteenth Int. Conf. on Thermoelectrics. Proceedings*, Dresden, Germany. 1997, p.287-290.

[5] A.Heinrich, C.Gladun, A.Burkov, Y.Tomm, S.Brehme, H.Lange, in *Proc. of the XIV Int. Conf. On Thermoelectrics*, St. Petersburg, 1995, p.259-263.

[6] V.K.Zaitsev, S.A.Ktitorov, Yu.V.Petrov, in *Materials for thermoelectric converters*, Leningrad, 1987, p.36.

[7] Yu.V.Ivanov, V.K.Zaitsev, M.I.Fedorov, Physics of solid state, **40**, p.1101-1106 (1998)

[8] U.Birkholz, H.Finkenrath, J.Naegele, N.Uhle, Phys. Stat. Sol., **30**, p.k81-k84, (1968)

[9] E.K.Arushanov, R.Carles, Ch.Kloc, E.Bucher, J.Leotin, D.V.Smirnov, Inst. Phys. Conf. Ser., **155**, p.1013-1016 (1997)

[10] E.Arushanov, Ch.Kloc, E.Bucher, Phys.rev. B, **50**, p.2653-2656, (1994)

[11] P.G.Klemens, Phys. Rev. **148**, p.845, (1966)

[12] A.R.Bhatt, K.W.Kim, M.A.Stroscio, J.Appl. Phys. **76**, p.3905, (1994)

ELECTRICAL PROPERTIES OF ORTHORHOMBIC IRON DISILICIDE

Jun-ichi Tani , Hiroyasu Kido
Department of Inorganic Chemistry, Osaka Municipal Technical Research Institute,
1-6-50 Morinomiya, Joto-ku, Osaka 536-8553, Japan, tani@omtri.city.osaka.jp

ABSTRACT

In order to clarify the electrical properties of Cr-doped β-$FeSi_2$ ($Fe_{1-x}Cr_xSi_2$) and Mn-doped β-$FeSi_2$ ($Fe_{1-y}Mn_ySi_2$), the Hall effect and electrical resistivity of $Fe_{1-x}Cr_xSi_2$ ($0.01 \leqq x \leqq 0.05$) and $Fe_{1-y}Mn_ySi_2$ ($0.01 \leqq y \leqq 0.10$) have been measured in the temperature range between 80 and 300 K. The solid solutions $Fe_{1-x}Cr_xSi_2$ and $Fe_{1-y}Mn_ySi_2$ are *p*-type over the measured temperature range. The observed features of R_H of these solid solutions are explained by using the two-band model with the existence of two acceptor levels. The hole concentration of $Fe_{1-x}Cr_xSi_2$ at 300 K ranges from 8.9×10^{18} cm^{-3} for x=0.01 to 1.1×10^{20} cm^{-3} for x=0.05, which is one order of magnitude higher than that of $Fe_{1-y}Mn_ySi_2$.

INTRODUCTION

In recent years the semiconducting phase of iron disilicide (β-$FeSi_2$) [1] has been studied as a candidate material for thermoelectric conversion application, because of its superior features such as large Seebeck coefficient, low electrical resistivity, and chemical stability [2-5]. There have been many attempts to dope some additives into β-$FeSi_2$ to alter its semiconducting properties. The conduction types are *p*-type, produced by doping with V, Cr, Mn, and Al, and *n*-type, produced by doping with Co, Ni, Pt, and Pd [2-9].

Komabayashi *et.al.* [8] reported the electrical resistivity and Seebeck coefficient of Cr-doped β-$FeSi_2$ film at room temperature. They concluded that Cr is superior to Mn as an additive for *p*-type β-$FeSi_2$ from the results of the power factor measurement. Tokiai *et al.* [9] reported the thermoelectric properties of sintered Cr-doped β-$FeSi_2$, and found the figure of merit (Z) of Cr-doped β-$FeSi_2$ increases by using composite powders prepared by the precipitation method. However, to our knowledge, there has been few investigation concerning the Hall effect of $Fe_{1-x}Cr_xSi_2$, and its several important transport properties have not been determined. It is very useful to have detailed information on the transport properties to improve the performance of this material.

In this paper, the Hall effect and electrical resistivity of $Fe_{1-x}Cr_xSi_2$ in the temperature range between 80 and 300 K are reported. We also present data for $Fe_{1-y}Mn_ySi_2$ for comparison.

EXPERIMENT

Constituent mixtures of Fe (purity > 99.9%), Si (purity > 99.9%), and Cr (purity > 99.9%) or Mn (purity > 99.9%) powders were ground together and heated in evacuated fused silica ampoules at 1273K for 3 hours. The product was ground into fine powder, and compacted into pellets by cold pressing and sintered at 1423 K for 3 hours and then annealed at 1073K for 48 hours in a vacuum ($< 10^{-3}$ Torr) to convert the mixture of metallic α-$FeSi_2$ and ε-FeSi into the semiconducting β-$FeSi_2$. The density of the annealed samples was approximately 70-80% of the theoretical figure. X-ray diffraction with Cu K_α radiation to the annealed $Fe_{1-x}Cr_xSi_2$ ($0.01 \leqq x \leqq 0.05$) and $Fe_{1-y}Mn_ySi_2$ ($0.01 \leqq y \leqq 0.10$) detected only orthorhombic β-$FeSi_2$ type structure.

The Hall coefficient (R_H) and electrical resistivity (ρ) were measured using van der Pauw's technique [10] on 1.2-cm-diam, 0.2-cm-thick samples with Toyo Corporation Resitest 8320. The contacts between the samples and lead Au wires were made by soldering with In. The Hall effect was measured in the temperature region between 80 and 300 K using an ac magnetic method, under an applied magnetic field of 0.39 T at a frequency of 200 mHz.

Mat. Res. Soc. Symp. Proc. Vol. 545 © 1999 Materials Research Society

RESULTS

Figure 1 shows the temperature dependence of electrical resistivity of $Fe_{1-x}Cr_xSi_2$ ($0.01 \leqq x \leqq 0.05$) and $Fe_{1-y}Mn_ySi_2$ ($0.01 \leqq y \leqq 0.10$), as compared with nondoped β-$FeSi_2$. The electrical resistivity of $Fe_{1-x}Cr_xSi_2$ at 300 K is lower than that of $Fe_{1-y}Mn_ySi_2$.

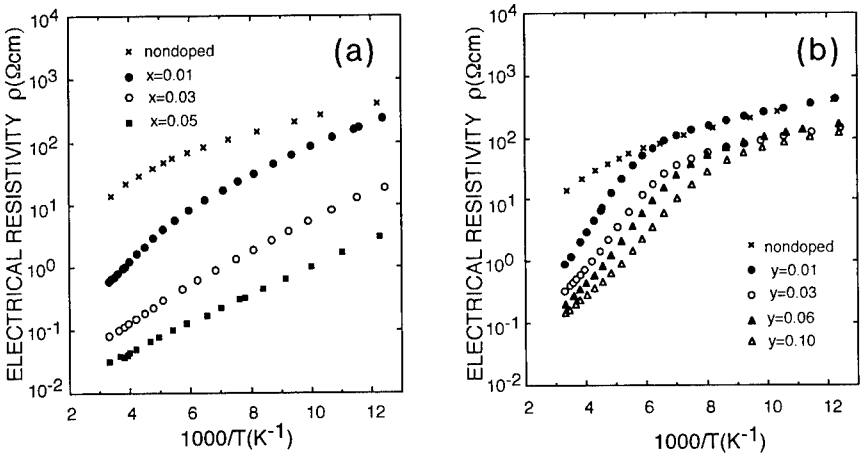

FIG. 1. The temperature dependence of electrical resistivity of $Fe_{1-x}Cr_xSi_2$($0.00 \leqq x \leqq 0.05$) (a) and $Fe_{1-y}Mn_ySi_2$ ($0.00 \leqq y \leqq 0.10$) (b).

Figure 2 shows the temperature dependence of Hall coefficient (R_H) of $Fe_{1-x}Cr_xSi_2$ ($0.01 \leqq x \leqq 0.05$) and $Fe_{1-y}Mn_ySi_2$ ($0.01 \leqq x \leqq 0.10$), as compared with nondoped β-$FeSi_2$. The signs of R_H for $Fe_{1-x}Cr_xSi_2$ and $Fe_{1-y}Mn_ySi_2$ are positive over the measured temperature range 80-300 K, indicating that the conductivity is mainly due to holes. For $Fe_{1-x}Cr_xSi_2$, R_H decreases with increasing temperature in the temperature range 80-300 K. For $Fe_{1-y}Mn_ySi_2$, however, with increasing temperature, R_H slightly decreases, increases, reaches a maximum, and then decreases. With increasing Mn content (x), the maximum of R_H shifts to lower temperature. The observed features of the temperature dependence of R_H of $Fe_{1-y}Mn_ySi_2$ ($0.01 \leqq y \leqq 0.10$) are very similar to *p*-type Al-doped single crystal in the temperature range of 30-300 K reported by Arushanov *et al.* [11]. They explained the results using the two-band model with the existence of an impurity band and an additional deep acceptor level. As has been pointed out by Arushanov *et al.* [11], $Fe_{1-x}Cr_xSi_2$ as well as $Fe_{1-y}Mn_ySi_2$ are also considered to have two acceptor levels, an level of dopant as well as a level of structural defects [12] and/or a small amount of unknown impurity which exist in both doped and nondoped β-$FeSi_2$.

If it is possible to neglect the effect of a level of structural defects and/or unknown impurity, the hole concentrations can be estimated by one carrier equation (1)[13]:

$$p = \frac{1}{eR_H} = \sqrt{\frac{n_v N_a}{2}} exp\left(\frac{-E_a}{2kT}\right) \qquad (1)$$

$$n_v = 2\left(\frac{2\pi m^* kT}{h^2}\right)^{\frac{3}{2}}$$

where N_a is the acceptor density and E_a is the activation energy of the acceptor level and m^* is the effective mass of the hole. In the $Fe_{1-x}Cr_xSi_2$ ($0.01 \leqq x \leqq 0.05$) system, the dependence of

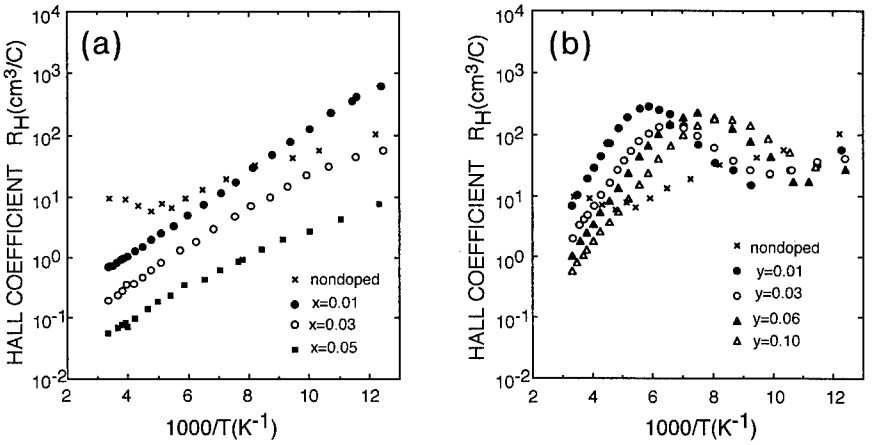

FIG. 2. The Hall coefficient (R_H) of $Fe_{1-x}Cr_xSi_2$ ($0.00 \leqq x \leqq 0.05$) (a) and $Fe_{1-y}Mn_ySi_2$ ($0.00 \leqq y \leqq 0.10$) (b) as a function of reciprocal absolute temperature.

$\log(1/R_HT^{3/4})$-$1/T$ plots is a straight line over the measured temperature range 80-300 K, which permits us to determined the hole concentration at 80-300 K in accordance with Eq.(1). For $Fe_{1-y}Mn_ySi_2$, however, the dependence of $\log(1/R_HT^{3/4})$-$1/T$ plots is a straight line only at high temperatures (220-300 K for y=0.01, 185-300 K for y=0.03, 160-300 K for y=0.06, and 150-300 K for y=0.10), which permits us to determined the hole concentration at high temperatures in accordance with Eq.(1).

Figure 3 shows the temperature dependence of hole concentration (p) of $Fe_{1-x}Cr_xSi_2$ ($0.01 \leqq x \leqq 0.05$) and $Fe_{1-y}Mn_ySi_2$ ($0.01 \leqq x \leqq 0.10$), as compared with nondoped β-$FeSi_2$. The hole concentrations (p) of $Fe_{1-x}Cr_xSi_2$ at 300 K are 8.9×10^{18} cm^{-3} for x=0.01, 3.3×10^{19} cm^{-3} for x=0.03, and 1.1×10^{20} cm^{-3} for x=0.05. However, the hole concentrations (p) of $Fe_{1-y}Mn_ySi_2$ are 8.9×10^{17} cm^{-3} for y=0.01, 2.9×10^{18} cm^{-3} for y=0.03, 5.7×10^{18} cm^{-3} for y=0.06, and 1.1×10^{19} cm^{-3} for y=0.10. Therefore, it was found that the hole concentration of $Fe_{1-x}Cr_xSi_2$ is one order of

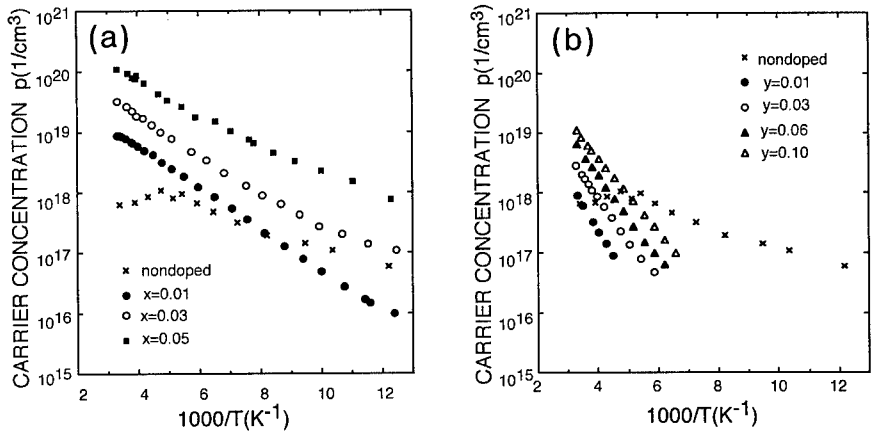

FIG. 3. The hole concentration (p) of $Fe_{1-x}Cr_xSi_2$ ($0.00 \leqq x \leqq 0.05$) (a) and $Fe_{1-y}Mn_ySi_2$ ($0.00 \leqq y \leqq 0.10$) (b) as a function of reciprocal absolute temperature.

magnitude higher than that of $Fe_{1-y}Mn_ySi_2$ at the same doping concentration. The acceptor activation energies (E_a) of $Fe_{1-x}Cr_xSi_2$ and $Fe_{1-y}Mn_ySi_2$ can be estimated from the slope of $\log(p/T^{3/4})$-$1/T$ plots. For $Fe_{1-x}Cr_xSi_2$, E_a is estimated to be 0.116 eV for x=0.01, 0.104 eV for x=0.03, and 0.083 eV for x=0.05. For $Fe_{1-y}Mn_ySi_2$, however, E_a is estimated to be 0. 299 eV for x=0.01, 0.258 eV for x=0.03, 0.248 eV for x=0.06, and 0.219 eV for x=0.10. E_a of $Fe_{1-x}Cr_xSi_2$ is much lower than that of $Fe_{1-y}Mn_ySi_2$.

CONCLUSIONS

We have measured the Hall effect and electrical resistivity of iron disilicide, $Fe_{1-x}Cr_xSi_2$ ($0.00 \leqq x \leqq 0.05$) and $Fe_{1-y}Mn_ySi_2$ ($0.01 \leqq y \leqq 0.10$) in the temperature range between 80 and 300 K, and its several important electrical properties of these solutions have been determined. The solid solutions $Fe_{1-x}Cr_xSi_2$ and $Fe_{1-y}Mn_ySi_2$ are *p*-type over the measured temperature range. The observed features of R_H of these solutions are explained by using the two-band model with two acceptor levels. The hole concentration of $Fe_{1-x}Cr_xSi_2$ at 300 K ranges from 8.9×10^{18} cm^{-3} for x=0.01 to 1.1×10^{20} cm^{-3} for x=0.05, which is one order of magnitude higher than that of $Fe_{1-y}Mn_ySi_2$.

REFERENCES

1. N. Kh. Abrikosov, Bull. Acad. Sci. U.S.S.R. **20**, 37 (1956).

2. R. M. Ware and D. J. McNeill, Proc. IEE **111** , 178 (1964).

3. U. Birkholz and J. Scelm, Phys. Status Solidi **27**, 413 (1968).

4. I. Nishida, Phys. Rev. B **7**, 2710 (1973).

5. T. Kojima, Phys. Status Solidi A **111**, 233 (1989).

6. J. Tani and H. Kido, J. Appl. Phys. **84**, 1408 (1998).

7. H. Nagai, I. Maeda, S. Katsuyama, and K. Majima, J. Jpn. Soc. Powder Powder Metall. **41**, 560 (1994) (in Japanese).

8. M. Komabayashi, K. Hijikata, and S. Ido, Jpn. J. Appl. Phys. **30**, 331 (1991).

9. T. Tokiai, T. Uesugi, and K. Koumoto, J. Ceram. Soc. Jpn. **103**, 670 (1995).

10. L. J. van der Pauw, Philips Res. Rep. **13**, 1 (1958).

11. E. Arushanov, Ch. Kloc, and E. Bucher, Phys. Rev. B **50**, 2653 (1994).

12. T. Miki, Y. Matsui, K. Matsubara and K. Kishimoto, J. Appl. Phys. **75**, 1693 (1994).

13. C.Kittel, *Introduction to Solid State Physics*, 7th ed. (J. Wiley, New York, 1986), p. 197.

THERMOELECTRIC TRANSPORT PROPERTIES OF $ReSi_{1.75}$ THIN FILMS

C.A. Kleint, A. Heinrich, H. Griessmann, D. Hofmann, H. Vinzelberg, J. Schumann,
D. Schlaefer, G.Behr, and L.Ivanenko

Institute of Solid State and Materials Research Dresden
Dept. of Thin Film Systems and Nanostructures,
Helmholtzstr. 20, D-01069 Dresden, Germany

ABSTRACT

Epitaxial $ReSi_{1.75}$ thin films of variable thickness between 15nm and 150nm have been prepared in an one step process by Facing Target Sputtering (FTS) onto heated (100) and (111)Si and SOS wafers. The epitaxial relations and film structure have been investigated by X-ray diffraction and transmission electron microscopy. Epitaxial growth was found at a substrate temperature of 1070K. Thermoelectric properties were measured between 100K and 450K and compared to the transport behavior of bulk $ReSi_{1.75}$ and polycrystalline films. A distinct dependence of both the conductivity and thermopower was found on the film thickness, on unintentional doping and on the film structure. The results show that epitaxial $ReSi_{1.75}$ films prepared by FTS can be a basis for further investigations of thermoelectric silicide/silicon multilayers.

INTRODUCTION

Semiconducting $ReSi_{1.75}$ with its small indirect band gap of about 0.15eV, formed by bonding and antibonding Re 5d-states, is a promising candidate for thin film applications near room temperature in infrared sensors [1] and thermoelectric couples [2]. Transport properties of $ReSi_{1.75}$ were investigated in thin films with mono-crystalline [3], polycrystalline [4] and nano-crystalline [2] structure and also in single crystals [5].

A particular feature of this compound is the good structural match to silicon. Up to now epitaxial $ReSi_{1.75}$ thin films on (100) and (111) oriented Si-substrates with thicknesses in the 10 to 100nm range have been prepared by Reactive Deposition Epitaxy (RDE) [6,7] and Solid Phase Epitaxy (SPE) [8], i.e. by the deposition of a Re metal film onto a Si substrate held at temperatures above or below the silicide formation temperature of about 920K, respectively. Post deposition annealing procedures were applied to form the silicide and/or to improve the crystalline quality. For both methods the silicide formation takes place under consumption of substrate silicon.

In this paper the question will be considered whether epitaxial $ReSi_{1.75}$ films can be prepared in an one step process, i.e. by simultaneous deposition of Re and Si onto a hot substrate without further annealing procedures, in order to establish conditions for future growth of $ReSi_{1.75}$ based multilayers. For the preparation of our $ReSi_{1.75}$-films we have utilized Facing Target Sputtering (FTS), an off-axis sputtering technology, which has been successfully applied to the deposition of epitaxial superconducting and magnetic thin films [9]. We will present first results on the structure and thermoelectric properties of epitaxial $ReSi_{1.75}$ thin films in comparison with bulk material and polycrystalline thin films, deposited on oxidized Si-wafers.

EXPERIMENTAL

$ReSi_{1.75}$ films were grown by Facing Target Sputtering in a high vacuum environment with a base pressure of $1*10^{-6}$ mbar. Two 90mm diameter DC-magnetron sources with opposite mag-

Mat. Res. Soc. Symp. Proc. Vol. 545 © 1999 Materials Research Society

netic polarity are placed face to face at a distance of 150 mm. The distance between the substrate and the source to source center line was 80 mm. The magnetrons were operated at 40W and an Ar-pressure of $7*10^{-3}$ mbar, resulting in deposition rates of typically 1Å/s. To achieve the correct rhenium silicide stoichiometry for the films, compound targets with excess silicon (Si/Re = 2.3) were prepared by conventional sintering techniques from 2N5 purity Re and 6N Si powders. Silicon wafers of (111) and (100) orientation with resistivities of 4800Ωcm and 1000Ωcm respectively and Silicon On Sapphire wafers with a 400 nm Si (100)-top layer (100Ωcm) were used as substrates for epitaxy. Polycrystalline thin films were deposited on Si/SiO_2-wafers. The deposition took place at 1070K, some 150K above the $ReSi_{1.75}$ phase formation temperature.

Structural properties were investigated by Transmission Electron Microscopy (Philips CN20 FEG) and X-ray diffraction (Philips X-pert). The electrical resistivity was measured with conventional dc four-probe technique, for thermopower measurements the differential method was used. Both properties were measured simultaneously in pure He atmosphere in the temperature range from 100K to 450K.

For comparison of thin film and bulk thermoelectric transport properties a bulk sample was grown by a modified Czochralski-process from high purity source material (4N Re and 6N Si). The crystal showed large single crystalline regions. The sample is single phase with a composition $ReSi_{1.8}$ measured by EPMA in the WDX mode.

RESULTS AND DISCUSSIONS

Structural properties

Epitaxial relationships and structural quality of the $ReSi_{1.75}$ films have been determined by X-ray diffraction from Bragg-Brentano scans and texture (pole figure) measurements. For $ReSi_{1.75}$ on (100) Si the silicide grows with its (100) plane parallel to the substrate surface (Fig.1).

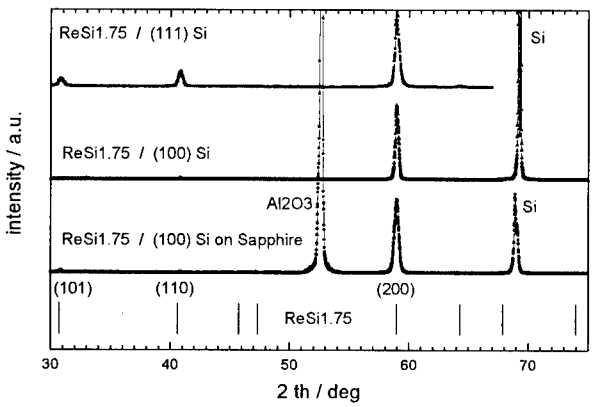

Fig.1: Bragg Brentano Scans (variable divergence slit) of FTS-grown $ReSi_{1.75}$ films on (111)Si, (100)Si and (100)Si on sapphire. Vertical bars mark $ReSi_{1.75}$ reflections for a polycrystalline sample

For the mosaic spread typically values between 2 and 3deg FWHM for different samples were found. Fig. 2 shows the (110) pole figure for a 15nm thick $ReSi_{1.75}$ film on (100) Si. Two

sets with four peaks separated by 90deg in Φ (azimuth) are observed. This fourfold symmetry can be ascribed to the existence of rotation twins since the $ReSi_{1.75}$ matching plane (100) has only twofold symmetry, whereas the (100) surface of silicon with its fourfold symmetry provides two distinct, but geometrically equivalent growth positions for the $ReSi_{1.75}$, separated by 90deg in azimuth. The two sets of peaks reflect two distinct epitaxial relationships with the same matching plane, occurring simultaneously but with large differences in their volume parts :

a) (100) $ReSi_{1.75}$ || (100) Si with [001] $ReSi_{1.75}$ || <110> Si (strong reflections) and

b) (100) $ReSi_{1.75}$ || (100) Si with [001] $ReSi_{1.75}$ || <100> Si (weak reflections).

The azimuthal orientation is characterized by a FWHM of 7 deg Φ.

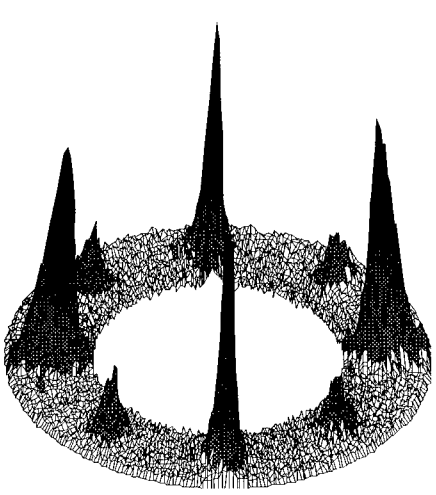

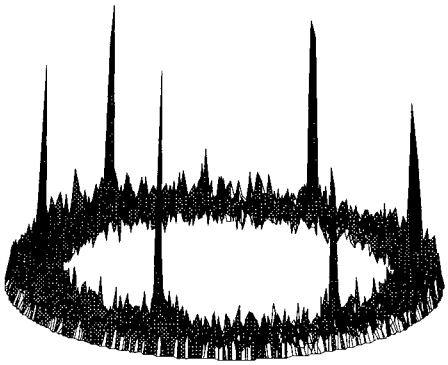

Fig. 3: (200) pole figure of a 15 nm thick $ReSi_{1.75}$ film, grown on (111) Si. The pole figure reflects the (110) oriented domains of the sample

Fig. 2 (left): (110) pole figure of a 15 nm, (100) oriented, $ReSi_{1.75}$ film on (100) Si

Whereas orientation a) with a maximum misfit of 2.1% and a common unit mesh of 120 $Å^2$ has been found for layers prepared by deposition of a Re-film onto a 'hot' Si-substrate too [7], orientation b), which is characterized by a similar maximum misfit but a larger common unit mesh of 600 $Å^2$, has not been reported in the literature.

Bragg-Brentano scans of $ReSi_{1.75}$-films on (111) Si exhibit three lattice planes oriented parallel to the film surface (101), (110) and (100) (Fig.1). It could be shown by pole figure measurements, that each of them is a matching plane of an epitaxial relationship. As an example Fig. 3 shows the (200) pole figure for the (110) film orientation. Similar to the films on (100) substrates the higher (threefold) symmetry of the Si (111) surface compared to the silicide matching plane leads to the appearance of three 120deg rotation twins. As for the layers on (100)Si the rotation twins occur with equal probability resulting in six peaks with equal intensity for $ReSi_{1.75}$ on (111)Si.

The peaks appear sharper in comparison to Fig. 2 indicating a better structural quality with a mosaic spread of 1.2 deg FWHM (ω) and 1.5 deg FWHM in Φ (azimuthal orientation). This might be due to the fact, that the maximum misfit between $ReSi_{1.75}$ (110) and Si(111) is only 0.1% with a common unit mesh of 102 $Å^2$. The complete epitaxial relationship is

a) (110) $ReSi_{1.75}$ || (111) Si; [001] $ReSi_{1.75}$ || <110> Si, which is also observed for layers on Si (111) prepared by RDE [6].

The epitaxial relationships for the two other matching planes (101) and (110) are

b) (100) $ReSi_{1.75}$ || (111) Si; [001] $ReSi_{1.75}$ || <110> Si with a maximum misfit of 5.7 % and a common unit mesh of 48 $Å^2$ and

c) (101) $ReSi_{1.75}$ || (111) Si; [001] $ReSi_{1.75}$ || <110> Si with a maximum misfit of 1.1 % and a common unit mesh of 312 $Å^2$.

which are typical only for our FTS-grown layers. From calculations of the corresponding volume fractions of orientations a) 20%, b) 68% and c) 12% it can be seen, that the (100) orientation dominates for the films on (111) Si.

Two 15 nm thick $ReSi_{1.75}$-films on (100) and (111) Si respectively have been investigated by TEM. Dark field images of cross section samples reveal a columnar microstructure with a sharp interface between film and substrate for both films. The average column width is 15 nm.

Electrical transport properties

The transport properties of the $ReSi_{1.75}$ thin films are expected to depend strongly on film structure, unintentional doping and deviations from strict stoichiometry. All these properties are mainly determined by the substrate surface and deposition temperature as well as the purity and composition of the sputtering targets. Because of the complicated microstructure found for the $ReSi_{1.75}$ films on (111)Si measurements have been performed only for layers on (100)Si. In Table 1 data of the electrical resistivity ρ, thermopower S and activation energy E_A (according to $\ln\rho \propto E_A/kT$) are summarized for all investigated samples: epitaxial films deposited onto (100)Si and (SOS) wafers by FTS and co-sputtering (CS) as well as polycrystalline films deposited onto oxidized Si wafers by FTS. For the co-sputtering high purity Re and Si targets have been used. We have also measured bulk material with large single crystalline regions to look whether it can be considered as a reference system for epitaxial films.

Table 1: Transport data of $ReSi_{1.75}$ thin films prepared by FTS, CS and of bulk $ReSi_{1.75}$

sample	thickness d_s/nm	structure	Resistivity ρ mΩcm		thermopower S μVK^{-1}		E_A/meV
			ρ(150K)	ρ(300K)	S(150K)	S(300K)	
FTS / SiO_2	150	poly	1.1	1.2	30	55	-
FTS / SiO_2	15	poly	1.5	1.3	18	35	-
CS / SOS	150	epi	70	35	-110	-75	47
FTS / SOS	150	epi	7.1	4.5	-75	-118	26
FTS / SOS	60	epi	-	5.3	-73	-105	33
FTS / (100)Si	300	epi	10.8	6.9	-70	-120	28
FTS / (100)Si	75	epi	14.5	8.3	-85	-160	-
FTS / SOS	15	epi	29	17.5	51	64	60
FTS / (100)Si	15	epi	-	-	40	-170	-
FTS / (100)Si	15	epi	20	13	40	90	-
Bulk	∞	poly	-	-	130	125	40

As shown in Table 1 the epitaxial films have to be classified according to their thickness d_s. Thick epitaxial films with $d_s \geq 50$nm show negative thermopower of similar size independent of the substrate (SOS or (100)Si) and target configuration (FTS or CS). Within the group of thick films only polycrystalline $ReSi_{1.75}$ on oxidized Si wafers show positive thermopower, i.e. dominant hole conduction. This different sign has to be related to the different film structure because in both cases the same sputtering targets have been applied and with that the same unintentional doping

was realized. The temperature dependence of the thermopower shown in Fig.4 confirms these results (The strong decrease of S(T) of the FTS sample on (100)Si above 400K is caused by the substrate and is not a film property). In Fig.4 the results on bulk $ReSi_{1.75}$ are also included. The large positive thermopower found in the bulk material is in contrast to the negative one in the epitaxial films. This difference is probably caused by the different purity of the source materials.

The results on thin films with d_s<30nm are more complex. As shown in Fig.5 the as deposited epitaxial films on SOS have a negative thermopower. During the first measuring cycle a change in sign is observed at about 450K. In all further heating and cooling curves the thermopower changes its size but keeps the positive sign. The values in Table 1 are those after the first cycle. The results of the films on (100)Si above 300K are strongly affected by the substrate. This influence yields the large negative values shown in Fig.5 and also the negative value of S(300K) in Table 1. This influence is also seen in the 75nm sample on (100)Si (Table 1). In contrast to the epitaxial films the polycrystalline layers show only dominant hole conduction.

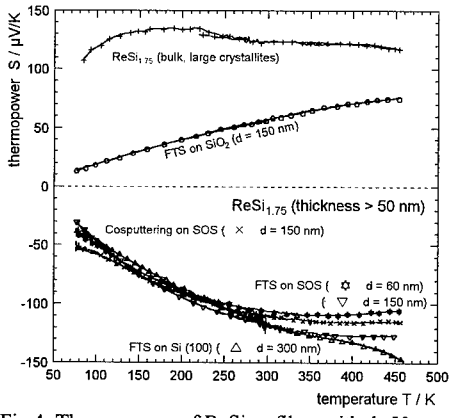

Fig.4 Thermopower of $ReSi_{1.75}$ films with d>50nm and bulk material

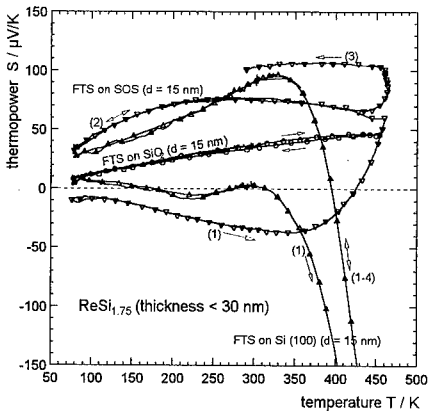

Fig.5 Thermopower of 15nm $ReSi_{1.75}$ films (numbers indicate the measuring cycle)

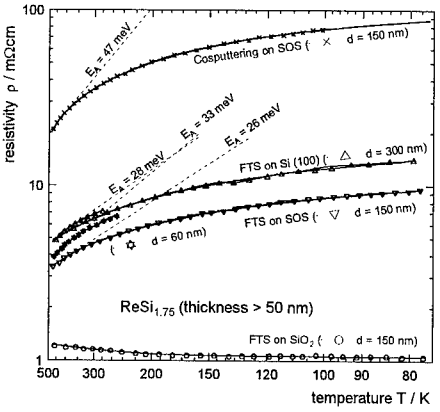

Fig.6 Resistivity and activation energies of $ReSi_{1.75}$ films with d>50nm

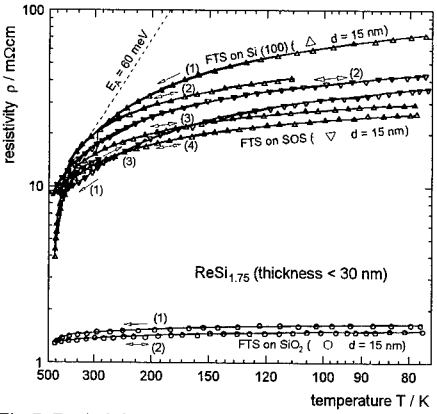

Fig.7 Resistivity of 15nm $ReSi_{1.75}$ films (numbers indicate measuring cycle)

There is up to now no final explanation of the change in sign of the thermopower in the thin epitaxial films. Because $ReSi_{1.75}$ is a small gap compound both types of carriers, holes and electrons, contribute to thermopower and conductivity. Only small shifts of the Fermi energy can cause a change in sign of the resulting thermopower. Such a shift can be caused by intrinsic defects which can disappear or made by structural relaxations during the heating process. This suggestion is in agreement with the positive thermopower found in poly- and nano-crystalline Re-Si films in the composition range of the $ReSi_{1.75}$ compound.

The resistivity of the thick and thin $ReSi_{1.75}$ films is shown in Figs. 6 and 7. The general temperature dependence is the same in all epitaxial films but the thin films exhibit larger resistivity values by about a factor 2 and show a steeper slope in the temperature range above 300K. This is caused in films on (100)Si by the substrate but is a film property on SOS wafers. There is no constant activation energy E_A but in the thin films on SOS the activation energy at 400K is equal to 0.60eV which is approximately ½ of the energy gap.

CONCLUSIONS

Epitaxial $ReSi_{1.75}$ thin films have been grown with variable thickness in an one step process without post deposition annealing by a FTS technique on single crystalline Si and SOS wafers. The silicide formation takes place without the consumption of substrate silicon and, therefore, our deposition method offers the opportunity to grow $ReSi_{1.75}$-thin films on substrates other than silicon too. Whereas $ReSi_{1.75}$ films on (100) Si exhibit a single epitaxial relationship in accordance with the literature, films grown on (111) Si show a complicated structure with three different epitaxial relationships occurring simultaneously.

Thermopower and electrical resistivity show different but reproducible behavior in thin (<30nm) and thick (>50nm) films. The correlation between transport behavior and preparation conditions including doping mechanisms and substrate influence has to be investigated in more detail to achieve a strategy to optimize the thermoelectric film properties.

ACKNOWLEDGEMENTS

This work was supported by the Bundesministerium für Bildung, Wissenschaft, Forschung und Technologie under contract number 03N2014B.

REFERENCES

[1] J.P. Becker, J.E. Mahan and R.G. Long, J. Vac. Sci. Technol., A13 (1995) 1133-1135.
[2] A.T. Burkov, A. Heinrich, C. Gladun, W. Pitschke and J. Schumann, J. Non-Cryst. Solids, 205-207 (1996) 737-741 and Phys. Rev. B58 (1998) 9644-9647.
[3] I. Ali, P. Muret and T.A. Nguyen Tan, Appl. Surf. Science, 102 (1996) 147-.
[4] R.G. Long, M.C. Bost and J.E. Mahan, Thin Solid Films 162 (1988) 29-40.
[5] U. Gottlieb, M. Affronte, F. Nava, O. Laborde, A. Sulpice and R. Madar, Appl. Surf. Science, 91 (1995) 82-86.
[6] T.A. Nguyen Tan, J.Y. Veuillen, P. Muret, S. Kennou, A. Siokou, S. Ladas, F. Lahatra Razafindrasima and M. Brunel, J. Appl. Phys., 77 (1995) 2514-2518.
[7] J.E. Mahan, G. Bai, M.-A. Nicolet, R.G. Long and K.M. Geib, Thin Solid Films, 207 (1992) 223-230.
[8] J.J. Chu, L.J. Chen and K.U. Tu, J. Appl. Phys., 62 (1987) 464-465.
[9] M. Naoe, S. Yamanaka and Y. Hoshi, IEEE Trans. Mag., 16 (1980) 646.

Single Crystal Growth and Thermoelectric Properties of $Ce_5Cu_{19}P_{12}$

K.J. Proctor and F.J. DiSalvo
Department of Chemistry and Chemical Biology, Baker Laboratory, Cornell University, Ithaca, NY 14853, USA

ABSTRACT

Single crystals of the known ternary cerium intermetallic $Ce_5Cu_{19}P_{12}$ were grown by Sn flux and I_2 transport methods. The long axis of the black hexagonal needles was confirmed to be the *c*-axis by single crystal X-ray diffraction. Electrical resistivity of both single crystals and a pressed pellet was measured from 4 - 300 K; the room temperature resistivity is about 400 $\mu\Omega$·cm for the needle axis of the crystals and about 5 mΩ·cm for the pressed pellet. The thermopower of the pressed pellet was found to be 34 μV/K at room temperature.

INTRODUCTION

Cerium intermediate valence (IV) compounds are potential thermoelectric materials since they often possess large thermopowers (S) and small electrical resistivities (ρ). Since IV materials only make up a small percentage of the known cerium compounds, the discovery of IV materials is a challenging problem. However, we have found several potentially interesting materials in the literature with IV signatures in the magnetic susceptibility (χ) and electrical resistivity but whose thermopower has not been measured. One such material is $Ce_5Cu_{19}P_{12}$ [1,2] with the hexagonal $Sc_5Co_{19}P_{12}$-structure type. The magnetic susceptibility of a powder suggested a reduced effective moment of Ce (1.71 versus 2.54 μ_B for a Ce^{3+} free ion) and the resistivity of a pressed pellet indicated single-ion Kondo interactions [1].

We are most interested in measuring the thermopower of IV materials, but we are also interested in exploring the anisotropy of transport properties. The transport properties of non-cubic materials, such as $Ce_5Cu_{19}P_{12}$, often display significant anisotropy. The anisotropy of transport properties has been studied in many materials, including the following cerium intermetallics: CeNiSn [3, 4], CeRhSb [5], $CeCu_2Si_2$ [6], $CeNi_2Ge_2$ [6], and $CeNiAl_4$ [7]. In fact, the thermoelectric materials commonly used today for room temperature cooling applications, alloys of Bi_2Te_3, is hexagonal and must be an oriented single crystal for maximum performance due to its anisotropy [8].

Exploring the anisotropy requires growing and measuring oriented single crystals. In addition, we want to measure the properties of single crystals to more accurately determine the electrical resistivity and thermal conductivity since reported pressed pellet data can be influenced by grain boundaries, preferred orientation, a low sintered density, and/or cracking due to anisotropic thermal expansion. Single crystals of intermetallic materials can be grown in several ways [9]. Common methods include metal fluxes [10], vapor or chemical transport, and Bridgeman and Czochralski methods. The relatively high phosphorus content of $Ce_5Cu_{19}P_{12}$ prevents using Bridgeman or Czochralski methods without suitable precautions to prevent P loss, such as a liquid encapsulant. A Sn flux is a common choice for intermetallics containing cerium, copper, and/or phosphorus. Some examples include CuP_2 [11], $CeCu_2Si_2$ [12], $CeFe_4P_{12}$ [13,14], $ZnSnP_2$ [15], $ZnSiP_2$ [15], $CdSiP_2$ [15], and $PtSi_3P_2$ [16]. In addition, crystals of $Ce_5Cu_{19}P_{12}$ have previously been grown utilizing I_2 as a transport agent [2]. We present here the results for our synthesis of single crystals of $Ce_5Cu_{19}P_{12}$ via Sn flux and I_2 vapor transport methods and a comparison of the transport properties of those crystals with a pressed pellet.

Mat. Res. Soc. Symp. Proc. Vol. 545 © 1999 Materials Research Society

EXPERIMENTAL

General Procedures

Prior to reaction, both cerium and iodine were purified in gram quantities. To remove any surface oxidation, cerium (Cerac, 12 mm pieces, 99.9 %) was melted in a tantalum susceptor under vacuum in an RF furnace and the molten metal allowed to drip into a water cooled copper cup [17]. Iodine (Fisher Scientific, 99.98 %) was sublimed onto a liquid nitrogen-cooled cold finger under static vacuum. After purification, these elements and phosphorus were handled only under an inert argon atmosphere. In general, the scale of reactions was limited by the maximum phosphorus pressure at the soak or annealing temperatures; calculated pressures of P_4 based on the initial phosphorus mass were kept below 5 atm and the reaction tubes were heated slowly to reduce the chance of tube explosion.

All products and intermediates were analyzed by powder X-ray diffraction (PXRD) on a Scintag XDS2000 (θ-2θ geometry and Cu Kα radiation) to determine the phase purity and crystallinity. Patterns were compared with a simulated pattern [18] using lattice constants and atomic coordinates from Reference 1. Lattice constants were refined with a least squares routine which corrects for small vertical displacement errors of the sample. The Ce-Cu-P phase diagram [2] was helpful in identifying extra reflections from impurity phases.

Crystals of $Ce_5Cu_{19}P_{12}$ were analyzed by standardless microprobe analysis (JEOL 733 SEM with x-ray detector). Energy versus intensity spectra were collected for 30 seconds from a 15 kV, 1 nA beam. The spectra were fitted to the Ce L, Cu K, P K, Sn L, and I L emissions with the SQ program in on a Flextran platform with a ZAF correction.

Pressed Pellet Synthesis

In order to intimately mix the metals and provide a brittle, grindable starting material, cerium and copper (>99.99 %) were arc melted in a 5 : 19 molar ratio (0.06 % mass loss). The resulting golden bead was ground with 12 molar equivalents of phosphorus (Johnson-Matthey, red lump, 99.999 %), pelleted (total mass $\approx$ 1.0 g), and placed in an alumina crucible. The crucible was sealed in quartz and annealed until there was no visible phosphorus remaining (4 D at 600°C and 8 D at 500°C). The resulting black pellet was spongy and a PXRD pattern contained extra reflections so it was repelleted and sintered for 12 D at 900°C and 9 D at 800°C with one intermediate repelleting. The PXRD pattern of the final pellet had no observable (>2 % of the intensity of the strongest reflection) impurity reflections and the refined lattice parameters of $Ce_5Cu_{19}P_{12}$ from 40 reflections agreed with previous reports [1,2]. Prior to measuring transport properties, the pellet was shaped into a rectangular bar of dimensions $7.0 \times 4.1 \times 3.8$ mm.

After measuring the transport properties of the pellet, we attempted to form a solid bead of the material by carefully arc melting a piece of the pellet. The large mass loss and extra reflections in the PXRD pattern suggest that the phosphorus vapor pressure above the melting temperature of $Ce_5Cu_{19}P_{12}$ is significant.

Vapor Transport Synthesis

Cerium, copper (Mallinckrodt, granular, 99.8 %), phosphorus, and resublimed iodine (5 mg/mL) were combined in a 5 : 21 : 12 : 2 molar ratio in a long quartz tube. The temperature was slowly ramped to 950°C and then a 100°C temperature gradient was established and held for about 3 weeks. $Ce_5Cu_{19}P_{12}$ was transported to the hot end of the tube as thin, shiny black,

hexagonal needles. The needles were washed with ethyl ether to remove any traces of iodine left on the surface of the crystals. A single crystal was mounted on a single crystal diffractometer (Bruker CCD SMART diffractometer with Mo Kα radiation). The reflections could be indexed with the correct hexagonal cell and the needle axis was determined to be the *c*-axis.

Sn Flux Synthesis

A stoichiometric mixture of cerium, copper (>99.99 %), and phosphorus were combined with Sn (mole ratio Ce : Cu : P : Sn = 5 : 19 : 12 : 11) in an alumina crucible. An inverted alumina crucible filled with quartz wool was placed on top of the first crucible and both were sealed in a quartz tube. The reaction mixture was soaked at about 1200°C (the quartz softened) for 4 D followed by cooling at 7°C/hr. It was found that temperatures of >1000°C were necessary for crystal formation. Some of the flux was removed by centrifuging the reaction mixture into the second crucible at 500°C. Crystals protruding from the surface of the sample were taken for property measurements. Attempts to remove the flux with a mixed HCl-HNO_3 etch resulted in a more pure PXRD pattern (only a few weak reflections from bronze Cu_6Sn_5 impurities) but the needle crystals were attacked by the acid and became too cracked and brittle for property measurements.

Property Measurements

Transport properties of the samples were measured as previously described [19,20]. Electrical resistivity was measured with the 4 probe AC method. Current contacts were made to the single crystals with ultrasonic In and 34 AWG copper wire; pressed pellet contacts were made with silver epoxy (Epoxy Technology, H20E) and Cu foil. All voltage contacts were made with silver epoxy and 40 AWG copper wire. Thermopower and thermal conductivity of the pressed pellet were measured simultaneously using the steady state technique [19,20]. The pellet was mounted to the apparatus with Pb:Sn solder. Temperatures were measured with two Au(0.07%Fe):Chromel-*p* thermocouples. The thermoelectric voltage of the sample was measured on and corrected for the contribution from the Chromel-*p* leads of the two thermocouples.

RESULTS AND DISCUSSION

Microprobe

Elemental analysis of fourteen crystals from Sn flux and transport reactions was performed via microprobe analysis. The refined percentages of Sn and I were negligible suggesting that there is no systematic contamination of the samples from the growth media. The average atomic percentages of Ce : Cu : P are $15.5 \pm 0.8 : 46.4 \pm 2.5 : 35.8 \pm 3.2$ (errors given as $\pm 1\sigma$) in comparison to the calculated percentages of 13.9 : 52.8 : 36.2 from the assumed 5-19-12 stoichiometry. No individual analysis was significantly outside of these values ($\pm 2\sigma$) and there were no statistically significant differences between the crystals from Sn flux and from I_2 transport. The data suggests that the crystals have a low Cu and a high Ce content. However, previous experience with standardless microprobe of ternary lanthanides, such as Ce_2CoSi_3, and the close similarity of lattice constants between the different synthetic techniques and to previous reports [1,2] suggests that the apparent deviation in Cu and Ce content is due to minor errors in the ZAF correction.

Electrical Resistivity

The resistivity of the pressed pellet (Figure 1) displays significant temperature hysteresis, probably due to the sample cracking or contacts shifting. Prior to temperature cycling, the room temperature magnitude (4.8 mΩ·cm) agrees with that previously reported (4.3 mΩ·cm) [1]. The temperature dependence of this data also suggests the presence of Kondo interactions. However, the rather abrupt rise and fall (4.3 to 5.2 mΩ·cm) in resistivity around 100 K observed previously [1] is more gradual here; we observe a nearly linear increase in resistivity with decreasing temperature (4.8 to 5.3 mΩ·cm) followed by a steep decline at temperatures below 100 K.

The resistivities of several single crystals were also measured along the *c*-axis. The room temperature resistivities (Table I) are more than an order of magnitude smaller than the values of the pressed pellet. The pressed pellet resistivity is likely higher than the single crystals because of grain boundary effects, a low sintered density, and cracking due to temperature cycling during the annealing process and the prior thermopower/thermal conductivity measurements. It is not surprising that the room temperature magnitudes of the I_2 transport crystals differ by more than a factor of 3 because of the difficulty in accurately determining the area factors for the thin needles.

The temperature behavior of the samples shows large differences between the three synthetic techniques (Figure 2). The identical temperature dependence of all four needles from vapor transport reactions confirms that the differences in magnitude (Table II) are a result of errors in the area factor. However, the small magnitude and metallic temperature behavior of the Sn flux needle suggests that the crystal surface was contaminated with Sn to form a metallic path between the voltage contacts. This may be possible since the crystal was never etched to completely remove the flux. The temperature dependence of the vapor

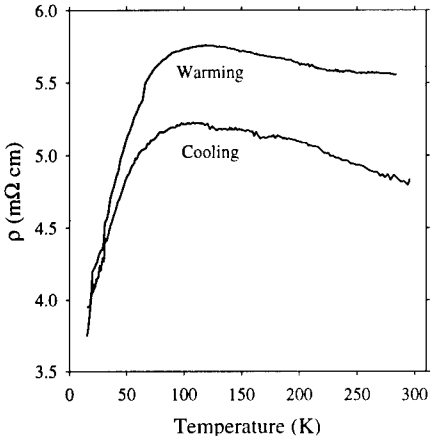

Figure 1. Electrical resistivity of $Ce_5Cu_{19}P_{12}$ pressed pellet.

Table I. Room temperature resistivities.

Synthetic Technique	ρ_{RT} (μΩ·cm)
Pressed Pellet	4820
Sn Flux	203
I_2 Transport (4 crystals)	201 - 681

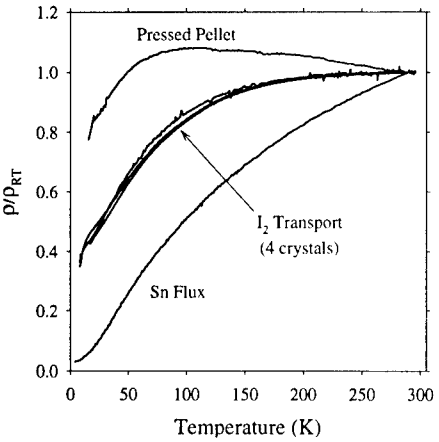

Figure 2. Electrical resistivity of $Ce_5Cu_{19}P_{12}$ scaled to room temperature.

transport needles is indicative of crystal field effects whereas the pressed pellet displays Kondo-like behavior. One possible explanation is that the Kondo interactions may be stronger in the basal plane. Unfortunately, the small diameter of all needle crystals prevented the measurement of a basal resistivity.

Thermopower and thermal conductivity

The thermopower and thermal conductivity of the pressed pellet are found to be 34 μV/K and 16 mW/K·cm at 298 K. By 204 K, the values drop to 31 μV/K and 10 mW/K·cm, respectively. These values of thermal conductivity cannot be trusted to more than an order of magnitude due to poor thermal contact between the sample and the heater/heat sink. An indication of the fragility of the contacts is that, while cooling the sample below 200 K, one solder contact failed and the heater fell off the sample. Preliminary results on a single crystal from an I_2 transport reaction suggest that the room temperature thermopower along the needle axis is 24 μV/K [21], a value reasonably consistent with that of our pressed pellet.

CONCLUSIONS

Single crystals of $Ce_5Cu_{19}P_{12}$ were grown via transport and flux techniques and their transport properties were measured. Large differences between the single crystal and pressed pellet data were found in both the magnitude and the temperature behavior of the electrical resistivity. With a thermopower of only 34 μV/K, $Ce_5Cu_{19}P_{12}$ is not likely to be a technologically interesting thermoelectric material.

ACKNOWLEDGMENTS

This research was funded by the Office of Naval Research. K.J.P. would also like to thank B. Cho and C.D.W. Jones for help with the initial setup and centrifuging of the flux reactions.

REFERENCES

1. R.J. Cava, T. Siegrist, S.A. Carter, J.J. Krajewski, W.F. Peck, Jr., H.W. Zandbergen, J. Solid State Chem. **121**, 51-55 (1996).
2. S.I. Chykhrij, G.V. Loukashouk, S.V. Oryshchyn, Yu. B. Kuz'ma, J. Alloys Compd. **248**, 224-232 (1997).
3. T. Takabatake, F. Teshima, H. Fujii, S. Nishigori, T. Suzuki, T. Fujita, Y. Tamaguchi, J. Sakurai, D. Jaccard, Phys. Rev. B. **41** (13), 9607-9610 (1990).
4. G. Nakamoto, T. Takabatake, Y. Bando, H. Fujii, K. Izawa, T. Suzuki, T. Fujita, A. Minami, I. Oguro, L.T. Tai, A.A. Menovsky, Physica B **206&207**, 840-843 (1995).
5. T. Takabatake, H. Tanaka, T. Bando, H. Fujii, S. Nishigori, T. Suzuki, T. Fujita, G. Kido, Phys. Rev. B **50** (1), 623-626 (1994).
6. H. Schneider, Z. Kletowski, F. Oster, D. Wohlleben, Solid State Comm. **48** (12), 1093-1097 (1983).
7. T. Mizushima, Y. Isikawa, K. Mori, J. Sakurai, J. Phys. Soc. Jpn. **65** Suppl B., 146-150 (1996).
8. H. Kaibe, Y. Tanake, M. Sakata, I. Nishida, J. Phys. Chem. Solids **50** (9), 945-950 (1989).

9. J.S. Abell, in *Handbook on the Physics and Chemistry of Rare Earths*, edited by K. A. Gschneidner, Jr., L. Eyring (North-Holland, Amsterdam, 1989), Vol. 12, p. 1.
10. Z. Fisk, J.P. Remeika, in *Handbook on the Physics and Chemistry of Rare Earths*, edited by K. A. Gschneidner, Jr., L. Eyring (North-Holland, Amsterdam, 1989), Vol. 12, p. 53.
11. J.P. Odile, S. Soled,C.A. Castro, A. Wold, Inorg. Chem. **17** (2), 283-6 (1978).
12. G.R. Stewart, Z. Fisk, J.O. Willis, Phys. Rev. B: Condens. Matter **28** (1), 172-7 (1983).
13. W. Jeitschko, D. Braun, Acta. Cryst. **B33**, 3401-3406 (1977).
14. K.J. Proctor (unpublished).
15. N.P. Luzhnaya, J. Cryst. Growth **3&4**, 97 (1968).
16. Ch. Perrier, M. Kirschen, H. Vincent, U. Gottlieb, B. Chenevier, R. Madar, J. Solid State Chem. **133**, 473-478 (1997).
17. R.A. Gordon, Ph.D. Thesis, Cornell University, 1995.
18. XPOW v2.0 ©1993; B. Downs and K. Bartelmehs, American Mineralogist **78**, 1104-1107 (1993).
19. K.J. Proctor, C.D.W. Jones, F.J. DiSalvo, J. Phys. Chem. Solids, in press.
20. C.D.W. Jones, K.A. Regan, F.J. DiSalvo, Phys. Rev. B. **58** (24), in press (1998).
21. J. Badding (private communication).

Thermoelectric and Structural Properties of $Bi_{1-x}Te_{1+x}$ Thin Films on CdTe(111)

Yunki Kim*, Sunglae Cho*, Antonio DiVenere*, George K. Wong*, Jerry R. Meyer**, and John B. Ketterson*
*Department of Physics and Astronomy, Northwestern University, Evanston, Illinois
**Code 5613, Naval Research Laboratory, Washington, D.C.

ABSTRACT

Thin films of the hexagonal phase of $Bi_{1-x}Te_{1+x}$ have been grown on CdTe(111) substrates using molecular beam epitaxy (MBE). Analysis of X-ray diffraction patterns (θ-2θ scans and rocking curves) of the films shows that their crystallinity depends upon the compositional deviation from stoichiometric BiTe. Measurements of the temperature-dependent thermoelectric power (TEP) of the films reveals that compositional changes cause the TEP to vary from electron dominant (n-type) to hole dominant (p-type), implying their possible application as a thermoelectric cooler or power generator. Measurements of the temperature-dependent resistivity of the films were conducted, and the analysis shows semimetallic behavior. These results demonstrate that $Bi_{1-x}Te_{1+x}$ is an appropriate model system to study the dependencies of thermoelectric and structural properties on binary composition.

INTRODUCTION

Little is known of the physical properties of hexagonal BiTe, compared with its well-known neighbor, the narrow-gap semiconductor Bi_2Te_3 with a bandgap of 0.13 eV. The hexagonal form of BiTe has been known to have a layered structure and can be regarded as a result of ordering in the solid solution of the two structures Bi_2 and Bi_2Te_3. [1,2] The stoichiometric Bi_1Te_1 with lattice constants of a=4.426 Å, c=24.069 Å can be achieved when the Bi_2 layers from bismuth are sandwiched with the two Te-Bi-Te-Bi-Te layers from Bi_2Te_3. The BiTe system naturally occurs near the stoichiometric composition as the Bi_2Te_3 and the Bi_4Te_3 systems do. [3]

There have been a couple of reports on the transport properties of bulk and thin film BiTe systems. [4,5] However, the transport properties of the hexagonal phase of BiTe system have not been studied carefully. Even the question of whether it is a metal, semimetal, or semiconductor is not yet answered.

In this report, growth of BiTe thin films on CdTe(111)B substrates and their structural properties will be presented. Their transport properties, from the viewpoint of structural deviations from the stoichiometric BiTe, and the temperature-dependent resistivity of the BiTe thin films near the stoichiometric composition will also be discussed.

EXPERIMENT

BiTe films were grown on semi-insulating CdTe(111)B substrates in a custom-built MBE system similar in design to a Varian Model 360. The base pressure of the growth chamber was in the range of 10^{-10} Torr. The substrates were etched in a solution of 1 % bromine in methanol prior to loading into a load-lock chamber. We first deposited a 3000 Å CdTe buffer layer on the

Mat. Res. Soc. Symp. Proc. Vol. 545 © 1999 Materials Research Society

CdTe substrate at 250 °C, followed by the co-deposition of Bi and Te at a rate of 0.3-0.4 Å/s. Reflection high energy electron diffraction (RHEED) was used to examine the specific surface reconstruction, the growth mode and growth orientation of the deposited layers. The growth temperature of BiTe films was 200 °C. The phase and growth orientation of the BiTe thin films were characterized using X-ray diffraction (XRD) including θ-2θ scans and rocking curves. Transport properties of the BiTe films have been studied using conventional four-probe-temperature-dependent-resistivity, Hall effect and temperature-dependent thermoelectric power measurements.

RESULTS

Figure 1 shows the RHEED pattern of a 3000 Å BiTe film on a CdTe(111)B substrate along (10.0) and (12.0) azimuth. It displays no surface reconstruction. The diffraction streaks are sharp and Kikuchi lines are apparent, representing a 2D layer-by-layer growth of BiTe on CdTe(111)B. The RHEED patterns, repeated at every 60°, imply the BiTe layers have 6-fold in-plane symmetry.

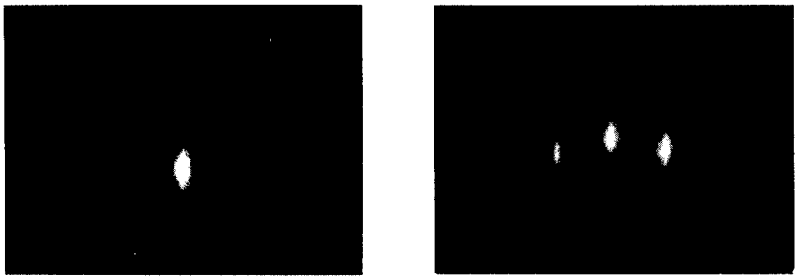

(10.0) (12.0)

FIG. 1. RHEED patterns of a 3000 Å (00.*l*) BiTe film on CdTe(111)B along (10.0) and (12.0) azimuth.

Figure 2 shows the XRD pattern (θ-2θ scan) of a BiTe thin film on CdTe(111)B. It has only (00.*l*) peaks. Several small peaks in the figure cannot be identified as peaks from the stoichiometric BiTe. This implies that the film is not perfectly stoichiometric and that the unit cell may be very large. However, if the compositional change is not large, from a practical point of view, the periodicity can be calculated from the position of XRD peaks, assuming that the sample has the same structure as a stoichiometric material. (See ref. 6.) In this work, c-axis lattice constants of the films have been calculated from the positions of BiTe (00.5) peaks in the XRD patterns. The rocking curve FWHM at the BiTe (00.12) peak of the BiTe film was measured to be 0.193°, as shown in Fig. 3, implying growth of a high quality film.

Figure 4 shows the dependence of the FWHM of the BiTe (00.12) peak on the c-axis lattice constants. It reveals that the FWHM values become smaller as the c-axis lattice constants approach the bulk value. This result indicates that the more stoichiometric the BiTe film is, the more periodic and ordered structure it has. This can be explained by assuming that as the BiTe system departs from the stoichiometric composition, one of the two substructures, Bi_2 and Te-Bi-Te-Bi-Te will be added randomly, resulting in a disordered structure. Another way to account

for this phenomenon is to assume that excess Te can occupy Bi sites and excess Bi can also occupy Te sites. [7] In this case, the difference in atomic size of Bi and Te makes a unit cell size change with composition. The FWHM is expected to reach a minimum when Bi and Te composition are the same, i.e. there is no excess Bi or Te.

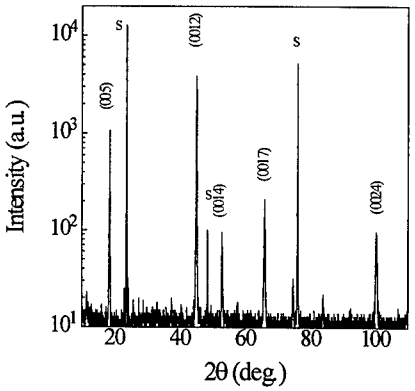

FIG. 2. XRD θ-2θ diffraction patterns of a BiTe thin film on CdTe(111)B; s denotes CdTe substrate peaks.

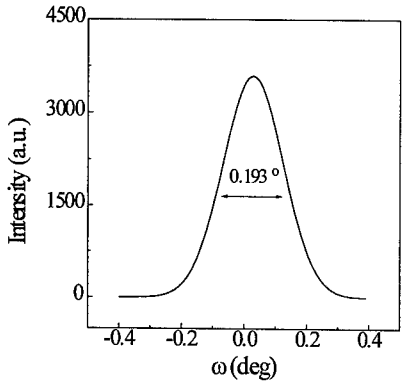

FIG. 3. The rocking curve of the BiTe film at the BiTe (00.12) peak. The FWHM was 0.193°.

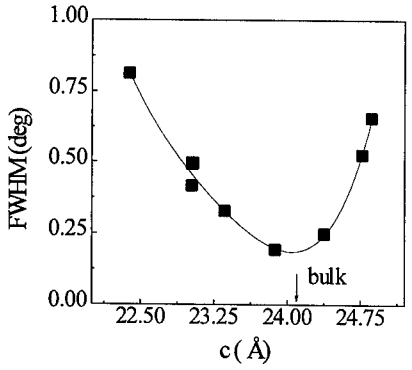

FIG. 4. FWHM values with respect to the c-axis lattice constants of BiTe thin films.

Temperature dependent thermoelectric powers of the BiTe thin films have been measured as shown in Fig. 5. There was a drastic change in the TEPs of the films with respect to the composition of Bi and Te. The TEPs of the BiTe films with smaller c-axis lattice constants display hole dominant (p-type) behavior whereas those with larger c-axis lattice constants display electron dominant (n-type) behavior. The TEP curves of the BiTe thin films show semimetallic characteristics. The TEPs of the films at room temperature with respect to the c-axis lattice constants are shown in Fig. 6. This figure shows an abrupt change of TEP values near the

stoichiometric BiTe. The point of the polarity change is slightly shifted from the stoichiometric BiTe composition composition. This implies that the ratio of electron and hole mobilities is not unity in the BiTe system. Similar polarity inversion on binary composition is found in the PbTe system.[8] This easy controllability of n- and p-type TEP characteristics by changing the binary composition in the BiTe system suggests this material should be considered as a possible thermoelectric element.

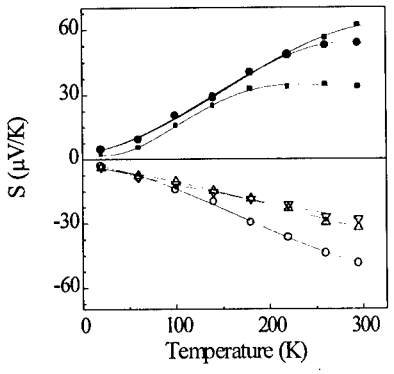

FIG. 5. Temperature-dependent thermoelectric powers of the BiTe thin films.

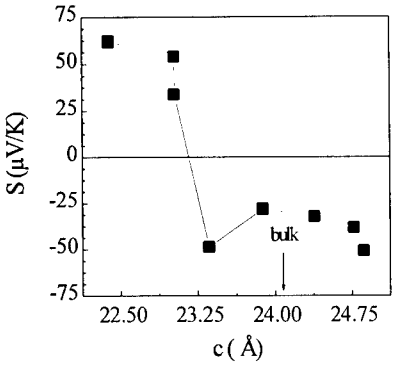

FIG. 6. Room temperature thermoelectric powers with respect to c-axis lattice constants of the films.

Temperature-dependent resistivity curves have been measured for a BiTe thin film near the stoichiometric composition and it displays a semimetallic behavior, as shown in Fig. 7. A Hall measurement was also performed on the same sample at room temperature. The electron density and mobility are measured to be 1.2×10^{20} cm^{-3} and 45.8 cm^2/Vs, respectively. From this high electron density, the temperature-dependent resistivity curve, and the temperature dependent TEP curves, BiTe thin films grown on CdTe(111)B can be classified as a semimetal.

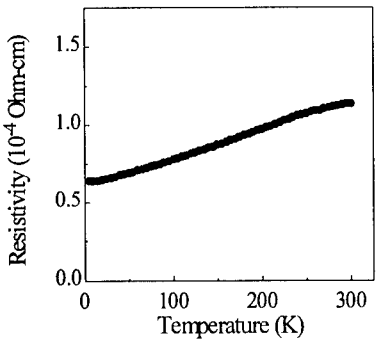

FIG. 7. Temperature-dependent resistivity of a BiTe thin film.

SUMMARY

Thin films of the hexagonal phase of $Bi_{1-x}Te_{1+x}$ have been grown on CdTe(111)B substrates using MBE. Analysis of X-ray diffraction patterns of the films (θ-2θ scans and rocking curves) shows that the BiTe thin films have highly periodic structures near the stoichiometric composition. Measurements of temperature-dependent thermoelectric powers (TEP) of the films reveals that the compositional change causes the TEP to vary from electron dominant (n-type) to hole dominant (p-type) near the stoichiometric composition. The temperature-dependent resistivity curve of a BiTe film has been measured, and the analysis shows semimetallic behavior. These results demonstrate that the structural and transport properties of the BiTe films are dependent on the binary composition.

ACKNOWLEDGMENTS

This work was supported by DARPA under Grant No. DAAG55-97-1-0130. Use was made of MRL Central Facilities supported by the National Science Foundation, at the Materials Research Center of Northwestern University, under Award No. DMR-9120521.

REFERENCES

1. M. M. Stasova, Zh. Struct. Khim **8**, 655 (1967) [transl. J. Struct. Chem. **8**, 584 (1967)]; M. M. Stasova, Zh. Struct. Khim **5**, 793 (1964) [transl. J. Struct. Chem. **5**, 731 (1964)]; M. M. Stasova, and O. G. Karpinskii, Zh. Struct. Khim **8**, 85 (1967) [transl. J. Struct. Chem. **8**, 69 (1967)].
2. P. M. Imamov, and S. A. Semiletov, Kristallogr. **15**, 972 (1971) [transl. Soviet Phys. Crystallogr. **15**, 845 (1971)].
3. Hidehiko Shimazaki, and Tohru Ozawa, Am. Mineralogist **63**, 1162 (1978).
4. M. M. Ibrahim, N. Afify, M. M. Hafiz, and M. A. Mahmoud, J. Phys. Chem. Solids **51**, 253 (1990).
5. M. J. McCulley, G. W. Neudeck, and G. L.Liedl, J. Vac. Sci. Technol. **10**, 391 (1973).
6. Allan Brown, and B. Lewis, J. Phys. Chem. Solids **23**, 1597 (1962).
7. G. R. Miller, and Che-Yu Li, J. Phys. Chem. Solids **26**, 173 (1965).
8. E. Miller, K. Komarek, and I. Cadoff, Trans. AIME **215**, 884 (1959).

MBE GROWTH AND THERMOELECTRIC PROPERTIES OF Bi_2Te_3 THIN FILMS

Sunglae Cho*, Yunki Kim*, Antonio DiVenere*, George K. L. Wong*, Jerry R. Meyer**, and John B. Ketterson*
*Department of Physics and Astronomy, Northwestern University, Evanston, IL 60208
**Code 5613, Naval Research Laboratory, Washington, D.C. 20375-5338

ABSTRACT

We have grown high quality Bi_2Te_3 thin films on CdTe(111)B substrates using MBE. Structural properties have been investigated using *in-situ* reflection high-energy electron diffraction (RHEED) and θ-2θ X-ray diffraction analysis. They show that Bi_2Te_3 films on CdTe(111) grow along the (00.*l*) in the hexagonal cell with a layer-by-layer growth mode, resulting in a smooth surface, and an X-ray Bragg peak FWHM of 0.2 °. The thermopower and electrical conductivity of the stoichiometric Bi_2Te_3 films were ~200 μV/K and 10^3 $(\Omega cm)^{-1}$, respectively, comparable to the single crystal bulk values. We have observed the antisite defect effect in Te-rich Bi_2Te_3 films: excess Te occupies Bi lattice sites and behaves as an n-type dopant. Crystallinity and transport properties are strongly affected by non-stoichiometry.

INTRODUCTION

High efficiency thin film thermoelectric devices are widely foreseen as having applications in the microelectronics industry such as dissipating the heat generated by various devices. Bi_2Te_3 and its solid solutions are well known thermoelectric materials for near-room temperature thermoelectric applications. Since one prerequisite is high mobility, this effort is directed toward achieving this goal.

A number of techniques have been used in the fabrication of Bi_2Te_3 thin films such as magnetron sputtering,[1,2] laser ablation,[3] MOCVD[4] and MBE[5,6] on various substrates (e.g. α-Al_2O_3, SiO_2, GaAs, glass, etc.). Little work has been reported on the growth of epitaxial Bi_2Te_3 thin films. Generally, all the previous studies show difficulties in obtaining a stoichiometric composition, because of the re-evaporation of Te at higher growth temperature,[5] and antisite defects: excess Te(Bi) occupies Bi(Te) lattice sites.[7]

In this article, we describe the growth, structural and transport properties of MBE-grown Bi_2Te_3 thin films on CdTe(111)B. The characterization of the films was performed by *in-situ* reflection high-energy electron diffraction (RHEED), X-ray diffraction (XRD), and transport measurements (resistivity, thermopower, and Hall effect).

THIN FILM GROWTH AND CHARACTERIZATION

Bi_2Te_3 thin films were grown on semi-insulating CdTe(111)B substrates in a custom-built MBE system similar to a Varian Model 360. It consists of growth, analysis, and load-lock chambers and is equipped with RHEED and Auger electron spectroscopy (AES). The experiments are carried out with different effusion cells containing CdTe for the growth of a CdTe buffer layer, and Bi and Te for the Bi_2Te_3 film growth. The CdTe(111)B wafers are etched in a solution of 2 % bromine in methanol prior to loading

Mat. Res. Soc. Symp. Proc. Vol. 545 © 1999 Materials Research Society

into the load-lock chamber. After thermal annealing at 300°C for 30 minutes, we first deposited a 3000 Å CdTe buffer layer on the CdTe substrate at 250°C, followed by deposition of the Bi_2Te_3 thin films at a rate of about 0.3 Å/s and at a growth temperature of 250 °C. Bi and Te were evaporated from different effusion cells. Bi_2Te_3 has a layered structure with a unit cell with lattice constants a=4.38 Å, c=30.45 Å in the hexagonal representation. The sequence of the layered structure is Te-Bi-Te-Bi-Te and three sequences make a unit cell: 6 Bi layers and 9 Te layers in a unit cell. The lattice mismatch of Bi_2Te_3 with CdTe(111)B (4.58 Å) substrate is 4.3 %. The base pressure of the growth chamber was in the 10^{-10} Torr range. RHEED was used to examine the specific surface reconstruction of the deposited layers.

Films were processed into bar-shape patterns using photolithography and lift-off techniques for electrical resistivity and Hall measurements. To measure the thermopower we used the differential method, in which a small temperature difference is maintained across the sample to produce the thermoelectric voltage: $\Delta V=S\nabla T+b(\nabla T)^2+\ldots$, where b is a constant. The thermoelectric voltage $(\Delta V)_i$ vs. temperature difference $(\nabla T)_i$ were plotted and from the slope of the linear region we could determine the thermopower.[8]

RESULTS AND DISCUSSION

Figure 1 shows the RHEED patterns of a 3000 Å Bi_2Te_3 thin film along the (120) and (100) azimuths. In the zinc-blende structure, the two (111) faces, designated by A and B, are both different and polar. The CdTe(111)B (Te-terminated) face has a $2\sqrt{3}\times 2\sqrt{3}$-R30° reconstruction which results in the RHEED pattern displaying 1/2 integer order streaks in the $(1\bar{1}0)$ azimuth and a 1/6 integer order in the $(11\bar{2})$ azimuth. However, there is no surface reconstruction of Bi_2Te_3 films on CdTe(111)B from the initial growth stages. In addition, the RHEED pattern of Bi_2Te_3 films exhibits a streaky pattern, representing layer-by-layer growth of Bi_2Te_3 films on CdTe(111)B, i.e. a smooth surface, and shows Kikuchi lines, attesting to a high structural quality of the films.

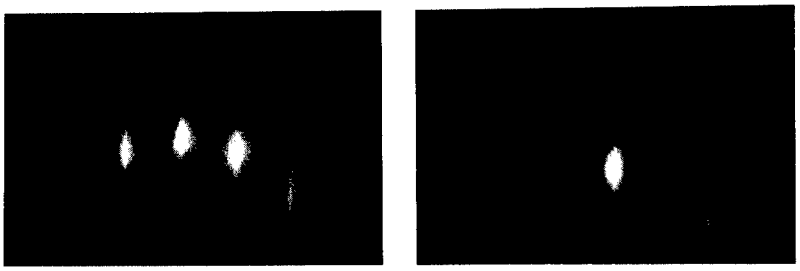

(120) (100)

FIG.1. RHEED patterns of a 3000 Å Bi_2Te_3 thin film along (120) and (100) azimuths.

Figure 2(a) shows a typical θ-2θ XRD pattern of a Bi_2Te_3 thin film of 1 μm thickness. It is observed that only (00.*l*) peaks in the hexagonal unit cell are present, implying the c-axis growth of Bi_2Te_3. Note that three substrate peaks (23.758: 76: 112) are observed. To evaluate the crystallinity of our films we have determined the full width at half maximum (FWHM) from the rocking curve at the highest peak (00.15). The stoichiometric sample yields 0.217° as shown in Fig. 2(b), which, to our knowledge, is the smallest value yet reported. From these XRD patterns we have determined the out-of-plane (c-axis) lattice constants for stoichiometric and off-stoichiometric samples with reference to the hexagonal unit cell using the following relation:

$$\frac{1}{d_{hkl}^2} = \frac{4}{3}\frac{h^2 + hk + k^2}{a^2} + \frac{l^2}{c^2}.$$

The c-axis lattice constant varies from 29.9 to 30.4 Å, compared to the bulk vale of 30.45 Å. In order to visualize the relationship between the crystallinity and the c-axis lattice constant, we have plotted the FWHM as a function of the c-axis lattice constant in Fig. 3. The FWHM increases with decreasing c-axis lattice constants from 0.2 to 1.2°. This indicates that the crystallinity become worse with increasing deviation from the bulk c-axis lattice constant.

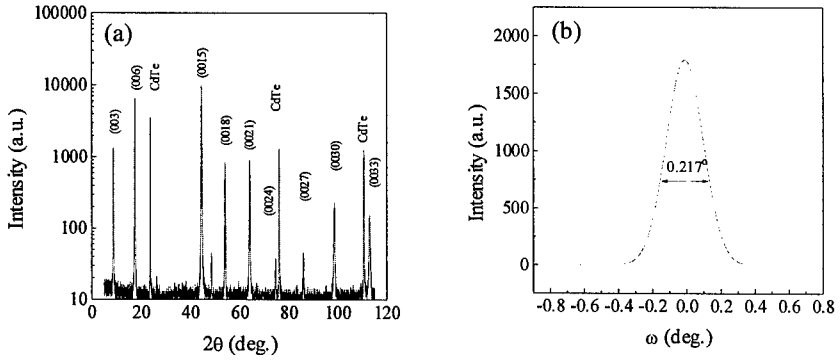

FIG.2. (a) θ-2θ XRD pattern of a 1 μm-thick stoichiometric Bi_2Te_3 thin film. (b) The rocking curve of the same film around the (00.15) peak. The FWHM is 0.217°.

Room-temperature thermopowers vs. c-axis lattice constant are plotted in Fig. 4. All films show a negative thermopower value, i.e. they are n-type. The stoichiometric film (having the largest lattice constant) shows the highest magnitude of the thermopower at room temperature. A decrease in the c-axis lattice constant induces a decrease in the magnitude of thermopower. The increased FWHM and the reduced magnitude of the thermopower with decreasing lattice constant is possibly explained in terms of antisite defects;[7] i.e., excess Te(Bi) occupies Bi(Te) lattice sites. The atomic radii of Bi and Te are 1.6 Å and 1.4 Å, respectively. Therefore, when excess Te occupies Bi lattice site, the

lattice constant decreases. It is known that excess Te also acts as an n-type dopant in the Bi_2Te_3 system. Therefore, the reduced value of the thermopower is likely due to the heavy doping via antisite defects.

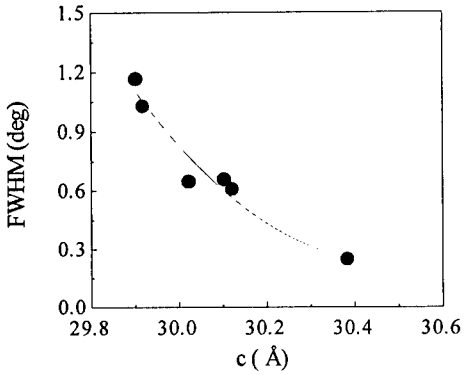

FIG. 3 FWHM vs. c-axis lattice constant of Bi_2Te_3 thin films.

In order to study the doping effect, we have determined effective carrier densities and mobilities by resistivity and Hall measurements. Figure 5 shows n-type carrier concentrations and mobilities as a function of c-axis lattice constants at 300 K. The carrier concentration and mobility of the stoichiometric sample are 6×10^{18} cm^{-3} and 670 cm^2/Vs, respectively. The electrical conductivity of the stoichiometric Bi_2Te_3 films was 10^3 $(\Omega cm)^{-1}$. As the lattice constant decreases, i.e. more excess Te occupies Bi lattice sites, the carrier concentration increases up to 1×10^{20} cm^{-3} and the mobility rapidly decreases. Our results indicate that stoichiometry has an important effect on the properties of Bi_2Te_3-based systems, especially with respect to thin films and superlattices.

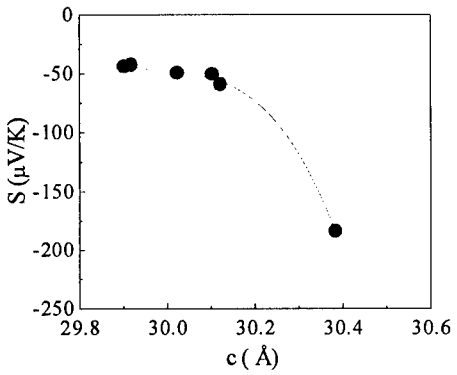

FIG. 4 Thermopower vs. c-axis lattice constant of Bi_2Te_3 thin films.

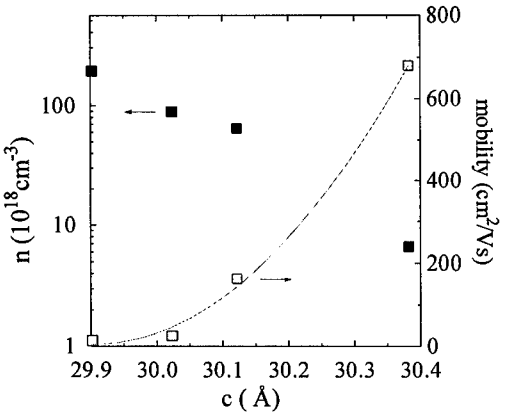

FIG. 5 n-type carrier concentration and mobility of Bi_2Te_3 thin films vs. c-axis lattice constant measured at 300 K.

SUMMARY

We have successfully grown high-quality Bi_2Te_3 thin films on CdTe(111)B substrates using MBE. Bi_2Te_3 films on CdTe(111) grow along the (00.*l*) with a layer-by-layer growth mode, resulting in a smooth surface. The X-ray Bragg peak FWHM of the stoichiometric sample was 0.2 °, attesting to the high crystallinity of the films. There is no surface reconstruction of Bi_2Te_3 films on CdTe(111)B. The thermopower and electrical conductivity of the stoichiometric Bi_2Te_3 films were ~200 μV/K and 10^3 $(\Omega cm)^{-1}$, respectively, comparable to single crystal bulk values. In Te-rich Bi_2Te_3 films, we observed antisite defects, i.e. excess Te occupies Bi lattice sites, based on XRD, resitivity, thermopower, and Hall measurements. Te-rich Bi_2Te_3 thin films show worse crystallinity and excess Te acts as an n-type dopant.

ACKNOWLEDGMENTS

This work was supported by DARPA under Grant No. DAAG55-97-1-0130. Use was made of MRL Central Facilities supported by the National Science Foundation, at the Materials Research Center of Northwestern University, under Grant DMR-9120521.

REFERENCES

1. Y. H. Shing, Y. Chang, A. Mirshafii, L. Hayashi, S. S. Roberts, J. Y. Josefowicz, and N. Tran, J. Vac. Sci. Technol. A **1**, 503 (1983).
2. H. Noro, K. Sato, and H. Kagechika, J. Appl. Phys. **73**, 1252 (1993).
3. A. Dauscher, A. Thomy, and H. Scherrer, Thin Solid Films **280**, 61 (1996).
4. R. Venkatasubramanian, T. Colpitts, E. Watko, M. Lamvik, and N. El-Masry, J. Cryst. Growth **170**, 817 (1997).
5. E. Charles, E. Groubert, and A. Boyer, J. Mater. Sci. Lett. **7**, 575 (1988).
6. A. Boyer and E. Cisse, Mater. Sci. Eng. B **13**, 103 (1992).

7. T. C. Harman. S. E. Miller, and H. L. Goeing, Bull. Amer. Phys. Soc. **30**, 35 (1955).
8. S. Cho, A. DiVenere, G. K. Wong, J. B. Ketterson, J. R. Meyer, and C. A. Hoffman, Solid State Commun. **102**, 673 (1997).

Synthesis and Thermoelectric Properties of $Cs_2Bi_{7.33}Se_{12}$, $A_2Bi_8Se_{13}$ (A = Rb, Cs), $Ba_{4-x}Bi_{6+2/3x}Se_{13}$, and $Ba_{3\pm x}Pb_{3\pm x}Bi_6Se_{15}$

Lykourgos Iordanidis[(a)], Paul W. Brazis[(b)], Carl R. Kannewurf[(b)], and Mercouri G. Kanatzidis*[(a)]

[(a)]Department of Chemistry and Center for Fundamental Materials Research, Michigan State University, East Lansing, MI 48824. [(b)]Department of Electrical Engineering and Computer Science, Northwestern University, Evanston, IL 60208.

Abstract

We are continuing our synthetic investigations in the ternary A/Bi/Se systems and also expanded our interests into the quaternary A/M/Bi/Se (A = Rb, Cs, Sr and Ba; M = lanthanide or Pb) systems. We have synthesized several new ternary and quaternary bismuth selenides with band gaps <0.6eV such as $Cs_2Bi_{7.33}Se_{12}$, $A_2Bi_8Se_{13}$ (A = Rb, Cs), $Ba_{4-x}Bi_{6+2/3x}Se_{13}$, and $Ba_{3\pm x}Pb_{3\pm x}Bi_6Se_{15}$. The synthesis, crystal structures and charge transports properties of these new compounds are presented.

Introduction

Bi chalcogenides exhibit a staggering compositional and structural complexity, and these two factors can lead to materials with corresponding complexities in the electronic structure and low thermal conductivity.[1] Our work on ternary bismuth chalcogenides such as β-,γ-$CsBiS_2$[2], KBi_3S_5[3], $KBi_{6.33}S_{10}$[4], $K_2Bi_8S_{13}$[4], α-[2], β-[5,6]$K_2Bi_8Se_{13}$, $K_{2.5}Bi_{8.5}Se_{14}$[5,6], $BaBiTe_3$[6,7] and quaternary such as $ALn_{1\pm x}Bi_{4\pm x}S_8$[8] (A = K, Rb; Ln = La, Ce, Pr, Nd) and $BaLaBi_2Q_6$[9] (Q = S, Se) shows that these kinds of compounds can possess low thermal conductivity, high thermopower and often high electrical conductivity. The incorporation of large electropositive ions such as alkaline earth and lanthanides into bismuth chalcogenide frameworks is expected to lead to materials with low thermal conductivity due to the high coordination sites they adopt and the ionic character of the surrounding M-Q bonds. High coordination sites and ionic bond character result in soft phonon modes which slow down heat transfer in these materials. Pb has similar coordination preferences with Bi and since it has one less electron, the charge balancing requirements are different. This means that the incorporation of Pb atoms into a A/Bi/Q framework is expected to yield new stoichiometries and interesting new structure types. Here we report the synthesis, crystal structures and charge transport properties of the ternary $Cs_2Bi_{7.33}Se_{12}$, $A_2Bi_8Se_{13}$ (A = Rb, Cs), $Ba_{4-x}Bi_{6+2/3x}Se_{13}$, and the quaternary $Ba_{3\pm x}Pb_{3\pm x}Bi_6Se_{15}$.

Results and discussion

The crystallographic data for all compounds described here are shown in Table 1.

Mat. Res. Soc. Symp. Proc. Vol. 545 © 1999 Materials Research Society

Table 1. Crystallographic data for $Ba_{4-x}Bi_{6+2/3x}Se_{13}$, $Ba_{3\pm x}Pb_{3\pm x}Bi_6Se_{15}$, $Cs_2Bi_8Se_{13}$ and $Cs_2Bi_{7.33}Se_{12}$.

	$Ba_{4-x}Bi_{6+2/3x}Se_{13}$	$Ba_{3\pm x}Pb_{3\pm x}Bi_6Se_{15}$	$Cs_2Bi_8Se_{13}$	$Cs_2Bi_{7.33}Se_{12}$
Space Group	$P2_1/m$	$P2_1/m$	$P2_1/m$	Pnma
Crystal Habit	needle	needle	needle	rod
a, Å	17.2295(6)	17.344(2)	13.742(1)	23.4559(2)
b, Å	4.2707(2)	4.2925(6)	4.1526(4)	4.1941(1)
c, Å	18.4658(2)	21.835(3)	25.030(2)	13.7317(3)
β, Å	90.605(2)	98.629(2)	96.813(2)	-
V, Å^3; Z	1358.7(1), 2	1607.3(4), 2	1418.3(2), 2	1350.88(5), 2
R1/wR2 [I>2σ(I)]	4.33/6.37%	3.31/7.93%	7.57/15.8%	7.04/14.4%
GOF on F^2	0.915	1.013	0.962	1.095

$R1 = \Sigma \, | |F_o| - |F_c| | / \Sigma \, |F_o|$, $wR2 = \{ \Sigma [w(F_o^2 - F_c^2)^2] / \Sigma [w(F_o^2)^2] \}^{1/2}$

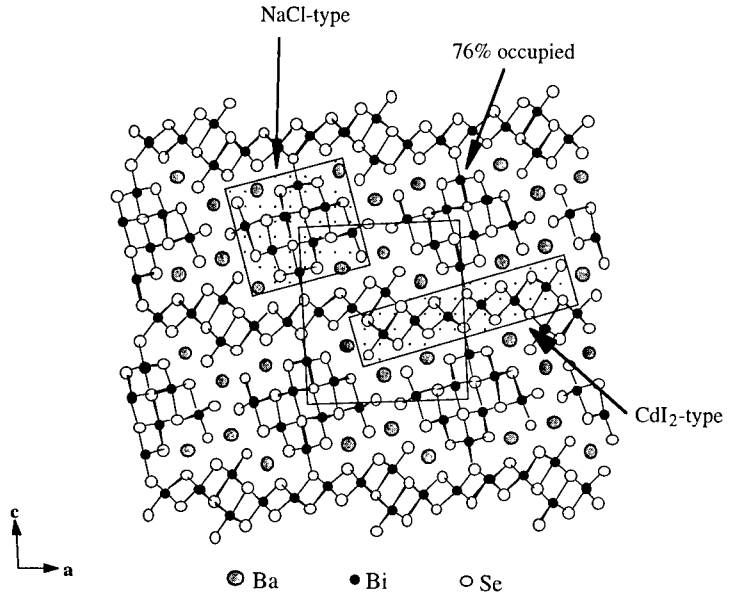

Figure 1. The structure of $Ba_{4-x}Bi_{6+2/3x}Se_{13}$. The boxed shaded areas indicate the NaCl- and CdI_2-type fragments.

$Ba_{4-x}Bi_{6+2/3x}Se_{13}$ was synthesized by reacting BaSe and Bi_2Se_3 at 1:2 ratio at 700°C for 3 days. It adopts the $Sr_4Bi_6Se_{13}$[10]-type structure with a general formula $M_{10}Q_{13}$ (M = metal, Q = S, Se), see Figure 1. This structure type is also adopted by several other ternary chalcogenides such as $K_2Bi_8Q_{13}$ (Q = S[4], Se[5]). The main characteristic is that the $[Bi_6Se_{13}]^{8-}$ part of the structure

remains intact while the remaining four Sr^{2+} positions can be substituted with a variety of similarly sized ions such as Ba^{2+}, K^{+}, Bi^{3+}, Pb^{2+} etc. Often these substitutions result in mixed occupancy between the alkali or alkaline earth metal and the bismuth atoms. The structure consists of Bi_2Te_3-, and CdI_2-type blocks which connect with each other to form a three-dimensional network.

One Ba site has a tricapped trigonal prismatic coordination with Ba-Se distances varying between 3.288(2)-3.534(3) Å while the other two Ba sites are bicapped trigonal prismatic with Ba-Se distances between 3.2789(2)-3.405(2) Å and 3.274(2)-3.410(3) Å. The rest of the metal positions are occupied by Bi atoms with a distorted octahedral coordination. An idealized formula of the compound would be $Ba_4Bi_6Se_{13}$, but there are only three positions for Ba atoms in the structure, so for neutrality reasons one Bi site is only 76% occupied. The remaining metal positions of the structure, as mentioned, occupy 6-coordinate sites, which are probably not large enough to accommodate a Ba^{2+} ion. Interestingly, $Sr_4Bi_6Se_{13}$ has four Sr^{2+} ions. Three of these ions occupy the same positions as the three Ba^{2+} ions and the fourth Sr^{2+} ion is situated in the partially occupied Bi position in $Ba_{4-x}Bi_{6+2/3x}Se_{13}$. This Sr^{2+} ion is reported to have a very small isotropic temperature factor (U_{iso} = 0.003 $Å^2$) compared to the other three Sr^{2+} ions in the structure (U_{iso} ~ 0.014 $Å^2$). This fact most probably indicates that the Sr^{2+} site is also partially occupied by Bi atoms and that the formula is better described as $Sr_{4-x}Bi_{6+2/3x}Se_{13}$. In the isostructural β-$K_2Bi_8Se_{13}$ phase the tricapped trigonal prismatic site is occupied by K^{+} ions while the two bicapped trigonal prismatic sites display mixed occupancy between K^{+} and Bi^{3+}. The partially occupied octahedral Bi site in $Ba_{4-x}Bi_{6+2/3x}Se_{13}$ is fully occupied in β-$K_2Bi_8Se_{13}$. This mixed occupancy can explain the heavy doping and metallic behavior observed for $Ba_{4-x}Bi_{6+2/3x}Se_{13}$. This type of non-stoichiometry can be difficult to control and can vary from preparation to preparation or even from crystal to crystal if serious precautions during synthesis and crystal growth are not taken. The temperature dependence of the electrical conductivity and thermopower of the needles of $Ba_{4-x}Bi_{6+2/3x}Se_{13}$ shows a n-type metallic behavior with a room temperature conductivity of ~2000 S/cm and a thermopower of ~-30 μV/K, see Figure 2.

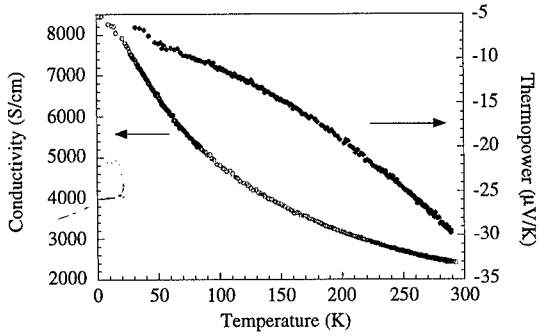

Figure 2: Variable temperature single crystal conductivity and thermopower of $Ba_{4-x}Bi_{6+2/3x}Se_{13}$.

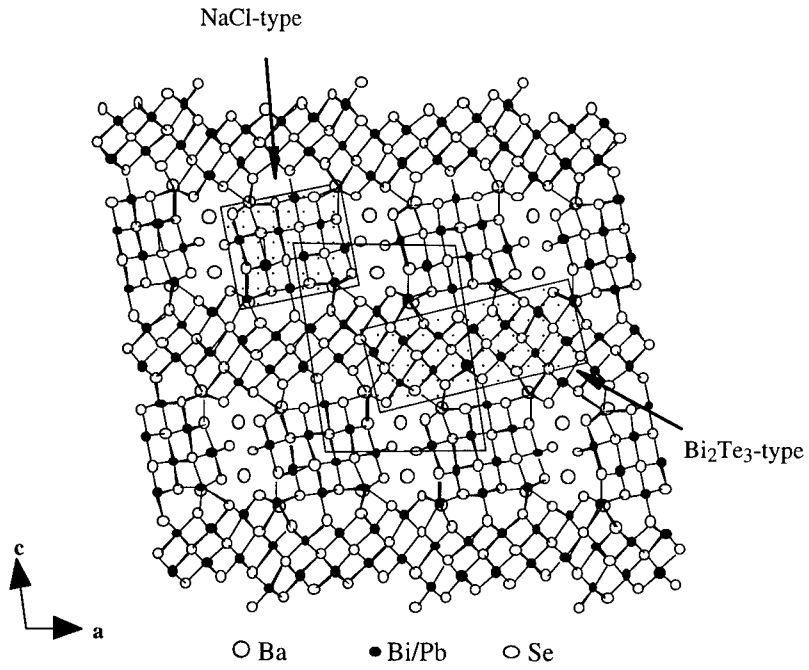

Figure 3: The structure of $Ba_{3\pm x}Pb_{3\pm x}Bi_6Se_{15}$. The boxed shaded areas indicate the NaCl- and Bi_2Te_3-type fragments.

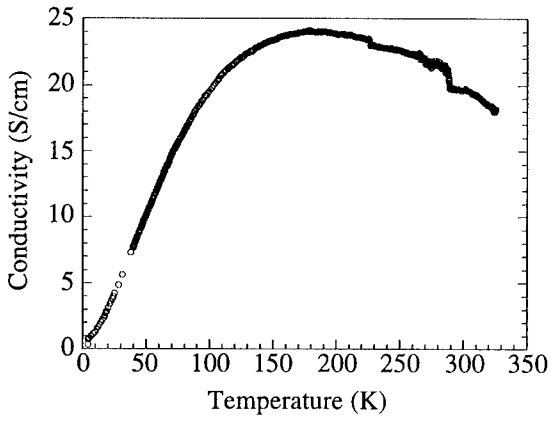

Figure 4: Variable temperature single crystal conductivity of $Ba_{3\pm x}Pb_{3\pm x}Bi_6Se_{15}$.

$Ba_{3\pm x}Pb_{3\pm x}Bi_6Se_{15}$ was synthesized by reacting BaSe, Pb, Se and Bi_2Se_3 in 1:1:1:1.5 ratio at 900°C for 6 days. It adopts a new structure type but is also related to $Ba_{4-x}Bi_{6+2/3x}Se_{13}$. The same size and shape NaCl-type block exists as in $Ba_{4-x}Bi_{6+2/3x}Se_{13}$ but now the CdI_2-type fragment is twice as thick. The structure consists only of Bi_2Te_3-, and NaCl-type fragments as shown in Figure 3. Again the high coordinate sites (>6) which are occupied mainly by Ba^{2+} ions display mixed occupancy between Ba^{2+} and Pb^{2+} ions. Needles of $Ba_{3\pm x}Pb_{3\pm x}Bi_6Se_{15}$ show a n-type semiconducting behavior with a room temperature conductivity of ~15 S/cm and a thermopower of ~360 μV/K as shown in Figure 4. The origin of the conductivity maximum at ~150 K is not known. $Ba_{3\pm x}Pb_{3\pm x}Bi_6Se_{15}$ has a band gap of 0.57eV.

$Rb_2Bi_8Se_{13}$ and $Cs_2Bi_8Se_{13}$ are analogs of the α–,β-$K_2Bi_8Se_{13}$ however they adopt a different structure. They were synthesized by reacting A_2Se (A = Rb, Cs) with Bi_2Se_3 at 1:3.3 ratio at 850°C for 6 days The structure is shown in Figure 5. It consists of infinite long rectangular NaCl-type rods running parallel to the b-axis. These rods have rectangular cross sections. Between the rods are included rows of Cs^+ ions. The different blocks are connected by small CdI_2-type fragments and two Bi atoms in a square pyramidal coordination (Sb_2Se_3-type). The same feature with square pyramidal Bi atoms exists also in α-$K_2Bi_8Se_{13}$[2] which adopts a different structure type. The two Cs^+ ions have a tricapped trigonal coordination environments with distances varying between 3.6439(6)-3.825(5) Å and 3.551(7)-3.921(5) Å respectively. With the exception of one Bi atom which is five-coordinate, with a square pyramidal environment (2.700(6)-2.956(4) Å), all Bi atoms in the structure have octahedral environments with varying degrees of distortion.

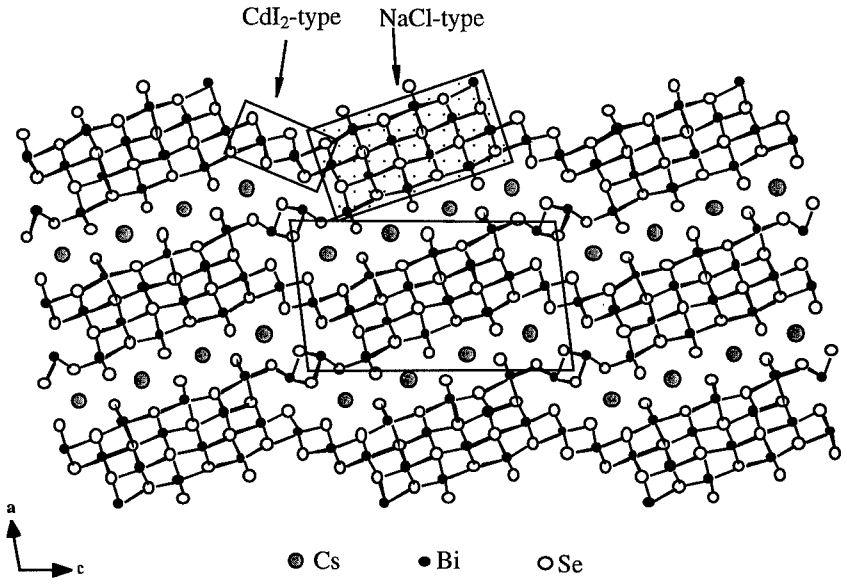

Figure 5. Structure of $Cs_2Bi_8Se_{13}$ viewed down the b-axis. The boxed areas indicate the NaCl- and CdI_2-type fragments.

The Rb analog, $Rb_2Bi_8Se_{13}$ is isostructural to $Cs_2Bi_8Se_{13}$ as evidenced by x-ray powder diffraction. Both compounds have band gaps around ~0.45eV. The temperature dependence of the electrical conductivity and thermopower of polycrystalline chunks of $Rb_2Bi_8Se_{13}$ shows a n-type metallic behavior. As shown in Figure 6, the room temperature electrical conductivity and thermopower of polycrystalline chunks of $Rb_2Bi_8Se_{13}$ is ~80 S/cm and thermopower of ~-72 μV/K respectively. Despite the metal-like temperature dependence, these values are characteristic of semiconductors and, as a result $Rb_2Bi_8Se_{13}$, can be described as a narrow band gap semiconductor.

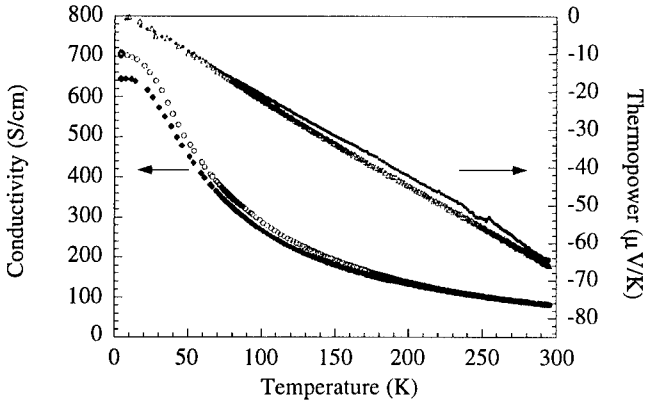

Figure 6. Variable temperature electrical conductivity and thermopower for polycrystalline chunks of $Rb_2Bi_8Se_{13}$.

$Cs_2Bi_{7.33}Se_{12}$ was synthesized by reacting Cs_2Se and Bi_2Se_3 at 1:3 ratio at 850°C for 6 days. Its structure consists of similar building blocks as $Cs_2Bi_8Se_{13}$ as shown in Figure 7. The infinite rods of NaCl-type run parallel to the b-axis. They are shorter in width compared to the those of $Cs_2Bi_8Se_{13}$. The rods share edges and each rod is rotated with respect to the neighboring rods, by ~13 degrees. The Cs^+ ions have the same trigonal prismatic coordination with distances varying between 3.672(4)-3.997(4) Å. All bismuth atoms are in octahedral coordination, again with varying degrees of distortion. For neutrality reasons the Bi atoms which connect the NaCl-type rods are 2/3 occupied.

The band gap of $Cs_2Bi_{7.33}Se_{12}$ is ~0.53eV and the room temperature conductivity measured on single crystal rods of $Cs_2Bi_{7.33}Se_{12}$ is ~200 S/cm. The thermopower is ~-110 μV/K at room temperature. The temperature dependence of the electrical conductivity and thermopower show a n-type metallic behavior but the actual values are consistent with semiconductors, so $Cs_2Bi_{7.33}Se_{12}$ can be described as a narrow band-gap semiconductor, see Figure 8. Qualitatively, the temperature dependence of this as well as the other compounds reported here is very similar to what is observed with samples of Bi_2Te_3.

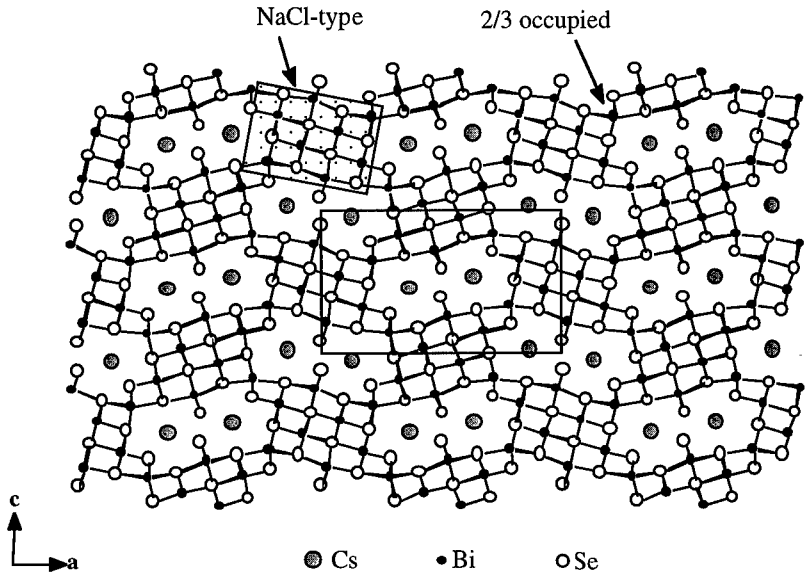

Figure 7. Structure of $Cs_2Bi_{7.33}Se_{12}$ viewed down the b-axis. The boxed shaded area indicates the NaCl-type fragment.

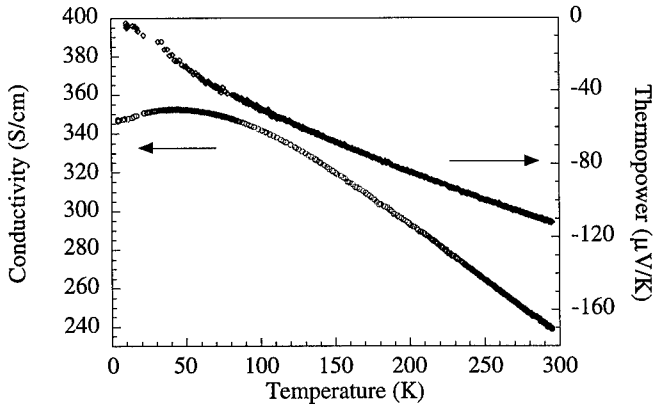

Figure 8. Variable temperature electrical conductivity and thermopower for a single crystal of $Cs_2Bi_{7.33}Se_{12}$.

Concluding Remarks

We have synthesized several new ternary and quaternary bismuth selenides such as $Cs_2Bi_{7.33}Se_{12}$, $A_2Bi_8Se_{13}$ (A = Rb, Cs), $Ba_{4-x}Bi_{6+2/3x}Se_{13}$, and $Ba_{3\pm x}Pb_{3\pm x}Bi_6Se_{15}$. All compounds have band gaps less than 0.6 eV and show n-type charge transport behavior. Due to vacancies and mixed Ba/Bi occupancy on certain crystallographic sites $Ba_{4-x}Bi_{6+2/3x}Se_{13}$, is heavily doped showing a metallic behavior.

Our exploratory research into the ternary and quaternary bismuth chalcogenide systems continues to yield new interesting compounds and several of them possess promising thermoelectric properties. Many of the compounds contain disordered or partially occupied sites. These sites are of great interest because they are amenable to chemical substitutions and allow us to study the effect of the substitutions on the electronic properties of the compounds without changing the structure. Some of the compounds synthesized are highly doped as a result of the synthesis procedure. Attempts will be made to control the doping levels and optimize the electrical conductivity and thermopower. Furthermore the thermal conductivity has to be measured and we expect, based on our previous results,[4,5] to be low.

Acknowledgments

This work was supported at NU and MSU by the Office of Naval Research (contract # N00014-98-10443). The work made use of the SEM facilities of the Center for Electron Optics at Michigan State University. The Siemens SMART platform CCD diffractometer at Michigan State University was purchased with funds from the National Science Foundation (CHE-9634638). At NU this work made use of the Central Facilities supported by the National Science Foundation through the Materials Research Center (DMR-96-32472).

References

[1] Kanatzidis, M. G.; DiSalvo, F. J. *Nav. Res. Rev.* **1996**, *4*, 14-22.
[2] McCarthy, T. J.; Ngeyi, S.-P.; Liao, J.-H.; DeGroot, D.; Hogan, T.; Kannewurf, C. R.; Kanatzidis, M. G., *Chem. Mater.*, **1993**, *5*, 331-340.
[3] McCarthy, T. J.; Tanzer, T. A.; Kanatzidis, M. G., *J. Am. Chem. Soc.*, **1995**, *117*, 1294-1301.
[4] (a) Kanatzidis, M. G.; McCarthy, T. J.; Tanzer, T. A.; Chen, L. -H.; Iordanidis, L.; Hogan, T.; Kannewurf, C. R.; Uher, C.; Chen, B. *Chem. Mater.*, **1996**, *8*, 1465-1474. (b) Chen, B.; Uher, C.; Iordanidis, L.; Kanatzidis, M. G. *Chem. Mater.*, **1997**, *9*, 1655-1658. (c) Kanatzidis, M. G.; McCarthy, T. J.; Tanzer, T. A.; Chen, L. -H.; Hogan, T.; Kannewurf, C. R.; Iordanidis, L. *Mat. Res. Soc. Symp.*, **1996**, *410*, 37-43.
[5] Chung, D-.Y.; Choi, K.-S.; Iordanidis, L.; Kanatzidis, M. G; Schindler, J. L.; Brazis, W.; Kannewurf, C. R.; Chen, B.; Hu, S.; Uher, C. *Chem. Mater.*, **1997**, *9* 3060-3071
[6] Chung, D-.Y.; Hogan, T.; Schindler, J. L.; Iordanidis, L.; Brazis, W.; Kannewurf, C. R.; Chen, B.; Uher, C.; Kanatzidis, M. G. *Mat. Res. Soc. Symp.*, **1997**, *478*, 333-344.
[7] Chung, D-.Y.; Jobic, S.; Hogan, T.; Kannewurf, C. R.; Brec, R.; Rouxel, R.; Kanatzidis, M. G. *J. Am. Chem. Soc.*, **1997**, *119*, 2505-2515.
[8] Iordanidis, L.; Schindler, J. L.; Kannewurf, C. R.; Kanatzidis, M. G. *J. Solid State Chem.*, **1999**, in press.
[9] Choi, K.-S.; Iordanidis, L.; Chondroudis, K.; Kanatzidis, M. G. *Inorg. Chem.*, **1997**, *36*, 3804-3805
[10] Cordier, G.; Schäfer, H.; Schwidetzky, C. *Rev. Chim. Miner.* , **1985**, *22*, 631-638.

THERMOELECTRIC PROPERTIES OF MIXED RHENIUM CHALCOGENIDES $Re_6Te_{15-x}Se_x$ ($0 \le x \le 8$)

S. KILIBARDA DALAFAVE, J. ZIEGLER, and H. MCALLISTER
The College of New Jersey, Dept. of Physics, Ewing, NJ 08628

ABSTRACT

Reported are the temperature dependencies of the thermoelectric power and electrical resistivity of mixed rhenium chalcogenides $Re_6Te_{15-x}Se_x$ ($0 \le x \le 8$) in the range 90-420 K. Influence of the partial chalcogen exchange on thermoelectric properties of these compounds is discussed. The samples are prepared by sintering elemental powders inside evacuated and sealed quartz ampoules at 1150 K for 170 hours. X-ray analysis reveals an orthorhombic lattice for samples with $x < 8$ and a tetragonal lattice for the $Re_6Te_7Se_8$ sample. The lattice parameters and the unit cell volume decrease with increasing selenium concentration.

The measurements indicate *p*-type semiconducting behavior for all samples. The presence of the energy gap is observed at higher temperatures ($T \gtrsim$ 180-220 K) for all *x*. Data suggest hopping conduction at lower temperatures. Room temperature resistivities increase non-linearly from 6.9 to 20.4 Ω·m with the increasing selenium content. Initially, the thermoelectric power α increases with temperature for all samples, with the fastest increase in $Re_6Se_8Te_7$ and the slowest in Re_6Te_{15}. The temperature at which α reaches maximum decreases with the increasing Se content. Above this temperature, α decreases uniformly as the temperature increases, the slowest increase being for $Re_6Se_8Te_7$ and the fastest for Re_6Te_{15}. Such $\alpha(T)$ dependence is also discussed. The temperature dependence of the power factor, α^2/ρ, is presented. Comparison of ρ, α, and the power factor in $Re_6Se_xTe_{15-x}$ with currently used state-of-the-art materials is given.

INTRODUCTION

A cluster type compound Re_6Te_{15} is closely related with the Chevrel phase molybdenum chalcogenides[1-5]. Although a large number of reports have been published on molybdenum chalcogenides with $[Mo_6]$ clusters, there is much less reported research on ternary rhenium chalcogenides with $[Re_6]$ units. Previous theoretical considerations[6] suggested that Re_6Te_{15} might have promising thermoelectric properties. Re_6Te_{15} is the only thermodynamically stable phase in the rhenium-telluride system[7] and it crystalizes in an orthorhombic structure[8,9]. A selenide of composition Re_6Se_{15} is not known. However, the existence of substitutional phases of type $Re_6Te_{15-x}Se_x$ has been proven[8,10]. The crystal structure and lattice parameters of these mixed selenotellurides were reported[6]. It was determined that the phase ends with $x = 8$.

Re_6Te_{15} consists of $[Re_6Te_8]$ and $[Te_7]$ clusters. In $Re_6Te_{15-x}Se_x$ only the Te atoms in the $[Re_6Te_8]$ cluster are substituted with Se atoms[10]. Atoms in the $[Te_7]$ cluster form the quasi-planar butterfly-like structure as in Re_6Te_{15}. In $Re_6Te_7Se_8$ (where the phase ends) all eight Te atoms from the $[Re_6Te_8]$ cluster are replaced[10]. Further addition of selenium leads to the formation of $ReSe_2$ as a second phase[10]. Other reported attempts[8] to make samples with $x > 8$ were unsuccessful.

Semiconducting behavior and large room temperature thermoelectric power for a phase with composition $ReTe_2$ were observed previously by Johnston *et al.*[11]. Later, Klaiber *et al.*[8] found similar value for the thermoelectric power of Re_6Te_{15} and room temperature resistivities of Re_6Te_{15} and $Re_2Te_3Se_2$ of ~ 10 Ω·m, but did not investigate intermediate compositions. Room temperatures resistivities and thermoelectric powers for various Se concentrations were reported[12].

Mat. Res. Soc. Symp. Proc. Vol. 545 © 1999 Materials Research Society

The temperature dependencies of these quantities for the two end compounds (Re_6Te_{15} and $Re_6Te_7Se_8$) were also measured[12].

As mentioned previously, in $Re_6Te_{15-x}Se_x$ only Te atoms in $[Re_6Te_8]$ clusters are replaced by Se atoms. It is therefore of interest to find how the chalcogen exchange inside the $[Re_6Te_8]$ cluster influences thermoelectric properties of these compounds. Presented here are the measurements of temperature dependant thermoelectric power and resistivity of $Re_6Te_{15-x}Se_x$ for the whole range of Se concentrations ($0 \le x \le 8$).

EXPERIMENT

Samples of $Re_6Te_{15-x}Se_x$ ($0 \le x \le 8$) used in this study were prepared from elemental powders (Se: 99.999%, Re: 99.997%, Te: 99.9985%). The elements, weighed in the stoichiometric ratios, were mixed using a high energy ball mill. The powder mixture was cold pressed and then reacted in an evacuated and sealed quartz ampoule at 1150 K for 170 hours. The resulting samples formed as gray, hard, and brittle polycrystalline materials.

Cell identification was performed and lattice parameters determined for $Re_6Te_{15-x}Se_x$ samples[12]. Samples with $x < 8$ were fitted to an orthorhombic cell and $Re_6Te_7Se_8$ to a tetragonal cell. The lattice parameters and the cell volume decrease with increasing selenium concentration[12]. These variations can be interpreted as being due to smaller selenium atomic radius as compared to the atomic radius of tellurium. This is consistent with the observed decrease in Re-Se distances inside the rhenium-chalcogen clusters in $Re_6Te_{15-x}Se_x$[10] as compared to Re-Te distances inside the $[Re_6Te_8]$ clusters in Re_6Te_{15}[8]. The decrease in the rhenium-chalcogen distances is about five times larger than the corresponding decrease of Te-Te distances in $[Te_7]$ units[8,10]. The electrical resistivity, ρ, and the thermoelectric power, α, of $Re_6Te_{15-x}Se_x$ ($0 \le x \le 8$) samples were measured as functions of temperature in the range 90-420 K.

RESULTS

The resistivity data indicate semiconducting behavior for all samples. Room temperatures resistivities vary between 6.9 Ω·m for Re_6Te_{15} and 20.4 Ω·m for $Re_6Te_7Se_8$. The plots of $ln\ \rho$ vs T^{-1} are shown in Fig. 1. At higher temperatures ($T > 190$-220 K) the fit of $ln\ \rho$ to a line was possible. This indicates the presence of the energy gap at the Fermi level and is consistent with previous theoretical considerations[13] and experimental observations[8] at room and higher temperatures in Re_6Te_{15}. For lower temperatures the fit to a straight line of $ln\ \rho$ vs T^{-1} was not possible. In this temperature range the resistivities were fitted with $\rho \approx \rho_0\ exp\ (T_0/T)^{1/y}$, where y varies between 1.6 and 2.8 for $0 \le x \le 8$. Such a dependence may indicate hopping conduction[14], which might be expected for these cluster-type structures. At this point we will not go any further in the analysis of such dependencies, since the measurements were done on sintered samples. A more detailed study of the conduction mechanism in $Re_6Te_{15-x}Se_x$ single crystals is necessary.

The observed semiconducting behavior of $Re_6Te_{15-x}Se_x$ system is accounted for by the saturation of valence bands. The six rhenium atoms in each rhenium-chalcogen cluster contribute a total of 42 valence electrons. Twenty-four of these electrons are used for 12 Re-Re bonds and 16 to fill the *p*-shells of the 8 chalcogen atoms[10,13]. The remaining two electrons are transferred to the quasi-planar anionic $[Te_7]$ cluster where they exactly fill the valence shells. The metal affinity increases from tellurium to selenium to sulfur. Therefore, the lighter chalcogen (in this case Se) in the mixed chalcogenide prefers to be bond heteronuclearly, while heavier chalcogen (in this case Te) favors homonuclear connections[10,15]. Due to electronegativity differences between rhenium and selenium and rhenium and tellurium, the electrons used in Re-Se bonds are more

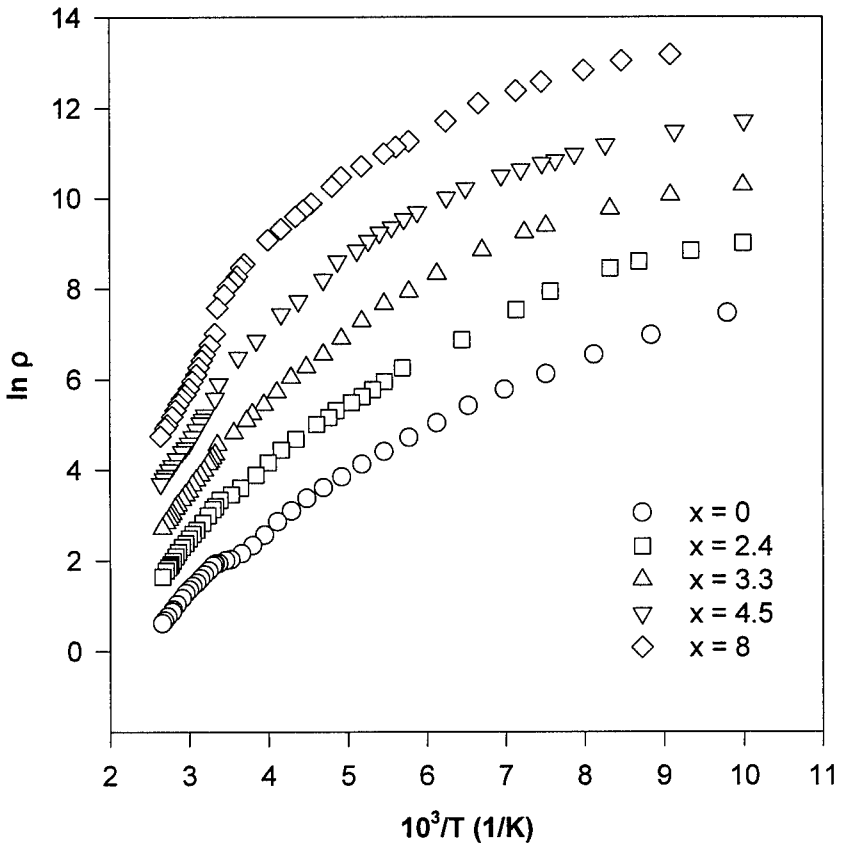

Fig. 1 Temperature dependence of the resistivity. Note: To improve the readibility of the graph, 1, 2, 3, and 4 were added to the graphs for x = 2.4, 3.3, 4.5, and 8, respectively.

localized than those in Re-Te bonds. The observed resistivity increase in $Re_6Te_{15-x}Se_x$ as selenium content increases is accounted for by the increased ionic nature of the rhenium-chalcogen bonding.

The variations of the thermoelectric power, α, with temperature are shown in Fig. 2. Positive values of α in the measured temperature range indicate that all samples were *p*-type semiconductors. The room temperature values of α for $Re_6Te_{15-x}Se_x$ increase by about 25% as x changes from 0 to 8. The steepest change in α ($\approx$ 16%) occurs for $2.5 \leq x \leq 5$. This is compared to less than 5% change in α for $x < 2.5$ and for $x > 5$. The reason for such a behavior remains to be investigated. The thermoelectric power in all samples initially increases with temperature. It reaches a maximum value and then decreases uniformly.

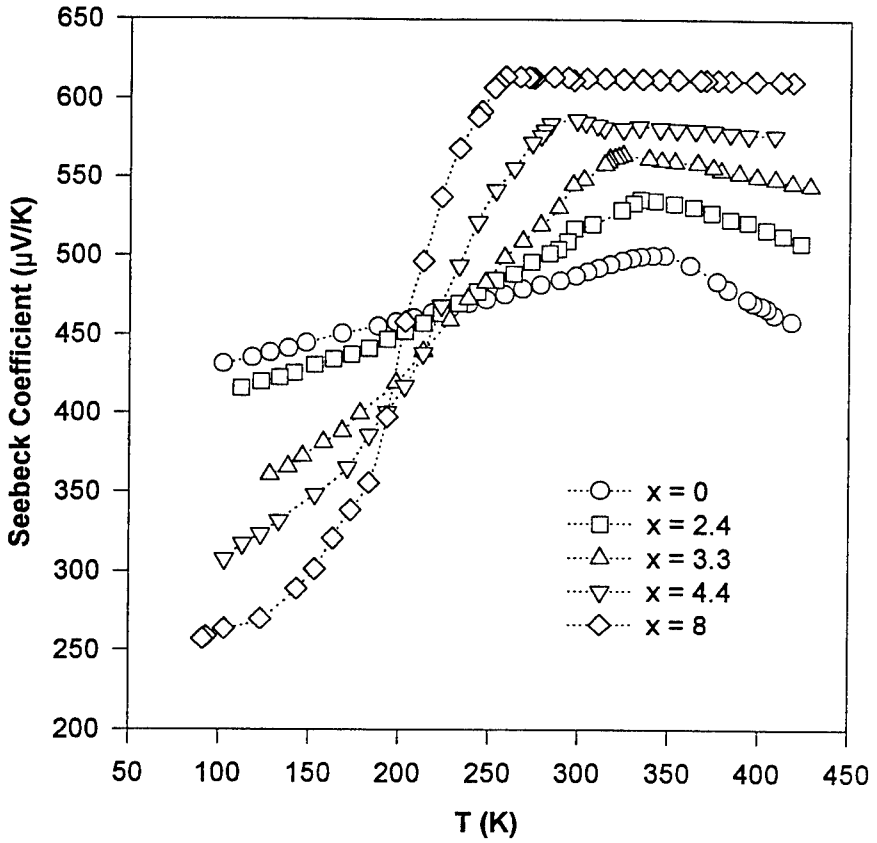

Fig. 2 Thermoelectric power vs temperature.

The power factor, α^2/ρ, of $Re_6Te_{15-x}Se_x$ normalized to room temperature values is presented in Fig.3. The power factor decreases almost two times as the selenium concentration increases from x = 0 to x = 8. This probably indicates that selenium substitution leads to the material that is, at best, of marginal use in thermoelectric devices at room temperatures when compared with state-of-the-art materials. Further measurements including the thermal conductivity and Hall mobility are necessary to make more definite conclusions. Single crystals preparation, their structure determination, as well as the temperature dependant measurements of the thermoelectric power, resistivity, and Hall mobility are planned.

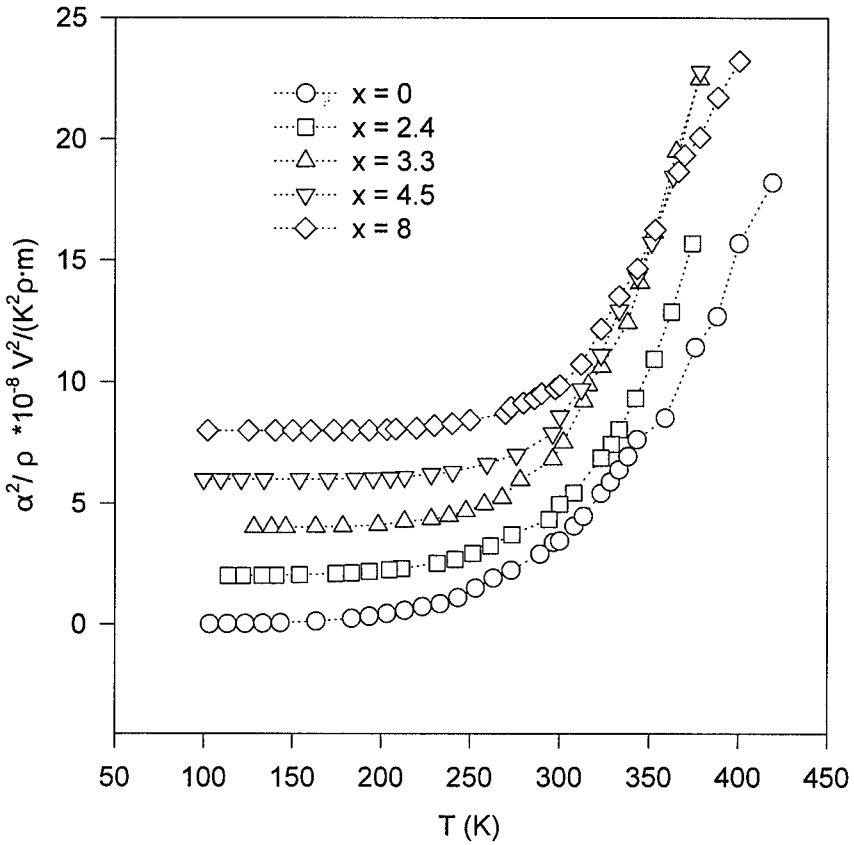

Fig. 3 Temperature dependence of the power factor in $Re_6Te_{15-x}Se_x$. Note: to make the graph more readable, 2, 4, 6, and 8 were added to the original data for x=2.4, 3.3, 4.5, and 8.

CONCLUSIONS

$Re_6Te_{15-x}Se_x$ ($0 \le x \le 8$) have been prepared and their structure analyzed. Measurements of the thermoelectric power and electrical resistivity over the temperature range 90-420 K indicate *p*-type semiconducting behavior for all of $Re_6Te_{15-x}Se_x$. The room temperatures thermoelectric power and electrical resistivity increase nonlinearly and the power factor decreases with increasing

selenium content. Electrical resistivity data suggest hopping conduction at lower temperatures. The presence of the energy gap is observed at higher temperatures. The thermoelectric power for all compounds initially increases with temperature. Excitations of optical phonons are most likely responsible for the observed increase of the thermoelectric powers as the temperature increases. Decrease of α at higher temperatures is probably due to the increase of the carrier mobility and decrease of the phonon free path with an increase in temperature. The relation of the mobility of charge carriers to the temperature dependence of α needs to be further investigated.

REFERENCES

1. W. Bronger and M. Spangenberg, J. Less Common Met. **76**, 73 (1980) .
2. W. Bronger and H. J. Miessen, J. Less Common Met. **83,** 29 (1982).
3. L. Leduc, A. Perrin, and M. Sergent, Acta Cryst. **C39,** 1503 (1983).
4. L. Leduc, A perrin, M. Sargent, F. Le Traon, J. C. Pilet, and A. Le Traon, Mat. Lett. **3,** 209 (1985) .
5. N. L. Speziali, H. Berger, G. Leicht, R. Sanjines, G. Chapuis, and F. Levy, Mat. Res. Bull. **23,** 1597 (1988).
6. G. A. Slack, in "*CRC Handbook of Thermoelectrics*", edited by D. M. Rowe (CRC Press, Boca Raton, 1995) p. 407-440.
7. A. A. Opalovskii, V. E. Fedorov, B. G. Erenburg, E. V. Lobkov, Y. V. Vasiliev, L. N. Senchenko, B. I. Sikanovski, Russ. Physical Chem. **45**, 2110 (1971).
8. F. Klaiber, W. Petter, and F. Hulliger, J. Solid State Chemistry **46,** 112 (1983).
9. A. A. Opalovskii, V. E. Fedorov, B. G. , B. G. Erenburg, E. V. Lobkov, Y. V. Vasiliev, L. N. Senchenko, B. I. Sikanovskii, Russ. Phys. Chem. **45**, 1197 (1971).
10. B. Harbrecht and A. Selmer, Z. anorg. allg. Chem. **620**, 1861-1866 (1994).
11. W. D. Johnston, R. C. Miller, and D. H. DAMON, J. Less-Common Met. **8,** 272 (1965).
12. S. Kilibarda-Dalafave and J. Ziegler, accepted for publication in J. Mat. Sci. Let.
13. D. W. Bullett, Sol. Stat. Com. **51** (1), 51 (1984).
14. H. Böttger and V. V. Bryksin, Phys. Stat. Sol. (b) **78**, (1976) 9; **78**, 415 (1976).
15. W. Bronger, H.-j. Miessen, R. Neugroeschel, D. Schmitz and M. Spangenberg, Z. anorg. allg. Chem. **525**, 41 (1985).

THERMOELECTRIC PROPERTIES OF DOPED RHENIUM CHALCOGENIDES $Re_6M_xTe_{15}$ (x = 0, 1, 2; M = Ga, In, Ag)

S. KILIBARDA DALAFAVE, H. BARCENA, and D. HENNINGSEN
The College of New Jersey, Dept of Physics, Ewing, New Jersey 08628

ABSTRACT

Temperature dependencies of the electrical resistivity, ρ, and the thermoelectric power, α, are reported for Re_6 M_xTe_{15} (M = Ga, In, Ag; x = 0, 1, 2) between 90-380 K. Theoretical discussion of the results is presented. The materials, synthesized by filling large voids in the Re_6Te_{15} cluster system, may have potential thermoelectric applications around and below room temperatures. The samples are prepared by reacting 99.99% pure elemental powders in evacuated and sealed quartz ampoules at 1070 K for 170 hours. The resistivity data indicate semiconducting behavior for all samples. Possible hopping conduction is present at lower temperatures. The energy gap is observed at higher temperatures in all the samples.

Positive values of α in $Re_6(Ga,In)_xTe_{15}$ (x = 0, 1, 2) indicate *p*-type semiconducting behavior in the studied temperature range. For these samples α increases initially with temperature, then levels off to a nearly constant value. The positions of the sharp peaks in α, observed at lower temperatures for x = 1, 2 only, depend on the Ga (In) concentration. High values of α (~ 300 μV/K) are measured at room temperatures. In Re_6AgTe_{15} α has small positive values (~ 20-40 μV/K) between 185 K and 270 K. Outside this range α is negative. It reaches local maxima of -340 μV/K at 105 K and -350 μV/K at 370 K. In $Re_6Ag_2Te_{15}$ α changes from positive to negative values above 295 K. A maximum positive value of +350 μV/K is reached at 250 K and maximum negative of -250 μV/K at 330 K. The power factor, α^2/ρ, increases with temperature for all studied samples. Theoretical fits to α(T) for all samples are discussed. Also discussed is the effect of filling the voids in the rhenium-telluride system on the figure of merit.

INTRODUCTION

Previous experimental observations[1-3] and theoretical considerations[4] suggested that Re_6Te_{15} cluster compound might have promising thermoelectric properties. It was also suggested that they might lead to development of new thermoelectric materials with efficiencies around and below room temperatures greater than that of presently used state-of-the-art thermoelectrics. In this paper we report the thermoelectric power and electrical resistivity of doped rhenium tellurides $Re_6M_xTe_{15}$ (x = 1, 2, M = Ga, In, Ag) in the temperature range 90-380 K.

Re_6Te_{15} is the only thermodynamically stable phase in the Re-Te system[2]. This cluster type compound is closely related to the Chevrel phase molybdenum chalcogenides[5-10]. While molybdenum chalcogenides with $[Mo_6]$ clusters have been studied extensively previously[5-10], only a limited amount of work has been reported on the thermoelectric properties below room temperatures on rhenium chalcogenides with $[Re_6]$ units.

Re_6Te_{15} contains $[Re_6Te_8]$ and $[Te_7]$ clusters[2,11]. In the $[Re_6Te_8]$ cluster six rhenium atoms form an $[Re_6]$ octahedron, which is surrounded with eight cubicly arranged tellurium atoms. Similar octahedral arrangement of Re atoms is found in $Na_2Re_3S_6$ and $K_2Re_3S_6$[5], $Sr_2Re_6S_{11}$ and $Ba_2Re_6S_{11}$[6], $Re_6Se_8Cl_2$[8], $Re_6Se_8Br_2$[9], $Cs_3Re_6S_{13}$[12], and the Chevrel phases $MoRe_4S_8$ and $MoRe_4Se_8$[13]. The $[Te_7]$ cluster consists of the remaining seven Te atoms. This cluster forms a quasi-planar structure[2] that connects $[Re_6Te_8]$ clusters.

Previous reports found *p*-type semiconducting behavior at room temperatures in the

Mat. Res. Soc. Symp. Proc. Vol. 545 © 1999 Materials Research Society

rhenium-telluride system[1-3]. The semiconducting behavior of Re_6Te_{15} is explained by the saturation of valence bands. In each rhenium-telluride cluster a total of 42 valence electrons are contributed by six rhenium atoms. Twenty-four of these electrons are needed for 12 Re-Re bonds. Sixteen are used to fill the *p*-shells of the 8 tellurium atoms[11,14]. The remaining two electrons exactly fill the valence shells of the [Te_7] structure. Large room temperature thermoelectric power ($\alpha \approx 500$ μV/K) and resistivities ~ 10 Ω·m were also reported[1-3]. Calculations[11] suggested a semiconducting band gap at room temperatures in Re_6Te_{15}.

It was found[2] that the Re_6Te_{15} structure includes voids large enough to contain additional metal atoms. It is of interest to find how the addition of these atoms influences thermoelectric properties of Re_6Te_{15}. We undertook a systematic study of $Re_6 M_x Te_{15}$ (x = 0, 1, 2; M = metal) systems. In this communication we report on thermoelectric power and electrical resistivity of $Re_6M_xTe_{15}$ (x = 0, 1, 2; M = Ga, In, Ag) compounds.

EXPERIMENT

Samples of $Re_6 M_x Te_{15}$ (x = 0, 1, 2; M = Ga, In, Ag) were prepared from elemental powders (99.99% pure). The powder mixture was cold pressed and then reacted under vacuum in a sealed quartz ampoule at 1070 K for 170 hours. The resulting samples formed as gray, hard, and brittle polycrystalline materials.

Cell identification was performed and lattice parameters determined for $Re_6M_xTe_{15}$ samples. All samples had the orthorhombic structure and all were of the single phase. The cell volume of the doped samples changes slightly depending on the dopant. The crystal structure will be covered in more details in a separate publication.

The electrical resistivity, ρ, and the thermoelectric power, α, of $Re_6M_xTe_{15}$ samples were measured as functions of temperature. Measurements were done in the range 90-380 K. The results were compared with the electrical resistivity and the thermoelectric power of Re_6Te_{15}[3].

RESULTS

The resistivity data indicate semiconducting behavior for all the samples. The room temperature resistivities, ρ_0, were as follows: Re_6GaTe_{15} : 2.2 Ω·m, $Re_6Ga_2Te_{15}$:3.3 Ω·m, Re_6InTe_{15} :3.2 Ω·m, $Re_6In_2Te_{15}$:3.6 Ω·m, Re_6AgTe_{15} :2.3 Ω·m, and $Re_6Ag_2Te_{15}$:0.6 Ω·m. The plots of $ln\ \rho$ vs T^{-1} are shown in Fig. 1. At higher temperatures (T > 160-220 K) the fit of $ln\ \rho$ to a line was possible for all samples. This indicates the presence of the energy gap and is consistent with previous theoretical considerations[11] and experimental observations[2] at room and higher temperatures in Re_6Te_{15}. For lower temperatures the fit to a straight line of $ln(\rho/\rho_0)$ vs T^{-1} was not possible. In this temperature range the resistivities were fitted with $\rho \approx \rho_0\ exp\ (T_0/T)^{1/y}$, where *y* is composition dependent. Such a dependence may indicate hopping conduction[15], which might be expected for these cluster-type structures. At this point we will not go any further in the analysis of such dependencies, since the measurements were done on sintered samples. A more detailed study of the transport mechanisms in $Re_6 M_xTe_{15}$ single crystals is necessary.

The variations of the thermoelectric power, α, with temperature are shown in Fig. 2. The room temperatures values of the thermoelectric power were measured to be between 260-310 μV/K for Ga and In doped samples. Values of α at room temperatures for Ag doped samples had negative values.

Positive values of α in the measured temperature range for M = (Ga, In) indicate that these samples were *p*-type semiconductors. These samples show similar temperature dependencies of α. The thermoelectric power in Re_6GaTe_{15} increases with temperature above 168 K. It reaches

274 μV/K at 336 K. It then levels off to a nearly constant value. The thermoelectric power in $Re_6Ga_2Te_{15}$ increases sharply above 157 K and then nearly levels off above 364 K to about 309 μV/K. The thermoelectric power in $Re_6In_2Te_{15}$ increases with temperature until it reaches a maximum of about 335 μV/K around 250 K. It then decreases slowly and nearly levels off to about 310 μV/K. The thermoelectric power in Re_6InTe_{15} increases from about 25 to 270 μV/K in the measured temperature range. Excitations of optical phonons are most likely responsible for the observed increase of the thermoelectric power of $Re_6M_xTe_{15}$ (M = Ga, In) as the temperature increases.

Galium and indium doped samples exhibit sharp peaks in the thermoelectric powers at lower temperatures. The peak positions shift to higher temperatures as the Ga(In) concentration

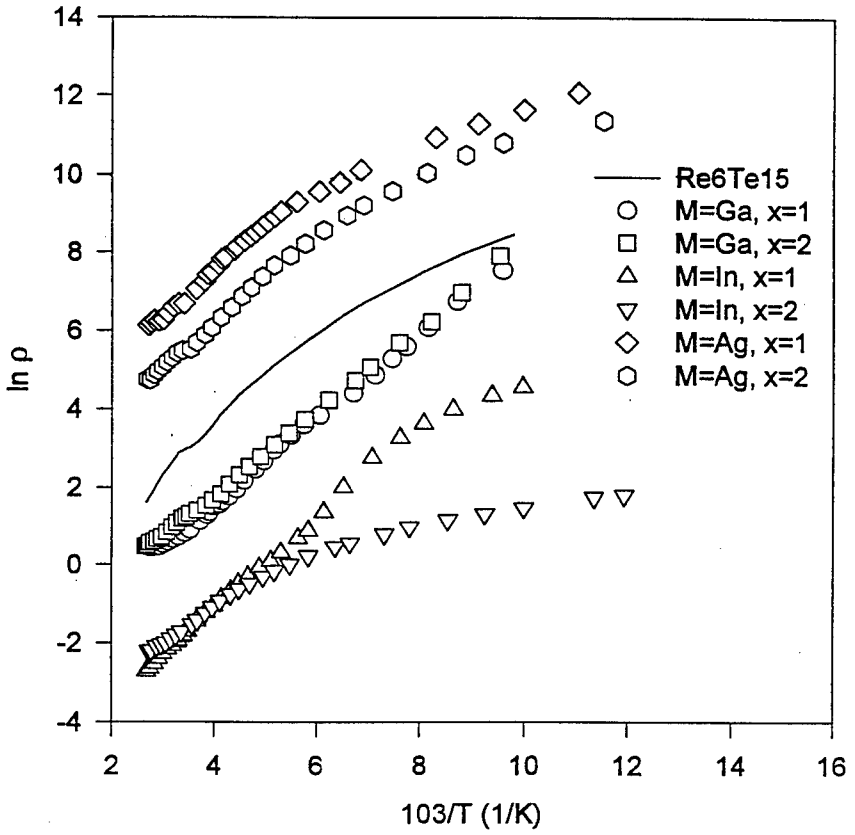

Fig. 1 Temperature dependence of resistivity in $Re_6M_xTe_{15}$. Note: To make it more readable, 2, 4, and -2 were added to ln ρ for Ga-, Ag-, and In-doped samples, respectively, and 1 was added to Re_6Te_{15}.

decreases. Similar peaks were not observed in Re_6Te_{15}. High values of α in these samples suggest low carrier concentration in the studied temperature range.

The thermoelectric power in Re_6AgTe_{15} changes from about -340 μV/K to about +20 μV/K between 105-185 K. It then nearly levels off. Above 270 K α decreases sharply and reaches a local maxima of -350 μV/K at 370 K. The thermoelectric power in $Re_6Ag_2Te_{15}$ increases to about 350 μV/K at 250 K. It then drops sharply and becomes negative above 295 K. At about 330 K it reaches a maximum negative value of approximately -250 μV/K. A broad shoulder is observed in both Re_6AgTe_{15} and $Re_6Ag_2Te_{15}$. The onset of the shoulder shifts toward higher temperatures as the Ag concentration increases.

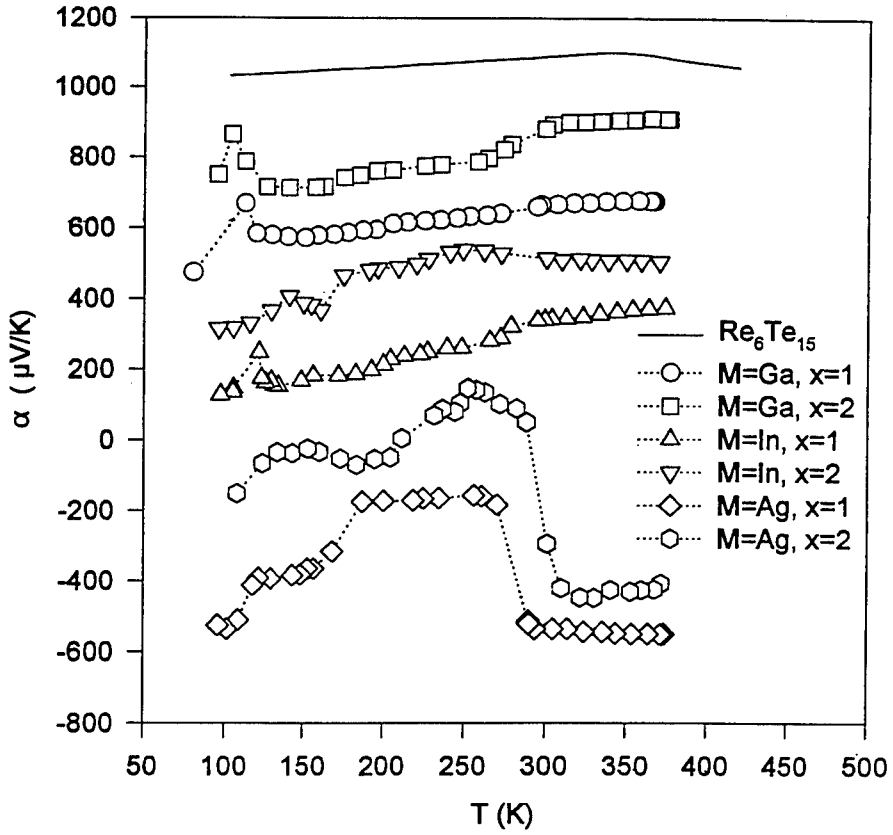

Fig. 2 α(T) in $Re_6M_xTe_{15}$. Note:To make the graph more readable, α(T) was increased, respectively, by 400, 100, and -200 μV/K for M=Ga, In, Ag and x=1; and respectively, by 600, 200, -200 μV/K for M=Ga, In, Ag and x=2.

In the measured temperature range $\alpha(T)$ was fitted assuming nondegenerate semiconductor model. The general trend of $\alpha(T)$ could be obtained using this model. The sharp peaks in Ga/In doped samples, broad shoulder in Ag doped samples, as well as the flattening of $\alpha(T)$ curve at higher temperatures could not be reproduced. We conclude that a nondegenerate semiconductor model cannot completely explain $\alpha(T)$ dependence of these materials. The temperature dependence of α and the existence of the peaks at lower temperatures need to be investigated further. Hall effect measurements are currently underway. They will help in providing better understanding of the relation of α (T) to the variation in concentration and mobility of charge carriers.

The power factors, $P_f = \alpha^2/\rho$, were calculated and shown in Fig. 3. For all the samples P_f increases with temperature. In the temperature range below 330 K the power factor of Re_6GaTe_{15}

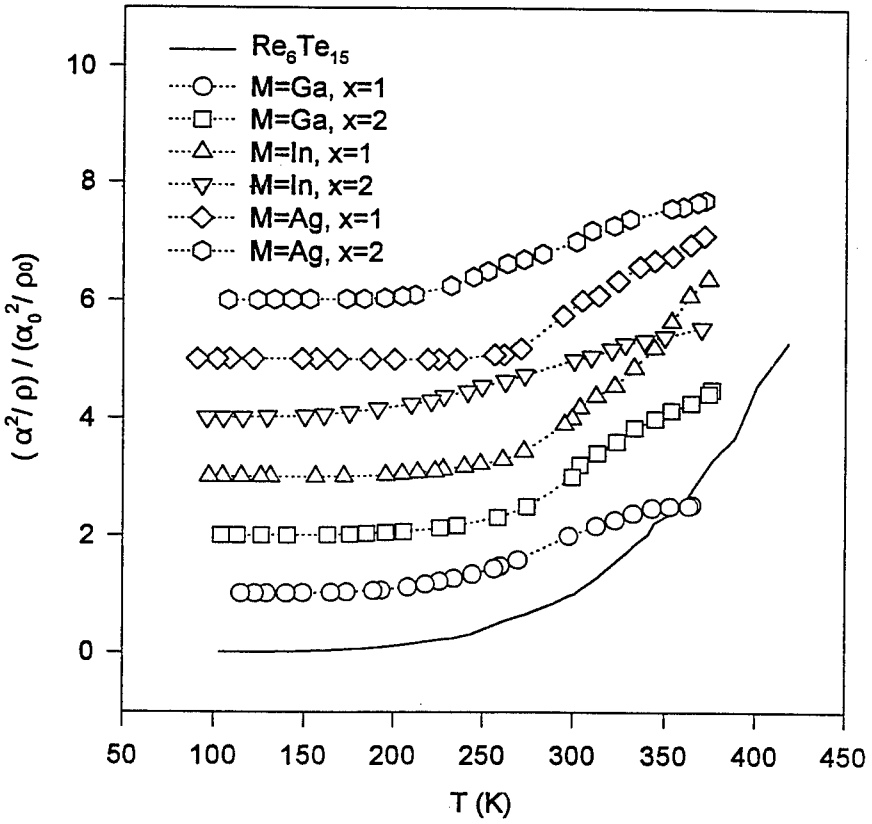

Fig. 3 Temperature dependence of the normalized power factor in $Re_6M_xTe_{15}$. Note: to make the graph more readable, 1, 2,3, and 4 were added to the original data for Ga, Ga_2, In, In_2, Ag, and Ag_2 doped samples, respectively.

is greater than that of $Re_6Ga_2Te_{15}$. Above 330 K P_f of Re_6GaTe_{15} levels off to a nearly constant value. In the whole temperature range the power factors of Re_6GaTe_{15} and $Re_6Ga_2Te_{15}$ are smaller than that of Re_6Te_{15}. The P_f in $Re_6In_2Te_{15}$ is greater that P_f in Re_6InTe_{15} up to 340 K. Above 265 K P_f in Re_6Te_{15} is greater that in $Re_6In_2Te_{15}$. P_f in Re_6Te_{15} is greater than P_f in Re_6InTe_{15} for the whole temperature range. Above 215 K P_f is greater in $Re_6Ag_2Te_{15}$ than in Re_6Te_{15}. For Re_6AgTe_{15} P_f becomes greater than in Re_6Te_{15} above 275 K. The P_f values of these materials might indicate that doping of Re_6Te_{15} with Ga, In, or Ag leads to the material that is, at best, of marginal use in thermoelectric devices in the studied temperature range. However, the existence of large voids in the rhenium-telluride system provides an opportunity for modifying the thermal conductivity by increasing the phonon scattering with the filling atoms.

CONCLUSIONS

The electrical resistivity, ρ, and thermoelectric power, α, of $Re_6M_xTe_{15}$ (x = 1, 2; M = Ga, In, Ag) have been measured over the range 90-380 K. The data indicate *p*-type semiconducting behavior for Ga and In doped samples. Ag doped samples change from *p*- to *n*-type semiconductors. The room temperature resistivities of all the samples are ~ 1-4 Ω·m. At higher temperatures the presence of the energy gap at the Fermi level is indicated. For lower temperatures hopping conduction might be present. A more detailed study of the transport mechanisms in $Re_6M_xTe_{15}$ single crystals is necessary to make more definite conclusions. Re_6GaTe_{15} shows the largest positive values of α, with the maximum of $\approx$ 370 μV/K at 380 K. Ga and In doped samples exhibit sharp peaks in α at lower temperatures, which need to be investigated further. At higher temperatures α in Ga and In doped samples increases with temperature non-uniformly. The α(T) dependencies cannot be completely explained by a nondegenerate semiconductor model.

Further measurements including the thermal conductivity and Hall mobility are necessary to make more definite conclusions about the usefulness of these materials as thermoelectric devices. Temperature dependant measurements of transport properties of single crystals are planned.

REFERENCES

1. Johnston, W. D., Miller, R. C., and Damon, D. H., J. Less-Common Met. **8**, 272 (1965).
2. Klaiber, F., Petter, W., and Hulliger, F., J. Solid State Chemistry **46**, 112 (1983).
3. Kilibarda Dalafave, S., accepted for publication in Materials Letters.
4. a) Slack, G. A., in "*CRC Handbook of Thermoelectrics*", edited by Rowe, D. M., CRC Press, Boca Raton, 1995, p. 407-440.
5. Bronger, W. and Spangenberg, M., J. Less Common Met. **76**, 73 (1980).
6. Bronger, W. and Miessen, H. J., J. Less Common Met. **83**, 29 (1982).
7. Leduc, L., Perrin, A., and Sergent, M., Acta Cryst. **C39**, 1503 (1983).
8. Leduc, L., Perrin, A., Sargent, M., Le Traon, F., Pilet, J. C., and Le Traon, A., Mat. Lett. **3**, 209 (1985).
9. Speziali, N. L., Berger, H., Leicht, G., Sanjines, R., Chapuis, G., and Levy, F., Mat. Res. Bull. **23**, 1597 (1988).
10. Fischer,C, Alonso-Vante, N, Fiechter,S, Tributsch,H, J Appl. Elec. **25**, (11), 1004-8 (1995).
11. Bullett, D. W., Sol. Stat. Com. **51** (1), 51 (1984).
12. Spangenberg, M. and Bronger, W., Angew. Chem. Int. Ed. Engl. **17**, 368 (1978).
13. Perrin, A., Sergent, M., and Fischer, O., Mat. Res. Bul. **13**, 259 (1978).
14. Harbrecht B. and Selmer, A., Z. anorg. allg. Chem. **620**, 1861-1866 (1994).
15. H. Böttger and V. V. Bryksin, Phys. Stat. Sol. (b) **78**, (1976) 9; **78**, (1976) 415.

The Nanofabrication of Quantum Wires for the Next Generation of Thermoelectrics

D. L. Demske*, J. L. Price*, N. A. Guardala*, N. Lindsey*, J. H. Barkyoumb*,
J. Sharma*, H. H. Kang† and L. Salamanca-Riba†
*Carderock Division, Naval Surface Warfare Center, West Bethesda, MD 20817
†Dept. of Materials and Nuclear Engineering, U. of Maryland, College Park MD 20742

ABSTRACT

The fabrication of a thermoelectric nanocomposite material consisting of nanometer scale bismuth (Bi) wires embedded in a porous mica template host is discussed in detail. In fabricating the mica templates, a positive ion accelerator is employed to irradiate 10 μm thick mica sheets with collimated beams of 15 MeV carbon ions at fluence levels of 1.5×10^{13} ions/cm^2. The normally incident beam generates latent nuclear damage tracks in the direction oriented perpendicularly to the mica basal plane. Atomic Force Microscope (AFM) pictures of etched tracks verify that we have fabricated porous templates containing arrays of channels with densities up to 10^{13}/cm^2 and diameters as small as 5 nanometers, thus providing pores having an aspect ratio of about 2000:1. Scanning electron micrographs of 50 nm diameter tracks show that these are parallel channels with smooth, non-tapered walls. In addition, to fabricate the wires we have developed a solution-electrodeposition process employing a PC processor-driven potentiostatic/galvanostatic system. Currently, we are electrochemically embedding 10 μm long Bi wires through the nanochannel templates. The potentiostatic electrodeposition behavior of these wires is described. Current-voltage waveforms confirm that the wires are electrically uninterrupted through the mica template. Transmission electron micrographs (TEM) show these wires are single crystals, of well-defined orientation with diameters down to 50 Å. We observe bundles of 80 Å wires with a packing density of about 10^9/cm^2. Energy Dispersive X-ray Spectroscopy (EDS) has corroborated the presence of Bi in the nanochannels. The observation of the bismuth crystal orientation in the porous mica template is examined.

INTRODUCTION

Recently, there has been considerable interest in low-dimensional, quantum size confined structures for improved thermoelectric materials. Bismuth is a group V semimetal with highly anisotropic electron energy-momentum properties; under proper size confinement and potential offset conditions, it has the capability of transitioning to a direct band gap semiconductor with a significantly improved material figure of merit (ZT).

Good thermoelectric materials are characterized by a high Seebeck coefficient and a high electrical-to-thermal conductivity ratio. In conventional TE materials the latter parameter generally has been restricted as the consequence of the Wiedemann-Franz law. Quantum size-confinement using nanowires provides a means to defeat this impasse and to enhanced ZT values in specific conventional TE materials such as Bi, Bi_2Te_3, and its alloys.[1] Quantum-confined nanocomposite systems exhibit profound changes in their

Mat. Res. Soc. Symp. Proc. Vol. 545 © 1999 Materials Research Society

transport properties as the result of marked differences in their electronic structures from those of their bulk counterparts. Theoretically, ZT starts to increase significantly when the externally adjustable quantum confinement dimension decreases below the intrinsic thermal de Broglie wavelength limit associated with the characteristic energy of the confinement and with wire density until the electrons can tunnel appreciably between the wires.[2] For Bi 2-d quantum wells in a particular configuration, this maximum in ZT has been determined to occur around 80 Å.[3] It has recently been demonstrated that quantum confinement resulting a semimetal-semiconductor transition in Bi quantum wires can occur at a substantially larger diameter wire than is needed for optimum improvement in ZT.[4,5] Ultimately, a more accurate assessment of ZT in Bi quantum wire thermoelectrics must also consider imposing additional fundamental requirements on "real" wire-nanochannel /barrier template structures.[2,3]

We report here on the two-part fabrication and subsequent verification of arrays of oriented, crystalline Bi wires from an aqueous solution electrodeposition of Bi^{3+} into channels in mica templates produced by positive ion nuclear damage tracks.

EXPERIMENT

The most important prerequisite for the experimental verification and characterization of TE quantum size-confined composites is the consistent and precise fabrication of the nanostructures. We construct these heterostructures using a two-part synthesis procedure:

1. Synthesis of the porous mica templates

The templates used in this work are made from high quality, transparent sheets of muscovite mica ($KAl_2(AlSi_3O_{10})(OH)_2$). The 1 cm^2 sheets are cleaved to a uniform thickness of 10 μm and irradiated with a uniform high energy (15 MeV) C^{4+}-ion bombardment to fluences as high as $10^{13}/cm^2$. At this ion-beam energy, the end-of-range is greater than 10 μm as confirmed by the SRIM96 code[6] and thus the carbon ions are not implanted in the substrate. Track densities are inferred from beam current flux measurements using in-line particle beam diagnostics and from AFM measurements. Calculations also show that the latent damage tracks formed should be on average 80 Å apart on the face of the substrate.

These tracks of structural damage are much more chemically active than the undamaged material. A suitable etchant needs to preferentially dissolve the damaged site with a very high selectivity compared to the undamaged material. After processing, the resulting etched pores have lateral dimensions down to about 50 to 80 Å. The etching of latent damage tracks is dependent on the etchant, its concentration, temperature, and the etch time. A 20% ultrapure hydrofluoric acid (HF) solution was used for etching. Robust ultrasonic agitation was found to be necessary to clear the nanochannels of etch product debris. Exploiting the birefringence of the mica templates, the nanochannel etching process was continuously monitored through the use of a laser polarization discrimination technique with phase-sensitive detection. We were able to calibrate this laser-monitoring technique to channel sizes which agrees with a conductance method.[7]

The breakthrough time of pore formation in 10 μm thick templates for 20% HF at 25 °C was about 50 seconds giving an etch rate along the wires (normal to the plane of the template of about 200 nm/s. The channel diameter growth rate was measured

to be 0.025 nm/s. This large asymmetry in the etching rates results in channels without a significant taper along their length. This was experimentally verified by SEM micrographs.

2. Wire Fabrication and Continuity Verification

The resultant nanochannels are filled with Bi wires using an electrochemical deposition process. A Bismuth metal electrode is vacuum deposited on one side of the mica template. The sample is then place in a custom-designed electrochemical cell with a Bi in ClO_4 electrolyte.

The deposition process can be carried using potentiostatic (constant voltage) control or galvanostatic (constant current) control. We determined that potentiostatic control gives the best results. With the potentiostatic method, the potential at which the adsorbed species collects at the electrode must be accurately known and the depositing current is not controlled. The equation

$$I_t = I_{dl} + I_{ct} \tag{1}$$

defines the total current where I_{dl} is the double layer charging current and I_{ct} is the charge transfer current which is proportional to the Bi^{3+} ion density. Because there is no way to determine I_{dl}, the true total current is not controllable. The uncertainty in I_{dl} introduces error in the total current and thus a lack of control of current and the deposition process. The potentiostatic method is more useful because the potential is controllable and known. Additionally the problem of competitive side reactions is overcome by use of a specific potential (where only a specific species will deposit). This assures that we are depositing the desired Bi species only.

The *IV* curve in Fig. 1 shows a sharp increase in the current at the initiation of the electrolysis process and while establishing a working potential of $\approx$600 mV between the electrodes. After a solid Bi wires from the an electrode the electric current is driven through both the wire and the ionic electrodeposition solution. Subsequently, the driving EMF decreases with increasing wire length. The process is terminated when the desired stage of the wire growth is achieved. The curve in Fig. 1 can be looked at as one half of a cyclic voltammogram.

TEM observations were performed at 100 keV in a Hitachi 600AB TEM with a Kevex EDS and 300 keV in a JOEL 4000 FX TEM for the high resolution lattice imaging of the mica with Bi wires. The TEM samples were thinned first using scotch tape and then cut with a scalpel. The area along the edge of the cut samples was thin enough to transmit electrons in the TEM without the need of ion milling. 50/100 mesh type folding copper grids were used to hold the samples. Optical diffractograms were obtained from the negatives of the high resolution images to identify the crystal structure of the wires.

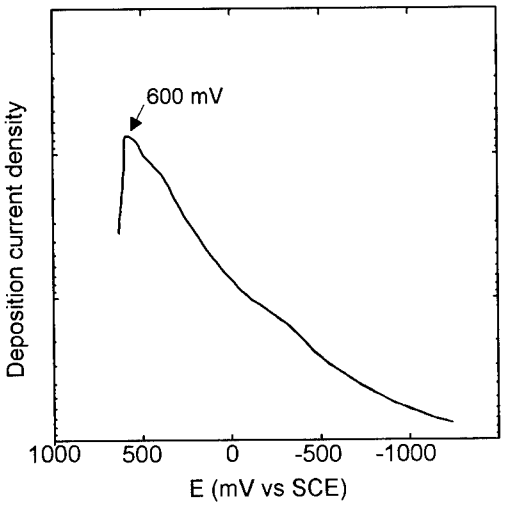

FIG. 1 *IV* curve generated during the electrochemical deposition of Bi nanowires in the mica templates. The $Bi^{3+} + 3e^{-} = Bi$ reaction starts at ≈600 mV and progresses with time to the right as the voltage goes more negative.

RESULTS

SEM pictures of cross-sectioned samples show that the etched channels had smooth, non-tapered walls. Fig. 2 is a bright filed TEM image showing Bi wires with diameters in the range of 80 to 450 Å. The high-Z Bi against the low-Z background of the mica yields good contrast in the TEM image. The white areas in this figure correspond to channels that were etched but not filled with Bi. The density of Bi wires was not homogeneous. In some sections densities were as high as 10^{13} ions/cm^2 (approximately equal to the ion-track density). EDS data confirmed that the dark areas contain Bi. The intensity of the Bi peaks is low in the EDS because the amount of Bi is quite small compare to other elements. Fig. 3 shows the lattice image of a Bi wire and mica. Optical diffractograms (inset of Fig. 3) taken from the negative of the high resolution image show high quality single crystalline Bi wire with the (012) plane preferentially oriented in the plane of the mica template (perpendicular to the nanowire axis). A number of wires were examined and all had the same (012) perpendicular orientation. The d-spacing between the (012) planes is the same as in the bulk suggesting that the wires are unstrained. The fact that we did not observe disordered structure in the wires or interference patterns between multiple planes in the Bi suggests that the wires were single crystals. Amorphous-like regions around the Bi wires were observed which plausibly could be due to the damage produced by the carbon ions during the irradiation process.

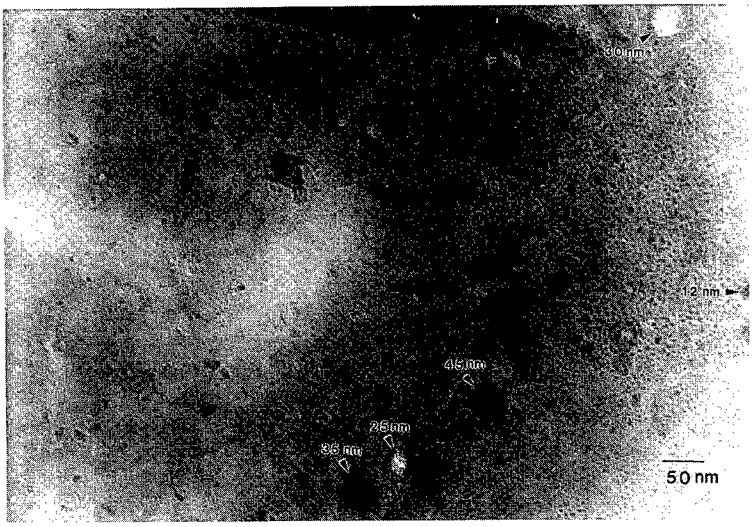

FIG. 2 Bright Field TEM of the Bi nanowires with sizes of some of the filled Bi nanowires (dark spots) and unfilled channels (white) labeled.

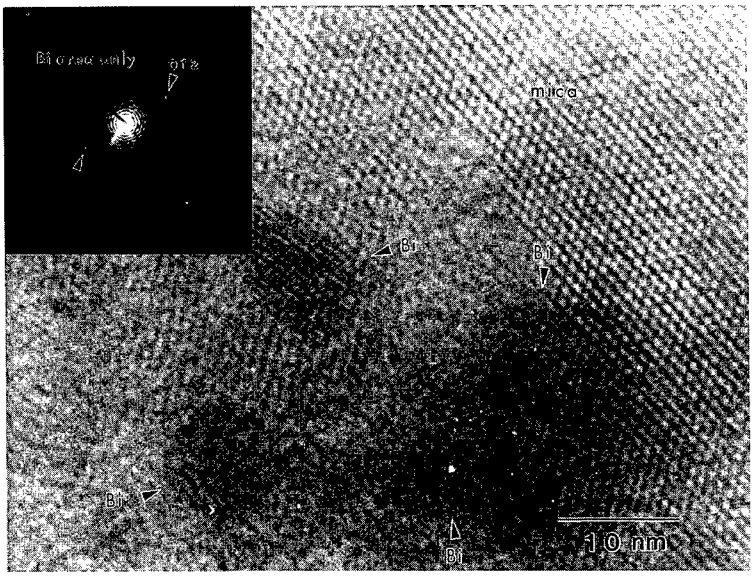

FIG. 3 High-resolution lattice image of Bi wires with sizes from ≈100 Å and smaller. The inset is a diffractogram of one of the wires showing (012) orientation normal to the wire axis.

CONCLUSIONS

This work concentrated on developing a practical and verifiable procedure for consistently fabricating dense arrays of nanometer size Bi wires in 10 micron thick mica sheets. It is crucial for the formation of quantum well wires that the tracks that are formed and subsequently etched be of fairly uniform dimensions throughout the entire length of the track. (Unfortunately, good polymer candidate materials have been shown to etch with conical tracks.) In addition, it has been established that the nuclear tracks must be kept ultra-pure and free from contamination in order to function properly as repositories for quantum wires. Our electrochemical deposition assured that we were only operating under conditions that would deposit Bi^{3+} thus assuring the purity of the Bi wires. With its exceedingly low thermal conductivity (0.79 W/m-K) in the direction normal to the basal plane, muscovite mica represents an excellent candidate as a thermoelectric template host material and should improve the effective ZT of any composite material. In addition, it is relatively inexpensive and is an established fabrication/channel track host with well known physical properties.

Mica also is an extremely good insulator with a band gap of approximately 7 eV which should result in a relatively high potential offset relative to the Bi Fermi level. If the mica is truly disordered in the region immediately adjacent to the Bi wires this could present a problem with the electrical properties of the system. A sufficient disorder in the mica would create band-tail states in the mica that would act as electron traps for the carriers in the bismuth quantum wires.

Other recent work has observed much larger Bi wires grown electrochemically that are polycrystalline with no preferred order.[8] In Bi quantum wires prepared by other methods, single crystal wires have been observed with orientations different from what we observed and the crystalline orientation also varies with wire diameter.[4] The orientation may depend on the fabrication technique, nanochannel diameter, and the template material. We did not attempt to study crystal orientation as a function of wire size in this work, but that maybe of interest to future studies.

ACKNOWLEDGMENTS

This work was supported by the Office of Naval Research and the Carderock Division's matching funds program (D. Demske) and NSF (L. Salamanca-Riba) through grant No. DMR-9321957.

REFERENCES

1. L. D. Hicks and M. S. Dresselhaus, Phys. Rev. B **47**, 16631 (1993).
2. D. A. Broido and T. L. Reinecke, Appl. Phys. Lett. **67**, 100 (1995).
3. D. A. Broido and T. L. Reinecke, Appl. Phys. Lett. **67**, 1170 (1995).
4. Z. Zhang, J. Y. Ying and M. S. Dresselhaus, J. Mater. Res. **13**, 1745 (1998).
5. Z. Zhang, X. Sun, M. S. Dresselhaus, J. Y. Ying and J. P. Heremans, Appl. Phys. Lett. **73**, 1589 (1998).
6. J. Ziegler, J. P. Biersack and U. Littmark, *Stopping and Range of Ions in Solids* (Pergamon, New York, 1985).
7. C. P. Bean, M. V. Doyle, and G. Entine, J. Appl. Phys. **41**, 1454 (1970).
8. K. Liu, C. L. Chien, P. C. Searson and K. Yu-Zhang, Appl. Phys. Lett. **73**, 1436 (1998).

PROSPECTS FOR BISMUTH NANOWIRES AS THERMOELECTRICS

M. S. Dresselhaus[a,b], Z. Zhang[a,#], X. Sun[a], J. Y. Ying[c], J. Heremans[e], G. Dresselhaus[f], and G. Chen[g]

[a]Department of Physics, Massachusetts Institute of Technology, Cambridge, MA 02139
[b]Department of Electrical Engineering and Computer Science, Massachusetts Institute of Technology, Cambridge, MA 02139
[c]Department of Chemical Engineering, Massachusetts Institute of Technology, Cambridge, MA 02139
[e]Physics and Physical Chemistry Department, General Motors R&D Center, Warren, MI 48090-9055
[f]Francis Bitter Magnet Laboratory, Massachusetts Institute of Technology, Cambridge, MA 02139
[g]Mechanical and Aerospace Engineering Department, University of California, Los Angeles, CA 90095-1597

ABSTRACT

The small effective mass of Bi, high anisotropy of its Fermi surface, and the high aspect ratio (length/diameter) of Bi nanowires make this an excellent system for studying quantum confinement effects of a one-dimensional (1D) electron gas in relation to electrical conductivity, thermoelectric power, and thermal conductivity. A theoretical model based on the basic electronic band structure of bulk Bi is suitably modified to describe 1D bismuth nanowires and is used to predict the dependence of these transport properties on nanowire diameter, temperature and crystalline orientation of the bismuth nanowires. Experiments have been carried out on ultra-fine single crystal Bi nanowires (10–120 nm diameter) with a packing density as high as 7×10^{10} wires/cm^2 to test the quantum confinement assumptions of the model and the occurrence of a quantum confinement-induced semimetal-to-semiconductor transition as the wire diameter becomes less than 100 nm. Prospects for the use of bismuth nanowires for thermoelectric applications are discussed.

INTRODUCTION

Bismuth is a very attractive material for low-dimensional thermoelectricity because of the large anisotropy of the three ellipsoidal constant energy surfaces for electrons at the L-point in the rhombohedral Brillouin zone ($m_x^* = 0.00651m_0$, $m_y^* = 1.362m_0$, $m_z^* = 0.00993m_0$ at the Fermi level [1]), and the high mobility of the carriers ($\mu = 3.5 \times 10^4$ cm^2/Vs for light mass electrons in the binary direction with a carrier density of 2×10^{18}/cm^3 at 300 K). In addition, bismuth has carriers with very long mean free paths for transport and heavy mass ions to scatter phonons better. Bismuth can be alloyed isoelectronically with antimony to yield a high mobility alloy with highly desirable thermoelectric properties. From the known bismuth-antimony phase diagram, it is possible to prepare semiconducting $Bi_{1-x}Sb_x$ for x in the range $0.09 < x < 0.17$. In this narrow composition range, the lowest conduction band and the highest valence band are both at the L-point in the Brillouin zone, and both bands have

Mat. Res. Soc. Symp. Proc. Vol. 545 © 1999 Materials Research Society

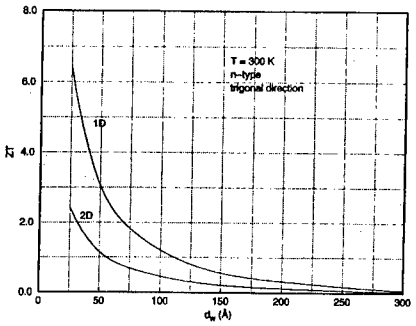

Figure 1: Calculated thermoelectric figure of merit ZT for 1D and 2D Bi systems in the trigonal direction as a function of d_W, the width of the quantum wire (1D) or quantum well (2D).

very similar highly anisotropic constant energy surfaces, giving rise to high mobility carriers, and good opportunities for preparing both n-type and p-type low-dimensional bismuth-based thermoelectric materials. As a bulk material, semimetallic Bi has a low Seebeck coefficient because of the approximate cancellation between the contributions from the electrons and holes. Low dimensionality, however, offers an opportunity to overcome this problem. As the quantum well (or wire) width decreases, the band edge for the lowest subband in the conduction band rises above that for the highest subband in the valence band, inducing a semimetal-semiconductor transition [2]. If the 2D (or 1D) bismuth system is then doped to the optimum doping level, a large enhancement in $Z_{2D}T$ (or $Z_{1D}T$) should be possible as the quantum well (or wire) width is decreased, as shown in Fig. 1. Of particular interest is the observation that significant enhancement in $Z_{2D}T$ (or $Z_{1D}T$) occurs for relatively large quantum well (or wire) widths ($\leq$ 50 Å). For example, Fig. 1 predicts a $Z_{2D}T > 1$ at room temperature for a 50 Å Bi quantum well confined in the trigonal direction. Such quantum well widths should be achievable experimentally, if one could only identify a suitable barrier material. This has turned out to present a difficult materials science problem, but steady progress has been made with improving the materials science for preparing bismuth-based 2D quantum well systems [3].

As shown in Fig. 1, even greater enhancement of ZT is predicted for 1D bismuth nanowires, if such wires can be fabricated with a suitably small wire diameter. This paper addresses progress that has been made to date on bismuth nanowire research for thermoelectric applications and prospects of this technology for rapid development in the near future.

STRUCTURE AND CHARACTERIZATION OF BISMUTH NANOWIRES

Arrays of hexagonally-packed parallel bismuth nanowires, 13–110 nm in diameter and 25–65 μm in length, have been prepared [4]. These nanowires are embedded in a dielectric matrix of anodic alumina, which, because of its array of nano-channels, is used as a template for preparing the Bi nanowires (see Fig. 2) [4]. Each of the nanowires is shown to be essentially a single crystal and the nanowires are highly oriented with a common crystallographic direction along the wire axis.

The anodic alumina templates, having an array of parallel near-cylindrical channels, are

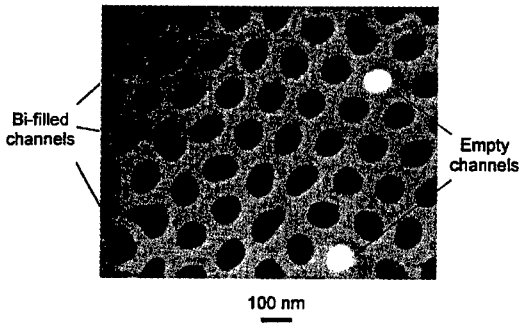

Figure 2: Cross-sectional view of the cylindrical channels of 65 nm average diameter of an anodic alumina template, shown as a transmission electron microscope (TEM) image. The template has been mostly filled with bismuth, and the TEM image was taken after the top and bottom sides of the sample had been ion milled with 6 kV Ar ions [5, 6].

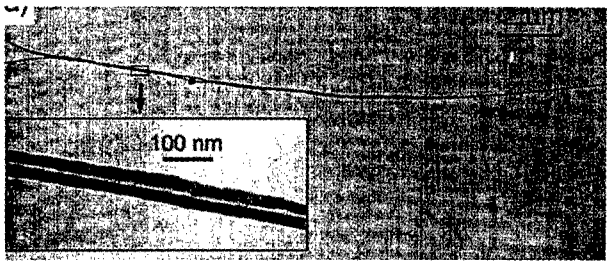

Figure 3: A TEM micrograph of two long free-standing Bi nanowires with ~23 nm diameters. The inset shows a high-magnification image taken from the indicated position on the long wires [5, 6].

produced by anodizing aluminum substrates in strong acid solutions [4, 7]. There are two ways that have been demonstrated for filling the nanotubes, one from the liquid phase [4] and the other from the vapor phase [8]. By both methods, arrays of essentially single crystal Bi nanowires are produced [4, 8].

The structural properties of the fabricated Bi nanowire arrays [4] have been investigated by various characterization techniques, such as X-ray diffraction (XRD), scanning electron microscopy (SEM), transmission electron microscopy (TEM), and selected area electron diffraction (SAED) [4, 9]. The single crystallinity and orientation of the Bi nanowires were confirmed by both high-resolution electron microscopy (HREM) and SAED studies on free-standing Bi nanowires (see Fig. 3), which were prepared by dissolving away the anodic alumina template in a special acid solution. The free-standing wires were found to have nearly uniform diameters (within 10%) along the long wire lengths. XRD experiments show that nearly all (~90%) of the wires in a nanowire array are oriented in the same crystallographic direction along the wire axis [2, 9], the most common being the $[10\bar{1}1]$ wire orientation in the hexagonal coordinate system (or [0,0.949,0.315] in the Cartesian system). In the XRD experiments, all the strong diffraction peaks are found to be close to the peak positions of a polycrystalline Bi standard, showing that the rhombohedral crystal structure of bulk Bi is also preserved in the small diameter Bi nanowires.[4]

ELECTRONIC STRUCTURE

To model the electronic structure, we assume an ideal 1D Bi quantum wire system, where the carriers are confined inside a cylindrical potential well with an infinite potential height. This is a reasonable approximation in view of the large band gap of the anodic alumina template (~3.5 eV). For the T-point holes, we assume parabolic bands, and describe the energy levels E_{ij} by

$$E_{ij}(k_l) = \frac{\hbar^2 k_l^2}{2m_l^*} + \frac{2\hbar^2 \chi_{ij}^2}{m_c^* d_W^2}, \tag{1}$$

where $2\pi\hbar$ is Planck's constant, m_c^* is the hole cyclotron effective mass in the plane normal to the wire axis, m_l^* and $\hbar k_l$ are the effective mass component and the carrier momentum along the wire axis direction, and χ_{ij} denotes the roots of the Bessel function $J_i(\chi_{ij}) = 0$ that define the energy of the subband edges. This dispersion relation $E_{ij}(k_l)$ represents free-electron-like motion along the wire axis and bound electron states in the cross-sectional plane [2].

The L-point electrons (see Fig. 4) are described by the non-parabolic Lax model [10], which is used because of the small L-point band gap, the strong coupling between the L-point conduction and valence bands, and the associated small electron effective mass components of Bi, especially at the band edge. The non-parabolic dispersion relation for the L-point electrons given by the Lax model [10] is:

$$E_{ij}(k_l) \approx \sqrt{\frac{E_{gL}^2}{4} + E_{gL}\left(\frac{\hbar^2 k_l^2}{2m_l^*} + \frac{2\hbar^2 \chi_{ij}^2}{m_c^* d_W^2}\right)} - \frac{E_{gL}}{2}, \tag{2}$$

where E_{gL} is the 3D band gap at the L-point, and this model results in heavier masses for electron states as we move away from the 3D band edge. Following Eq. (2), we calculate the L-point electron subband structure for Bi nanowires for different wire diameters and

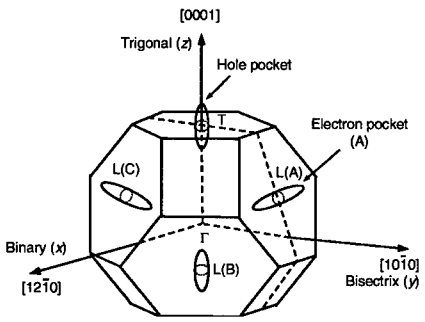

Figure 4: The Fermi surfaces of Bi, showing the Brillouin zone with the fifth-band hole pocket about the T-point and the three sixth-band L-point electron pockets labelled A, B, and C. For nanowires having their wire axes in the bisectrix-trigonal plane, the mirror plane symmetry of the bulk bismuth structure results in the crystallographic equivalence of the L-point carrier pockets B and C. However, the L-point carrier pocket A is not equivalent crystallographically to carrier pockets B or C.

crystallographic orientations, using the full Lax model to obtain the band edge electron states for $k_l = 0$ for each subband. The term in $(\hbar^2 k_l^2/2m_l^*)$ is treated in perturbation theory and the non-parabolic effects associated with m_l^* for energies greater than the subband edge are neglected, so that m_l^* for a given subband is treated as an energy-independent constant. The Fermi level is adjusted so that in the absence of dopants, the electron concentration is equal to the hole concentration.

Since transport measurements have been made on several Bi nanowire samples having their wire axes along the [10$\bar{1}$1] axis, we show in Fig. 5 a schematic of the dispersion relations for the electronic subband structure of bismuth nanowires oriented along the [10$\bar{1}$1] direction, treating the L-point electron and hole bands as mirror bands, following the two-band Lax model. For the [10$\bar{1}$1] crystal orientation, one of the electron pockets (denoted by A) has a very small electron cyclotron effective mass, while the other two electron pockets (denoted by B and C) are equivalent and have a cyclotron effective mass about two times heavier than that of electron pocket A. Thus, the energy of the lowest subband edge of electron pocket A increases faster with decreasing wire diameter d_W than for the lowest subband edge of electron pockets B and C, thus resulting in the splitting of the L-point band edge as shown in Fig. 5. Since m_l^* for electron pockets B and C is smaller than for electron pocket A, the band curvature for the dispersion relation $E_{ij}(k_l)$ is greater for carrier pockets B and C than for A, as shown in Fig. 5. In this figure we see that as the wire diameter d_W decreases, the energy gap between the highest L-point valence subband extremum and conduction subband extrema increases, while the band overlap energy decreases. Bi nanowires thus are expected to undergo a semimetal-to-semiconductor transition when the wire diameter is reduced below a critical value d_c, as discussed below.

Following Eqs. (1) and (2), the indirect bandgap E_g' between the highest T-point hole subband edge and the lowest L-point electron subband edge for the heavy mass direction is given by

$$E_g' = \frac{2\hbar^2\chi_{10}^2}{m_{ch}^* d_W^2} + \sqrt{\frac{E_{gL}^2}{4} + E_{gL}\left(\frac{4\hbar^2\chi_{10}^2}{m_{ce}^* d_W^2}\right)} - \frac{E_{gL}}{2} + E_g, \tag{3}$$

where m_{ch}^* and m_{ce}^* denote the cyclotron effective masses for holes and electrons given above,

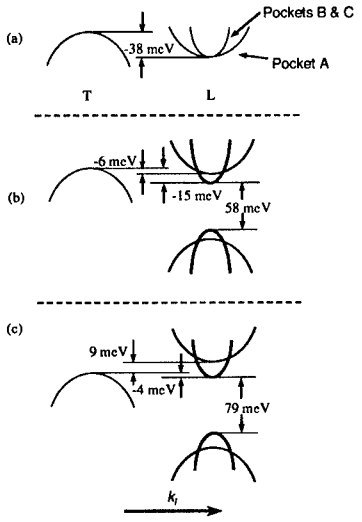

Figure 5: Schematic energy band diagram showing the energies of the lowest subband edges for the three L-point electron pockets (A, B, and C) and the highest subband edge for the T-point and L-point holes for: (a) bulk Bi, where the L-point bulk bandgap is ~15 meV, (b) 90 nm-diameter Bi nanowires, and (c) 65 nm-diameter Bi nanowires, both oriented along the $[10\bar{1}1]$ or [0,0.949,0.315] direction. The energy dispersion relation for each subband shown is for the wave vector along the wire axis k_l, while the band edge energy of each subband is determined by the average in-plane effective mass, approximated here by the cyclotron mass m_c^* (see Eq. 2). The locations of the electron and hole carrier pockets in the Brillouin zone are shown Fig. 4.

χ_{10} is the Bessel function for the extremal subbands ($i, j = 1, 0$), d_W is the wire diameter, E_{gL} is the direct bulk L-point band gap, and E_g is the 3D band gap between the T-point hole band extremum and the L-point conduction band extremum ($E_g = -0.038$ eV, the band overlap energy being negative in the semimetallic regime). As the wire diameter d_W decreases, E_g' increases (as shown in Fig. 6) until eventually E_g' becomes positive, with $E_g' = 0$ defining d_c, the critical nanowire diameter for the semimetal ($E_g' < 0$) to semiconductor ($E_g' > 0$) transition. Since the details of the band structure in Fig. 5 are sensitive to the nanowire crystallographic direction, d_c also depends on crystallographic direction (see Fig. 6). Bismuth nanowires are of interest for thermoelectric applications in the semiconducting regime, under heavy doping conditions which optimize ZT for a given wire diameter.

Based on Fig. 5, we can calculate the carrier concentration for each ellipsoid of the Fermi surface for Bi as a function of temperature and thereby obtain the total electron and hole concentration by summation. Figure 7 shows the calculated results for the concentrations of the various carriers for Bi nanowires with wire diameters of 90 nm and 65 nm oriented along the $[10\bar{1}1]$ direction, plotted on a semilog plot to cover the wide range of relevant carrier densities. We note here that the carrier concentrations for these nanowires are very different between the electron carrier pocket A and pockets B and C. At very low temperatures, for both the 90-nm and 65-nm Bi nanowires, only electron pockets B and C and the T-point hole pocket are populated; the total electron (hole) concentrations at $T = 2.0$ K are 2.40×10^{16} cm^{-3} and 8.11×10^{15} cm^{-3} for the 90-nm and 65-nm nanowires, respectively. At room temperature ($T = 300$ K), the carrier concentrations for the 90-nm nanowire [Fig. 7(a)] are 3.09×10^{17} cm^{-3}, 1.35×10^{18} cm^{-3}, 2.11×10^{18} cm^{-3} and 8.89×10^{17} cm^{-3} for electron

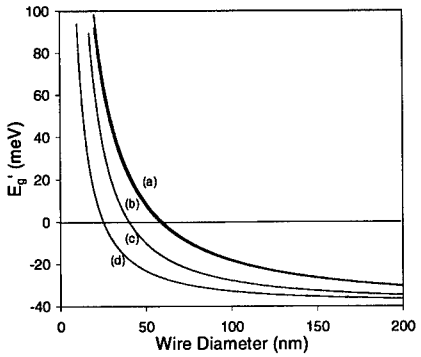

Figure 6: Calculated band gap energy between the lowest electron subband and the highest hole subband of Bi nanowires oriented along (a) $[10\bar{1}1]$, (b) bisectrix, (c) trigonal, and (d) binary directions, as a function of wire diameter. The non-parabolic effect of the L-point electron pockets has been taken into account in the calculations. The values of d_c, the critical wire diameter, where the semimetal to semiconductor transition occurs, are: 59 nm, 58 nm, 40 nm, and 25 nm, respectively, for Bi nanowires oriented along the $[10\bar{1}1]$, bisectrix, trigonal and binary directions, respectively [5, 6].

pocket A, electron pocket B or C, the T-point hole pocket, and the L-point hole pockets, respectively, yielding a total carrier concentration of 3.00×10^{18} cm^{-3} for electrons (holes). Likewise, the carrier concentrations for the 65-nm nanowire [Fig. 7(b)] are 4.23×10^{16} cm^{-3}, 7.49×10^{17} cm^{-3}, 1.45×10^{18} cm^{-3} and 8.93×10^{16} cm^{-3} for electron pocket A, electron pocket B or C, the T-point hole pocket, and the L-point hole pockets, respectively, yielding a total electron (hole) concentration of 1.54×10^{18} cm^{-3} at 300 K. Thus, thermal excitation to 300 K increases the carrier density by two orders of magnitude for these Bi nanowires.

At high temperatures, the Fermi energy decreases with increasing temperature, so that the carrier concentration of electron pocket A becomes almost insensitive to temperature. In Fig. 7(b), the small decrease of the carrier concentration for electron pocket A above 260 K is also due to the same mechanism (the decrease of E_f with increasing T). The model calculations presented here should be considered as approximate at high temperatures for three reasons. First, the Lax model is not accurate for electron energies far away from the 3D conduction band edge. Secondly, the T-point valence band is also expected to be non-parabolic when hole energies are far away from the band edge, and the non-parabolic effects of the T-point valence band are ignored in the model presented here. Thirdly, the band structure is known to vary with temperature [11], and this effect is neglected here.

Based on these approximations, the calculated Fermi energies as a function of temperature for Bi nanowires with 65 and 90 nm diameters along the $[10\bar{1}1]$ direction are presented in Fig. 8, where the Fermi energies are measured from the 3D T-point valence band edge. The Fermi energies at $T = 2.0$ K are -8.500 meV and -3.625 meV for the 90-nm and 65-nm Bi nanowires, respectively, which are considerably higher than the -15 meV for bulk Bi [12], reflecting the lower carrier densities of the nanowires relative to bulk Bi. Since the energy separations in Bi nanowires between the electron subbands close to the 3D conduction band edge are much larger than those of the T-point hole subbands, the density of states of electrons close to the 3D conduction band edge is smaller than that of holes close to the 3D valence band edge. Consequently, E_f increases with increasing temperature at

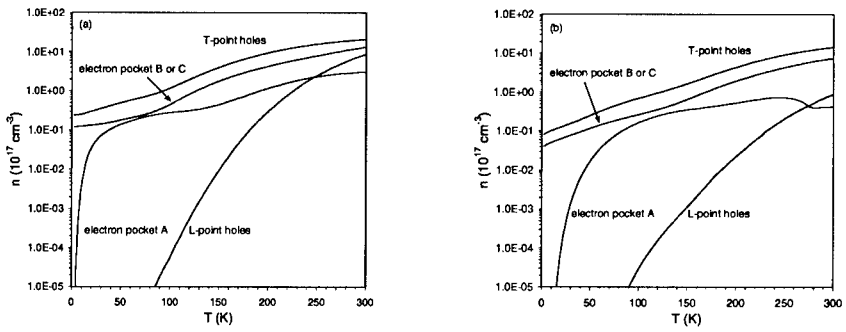

Figure 7: Semilog plot of the calculated carrier concentration as a function of temperature for each ellipsoid of the Fermi surface of Bi, including T-point holes and L-point electrons and holes, for Bi nanowires with diameters of (a) 90 nm and (b) 65 nm, oriented along the $[10\bar{1}1]$ direction. The calculations are based on the electronic subband structures shown in Fig. 5. Since the electron pockets B and C are equivalent for Bi nanowires oriented along $[10\bar{1}1]$ direction, the carrier concentration for only one of them is shown here. The temperature dependence of the carrier concentration for electron pocket A is seen to differ markedly from that of pocket B or C. The L-point hole concentration shown in the figure is the sum for the three L-point hole pockets.

low temperatures to balance the different density of states for L-point electrons and T-point holes. The small decrease of the Fermi level E_f with increasing T at $T \leq 40$ K for the 65-nm nanowire is due to E_f being very close to the lowest electron subband edge at 2.0 K, and the density of states of electrons close to the subband edge is very large due to the divergence of the 1D electron density of states at the subband edge. Therefore, when the temperature increases from 2.0 K to 40 K, E_f moves down slightly to avoid the very large electron density states at the subband edge. Due to the large non-parabolic effects of the L-point electrons, the energy separations between the electron subbands decrease and the effective masses of the electrons increase quickly when the electron energy moves away from the 3D band edge. Therefore as the carrier energy increases relative to the Fermi level, the density of states for electrons increases much faster with energy than that for holes. This effect tends to lower the Fermi level at high temperatures, where thermal excitation of the carriers results in increased occupation of these higher-lying energy states, as shown in Fig. 8.

TRANSPORT PROPERTIES

Although the transport measurements on the Bi nanowire arrays have been very informative about the electronic structure, and encouraging about the eventual use of these nanowire arrays for thermoelectric applications, these measurements and their interpretation are still at an early stage of development, as summarized below.

Measurements of the temperature dependence of the resistance $R(T)$ of Bi nanowire arrays have been carried out on samples prepared both from the liquid phase by pressure injection [4] and by vapor phase deposition [8], yielding results consistent with each other.

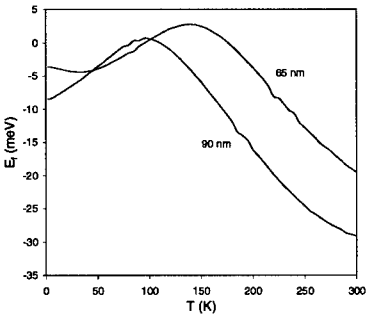

Figure 8: Calculated Fermi energy E_f (measured from the 3D T-point valence band edge) as a function of temperature for Bi nanowires of wire diameters 90 nm and 65 nm, oriented along the $[10\bar{1}1]$ direction. The calculations are based on the electronic subband structures shown in Fig. 5 [5, 6].

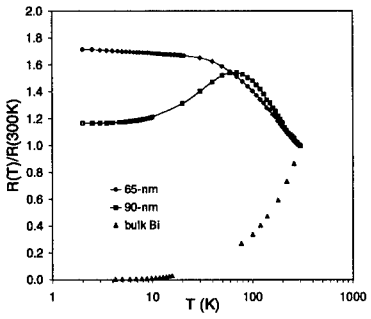

Figure 9: Temperature dependence of the resistance for Bi nanowire arrays oriented along the $[10\bar{1}1]$ direction with average diameters of 65 nm and 90 nm, and $\sim$40 μm long, after thermal annealing at 150 °C for 8 hours [5, 6]. The data for bulk Bi are obtained from references [13, 14].

The resistance measurements $R(T)$ are made with a 2-probe method showing low contact resistances, and the results (Fig. 9) are normalized to the room temperature value R(300 K), because the filling factor of the templates is not known for these samples [5, 6].

As shown in Fig. 9, the temperature dependence of the resistance of Bi nanowires is very different from that of bulk Bi and is very sensitive to the wire diameter. At high temperatures ($T > 70$ K), the resistivity of both nanowire arrays (90 nm and 65 nm diameters) shown in this figure decreases with increasing T, while at low temperatures, the T dependences are very different for the two arrays. When $T < 70$ K, the resistivity of the 65-nm sample continues to increase with decreasing temperatures, while the resistivity decreases with decreasing temperatures for the 90-nm sample. The general trend observed in Fig. 9 is consistent with previous results on single-crystal Bi thin wires of larger diameters ($d \geq 200$ nm) [15, 16].

For both bismuth nanowires and bulk Bi, the temperature dependence of the resistance is strongly influenced by both the temperature-dependent increase in carrier density (because of the very low Fermi level) and the decrease in carrier mobility. The carrier densities, calculated from the model and presented in Fig. 7 [5, 6], show that at low temperatures ($T < 70$ K), the carrier concentration of the 65-nm Bi wire increases with T more rapidly than that of the 90-nm Bi wire. In the 65-nm Bi nanowire, the decrease of the carrier

concentration with decreasing T outweighs the increase in carrier mobility with decreasing T below 70 K, and therefore the resistivity continues to increase slowly with decreasing T. However, for the 90-nm Bi wire, the T dependence of the carrier concentration is weaker, so that the increase in carrier mobility with decreasing T is relatively more important. Therefore, the total resistivity for the 90-nm nanowire decreases with decreasing T below 70 K producing a maximum in $R(T)$ at $\approx$100 K. At high temperatures ($T > 70$ K), the T dependences of the carrier concentration for both the 65-nm and 90-nm nanowire samples are quite similar, and the carrier concentration increases by about 40 times when T increases from 70 K to 300 K. The increase in the carrier concentration with increasing T for $T > 70$ K outweighs the decrease of carrier mobility for both nanowire samples, and therefore their resistivities decrease with increasing T over this higher temperature range.

The different behavior between $R(T)$ for the Bi nanowires and for bulk bismuth is striking. Because of the very low Fermi level for both bulk Bi and for the Bi nanowires, the total carrier concentration n for electrons and holes depends strongly on temperature. This temperature dependence of $n(T)$ is stronger for the nanowires than for bulk Bi, and becomes stronger as the wire diameter decreases. Furthermore, the temperature dependence of $n(T)$ becomes increasingly strong as d_W decreases in the semiconductor regime. Regarding the carrier mobility, the dominant scattering mechanism for bulk bismuth is phonon scattering, whereas for the nanowires, boundary scattering at the nanowire interfaces becomes increasingly important at low temperatures (< 70 K) and for the small nanowire diameters d_W of interest for thermoelectric applications. The general behavior shown in Fig. 9 for the 65-nm wire array has been observed for smaller nanowire diameters, including d_W values in the semiconducting regime (down to 28 nm), for Bi nanowires prepared from the vapor phase [8, 17].

The ability to remove the bismuth nanowires from the anodic alumina templates and to prepare free-standing Bi nanowires indicates a workable strategy for quantitative measurement of the temperature dependence of the resistivity $\rho(T)$ [or of the conductivity $\sigma(T)$] for bismuth nanowires of various diameters. The measurement of $\rho(T)$ on such small diameter wires represents a significant experimental challenge. The ability for n-type doping of bismuth nanowires by Te addition to the molten bismuth represents the first step necessary to control the carrier concentration in the Bi nanowires [2, 5, 6]. The p-type doping of bismuth nanowires should be possible with Pb, using the same technique as was successfully employed for the n-type doping of bismuth nanowires.

Thus far, there have been very few measurements on the Seebeck coefficient of bismuth nanowires [18], though recent achievement of reliable measurements on 200-nm Bi nanowire arrays [17] is encouraging. Improvement in the measurement technique for the Seebeck coefficient is still needed to extend the measurements to the smaller nanowire diameters of interest for thermoelectric applications [19].

Also encouraging for thermoelectric applications are the results on the high-field classical size effect in the longitudinal magnetoresistance [2, 5], showing that the defect and impurity levels in the nanowires are sufficiently low so that the wire diameter is comparable to or smaller than the carrier mean free path [20], and ballistic transport can occur in the nanowires in a high longitudinal magnetic field. The ability of the electronic structure and transport models for Bi nanowires to account for the dependence of the classical size effect in the magnetoresistance on temperature, magnetic field, nanowire diameter and annealing conditions [2, 5, 6] is important for predicting the behavior of Bi nanowires in the smaller diameter range, well below 10 nm, where enhancement in ZT is expected [19]. Previously

reported results for the low-field magnetoresistance [2] lend direct confirmation for the general features of the model for the electronic structure of bismuth nanowires presented above, which is used for calculating the transport properties, yielding estimates for the thermoelectric figure of merit [19]. Studies of localization effects in the Bi nanowires [8] show that these effects only become measurable below 5 K. Although localization effects increase in importance with decreasing T, even at 2 K, they are quite small in magnitude for single crystal Bi nanowires [6], though they are very important in disordered polycrystalline thin Bi wires and films [21].

Thermal conductivity studies of 1D nanowire systems [22] also indicate the possibility of very low phonon thermal conductivity values for Bi nanowires because of the strong phonon scattering at the Bi nanowire-anodic alumina interfaces. Near-term efforts on Bi nanowire research for thermoelectric applications will therefore focus heavily on establishing the physics, materials science and measurement techniques for nanowires in the 50–70 nm range, where the fabrication techniques have already been developed. Concurrently, attention will be given to extending the fabrication technology using a variety of possible techniques so that smaller diameter nanowires can be fabricated. It is in the smaller diameter range, well below 10 nm, where enhanced $Z_{1D}T$ is expected. It is important that reliable measurements of the Seebeck coefficient, of the electrical conductivity and of the thermal conductivity can soon be made in the interesting wire diameter range where enhanced thermoelectric performance is expected.

ACKNOWLEDGMENTS

The authors would like to thank J.-P. Issi and P. C. Eklund for valuable discussions. The authors gratefully acknowledge support by the US Navy under Contract No. N00167-98-K-0024 (MIT), and ONR under MURI (UCLA), UCLA Subgrant No. 0205-6-G-7A114-01 (MIT).

REFERENCES

[#] Present address: Lucent Technologies Bell Labs, 9333 S. John Young Pkwy, Orlando, FL 32819.

[1] R. T. Isaacson and G. A. Williams, Phys. Rev. **185**, 682 (1969).

[2] Z. Zhang, X. Sun, M. S. Dresselhaus, J. Y. Ying, and J. Heremans, Appl. Phys. Lett. **73**, 1589–1591 (1998).

[3] S. Cho, A. DiVenere, G. K. Wong, J. B. Ketterson, J. R. Meyer, and C. A. Hoffman. In *Thermoelectric Materials - New Directions and Approaches: MRS Symposium Proceedings, San Francisco, volume* **478**, edited by T. M. Tritt, M. G. Kanatzidis, H. B. Lyon, Jr., and G. D. Mahan, page 67, Materials Research Society Press, Pittsburgh, PA, 1997.

[4] Z. Zhang, J. Y. Ying, and M. S. Dresselhaus, J. Mater. Res. **13**, 1745–1748 (1998).

[5] Z. B. Zhang. *Fabrication, characterization and transport properties of bismuth nanowire systems.* Ph. D. thesis, Massachusetts Institute of Technology, Department of Physics, February 1999.

[6] Z. Zhang, X. Sun, M. S. Dresselhaus, J. Y. Ying, and J. Heremans, (unpublished).

[7] Z. Zhang, M. S. Dresselhaus, and J. Ying. In *Thermoelectric Materials-The Next Generation Materials for Small-Scale Refrigeration and Power Generation Applications: MRS Symposium Proceedings, Boston, volume* **544**, edited by T. M. Tritt, H. B. Lyon, Jr., G. Mahan, and M. G. Kanatzidis, Materials Research Society Press, Pittsburgh, PA, 1999.

[8] J. Heremans, C. M. Thrush, Z. Zhang, X. Sun, M. S. Dresselhaus, J. Y. Ying, and D. T. Morelli, Phys. Rev. B **58**, R10091 (1998).

[9] Z. B. Zhang, D. Gekhtman, M. S. Dresselhaus, and J. Y. Ying, (unpublished).

[10] B. Lax and J. G. Mavroides, in *Advances in Solid State Physics*, (Academic Press, New York, 1960), Vol. 11.

[11] M. P. Vecchi and M. S. Dresselhaus, Phys. Rev. B **10**, 771 (1974).

[12] R. J. Dinger and A. W. Lawson, Phys. Rev. B **7**, 5215 (1972).

[13] R. Hartmann, Phys. Rev. **181**, 1070 (1969).

[14] J. P. Michenaud and J. P. Issi, J. Phys. C **5**, 3061 (1972).

[15] N. B. Brandt, V. V. Moshchalkov, and S. M. Chudinov, Sov. Phys. JETP **45**, 953 (1977).

[16] M. Gurvitch, J. Low Temp. Phys. **38**, 777 (1980).

[17] J. Heremans and C. M. Thrush, (private communication).

[18] T. E. Huber and R. Calcao. In *Sixteenth International Conference on Thermoelectrics: Proceedings, ICT '97; Dresden, Germany*, edited by Armin Heinrich and Joachim Schumann, page 404, Institute of Electrical and Electronics Engineers, Inc., Piscataway, NJ 09955-1331, 1997. IEEE Catalog Number 97TH8291; ISSN 1094-2734.

[19] X. Sun, M. S. Dresselhaus, Z. Zhang, and G. Chen. In *Thermoelectric Materials-The Next Generation Materials for Small-Scale Refrigeration and Power Generation Applications: MRS Symposium Proceedings, Boston, volume* **544**, edited by T. M. Tritt, H. B. Lyon, Jr., G. Mahan, and M. G. Kanatzidis, Materials Research Society Press, Pittsburgh, PA, 1999.

[20] R. G. Chambers, Proc. Roy. Soc. London A **202**, 378 (1950).

[21] D. E. Beutler and N. Giordano, Phys. Rev. B **38**, 8 (1988).

[22] Gang Chen, S. G. Volz, T. Borca-Tasciuc, T. Zeng, D. Song, K. L. Wang, and M. S. Dresselhaus. In *Thermoelectric Materials-The Next Generation Materials for Small-Scale Refrigeration and Power Generation Applications: MRS Symposium Proceedings, Boston, volume* **544**, edited by T. M. Tritt, H. B. Lyon, Jr., G. Mahan, and M. G. Kanatzidis, Materials Research Society Press, Pittsburgh, PA, 1999.

THERMOELECTRIC BISMUTH WIRE ARRAY COMPOSITES

T.E. HUBER *, M.J. GRAF **, C. A. FOSS ***
*Howard University, Washington, DC 20059, thuber@howard.edu, edtech01@erols.com
**Department of Physics, Boston College, Chestnut Hill, MA 02467, grafm@bc.edu
***Department of Chemistry, Georgetown University, Washington, DC , cfoss@gusun.edu

ABSTRACT

The resistance R of a high density array of 200 nm diameter wires in anodic alumina is studied experimentally. R decreases from 300 K down to 0.3 K. An anomalous drop in R was found at T<50 K. Possible explanations are considered, including one based on the one-dimensional quantum size effect. Also, the large magnetoresistance is suggestive of weak-localization effects. The implication for the thermoelectric properties is discussed.

INTRODUCTION

Theoretical studies indicate that a one-dimensional wire or array of wires of diameter d where $d < \lambda_F$, and where λ_F is the Fermi wavelength equal to 25 nm for the electrons in bulk Bi, may have outstanding thermoelectric properties. It is well known that Bi has a large thermoelectric figure of merit ZT at intermediate temperatures at around 100 K in the presence of a magnetic field B ~ 1 T. Bulk bismuth is a semimetal. The electron effective mass along certain axes is very small and therefore quantum confinement effects can be very large. Lutskii [1] pointed out the possibility of a SMSC transition to occur when the energy shift due to confinement becomes large. This would make Bi even more desirable for thermoelectric applications because semiconductors are typically better thermoelectric materials than semimetals. The critical diameter d_c of this transition is expected to be around 30 nm. Recently, Z. Zhang, J.Y. Ying, and M.S. Dresselhaus have reported on the fabrication of Bi wire arrays in anodic alumina with wire diameters ranging between 56 nm and 13 nm[2]. They do not present direct transport measurements but instead optical absorption spectra of the nanowire arrays which suggests an SMSC transition. E.N. Bogachek, A.G. Scherbakov and U. Landman[3] studied theoretically the quantum transport in 3D nanowires. For small diameter wires they predict conductance quantization . Also, the on-off switching of the conducting channels in the wires is manifested not-only by the step-like behaviour of the conductance but also the appearance of thermopower peaks as a function of constriction diameter. Similar phenomena, ZT increases, have been discussed theoretically by L.D Hicks and M. Dresselhaus[4] for 1D conductors. Confinement introduces scattering and it is known that electronic transport in disordered conductors can occur in ballistic, diffusive (resistive) or localized regimes. The mode of electron transfer, i.e. localized or ballistic, is relevant to thermoelectricity because the predicted increase in ZT occurs only if the mobility is not detrimentally affected by the confinement[5].

The transport of a single 200 nm diameter wire has been studied before[6]. M. Gurvitch found

Mat. Res. Soc. Symp. Proc. Vol. 545 © 1999 Materials Research Society

that the resistance is metallic (dR/dT>0) with an anomalous drop at about 40 K. The transport measurements were interpreted in terms of the quantum size effect. Here we report an experimental study of 200 nm diameter Bi wire array. The resistivity value and its temperature dependence are roughly the same as that of the single wire. Clearly, results on wire arrays are of more direct interest to thermoelectrics because the insulator matrix does not thermally "short" the conductor.

The electronic transport properties of confined Bi have attracted interest early on. Experimental work on thin films shows that the elastic lifetime of an electron l_e in an eigenstate of momentum is much smaller that the inelastic pathlength of an eigenstate of energy l_ϕ. In the presence of strong spin-orbit coupling, this weak localization phenomenon is called anti-localization[7] because it decreases the resistance at low temperatures. Magnetic field dependent corrections to the Drude result have been derived in the localization and interaction models in 1-D conductors, and also thin films [8]. Our electronic transport measurements of a 200 nm diameter wire array can be interpreted in terms of the weak localization model . Assuming this model we find that $l_e << l_\phi$, indicating that the mode of electronic transport is ballistic.

EXPERIMENT

In this research we used commercial 90 μm thick Anopore membranes. The channels are injected at 10,000 PSI with pure Bi. Scanning Electron Microscope images of the wire arrays have already being presented[9]. The X-ray diffraction (XRD) spectrum of the Bi array, with scattering geometry set normal to the wire's direction, is shown in Fig. 1. XRD peaks are very narrow, which indicates the long-range periodicity of the lattice structure along the wire. The main scattering peaks are labeled. Since the position of these peaks correspond within experimental resolution with those for the bulk we obtain that the crystalline structure is rhombohedral. Bismuth expands significantly upon cooling and is stressed by the matrix walls. However, our XRD spectrum shows no shifts in the peak position indicating little strain. We further conclude that the wires crystalline direction is oriented preferentially with the trigonal axis along the wirelength because of the prominence of the (003), (006) and (009) in comparison to the (102) peak. It is for this orientation that bulk Bi has the highest figure of merit..

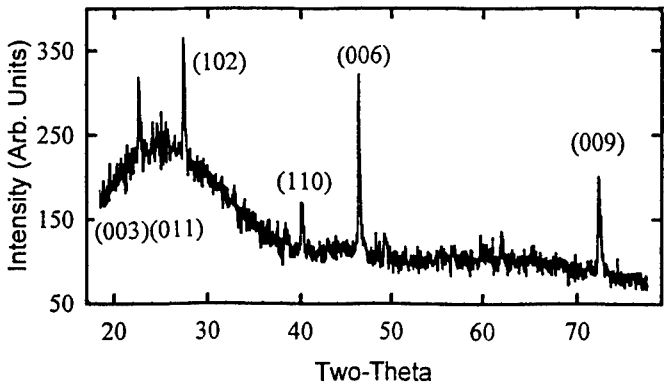

Fig. 1. XRD spectra of Bi in a 200 nm diameter wire array. The peaks are labeled with the Miller indices of the corresponding lattice planes.

With a view at thermoelectric applications we looked for a way to minimize the electrical and contact resistance. The method that we have used is illustrated in Fig. 2.. Electrical contact was made via copper leads attached to copper electrodes. The space between the electrodes and the Anopore, as well as the Anopore channels, was injected with molten Bi. We also show in Fig. 2 a reference sample of pure Bi prepared in the same manner. The sample resistance was measured using four terminal a.c. techniques. The contact resistance of these devices is estimated to be less than 1 mΩ.

Bi wires of diameter $d>>d_c$, such as ours, can be considered to be made of a semimetal where the overlap is modified only a little from the bulk value of 40 meV[10]. The resistivity is presented in Fig. 3. At 300 K the resistivity of the composite is roughly 3.0 mΩ. Since the wire array area is 0.03 square-cm we obtain the composite resistivity is 10^{-2} Ω-cm. However, the Anopore filling fraction is 0.5. Therefore, the room temperature resistivity of Bi in the channels ρ is 5×10^{-3} Ω-cm. Since the bulk resistivity is 1.1×10^{-4} Ω–cm for bulk samples for which the trigonal axis is oriented perpendicular to the wire direction[11], the resistance of the room temperature resistivity of the Bi nanowire to that of the bulk is 45. The ratio r of the room temperature resistance to that at 4 K is approximately 2. The resistivity of our sample is shown in Fig. 3. Most interesting is the wide plateau at around 40 K.

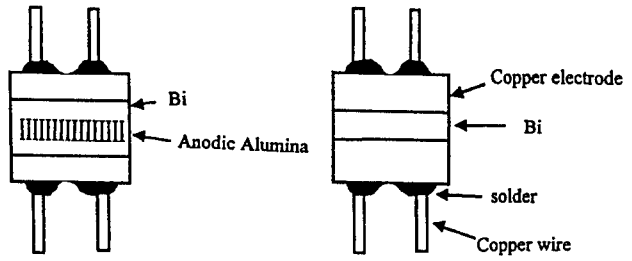

Fig. 2. Four contact devices used in this work. (a) Bi injected Anopore is sandwiched between two copper electrodes that serve as contacts using Bi. (b) Bi between the two copper electrodes.

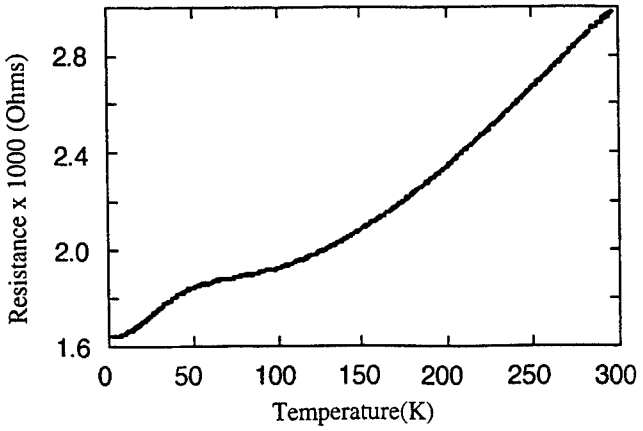

Fig. 3. Resistance as a function of temperature.

We have also measured the magnetoresistance MR = R(T, H) -R(T, 0), where R(T,H) is the resistance at a given temperature and magnetic field, up to a field of 3 T. This is shown in Fig. 4. MR/R(T,0) is more than 75 at 4 K and 3 T. It should be noted that the MR is positive. The configuration is very close to transverse but we have found that the sample was miss-aligned by 20° after the experiment was concluded. The transverse MR of wires is different from that of bulk Bi which exhibits a $B^{1.6}$ dependence in the high magnetic field range[12]

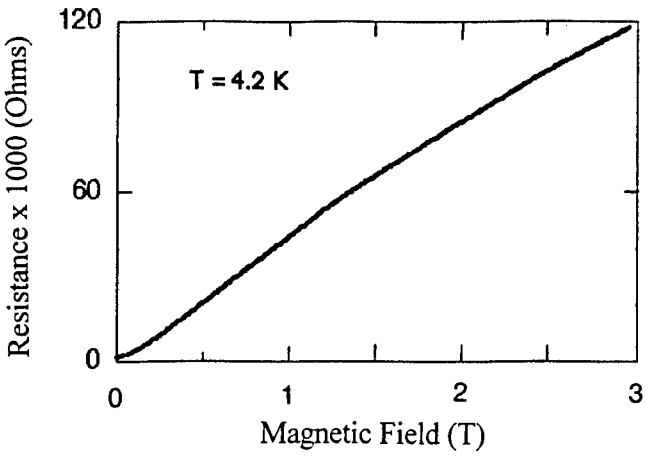

Fig. 4.
The magnetoresistance for T=4.2 K.

We can look at the resistivity as a manifestation of wall scattering. Using Sondheimer[13] relation, $\rho_{wire}/\rho_{Bulk} - 1 = ((1-P)/(1+P))\, l_{Bulk}/d$, where P is the fraction of carriers that are being reflected specularly and l_{Bulk} is the mean free path in the bulk at a given temperature. Taking l_{Bulk} to be 100 μm at 4.2 K we obtain that P~0.9. Gurvitch correctly points out that P increases in the presence of size quantization. He proposed this mechanism for the resistance plateau at 40 K. However, we are not aware of a theoretical calculation of this effect. A recent paper, Liu, Chien, and Searson[14], present magnetoresistance (H<6T) measurements of Bi wire arrays (200 nm<d<2 μm) prepared using an electrochemical technique. In their interpretation they adhere to Gurvitch's view.

Another interpretation is that the low temperature drop in the resistivity as a manifestation of disorder in a 1-D conductor or weak localization, where disorder is introduced by the wall scattering.. It is clear that this is only an approximation since $\lambda_F < d$. However, evidence of weak localization have been found in all dimensionalities, and in particular in 2D films and also thick films. It is known that :

$$R(T,H) = R_{Drude} + \Delta R_{loc}(T,H) + \Delta R_{Int}(T) \qquad (1)$$

Here R_{Drude} is the classical scattering . $\Delta R_{loc}(T,H)$ and $\Delta R_{Int}(T)$ are the quantum corrections due to disorder. Whereas the first term is negative and H-dependent, the latter term is positive. Fitting our

experimental data is beyond the scope of this paper but the field dependence is reminiscent of the data for thin Bi films[7] which have been interpreted in terms of this model. Weak localization efects are not restricted to thin films and the theory has been extended to 1-D wires also. S. Wind et al [15] calculated the localization contribution to the magnetoresistance of 1-D wires, including spin-orbit effects, by treating the magnetic field as a perturbation. Typically one finds $d < l_e << l_\phi$, that is the electron are transported by collisions with the walls without energy loss as in an electron waveguide. However, we are not aware of a theoretical calculation of these effects for semiclassical ($d > \lambda_F$) wires in the presence of strong size effects and we cannot make a careful estimate. Also, such analysis is beyond the scope of this experimental paper.

The magnetoresistance is very large. We have already presented the magnetoresistance of wire arrays at very small fields (0.02 T) in a previous publication[16]. We have observed that 1 T field changes the metallic (dR/dT>0) character of the resistance, for one where (dR/dT<0). This is shown in Fig. 5.

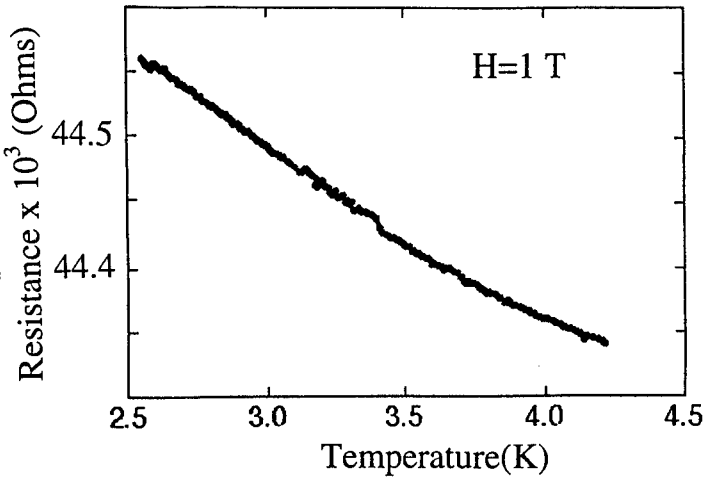

Fig. 5. Resistance as a function of temperature in the presence of a large magnetic field (H= 1 T).

We have recently observed that similar effects are at play in the composite formed by 6 nm wire diameter Bi wires in a porous Vycor glass matrix [17].

Technical assistance was provided by W. Fernando, S.J.. The work of T.E.H was supported by the Army Research Office through DAA H04-95-1-0117 and by the National Science Foundation through DMR-9632819. M.J.G. was supported in part through Research Corporation grant RA0246. C.F.'s research was supported by the Division of Materials Research of the National Science Foundation.

CONCLUSION

We have prepared Bi wire arrays using the high-pressure injection of the melt. Low contact resistance "devices" of contact resistances lower than 1 mΩ have been prepared. 200 nm diameter Bi wires are "metallic", that is dR/dT>0, between 2 K and room temperature. A discussion in terms of quantum size effects and weak localization is presented that suggest that Bi nanowires are good candidates for electron waveguides. Clearly smaller diameter wires are highly desirable as thermoelectric materials and we plan to study wire arrays of d= 30 nm and 15 nm.

REFERENCES

1. V.N. Lutskii, JETP Lett. **2**, 245 (1965).
2. Z. Zhang, J.Y. Ying, and M.S. Dresselhaus, J. Mater. Res. **13** 1745 (1998).
3. E.N. Bogacheck, A.G. Scherbakov, and U. Landman, in Nanowires, edited by P.A. Serena and N. Garcia (Kluwer, Dordrecht, 1997).
4. L.D. Hicks and M.S. Dresselhaus, Phys. Rev. **B47**, 16631 (1993).
5. A. Casian, I. Sur, A. Sandu, H. Scherrer, and S. Scherrer, Proc of the 1997 International Conference on Thermoelectrics, edited by A. Heinrich (IEEE, 1997), pp. 442.
6. M. Gurvitch, J. Low. Temp. Phys. **38**, 777 (1980).
7. Y.F. Komnik, E.I. Bukhshtab, and Y.V. Nikitin, Sov. J. Low. Temp. Phys. 7, 656 (1982). Y.F. Kommik, E.I. Bukhshtab, A.V. Butenko, and V.V. Andrievsky, Solid State Comm., **44**, 865 (1982).
8. Y. Imry in Introduction to Mesoscopic Physics (Oxford University Press, Oxford, 1997).
9. C.A. Huber, T.E. Huber, M. Sadoqi, J.A. Lubin, S. Manalis, and C.B. Prater, Science **263** 800(1994).
10. The new band overlap can be estimated from $\Gamma=\Gamma_B(1-(d_c/d)^2)$, where d_c is taken to be 30 nm and the bulk phase overlap Γ_B is 40 meV. For d= 200 nm we obtain that Γ= 39 meV, which is not very different from the bulk value. In a first approximation this difference is neglected.
11. H.J. Goldsmid in Electronic Refrigeration, 2nd edition (Pion Limited, London, 1986).
12. L.A. Falkovskii, Sov. Phys. Uspekii **94**, 1 (1968).
13. E.H. Sondheimer, Proc. Phys. Soc. London, **A65**, 561 (1952).
14. K.Liu, C.L. Chien, and P.C. Searson, Phys. Rev. **B58**, 14681 (1998). It is not clear to us if the samples used in this paper, exhibiting a non-metallic resistance, dR/dT<0, can be compared to the samples presented in the present paper, or Gurvitch's single wire sample, that exhibit "metallic" behaviour (dR/dT>0).
15. S. Wind, M.J. Rooks, V. Chandrasekhar, and D.E. Prober, Phys. Rev. Lett. **57**, 633 (1986).
16. T.E. Huber, M.J. Graf, and C.A.Foss, submitted to the Proceedings of the 1998 International Conference in Nagoya , Japan. (K. Koumoto and S. Yamaguchi, Eds.).
17. T.E. Huber and M.J. Graf, submitted to Phys. Rev..

Solid State Chemistry Approach to Advanced Thermoelectrics. Ternary and Quaternary Alkali Metal Bismuth Chalcogenides as Thermoelectric Materials

Mercouri G. Kanatzidis[(1)], Duck-Young Chung[(1)], Lykourgos Iordanidis[(1)], Kyoung-Shin Choi[(1)], Paul Brazis[(2)], Melissa Rocci[(2)], Tim Hogan[(3)] and Carl Kannewurf[(2)]

(1) Dept. of Chemistry, Michigan State University and Center for Fundamental Materials Research, East Lansing, MI 48824. (2) Dept. of Electrical Engineering and Computer Science Northwestern University, Evanston, Illinois, 60208. (3) Dept. of Electrical Engineering, Michigan State University, East Lansing, MI 48824.

Abstract

Our exploratory research to identify new promising candidates for next generation thermoelectric applications has produced several interesting new materials which are briefly described here. We present their compositions, solid state structures, properties and charge transport behavior. The compounds $CsBi_4Te_6$, β-$K_2Bi_8Se_{13}$, $Ba_4Bi_6Se_{13}$, $Eu_2Pb_2Bi_6Se_{13}$, $KBi_{6.33}S_{10}$, $Eu_2Pb_2Bi_4Se_{10}$, $Ba_2Pb_2Bi_6S_{13}$ and $K_{1.25}Pb_{3.5}Bi_{7.25}Se_{15}$ are particularly noteworthy.

Introduction

The subject of thermoelectric materials is now a growing and active field primarily due to several new concepts and also because of a recognized technological need.[1,2] Several new ideas and approaches to the design of improved thermoelectric materials have stimulated a resurgence of interest in this old field.[3,4,5] Although there are many different avenues taken by different groups around the world,[6,7,8] here we discuss our approach to new thermoelectric materials,[9] exploring complex chalcogenide materials using newly developed solid state synthetic techniques for these systems.[10]

An efficient thermoelectric device is fabricated from two materials, one n-type and the other a p-type conductor. Each material is separately chosen to optimize the figure of merit, ZT, where $Z = S^2\sigma/\kappa$; T is the temperature, S the thermopower, σ the electrical conductivity, and κ the thermal conductivity. All three of these properties are determined by the details of the electronic structure and scattering of charge carriers (electrons or holes) and thus are not independently controllable parameters.[11] κ has a contribution from κ_{ph}, the phonon thermal conductivity as well as the carrier thermal conductivity κ_{el}. In order to carry a heat flux of reasonable magnitude, moderate to high carrier densities are needed (small band gap semiconductors with carrier densities of 10^{18}-10^{19}/cm^3 to metals at 10^{23}/cm^3). When the carrier densities approach 10^{23}/cm^3, κ_{el} usually is much larger than κ_{ph}. In that case, the ratio κ/σ is given approximately by the Wiedemann-Franz law, $\kappa/\sigma = L_oT$, where L_o is a constant.[12] Because cancellations in thermoelectric power can occur when both electrons and holes are dominant (i.e. $S = S_e + S_h$) one needs materials with preferably one type of carrier. The material used in commercial devices today is $Bi_{2-x}Sb_xTe_{3-y}Se_y$ alloy (thermopower of $\pm$ 220 μV/K[13]), and its ZT value at room temperature is ~0.9-1.0. Improving device performance means improving ZT or increasing S while keeping moderate to large carrier densities of one carrier type. Significant improvements in thermoelectric conversion efficiencies could occur if bulk materials of similar thermal conductivity with thermopowers of 300 to 400 μV/K and electrical conductivities of 1000-2000 S/cm were found.

We seek to identify new materials with higher figures of merit than those available today. A desirable feature for these materials is a higher compositional and structural complexity than Bi_2Te_3. Boltzmann transport theory describes both electrical and thermal transport in the vast majority of solids. This theory provides a general understanding of the thermopower that is expressed in the Mott equation:

Mat. Res. Soc. Symp. Proc. Vol. 545 © 1999 Materials Research Society

$$S = \frac{\pi^2}{3} \cdot \frac{k^2 T}{e} \cdot \frac{d ln\sigma(E)}{dE} \Bigg|_{E=E_f} \qquad \text{Eq. (1)}$$

$\sigma(E)$ is the electrical conductivity determined as a function of band filling or Fermi energy, E_F. If the electronic scattering is independent of energy, then $\sigma(E)$ is just proportional to the density of states at E. In the general case, S is a measure of the difference in $\sigma(E)$ above and below the Fermi surface, specifically through the logarithmic derivative of σ with E. Since the thermopower of a material is a measure of the asymmetry in electronic structure and scattering rates near the Fermi level, we desire to produce complexities in either or both in a small energy interval (a few kT) near E_F.

Structural and compositional complexity can result in corresponding complexities in the electronic structure, which may produce the required asymmetry in $\sigma(E)$ (see eq. (1)) to obtain large thermopowers. The phonon contribution to the thermal conductivity can also be lowered by such structural complexity, by choosing heavy elements as components of the material and by choosing combinations of elements that normally make moderate to weak chemical bonds. Since the known materials that are used in thermoelectric devices are chalcogenide compounds, we are searching for more complex semiconducting compounds of this type.

A significant development is the emergence of materials that conduct electricity like a crystalline solid but heat like a glass. In these materials a weakly bound atom or molecule 'rattler' is used to lower the thermal conductivity of the solid without severely affecting electronic conduction, thus leading to improved thermoelectric efficiency.[14,15] The class of chalcogenide materials described here fall under this description because, as it will become apparent below, they are made of three-dimensional or two-dimensional bismuth-chalcogenide frameworks, stabilized by weakly bonded alkali atoms which reside in cavities, tunnels or galleries of the framework. These electropositive atoms almost always possess the highest thermal displacement parameters in the structure, which is evidence that a certain degree of "rattling" is going on. This feature is very important in the low observed thermal conductivities of these materials.

Ternary and Quaternary Bismuth Chalcogenides with Alkali- and Alkaline Earth Metals

For chalcogenide materials discovery, the use of molten alkali metal polychalcogenides, of the type A_2Q_x (A=alkali metal, Q=chalcogen) as solvents is very appropriate as we and others have demonstrated already.[10] Low melting A_2Q_x fluxes remain nonvolatile over a wide temperature range, and so once above the melting point, reaction temperatures can be varied considerably without concern for solvent loss. Polychalcogenide fluxes are highly reactive towards metals because they are very strong oxidants. Reactions between metals and molten A_2Q_x are performed *in situ*. The advantage of the flux method is that it allows the reaction system to choose where it wants go (in a kinetic or thermodynamic sense) without attempting to force upon it a certain stoichiometry or structure. Provided the temperature and time are appropriate, the reaction system has the opportunity (and all the ingredients) to form new phases. The benefit of this synthetic approach becomes apparent from the unusual compositions often found for the new materials which most certainly could not have been predicted *a-priori*.

What are the empirical guidelines with which we have to design thermoelectric materials and how do we go about choosing a particular system for exploration? We know that heavy atoms are desirable since they tend to give rise to low frequency phonons which help slow down heat transfer through a material leading to low thermal conductivity. The fact that Bi_2Te_3 is the best material known to date suggests that it combines many of the necessary features for high figure of merit. If there is something special about bismuth in giving rise to simultaneously high electrical conductivity and thermoelectric power, it could be manifested in other compounds of bismuth as well. This suggests a research direction where we could explore other, more complex,

chalcogenides of bismuth in the hope that some (or all) of the key properties would be superior to those of Bi_2Te_3. Further, structurally and compositionally more complex bismuth chalcogenides would, most likely, have a low lattice thermal conductivity. This is because a structure with a large unit cell is expected for such materials, which would decrease the acoustic phonon mode velocities that are responsible for the transfer of heat in materials. The relatively weak Bi-Te bonding and the large atomic masses contribute as well to the low phonon velocities. As an additional guideline we choose the elements in the framework so that they have similar electronegativities. A binary framework in which the atoms differ little in electronegativity can support charge carriers with high mobilities. Therefore, we aim to perform exploratory synthesis in this region of the periodic table involving the elements Bi, Sb, Se, Te etc.

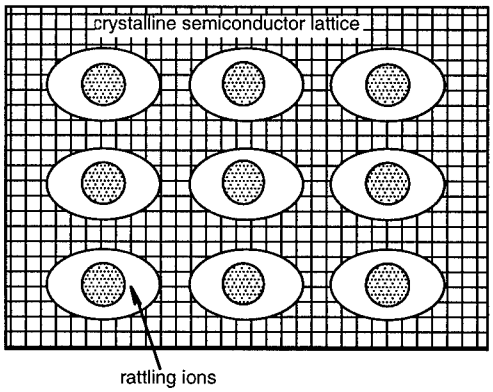

Figure 1. Schematic representation of a material with a crystalline semiconducting framework with cages, or tunnels in which electropositive or neutral atoms, with weak bonds to the framework, reside. The weak interactions give rise to very soft phonon modes due to "rattling" type motions which scatter the thermal phonons traveling through the material. If the charge carriers can move through the crystalline framework and around the cages or tunnels, without much scattering, then most of the necessary ingredients are there for a good thermoelectric material.

While there are several approaches to minimizing κ_{ph} the most intriguing is the one associated with the concept of "phonon glass electron crystal" which was introduced by Slack as the limiting characteristic for a superior thermoelectric.[16] Because $\kappa = \kappa_{el} + \kappa_{ph}$, one way to increase ZT is to minimize κ_{ph}. A material which is a "phonon glass electron crystal" features cages (or tunnels) in its crystal structure inside which reside atoms small enough to "rattle", see Figure 1. This situation produces a phonon damping effect which results in dramatic reduction of the solid's lattice thermal conductivity. If the atomic orbitals of the "rattling" ions do not participate in the electronic structure near the Fermi level, the mobility of carriers throughout the rest of the structure may not be substantially affected, potentially giving rise to high electrical conductivity as well as thermopower. The presence of alkali metals in the structures of ternary and quaternary bismuth chalcogenides induce the stabilization of Bi-chalcogen frameworks with cages or tunnels which accommodate the charge-balancing alkali atoms. The set of guidelines outline above is not complete and there are other selection criteria. Furthermore it is unclear at this state of development of this field, if the above criteria are either sufficient or even necessary for the design of new thermoelectric materials. This fact renders the synthetic efforts in this area somewhat empirical.

A Promising Ternary Bismuth Telluride. The low dimensional phase $CsBi_4Te_6$ seems promising.[17,18] The compound is a layered anisotropic material which grows in a needle type morphology. It is composed of anionic $[Bi_4Te_6]$ layers alternating with layers of Cs ions, see Figure 2. The compound is in essence a reduced version of Bi_2Te_3. Apparently the addition of

one electron per two equivalents of Bi_2Te_3 does not form a formal intercalation compound, but causes a rather large reorganization of the bismuth telluride framework and reveals an inability to delocalize such electrons in the framework. The structure of $CsBi_4Te_6$ departs rather drastically from that of the binary compound. The added electrons then localize on the Bi atoms forming Bi-Bi bonds. The presence of these bonds is very unusual in bismuth chalcogenide chemistry and it is not clear whether they play a role in the enhanced thermoelectric properties of the material. The Bi coordination geometry is octahedral.

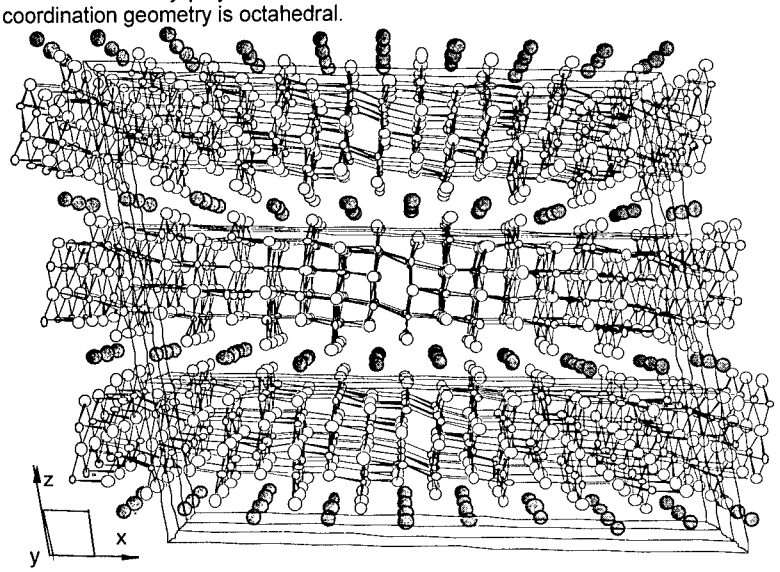

Figure 2. The structure of $CsBi_4Te_6$ looking down the b-axis direction. Large open circles are Te atoms. Large shaded circles are Cs atoms.

Crystals of $CsBi_4Te_6$, prepared with no attempt to deliberately dope them, have high room temperature electrical conductivities ranging from 900- 440 S/cm. By comparison $Bi_{2-x}Sb_xTe_{3-y}Se_y$ alloy has ~800-1000 S/cm. The room temperature thermopower ranges from 90 to 120 μV/K, lower than the 220 μV/K value typically found for optimized Bi_2Te_3. Thermal conductivity measurements on pressed pellets show values in the range 0.9-1.8 W/mK which is comparable to that of Bi_2Te_3. These values give rise to a relatively high room temperature ZT of 0.2-0.5, enough to make them good candidates for further investigations with respect to optimization via doping, solid solution work and crystal processing and growth. We are optimistic that improvements in the sample preparation of $CsBi_4Te_6$ as well as appropriate doping will result in significant ZT enhancements in this material.

Work to dope this material with various chemical impurities has begun. We investigated SbI_3, BiI_3, In_2Te_3 and excess Te in amounts varying from 1-4 % by wt. These are very heavy doping levels by the standard of Si or GaAs doping, but at this stage we wanted to explore the sensitivity of the material to such chemical perturbations. We are also investigating much smaller doping levels. These dopants were chosen with the purpose of placing halide atoms in the Te sites (to produce n-type doping) and In atoms in the Bi sites (to produce p-type doping). Although doping with these agents seems to occur, it is currently not clear what sites in the crystal structure are being affected. In fact the results with SbI_3 and BiI_3 have been surprising because the materials seem to be consistently p-doped rather than n-doped. This observation is not consistent with iodine atoms occupying Te sites but instead is in agreement with what would be expected if Sb atoms were replacing Te atoms. The Sb atoms having only five electrons would introduce a hole in the valence Te-based band in which each Te atom brings six electrons. In_2Te_3 dopes the materials

n-type. Also depending on the amount of doping all values of room temperature thermopower between 150 and -110 μV/K have been observed, see Figure 3. This is very encouraging because it shows that the $CsBi_4Te_6$ is subject to considerable doping manipulation, much like Bi_2Te_3, and more research is warranted to find the proper dopands for maximum ZT. More detailed studies regarding this compound can be found elsewhere in this volume.[19]

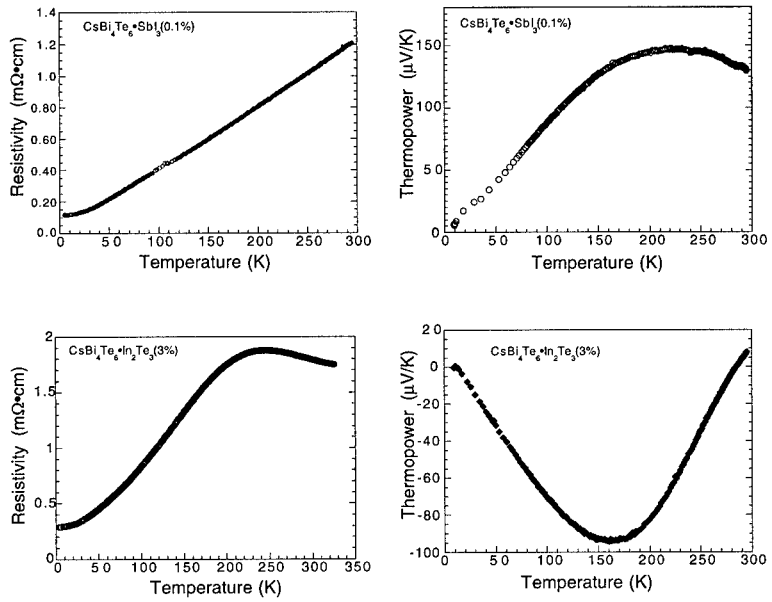

Figure 3. shows variable temperature electrical conductivity and thermoelectric power of a p-type and n-type doped crystal.

A band structure calculation for $CsBi_4Te_6$ would be insightful in helping us understand at a deeper level the electronic properties of this material. Such work is now in progress.

Ternary and Quaternary Bismuth Chalcogenides

Several structure types have been discovered in this laboratory which exhibit promising enough thermoelectric properties and thermal conductivity to deserve further investigations concerning their chemical modification to generate isostructural derivatives as well as doping with judiciously selected impurities. Table 1 summarizes some of these new compounds along with some of the property data obtained thus far on them. Given the rather large list of prospective materials, we have only had the time to extensively investigate a few of them. In this paper we will highlight some of these systems and comment on the prospect of obtaining very high ZTs.

Materials with the $Sr_4Bi_6Se_{13}$ Structure. The $Sr_4Bi_6Se_{13}$ structure type combines elements from two different structure types which are interconnected to form a three-dimensional network. These structural elements are fragments (e.g. blocks, layers, rods etc) excised out of the Bi_2Te_3-(NaCl-type) and CdI_2-structure types. The fragments then connect to form tunnels filled with eight-coordinate Sr^{2+} cations, see Figure 4. The Sr^{2+} ions in the structure of $Sr_4Bi_6Se_{13}$ occupy high coordination sites (i.e. coordination greater than six) while the $[Bi_6Se_{13}]^{4-}$ framework features only octahedral (albeit distorted) Bi^{3+} centers. In compounds of this type, the alkali and alkaline earth atoms interact with the bismuth chalcogenide framework via weak ionic bonds. The

sizes of the tunnels in which they reside are often larger than the ionic size of the alkali metals and this gives rise to either vibrational motion or slight positional disorder.

Table 1. Selected Bismuth Chalcogenide Compounds with Promising Thermoelectric Properties

Compound	Space Group	E_g·RT (eV)	σ_{RT} (S/cm)	S_{RT} (μV/K)	κ_{RT} (W/m·K)	mp (°C)
Bi_2Te_3	R-3m	*0.15*	*900*	*±210*	*1.4 - 1.6*	*585*
$CsBi_4Te_6$	C2/m	0.11	700 - 2440	110	0.9 - 1.9	545
$Rb_{0.5}Bi_{1.83}Te_3$	Cmcm	< 0.03	800	-40	—	540
β-$K_2Bi_8Se_{13}$	$P2_1/m$	0.59	250	-200	0.8 - 1.6	672
$K_{2.5}Bi_{8.5}Se_{14}$	$P2_1/m$	0.56	1600	-6	1.2 - 2.3	692
$Eu_2Pb_2Bi_4Se_{10}$	P nma	<0.2	380	-30	—	—
$Ba_2Pb_2Bi_6S_{13}$	$P2_1/m$	-	-	-	-	-
$Sr_2Pb_2Bi_6Se_{13}$	$P2_1/m$					
$Ba_{4-x}Bi_{6+0.66x}Se_{13}$	$P2_1/m$	<0.2				
$Eu_2Pb_2Bi_6Se_{13}$	$P2_1/m$	<0.2	280-5362	-35		
$KBaBiSe_3$	Fm-3m	0.78	—	—	—	764
$KPbBiSe_3$	Fm-3m	0.58	—	—	—	923
$KPbBiTe_3$	Fm-3m	—	—	—	—	—
$CsPb_2Bi_3Te_7$	Cmcm	< 0.05	965	-20	—	582
$RbPb_2Bi_3Te_7$	Cmcm	< 0.05	1270	-20	—	597
$BaBiTe_3$	$P2_12_12_1$	0.28, 0.42	42	205	0.63	644(dec)
$K_{1.25}Pb_{3.5}Bi_{7.25}Se_{15}$	$P2_1/m$	0.53	260	-150	—	685
$KBi_{6.33}S_{10}$	P nma		100-300	-30 to -120	1.2	—

The structure of β-$K_2Bi_8Se_{13}$ is closely related to that of $Sr_4Bi_6Se_{13}$[20] by replacing two Sr^{2+} ions with two K^+ ions and the remaining two Sr^{2+} ions with two Bi^{3+} ions. These substitutions are isoelectronic on average and do not require compositional changes in the "Bi_6Se_{13}" part of the compound. Therefore an alternative way of representing this phase is $(K,Bi)_4Bi_6Se_{13}$. The high coordination sites of Bi in the structure of β-$K_2Bi_8Se_{13}$ are distinct from the rest of the metal sites which are essentially octahedral. The high coordination sites (i.e. Sr^{2+} sites) are amenable to a substantial degree of chemical substitution provided cations of similar size are used and electroneutrality is preserved. Another interesting substitution here is the replacement of the four Sr^{2+} ions in $Sr_4Bi_6Se_{13}$ with two Ba^{2+} ions and two Pb^{2+} ions, or the replacement of two Sr^{2+} ions with two Pb^{2+} ions. This results in the isostructural compounds $Ba_2Pb_2Bi_6S_{13}$ and $Sr_2Pb_2Bi_6Se_{13}$ as well as the solid solution compounds $Ba_{2-x}Pb_{2+x}Bi_6S_{13}$ and $Sr_{2-x}Pb_{2+x}Bi_6Se_{13}$. Interestingly, the selenide analog $Ba_{2-x}Pb_{2+x}Bi_6Se_{13}$ has not been observed yet, instead a different structure type is adopted related to that of $A_{1+x}Pb_{4-2x}Sb_{7+x}Se_{15}$, see below.

A characteristic feature in the K-Bi-Q materials is that whenever high coordination sites are found in the lattice (i.e. >6) a positional K/Bi disorder is almost always encountered. This is attributed to the similar ionic sizes of K^+ and Bi^{3+} in high coordination. The corresponding sulfide $K_2Bi_8S_{13}$ also adopts the same structure type. Furthermore the corresponding Sb analogs of β-$K_2Bi_8Se_{13}$ are also known. The great variety of analogs available makes these systems excellent for an enormous variety of chemical manipulation while at the same time preserving the structure. This is very desirable when one is engaged in ZT optimization studies.

The electrical properties of β-$K_2Bi_8Se_{13}$ were measured from single crystal samples and polycrystalline ingots. Up until very recently, the highest room temperature conductivity value obtained for single crystals of β-$K_2Bi_8Se_{13}$ was 250 S/cm with a weak negative temperature dependence consistent with a semi-metal or a narrow band-gap semiconducting material. Recently, however, we have refined the crystal growth procedure and have obtained higher quality n-type samples with room temperature conductivity of ~550 S/cm and a room thermopower of -220 μV/K, see Figure 5. The thermopower is trending to high values above room temperature suggesting a maximum ZT at higher temperatures.

The $K_2Bi_8S_{13}$ is also promising with maximum conductivity and thermopower of ~200 S/cm and ~90 μV/K, respectively.[23] These are unoptimized values, and we believe they can be greatly improved by further processing and systematic doping studies. Preliminary results with polycrystalline samples indicate that $K_2Bi_8S_{13}$ have carrier concentrations of $3x10^{20}$. Doping experiments with SbI_3 indicate that the conductivity type of $K_2Bi_8S_{13}$ can be controlled to be n-type with room temperature thermopowers reaching -100 μV/K. Further doping experiments are in progress.[21]

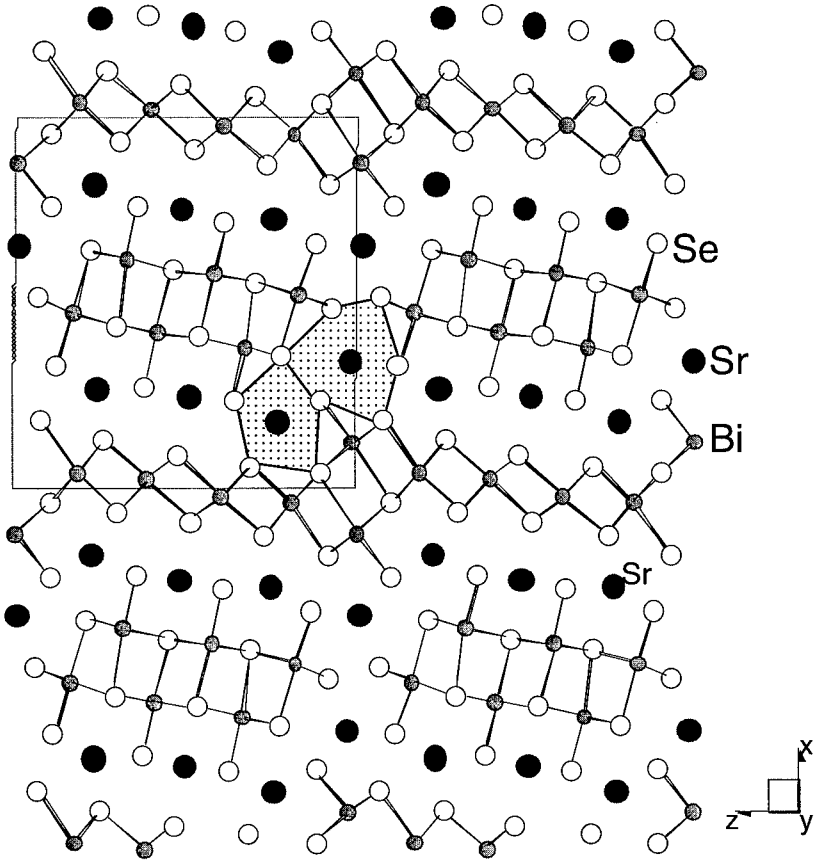

Figure 4. Projected view of the structure of $Sr_4Bi_8Se_{13}$. Large gray circles represent Sr ions, open circles represent selenium atoms. Shaded areas highlight the location of high coordination sites (>6) which are subject to chemical substitution.

Despite the metal-like temperature dependence of the electrical conductivity and thermopower of β-$K_2Bi_8Se_{13}$ the valence precise character indicated by their structure and formulation suggest they should be semiconductors. Indeed, diffuse reflectance spectroscopy on β-$K_2Bi_8Se_{13}$ at room temperature reveals the presence of well defined electronic transitions associated with a band gap of 0.59 eV.

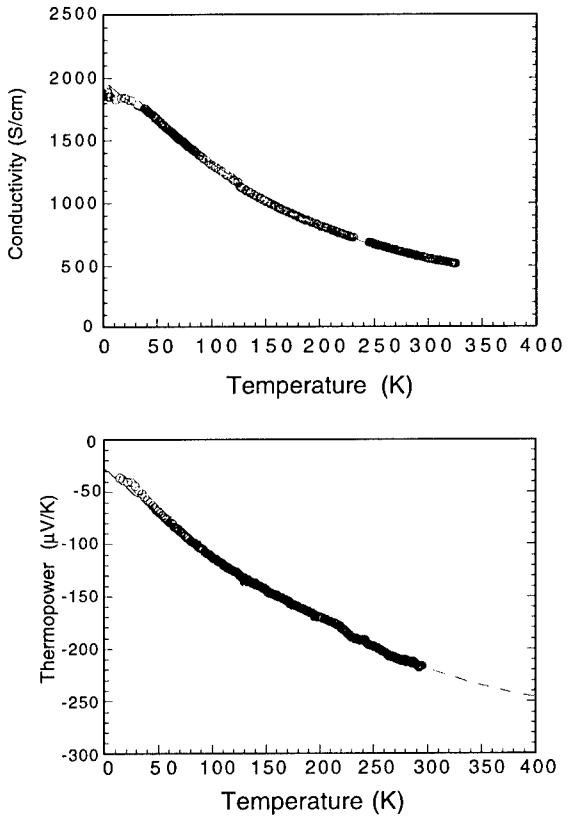

Figure 5. Electrical conductivity and thermoelectric power of a single crystal of β-$K_2Bi_8Se_{13}$.

The room temperature thermal conductivity of β-$K_2Bi_8Se_{13}$ (measured on polycrystalline ingot) does not vary much from sample to sample and lies around 1.3 W/m·K. It is similar to that of optimized $Bi_{2-x}Sb_xTe_{3-y}Se_y$ alloy ~ 1.3 W/m·K. These results demonstrate that it is possible to achieve lower thermal conductivity in ternary compounds with complex compositions and crystal structures compared to corresponding high symmetry binary compounds. Another reason for the very low thermal conductivities of these compounds may be the presence of "rattling" alkali atoms in tunnels which are only electrostatically interacting with Se atoms on the tunnel walls. This means that these atoms are loosely bound and the fact that the average isotropic thermal displacement (ADP) parameters of the K atoms are the largest in the unit cell of both compounds corroborates this. This is in agreement with Slack's suggestion of an "electron-crystal phonon-glass" being a key feature of a thermoelectric material. Loosely bound atoms with large (ADP) parameters scatter phonons much more strongly than electrons, producing a glass-like thermal conductivity without affecting the carrier mobility which is associated with the covalently bound part of the structure that is the $[Bi_xSe_y]^{n-}$ framework. The thermal conductivity of β-$K_2Bi_8Se_{13}$ in the temperature range of 4-300 K is significantly lower than that of the isostructural compound

$K_2Bi_8S_{13}$, which is consistent with the fact that the heavier Se atoms soften the lattice phonons thereby suppressing heat transport in the material. Also in the sulfide the K^+ ions experience smaller cages in which to rattle which is brought about by the shrinking of the bismuth chalcogenide framework. This causes "hardening" of the rattling modes. Using the measured values of the electrical resistivity in conjunction with the Wiedemann-Franz law, the maximum possible values of the κ_{el} contribution in both cases were estimated to be less than 10 % of κ_{total}. Thus, essentially all heat in β-$K_2Bi_8Se_{13}$ is carried by lattice phonons.

There is no doubt that the compound β-$K_2Bi_8Se_{13}$ is quite promising as a thermoelectric material. Based on the values σ~550 S/cm, S~-200 μV/K and κ_{ph} ~1.3 W/m·K, a room temperature ZT value of ~0.5 can be estimated. By comparison *optimized* Bi_2Te_3 has a ZT of ~0.9. The better performance of Bi_2Te_3 alloy derives mainly from its higher electrical conductivity (σ_{RT} ~ 950 S/cm) since the thermopower of β-$K_2Bi_8Se_{13}$ is comparable, while its thermal conductivity is equal or lower. Another dimension in the problem of ZT optimization comes from solid solutions of the type $K_xBi_y(Se,S)_z$ and $K_x(Bi,Sb)_ySe_z$. This type of alloying is expected to lower the κ_{ph} further and increase the thermopower by increasing energy band-gap.

The compounds $Ba_4Bi_6Se_{13}$ and $Eu_2Pb_2Bi_6Se_{13}$ are also isostructural to $Sr_4Bi_6Se_{13}$, again deriving from substitutions on the high coordination sites of the prototypical structure. The remaining $[Bi_6Se_{13}]^{4-}$ framework is the same. Such modifications are useful in this research because they provide us with the ability to change the thermoelectric properties a great deal without changing the structure type. This should eventually help us learn more about structure-property relationships.

Preliminary charge transport data shows that $Ba_4Bi_6Se_{13}$ is obtained highly doped when first synthesized, with a room temperature conductivity and corresponding Seebeck coefficient of 2500 S/cm and -32 μV/K. Not surprisingly, this degree of doping is not optimum for maximum ZT. The analogous $Eu_2Pb_2Bi_6Se_{13}$ is also not optimally doped with room temperature conductivity and Seebeck coefficient of 300 S/cm and -37 μV/K, see Figure 6. Both of these compounds show n-type charge transport, which is consistent with a number of possibilities including Se deficiency, Se occupation of Bi sites or presence of accidental n-doping impurities. Systematic doping studies on these materials to find out whether the compounds can be doped p-type and to explore the prospects for optimization would be interesting.

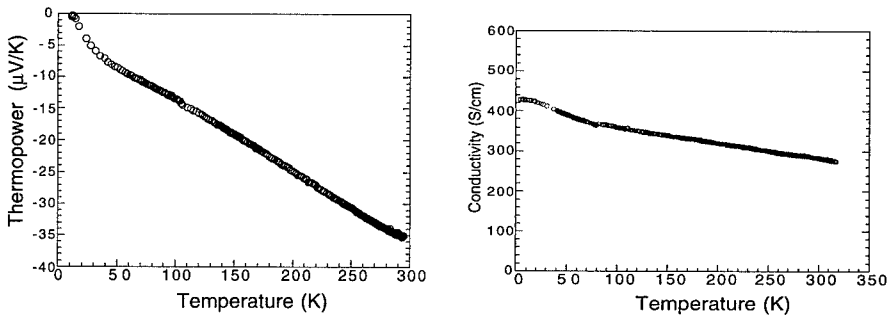

Figure 6. Thermoelectric power and electrical conductivity and as a function of temperature for a single crystal of $Eu_2Pb_2Bi_6Se_{13}$.

Materials with the Cosalite Structure. The structure of $KBi_{6.33}S_{10}$ is closely related to that of the mineral cosalite $Pb_2Bi_2S_5$.[22] The relationship becomes more apparent if the formula is doubled and written as $Pb_2Pb_2Bi_4S_{10}$ and then compared to the rearranged formula of ($\square_{0.67}K_1Bi_{0.33}$)$Bi_2Bi_4S_{10}$ ($\square$=vacancy). The structure of $KBi_{6.33}S_{10}$ is a defect cosalite type in which the high coordination positions in the lattice are occupied by a mixture of K and Bi atoms. The

$[Bi_{6.33}S_{10}]^-$ framework is made of edge-sharing BiS_6 octahedra, as shown in Figure 7. Perhaps this defect character of the structure gives rise to the observed very low thermal conductivity (for a sulfide compound) which is ~1.4 W/m-K of $KBi_{6.33}S_{10}$.

Taking as a benchmark the room temperature value of the total thermal conductivity of Bi_2Te_3 (κ= 1.7 W/m·K)[11], we note that the total thermal conductivity of $KBi_{6.33}S_{10}$[23] is actually lower. This is an important finding because $KBi_{6.33}S_{10}$, being a sulfide, is expected to possess higher thermal conductivity compared to the heavier tellurides. If controlled doping can enhance the electrical conductivity and at the same time preserve or even increase the thermopower, in the case of $KBi_{6.33}S_{10}$ we indeed might have a promising thermoelectric material. To achieve this, we need additional information regarding the transport properties including carrier concentrations and mobilities. Preliminary results with polycrystalline samples indicate that $KBi_{6.33}S_{10}$ has carrier concentrations of $3x10^{19}$.

The prospect that a bismuth sulfide compound might yield a high ZT is quite attractive even if that ZT were only as good as that of bismuth telluride alloy, because considerable weight savings could be achieved in thermoelectric devises. Sulfur is inexpensive compared to Te and Se and environmentally more acceptable.

An additional compound which deserves mention here is $Eu_2Pb_2Bi_4Se_{10}$. In this system, instead of vacancies in the high coordination sites we have full albeit mixed occupancy with Eu/Pb pairs. The $Eu_2Pb_2Bi_4Se_{10}$ exhibits very interesting charge transport properties with high room temperature values of conductivity and thermopower at 550 S/cm and -135 μV/K respectively. Figure 8 shows the temperature dependence of these properties measured on single crystal samples. The maximum in the conductivity at 150 K is not understood and needs further study. The thermopower is very linear over the entire 8K-300 K range and will probably get much higher at elevated temperatures. Thermal conductivity data are not available yet. Based on these preliminary values doping studies would be most interesting and are being pursued.

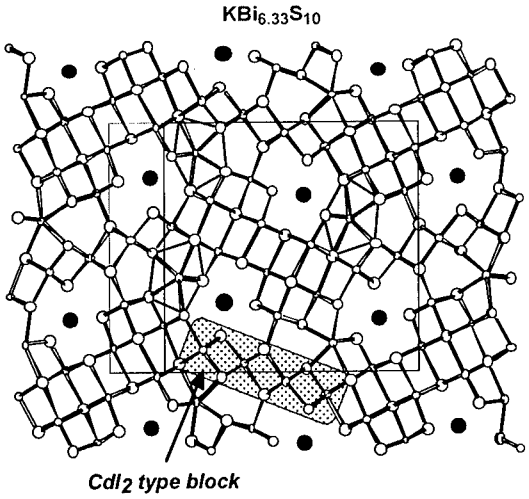

Figure 7. Structure of $KBi_{6.33}S_{10}$. The shaded areas represent the high coordination sites which are occupied by both Bi and K atoms. The CdI_2 type block is also shown. Small open circles are Bi atoms and large dark gray circles are K atoms.

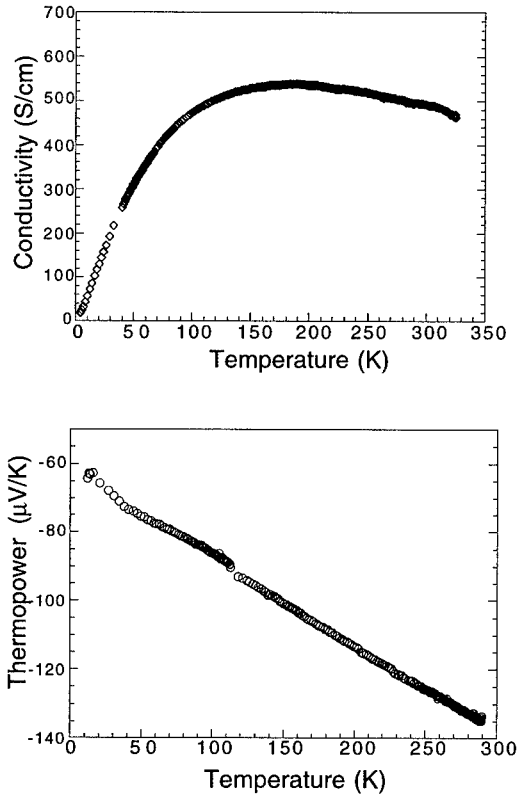

Figure 8. Four probe electrical conductivity and thermopower as a function of temperature for single crystal $Eu_2Pb_2Bi_4Se_{10}$.

The $A_{1+x}Pb_{4-2x}Sb_{7+x}Se_{15}$ Class

The new isostructural compounds, $A_{1+x}Pb_{4-2x}Sb_{7+x}Se_{15}$ (A=K, Rb; 0<x<2) and $K_{1.25}Pb_{3.5}Bi_{7.25}Se_{15}$, are closely related to β-$K_2Bi_8Se_{13}$ have recently been prepared. Figure 9 shows that these compounds also have a three-dimensional anionic framework composed of NaCl- and Bi_2Te_3-type units and K^+/Rb^+- filled channels running along the b-axis. The local environments of the alkali metal ions and sizes of the NaCl-type blocks for β-$K_2Bi_8Se_{13}$, $K_{2.5}Bi_{8.5}Se_{14}$, and $A_{1+x}Pb_{4-2x}Sb_{7+x}Se_{15}$(A=K, Rb) are exactly the same. Only the width of the Bi_2Te_3-type unit in each compound is different. In the structure of $A_{1+x}Pb_{4-2x}Sb_{7+x}Se_{15}$ the alkali atoms display the largest ADPs suggesting a certain degree of rattling motion in these sites. This suggests that the thermal conductivity of these compounds should be low.

The relationship between these compounds can easily be seen if their composition is rewritten as the sum of the atoms in the anionic framework and the alkali metal in the channel. For example, in β-$K_2Bi_8Se_{13}$, one K^+ ion is stabilized in the channel and the other K^+ ion is disordered with Bi^{3+} ions in the anionic framework. Therefore, the formula can be described as $K^+[KBi_8Se_{13}]^-$ or $K^+[M_9Se_{13}]^-$ (where M = K+Bi in the anionic framework). Similarly, $K_{2.5}Bi_{8.5}Se_{14}$ can be described as $K^+[M_{10}Se_{14}]^-$ and $K_{1.25}Pb_{3.5}Bi_{7.25}Se_{15}$ as $A^+[M_{11}Se_{15}]^-$ (M=K+Bi+Pb in the anionic

framework). Therefore, $K_{2.5}Bi_{8.5}Se_{14}$ and $A_{1+x}Pb_{4-2x}Sb_{7+x}Se_{15}$(A=K, Rb) are the results of successively adding of "MSe" unit to β-$K_2Bi_8Se_{13}$.

$$K[KBi_8Se_{13}] \xrightarrow{+MSe} K[KBi_9Se_{14}] \xrightarrow{+MSe} K[K_{0.25}Pb_{3.5}Bi_{7.25}Se_{15}]$$

$$K[M_9Se_{13}] \xrightarrow{+MSe} K[M_{10}Se_{14}] \xrightarrow{+MSe} K[M_{11}Se_{15}]$$

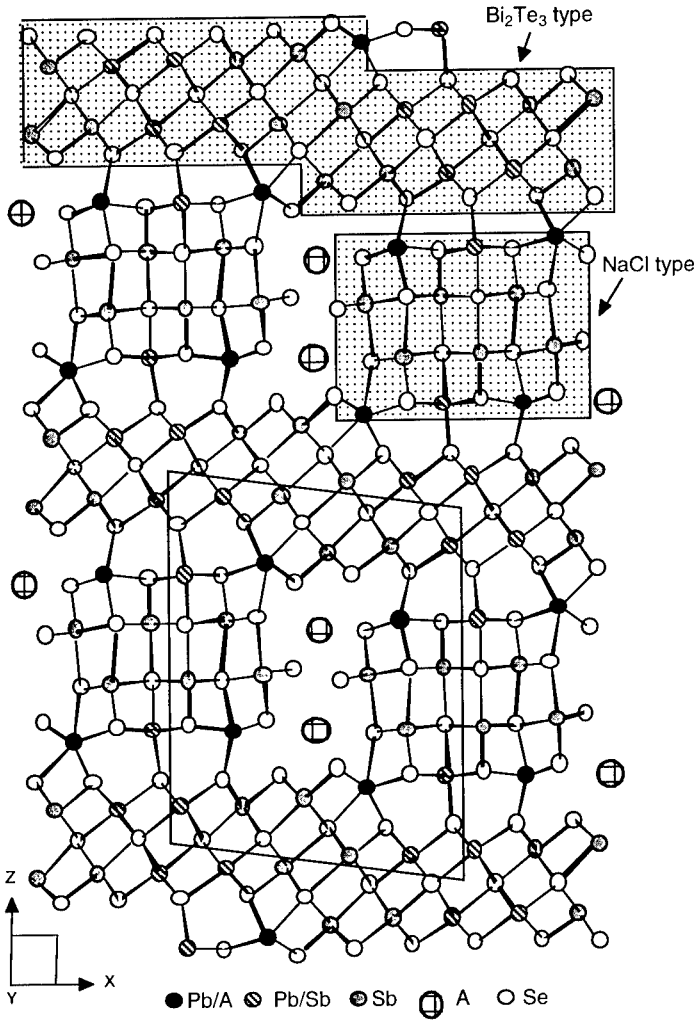

Figure 9. Structure of $A_{1+x}Pb_{4-2x}Sb_{7+x}Se_{15}$ (A=K, Rb; 0<x<2). The shaded areas indicate the fundamental building blocks which make up the structure.

Further information about these compounds can be found elsewhere in this volume.

This structure type is flexible enough to preserve the basic framework through successive addition of "MSe" units by adjusting the width of the Bi_2Te_3-type blocks. $A_{1+x}Pb_{4-2x}Sb_{7+x}Se_{15}$(A=K, Rb) are expected to have substantially low thermal conductivity due to the presence of heavy Pb atoms which also enhance the degree of disorder in the structure. The Pb^{2+} ions are disordered with the alkali metal ions in 8-coordinate sites and disordered with Bi^{3+} or Sb^{3+} ions in octahedral sites in the framework.

An interesting feature of $A_{1+x}Pb_{4-2x}Sb_{7+x}Se_{15}$ is that these materials can be synthesized with various Pb contents as long as the formula, $A_{1+x}Pb_{4-2x}Sb_{7+x}Se_{15}$ ($0<x<2$) is satisfied. The band gap values increase (0.35-0.75 eV) as the Pb content in the compound decreases. At room temperature, these compounds show very high thermopower (~900 μV/K) but low electrical conductivity (~0.01 S/cm). While the $A_{1+x}Pb_{4-2x}Sb_{7+x}Se_{15}$ compounds exhibit low conductivities, the Bi-analog, $K_{1.25}Pb_{3.5}Bi_{7.25}Se_{15}$, shows very promising properties with room temperature conductivity and thermopower of 260 S/cm and -150 μV/K[24] respectively. We will be working to improve these properties through doping investigations and high quality crystal growth.

Concluding Remarks

It is evident from the above discussion that through systematic exploratory synthesis a number of new and interesting materials are emerging for further development. Alkali metal as well as alkaline earth bismuth chalcogenides have all the desirable features sought in an efficient thermoelectric material. These include very low thermal conductivities by virtue of their "phonon-glass electron crystal" characteristics as well as low symmetry large unit cell structures. They also possess high thermopowers and electrical conductivities and complex electronic structures. It must be emphasized that because the nature of this research is highly exploratory and the available guidelines are only general, many new compounds have been discovered which are interesting from a chemical and structural perspective but are not at all suitable for thermoelectric applications.[25,26] However, a substantial number of new candidate compounds have been identified through this research which were not known only a few years ago.

In addition to the ones described here and elsewhere in this volume, many more new compounds involving, not only alkali metal as well as alkaline earth bismuth chalcogenides, but also alkali metal/Pb/Bi/Q, Pb/Bi/Q and Pb/Sb/Q (Q=S, Se and Te) have been discovered in our laboratory which are currently under investigation. They will be reported in future publications. The application of dopants to manipulate the electron density at the Fermi level and to control the conductivity type in these materials is necessary to maximize ZT.

Acknowledgments

Financial support from the Office of Naval Research (N00014-98-1-0443) and DARPA (DAAG55-97-1-0184) is gratefully acknowledged. The work made use of the SEM facilities of the Center for Electron Optics at Michigan State University. The work at Northwestern made use of the Central Facilities supported by NSF through the Materials Research Center (DMR-9632472).

References

1 *Thermoelectric Materials - New Directions and Approaches*, Tritt, T. M.; Kanatzidis, M. G.; Lyon, H. B.; Mahan, G. D. Ed., *Mat. Res. Soc. Symp. Proc.* **1997**, *478*, and references therein.

2 Kanatzidis, M. G.; DiSalvo, F. J. *"Thermoelectric Materials:Solid State Synthesis", ONR Quarterly Review* **1996**, *XXVII*, 14-22.

3 (a) Sales, B. C. *Mater. Res. Bull.*. **1998**, *23*, 15-21. (b) Sales, B. C.; Mandrus, D; Williams, R. K. *Science* **1996**, *272*, 1325-1328. (c) Sales, B. C.; Mandrus, D; Chakoumakos, B. C.; Keppens, V.; Thompson, J. R. *Phys. Rev. B.* **1997**, *56*, 15081-15089.

4 (a) Caillat, T; Fleurial, J. P. *J. Phys. Chem. Solids* **1998**, *59*, 1139-1144. (b) Roche, C.; Pecheur, P.; Toussaint, G.; Jenny, A.; Scherrer, H., Scherrer, S. *J. Phys. B.* **1998**, *10*, L333-L339.

5 Tritt, T. M. *Science* **1996**, *272*, 1276-1277.

6 Sellinschegg, H.; Stuckmeyer, S. L.; Hornbostel, M. D.; Johnson, D. C. *Chem. Mater.* **1998**, *10*, 1096-1101.

7 Littleton, R. T.; Tritt, T. M.; Feger, C. R.; Kolis, J.; Wilson, M. L.; Marone, M.; Payne, J.; Verebeli, D.; Levy, F. *Appl. Phys. Lett.* **1998**, *72*, 2056-2058.

8 (a) Karpinsky, O. G.; Shelimova, L. E.; Kretova M. A. *J. Alloys Compd.* **1998**, *268*, 112-117. (b) Karpinskii, O. G.; Shelimova, L. E.; Kretova, M. A. *Inorg. Mater.* **1998**, *34*, 225-232. (c) Karpinsky, O. G.; Shelimova, L. E.; Kretova M. A. *J. Alloys Compd.* **1998**, *265*, 170-175. (d) Caillat, T.; Fleurial, J. P.; Borshchevsky, A. *J. Phys. Chem. Solids* **1997**, *58*, 1119-1125.

9 Chung, D.-Y.; Hogan, T.; Schindler, J.; Iordanidis, L.; Brazis, P.; Kannewurf, C. R.; Chen, B.; Uher, C.; Kanatzidis, M. G. *"Searching for New Thermoelectrics in Chemically and Structurally Complex Bismuth Chalcogenides"* in *Thermoelectric Materials - New Directions and Approaches*, Tritt, T. M.; Kanatzidis, M. G.; Lyon, H. B.; Mahan, G. D. Ed., *Mat. Res. Soc. Symp. Proc.* **1997**, *478*, 333-344.

10 Kanatzidis, M. G.; Sutorik, A. *"The Application of Polychalcogenide Salts to the Exploratory Synthesis of Solid State Multinary Chalcogenides at Intermediate Temperatures"*, *Prog. Inorg. Chem.* **1995**, *43*, 151-265.

11 *CRC Handbook of Thermoelectrics*; Rowe, D. M. Ed., CRC Press, Inc.: Boca Raton, FL, 1995; references therein.

12 Kittel, C. *Introduction to Solid State Physics*, 6th Eds.; John Wiley & Sons, Inc.: New York, 1986; p 150.

13 *Encyclopedia of Materials Science and Engineering, Thermoelectric Semiconductors*; MIT Press: Cambridge, MA; Pergamon Press: Oxford, 1986; p 4968.

14 Sales B. C. *"Novel thermoelectric materials"*, *Curr. Opin. Solid St. Mater.* **1997**, *2*, 284-289.

15 (a) Nolas G. S.; Cohn, J. L.; Slack, G. A.; Schujman, S. B. *Appl. Phys. Lett.* **1998**, *73*, 178-180. (b) Nolas G. S.; Slack, G. A.; Morelli, D. T.; Tritt, T. M.; Ehrlich, A. C. *J. Appl. Phys.* **1996**, *79*, 4002-4008.

16 (a) Slack, G. A. *"New Materials and Performance Limits for Thermoelectric Cooling"* in *CRC Handbook of Thermoelectrics*, Rowe, D. M. Ed., CRC Press, Inc.: Boca Raton, FL, 1995; p 407-440. (b) Slack, G. A., in *Solid State Physics*, Ehrenreich, H.; Seitz, F.; Turnbull, D. Ed., Academic Press, New York, 1997; vol. 34, p 1.

17 Chung, D.-Y.; Hogan, T.; Schindler, J. L.; Iordanidis, L.; Brazis, P. W.; Kannewurf, C. R.; Chen, B.; Uher, C.; Kanatzidis, M. G. *"Complex Bismuth Chalcogenides as Thermoelectrics"*, *Proc. Inter. Conf. Thermoelect.* 1997, Aug. (7th), pp. 459, Dresden, Germany.

18 Schindler, J. L.; Hogan, T. P.; Brazis, P. W.; Kannewurf, C. R.; Chung, D.-Y.; Kanatzidis, M. G. *"Electrical Properties and Figures of Merit for New Chalcogenide-Based Thermoelectric Materials"* in *Thermoelectric Materials - New Directions and Approaches*, Tritt, T. M.; Kanatzidis, M. G.; Lyon, H. B.; Mahan, G. D. Ed., *Mat. Res. Soc. Symp. Proc.* **1997**, *478*, 327-332.

19 P. W. Brazis, M. Rocci, D.-Y. Chung, M. G. Kanatzidis, C. R. Kannewurf "Transport Properties of Doped $CsBi_4Te_6$ Thermoelectric Materials", see elsewhere in this volume.

20 Cordier, G.; Schäfer, H.; Schwidetzky, C. *Rev. Chim. Miner.* , **1985**, *22*, 631-638

21 Brown, S.; Chung, D.-Y.; Kanatzidis, M. G. work in progress.

22 Srikrishnan, T.; Nowacki, W. Z. *Z. Kristallogr.* **1974**, *140*, 114-136.

23 Chen, B.; Uher, C.; Iordanidis, L.; Kanatzidis, M. G. *Chem. Mater.* **1997**, *9*, 1655-1658.

24 Choi, K-S.; Chung, D.-Y.; Rocci, M.; Brazis, P.; Kannewurf, C. R.; Kanatzidis M. G.; work in progress.

25 Choi, K.-S.; Iordanidis, L.; Chondroudis, K.; Kanatzidis, M. G. *Inorg. Chem.* **1997**, *36*, 3804-3805.

26 Iordanidis, L.; Schindler, J. L.; Kannewurf, C. R.; Kanatzidis, M. G. *J. Solid State Chem.*, in press.

MATERIALS WITH OPEN CRYSTAL STRUCTURE AS PROSPECTIVE NOVEL THERMOELECTRICS

CTIRAD UHER, JIHUI YANG*, and SIQING HU
Department of Physics, University of Michigan, Ann Arbor, MI 48109, cuher@umich.edu
*also at Physics & Physical Chemistry Department, General Motors Research and Development Center, Warren, MI 48090-9055

ABSTRACT

A useful approach to identify materials with high thermoelectric figure of merit is to search for solids that offer great flexibility to modify and tailor the structure so as to achieve the optimal transport behavior. Among the most promising novel thermoelectric materials are solids with "open crystal structure". They may be typified by structures with unfilled cages, crystals with an empty atomic sublattice, and by a network of polyhedral cages enclosing guest species. In this paper we present our latest results concerning transport properties in the above classes of solids. Specifically, we focus on the filled skutterudites, half-Heusler alloys, and clathrates.

INTRODUCTION

The past half-dozen years or so have witnessed a major rejuvenation of interest in thermoelectricity and in the novel thermoelectric materials that may enhance the coefficient of performance (COP) of thermoelectric devices. The impetus for carrying out research in thermoelectricity comes from a variety of sources that recognize the impressive potential this technology holds for both cooling and power generation applications. Among the strongest motivational factors are the environmental concerns about certain established technologies, the by-products of which are viewed as major environmental hazards. In this context we note the coolants used in the refrigeration industry, particularly the harmful, ozone depleting R-12 and even its replacement R-134a that poses a threat because it contributes to global warming. Moreover, a considerable quantity of waste heat generated in industrial plants and in automobile operations calls for ways to capture it and convert it into useful forms of energy. Equally important, thermoelectricity has a potential to address the issues of cooling and air conditioning in areas where a compact and reliable means of lower-temperature operation is desirable.

The benefits that thermoelectricity offers are well known and much appreciated—all solid state design, environmentally friendly devices, quiet and vibration-free operation, long life with extreme reliability, a reversible and easily controlled operation, and competitive cost. Indeed, in the niche areas of applications, thermoelectric devices are second to none. Unfortunately, the niche areas represent only a minute segment of technology where thermoelectricity could potentially make an impact. A more widespread use of thermoelectrics has been precluded by a rather low COP of the thermoelectric devices in comparison to established technologies. The crux of the problem is the material base of thermoelectricity that has stagnated since the early 1960s. It is surprising that the thermoelectric devices on today's market are based on materials developed some forty years ago with only "cosmetic" improvements made in the interim.

The low COP is predicated on less-than-impressive values of the figure of merit Z of the materials constituting the legs of a thermocouple. The figure of merit Z, or its dimensionless equivalent ZT, are convenient parameters to assess the material's potential as a suitable thermoelectric. The figure of merit is defined as $Z = S^2\sigma/\kappa$ where S is the thermopower, σ the electrical conductivity, and κ the thermal conductivity. The product $S^2\sigma$ is often referred to as the power factor. It turns out that a promising thermoelectric is a semiconductor or, in very rare

Mat. Res. Soc. Symp. Proc. Vol. 545 © 1999 Materials Research Society

cases a semimetal, with high carrier mobility and, at the same time, high effective mass. Moreover, it must be a poor conductor of heat or more precisely, a material with as low lattice thermal conductivity as possible. While no a priori limit exists on the value of Z, it is unlikely that an ordinary 3-dimensional solid would have ZT much in excess of 4-5. However, doubling or tripling the dimensionless figure of merit from the current values of less than unity would go a long way toward making thermoelectricity a more widely accepted technology. It is in this context that a vigorous search for novel thermoelectric materials has sprang out during the past few years.

The transport properties that govern how well a material performs as a thermoelectric are not mutually independent and thus one cannot make use of the extremal transport parameters of any given material. There is always a compromise to be made that leads to optimization of the thermoelectric figure of merit. Although one cannot completely overcome the constrains nature imposes on the electronic and vibrational structure of solids, it is not unreasonable to search for the novel structural forms where the linkage between the electronic and phonon states is weaker or where one can, by judicious structural modifications, alter the coupling between the electronic and lattice degrees of freedom. This is the approach advocated by Slack [1] which in its ultimate form is referred to as the "phonon glass/electron crystal" (PGEC) concept. The premise is that one can design a solid that will be a poor conductor of heat, like glass, yet possess excellent electronic properties one normally associates with crystals. This approach has been tried by a number of laboratories worldwide and encouraging progress has been achieved with several classes of materials.

At the University of Michigan, in collaboration with General Motors Research and Development Center, we have focused on the study of novel thermoelectrics with open crystal structure. These are materials typified by their unique structural features such as unfilled cages, crystals with empty atomic sublattices, and solids consisting of a network of polyhedral cages enclosing guest species within the cages. Materials of this kind allow considerable freedom to modify and tailor their structure, alter the electronic and lattice properties and, in turn, optimize transport properties. In this paper we briefly discuss three archetypal examples of these novel thermoelectrics, present our latest results, and suggest directions for future research efforts.

FILLED SKUTTERUDITES

The name skutterudite refers to the class of solids with a generic formula AB_3 where A=Co, Rh, or Ir and B=P, As, or Sb. Skutterudites crystallize in a body-centered structure consisting of a simple cubic array of A atoms at the (¼ ¼ ¼) crystallographic site, each surrounded by distorted octahedra of B atoms. The tilt of the octahedra results in formation of four-membered square planar rings of pnictide B atoms, and somewhat irregular dodecahedron "cages" of B atoms centered at the corner (000) and body center (½ ½ ½) of the unit cell. In a cubic unit cell, there are eight formula units including two voids. An equivalent representation of the structure that specifically notes the presence of the two voids is $Co_8\square_2Sb_{24}$. In their binary (unfilled) form, skutterudites possess high mobility and large thermopower, but unfortunately also high thermal conductivity [2,3]. The presence of the voids, i.e., the open structure of skutterudites, lends itself to an important modification of transport properties. By filling the voids with undersized rare-earth atoms—forming the so-called filled skutterudites—one achieves a drastic reduction in the lattice thermal conductivity [4]. The rare-earth atoms exercise large local anharmonic vibrations—they "rattle" in the cages—and this disrupts the normal modes of the structure. Although the electronic properties are sensitive to the presence of rattling ions in the voids, the power factors ($P = S^2\sigma$, where S is the thermopower and σ the electrical conductivity) remain reasonably high and contribute to an overall high figure of merit [5]. The two most popular rare-

earth fillers are Ce and La. The major distinction between the two is the presence of 4f electrons in the shell structure of Ce that have a tendency to hybridize and that are responsible for a plethora of magnetic and band structure effects in compounds containing Ce.

In our studies we have used as a model system the family of filled skutterudites designated as $Ce_yFe_{4-x}Co_xSb_{12}$. The subscript y indicates that the filling fraction of Ce is not a constant but depends on the amount of Co in the system. Thus, while for x=0 one can fill essentially all cages with Ce, the presence of Co limits the amount of Ce that can be accommodated in the voids. In our previous work we have established [6] that the filling fraction rapidly decreases with an increasing amount of Co and that in purely Co-based filled skutterudites, $Ce_yCo_4Sb_{12}$, one can fill at most only about 10% of the voids. For comparison, using La, one can fill up to 23% of voids before one saturates $La_yCo_4Sb_{12}$ [7].

Alloying Co with Fe in $Ce_yFe_{4-x}Co_xSb_{12}$ serves two main purposes: As one fills the voids, one adds three electrons to the structure for every Ce ion. In order to preserve structural stability, one must replace some of the Co atoms with a metal with fewer electrons, in our case with Fe which has one electron less than Co. Assuming an extreme case and replacing all Co with Fe, one creates four holes in the valence band and the three Ce electrons cannot fully compensate the structure. Hence, a filled ternary skutterudite $CeFe_4Sb_{12}$ is a metal. Based on this simple crystal chemistry, a complete compensation is expected for $CeFe_3Co_1Sb_{12}$, and structures with $x > 1$ should be n-type. In reality, all compounds with $x \leq 3.5$ remain p-type. This finding provided an early hint that the occupancy of cages is incomplete and decreases with increasing Co content. The Fe/Co ratio governs not just the electronic properties but also has considerable influence on the transport of heat. While Ce "rattling" leads to a dramatic suppression of thermal conductivity, the presence of Fe leads to an additional significant (~50%) reduction in the phonon thermal conductivity. The effect of Fe is especially notable near room temperature where the thermal conductivity is substantially independent of the Ce content. This fact led us to interpret the thermal conductivity of partially filled skutterudites as that due to solid solutions of fully filled $CeFe_4Sb_{12}$ and unfilled $\square Co_4Sb_{12}$, where $\square$ stands for a vacancy [8]. Promising results concerning substitution on the simple cubic array of A atoms encourage one to consider substitution on the sites occupied by pnicogen atoms. This is what we have undertaken recently and here we report our results.

We prepared a new batch of filled skutterudites with a composition close to that shown previously to yield the lowest lattice thermal conductivity, $Ce_{0.65}Fe_2Co_2Sb_{12}$. We then altered the structure by replacing some of the Sb atoms with Sn and Ge, the group IV elements. The respective samples have compositions $Ce_{0.65}Fe_2Co_2Sb_{11}Sn_1$ and $Ce_{0.65}Fe_2Co_2Sb_{10}Ge_2$, and were made according to a recipe described previously. Samples were annealed at 700°C for 20 hours to promote further homogenization. Hall effect and electrical resistivity were measured using a Linear Research ac bridge with 16Hz excitation in a magnet cryostat capable of fields up to 5 Tesla. Thermal transport properties (thermopower and thermal conductivity) were determined using longitudinal steady-state technique over the temperature range of 4-300K. Samples were enclosed inside a radiation shield to minimize radiation heat loss.

Figures 1 and 2 show the temperature dependence of the carrier density obtained from Hall effect measurements, and the behavior of electrical resistivity. Holes are added to the structure upon a partial replacement of Sb with Ge or Sn and this enhances free carrier density. The effect is particularly notable for Sn the presence of which increases the carrier density of $Ce_{0.65}Fe_2Co_2Sb_{12}$ by a factor of twenty in spite of Sn substituting on only half as many Sb sites as Ge. While Ge seems to lower the resistivity of the structure, the presence of Sn increases carrier scattering. Electrical resistivity of the Sn-substituted sample is much larger than that of the undoped sample, and below 25K it actually rises with decreasing temperature. Carrier mobility is clearly strongly degraded in this Sn-substituted sample.

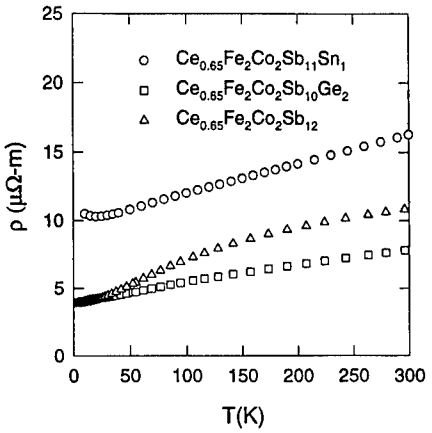

Figure 1: Resistivity versus temperature for undoped, Sn-doped, and Ge-doped filled skutterudites.

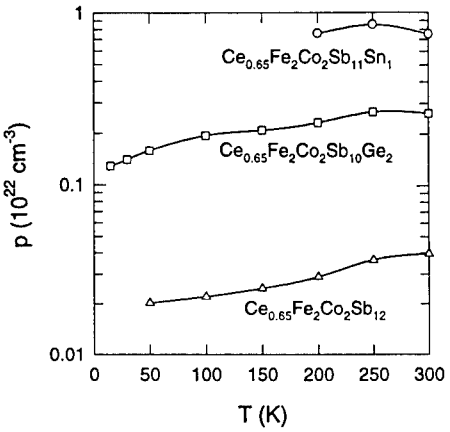

Figure 2: Carrier density versus temperature obtained from the Hall effect data for samples shown in Fig.1.

Turning our attention to the behavior of the thermopower we note, see Fig.3, nearly linear temperature dependence for the undoped $Ce_{0.65}Fe_2Co_2Sb_{12}$ but substantial curvatures in the data of the two doped samples. While the thermopower of $Ce_{0.65}Fe_2Co_2Sb_{12}$ and of its Sn-doped cousin are reasonably large, the much enhanced carrier density in the Ge-substituted sample appears to have a very detrimental effect on the thermopower.

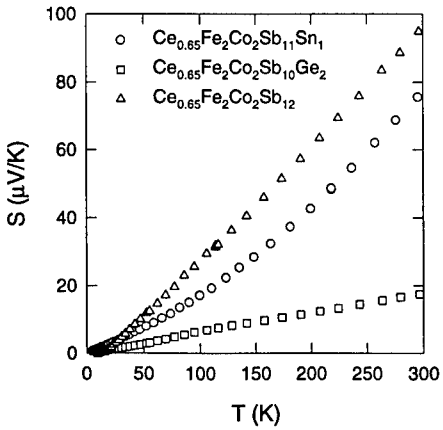

Figure 3: Thermopower for the undoped, Sn-doped, and Ge-doped filled skutterudites.

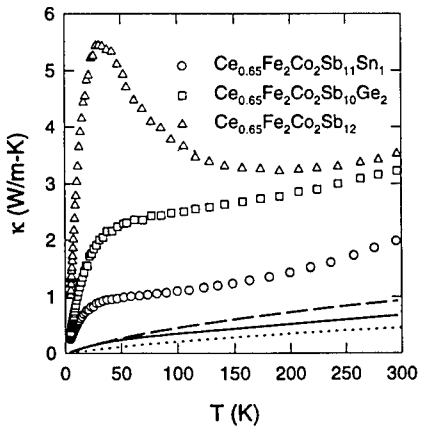

Figure 4: Thermal conductivity vs. temperature. Electronic contributions are shown as curves: solid line for $Ce_{0.65}Fe_2Co_2Sb_{12}$, dashed line for $Ce_{0.65}Fe_2Co_2Sb_{10}Ge_2$, dotted line for $Ce_{0.65}Fe_2Co_2Sb_{11}Sn_1$.

Disorder on the Sb network has a distinct influence on the phonon transport. Figure 4 illustrates a strong suppression of the thermal conductivity, particularly for the Sn-doped sample. The prominent dielectric peak seen in the thermal conductivity of $Ce_{0.65}Fe_2Co_2Sb_{12}$ is completely washed out and the conductivity is monotonically rising with increasing temperature. A contributing factor to this rise is the electronic thermal conductivity estimated from the resistivity data and the Wiedemann-Franz law, and plotted as curves in Fig.4. Based on these preliminary measurements, doping on the Sb sites has a strong influence on both the electronic and vibrational properties of the filled skutterudites. Unfortunately, our trial concentrations of Ge and Sn do not lead to an enhancement in the thermoelectric properties. Too high carrier concentrations combined with a strong influence of ionized-impurity scattering weigh more in this case than the gain arising from a reduction in the lattice thermal conductivity. A small amount of isoelectronic impurity such as As or even Bi should be tried on the Sb site. Such impurity should have a much weaker effect on the electronic properties yet; it may help in reducing thermal conductivity.

HALF-HEUSLER ALLOYS

Half-Heusler alloys are interesting ternary intermetallics with the general formula MNiSn (M=Zr, Hf, Ti). They are closely related to the full Heusler alloys MNi_2Sn built up of four interpenetrating fcc sublattices mutually shifted along the body diagonal by a ¼ distance. Full Heusler alloys are good metals. Quite remarkably, the integrity of the structure is preserved when one of the two Ni sublattices is replaced by an ordered lattice of vacancies—the configuration representing the half-Heusler alloys. From the band-structure perspective, the removal of the Ni sublattice leads to a lowering of the point group symmetry, shifts of the valence and conduction bands, and the onset of a small gap in the density of states [9]. The nature of transport thus changes from that of a good metal to one representing a small gap semiconductor, at least at ambient and higher temperatures. Because the half-Heusler alloys exhibit large thermopower while having a relatively low resistivity, it was suggested that they might be of interest as prospective thermoelectric materials [10]. We share the enthusiasm concerning these materials and we have recently reported on the transport and thermoelectric properties of pure ZrNiSn and its isoelectronic alloys with Hf [11]. With the atomic species occupying clearly delineated sublattices (and noting the presence of an empty Ni sublattice), the structure presents numerous opportunities to explore the specific role each sublattice plays in the carrier and lattice dynamics and in the overall transport behavior. In this highly structured environment any disorder on any one of the sublattices is likely to have a profound effect on the band structure and consequently on the transport properties. To gain insight into the properties of these interesting intermetallics, our approach is to systematically modify one sublattice at a time and learn how such a structural modification influences transport properties and what implications there are for maximizing the thermoelectric figure of merit. Hopefully, by combining the "beneficial" structural modifications on each respective sublattice one would obtain a fine-tuned material with outstanding thermoelectric properties. In this sense we view the half-Heusler alloys as another example of materials with open structure.

Realizing that intermixing might be a serious problem in the system consisting of fast and slow diffusing species (the small ion-core Ni has a high diffusion rate in the matrix consisting of both the M metal and Sn, while interdiffusion between M and Sn is a rather slow process), we first attempted to establish appropriate annealing conditions that yield homogeneous alloys. We found that annealing the as-grown structure for one week at 800°C under argon is usually sufficient.

In our earlier work [11] we focused on the M sublattice. We have shown that by alloying Zr with its isoelectronic partner Hf, we were able to reduce dramatically the lattice thermal conductivity while the electronic properties were left substantially intact. Mass-defect between Zr (M_{Zr}=91) and Hf (M_{Hf}=179) is large enough to cause a suppression of the lattice thermal conductivity of $Zr_{0.5}Hf_{0.5}NiSn$ by a factor of more than three in comparison to pure ZrNiSn and HfNiSn, see Fig.5. From the perspective of thermoelectricity, this is an encouraging result.

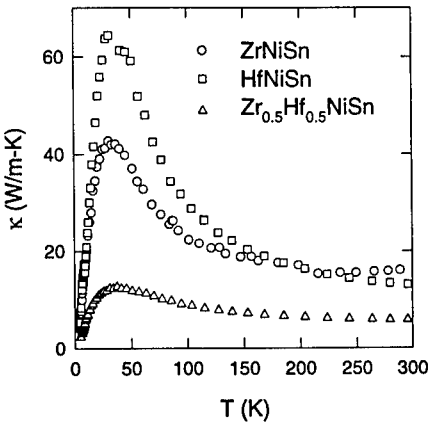

Figure 5: The effect of isoelectronic alloying on the thermal conductivity of half-Heusler alloys.

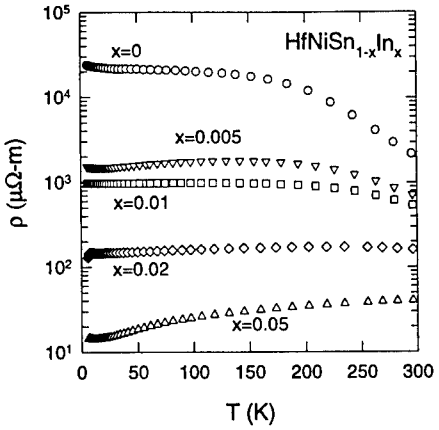

Figure 6: Resistivity of In-doped HfNiSn as a function of temperature.

Already in these early studies it was apparent that the nature of transport changes dramatically as the temperature varies. In the temperature regime below 150K, the transport properties (electrical resistivity, thermopower and the Hall effect) displayed a distinctly metallic character. In contrast, at elevated temperatures the alloys rapidly attained a semiconductor-like behavior dominated by a band of electrons with heavy mass. It was essential to explore how doping might alter the band structure and we targeted the Sn sublattice to elucidate the point. In [12] we report on a spectacular change in the nature of transport upon doping on the Sn sublattice with a rather small amount of Sb (0.5 – 1 at.%). Introducing an extra electron with each Sb atom that replaces Sn results in an entirely metallic structure with two orders of magnitude lower resistivity than that of the undoped alloy. Remarkably, the high values of the thermopower (–150 to –200 μV/K at 300K)—the feature that drew our attraction to these alloys in the first place—were preserved and the temperature dependence of thermopower suggested that these values would be even higher above room temperature. A combination of high thermopower and low resistivity resulted in power factors on the order of 25-30 $\mu W/cm\text{-}K^2$. These promising values are undoubtedly associated with the heavy electron band for which we estimated the effective mass $m^* \approx 5m_e$. It is of interest to find out what happens when one substitutes for Sn with an element one column to the left of Sn, i.e., when one tries to introduce holes into the structure. We have attempted to do so with indium and here we report our results.

We made a series of Hf-based half-Heusler alloys and doped them with up to 5at.% of In. Alloys were annealed for 1 week at 800°C under argon, our standard annealing treatment. Figure 6 shows the resistivity as a function of temperature for samples with various amounts of In impurity. The trend is clear—as the amount of In increases, resistivity decreases by a couple of

orders of magnitude and the activation character of transport gives way to a purely metallic dependence. The crossover at which the temperature coefficient of resistivity changes sign shifts progressively to higher temperatures and for the most heavily doped sample, the crossover, if any, takes place above 300K. The trend towards a more metallic structure is also reflected in the carrier density that increases monotonically from 8×10^{18} cm^{-3} for the 0.5at.% In sample to near 10^{21} cm^{-3} for the most heavily doped sample.

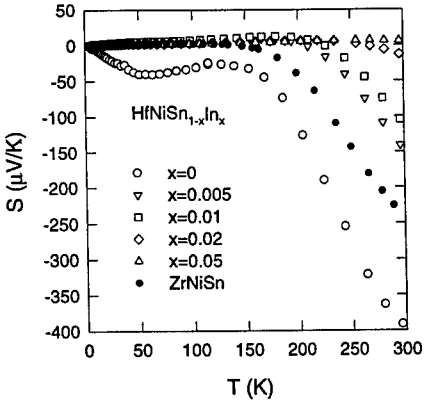

Figure 7: Thermopower of In-doped HfNiSn. For reference, we also include data obtained on ZrNiSn

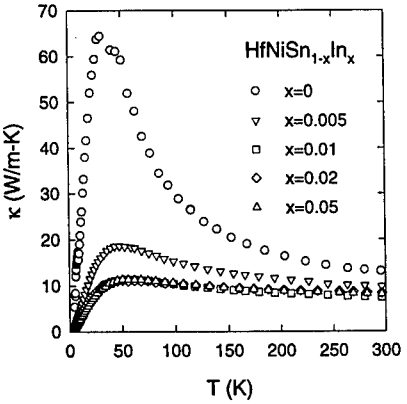

Figure 8: Thermal conductivity of In-doped HfNiSn as a function of temperature.

The crossover from the metallic regime of conduction at low temperatures to an activated transport at elevated temperatures is also well documented by the trend in the thermopower, Fig.7. Although the data for pure HfNiSn are complicated by a dip near 50K that we have not seen previously in the data of ZrNiSn nor in $Zr_{0.5}Hf_{0.5}NiSn$, the thermopower nevertheless shows a sharp break near 150K that was a typical and prominent feature of the thermopower data in all pure half-Heusler alloys and in their isoelectronic variants. We include in Fig.7 a curve for pure ZrNiSn to serve as a reference. In comparison to it, the thermopower of HfNiSn is considerably larger near the ambient temperature and the highest values are reached above 300K, beyond the range we can access in these measurements. In indium-doped alloys we observe a small, positive and nearly T-linear thermopower that extends to considerably higher temperatures than 150K. Depending on the amount of In, a sharp break eventually sets in at higher temperatures and the thermopower rapidly attains large negative values. The two most heavily doped samples would presumably follow the same trend above 300K. Obviously, the heavy electrons take over and govern the transport the same way they do in the undoped alloys except that now their influence is shifted to considerably higher temperatures. These data further reinforce our viewpoint [12] that half-Heusler alloys undergo a transition from a metallic (or possibly semimetallic) state at low temperatures to that of a single carrier-dominated semiconductor at elevated temperatures, and this transition can be tuned by doping the structure.

How phonons react to the presence of indium impurity on the Sn sublattice is illustrated in Fig.8. We note a drastic reduction in the thermal conductivity; particularly the dielectric peak at low temperatures is quickly wiped out with increasing amounts of In. It is quite remarkable that the relatively small amount of In we substitute on the Sn sublattice has such a profound effect on the thermal conductivity. As impressive as the reduction in thermal conductivity is, it is

nevertheless not large enough for the purposes of thermoelectricity. However, by combining the doping process with isoelectronic alloying, see Fig.6, i.e., simultaneously modifying both M and Sn sublattices, one should be able to achieve further significant reduction in thermal conductivity. Half-Heusler alloys hold considerable potential as novel thermoelectrics and it is essential to extend their studies to temperatures above 300K where their thermoelectric properties are likely to peak.

GROUP IV CLATHRATES

Among the most interesting open structures are compounds called clathrates [13]. They are inclusion compounds in which cages of polyhedra of the host structure can accommodate various types of guest molecules. Perhaps the best known examples are the clathrate hydrates where the host is H_2O molecules forming polyhedral cages through hydrogen bonds, and the guest species are various kinds of gases. Clathrate structures form also with the group IV elements Si, Ge (occasionally also with Sn), where the guest species are either alkali metals or alkaline-earth elements. In their binary form there are two main compositions: type-I clathrates A_xSi_{46} (equivalent structure for Ge) with maximum x=8, and type-II clathrates A_xSi_{136} with the maximum alkali metal content x=24. The former crystallize with a simple cubic structure and consist of two pentagonal dodecahedra and six 14-face polyhedra in a unit cell. The latter form the face-centered-cubic lattice with sixteen pentagonal dodecahedra and eight 16-face polyhedra in a unit cell. In both structures, every Si (Ge) atom has four Si (Ge) nearest neighbors at distances only slightly greater than in crystalline diamond structure of Si (Ge). The structures are an analog to C_{60} and related carbon fullerene networks, except that Si (Ge) prefers sp^3 bonding that leads to sharing of polyhedra faces in the clathrate structure. The actual bond lengths do not differ much from the crystalline diamond structure of Si (Ge) and the average bond angle is very close to the perfect tetrahedral angle of 109.4°. It should be stressed that Si (Ge) polyhedra network can only be sustained in the presence of the guest species that stabilize the structure; without them, the cage structure collapses. Clathrates of this kind are sometimes referred to as crypto-clathrates, i.e., hidden clathrates.

Although the group IV clathrates were discovered in mid-1960s [14], very little is known about their transport properties. Band structure calculations indicate that the binary Si-based clathrates are semiconductors with a gap that exceeds that of ordinary Si by about 0.7 eV [15]. Ge-based clathrates have a smaller gap and may even be semimetals. What make these systems of interest from the perspective of thermoelectricity are two things:

i) the likelihood that the lattice thermal conductivity will be extremely small,
ii) a possibility to dope the structure by controlling the guest species.

The hope that thermal conductivity of the group IV clathrates might be very low is based on the well documented behavior of its cousins--clathrate hydrates-- that show anomalously low thermal conductivity and have a positive coefficient, $d\kappa(T)/dT > 0$, at all temperatures below the freezing point of water [16,17]. In spite of their crystalline nature, the thermal conductivity of clathrate hydrates resembles that of an amorphous solid. If this behavior is common, the group IV clathrates might be an archetypal example of the PGEC solids. By selecting suitable guest species to fill the cages and by doping on the Si (Ge) polyhedra network, one has a way to control and alter the carrier density.

Synthesis of the binary clathrates is rather complicated and requires a two-stage process to control the exact alkali metal content [18]. An easier approach to make the group IV clathrates, and the one that offers more options to tailor the physical properties by incorporating also alkaline-earth elements, is to synthesize ternary clathrates of the form $X_8Y_{16}Si_{30}$ and their Ge and Sn variants. This can be achieved by melting stoichiometric quantities of the alkaline-earth

element X, a group III element Y, and Si (Ge, Sn) [19]. Each alkaline-earth atom resides in the cage and donates two electrons. To compensate, twice as many atoms of the group III element must randomly substitute for Si (Ge, Sn) in the tetrahedral network. By opting not to compensate the charge fully, one has, in principle, means of altering the carrier density. To make group IV clathrates a useful thermoelectric, one has to establish the optimum carrier concentration that yields maximum power factor. Combining the optimized power factor with the exceptionally low thermal conductivity, one has a real prospect of finding a novel thermoelectric material with superior properties.

We prepared ternary clathrates based on germanium, $Ba_8Ga_{16}Ge_{30}$ and Sr_8 $Ga_{16}Ge_{30}$, and determined their transport properties. Our initial attempts to grow clathrates in quartz tubes under argon were often unsuccessful as the quartz tube broke, particularly when Ba was present. Subsequently, we opted to grow the material in a pyrolytic boron nitride crucible placed inside a larger quartz tube filled with argon and heated for one week at 1000-1100°C. Clathrates grown close to their stoichiometric composition came out as robust, silvery, polycrystalline ingots from which samples were cut using a diamond wheel saw. Typical dimensions of our samples are 2x3x8 mm^3. We used crystal growth facilities at both University of Michigan and at GM Research Center with virtually identical outcome as far as the quality and the properties of the clathrates were concerned. Transport measurements were made over the range 4-300K using techniques described in the preceding sections.

Figure 9 shows x-ray powder scan of a well developed, single-phase clathrate structure obtained on our $Ba_8Ga_{16}Ge_{30}$. Scans of comparable quality were obtained for other clathrates. In Table I we collect room temperature values for some of the transport parameters.

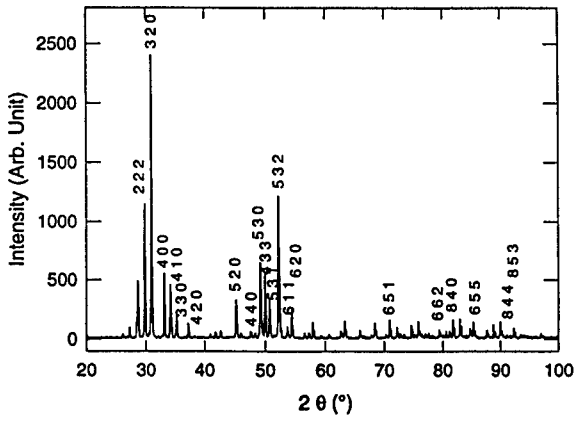

Figure 9: x-ray powder scan of $Ba_8Ga_{16}Ge_{30}$.

Table I: Room temperature parameters of some of the investigated clathrates

Structure	ρ(μΩ–m)	S(μV/K)	κ(W/m–K)	n(cm^{-3})	μ(cm^2/V–s)
$Sr_8Ga_{16}Ge_{30}$-sintered	21.9	–105	1.25	7.7×10^{20}	3.7
$Sr_8Ga_{16}Ge_{30}$ (in pBN)	7.5	–82.4	2.52	1.2×10^{21}	7.0
$Sr_8Ga_{16}Ge_{30}$ (in quartz)	4.4	–52	3.3	1.8×10^{21}	7.6
$Ba_8Ga_{16}Ge_{30}$ (in quartz)	6.8	–34	2.85	1.1×10^{21}	8.3

Figure 10 shows the temperature dependence of electrical resistivity of our clathrates. We note a metallic dependence for all structures throughout the temperature range covered. Hall constant is negative indicating the dominant contribution of electrons. Although we prepared several ingots with a slightly off-stoichiometric amount of Ga and Sr (Ba), this had little effect on the resistivity and carrier density, the latter remaining around 10^{21} cm^{-3}. Consequently, carrier mobilities are rather low, only a few cm^2/V-s. These values stand in sharp contrast with the

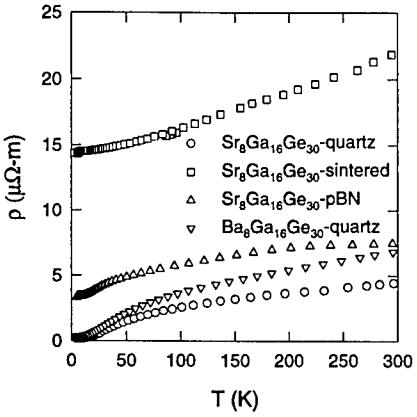

Figure 10: Resistivity of Ge-clathrates as a function of temperature.

results reported recently by Nolas et al. [20]. Their samples are nominally of the same composition as ours, except that they do not measure the as-grown material but powder it and sinter it in a carbon die. While two of their three samples have comparable resistivities to our structures—one sample displayed an activation behavior below 100K—the carrier densities reported in Ref.20 are in the range 10^{17}–3×10^{18} cm^{-3}, some three to four orders of magnitude lower than what we measure. These surprisingly low carrier densities imply very high mobilities of a few thousands cm^2/V-s, well above the values we measure. To try to make a fair comparison with the data of Ref.20, we crushed one of our Sr_8 $Ga_{16}Ge_{30}$ ingots (the ingots grown in a pyrolytic boron nitride crucible and entered in Table I as Sr_8 $Ga_{16}Ge_{30}$ (in pBN)) and sintered it in a carbon die under similar conditions as reported in Ref.20. While the smaller grain size in this sample has a significant effect on electrical resistivity and on thermal conductivity (discussed later), we observe only small change in the carrier density. We thus have no idea what is the source of such major discrepancy in the carrier concentrations between the data sets of Ref.20 and our results.

Thermopower is shown in Fig.11. In general, Sr-loaded samples have higher thermopower than samples with Ba. We observed a rather strong dependence of thermopower on the crucible material. We tried different crucibles and the thermopower of Sr_8 $Ga_{16}Ge_{30}$ seemed to improve as we progressed from quartz to tantalum to pyrolytic boron nitride crucibles. The highest thermopower was measured following crushing and sintering Sr_8 $Ga_{16}Ge_{30}$ grown in a p-BN crucible. Thermopower of this sample is comparable to the two metallic samples reported in [20].

The group IV clathrates are very poor conductors of heat as attested to by the magnitude of thermal conductivity and by its temperature dependence, see Fig.12. While $Ba_8Ga_{16}Ge_{30}$ behaves as a good crystalline solid ($\kappa \propto 1/T$ and a large peak at low temperatures), all $Sr_8Ga_{16}Ge_{30}$ samples display a positive temperature coefficient of thermal conductivity. However, neither of the two "as-grown" $Sr_8Ga_{16}Ge_{30}$ ingots approaches a glass-like behavior because they both show

a clear peak at helium temperatures indicating that well-defined normal phonon modes are present. It is only when we powder and sinter the "as-grown" ingot that we observe a very distinct change in the character of thermal transport. This is the case of a sample labeled $Sr_8Ga_{16}Ge_{30}$ –sintered in Fig.12. Thermal conductivity here is much depressed (by a factor of two at 300K and more at lower temperatures), the slope dκ/dT is positive throughout the temperature range covered, and there is no hint of the phonon peak at low temperatures. Heat transport in this sample looks more like that of an amorphous solid than that of a crystalline material. Nolas et al.[20] reported recently on a glass-like behavior in their clathrate structures that also displayed a plateau-like feature in the thermal conductivity.

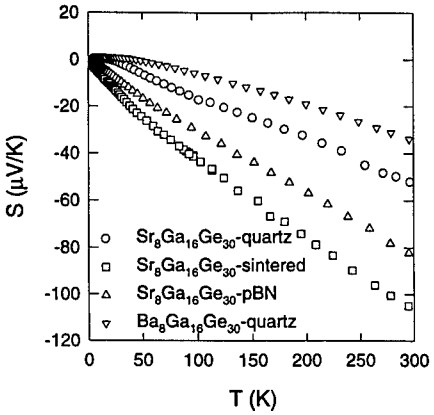

Figure 11: Thermopower of Ge-clathrates.

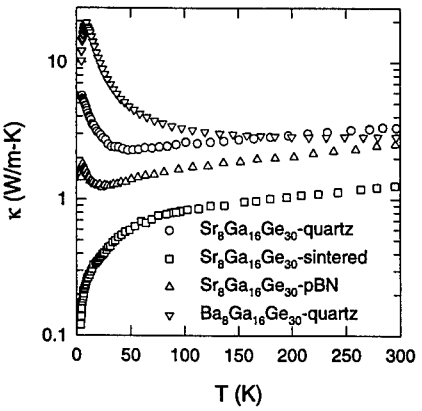

Figure 12: Thermal conductivity of Ge-clathrates

Low thermal conductivity of clathrate hydrates is believed to be associated with unusually strong interactions between the guest and host lattice vibrations. A possible scenario for strong vibrational coupling assumes avoided crossings of the localized rattling modes of the guest species and of the acoustic phonon modes of the host lattice [16, 21]. Having similar structures, it is likely that the same strong coupling exists in the group IV clathrates and is responsible for the anomalously low and amorphous-like thermal conductivity. It is important to find out what happens to clathrates—beyond reducing the size of the grains—in the process of crushing and sintering the "as-grown" ingots. Smaller grain size by itself would merely increase the electrical resistivity and reduce thermal conductivity but normally would not induce amorphous behavior on the otherwise polycrystalline structure.

Clathrates are certainly very intriguing materials and if one is able to control their doping and achieve high power factors, their very low thermal conductivity would make them strong competitors as thermoelectrics.

ACKNOWLEDGMENT

It is our pleasure to acknowledge fruitful collaborations with Drs. D. T. Morelli and G. P. Meisner. The work was supported by ONR Grant No. 0014-96-10181.

REFERENCES

1. G. A. Slack, in *CRC Handbook of Thermoelectrics*, Chapter **34**, edited by D. M. Rowe, Chemical Rubber, Boca Raton, FL, 1995, p. 407.

2. J.-P. Fleurial, T. Caillat, A. Borshchevsky, D. T. Morelli, and G. P. Meisner, in Proceedings of the 15th International Conference on Thermoelectrics, edited by T. Caillat (Institute of Electrical and Electronics Engineering, Piscataway, NJ, 1996), p. 91.

3. D. T. Morelli, T. Caillat, J.-P. Fleurial, A. Borshchevsky, J. Vandersande, B. Chen, and C. Uher, Phys. Rev. **B51**, p. 9622 (1995).

4. G. A. Slack and V. G. Tsoukala, J. Appl. Phys. **76**, p. 1665 (1994).

5. B. C. Sales, D. Mandrus, and R. K. Williams, Science **272**, p. 1325 (1996).

6. B. Chen, J.-H. Xu, C. Uher, D. T. Morelli, G. P. Meisner, J.-P. Fleurial, T. Caillat, and Borshchevsky, Phys. Rev. **B55**, p. 1476 (1997).

7. G. S. Nolas, J. L. Cohn, and G. A. Slack, Phys. Rev. **B58**, p. 164 (1998).

8. G. P. Meisner, D. T. Morelli, S. Hu, J. Yang, and C. Uher, Phys. Rev. Letters **80**, p. 3551 (1998).

9. S. Ögüt and K. M. Rabe, Phys. Rev. **B51**, p. 10443 (1995).

10. B. A. Cook, J. L. Harringa, Z. S. Tan, and W. A. Jesser, Proc. 15th International Conference on Thermoelectrics, Pasadena, CA, IEEE Catalog Number 96TH8169, p. 122 (1996).

11. C. Uher, S. Hu, J. Yang, G. P. Meisner, and D. T. Morelli, Proc. 16th International Conference on Thermoelectrics, Dresden, Germany, IEEE Catalog Number 97TH8291, p. 485 (1997).

12. C. Uher, J. Yang, S. Hu, D. T. Morelli, and G. P. Meisner, Phys. Rev. B, submitted for publication.

13. L. Pauling and R. Marsh, Proc. Nat. Acad. Sci. **38**, p. 112 (1952).

14. C. Cros, M. Pouchard, and P. Hagenmuller, Compt. Rend. **260**, p. 4764 (1965).

15. G. B. Adams, M. O'Keeffe, A. A. Demkov, O. F. Sankey, and Y.-M. Huang, Phys. Rev. **B49**, p. 8048 (1994).

16. J. S. Tse and M. A. White, J. Phys. Chem. **92**, p. 5006 (1988).

17. M. Zakrzewski and M. A. White, Phys. Rev. **B45**, p. 2809 (1992).

18. C. Cros, M. Pouchard, and P. Hagenmuller, J. Solid State Chem. **2**, p. 570 (1970).

19. B. Eisenmann, H. Schäfer, and R. Zagler, J. Less-Common Metals **118**, p. 43 (1986).

20. G. S. Nolas, J. L. Cohn, G. A. Slack, and S. B. Schulman, Appl. Phys. Lett. **73**, p. 178 (1998).

21. J. S. Tse, V. P. Shpakov, V. V. Murashov, and V. R. Belosludov, J. Chem. Phys. **107**, p. 9271 (1997).

PRESSURE-TUNING IN THE SEARCH FOR IMPROVED THERMOELECTRIC MATERIALS

D.A. Polvani*, J.F. Meng*, C.D.W. Jones**, F.J. DiSalvo** and J.V. Badding*
*Department of Chemistry, Pennsylvania State University, University Park, PA 16802
**Department of Chemistry, Cornell University, Ithaca, NY 14853

ABSTRACT

The traditional approach to the search for improved materials, such as thermoelectric materials, involves the sequential synthesis and characterization of new compounds, followed by the investigation of their properties. Each single solid state compound has materials interaction parameters (e.g., degree of orbital overlap, orbital energy, band energies etc.) that determine its thermoelectric properties. These interaction parameters can be used to define a phase space, in which individual compounds are represented by a single point. Because this phase space can be rapidly explored with pressure, our efforts have focused on the synthesis of complex semiconductors and rare earth based materials, followed by pressure-tuning studies of their thermoelectric properties. This approach to exploring interaction parameter phase space potentially allows the thermoelectric power to be more rapidly and cleanly optimized than is possible with the traditional approach. Here we present some results for rare earth thermoelectric compounds that have been pressure-tuned. Demonstration of the existence of materials with improved ZT at high pressure can also provide insight into the structural and electronic parameters necessary to achieve high figures of merit at ambient pressure.

INTRODUCTION

Renewed interest in thermoelectric devices has reinvigorated the search for new compounds that exhibit improved thermoelectric properties. The traditional approach to this search involves the sequential synthesis and characterization of new solid state compounds. Combinatorial techniques, in which large numbers of compounds are synthesized in parallel, are being investigated as a means of increasing the rate of discovery of useful materials, such as thermoelectric materials.[1, 2, 3] Here we discuss a different strategy, involving pressure tuning, that has the potential to increase the rate of discovery of novel materials that exhibit larger thermoelectric figures of merit ($Z=S^2\sigma/\kappa$).

Pressure tuning involves the use of pressure to change the interatomic distance in a material while probing one or more physical properties. Large changes in electronic structure and properties can be induced with pressure. For example, the fundamental band gap of many semiconductors can be closed under pressure, resulting in a semiconductor-metal transition that can be observed in properties such as the optical reflectivity, electrical conductivity, and thermoelectric power.[4] At pressures below the semiconductor-insulator transition, the band structures of semiconductors (and other types of solid state materials) can be rapidly tuned with exquisite precision. Pressure tuning is therefore a powerful tool for probing and exploring electronic structure and properties.

If we define a phase space that consists of the materials interaction parameters that determine the thermoelectric properties of a solid state material, we can think of the search for improved thermoelectric materials as an exploration of this phase space.[5] Each solid state compound can be represented by a single point in phase space. The traditional approach involving sequential synthesis and characterization explores phase space one point at a time. To increase the rate of discovery of new thermoelectric materials, it would be desirable to be able to more rapidly explore phase space. For semiconductors, the phase space parameters that determine the thermoelectric power are the band energies. Because band energies can be rapidly and precisely tuned with pressure, pressure tuning allows the relevant phase space to be explored more rapidly than is possible with conventional approaches. For other classes of thermoelectric materials, the relevant phase space parameters can typically also be tuned with pressure.

Pressure will also change two other properties that are important for thermoelectric materials, the electrical and thermal conductivities. However, because both conductivities typically increase with pressure (phonon frequencies typically increase with pressure; band gaps

Mat. Res. Soc. Symp. Proc. Vol. 545 © 1999 Materials Research Society

often decrease), the effect on the thermoelectric figure of merit is less significant than that of the thermoelectric power, which is squared in the expression $Z=S^2\sigma/\kappa$.

Once an improved thermoelectric material is found at high pressure, it provides a target for synthesis at ambient pressure. Demonstration of a thermoelectric material with a ZT of 2 or greater at high pressure, which is better than the best known ambient pressure thermoelectric material, bismuth/antimony telluride, would be a significant "proof of principle" accomplishment. This would drive considerable effort to reproduce the improved properties at ambient pressure as well as provide fundamental insight into the parameters necessary for high ZT. In many materials, a chemical pressure can be effected by substituting smaller atoms into the crystal structure. This could allow the properties achieved at high pressure to be realized at ambient pressure. Alternatively, the lattice parameter of an ambient pressure phase may be tuned with chemical pressure. Complex ternary and quaternary compounds offer more degrees of freedom for chemical tuning. A feedback loop involving pressure tuning and chemical tuning efforts is likely to be most effective.

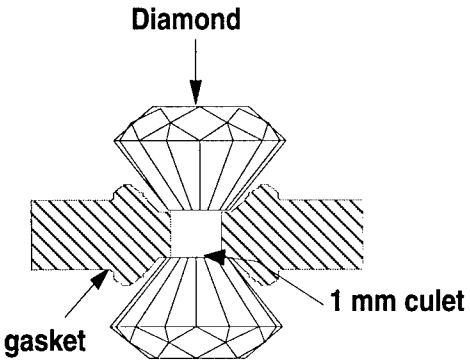

Figure 1: Two opposing brilliant cut diamonds serve as anvils in the diamond anvil cell. The sample and the sample medium (typically monoclinic zirconia) surrounding the sample are contained by a metal gasket (T301 stainless steel), which is approximately 150 μm thick. The culet is 1 mm in diameter. When load is applied to the diamonds, the sample contained by the gasket and diamonds is compressed.

EXPERIMENTAL

For pressure tuning studies of thermoelectric materials it is necessary to measure thermoelectric power as a function of pressure. There are several reports of methods for the measurement of thermoelectric power as a function of pressure using tungsten carbide type opposed anvil systems.[6, 7, 8] We have been developing diamond anvil cell (DAC) (Figure 1) techniques for thermoelectric power measurements on small samples at both ambient and high pressures. The advantages of the DAC include its low cost, versatility, and ability to work with samples that are as small as 100 μm. A schematic of the sample arrangement for thermoelectric power measurements in a DAC is shown in Figure 2. Two chromel-alumel thermocouples (A_1C_1 and A_2C_2) are placed across the sample. A temperature gradient is induced at one end of the sample typically by means of resistive or radiative heating. The overall sample TEP (S_S) is calculated from the following equations, which relate the TEP of each of the thermocouple wires (S_A and S_C) to the absolute sample thermoelectric power:[8]

$$S_S - S_A = \Delta E_{AA} / \Delta T \quad (2)$$
$$S_S - S_C = \Delta E_{CC} / \Delta T \quad (3)$$

ΔE_{AA} and ΔE_{CC} are the emf's between the thermocouple wires A_1-A_2 and C_1-C_2, respectively. ΔT is the temperature difference between the two thermocouple junctions (J_{A1C1} and J_{A2C2}). An equation independent of ΔT is obtained when (1) and (2) are combined:

$$S_S = (S_A - rS_C)/(1-r) \quad (4)$$

where $r = \Delta E_{AA}/\Delta E_{CC}$. Therefore, the TEP of the sample can be calculated from Equation (4) when S_A and S_C are known and ΔE_{AA} and ΔE_{CC} are measured.

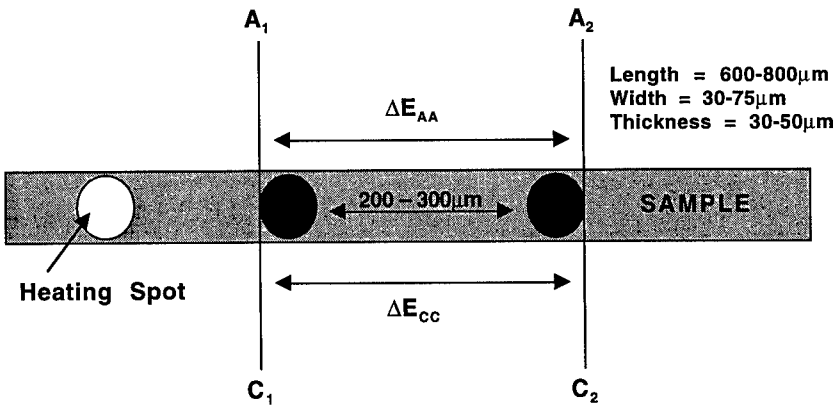

Figure 2: Schematic sample geometry and thermocouple arrangement. Laser heating one side of the sample induces a temperature gradient.

A YLF infrared laser (Quatronix model 4216D CW Nd:YLF, 1053nm) is used to induce a temperature gradient across the sample. The location of the heated spot is monitored with an infrared video camera (Hitachi KP-160 CCD). The temperature gradient is monitored by a pair of Hewlett-Packard nano-voltmeters. The nano-voltmeters are also used to measure ΔE_{AA} and ΔE_{CC} from equations (2) and (3). The two voltmeters are interfaced with a Macintosh computer so that ΔE_{AA} and ΔE_{CC} are measured at the same time. It is necessary to perform the measurements simultaneously because small fluctuations in laser power (1% or less) result in fluctuations in the voltages of the thermocouples, which are canceled out when simultaneous measurements are made.

RESULTS AND DISCUSSION:

Pressure tuning $Nd_{0.45}Ce_{2.55}Pt_3Sb_4$

Because techniques for the measurement of thermoelectric power under pressure are not as well established as other measurement techniques, such as electrical resistivity, it is important to perform measurements on many standards. The thermoelectric powers of standards such as Bi, Ni, Yb, $CePd_3$, $CeSn_3$ were calculated from equation (4) using $S_A = -18.39\mu V/K$ and $S_C = 21.65\mu V/K$. The thermoelectric power of chromel-alumel type thermocouples do not change by more than $0.6\mu V/K$ at pressures to 10 GPa.[9] The data for Bi and Yb are in good agreement with previous reports.[10] Because there is little change in its electronic structure at pressures up to 10 GPa, thermoelectric power of Ni is expected to stay constant with respect to pressure up to 10 GPa,[11] which is what is observed. Measurements on two more complex metallic samples, $CePd_3$ and $CeSn_3$ are also in good agreement with previously reported data.[12, 13]

We have made measurements on many different samples ranging from narrow band gap semiconductors to intermediate valence compounds. Several of the samples which show promise as thermoelectric materials at ambient pressure exhibited significant increases in thermoelectric

power under pressure. Results for the Nd doped Kondo insulator, $Nd_{0.45}Ce_{2.55}Pt_3Sb_4$,[14] which has an ambient pressure ZT of 0.09 at 295K, are presented in Figure 3.

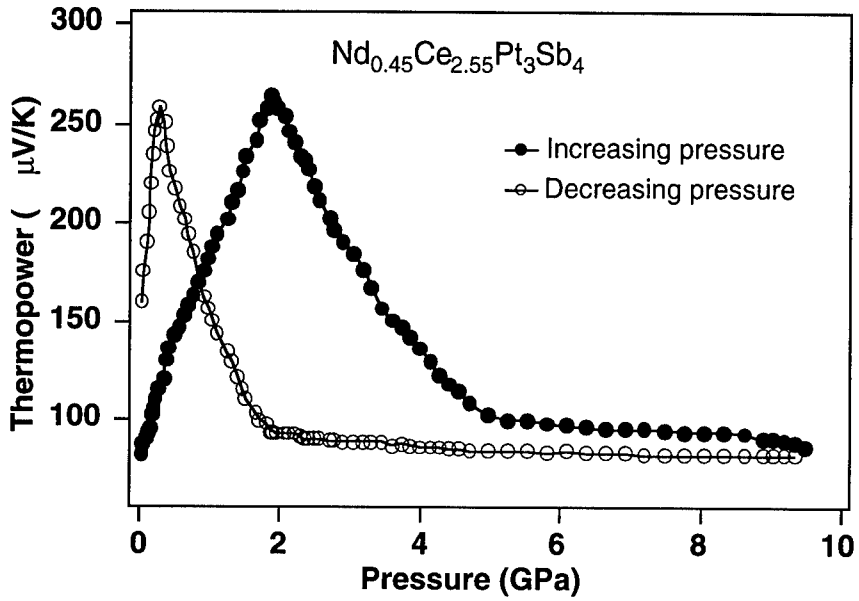

Figure 3: Pressure dependence of thermoelectric power for the doped Kondo insulator $Nd_{0.45}$ $Ce_{2.55}Pt_3Sb_4$ at room temperature.

The ambient pressure thermoelectric power agrees well with independent ambient pressure measurements on larger samples.[14] A significant increase in the thermoelectric power is observed up to approximately 2 GPa, indicating that the thermoelectric properties of this material can be successfully pressure tuned. Qualitatively similar behavior was observed for several other samples in the $Nd_xCe_{3-x}Pt_3Sb_4$ series. The measurements were reversible in increasing and decreasing pressure directions (not shown in Figure 3 for clarity) as long as the pressure was not increased above about 2 GPa. This reversibility up to 2 GPa rules out the presence of many types of errors including movement of the thermocouples and changes in thermal contact upon compression. If the pressure is increased to almost 10 GPa, hysteresis is observed upon releasing the pressure, suggesting that irreversible changes in the sample may occur upon compression to higher pressures. Similar irreversible behavior upon compression to pressures in excess of 6 GPa has been observed in other semiconductors, such as Bi_2Te_3.[15]

The $Nd_{0.45}Ce_{2.55}Pt_3Sb_4$ samples compressed in the DAC likely experience a significant amount of non-hydrostatic stress. We have found that upon compression under hydrostatic conditions using a large volume high pressure apparatus, an increase in the thermoelectric power is still observed but is more modest (to about 110 μV/K). This suggests that non-hydrostatic stress may play a significant role in pressure tuning $Nd_{0.45}Ce_{2.55}Pt_3Sb_4$ and other thermoelectric materials. Our current research efforts are focussed on understanding the effects of non-hydrostatic stress upon the thermoelectric power of these materials.

ACKNOWLEDGEMENTS

Financial support from the Defense Advanced Research Projects Agency and the Office of Naval Research is gratefully acknowledged. We thank one of our collaborators, G.D. Mahan, for helpful discussions and contributions. CDWJ would also like to thank K.A. Regan for experimental assistance and the Natural Sciences and Engineering Research Council of Canada for fellowship support.

REFERENCES

1. X. D. Xiang, X. Sun, P. G. Schultz, Science. **268**, 1738 (1995).
2. R. B. VanDover, L. F. Schneemeyer, R. M. Fleming, Nature. **392**, 162 (1998).
3. G. Briceno, H. Chang, X. Sun, P. G. Schultz, X. D. Xiang, Science. **270**, 273 (1995).
4. W. Paul, J. H. Burnett, H. M. Cheong, in *High Pressure Science and Technology - 1993*, edited by S. C. Schmidt, J. H. Shaner, G. Samara, M. Ross (American Institute of Physics, New York, 1994) p. 545.
5. J. V. Badding, J. F. Meng, D. A. Polvani, Chemistry of Materials. **10** (10), 2889 (1998).
6. G. Ramani, A. K. Singh, Solid State Communications. **29**, 583 (1979).
7. G. Ramani, C. Divikar, A. K. Singh, Physical Review B. **35** (3), 1440 (1987).
8. A. K. Singh, G. Ramani, Rev. Sci. Instrum. **49** (9), 1324 (1978).
9. F. P. Bundy, in *Progress in Very High Pressure Research*, edited by F. P. Bundy, J. W. R. Hibbard, H. M. Strong (Wiley, New York, 1961) p. 256.
10. B. T. Ferdin, N. V. Jaya, K. Anbukumaran, S. Natarajan, Rev. Sci. Instrum. **66** (12), 5636 (1995).
11. D. A. Young, in *Phase Diagrams of the Elements*, (University of California Press, Berkeley, 1991).
12. V. Vijayakumar, S. N. Vaidya, E. V. Sampathkumaran, R. Vijayaraghavan, Solid State Communications. **46**, 549 (1983).
13. H. Sthioul, D. Jaccard, J. Sierro, in *Valance Instabilities*, edited by P. Wachter ,H. Boppart (North-Holland Publishing Co., 1982).
14. C. D. W. Jones, K. A. Regan, F. J. DiSalvo, Phys. Rev. B. in press.
15. L. G. Khvostantsev, Phys. Stat. Sol. **71** (a), 49 (1982).

BOUNDARY EFFECTS IN THIN-FILM THERMOELECTRICS

M. BARTKOWIAK and G.D. MAHAN
Department of Physics and Astronomy, University of Tennessee, Knoxville, TN 37996-1200, and Solid State Division, Oak Ridge National Laboratory, Oak Ridge, TN 37831-6030, bartkowiakm@ornl.gov

ABSTRACT

Equations describing the resistances to the transport of heat and electricity through boundaries of thin-film thermoelectrics are derived. We show that these boundary resistances obey a boundary form of the Wiedemann-Franz law and cause a new type of thermal instability for short thermoelectric devices. We consider boundary thermal resistances both for phonons (Kapitza resistance) and for electrons, the contact electrical resistance at the junctions, and the boundary thermoelectric effects. It is shown that the Kapitza resistance causes reduction of the effective thermal conductivity of the system only if the electron and phonon subsystems are out of equilibrium. In this case, the thermoelectric figure of merit Z can be increased by reducing the thickness of the film. The electrical contact resistance at the junctions is shown to degrade the performance of the device. However, according to the boundary Wiedemann-Franz law, electrical contact resistance is accompanied by a thermal boundary resistance for the electron subsystem, which can cause an additional enhancement of Z. In some cases, this can lead to a device with ZT as high as 3 at room temperatures.

INTRODUCTION

There has been a resurgence of interest in improving the performance of thermoelectric devices [1]–[5]. One approach is to find new materials. Another approach is to improve the performance by using multiple quantum wells of thermoelectrics [6, 7]. Here we derive the general equations for transport of heat and electricity in the direction perpendicular to the boundaries of a thermoelectric thin film or a superlattice and show that the boundary effects can cause a multiple increase of the thermoelectric figure of merit. There is a boundary value of the electrical conductivity σ_B, the Seebeck coefficient S_B, and the thermal conductivities of phonons K_{Bp} and electrons K_{Be}. We find that the electrical components obey a law $K_{Be} = \mathcal{L}_0 \sigma_B T (k_B/e)^2$ similar to the Wiedemann-Franz law for bulk transport. Here the dimensionless coefficient $\mathcal{L}_0$ is between 2 and $\pi^2/3$. These boundary effects become important for short devices, and should be used in the modeling of superlattice transport.

There is a well-known thermal boundary resistance to the flow of heat by phonons [8]. There have been suggestions for similar resistances to the flow of electrons through boundaries [9]–[11]. Here we provide, for the first time, the complete equations for the electrical and thermal resistances of electron flow through boundaries. We regard this result as new and important. Using these equations, we solved for the thermoelectric properties of a two terminal device consisting of a thermoelectric of length L with metal electrodes on each end. The equations show a new thermal instability. Thermal instabilities associated with Joule

Mat. Res. Soc. Symp. Proc. Vol. 545 © 1999 Materials Research Society

heating are well understood. The present instability does not involve Joule heating but is a thermal boundary instability. Nevertheless, it could cause the temperature of the device to rise uncontrollably when L becomes small.

It may seem obvious that the presence of Kapitza resistance at the boundaries, i.e., the boundary thermal resistance for phonons leads to the reduction of the thermal conductivity of the system. However, we show that this is the case only when electron and phonon subsystems are out of equilibrium at a finite distance from the junctions. In this case, the thermoelectric figure of merit Z can be increased by reducing the thickness of the film. The maximum degree of the enhancement depends on the properties of the semiconductor, and, for example for InSb, can be as high as 17, leading to a device with $ZT \approx 2.4$ at room temperatures. Moreover, when the junctions additionally have a finite thermal boundary resistance for the electron subsystem, even when the boundary Wiedemann-Franz law is taken into account, the effective figure of merit Z of a power generator can be further increased to reach a maximum for micron or submicron thickness of the film.

WIEDEMANN-FRANZ LAW AT BOUNDARIES

Recent work[10, 11] has included a thermal boundary resistance for the electronic heat flow. Here we wish to derive the full set of boundary impedances. We begin with the equation for transport of electricity (J) and heat (J_Q) in a bulk thermoelectric

$$J = -\sigma\left(\frac{dV}{dx} + S\frac{dT}{dx}\right) \tag{1}$$

$$J_Q = -\sigma TS\frac{dV}{dx} - K'\frac{dT}{dx} \tag{2}$$

$$J_Q = JST - K\frac{dT}{dx} \tag{3}$$

$$K = K' - \sigma TS^2 \tag{4}$$

here K' is the thermal conductivity at zero potential, which is different than the thermal conductivity K at zero current. The efficiency of a bulk thermoelectric device depends on the material properties through the dimensionless parameter ZT, where

$$Z = \frac{S^2\sigma}{K} \tag{5}$$

is called the figure of merit [1, 2, 3]. For $ZT \to \infty$, Carnot efficiency is obtained, but the best materials currently used in thermoelectric devices have $ZT \approx 1$ at room temperatures. By analogy, we write down similar equations for a boundary

$$J = -\sigma_B(\Delta V + S_B\Delta T) \tag{6}$$

$$J_Q = -\sigma_B TS_B\Delta V - K'_B\Delta T \tag{7}$$

$$J_Q = JS_BT - K_B\Delta T \tag{8}$$

$$K_B = K'_B - \sigma_B TS_B^2 \tag{9}$$

Here we have introduced the boundary impedances: σ_B (S/m^2), S_B (V/K), and $K_B = K_{Bp} + K_{Be}$ (W/m^{2}K). This is the most general result. The flow of current has impedances if there is a temperature difference ΔT across the boundary, or if there is a potential difference

ΔV, or both. The heat current behaves similarly. An Onsager relation proves that the same Seebeck coefficient S_B enters both terms. These are the general equations which describe a non-Ohmic contact.

We give an example of these results. We assume the boundary impedances are due to a grain boundary with a thickness of a few atoms. This is modeled as a potential barrier with a square shape. Electrons can either tunnel through this barrier, or else be thermally excited over it. Earlier we derived [9] the boundary impedances for the thermal excitations of electrons over the boundary. It is given in terms of Richardson's equation, where $A \approx 120\text{A}/(\text{cm}^2\ \text{K}^2)$, and T is the average temperature in the barrier:

$$J_R = AT^2 e^{-U_0/k_B T} \tag{10}$$

$$\sigma_B = \frac{eJ_R}{k_B T}, \quad S_B = \frac{1}{eT}[U_0 + 2k_B T] \tag{11}$$

$$K_{Be} = \frac{2k_B J_R}{e} = 2\sigma_B T \left(\frac{k_B}{e}\right)^2 \tag{12}$$

Here U_0 is the barrier height, as measured from the chemical potential. Note that S_B is *not* the difference of the Seebeck coefficients of the two sides of the junction. The last equation is the boundary form of the Wiedemann-Franz law.

Next consider the case that the barrier is thin. The electrons can tunnel through the barrier with a higher probability than they can be thermally excited over it. For simplicity assume the junction is symmetric, with the same material on both sides. We follow the general derivation as used in the tunneling Hamiltonian [12] to get for the case that there is a voltage V

$$J = 2e \int \frac{d^3k}{(2\pi)^3} v_z \mathcal{T}[n_F(\varepsilon) - n_F(\varepsilon + eV)] \tag{13}$$

$$J_Q = 2 \int \frac{d^3k}{(2\pi)^3} v_z (\varepsilon - \mu) \mathcal{T}[n_F(\varepsilon) - n_F(\varepsilon + eV)] \tag{14}$$

The difference in Fermi functions can be expanded to first power in the voltage. The tunneling probability $\mathcal{T}$ is small, and is assumed to be dominated by an exponential dependence upon the energy ξ of the electron as measured from the chemical potential: $\mathcal{T}(\varepsilon) = \mathcal{T}(\mu)\exp\{\Lambda\xi\}$, where the constant $\Lambda = 1/\sqrt{E_d U_0}, E_d = \hbar^2/2md^2$ and where d is the barrier thickness. Tunneling occurs only if $\Lambda k_B T < 1$. Otherwise, the electron is thermally excited over the barrier and one uses the above results for thermionic emission. This inequality sets the maximum value of d for tunneling to occur. It is now easy to evaluate the above expressions for the currents, and derive the boundary resistances

$$\sigma_B = \frac{e^2 m}{2\pi^2 \Lambda \hbar^3} \mathcal{T}, \quad S_B = \left(\frac{k_B}{e}\right) \frac{\pi^2}{3} \Lambda k_B T \tag{15}$$

$$K'_{Be} = \frac{\pi^2}{3} \sigma_B T \left(\frac{k_B}{e}\right)^2 \tag{16}$$

The thermal boundary conductivity given exactly by the boundary form of the Wiedemann-Franz law. This completes the discussion of tunneling through a barrier between identical materials. Other cases will be reported elsewhere. However, since an electron always will

tunnel through thin barriers, and be thermally activated over thick barriers, these two cases include most physical situations.

The coefficients in Eqs. (12) and (16) give $\mathcal{L}_0 = 2$ and $\pi^2/3$, respectively. These are the usual coefficients for Maxwell-Boltzmann and Fermi-Dirac statistics, respectively. In bulk transport, the Wiedemann-Franz law is proven by assuming that the same relaxation time for scattering the electrons enters into the flow of electricity and the flow of heat. There is no such approximation in the boundary case. There is no relaxation time in the derivation of these equations. Indeed, Eq. (12) is derived assuming ballistic flow of the electrons over the barrier, i.e., there is no relaxation time!

One must also include at the boundary the phenomena of Joule heating. It occurs whenever there is a current J and voltage difference $\Delta V = (\rho_B J + S_B \Delta T)$, and the heating is $J\Delta V$. The boundary electrical resistance is $\rho_B = 1/\sigma_B$. We assume that half of this heat ends up on each side of the boundary. For example, if heat is flowing from left to right, then there are three heat currents: the amount (J_{QL}) approaching from the left, the boundary current (J_{QB}), and the amount (J_{QR}) departing on the right. The relationship between them is

$$\begin{aligned} J_{QB} &= J_{QL} + \frac{1}{2} J(\rho_B J + S_B \Delta T) \\ J_{QR} &= J_{QB} + \frac{1}{2} J(\rho_B J + S_B \Delta T) \ , \end{aligned}$$

so that, by adding these equations, we get $J_{QR} = J_{QL} + J(\rho_B J + S_B \Delta T)$. These equations, along with the definition (8), provide all of the needed information to match the flow of heat and current at the boundary.

THERMAL INSTABILITY

Next we show the existence of a possible thermal instability associated with the boundary impedances. We solve for the case of a bar of length $L = 2a$ which extends $-a < x < a$. It is connected to a cold reservoir T_c at $x = -a$ with one boundary, and to a hot reservoir T_h at $x = a$ through another boundary.

Consider the coupled equations for the heat balance between electrons and phonons[10, 11]. They can only exchange energy if their temperatures $T_p(x)$ and $T_e(x)$ are different. Because the boundary resistances of electrons and phonons are not the same, these systems have different temperatures at the boundary, and require a distance $1/\lambda$ to equilibrate.

$$-K_e \frac{d^2 T_e}{dx^2} = \rho J^2 - P\delta T \tag{17}$$

$$-K_p \frac{d^2 T_p}{dx^2} = P\delta T \tag{18}$$

Here, $\delta T = T_e - T_p$, and the parameter P represents the strength of the electron-phonon interaction. A formula for P for metals was given by Allen[13]. For doped semiconductors, dimensional analysis gives the approximate formula $P \sim n_e k_B \omega_D$ where n_e is the density of electrons and ω_D is the Debye frequency. We regard all quantities such as ($\rho, P, K_{e,p}$) as constants. These are solved in the standard way[10, 11] by defining a "center-of-thermal conductivity" temperature T_{ctc}, $KT_{ctc} = K_e T_e + K_p T_p$, where $K = K_e + K_p$. The solutions

are

$$T_{ctc} = T_a + T_b\frac{x}{L} + \frac{\rho J^2}{2K}(a^2 - x^2) \tag{19}$$

$$\delta T = \frac{\rho J^2}{K_e\lambda^2} + A\cosh(\lambda x) + B\sinh(\lambda x) \tag{20}$$

$$\lambda^2 = P\frac{K}{K_eK_p} \tag{21}$$

The four unknown constants A, B, T_a, T_b are determined by the following boundary conditions for the flow of heat for electrons and phonons

$$-K_p\left(\frac{dT_p}{dx}\right)_{\pm a} = \pm K_{Bp}[T_p(\pm a) - T_{h/c}]$$

$$ST_e(\pm a)J - K_e\left(\frac{dT_e}{dx}\right)_{\pm a} \pm \frac{J}{2}[\rho_B J \pm S_B(T_{h/c} - T_e(\pm a))]$$
$$= JS_B\frac{T_e(\pm a) + T_{h/c}}{2} \mp K_{Be}[T_{h/c} - T_e(\pm a)]$$

These four linear algebraic equations can be solved for the four unknown variables. Detailed solutions will be presented elsewhere. The existence of the instability can be shown in a simple fashion. Write these equations as $MY = C$ where $Y = (A, B, T_a, T_b)$ is a vector, M is a matrix, and C are the source terms which contain the known constants T_c, T_h and J^2. The determinant of matrix M has the form

$$\begin{aligned}
\det M &= D_0 - j_s^2 D_2 \\
j_s &= \frac{J}{K_{Be}}(S - S_B) \\
D_0 &= (\delta_p c_e + \delta_e c_p)[(1 + 2f_e)\delta_e s_p + (1 + 2f_p)\delta_p s_e] \\
D_2 &= (\delta_e c_p + \delta_p c)[(1 + 2f_p)\delta_p s + \delta_e s_p] \\
f_p &= \frac{K_p}{LK_{Bp}},\quad f_e = \frac{K_e}{LK_{Be}},\quad \delta_p = \frac{K_p}{K},\quad \delta_e = \frac{K_e}{K} \\
c &= \cosh(\lambda a),\quad s = \sinh(\lambda a),\quad u = 2\lambda a \\
c_{(e,p)} &= c + suf_{(e,p)},\qquad s_{(e,p)} = s + cuf_{(e,p)}
\end{aligned}$$

The constants D_0, D_2 are both positive. So the determinant is zero when the current has a value given by

$$j_s = \pm\sqrt{\frac{D_0}{D_2}} \tag{22}$$

When the determinant vanishes, the various quantities A, B, T_a, T_b all diverge to infinity. Clearly, this signifies an instability. Our first thought was that it was a thermal runaway caused by Joule heating. However, Joule heating is caused by the terms ρJ^2 or $\rho_B J^2$ which are not in the determinant, so that the instability is not caused by Joule heating. It seems to be a new type of thermal instability.

The cause of the instability is revealed by the dimensionless parameter j_s. It depends on an interesting combination of bulk parameters (e.g, S) and interface parameters (e.g,

K_{Be}, S_B). The numerator $\sim J(S - S_B)$ is the rate (JS) at which heat is sent towards the interface by the current minus the rate (JS_B) at which it goes through the boundary. The difference is the rate at which it accumulates at the boundary. The denominator contains the thermal boundary conductivity K_{Be} for electrons, which measures the ease with which this energy gets through the boundary. Low values of K_{Be} make it hard for the energy JS to get through the interface. So the instability is due to inability of the system to transport through the interface the heat coming at it. Energy accumulates in the system, which causes overheating. Since every material has these coefficients, this instability could exist at every interface. However, in thermoelectrics the Seebeck coefficient is relatively large, which makes it occur at lower current densities.

It is interesting to examine how the instability varies with the length $L = 2a$ of the system. The ratio D_0/D_2 is of order unity in both limits of $a\lambda >> 1$ and $a\lambda << 1$. So this ratio has no great variation with sample length. Nevertheless, the instability is more important for short devices. This comes from the current density J. The voltage scale of a thermoelectric device[1, 2] is set by $\Delta V \approx S\Delta T \approx IR$ which is independent of thickness. However, the resistance $R = \rho L^*/(\text{Area})$, where $L^* = L + 2\sigma\rho_B$. Thus, if one chooses the current density J to operate at the value of maximum efficiency, it has the approximate value of $J_M \sim S\Delta T/\rho L^*$ which increases as L^* becomes smaller. Short devices have smaller resistances and take larger currents to operate at maximum efficiency. Then values of j_s are larger and one approaches the instability point.

In actual practice, the boundary form of the Wiedemann-Franz law prevents the occurrence of the instability. Note that j_s depends upon K_{Be} while J_M depends upon ρ_B. The constraint on the product $K_{Be}\rho_B = \mathcal{L}_0 T(k_B/e)^2$ prevents J_M from reaching the singular point given by $j_s \sim 1$. Our computer solutions only found an instability when we took values of K_{Be} to be larger than proscribed by the boundary form of the Wiedemann-Franz law.

EFFICIENCY AND EFFECTIVE ZT

The formulas for the efficiency, including boundary phenomena, are too complicated to have an analytical expression for the coefficient of performance. One simple analytical result that can be obtained is the equation for the effective thermal conductivity (K^*) at zero current

$$K^* = K\frac{\frac{\delta_e}{s_e} + \frac{\delta_p}{s_p}}{(1+2f_e)\frac{\delta_e}{s_e} + (1+2f_p)\frac{\delta_p}{s_p}} \tag{23}$$

This formula exhibits symmetry between the electronic (e) and phonon (p) contributions to the thermal conduction. K^* depends on the thickness of the film and is less than K, so that the figure of merit should be corresponding larger. The reason for this is well-known: the thermal boundary resistances reduce the thermal conductivity [14, 15, 16]. In fact, Eq. (23) implies that as the thickness of the film $L \to 0$, then also $K^* \to 0$. However, this is true only when *both* K_{Be} *and* K_{Bp} are finite. Otherwise, if for example $K_{Be} \to \infty$ and K_{Bp} was finite, phonons would transfer their energy to the electrons, which in turn would carry the heat across the junction, so that the phonon thermal boundary resistance $1/(aK_{Bp})$ could not stop the heat conduction. The fact that electrons and phonons can be out of equilibrium causes the appearance of the length scale λ in Eq. (23) in the factors $s_{e,p}$, but does not

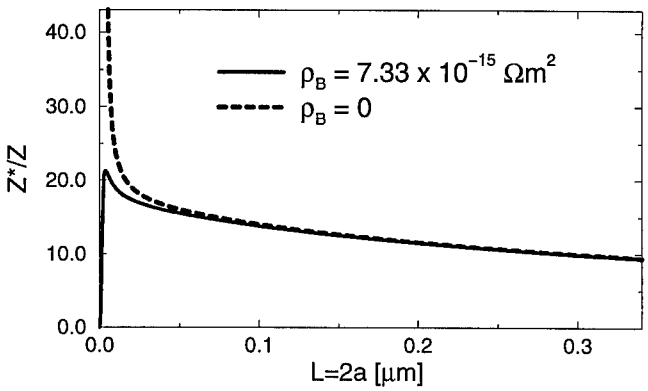

Figure 1: Enhancement of the figure of merit for power generation as a function of the thickness of InSb film for the boundary electrical resistance ρ_B satisfying the boundary Wiedemann-Franz law (solid curve) and for $\rho_B = 0$ (dashed curve).

alter the above conclusion. Therefore, as long as both K_{Be} and K_{Bp} are finite (which is indeed true in reality), effective thermal conductivity can be made arbitrary small just by reducing the thickness of the semiconducting sample. Unfortunately, this does not mean that the effective figure of merit can be made arbitrary large [see Eq. (5)]. Nonzero electronic thermal boundary resistance, according to the boundary Wiedemann-Franz law, is always accompanied by the boundary electrical resistance ρ_B and the boundary Joule heating $\rho_B J$, which inevitably degrades the performance of the device. Can we still gain? There is no unique answer to this question. It depends on whether the device is a refrigerator or a power generator and on values of the material and boundary parameters. But, at least sometimes, we can gain. This is illustrated in Fig. 1, where the ratio of the effective figure of merit Z^* of an InSb thin film to the figure of merit Z of bulk InSb is plotted as a function of the film thickness. Here Z^* corresponds to a power generator and was calculated by maximizing the efficiency and by using the standard relation between the maximum efficiency and the figure of merit [1, 2, 3]. Values of the phonon and the electron contributions to the boundary thermal resistance were assumed as $K_{Bp} = 5 \times 10^6$ W/(m^{2}K) and $K_{Be} = 10^9$ W/(m^{2}K). The boundary electrical resistance was chosen to satisfy the boundary Wiedemann-Franz law. $Z^*/Z \approx 22$ at the maximum corresponds to the effective dimensionless figure of merit $Z^*T \approx 3$ at room temperatures, i.e., about three times more than the best thermoelectric device ever made. The dashed curve, presented in Fig. 1 for comparison, corresponds to the vanishing boundary electrical resistance.

In summary, we present for the first time the equations which describe the boundary impedance of a thermoelectric. Since all materials have a conductivity and a Seebeck, these equations apply to all boundaries. We also give examples of these impedances for the cases of tunneling or thermionic emission. Finally, in solving the equations for the transport of heat through a device with a boundary at each end, we find a new type of thermal instability associated with the boundary. This instability should be present in short thermoelectric devices. The boundary effects can also lead to a substantial improvement of the performance of such devices.

ACKNOWLEDGEMENTS

We thank Dr. J. Sharp for suggesting that we read the Russian papers. Research support is acknowledged from the University of Tennessee, from Oak Ridge National Laboratory managed by Lockheed Martin Energy Research Corp. for the U.S. Department of Energy under contract DE-AC05-96OR22464, and from a Research Grant No. N00014-97-1-0565 from the Applied Research Projects Agency managed by the Office of Naval Research.

References

[1] D.M. Rowe and C.M. Bhandari, *Modern Thermoelectrics* (Reston, 1983).

[2] J. Goldschmid, *Electric Refrigeration* (Pion, London, 1986).

[3] G.D. Mahan, B. Sales, J. Sharp, Phys. Today **50** (3), 42 (1997).

[4] *Thermoelectric Materials — New Directions and Approaches*, edited by T.M. Tritt, M.G. Kanatzidis, H.B. Lyon Jr and G.D. Mahan, (Mater. Res. Soc. Proc. **478**, 1997).

[5] G.D. Mahan, *Solid State Physics*, Vol. 51, ed. H. Ehrenreich and F. Spaepen (Academic Press, 1998) p. 81.

[6] L.D. Hicks, T.C. Harman, X. Sun, and M.S. Dresselhaus, Phys. Rev. B **53**, R10493 (1996).

[7] R. Venkatasubramanian and T. Colpitts, in Ref. [4], p. 73.

[8] E.T. Swartz and R.O. Pohl, Rev. Mod. Phys. **61**, 605 (1989).

[9] G.D. Mahan, J.O. Sofo and M. Bartkowiak, J. Appl. Phys. **83**, 4683 (1998).

[10] Yu.G. Gurevich and G.N. Logvinov, Fiz. Tekh. Poluprovodn. **26**, 1945 (1992) [Sov. Phys. Semicond. **26**, 1091 (1992)].

[11] V.S. Zakordonets and G.N. Logvinov, Fiz. Tekh. Poluprovodn. **31**, 323 (1997) [Semiconductors **31**, 265 (1997)].

[12] G.D. Mahan, *Many-Particle Physics*, (Plenum, Sec. Ed., 1990) chap. 9.

[13] P.B. Allen, Phys. Rev. Lett. **59**, 1460 (1987).

[14] G. Chen, *Dynamic Systems and Control Vol.59, Microelectromechanical Systems*, (MEMS), p. 13 (ASME,1996).

[15] W.S. Capinski and H.J. Maris, Physica B **219 & 220**, 699 (1996).

[16] S.M. Lee, D.G. Cahill and R. Venkatasubramanian, Appl. Phys. Lett. **70**, 2957 (1997).

PREPARATION AND PROPERTIES OF POROUS BISMUTH FILMS

W.-N. Shen, B. Dunn, F. Ragot, M.S. Goorsky, C.D. Moore, G. Chen *, R. Gronsky **,
W.W. Fuller-Mora [∀], D.J. Gillespie [∀] and A.C. Ehrlich [∀]
Department of Materials Science and Engineering, *Department of Mechanical and Aerospace Engineering, University of California, Los Angeles, CA 90095
**Department of Materials Science and Mineral Engineering, University of California, Berkeley, CA 94720
[∀]Naval Research Laboratory, Washington, DC 20375

ABSTRACT

The use of chemical solution routes to form inorganic thin films is a relatively new method which represents an alternative to vapor phase routes. The present study involves the use of a chemical solution route, the decomposition of metal carboxylates, to prepare bismuth thin films of controlled porosity. Such morphologies offer the opportunity to disrupt phonon transport without greatly affecting electrical conductivity and bismuth represents a well known system in which to investigate these effects. Porous bismuth thin films have been prepared using bismuth 2-ethylhexanoate ($Bi[OOCCH(C_2H_5)C_4H_9]_3$) as the precursor in a solvent of 2-methyl-1-propanol. The solution is deposited on glass, Kapton, silicon, alumina or magnesia substrates by spin coating and heated to between 250 - 300°C in hydrogen. Heat treatment temperature and time are important for controlling film microstructure as both pore volume (25 to 50%) and preferred orientation depend upon heat treatment conditions. Bismuth films (62 nm thick) with 32% porosity exhibit conductivities in the range of 150 S/cm with Seebeck coefficients comparable to that of bulk materials.

INTRODUCTION

Bismuth is one of the most well studied thermoelectric materials. The combination of high carrier mobilities, very long electron mean free path, and heavy mass to scatter phonons enables bismuth to exhibit one of the highest thermoelectric figure of merit (ZT) values of any metal. The prospect of inducing a semimetal-semiconductor transition promises to lead to enhancement of these values.[1] However, the characteristic property of bismuth which is most important for the present work is the substantial difference in the mean free path of electrons and phonons. It is this disparity which enables us to consider using nanoporosity as a strategy for enhancing ZT.

The influence of porosity on thermoelectric properties has received very little attention despite some tantalizing results on bulk Si-Ge solid solutions.[2] This work indicated that in a certain porosity range, the ratio of electrical to thermal conductivity (σ/κ) exceeded that of the nonporous material. It was proposed that the decrease in thermal conductivity with increasing porosity followed a slightly different characteristic than that of the corresponding change in electrical conductivity with porosity. As a result, at porosities of 15 to 20%, σ/κ values were as much as 30% higher than that of nonporous materials of the same composition. It is important to note that this work made no serious attempt to control pore size or pore size distribution and that micron size pores were reported.

This prior work suggests that microstructure control may offer a novel approach for increasing the thermoelectric figure of merit for appropriate materials. Bismuth represents a

Mat. Res. Soc. Symp. Proc. Vol. 545 © 1999 Materials Research Society

model system in which to investigate this effect. With the electron mean free path of bismuth being so much greater than that of the phonon mean free path, there is an opportunity to use nanometer sized pores to selectively disrupt phonon transport without seriously affecting electron transport. One of the principal objectives of this paper is to establish synthetic methods for achieving the desired nanoporous microstructure.

The synthesis approach used to obtain nanoporous bismuth is termed metalorganic deposition or MOD.[3] MOD is a nonvacuum, liquid-based technique which readily lends itself to the preparation of thin films by spin-coating methods. Upon heating, the soft metalorganic film is converted to its constituent elements. It is important to mention that MOD is one of several solution-based methods for synthesizing inorganic materials.[4, 5] Such methods have become increasingly popular because of low processing temperatures, environmentally benign conditions and the ability to directly fabricate inorganic films, coatings or fibers at ambient temperature and pressure. The use of MOD to prepare metals is not as common as inorganic oxides but several systems have been reported including Au, Ag, Cu, Pb and Sn.[3]

The present paper describes the use of MOD to prepare thin bismuth films which remain nanoporous because the sintering process has been arrested. The paper addresses the synthesis conditions and heat treatments required to obtain phase pure bismuth of controlled thickness. An important feature in this work is the use of hydrogen plasma etching to remove residual carbon. The values measured for the electrical conductivity and thermoelectric power are consistent with the percent porosity existing in the film.

SYNTHESIS OF POROUS BISMUTH FILMS

The general approach taken in synthesizing porous bismuth films is to decompose an organometallic precursor at temperatures below the melting point of bismuth. A convenient feature of this MOD approach is that it is possible to prepare a homogeneous solution of organometallic precursors which are then deposited on various substrates by spin-coating. Upon pyrolyzing the organometallic precursors, the organic ligands decompose and release gases such as carbon dioxide, carbon monoxide and water vapor. This process produces voids which lead to the formation of the desired porous bismuth films. The paragraphs below describe the details of film formation.

Precursor and Solvent Selection

The two principal constituents involved in the preparation of porous bismuth films are the organometallic source of bismuth (the bismuth precursor) and the solvent system. Each component must satisfy several criteria. The bismuth precursors must exhibit a relatively low volatility for room temperature processing, along with thermal decomposition at temperatures less than the melting point of bismuth. Metal carboxylates are better precursors than metal alkyls or metal alkoxides. The relative volatility for Bi precursors are:

$$BiR_3 > Bi(OR)_3 > Bi(OOCR)_3, \qquad (1)$$

where R represents a saturated hydrocarbon group (e.g. CH_3 for Bi^{III} acetate or $CHC_2H_5C_4H_9$ for Bi^{III} 2-ethylhexanoate). The nature of the organic ligand is quite important as this is responsible for producing pores within bismuth. During pyrolysis of the metalorganic precursors, the organic ligands are decomposed to release gases (CO, CO_2 and H_2O) which

create pores. Due to the low melting temperature of bismuth (m.p. = 271°C), the temperature range for the decomposition reactions should be below the bismuth melting point in order to control porosity in the final film.

We have used a combination of x-ray diffraction (XRD), mass spectrometry and thermogravimetric analysis (TGA) to characterize the decomposition behavior of different bismuth precursors. This information provides appropriate guidance for heat treating the films to produce porous bismuth. Studies with bismuth acetate show two important features: (a) that bismuth oxide is formed upon heating in inert gas (e.g. N_2) and (b) it is feasible to decompose the Bi precursors at temperatures as low as 250°C provided there is adequate reaction time (Fig. 1). The decomposition of bismuth acetate in air occurs in three stages as shown in the following equations.

$$Bi(OOCCH_3)_{3(s)} \xrightarrow{\Delta} BiO(OOCCH_3)_{(s)} + CH_3COCH_{3(g)} + CO_{2(g)}, \quad (2)$$

$$BiO(OOCCH_3)_{(s)} \xrightarrow{\Delta} 1/2\ (BiO)_2CO_{3(s)} + 1/2\ CH_3COCH_{3(g)}, \quad (3)$$

$$1/2\ (BiO)_2CO_{3(s)} \xrightarrow{\Delta} 1/2\ Bi_2O_{3(s)} + 1/2\ CO_{2(g)}. \quad (4)$$

The initial reaction (Eq. 2) occurs over the range of 100 to 150°C leading to the formation of Bi oxide acetate, $BiO(OOCCH_3)$, which remains stable until 300°C when it decomposes to Bi basic carbonate, $(BiO)_2CO_3$ (Eq. 3). The final stage involves the formation of bismuth oxide at 350°C (Eq. 4). It is not surprising that decomposition in air leads to Bi_2O_3. What is unexpected is that these reactions occur at comparable temperatures when heated in N_2. That is, under inert gas, the final product becomes bismuth oxide as the carboxylate ligand itself serves as the oxygen source. It is evident that reducing conditions are required and, using pure hydrogen, the last step of the decomposition reaction becomes Eq. 5 instead of Eq. 4:

$$1/2\ (BiO)_2CO_{3(s)} + 3/2\ H_{2(g)} \xrightarrow{\Delta} Bi_{(s)} + 1/2\ CO_{2(g)} + 3/2\ H_2O_{(g)}. \quad (5)$$

The kinetics of the reduction process are quite important. It is possible to obtain pure bismuth at temperatures as low at 250°C provided there is adequate reaction time. TGA using 10% H_2 in He (Fig. 1) demonstrates that if the temperature is held sufficiently long, the precursor decomposes and bismuth is formed. It is interesting to note that the environment must be sufficiently reducing in order for Eq. 5 to occur. A gas mixture of N_2 containing 4% H_2 produced a mixture which was primarily bismuth oxide with a small fraction of bismuth.(Fig. 2) The above decomposition studies were carried out with both bismuth acetate and Bi 2-ethylhexanoate. As indicated by Eqs. 3-5, the former led to by-products which could be identified readily using XRD and TGA. The decomposition mechanism for Bi 2-ethylhexanoate is somewhat more complicated than Bi acetate, and although not all the decomposition products could be identified, it was evident that heat treatment in pure H_2 gas was required in order to obtain pure bismuth from this precursor.

The choice of solvent is dependent on several factors with solubility being the most important one. Solvents must have low volatility at room temperature and not react with the organometallic precursors. Controlling solvent viscosity and wettability on substrates is required for spin-coating thin films. Another important consideration is that the solvent must evaporate at temperatures below that of thermal decomposition of the precursor. In addition, all chemicals have to be examined for safety and toxicity. Several solvent systems have been examined including xylene, 2-methyl-1-propanol, 2-methoxyethanol, 2-ethylhexanoic acid, acetic acid,

propionic acid, cyclohexanone, water and ethylene glycol. We have focused our efforts on using the 2-methyl-1-propanol solvent system as it meets the various criteria and produces the best quality films when used in combination with the precursor Bi 2-ethylhexanoate.

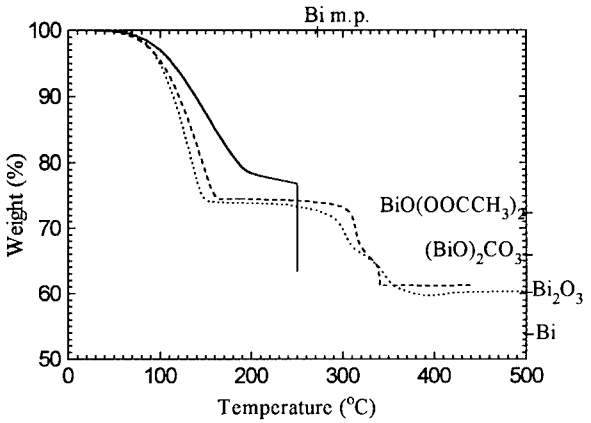

Figure 1. Thermogravimetric analysis results for Bi acetate. Ramping rate is 10 °C/min. and carrier gas flow is 15 ml/min. Dotted lines (·····) indicate reaction under N_2 atmosphere; dashed lines (-----) under air; solid lines (——) held at 250°C for 15 hours under 10% H_2 in He. The labels on the right side represent the theoretical weight losses for Bi acetate to transform to the different compounds.

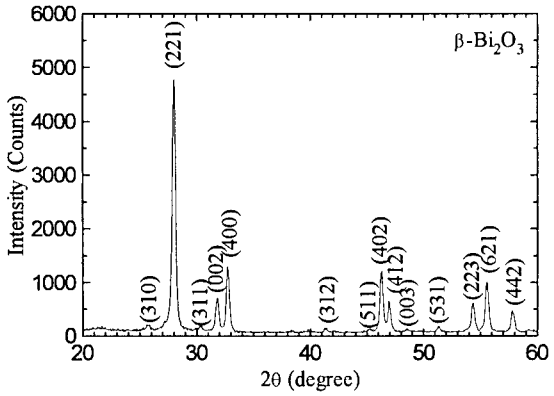

Figure 2. X-ray diffraction result for β-Bi_2O_3 obtained from Bi 2-ethylhexanoate heated at 450°C under 4% H_2 in N_2 for 10 hours. X-ray peaks for Bi occur at 2θ = 27.1, 37.9 and 39.6.

Film Synthesis

The synthesis of porous bismuth thin films is based on dissolving the bismuth 2-ethylhexanoate precursor into 2-methyl-1-propanol. This system exhibits excellent solubility and uniform solutions with as much as 70 wt.% Bi 2-ethylhexanoate precursor concentration can be prepared. After filtering, the solution is spin-coated onto various substrates with typical conditions being 4000 rpm of rotation speed and 30 seconds of rotation time. Several substrates are successfully wet by the precursor solutions and lead to good quality films. These include Pyrex, Si(100), Kapton, polycrystalline MgO and polycrystalline Al_2O_3. In the case of Pyrex, the as received surfaces were too smooth (roughness about 6 nm) to provide adequate wettability of the precursor solutions. To overcome this problem and obtain excellent wettability, the Pyrex substrates were pretreated by reactive ion etching (RIE) using a gas mixture of CF_4 and O_2. In the studies reported here, Pyrex was used as the substrate because its low electrical conductivity (10^{-13} $\Omega^{-1}m^{-1}$ at room temperature) causes less interference with the transport property measurements for thin films.

After spin coating, the films were dried and heated to temperatures between 250°C and 300°C in pure H_2. The films required at least one hour at elevated temperatures to have complete conversion of the precursors to metallic bismuth. X-ray diffraction shows that the resulting films are polycrystalline although there is preferred orientation (Fig. 3). Films heated for less than 3 hours exhibited an orientation in which the (012) plane was parallel to Bi thin film surface. After 6 hours heating, the thin films exhibited a trigonal orientation.

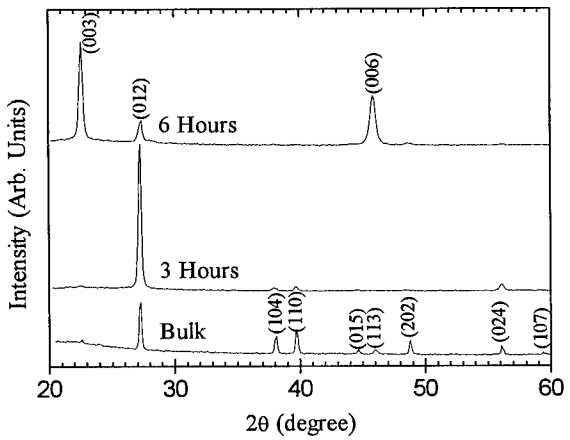

Figure 3. X-ray diffraction results for bulk and porous bismuth thin films obtained using 43 wt.% Bi 2-ethylhexanoate heated at 250°C. Heating times are labeled individually.

Film thickness is determined by a number of parameters including solution viscosity, spin-coating rotation speed, substrate wettability, precursor solution concentration and heat treatment conditions. Fig. 4 shows that by controlling these parameters it is possible to vary the resulting bismuth film thickness from 22 to 570 nm. These data were obtained by profilometry

measurements in which the corners of the bismuth films were etched by nitric acid to expose the Pyrex substrate surface and create the required step. The more dilute solutions (43 wt.% Bi 2-ethylhexanoate solutions) with longer heating times (6 hours at 250°C) led to a film thickness of 80 nm (Fig. 4a) Increasing the heat treatment temperature reduces the thickness still further and films heated to somewhat above the melting point of bismuth were on the order of 20 nm (Fig. 4b). More concentrated Bi 2-ethylhexanoate solutions produced thicker bismuth films due to the higher viscosity of the precursor solution (Fig. 4a). Another means of producing thicker films is to spin-coat multiple layers of the precursor solution prior to the pyrolysis treatment. SEM investigations of the various films confirmed that they were continuous, but the microstructural details of these films could not be characterized as these features were beyond the resolution of the instrumentation. TEM studies of film microstructure as a function of heat treatment are in progress.

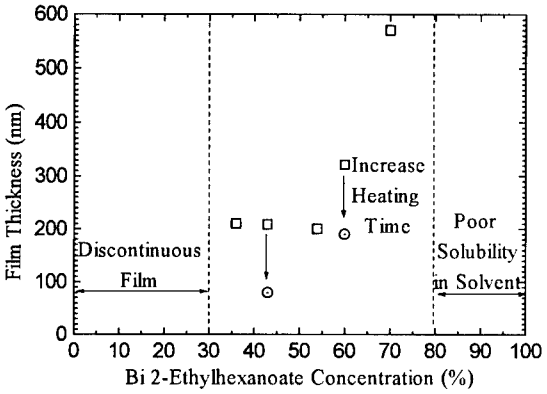

(a)

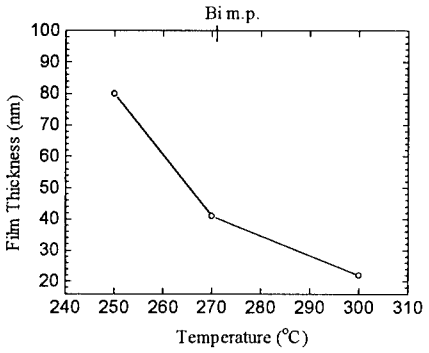

(b)

Figure 4. Thickness dependence for single layer, spin-coated Bi thin films (using 43 wt.% Bi 2-ethylhexanoate). (a) Heated at 250°C for 3 hours (□) and 6 hours (o) respectively. (b) Heated to higher temperature for 6 hours (250°C, 270°C) or one hour (300°C).

The porous bismuth thin films obtained from Bi 2-ethylhexanoate were found to contain a small fraction of residual carbon from the decomposition reactions. FTIR measurements made on bismuth films deposited on Si(100) substrates showed the presence of a cycloolefin peak near 1560 cm^{-1} (Fig. 5). This impurity was believed to cause low conductivity in the porous bismuth films and for this reason methods to remove it were investigated. Hydrogen plasma etching was chosen as this technique has been found to be a useful means of removing carbon impurities from metal films.[6] In the present experiments, a mixture gas of 10% H_2 and 90% N_2 was selected as the source gas for the H_2 plasma. Experiments showed that with a 30 mTorr source gas pressure, a 10 Watt plasma (operating at 2.45 GHz) and 30 second etching time were

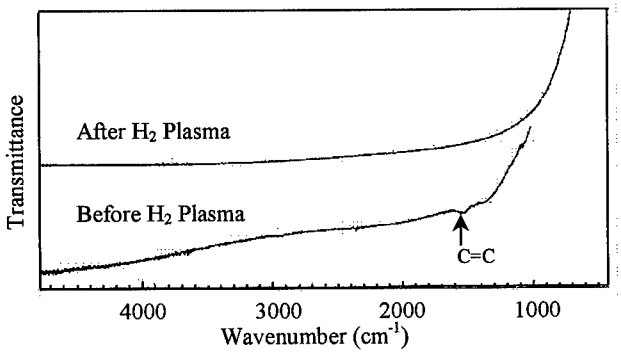

Figure 5. FTIR results for porous Bi thin films. C=C indicates the cycloolefin absorption. Porous bismuth thin films were spin-coated on Si(100) substrates and heated at 270°C for 6 hours with 60 wt.% Bi 2-ethylhexanoate.

optimum conditions for removing the cycloolefin peak as shown in Fig. 5. It is important to note that the conductivity for the porous Bi thin films increased dramatically, by nearly 1000 times, from 0.2 to 1.5 x 10^2 S/cm at room temperature. These results show the importance of removing carbon from the film and the effectiveness of the H_2 plasma etching treatment. It is interesting to note that the plasma etching process also removes oxide impurities (e.g. β-Bi_2O_3). This process is expected to occur since the bonding energy of Bi-O (337 kJ/mol) is less than that of O-H (428 kJ/mol).

Properties of Porous Bismuth Films

The porosity of bismuth films was measured using x-ray reflectivity.[7] The technique is non-destructive, requires no sample preparation and is sensitive to amorphous as well as crystalline materials From the experiment one obtains material density along with quantitative information concerning surface and interfacial roughness. The measurements were made on a modified Bede D^3 diffractometer, using Cu $K_{\alpha 1}$ radiation, a two bounce Si(111) collimator and one bounce Si(111) monochromator. As the angle between the surface and the x-ray beam increases, the beam undergoes total external reflection until it reaches the critical angle where the x-rays penetrate the surface. Beyond this angle the intensity collected is determined by the roughness of the surface (and buried interfaces), with smooth samples showing a decrease in intensity proportional to θ^{-4}, and rough samples showing a steeper gradient. The position of the critical angle depends on the square root of the material density as indicated from the following equation:

$$\theta_c = \lambda \sqrt{\frac{N_A r_o}{\pi} \sum_j \frac{\rho_j}{A_j} \left(Z_j + f_j' \right)} \qquad (6)$$

where θ_c = critical angle, N_A = Avogadro's number, r_o = classical electron radius, ρ_j = density, A_j = atomic mass, Z_j = atomic number, f_j' = form factor and λ = photon wavelength.

Since the x-ray beam is incident on the sample at low angles, the values obtained are an average across the entire sample surface. To reduce the potential for errors with small samples, the experimental data has been matched with a simulated scan.[8] Although the x-ray reflectivity technique is most commonly employed to study buried interface roughness, we find that it is quite applicable to the analysis of porous films.

Figure 6 shows typical data for two porous bismuth films. As indicated in Eq. 6, the θ_c values enable one to obtain film density relative to pure bismuth. It is somewhat clearer to use the data to determine film porosity, P :

$$P = 1 - \rho/\rho_o, \tag{7}$$

where ρ_o is the density of bulk bismuth. The two films in Fig. 6 possess porosity levels of 25% (before H_2 plasma treatment) and 32% (after H_2 plasma treatment) while the gradient indicates a film roughness of approximately 5 nm. In general, film density follows a pattern similar to that of film thickness. That is, higher precursor concentration, longer heat treatment times and higher temperatures lead to denser films (i.e. lower porosity). For the films shown in Fig. 7, film porosity ranges from 25% (film heated at 300°C) to 50% (film heated at 250°C).

The use of hydrogen plasma etching to remove carbon from the bismuth films also affects film thickness and porosity. It is likely that exposure of the bismuth to the hydrogen plasma leads to the formation of BiH_3, an unstable species, which decomposes and redeposits bismuth on the surface of the film. This process effectively causes the film thickness to increase because the redeposited layer has not been sintered. Thus, as shown in Fig. 7, the porosity of the plasma-treated film, 32 - 35%, is greater than that of the initial film. The corresponding film thickness increases as well, to approximately 60 nm.

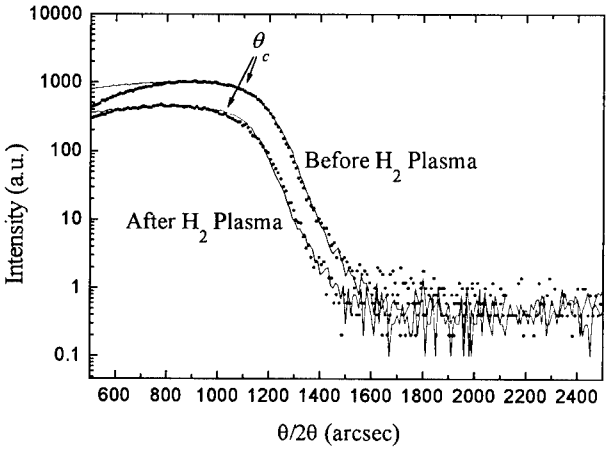

Figure 6. Density measurement and simulation for porous Bi thin films obtained from 43 wt.% Bi 2-ethylhexanoate. Dots (•) represent the experimental data; lines (—) represent the simulation results

Electrical conductivity and thermoelectric power measurements have been made on the plasma-treated bismuth films with 32% porosity. The measurement methods have been described previously.[9] The porous bismuth films have a conductivity of ca. 1.5 x 10^2 S/cm at

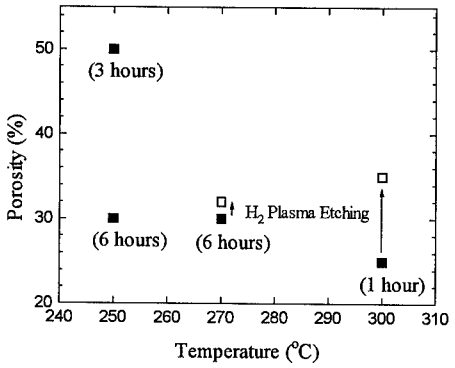

Figure 7. Effect of hydrogen plasma treatment on thickness and porosity of porous Bi thin films. Values in parentheses ( ) indicate heating time to synthesize porous Bi thin films from 43 wt.% Bi 2-ethylhexanoate.

room temperature which decreases very slightly upon cooling (Fig. 8a). The data reported for dense bismuth films of comparable thickness (71 nm) indicate a similar temperature dependence but with conductivity values which are approximately a factor of 10 higher than those of the porous films.[10] This comparison suggests that the nanoscale porosity is responsible for the lower electrical conductivity. The conductivity - temperature plots for dense and porous thin films are compared to that of bulk bismuth in Fig. 8a. The lower conductivity and different temperature dependence of thin films as compared to bulk has been observed previously.[10]

As shown in Fig. 8b, the Seebeck coefficient of the porous thin films was comparable to that of both the dense film and the bulk material. Moreover, the observed temperature dependence, decreasing Seebeck coefficient with decreasing temperature, was the same for all samples. These results suggest that porosity has no significant effect on the thermoelectric power.

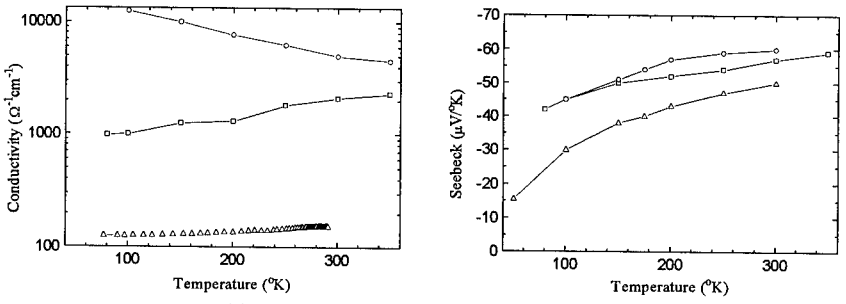

Figure 8. Transport properties for porous Bi thin film (62 nm in thickness and 32% in porosity): (a) Electrical conductivity; (b) Seebeck coefficient. Symbols indicate the results of porous Bi thin film (Δ); dense Bi thin film (□) by thermal evaporation (71 nm thick) [10]; bulk polycrystalline Bi (o).

CONCLUSION

Porous thin films of bismuth have been prepared by a MOD process based on dissolving bismuth 2-ethylhexanoate into 2-methyl-1-propanol. Thermal decomposition studies establish that heat treatment in pure hydrogen is necessary in order to fully convert the bismuth carboxylate precursor to metallic bismuth. By controlling the sintering process, it is possible to produce films which contain between 25% and 50% porosity. The presence of a small fraction of residual carbon in the films is effectively removed by a hydrogen plasma treatment. Initial results for the electrical conductivity and Seebeck coefficient for 62 nm thick bismuth films with 32% porosity gave values consistent with film microstructure.

ACKNOWLEDGMENTS

The authors greatly appreciate the support of the research under DOD/ONR MURI program on thermoelectrics (N00014-97-1-0516).

REFERENCES

1. M.S. Dresselhaus, X. Sun, S.B. Cronin, T. Koga, G. Dresselhaus and K.L. Wang, Mat. Res. Soc. Symp. Proc. **478**, 55 (1997).
2. N.S. Lidorenko, O.M. Narva, L.D. Dudkin and R.S. Erofeev, Neorg. Mater. **6**, 2112 (1970).
3. J.V. Mantese, A.L. Micheli, A.H. Hamdi and R.W. Vest, MRS Bull. **14**, 48 (1989)
4. D. Segal, J. Mater. Chem. **7**, 1297 (1997).
5. F.F. Lange, Science **273**, 903 (1996).
6. G.S. Sandhu, U.S. Patent No. 5691009 (1997).
7. M. Wormington, I. Pape, T. P. A. Hase, B. K. Tanner and D. K. Bowen, Phil. Mag. Lett. **74**, 211 (1996).
8. Grazing Incidence X-Ray Scattering Software, Bede Scientific Inc.
9. T.M. Tritt, G.S. Nolas, G.A. Slack, A.C. Ehrlich, D.J. Gillespie, J.L. Cohn, J. Appl. Phys. **79**, 8412 (1996).
10. F. Völklein and E. Kessler, Phys. Stat. Sol. A **81**, 585 (1984); Phys. Stat. Sol. B **134**, 351 (1986); **143**, 121 (1987).

$Bi_{1-x}Sb_x$ ALLOY THIN FILM AND SUPERLATTICE THERMOELECTRICS

S. Cho*, I. Vurgaftman**, A. B. Shick*, A. DiVenere*, Y. Kim*, S. J. Youn*, C. A. Hoffman**, G. K. L. Wong*, A. J. Freeman*, J. R. Meyer**, and J. B. Ketterson*,
*Department of Physics and Astronomy, Northwestern University, Evanston, IL 60208
**Code 5613, Naval Research Laboratory, Washington, D.C. 20375-5338

Abstract

We have grown $Bi_{1-x}Sb_x$ alloy thin films on CdTe(111)B over a wide range of Sb concentrations ($0 \le x \le 0.183$) using MBE. We have observed several differences with the bulk system. The 3.5 and 5.1% Sb alloys show semiconducting behavior, and the Sb concentration with the maximum bandgap is shifted to a lower Sb concentration, from 15% in bulk to 9%. The power factor S^2/ρ (where S is thermoelectric power(TEP) and ρ electrical resistivity) peaks at a significantly higher temperature (250K) than previously reported for the bulk alloy (80K). The magnetotransport properties of $Bi_{1-x}Sb_x$ thin films (x = 0, 0.09, and 0.16) and Bi/CdTe superlattices have been determined by applying the Quantitative Mobility Spectrum Analysis (QMSA) and multicarrier fitting to the magnetic-field-dependent resistivities and Hall coefficients, using algorithms which account for the strong anisotropy of the mobilities. The calculated S values are in good agreement with experimental results. The structural stability of bulk Bi is studied using the local density linear muffin-tin orbital method. It is shown that the internal displacement changes the Bi electronic structure from a metal to a semimetal, in qualitative agreement with a Jones-Peierls-type transition. The total energy is calculated to have a double well dependence on the internal displacement, and to provide a stabilization of the trigonal phase. We show that an increase of the trigonal shear angle leads to a semimetal-semiconductor transition in Bi.

I. Introduction

Bi and Sb are semimetals with a rhombohedral structure. They have a small energy overlap between the conduction and valence bands, high carrier mobilities, and small effective masses. Because of these properties, Bi and Sb have frequently been used for quantum size effect studies. The $Bi_{1-x}Sb_x$ alloy system can be either a semiconductor or semimetal depending on the Sb concentration.[1-17] The addition of Sb to Bi causes the L_s and T bands to move down with respect to the L_a band. At x=0.04 the L bands invert[2,3] and at x=0.07 the overlap between the hole T and L_a bands disappears[4], resulting in an indirect bandgap semiconductor for $x<0.09$. For $0.09<x<0.15$, $Bi_{1-x}Sb_x$ is a direct gap semiconductor with a maximum bandgap in the range 18-20 meV for 12~15 % Sb concentration.[1,6,7] For $x>0.15$, the hole H band lies above L_s and we again have an indirect semiconductor. Finally at x=0.22, H crosses L_a, and the alloys are again semimetallic up to x=1 (pure Sb). With properties such as a small bandgap, high mobility and a reduced lattice thermal conductivity, semiconducting Bi-rich $Bi_{1-x}Sb_x$ alloys may potentially be used as an n-type thermoelement operating around 80 K. The thermoelectric figure of merit, defined by $ZT=(S^2/\rho\kappa)T$, is 0.88 at 80 K in a magnetic field of 0.13 T,[6] where S is the thermoelectric power (TEP) or Seebeck coefficient, ρ is the electrical resistivity, and κ is the thermal conductivity.

In this article, we report a detailed experimental study of the electrical resistivity and thermoelectric properties of $Bi_{1-x}Sb_x$ alloy films grown on CdTe(111)B substrates over a wide range of Sb concentrations ($0 \le x \le 0.183$).(Sec. III. 1) We also discuss a detailed

Mat. Res. Soc. Symp. Proc. Vol. 545 © 1999 Materials Research Society

model for the thermoelectric properties of BiSb-based heterostructures which self-consistently incorporates the field-dependent Hall and resistivity data. The Quantitative Mobility Spectrum Analysis (QMSA),[18] which derives multiple electron and hole densities and mobilities from the magnetotransport measurements, has been modified to account for the strong anisotropy of the electrical conduction in these materials. We will show that the experimental TEPs can be accounted for in detail. The potential for using the transport/TEP data to extract band parameters will also be examined.(Sec. III. 2) On the other hand, we have studied quantitatively (i.e. in terms of the all-electron total energy) the effects of the two distortions of the rhombohedral A7 structure (internal displacement and trigonal shear) on the electronic structure of Bi. We also discuss the metal-semimetal transition in terms of a Jones-Peierls mechanism driven by these distortions. (Sec. III.3)

II. Thin Film and Superlattice Growth and Transport Measurements

The growth of Bi thin films, BiSb alloy thin films, and Bi/CdTe superlattices on semi-insulating (111)B CdTe substrates by molecular beam epitaxy has been described in detail elsewhere.[19] $Bi_{1-x}Sb_x$ alloy thin films with x=0, 0.019, 0.035, 0.051, 0.072, 0.088, 0.112, 0.143, 0.164, and 0.183 were prepared. The $Bi_{1-x}Sb_x$ epilayers had nominal thicknesses of 0.5-1 μm. Two Bi/CdTe superlattices with 400 Å/100 Å (9 periods) and 800 Å/100 Å (5 periods) well/barrier thicknesses were also grown. CdTe is eminently suitable as a barrier for superlattice thermoelectric devices owing to its near lattice match with Bi, large energy gap, and low thermal conductivity. In all cases, the growth direction was parallel to the trigonal axis of the Bi-based materials. The $Bi_{1-x}Sb_x$ composition was controlled by a quartz thickness monitor where the accuracy was confirmed by inductively coupled plasma (ICP) spectroscopy analysis. The structural properties will be reported elsewhere.[19]

The resistivities and Hall coefficients of all structures were measured as a function of magnetic field ($0 \le B \le 7$ T) and temperature ($4.2 \le T \le 300$ K) by the van der Pauw technique, with current flow in the plane perpendicular to the trigonal axis. To measure the TEP we used the differential method, in which a small temperature difference is maintained across the sample to produce the thermoelectric voltage: $\Delta V=S\nabla T+b(\nabla T)^2+\ldots$, where b is a constant. The thermoelectric voltage $(\Delta V)_i$ vs. temperature difference $(\nabla T)_i$ were plotted and from the slope of the linear region we could determine the TEP.

III. Results and Discussion

1. Transport properties of $Bi_{1-x}Sb_x$ alloy thin films grown on CdTe(111)B

We have measured electrical resistivities and TEPs for 1 μm thick $Bi_{1-x}Sb_x$ alloy thin films over a wide range of Sb concentrations ($0 \le x \le 0.183$). Detailed transport properties were discussed elsewhere.[20] From temperature-dependent electrical resistivity we could define an effective thermal energy gap. The fitted thermal bandgaps are shown in Fig. 1, compared with similarly calculated literature values for bulk[1,6-8] and 1 μm-thick-epitaxial thin films grown on BaF_2(111).[16] As mentioned in the Introduction, the semiconducting behavior in bulk occurs at alloys compositions between 7 and 22% Sb with a maximum bandgap (18-20 meV) at x=0.15. However, we have observed several differences relative to the bulk system. The 3.5 and 5.1% Sb alloys (corresponding to semimetals in bulk) show semiconducting behavior. The Sb concentration for the maximum bandgap shifts to a lower Sb concentration, from 15% in bulk to 9%. It is seen

that the effective bandgaps of thin films grown on CdTe(111) are larger than the bulk values, with a maximum gap of 40 meV.

Figure 2 shows a comparison of the TEP between our thin films and bulk values as a function of Sb concentration at several temperatures. Three important points are evident: i) The magnitude of the TEP of the alloys with Sb concentrations of 3.5 and 5.1% increases with decreasing temperature above 220K, indicative of semiconducting behavior. ii) The Sb concentration for the maximum TEP has shifted to lower Sb concentrations, from 15 % to 9 %. iii) The TEPs of the alloy thin films grown on CdTe(111) are larger than for bulk alloys, which is consistent with an enhanced gap. All these differences observed in TEP measurements are consistent with the electrical resistivity results. In both transport measurements (electrical resistivity and TEP), the 8.8% Sb alloy has highest effective gap and the highest TEP.

The temperature-dependent power factor (S^2/ρ) for a 7.2 % BiSb alloy thin film is compared to bulk Bi and $Bi_{0.88}Sb_{0.12}$ alloy crystals as shown in Fig. 3. Only the largest literature values are graphed. These results show that power factors for the BiSb thin films peak at a significantly higher temperature (250K) than for previous results for the bulk alloy (80K). The peak temperature mainly depends on the electrical resistivity behavior. With a small bandgap of 20 meV in bulk, the electrical resistivities of the alloys decreases with decreasing temperature below room temperature until a certain temperature, related to the thermal energy (e.g. at 300 K, k_BT~25 meV). We observe that the 1.9, 3.5, 16.4, and 18.3% alloys have a minimum in the resistivity below room temperature. However, for other films, e.g. 7.2% Sb alloy (having maximum power factor), the electrical resistivity increases with decreasing temperature. Therefore the peak occurs at a higher temperature. These results imply that thermoelectric properties such as the optimum operating temperature and the magnitude of the figure of merit Z, depend on the magnitude of the bandgap of the material and can be controlled by band engineering.

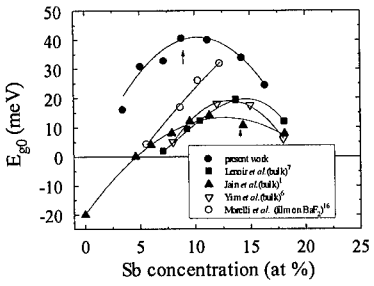

Fig. 1. Effective thermal bandgap E_{g0} at 0 K as determined from temperature dependent electrical resistivity versus Sb concentration.

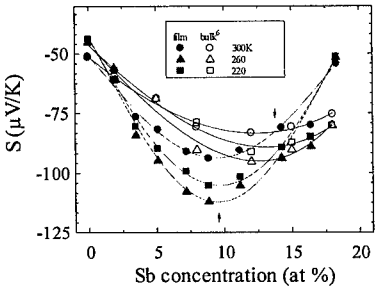

Fig. 2. TEPs of $Bi_{1-x}Sb_x$ alloy thin films and bulk crystal as a function of Sb concentration at several temperatures: 220K, 260K, and 300K.

A possible explanation for the appearance of semiconducting behavior in the 3.5 and 5.1% Sb alloys, a shift in Sb concentration with maximum bandgap and an enhanced effective bandgap over bulk BiSb alloy, may be the strain effect, which modifies the electronic band structure, resulting in a shift of the relative position of the electron and hole

bands. The presence of tensile strain was verified in the θ-2θ X-ray diffraction studies. The c-axis lattice constant with respect to the hexagonal unit cell of BiSb for our films is consistently smaller than that of the bulk for a given Sb concentration. The strain-related electronic structure will be discussed in section III. 3.

2. Magnetotransport Properties and Theoretical Modeling of TEP of Thin Films and Superlattices

The magnetotransport results were analyzed using a Quantitative Mobility Spectrum Analysis (QMSA) procedure[21,22] which derives carrier densities and mobilities for all of the species present. The TEP has been calculated using a band structure, statistical, and transport model that incorporates electron and hole densities and mobilities derived from field-dependent Hall and resistivity measurements that were analyzed by the anisotropic QMSA and multicarrier fitting approaches. The details of the anisotropic QMSA procedure have been presented elsewhere.[18]

A. Bi Thin Film

We first consider the Bi thin film, which is taken to be semimetallic with a 38-meV overlap between the conduction band minima at the L valleys and the valence band maximum at the T valley. In QMSA the holes are therefore assumed to be isotropic, whereas a large mobility ratio of $\mu_{l2}/\mu_{l1} = 60$ is employed for anisotropic electrons residing in the L valleys.[23,24] QMSA results for the carrier densities and mobilities as a function of temperature are shown in Figs. 4 and 5, respectively. The concentration results are in good agreement with those of previous investigations of bulk Bi samples[25] and with the densities predicted by carrier-statistical calculations described elsewhere. At $T = 6.3$ K, the electron mobility is found to be 6.4 x 10^4 cm^2/Vs and the hole mobility is 6600 cm^2/Vs, whereas nearly equal electron and hole mobilities are obtained if the electrons are taken to be isotropic.[18]

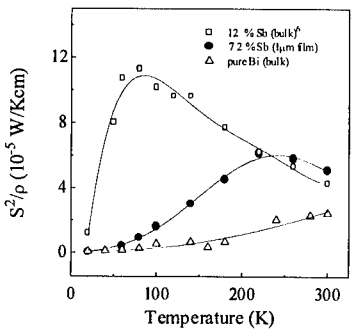

Fig. 3. Temperature dependence of the power factor (S^2/ρ).

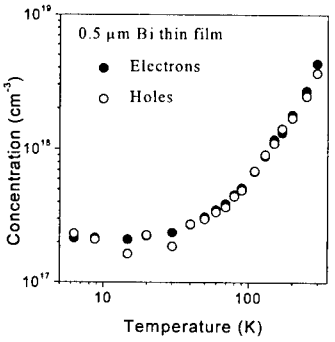

Fig. 4. Electron and hole densities as a function of temperature, as determined from analysis of the Hall data with the anisotropic QMSA procedure.

TEPs were calculated, using the QMSA densities to derive the Fermi energies and the QMSA mobilities to fix the normalization of the momentum relaxation times. The result is given by the solid curve of Fig. 6, which is in good agreement with the experimental data represented by the filled points, when it is considered that the model incorporating input from the transport measurements contains no adjustable parameters. The relatively modest discrepancy at lower temperatures is probably due to a slight underestimate of the electron-to-hole mobility ratio obtained from the magnetotransport characterization.

B. Bi/CdTe Superlattices

Similar analyses were carried out on data from the two Bi/CdTe superlattice samples. Experimental[26] and theoretical TEP results for the 400 Å/100 Å superlattice are indicated by the open points and dashed curve, respectively, in Fig. 6. In this case, the agreement is even better than for the Bi thin film. While at low temperatures, the magnitude of the TEP is smaller than that for the Bi thin film due to the much stronger degeneracy of the electrons, S increases rapidly with T as the degeneracy is reduced. At high T, the TEP exceeds that in the Bi film owing to a smaller hole population even though the mobility ratio is closer to unity than in Bi. The agreement between the theoretical and experimental results for the 800 Å/100 Å superlattice is quite similar.

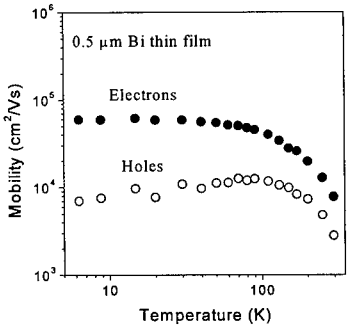

Fig. 5. Electron and hole mobilities as a function of temperature derived from the anisotropic QMSA of the Hall data.

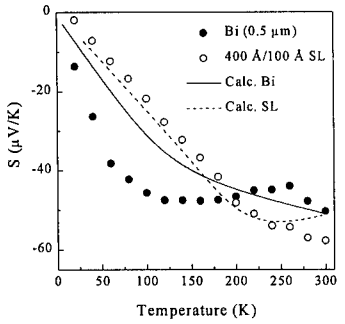

Fig. 6. Experimental and theoretical TEPs for thin film and a 9-period 400 Å/100 Å Bi/CdTe superlattice.

C. $Bi_{1-x}Sb_x$ alloys

In analyzing the transport data for the two $Bi_{1-x}Sb_x$ samples (x=0.09 and 0.16), a larger mobility ratio of 250 was assumed.[27] The data were insufficiently sensitive for the QMSA procedure to be used with no constraining conditions. Therefore, we performed a standard multicarrier fit including anisotropy and assuming the presence of three carrier species: electrons in the L_a valley, holes in the T valley, and holes in the L_s valley. Results for the electron concentration (filled circles) and net hole concentration (both L and T valleys, open circles) in this film are shown in Fig. 7. Corresponding fits for the electron mobility (filled circles), average hole mobility when the values for both hole species are allowed to float (open circles) and average hole mobility when μ_{pT} is fixed at the value for

Bi (open boxes) are given in Fig. 8. The two hole mobilities are seen to differ by a factor of 2-3. The curve in Fig. 7 is from a statistical calculation of the electron density, in which the electron and hole effective masses near the band edges have been adjusted from their literature values by a constant multiplicative factor of 1.2. This is done in order to fit the experimental room-temperature density of $n = 1.7 \times 10^{18}$ cm^{-3}, which is in good agreement with previous determinations. Note that the model then reproduces the experimental dependence $n(T)$ quite well. For the temperature range of 60-100 K, in which thermally excited intrinsic carriers begin to appear, the agreement is slightly better by using a gap smaller than 12 meV, and somewhat worse when a larger indirect gap (e.g., 35 meV) is assumed.

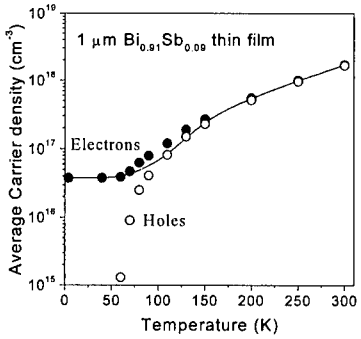

Fig. 7. Electron concentration (averaged over the total thickness) and net hole concentration from the multicarrier fit to the magnetotransport data. Also shown is the carrier-statistical calculation of the electron density obtained assuming a gap of 12 meV (curve).

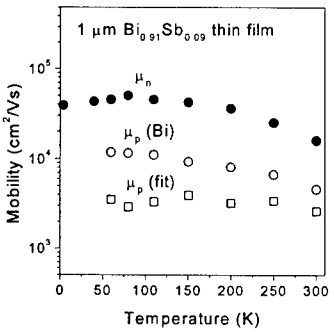

Fig. 8. Electron mobility (filled circles) and hole mobility, averaged over L and T-valley contributions, with floating mobilities for both species (open circles), and average hole mobility when the T-valley mobility is fixed at its value for Bi (open boxes) as a function of temperature.

Figure 9 compares the experimental and theoretical TEPs for the $Bi_{0.91}Sb_{0.09}$ film. If the calculation employs the density and mobility values given in Fig. 7, the theoretical TEP presented by the dotted curve in Fig. 9 significantly exceeds the measured values at low temperatures. The discrepancy must be in the description of the electrons, since few holes are present at temperatures below 100 K. In fact, previous studies of Bi-based thin films observed a carrier component whose concentration did not scale with film thickness.[28,29] This component presumably results from interface defects and, due to band bending, tends to be localized in the vicinity of the interface. The solid and dashed curves of Fig. 9 represent the results of assuming that the electrons observed at low temperatures are concentrated with a sheet density of $N_l = 4 \times 10^{12}$ cm^{-2} (intermediate between the values reported in Refs. 28 and 29) over a thickness of 2000 Å rather than over the total film thickness of 1 μm. With this assumption, the local electron density is 2×10^{17} cm^{-3}, and the degeneracy is great enough to account for the experimental TEP at low T. As the

temperature increases to the point where additional electrons and holes are thermally excited, those carriers are expected to spread out uniformly through the entire film. The dashed and solid curves, which account for both localized and bulk carriers and take the energy gap to be 12 meV are seen to bracket the measured values. If the same procedure is followed while assuming a larger energy gap of 35 meV, the agreement between theory and experiment is not as good at intermediate temperatures. However, as for the intrinsic carrier concentration (Fig. 7), the difference is not great enough to represent a definitive argument against a larger value for E_g.

Fig. 10 shows the experimental (points) and theoretical (curves) results for the TEP as a function of temperature in the $Bi_{0.84}Sb_{0.16}$ thin film, for which an indirect energy gap was assumed to have its bulk value of 30 meV. The increased (non-uniform) carrier density and hence greater electron degeneracy forces theory and experiment to agree at low temperatures. The agreement at high temperatures is also quite good, although the magnitude of S from the theory is somewhat too large at intermediate temperatures. The calculated results are again relatively insensitive to variations of the energy gap.

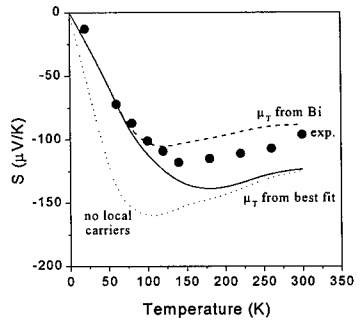

Fig. 9. Experimental and theoretical TEPs as a function of temperature for the 1 μm $Bi_{0.91}Sb_{0.09}$ thin film. The solid curve corresponds to a floating T-valley mobility, whereas the dashed curve results from assuming the T-valley mobility equal to that in the Bi thin film.

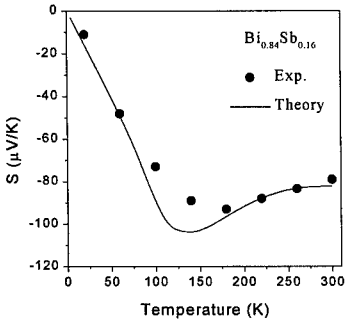

Fig. 10. Experimental and theoretical TEPs as a function of temperature for the 1 μm $Bi_{0.84}Sb_{0.16}$ thin film.

3. Electronic Structure, Phase Stability and Semimetal-Semiconductor Transition in Bi

The relativistic version of the FLMTO - plane wave method[30] is used to obtain self-consistent solutions of the Kohn-Sham-Dirac equations and the total energy. A 65 k-point mesh with the tetrahedron method in the irreducible part of the A7 Brillouin zone was used for the k-space integration. A three-κ basis set (including 5d, 6s, 6p and 6d electron states) is used to construct the band Hamiltonian. An $l_{max} = 6$ is used for the tail- decomposition and charge density calculations. Convergence to better than 10^{-4} e/(a.u.)^3 for the charge density and 10^{-5} Ry for the total energy is achieved.

Bi belongs to the group-V elements with the α-arsenic, A7, crystal structure. The A7 structure may be obtained from a simple cubic (SC) structure under two separate distortions: (i) an internal displacement of the two inter-penetrating fcc lattices (into which a SC structure can be resolved) along a (111) cube diagonal, and (ii) a trigonal shear. The electronic band structure of bulk Bi obtained with the experimental lattice parameters[31] is shown in Fig. 11. (In a hexagonal basis a=8.5678 a.u., and c=22.2958 a.u., the trigonal shear angle α= 57°19', and the internal displacement u=0.234 (in units of the c-axis).)

The main features of the band structure consist of a hole pocket at the T-point and an electron pocket at the L-point, and are in agreement with both previous first-principles pseudopotential[32] and a variety of semi-empirical calculations.[33] As follows from Fig. 11, bulk Bi is a semimetal with a small conduction-valence band overlap involving the T and L points. The electron binding energies at Γ and T are compared with the data of XPS measurements and previous semi-empirical calculations. There is a reasonable agreement (rather qualitative) between our results and experiment. The lower energy of the valence band bottom obtained in most semi-empirical tight-binding calculations is due to the use of older experimental data for the parametrization of the Hamiltonian matrix elements. As follows from the results of our calculations and recent experiments,[34] the position of the valence band bottom measured in the earlier experiments is too low, and hence the semi-empirical results must be revised.

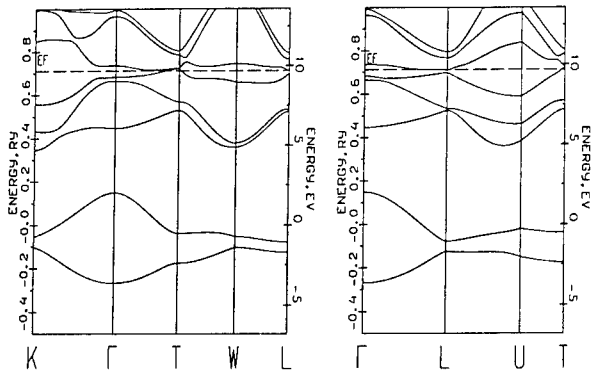

Fig. 11. Band structure of A7 - Bi for the experimental volume, internal displacement and trigonal shear.

The total energy as a function of the internal displacement (δ= 0.25 - u) for different volumes, but with the trigonal shear angle fixed at the experimental value, is shown in Fig. 12a. The total energy clearly has a double-well character. A similar total energy dependence on the internal displacement was obtained previously for P and Sb within the framework of first-principles pseudopotential calculations.[35] The equilibrium value of the internal displacement decreases with decreasing volume and for V = 0.85 V_{exp} the dependence becomes practically flat. This shows that at high pressure an A7 to SC phase transition is expected, in agreement with experiment.[36] It should be mentioned that, as in the case of P and Sb, the dependence of the total energy on the internal displacement describes a second-order phase transition from A7 to SC in disagreement with the first-

order phase transition observed experimentally. Therefore the mechanical work has to be added to the total energy to obtain a free energy at zero temperature and the first-order phase transition observed experimentally.

Using a Landau-type expansion of the total energy, $\delta E = A\delta^2 + B\delta^4$, we obtain an equilibrium internal displacement parameter $\delta = 0.016$ which is in fairly good agreement with the experimental volume. The density of states at the Fermi-level as a function of the internal displacement parameter is shown in Fig. 12b. A decrease of the DOS with increasing δ demonstrates the role of the internal displacement in the metal-semimetal transition. At some value of δ larger than the equilibrium value an energy gap appears.

The total energy vs. unit cell volume dependence for the experimental value of the trigonal angle is shown in Fig. 13. There is an excellent agreement between the LDA and experiment. We also varied the angle around the experimental value and obtained E(60°) - E(57°19') = 0.53 meV and E(54°) - E(57°19') = 39.44 meV. Thus, we can conclude that the LDA provides the correct minimum of all three parameters for trigonal Bi : volume, trigonal angle, and internal displacement. To analyze the character of the metal-semimetal transition we performed calculations of Bi with the experimental Bi volume and (a) internal displacement u = 0.25 and trigonal angle = 60° (which is an equivalent to the SC -structure); (b) an internal displacement u = 0.234 and a trigonal angle = 60° (no trigonal shear); and (c) the actual trigonal structure of Bi .

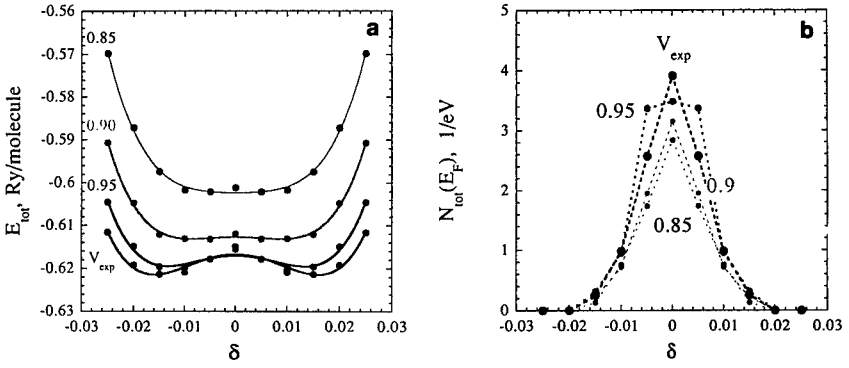

Fig. 12. (a) Total energy vs. internal displacement for different volumes. (b) Total DOS at E_F vs. internal displacement for different volumes (for experimental trigonal shear).

An "artificial" SC Bi (a) has a metallic ground state (Fig. 14a). The shift of one of the fcc sublattices along the (111) diagonal (Fig. 14b) (trigonal distortion) leads to the opening of a gap at L and T and is consistent with a splitting of the degenerate states near E_F for SC - Bi . Thus, Bi becomes a very narrow band gap semiconductor (a direct gap at T of 30 meV). The energy gain of this transition (E_B - E_A) is calculated to be -66.4 meV; i.e. this transition lowers the total energy. Then, introducing a change in the trigonal angle from SC value of 60° to the experimental value, with the same volume and internal displacement as in the case (b) (cf. Fig. 14c), leads to a semimetal with a very small negative energy gain (E_C - E_B) -0.53 meV. Thus, an internal displacement leads to a metal -

insulator transition, which is qualitatively similar to a Jones-Peirels transition. The trigonal shear, however, drives a semiconductor-semimetal transition.

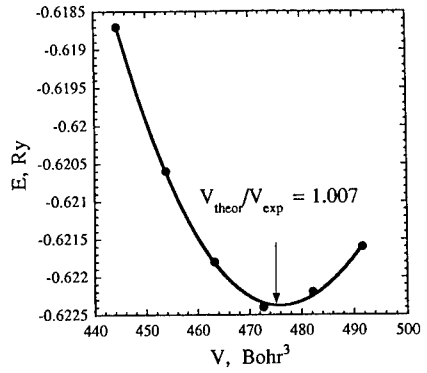

Fig. 13. Total energy vs. unit cell volume.

As a model to analyze qualitatively the effect of a strain in the plane perpendicular to the c-axis on the electronic structure of Bi-films, we assume the following model of a strained film: we chose the lattice parameter a to be the same as for the assumed substrate (CdTe) and determine the c/a -ratio in accordance with the experimental volume of Bi. We also choose the experimental value for the internal displacement. There is a decrease of the E_{Fe} and E_{Fh} overlaps with an increase of the "in-plane" lattice constant and trigonal angle. Finally, at $\alpha = 60°$, Bi becomes a narrow-band semiconductor. This calculation suggests that the presence of tensile strain in our films grown on CdTe(111) leads to an increase in the rhombohedral angle, which drives the electronic band structure of BiSb toward semiconducting behavior as mentioned above. The appearance of semiconducting behavior in the 3.5 and 5.1% Sb alloys, the shift of the Sb concentration for the maximum bandgap, and the enhanced bandgap over bulk BiSb alloys are all consistent with a strain-altered band structure.

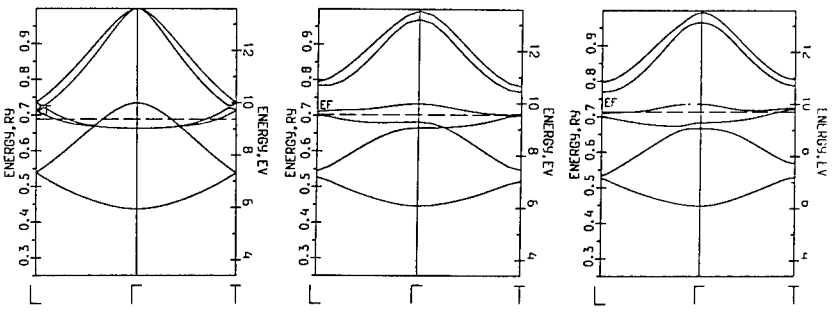

Fig. 14. The band structure along various symmetry lines: (a) for u=0.25 and $\alpha = 60°$ (note L and T are equivalent in this case); (b) for u=0.234 and $\alpha = 60°$; (c) for u=0.234 and $\alpha = 57°19'$

IV. Conclusions

We have studied the transport properties of 1μm-thick $Bi_{1-x}Sb_x$ alloy thin films on CdTe(111)B over a wide range of Sb concentrations ($0<x<0.183$). Compared to the bulk alloy system, there are three important conclusions. i) Semiconducting behavior was observed for the 3.5 and 5.1% Sb alloy thin films. ii) The Sb concentration for the maximum TEP and thermal bandgap shifts toward lower Sb concentrations, from 15 % to 9 %. iii) The effective thermal bandgap and TEPs of the alloy thin films grown on CdTe(111) are larger than for bulk alloys. In addition, we have observed that the power factor S^2/ρ peaks at a significantly higher temperature (250K) relative to that for the bulk alloy, which peaks at (80K).

The TEP has been calculated using a band structure, statistical, and transport model that incorporates electron and hole densities and mobilities derived from field-dependent Hall and resistivity measurements that were analyzed by the anisotropic QMSA and multicarrier fitting approaches. For a Bi thin film and two Bi/CdTe superlattices, the model achieves good agreement with experimental TEPs with no adjustable parameters. However, the low-temperature TEPs for $Bi_{1-x}Sb_x$ alloy thin films with $x = 0.09$ and $x = 0.16$ can only be accounted for by assuming that the electrons associated with additional donors (presumably associated with interface defects) localized in a region adjacent to the substrate rather than being distributed uniformly throughout the 1 μm total film thickness. This is in contrast with the case of the Bi/CdTe superlattices with well thicknesses of 800 Å because in those structures, with frequently occurring interfaces, each well is thinner than the region over which band bending localizes the carriers.

The relativistic total energy LDA calculations of Bi provide rather good agreement with experiment for the Bi ground state properties: equilibrium volume, internal displacement, and trigonal shear angle. The total energy as a function of internal displacement has a double - well character. A decrease of the equilibrium value of the internal displacement with compression promotes an A7 to SC phase transition under pressure. The metal-semiconductor transition in Bi is shown to be qualitatively consistent with the Jones-Peierls model. By varying the trigonal shear angle (e.g., through the action of coherency strain with various substrates) one can control the semi-metal-to-semiconductor transition. This may provide a means to produce, with the right substrate, an improved thermoelectric from strained Bi itself, without impurity doping or superlattice formation. These results suggest that band-engineered Bi-based materials may be useful in thermoelectric devices.

Acknowledgments

This work was supported by DARPA under Grant No. DAAG55-97-1-0130. Use was made of MRL Central Facilities supported by the National Science Foundation, at the Materials Research Center of Northwestern University, under Grant DMR-9120521. The anisotropic QMSA work at NRL was also supported by a CRDA with LakeShore Cryotronics, Inc.

References

1. A. L. Jain, Phys. Rev. **114**, 1518 (1959).
2. S. Golin, Phys. Rev. **176**, 830 (1968).
3. E. J. Tichovolski and J. G. Mavroides, Solid State Commun. **7**, 927 (1969).
4. G. A. Mironova, M. V. Sudakaova, and Ta. G. Ponomarev, Sov. Phys. Solid State **22**,

2124 (1980).
5. G. Oelgart, G. Schneider, W. Kraak, and R. Herrmann, Phys. Stat. Sol. (b) **74**, K75 (1976).
6. W. M. Yim and A. Amith, Solid-State Electron. **15**, 1141 (1972).
7. B. Lenoir, M. Cassart, J.-P. Michenaud, H. Scherrer, and S. Scherrer, J. Phys. Chem. Solids **57**, 89 (1996).
8. D. M. Brown and S. J. Silverman, Phys. Rev. **136**, A290 (1964).
9. V. G. Alekseeva, N. F. Zaets, A. A. Kudryashov, and A. B. Ormont, Sov. Phys. Semocond. **10**, 1332 (1976).
10. N. B. Brandt and E. A. Svistova, J. Low Temp. Phys. **2**, 1 (1970).
11. N. B. Brandt and Ya. G. Ponomarev, Sov. Phys. JETP **28**, 635 (1969).
12. N. B. Brandt, S. M. Chudinov, and V. G. Karavaev, Sov. Phys. JETP **34**, 368 (1972).
13. N. B. Brandt, Kh. Dittmann, and Ya. G. Ponomarev, Sov. Phys. Solid State **13**, 2408 (1972).
14. E. E. Mendez, A. Misu, and M. S. Dresselhaus, Phys. Rev. B **24**, 639 (1981).
15. M. Lu, R. J. Zieve, A. van Hulst, H. M. Jaeger, T. F. Rosenbaum, and S. Radelaar, Phys. Rev. B **53**, 1609 (1996).
16. D. T. Morelli, D. L. Partin, and J. Heremans, Semicon. Sci. Technol. **5**, S257 (1990).
17. D. M. Brown and S. J. Silverman, Phys. Rev. **136**, A290(1964).
18. I. Vurgaftman, J. R. Meyer, C. A. Hoffman, S. Cho, J. B. Ketterson, L. Faraone, J. Antoszewski, and J. R. Lindemuth, submitted to J. Electron. Mater.
19. S. Cho, A. DiVenere, G. K. Wong, J. B. Ketterson, and J. R. Meyer, J. Vac. Sci. Technol. A (in press).
20. S. Cho, A. DiVenere, G. K. Wong, J. B. Ketterson, and J. R. Meyer, (submitted to Phys. Rev. B).
21. J. Antoszewski, D. J. Seymour, L. Faraone, J. R. Meyer, and C. A. Hoffman, J. Electron. Mater. **24**, 1255 (1995).
22. J. R. Meyer, C. A. Hoffman, J. Antoszewski, and L. Faraone, J. Appl. Phys. **81**, 709 (1997).
23. G. A. Saunders and Z. Sümengen, J. Phys. F **2**, 972 (1972).
24. B. Abeles and S. Meiboom, Phys. Rev. **101**, 544 (1956).
25. J.-P. Michenaud and J.-P. Issi, J. Phys. C **5**, 3061 (1972); I. F. I. Mikhail, O. P. Hansen, and H. Nielsen, J. Phys. C **13**, 1697 (1980).
26. S. Cho, A. DiVenere, G. K. Wong, J. B. Ketterson, J. R. Meyer and C. A. Hoffman, Solid State Commun. **102**, 673 (1997).
27. T. Yazaki and Y. Abe, J. Phys. Soc. Japan **24**, 290 (1968).
28. C. A. Hoffman, J. R. Meyer, F. J. Bartoli, A. DiVenere, X. J. Yi, C. L. Hou, H. C. Wang, J. B. Ketterson, and G. K. Wong, Phys. Rev. B **48**, 11 431(1993).
29. Yu. F. Komnik et al., Zh. Eksp. Teor. Fiz. **60**, 669 (1971) [Sov. Phys. JETP **33**, 364 (1971)].
30. S.Y. Savrasov, Phys.Rev. B **54**, 16470 (1996).
31. S. Golin, Phys. Rev. **166**, 643 (1968).
32. X. Gonze, J.-P. Michenaud, J.-P. Vigneron, Phys. Rev. B **41**, 11827 (1990).
33. Y. Liu and R. Allen, Phys.Rev.B **52**, 1566 (1995).
34. G. Jozequel et al., Phys. Rev. B **56**, 6620 (1997).
35. K. J. Chang and M. L. Cohen, Phys. Rev. B **33**, 7371 (1986).
36. P. Cucka and C. S. Barrett, Acta Cryst. **16**, 461 (1962).

MATERIALS DEVELOPMENT FOR THERMOMAGNETIC COOLING

F. Freibert, A. Migliori, T.W. Darling, S. A. Trugman, Thermal and Condensed Matter Physics, MS K764, Los Alamos National Laboratory, Los Alamos, NM 87545, (505) 667-2515, migliori@lanl.gov

ABSTRACT

We review thermoelectric effects in a magnetic field at a phenomenological level. The measurement problem is discussed in detail, and results are presented based on the time-dependent voltages developed by thermoelectric materials in zero field and in large magnetic fields. These time dependent voltages provide a direct and unambiguously accurate measurement of both the Peltier and Ettingshausen figures of merit, and can be used to obtain all the relevant transport including thermal conductivity. Discussion of the limiting performance of both Peltier and Ettingshausen coolers are discussed. Data are shown for Ettingshausen materials with part-per-million levels of Sn doping. Thought these materials exhibit high Ettingshausen figures of merit, Sn doping does not appear to improve performance.

INTRODUCTION

Thermoelectric/thermomagnetic materials are used to generate either electrical power or to produce refrigeration. Measurement of the power-generation properties is equivalent to measurement of the refrigeration properties. The quantity ZT is a measure of the effectiveness of either function and is a dimensionless quantity that arises from a simple phenomenological description of charge and heat transport. That description includes the influence on charge transport by thermoelectric voltages and the influence on heat transport by electrical currents such that

$$\boldsymbol{j} = \sigma(\boldsymbol{E} - \mathbf{S}\nabla\boldsymbol{T}) \tag{1}$$

$$\boldsymbol{j}_q = \sigma\mathbf{S}\boldsymbol{T}\boldsymbol{E} - (\sigma\mathbf{S}^2\boldsymbol{T} + \mathbf{K})\nabla\boldsymbol{T} \tag{2}$$

where $\boldsymbol{j}$ is the electric current, $\boldsymbol{j}_q$ is the heat current, $\boldsymbol{E}$ is the internal electric field, $\nabla\boldsymbol{T}$ is the temperature gradient, σ is the electrical conductivity tensor, $\mathbf{S}$ is the thermopower tensor, and $\boldsymbol{K}$ is the thermal conductivity tensor. These equations, combined with a continuity equation for time-independence,

$$\bar{\nabla} \bullet \bar{j}_q - \bar{E} \bullet \bar{j} = 0 \tag{3}$$

can be manipulated to obtain for a one-dimensional Peltier cooler

$$T_h - T_c = \frac{\sigma_{11} S_{11}^{\ 2}}{2K_{11}} T_c^2 = \frac{1}{2}(ZT)T_c \tag{4}$$

Mat. Res. Soc. Symp. Proc. Vol. 545 © 1999 Materials Research Society

where T_h and T_c are the hot and cold temperatures of the device and the temperature gradient and electric field are in the 1-direction. Note that ZT is only expected to be useful over a small range of temperatures where it is expected that the physical properties do not vary much, and ZT can, in principle, have any positive value.

Similarly, for a perfect Ettingshausen material, with magnetic field along the 3-axis, applied electric field along the 1-axis and heat flow along the 2-axis (requiring that $\sigma_{12}=S_{11}=K_{12}=0$)

$$T_h - T_c = -\frac{\sigma_{11}S_{12}S_{21}}{2K_{22}}T_c^2 = \frac{1}{2}(ZT)T_c \tag{5}$$

but unlike the Peltier case, ZT cannot exceed unity (or else heat flows from cold to hot even with no electric power input). However, in general, neither Eq. 4, nor Eq. 5 describe what happens when heat flows and current flows are not perpendicular or parallel, as would occur in a system in a magnetic field that has comparable Peltier and Ettingshausen [1] effects, such as Bi.

EXPERIMENT

We can see that to determine the effectiveness of any thermoelectric device, we must measure the electrical conductivity, the thermoelectric power, and the thermal conductivity. Each of these quantities is a tensor in a magnetic field, and is also a tensor for oriented materials (such as a single crystal) even if a magnetic field is not present. Thermal conductivity is traditionally difficult to measure accurately, but is crucial to ZT, while thermopower, though somewhat more easily measured, is also more important. Surprisingly, the electrical conductivity, usually considered to be easy to measure, also presents problems for good thermoelectric materials, primarily because of Eq.

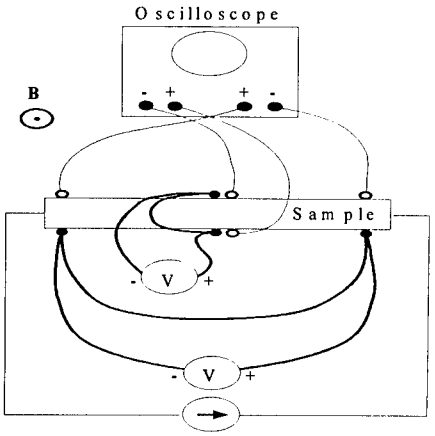

Figure 1. Shown is a sample that is thermally anchored at one end (not shown), with thermocouples (solid contacts) and voltage leads (open contacts) in an arrangement to measure ZT directly.

1. That is, in a thermoelectrically active material, hooking up leads and a constant current source and measuring voltages does *not* yield the electrical conductivity, nor the Hall conductivity. The reason is that substantial thermoelectric voltages and temperature gradients develop that are linearly dependent on the measuring current. Thus accurate resistivity measurements require that the entire sample be thermally anchored. Thermopower and thermal conductivity measurements, however, require that the sample not be thermally anchored. Thus at least two independent measurement set-ups are required to measure the parameters that determine ***ZT***.

There is, however, another approach and that is to determine ***ZT*** directly. To illustrate how this works, consider the sample arrangement of Figure 1. For such an arrangement, a constant current source drives current through the sample in alternating directions (a "square wave") with a frequency of a few Hz. Thermoelectric/thermomagnetic effects generate an alternating temperature gradient that takes some time to build up. That is, the heat capacity and thermal diffusivity of the sample ensure that at the instant of current reversal, there is no instantaneous change in the temperature gradients; temperature gradients develop in an approximately exponential way, taking tens of milliseconds for our mm-size-sample. This is shown in Figure 2. Thus the voltage changes that occur at the instant of current reversal are accurate measures of the conductivity and Hall conductivity. Note that this is true even if temperature gradients are present. After some time determined by the thermal time constant of the sample, thermoelectric voltages change the measured voltage. The ratio of this slower change to the faster one at the instant of current reversal is ***ZT,*** shown explicitly in

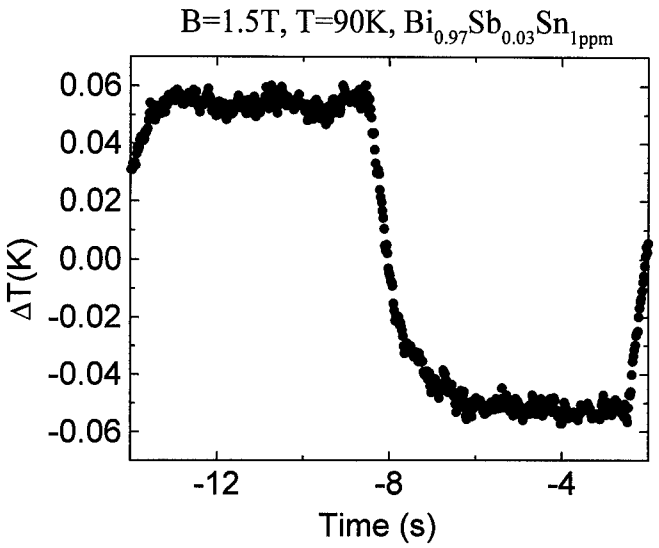

Figure 2. The temperature difference developed across a sample of $Bi_{0.97}Sb_{0.03}Sn_{1ppm}$ in a magnetic field of 1.5T at 90K. This temperature difference is perpendicular to both the field and the current and was measured with chromel-constantan thermocouples.

Figure 3 for an Ettingshausen material. Thus unambiguous and direct measurements of ZT can be made [1-3]. Such measurements determine refrigeration efficiency by using the refrigeration effects directly to determine the changes in electrical work that occur as the sample is cooled by the measuring current. There are several advantages to this measurement, including that thermal EMFs need not be corrected for and that none of the physical parameters need be known or measured (excepting the sample width for Ettingshausen measurements only), nor does this method require measurements of small temperature differences in magnetic fields. The only caution is that the free end of the sample be connected to the thermal anchor with leads whose thermal conductance is much less than the sample's. This method has been very rarely used for Peltier materials [1-3], and our work is the first on direct measurements of Ettingshausen ZT.

If, as in Figure 1, chromel-constantan thermocouples (which are insensitive to magnetic fields) are attached to the sample, then the small temperature differences that develop ΔT can be measured as well (Figure 2). Note that rather simple computer data acquisition systems are all that is required. The asymptote of the drop in voltage after reversal of the current is shown in Figure 3 to be proportional to S_{12} and ΔT and dependent on the sample dimensions **L**, the length and **W** the width, thus S_{12} can be determined easily. Because the instantaneous voltage drop is proportional to j_{11} (which is measured), σ_{12} is also determined. Finally, noting that because $\mathbf{W}ZT$ is measured directly as a voltage ratio, and using Eq. 5, and the computed S_{12}, σ_{11}, and W, we can determine K_{22} approximately. The reason that it is not determined exactly is that S_{12} is not in general equal to $-S_{21}$. The differences arise from the so-called Umkehr [4] effect which is certainly present in Bi alloys

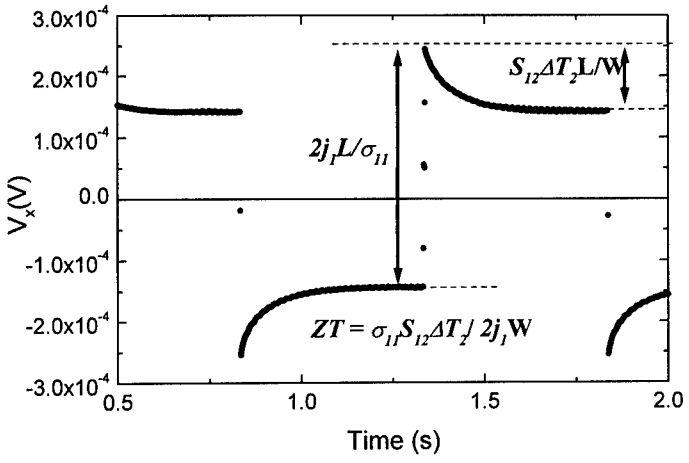

Figure 3. The time-dependent voltage measured along the direction of current j_1 in an Ettingshausen sample of $Bi_{0.97}Sb_{0.03}Sn_{1ppm}$ of width **W** in a magnetic field of 1.5T. The formula for ZT is show as well.

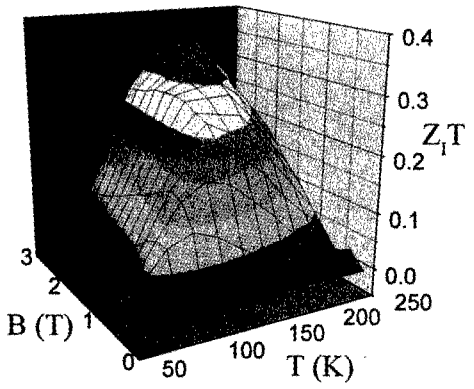

Figure 4. ***ZT*** measured over a broad parameter range for single crystals oriented for best refrigeration of $Bi_{0.97}Sb_{0.03}Sn_{1ppm}$. The measurements of ***ZT*** were made using the technique described here.

used here, but it less than a 10% correction and is beyond the scope of this article. Of course, because the temperature differences used to probe thermopower and thermal conductivity are generated by the refrigeration performance of the material itself, our accuracy for these quantities degrades quadratically with decreasing ***ZT***. However, if ***ZT*** is low then in some absolute sense, we don't care. If ***ZT*** is large, then our accuracy for all quantities is better than, or at least as good, as accuracy obtained using separate measurements.

RESULTS

We used this technique to study the predicted effects of hole-dopants [5] on semi-metallic Bi-Sb alloys, in an attempt to optimize their already favorable Ettingshausen ***ZT***. The basic reasoning behind this approach is roughly as follows. In order to optimize thermomagnetic performance it is desirable to 1) reduce phonon thermal conductivity which is a parasitic effect on refrigerator performance and 2) to increase the effective electron-hole transport symmetry so that the Hall effect is reduced and therefore heat transport is increased. The addition of Sb to Bi, because of the mass difference, should scatter phonons effectively, while the electronic similarity to Bi should minimize electronic scattering. The addition of small concentrations of Sn has a different effect. Because Bi 3%Sb is expected to have of order 10^{-5} carrier electrons/atom, and because this alloy has more very light electrons than very light holes (there is also a heavy hole that plays a role, but we expect that hole to be less important in Ettingshausen refrigeration than the light hole) addition of parts per million of Sn should move the system toward equal numbers of very light electrons and very light holes, thereby reducing the Hall effect and increasing ***ZT***. To Test these ideas, it is important to determine trends in ***ZT*** accurately as Sn doping is varied. Because the parameter space is large

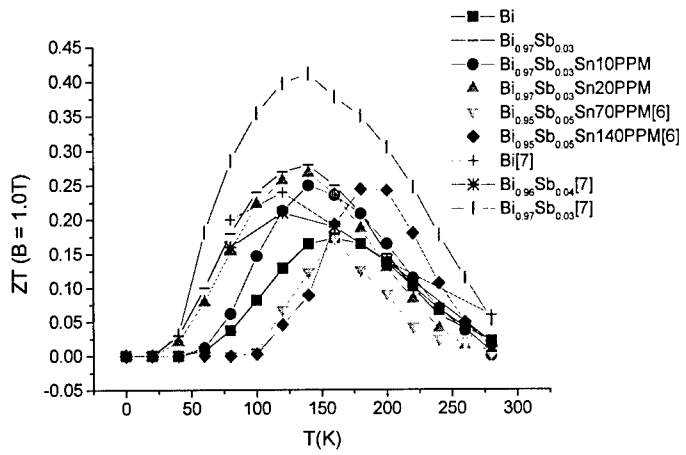

Figure 5. Direct measurements of ***ZT*** made by us and by others [6,7] for various Bi Sb Sn alloys. All samples were single crystals. Data are for an applied field of 1T, and samples were oriented for best Ettingshausen effect.

(measurements must be made as a function of temperature, magnetic field and Sn concentration), and because high accuracy is desirable, the only practical experimental approach is to measure ***ZT*** directly. It is also desirable to obtain the thermopower tensor, resistivity tensor and diagonal thermal conductivity as well. In Figure 4 we show a complete result on $Bi_{0.97}Sb_{0.03}Sn_{1ppm}$ single crystal oriented for most favorable refrigeration. In Figure 5 we show data obtained by us and others for different compositions and at a magnetic field of 1T, chosen because Neodymium Iron Boron permanent magnets can achieve this field. Our measurements have errors of order 1%, are in substantial agreement with some published work [6], but are in substantial disagreement with the work of Cuff et al. [7], who obtain Ettingshausen ***ZT***s that are a factor of two larger than those measured by us and others. We attribute this to the use of unrealistic values by Cuff et al. in computing ***ZT***.

We also measured all the parameters that go into ***ZT*** as well. In Figure 6 are shown the relevant (for Ettingshausen) thermopower, resistivity, thermal conductivity and ***ZT*** for $Bi_{0.97}Sb_{0.03}Sn_{10ppm}$ with subscripts referring to the conventional labeling of crystallographic axes. As is expected, for the data taken near 60K where ***ZT*** is small, the scatter in the thermal conductivity is excessive. However once into the regions where ***ZT*** is appreciable, the thermal conductivity is well determined. It also appears that there may be some evidence of quantum oscillations in the thermopower data at the lowest temperatures.

The data taken by us and by Jandl et al. appear to agree well. What is puzzling, however, is the insensitivity of ***ZT*** to Sn, and the surprising consistency of the peak value of ***ZT*** for many different concentrations. We do not understand this.

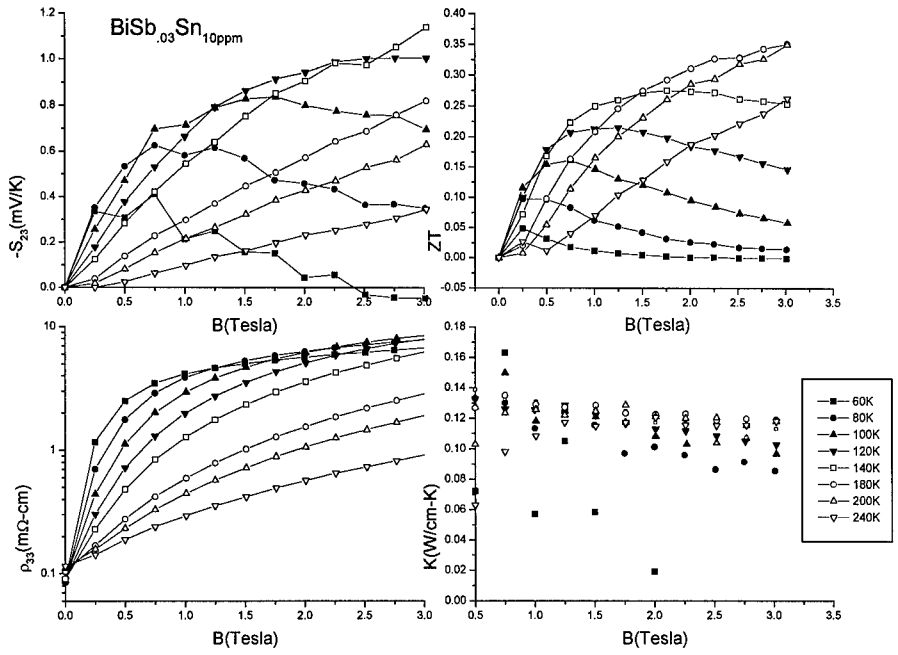

Figure 6. Measurements of ***ZT***, diagonal thermal conductivity K, resistivity ρ_{33}, and off-diagonal thermopower S_{23} using the time-dependent approach described in the text. The sample was a single crystal of $Bi_{0.97}Sb_{0.03}Sn_{10ppm}$ grown using an RF zone melter from the quenched alloy.

CONCLUSIONS

The direct measurement of ***ZT*** is an excellent approach to the study of thermoelectric/thermomagnetic materials because it actually uses the key effect-refrigeration-to measure accurately the key parameter that determines refrigerator efficiency, ***ZT***. We used this technique to measure the Ettingshausen ***ZT*** for a variety of Bi/Sb/Sn alloys as a function of Sn concentration, temperature and magnetic field. We found that the best value of ***ZT*** was insensitive to Sn concentration, contrary to what we expected.

ACKNOWLEDGEMENTS

This work performed under the auspices of the United States Department of Energy, Advanced Energy Projects Office.

REFERENCES

1. F. Freibert, T. Darling, A. Migliori, and S. Trugman, J. Appl. Phys., submitted for publication.
2. T. C. Harman, J. Appl. Phys. **29**, 1373 (1958).
3. G. L. Gutherie and R. L. Palmer, J. Appl. Phys. **37**, 90 (1966).
4. Y. C. Akgoz, G. A. Saunders,Phys. C: Solid State **8**, 2962 (1975).
5. A. Migliori, T. W. Darling, F. Freibert, S. A. Trugman, E. Moshopoulu, J. S. Sarrao, Mat. Res. Soc. Symp. Proc. **478** , 231 (1997).
6. P. Jandl, U. Birkholz, J. Appl. Phys. **76**, 7351 (1994).
7. K. F. Cuff, R. B. Horst, J. L. Weaver, et al. Appl. Phys. Lett. **2**, 145 (1963).

THERMOELECTRIC PROPERTIES OF SINGLE-WALL CARBON NANOTUBES

L. GRIGORIAN, G. SUMANASEKERA, and P.C EKLUND
Department of Physics and Astronomy
University of Kentucky, Lexington, KY 40506-0055
lgrigor@pop.uky.edu; gamini@monica.gws.uky.edu; eklund@pop.uky.edu

ABSTRACT

Results of the temperature dependence of the thermoelectric power and four-probe resistance of single wall carbon nanotube mats are presented. The data are interpreted in terms of the response of a percolating network of metallic nanotube bundles. To the best of our knowledge, the work represents the first systematic study of the transport properties of a series of samples prepared using different transition metal-Y growth catalysts. Although x-ray diffraction and Raman scattering data indicate these samples are nominally the same, we find that the identity of the catalyst has a pronounced effect on the electrical transport properties. The data are interpreted qualitatively in terms of a dilute Kondo system involving the coupling of the the localized magnetic moments of impurity atoms (derived from the catalyst), and the conduction electron spins in the nanotube walls.

INTRODUCTION

A single wall carbon nanotube (SWNT) can be envisioned as a graphene sheet rolled into a seamless cylinder (Fig.1) [1]. The structure of a carbon nanotube can be uniquely defined by two integers (n,m) which define the "roll-up" vector $\mathbf{C} = n\mathbf{a}+n\mathbf{b}$, where **a** and **b** are the primitive translation vectors of the flat graphene sheet. The length of **C** is equal to the circumference of the (n,m) nanotube (Fig.1).

Fundamental symmetry considerations applied to the electronic band structure indicate that tubes with symmetry (n,n), as well as 1/3 of all the other possibilities (n,m≠n), are metallic. The remaining (n,m) tubes are semiconductors with energy gaps $E_g \sim 2\ \gamma\ a_{C\text{-}C}/d$, where γ is the C-C tight

Mat. Res. Soc. Symp. Proc. Vol. 545 © 1999 Materials Research Society

binding overlap energy, $a_{C\text{-}C}$ the nearest-neighbor C-C distance, and d the tube diameter given by $d = \{n^2+nm+m^2\}^{1/2}$. Theoretical prediction of a perturbation in the electronic band structure due to tube-tube interactions within the same bundle have been reported which introduce, in the case of metallic tubes, a pseudogap in the density of stares (DOS) at the Fermi energy [2]. Small diameter ($1< d <2$ nm) single-wall carbon nanotubes (SWNT) have now been prepared in sufficient yield from catalyzed carbon plasmas to allow the widespread study of the chemical and physical properties of these novel molecular filaments [1]. In this diameter range, scanning tunneling spectroscopy (STS) has shown that the semiconducitng tubes typically exhibit gaps $E_g \sim 0.6$ eV [3].

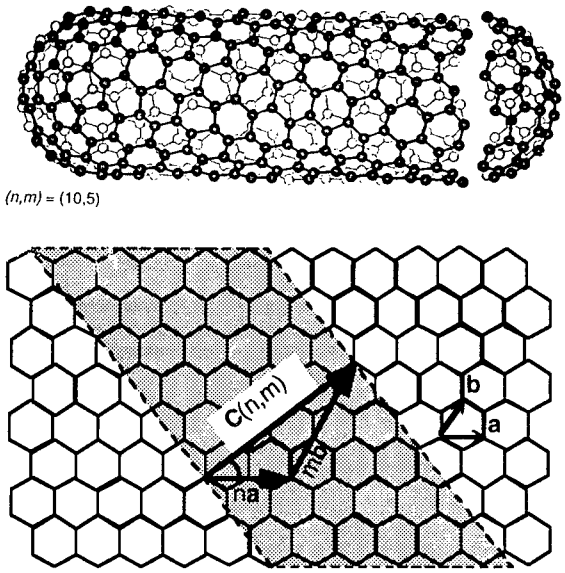

Fig.1. Single wall carbon nanotube formed from the piece of flat graphene sheet also shown in the figure. The "roll-up" vector C(n,m) defines the symmetry of the particular nanotube whose nuclear diameter d is given by $d = C(n,m)/\pi$ [1]. All possible SWNT structures can be realized for $n \leq 0$, $0 \leq m \leq n$.

Quite long tubes are produced with aspect ratios 10^4 - 10^5, provided that a few atomic % transition metal (M) catalyst is also present in the plasma. Transition metals M = Fe, Ni, Co, or these metals in combination, e.g., Ni-Co,

or a transition metal in combination with a rare earth, e.g., Ni-Y, have been found to be successful catalysts. So far, whether these SWNTs are produced in an arc discharge (AD) [4-6], or in a pulsed laser vaporization (PLV) apparatus [7, 8], they are usually observed to be gathered in ordered arrays or "crystalline" bundles containing tens to hundreds of individual tubes. Some of the metal catalyst first incorporated into the arc electrodes or laser targets will ultimately reside as interstitial impurity atoms or chains of atoms in close contact with the nanotube walls.

The first measurements of the thermopower in SWNT mats produced both by PLV (Ni-Co catalyst) and AD (Ni-Y catalyst) yielded surprising results: large positive values at room temperature, i.e., S(300 K) ~ +40 to +60 μV/K, and a strongly non-linear T- dependence [9, 10]. This behavior is in a sharp contrast to that observed for the basal plane of graphite which exhibits a S(300 K) ~ -4 μV/K and a nearly linear T-dependence. Graphite has a pair of weakly overlapping electron and hole sp^2 or π-bands with near mirror symmetry about the Fermi energy E_F. Approximately equal numbers of electrons and holes in these π-bands are consistent with the small (negative) linear thermopower observed below room temperature. Similarly, the one-dimensional band structures of isolated, defect-free, metallic carbon nanotubes [1] are also found to be quite symmetric about E_F, although the bands, in this case, overlap by ~ 2 eV. One should therefore anticipate small values for the room temperature thermopower of SWNTs as well, contrary to experiment.

The four-probe resistance R(T) of SWNT mats, a single bundle, and even a single nanotube, have all been reported to exhibit anomalous behavior. These nanotube systems exhibit a shallow minimum in R at T*~ 40-300 K with $dR/dT < 0$ for $T < T^*$ [11]. Several mechanisms have been proposed to explain the anomalous R(T) behavior, i.e., weak localization [9, 11], contact tunneling resistance between tube bundles in the mat [12], tube-tube interactions within a bundle [2, 9], conductivity contributions from both semiconducting and metallic tubes in the sample [9], and backscattering by "twistons" [13]. In this work, consistent with the model proposed recently by A. Kaiser et al. [12], the electrical transport properties of mats of SWNT bundles are viewed as dominated by the contribution from bundles of metallic tubes (and

interbundle electrical contacts) which allow the formation of percolating metallic pathways throughout the sample. Hereafter, when we refer to the SWNT mat thermopower or resistance, these quantities are discussed in terms of the dominant contribution from the metallic percolating network of SWNT bundles.

RESULTS AND DISCUSSION

Transport data were collected on mats of tangled bundles of SWNTs taken directly from an arc discharge apparatus (CarboLex Inc., Lexington, KY; www.carbolex.com). The thermopower (S) and four-probe resistance (R) measurements were carried out by methods described elsewhere [14-16]. Briefly, the data were collected between 10 and 400 K by attaching two thermocouples and two additional electrical leads to each sample using silver paint. Two of the thermocouple leads were also used as "voltage leads" in the four probe ac resistance measurements; current and voltage were measured at 100 Hz using a lock-in amplifier. Thermopower data were collected using the "analog subtraction" method which involves measuring the time-dependent thermoelectric response of the sample at each temperature to a heat pulse ($\Delta T < 0.5$ K) and extracting the Seebeck coefficient by a linear least squares fit to the data [14].

The approximate volumetric yield of nanotubes was estimated on the basis of Raman scattering [17] to be ~20-70%, depending on the specific catalyst, i.e., M-Yttrium (M= Mn, Cr, Fe, Co, Ni; M=4 at.%, Y=1 at.%). The balance of the material in the mats was in the form of ~10-20 nm diameter carbon nanospheres and carbon-coated catalyst particles. For comparison, an "as-produced" sample made by PLV (Rice University) [7, 8] using Ni-Co catalyst was also studied. After the initial transport measurements on the mats, a post-synthesis iodine-treatment of the samples was carried out in an attempt to convert the interstitial M into M-I complexes. The treatment involves the intercalation of charged linear polyiodide chains (I_n^-) into the interstitial channels between the tubes in the bundle [10]. Z-contrast transmission electron microscopy images, sensitive to the large atomic number (Z) of iodine, has shown that iodine can be reversibly intercalated into the channels; iodine is easily de-intercalated by heating in a vacuum (100°C). As we shall

show, this iodine treatment has a dramatic effect on the thermopower and resistance of the mats.

X-ray diffraction (XRD), scanning and transmission electron microscopy (SEM and TEM) were used to characterize the SWNT materials. The SWNT samples exhibited an XRD peak in the range $2\theta \sim 5.9°\text{-}6.1°$ (CuK_a radiation) associated with the average tube separation in bundles [7]. The existence of the XRD peak confirms the presence of well-ordered, large bundles of nearly monodispersed tubes. For the Fe-Y, Co-Y and Ni-Y derived samples, we estimate the same mean diameter d ~1.3 nm, midway between the values expected for (9,9) and (10,10) tubes, where the notation (n,m) refers to the SWNT symmetry [1]. However, insufficient material was available for XRD analysis of the Cr-Y and Mn-Y catalyzed samples. Raman scattering spectra for all SWNT samples (including those made using Cr-Y and Mn-Y) were taken with YAG laser (1064 nm) excitation and were found very similar (Fig. 2).

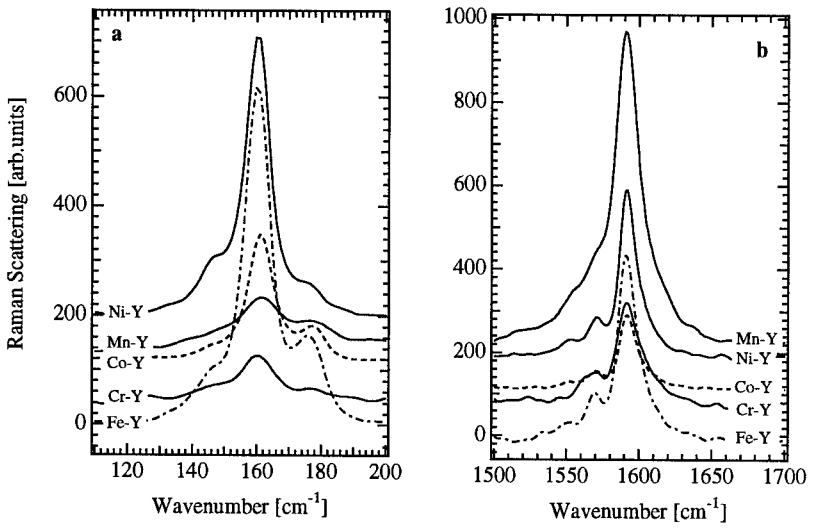

Fig.2. Room temperature Raman spectra of SWNT bundles synthesized by the arc discharge method using the M-Y catalysts indicated: (a) the radial mode and (b) the tangential mode regions.

Previous work has shown that the scattering is resonant [18]. The two strongest features are at opposite ends of the spectrum and involve low frequency radial modes and high frequency tangential modes. Theory has shown that the radial mode frequency of isolated SWNTs is inversely proportional to the tube diameter. So these modes are quite useful in estimating the diameter distribution. In all the mat samples studied here, a doublet with peaks at ~165 cm^{-1} and ~178 cm^{-1} was observed, consistent with only small differences in tube diameter distribution [18] from one sample to the next. In the AD samples, the 165 cm^{-1} peak is the stronger component of the doublet, whereas in the PLV sample the 178 cm^{-1} peak is more dominant. The similarity in the Raman spectra in the various AD-derived mats stems from the fact that the arc conditions (He gas pressure, current, voltage) were maintained identical; only the catalyst was changed from run to run. Fig.3 shows typical thermopower data in the range 10 <T< 400 K. S is found to be positive over the entire T range, indicating that the contribution from the

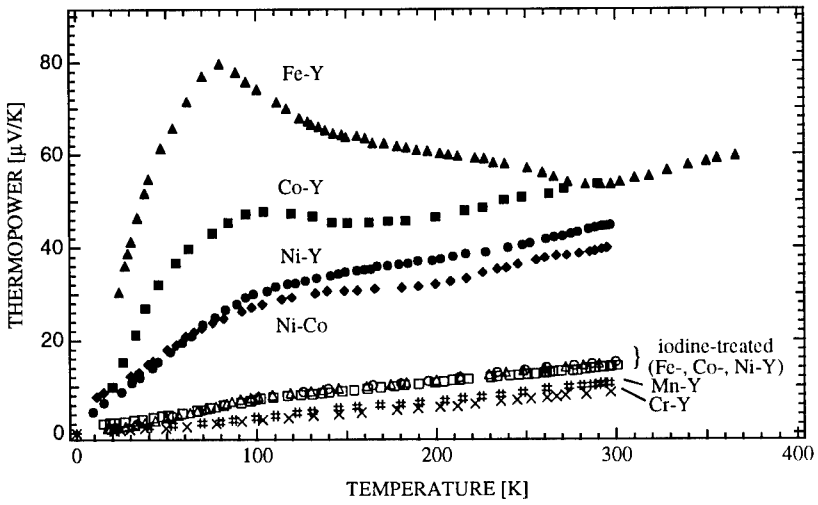

Fig.3. Temperature dependence of the Seebeck coefficient (S) for the various samples indicated. A post-synthesis "iodine treatment" (see text) on mats produced using Fe-Y, Ni-Y or Co-Y catalysts strongly suppresses the broad peak in S.

positive hole carriers dominates the response. The data for mats grown using M-Y (M = Fe, Co, Ni) can be viewed as a superposition of a broad peak on a linear diffusion term (aT). The large non-linear contribution to the data is identified here with a coupling of the tube conduction electron spins and those on localized magnetic impurities within the SWNT bundles, i.e., the Kondo effect. As little as ~100 ppm Fe impurity in Au [19] has been shown to introduce a "giant" thermopower peak similar in form to those shown in Fig.3. The thermopower data for the "as-prepared" PLV-produced (Ni-Co) SWNT sample (Fig.1) is similar to the "as-prepared" AD-produced samples (Ni-Y), evidencing that the anomalous thermopower peak is not associated with one nanotube synthesis method or the other. Interestingly, mats produced using Cr-Y and Mn-Y are nearly identical, much smaller in magnitude, and linear. This is taken as evidence that Mn and Cr are not active Kondo centers in SWNT bundles.

The pronounced effect of the *post-synthesis iodine treatment* on the thermopower data from mats grown using Fe-Y, Co-Y and Ni-Y catalysts is also evident in Fig.3. As can be seen, the iodine-treatment very nearly suppresses the broad (Kondo) peak, leaving an almost linear thermopower, slightly larger than obtained with as-grown mats grown from Cr-Y and Mn-Y. After iodine treatment, the data for these three different samples are now almost equal. This observation, and a similar response of the mat resistance R(T) to iodine treatment are consistent with the formation of metal iodide complexes within the bundle, altering the valence of the interstitial metal (M) and suppressing the Kondo effect. Similar chemical effects have been observed previously, i.e., oxygen in the classic Kondo system Au:Fe, where the Fe is complexed as an oxide suppressing the Kondo anomaly [20].

To more quantitatively examine the broad peak in the thermopower, the data S(T) in Fig. 3 were fit to the sum of a metallic diffusion term (S_d = aT) and a peak $S_K = S\text{-}S_d$, where S_K is the proposed contribution resulting from the magnetic impurity. In Fig.4, as is usually done in Kondo systems [21, 22], we plot S_K (Fig.4a) and the normalized thermopower $S_K/S_{K,max}$ (Fig.4b) on a logarithmic temperature scale. In Fig.4a, it can be seen that the Kondo contribution to S decreases as we pass through the end of the 3d transition metal row (Fe, Co, Ni), and is not discernible for the early transition metals

(Cr, Mn). On the scale of Fig.4a, a small residual Kondo behavior is evident after iodine-treatment. In Fig.4b, the normalized thermopower is plotted *vs.* $\ln(T/T_{max})$, where T_{max} is the temperature at the maximum value of S ($S_{K,max}$). Values for (T_{max} , $S_{K,max}$) for each sample are listed in the figure. It is common to use values of T_{max} locating the thermopower peak as an estimate for the Kondo temperature, i.e., $T_K \sim T_{max}$ [21, 22]. For these samples, we find T_K in the range 80 K < T_K < 100 K, depending on M. These values for T_K fall about midway in the range discovered so far for Kondo systems, i.e., from a few degrees K to as high as 1000 K [21, 22]. The fact that the normalized thermopower data all fall on the same universal curve (Fig.4b) is taken as strong evidence for the proposed Kondo effect in SWNT [21, 22]. To the best of our knowledge, SWNTs may provide the first example of a Kondo anomaly in a carbon material.

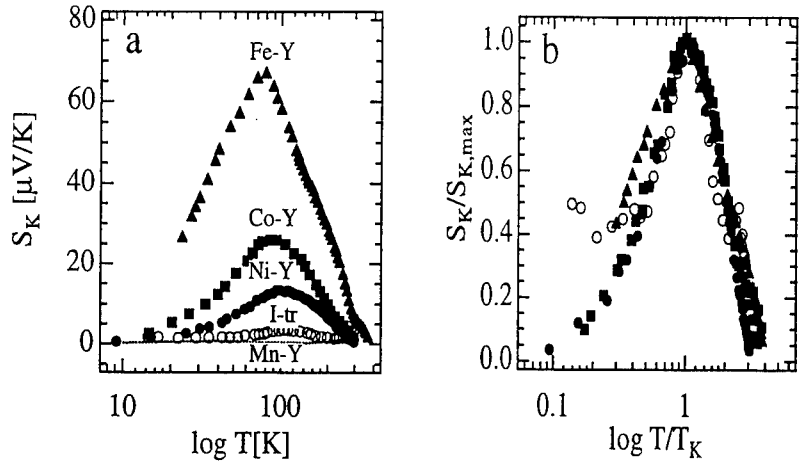

Fig. 4. (a) Temperature dependence (log T) of the thermopower $S_K = S - S_d$, where $S_d = aT$ has been subtracted from the data. "I-tr" stands for the iodine-treated sample. (b) Normalized data plotted vs. $\log(T/T_K)$; see text. Symbols in (b) are the same as in (a).

The Kondo effect has also been shown in the past to exhibit a strong influence on the electrical resistivity of metals, although its signature varies substantially from one system to another [21, 22]. Typically, a metallic Kondo system exhibits linear resistance for T well above T_K. On cooling, approaching

T_K from above, R passes first through a characteristic "Kondo minimum" and then increases as R ~ ln T. On further cooling a power law dependence R ~ T^n is then obtained at the T << T_K [21]. In Fig.5, we plot the logarithm of the *normalized* four-probe resistance $R_N(T)$ = R(T)/R(300 K) vs. logT for mats whose S(T) data appear in Fig. 3,4. The strong low-T upturn in the R_N data is evident, and this anomaly has been the subject of much discussion in the literature on SWNTs [9-13]. The strength of the R_N upturn correlates well with the strength of the broad peak in the thermopower (Fig.2a), suggesting

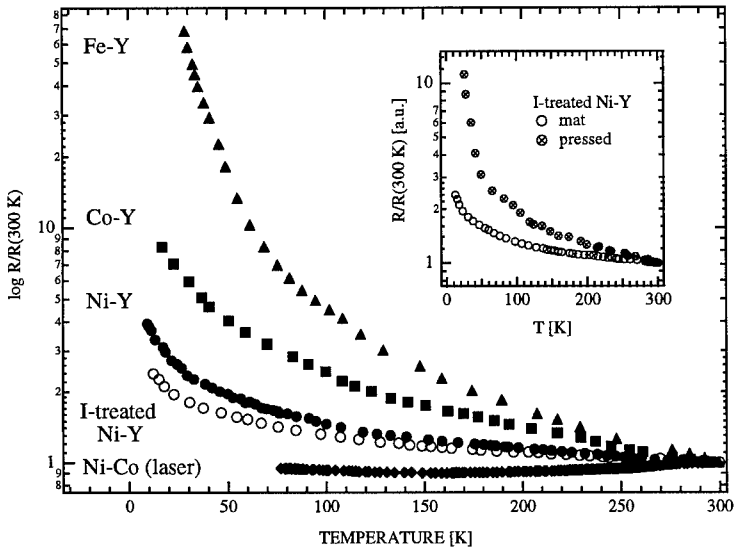

Fig.5. Log [R(T)/R(300 K)] vs log T. Data were collected on the same mats as used for the thermoelectric power studies (Fig.3,4). Inset: effect on R(T) of mild pressure to densify the material in the mat. Open (crossed) symbols represent R before (after) densification.

that Kondo scattering makes a substantial contribution to the low-T resistance, although we feel it is likely that other mechanisms are contributing to this low-T upturn in R_N as well. It is important to note that the iodine-treated mats all exhibit similar data, with a significantly reduced low-T upturn in R_N. The fact that a residual low-T upturn remains after

iodine treatment is certainly consistent with an incomplete attempt to complex all the M (with iodine). But an equally likely explanation, may lie in contributions from other mechanisms (e.g., interbundle contacts, weak localization, twistons, etc.). All our AD-derived mats exhibited negative dR_N/dT over the entire range of temperature, in contrast to the behavior of the LV (Ni-Co) SWNT sample which exhibited weakly positive resistance for T > 150 K, in agreement with previous work on other PLV material [7]. In fact, the weakly negative dR_N/dT for AD derived mats surviving up to room temperature may well stem from *inter*bundle contact resistance, as proposed by Kaiser et al. [11]. In the inset to Fig.5 we demonstrate the effect of modest applied pressure on R(T); the pressure was simply used to densify the bundles in the mat and then removed to study the effect on the transport properties. The solid and dashed lines represents data taken on the same "as-prepared" mat before and after densification, respectively. The significant effect of a rather mild compaction of the mat on R(T) indicates the importance of interbundle contacts. This effect has been noted previously for hot-pressed

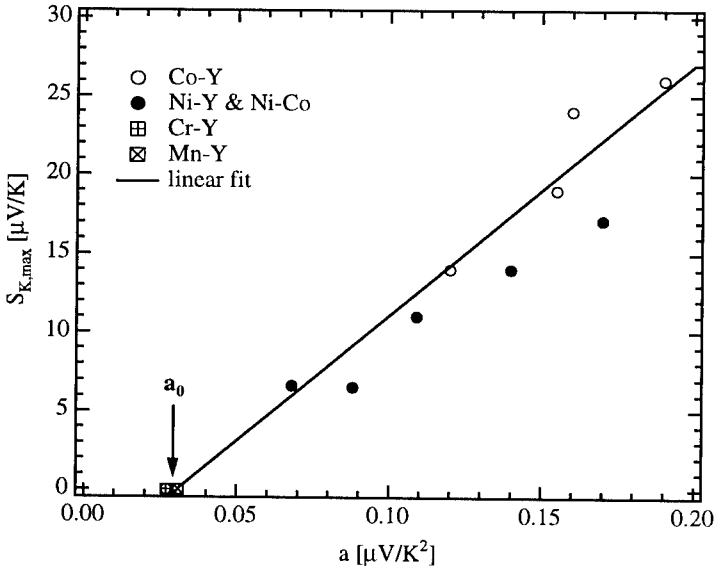

Fig.6. Correlation between $S_{K,max}$ and "a" for a variety of SWNT mat samples. Data for samples produced with Fe-Y are out of range and therefore are not shown.

PLV-grown SWNT mats [9, 11]. As the thermopower is measured at zero current, the effect of these contacts on S is observed here to be very small.

In Fig.6, we display an interesting linear correlation between $S_{K,max}$ and the slope "a" of the diffusion term $S_d = aT$ obtained by analyzing the data in Fig.3, as described above. Data are presented for a variety of samples prepared from several M-Y catalysts, and iodine-treated mats. Interestingly, data from all samples except those produced with Fe-Y are well described by the linear correlation (solid line) obtained by a least squares fit to the data. The data points for Fe-Y derived mats are far off scale, however. The intercept of the solid line on the ordinate (a) might be interpreted as the "intrinsic" diffusion coefficient $a_0 = 0.0314\ \mu V/K^2$ for a metallic nanotube bundle. This value for a_0 translates into a room temperature thermopower $S \sim +9.4\ \mu V/K$, a factor of 2-3 times larger than the basal plane of graphite. This interpretaion of a_0, however, ignores the role of possible tube wall defects, such as "5-7" defects [1]. Their presence may shift the Fermi energy, or alter $D(E_F)$, the electronic DOS near E_F. Because $D(E_F)$ is low in metallic SWNTs, small concentrations of wall defects could shift E_F considerably, upsetting the balance of electrons and holes in the system. Further work will be necessary to sort out whether or not these defects are present in significant numbers, and whether or not they impact significantly the thermopower and resistance.

ACKNOWLEDGMENTS

This work was supported in part by the NSF #DMR-9809686 (MRSEC), NSF #OSR-9452895 (EPSCOR), and DARPA #DAAB-07-97-C-J036. The PLV SWNT sample was kindly provided by Professor Richard Smalley at Rice University. The authors greatfully acknowledge stimulating discussions with Professors M.S. Dresselhaus (MIT) and G.D. Mahan (U. Tenn.).

REFERENCES

1. M.S. Dresselhaus, G. Dresselhaus, and P.C. Eklund, Science of Fullerenes and Carbon Nanotubes, (Academic Press, New York), 1996.
2. P. Delaney, H.J. Choi, J. Ihm, S.G. Louie, and M.L. Cohen, Nature **391**, 466 (1998).
3. J.W.G. Wildoer, L.C. Venema, A.G. Rinzler, R.E. Smalley, and C. Dekker, Nature **391**, 59 (1998).
4. S. Iijima, T. Ichihashi, Nature **363**, 603 (1993).
5. D.S. Bethune et al, Nature **363**, 605 (1993).
6. C. Journet et al, Nature, **388**, 756 (1997).
7. A. Thess et al, Science **273**, 483 (1996).
8. A.G. Rinzler et al, Appl. Phys. A **67**, 29 (1998).
9. J. Hone et al., Phys. Rev. Lett. **80**, 1042 (1998).
10. L. Grigorian et al., Phys. Rev. Lett. **80**, 5560 (1998).
11. J.E. Fischer et al, Phys. Rev. B **55**, R4921 (1997).
12. A.B. Kaiser, G. Dusberg and S. Roth, Phys. Rev. B **57**, 1418 (1998).
13. C.L. Kane, E.J. Mele, Phys. Rev. Lett. **78**, 1932 (1997).
14. P.C. Eklund and A.K. Mabatah, Rev. Sci. Instrum. **48**, 775 (1977).
15. G.U. Sumanasekera, L. Grigorian, and P.C. Eklund, submitted to Rev. Sci. Instrum.
16. L. Grigorian et al., Phys. Rev. B **58**, R4195 (1998).
17. S.L. Fang et al., to be published.
18. A.M. Rao et al., Science **275**, 187 (1997).
19. D.K.C. MacDonald, W.B. Pearson, and I.M. Templeton, Proc. Roy. Soc. **A266**, 161 (1962).
20. A.V. Gold, D.K.C. MacDonald, W.B. Pearson, and I.M. Templeton, Phil. Mag. **5**, 765 (1960).
21. R.D. Barnard, Thermoelectricity in Metals and Alloys (Taylor & Francis Ltd, London, UK) 1972.
22. G.D. Mahan, in Solid State Physics, Eds.H. Ehrenreich and F. Spaepen (Academic Press, New York), 1997.

Electronic Structure and Transport Properties of $CoSb_3$: A Narrow Band-Gap Semiconductor

J. O. Sofo *, G. D. Mahan **
*Centro Atómico Bariloche and Instituto Balseiro,
Comisión Nacional de Energía Atómica, (8400) Bariloche RN, Argentina, sofo@cab.cnea.edu.ar
** Solid State Division, Oak Ridge National Laboratory
P.O.Box 2008, Oak Ridge, TN 37831-6030, and
Department of Physics and Astronomy, The University of Tennessee, Knoxville, TN 37996-1200

Abstract

We report calculations which show that the band structure of $CoSb_3$ is typical of a narrow band-gap semiconductor. The gap is strongly dependent on the relative position of the Sb atoms inside the unit cell. We obtain a band gap of 0.22 eV after minimization of these position. This value is more than four times larger than the result of a previous calculation which reported that the energy bands near the Fermi surface are unusual. The electronic states close to the Fermi level are properly described by a two-band Kane Model. The calculated effective masses and band gap are in excellent agreement with Shubnikov de Haas and Hall effect measurements. Recent measurements of the transport coefficients of this compound can be understood assuming it is a narrow band gap semiconductor, in agreement with our results.

Introduction

$CoSb_3$ is one of several compounds with the $CoAs_3$ or skutterudite structure. This family of compounds has been recently identified as candidate for good thermoelectric materials.[1, 2] They are good thermoelectrics at high temperatures and offer a possibility for improvement at room temperature.

In addition to their potential applications, skutterudites are a fascinating family of compounds. Their crystal structure, is characterized by the formation of four-membered pnictide rings which are located in the centers of cubes formed by the metal atoms. For every four metal cubes there is one empty, without the four-membered pnictide ring. This void space can be filed with different atoms like La or Ce, to obtain the related family of compounds called *filled skutterudites* or *stuffed skutterudites*. The filling can be useful for doping or decreasing the thermal conductivity.

Before Caillat and coworkers [1] pointed out the potential of skutterudites as high performance thermoelectrics, these materials were studied because of their interesting bonding properties [3, 4, 5, 6, 7]. This potential was the reason for several experimental [8, 9, 10, 11, 12] and theoretical [13, 14, 15, 16, 17, 18] studies. Most of this effort have been focused on the transport properties of $CoSb_3$ pure, single crystals. This understanding is necessary to assess the potential and directions for improvement of its thermoelectric properties. Our work builds the basic ingredient for a model of the transport properties of $CoSb_3$. It provides a simple analytical expression for the bands close to the Fermi level, i.e. those bands that are involved in the transport process.

Singh and Pickett [13] described the valence band as parabolic at the Γ point but with a cross over to linear behavior extremely close to the band edge. Based on this characteristic, they called unusual the transport properties predicted for this compound. Most of the recent experimental work on transport properties of $CoSb_3$ [8, 9, 10, 11, 12] has been motivated or focused on this prediction.

Here we show that the band structure of $CoSb_3$ is in fact typical of narrow band-gap semiconductors. We found that the bands close to the Fermi level are well described by the two-band Kane model.[20] We obtain the valence and conduction bands effective masses by fitting this model to the calculated bands. Our results are in excellent agreement with Hall and Shubnikov de Haas measurements. We also show that the band gap is extremely sensitive to the position of Sb atoms, i.e. the size of the pnictides rings. When the pnictide atoms are located at the relaxed (zero force) positions, we obtain a band gap bigger than the result obtained previously by Singh and Pickett [13]. This result is analyzed under the chemical picture given by Jung et al. [3] where it is shown that the top of the valence band at Γ is formed by the most anti-bonding combination of the π_4 orbitals of the ring.

Mat. Res. Soc. Symp. Proc. Vol. 545 © 1999 Materials Research Society

	a (Å)	u	v
Arushanov, et al. Ref. [11]	9.036		
Caillat, et al. Ref. [10]	9.0345		
Mandrus, et al. Ref. [9]	9.03573(3)	0.3348(1)	0.1570(1)
Schmidt, et al. Ref. [4]	9.0385(3)	0.33537(4)	0.15788(4)
This work LDA	8.94	0.3328	0.1599
This work GGA	9.14	0.3332	0.1594

Table 1: Comparison between experimental (first four) and theoretical (last two) results for the lattice and internal parameters of the $CoSb_3$ structure.

Computational Method

For our calculations we use the Full-Potential Linearized Augmented Plane Wave method (FP-LAPW) [21]. In brief, this is an implementation of density functional theory with different possible approximations for the exchange and correlation potential, including the local spin density approximation (LSDA) or generalized gradient approximation (GGA). The Kohn-Sham equations are solved using a basis of linearized augmented plane waves.[22] For the exchange and correlation potential we use the Perdew and Wang[23] parameterization of the Ceperley-Alder data in the LSDA case. The LSDA results are also compared with the GGA of Perdew, Burke, and Ernzerhof [24]. We found that there is no difference between GGa and LDA for this compound. Local orbital extensions to the LAPW basis[25] are used to describe the $3s$ and $3p$ orbitals of Co, the $4p$ orbitals of Sb, and to reinforce the description of the $4d$ orbitals of Sb.

We use a well converged basis set of around 2000 plane waves and a sampling of the Brillouin zone (BZ) of 400 points, corresponding to 24 in the irreducible wedge (IBZ). To confirm the convergence of our results, we have check that the atomic positions and lattice parameters does not change when using 2300 plane waves and 3000 points in the BZ, corresponding to 147 k-points in the IBZ. We use a muffin-tin radius of 2.2 Bohr for Co and 2.4 Bohr for Sb.

Crystal Structure and Elastic Properties

The skutterudite structure of $CoSb_3$ is formed by a *bcc* lattice with four formula units per cell. The unit cell symmetry corresponds to the space group $Im\bar{3}$ (T_h^5), with 4 Co atoms in the $8e$ positions and 12 Sb in the $24d$.[19] This arrangement has two internal parameters u and v governing the position of the Sb atoms and consequently the size of the Sb_4 rings.

The lattice and internal parameters of the crystal structure have been determined experimentally by several authors in the past[11, 10, 4], and further refinement of these values were obtained by Mandrus and coworkers [9]. These values are summarized in Table 1 together with our LSDA and GGA results. Our LSDA result for the lattice constant is 1% smaller than the experimental value. This discrepancy is a typical and well known consequence of the LSDA. The same result is obtained by Feldman and Singh [16] using similar approximations. The GGA for the exchange and correlation potential yields a lattice constant 1% larger than the experimental value. The internal parameters defining the position of the pnictides are in good agreement with the experimental values for both LDA and GGA.

As a check for our structural results we calculated the bulk modulus obtaining 102 GPa when LDA is used for the exchange and correlation potential, and 89 GPa when using GGA for the calculation. Although we could not find an experimental value reported for the bulk modulus of $CoSb_3$, our LDA result is in close agreement to the 105 GPa calculated by Feldman and Singh [16]. As in the case of Feldman and Singh, the bulk modulus was calculated without relaxing the internal parameters u and v, which determine the position of the Sb atoms. These parameters are kept fixed at the values given in Table 1, in this way the forces on the Sb atoms are zero for the equilibrium volume only. As a test that this is not a bad approximation to the bulk modulus we checked that these forces remained small, i.e. less than 1 mRyd/Bohr, even for a 5% compression in the volume. All these values are in the range of the 112.4 GPa measured by Slack and Tsoukala [2] for $IrSb_3$, which is other member of the same family of compounds.

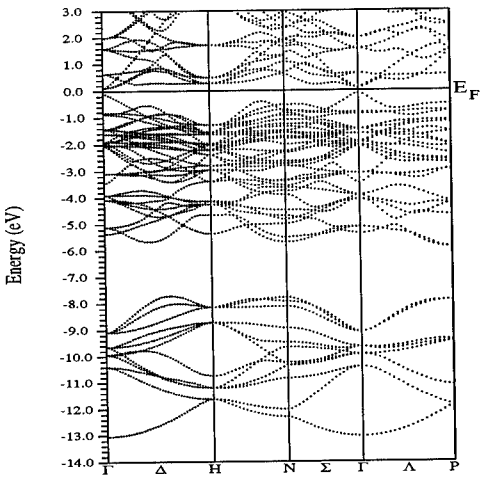

Figure 1: Electronic band structure of the skutterudite $CoSb_3$ for a path along symmetry points of the bcc Brillouin zone.

Electronic Band Structure and Transport Properties

The band structure of $CoSb_3$ obtained at the LDA equilibrium lattice constant and internal parameters is shown in Fig. 1. The lower set of bands, from around -13 eV to -8 eV are the 12 Sb $5s$ bands. The upper set of bands from around -6 eV up to the Fermi level are a mixture of Sb $5p$ and Co $3d$ states. An important feature to notice in the figure is the direct band gap at Γ $E_G = 0.22$ eV when u and v are relaxed to their minimum energy value. This gap is more than four times bigger than the value found by Singh and Pickett[13]. We found their value of 0.05 eV when, instead of using the internal parameters u and v that minimize the energy, we use the corresponding experimental values. The difference between both sets of parameters is small (Table 1) and the energy of the state at the top of the valence band at Γ is very sensitive to these changes.

The sensitivity to the atomic positions of the gap, together with the well known problem of underestimation of the gap by LDA, makes it very difficult to draw a definite answer about the energy gap of this compound.. However, to be consistent, the result of the theory should be obtained with the parameters predicted by theory. Following this rule, our result for the band gap of $CoSb_3$ is 0.22 eV, and it should be considered a lower bound to the actual value. The final answer should be given by the proper spectroscopic experiment.

The sensitivity of the band gap to the Sb position can be understood using the chemical picture given by Jung and coworkers [3]. The top of the valence band at Γ corresponds to the anti-bonding combinations of the π_4 orbital of the ring along a crystallographic axis. The energy of these states is mainly determined by the energy of this molecular orbital of the ring. Small changes in the positions of the Sb atoms affect strongly the energy of this molecular orbital opening or closing the gap.

The electronic band gap of the order of 0.2 eV, is shown in the density of states plot of Fig. 2. The density of states around the Fermi level is small compared with the contribution of the Co d bands. This feature is clearly seen in the close up of the DOS around the Fermi level shown in the inset of this figure.

As we mentioned before, we do not find the bands of $CoSb_3$ unusual, but typical of a narrow band-gap semiconductor. To show this, we fitted the two-band Kane model to our calculated bands close to the Fermi level. Other narrow band-gap semiconductors described by the Kane model [26], like InSb, HgTe, and CdSe,

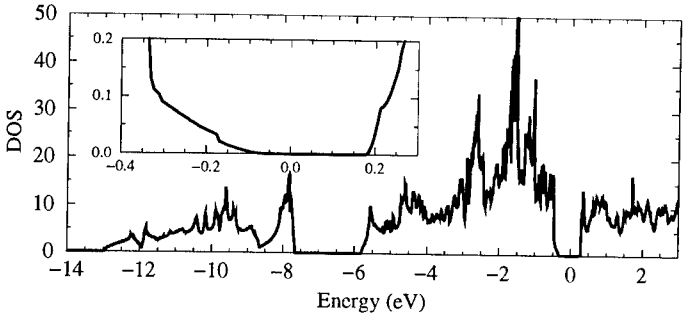

Figure 2: Electronic density of states of the skutterudite $CoSb_3$ as a function of the energy measured from the Fermi level. The inset shows a close up of the region around the Fermi level.

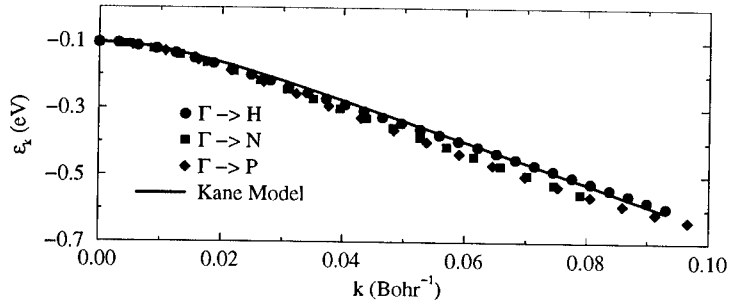

Figure 3: Close up of the non-parabolic valence band of $CoSb_3$, along three different high symmetry directions of the Brillouin zone, together with the fitted Kane model band.

have a band of heavy holes degenerate at the top of the valence band with the non-parabolic band of light holes. In $CoSb_3$ this band is a heavy electrons band degenerate at the bottom of the conduction band with the non-parabolic band of light electrons.

The non-parabolic valence band of $CoSb_3$ is shown in Fig. 3 along three different high symmetry directions of the Brillouin zone. This band is spherical in k space as can be seen from the small difference in energy between different directions.

In the two-band Kane model, the dispersion relation ε_k of the bands is obtained by $\mathbf{k}\cdot\mathbf{p}$ perturbation theory, and is given by the solution of

$$\frac{\hbar^2 k^2}{2m^*} = \varepsilon_k \left(1 + \frac{\varepsilon_k}{E_G}\right), \tag{1}$$

where m^* is the effective mass at the band edge, E_G is the band gap and the other symbols have the usual meaning. We fitted our LDA results to the solution of Eq. (1), fixing E_G=0.22eV and adjusting the effective mass in order to get the best fit. The effective mass obtained in the fitting is $m^*/m_0 = 0.071$ for the $\Gamma \rightarrow$ H dispersion relation, and 0.069 for the $\Gamma \rightarrow$ N and $\Gamma \rightarrow$ P directions. The Kane model band obtained for the $\Gamma \rightarrow$ H direction is shown with full line in Fig. 3. The agreement makes clear that the bands of $CoSb_3$ are properly described by this model.

Our value of effective mass is in remarkable agreement with both, transport and Shubnikov de Haas effect measurements. Caillat et al. [10] found that their Hall results are explained assuming a hole effective mass of 0.071. Arushanov et al. [12], performed Shubnikov de Haas oscillation measurements. These authors found a value of $m^*/m_0 = 0.07 \pm 0.01$ from the temperature dependence of the oscillation amplitude.

The conduction band is formed by the non-parabolic band described before, plus a triply degenerate parabolic band degenerate with this at Γ. The effective mass of this band is $m_e^*/m_0 = 0.35$. To the best of

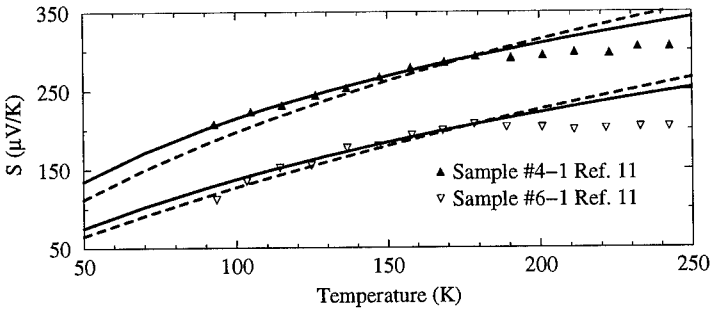

Figure 4: Seebeck coefficient as function of temperature. The triangles are experimental data taken from Ref. 11. Solid lines are calculated using the bands obtained in this work. Dashed lines are obtained using the bands reported by Singh and Picket (Ref. 13). Both calculations assume a constant relaxation time.

our knowledge there is no experimental value of this quantity reported.

The Seebeck coefficient is mainly determined by the band structure of the material. The carrier's scattering processes do not affect its value in a predominant way. In the limiting case where the relaxation time is assumed independent of energy, the Seebeck coefficient becomes independent of the relaxation time. We calculated the Seebeck coefficient assuming a constant relaxation time. The results are shown with solid line in Fig. 4 and compared with experimental results from Arushanov and coworkers[11], and with the same calculation performed with the bands obtained by Singh and Pickett[13]. We adjusted the carrier's concentration in the calculation in order to reproduce the experimental data at around 180K. Below this temperature the agreement between our results and the experimental data is excellent for both samples. Only the valence band is taken into account for the calculation. The disagreement above 180K may be due to the appearance of minority carriers, an effect not taken into account in the calculation. For the sample with the highest doping level (empty triangles in Fig. 4) both band structures reproduce the experimental data, as expected, because the difference between both calculations is at the top of the valence band. However, for the sample with the lowest doping level, where the disagreement between both band structures is shown more evidently, the agreement of our calculation is clearly better.

As a result of the calculations described in the previous paragraph, we noticed that at room temperature and for the doping levels obtained for this samples, this compound is not in the degenerate limit assumed to obtain Eq. (1) of Ref. [13]. The chemical potential is, for all the cases considered, within the gap.

Conclusions

We have performed ab-initio calculations of the skutterudite $CoSb_3$. Our results on structural and electronic properties are in excellent agreement with reported measurements on this system. We found that the two-band Kane model is a natural description of the $CoSb_3$ bands close to the Fermi level. From our calculations we obtain the two parameters necessary for the full determination of the model, the band gap $E_G = 0.22eV$ and the effective mass $m^*/m_0 = 0.071$. A proper description of the bands is the first step towards a model of the transport properties of this compound. This model is a necessary tool for the optimization of $CoSb_3$ as a good thermoelectric material.

Acknowledgments

We acknowledge research support from the D.O.D. Advanced Research Projects Agency under contract DAAB07-97-J036 with the Allied Signal Corporation. One of us J.O.S. is supperted by CONICET, Argentina.

References

[1] T. Caillat, A. Borshchevsky, and J.-P. Fleurial, in *Proceedings of the XIth International conference on Thermoelectrics, University of Texas at Arlington, 1992*, edited by K. A. Rao (University of Texas at Arlington Press, Arlington USA, 1993), p 98.

[2] Glen A. Slack and Veneta G. Tsoukala, J. Appl. Phys. **76**, 1665 (1994).

[3] Dongwoon Jung, Myung-Hwan Whangbo, and Santiago Alvarez, Inorg. Chem. **29**, 2252 (1990).

[4] Th. Schmidt, G. Kliche, and H. D. Lutz, Acta Crystallogr. Sect. C **43**, 1678 (1987).

[5] H. D. Lutz and G. Kliche, Phys. Stat. Sol. (b) **112**, 549 (1982).

[6] J. Ackermann and A. Wold, J. Phys. Chem Solids **38**, 1013 (1977).

[7] L. D. Dudkin and N. Kh. Abrikosov, Sov. Phys. Solid State **1**, 126 (1959).

[8] D. T. Morelli, T. Caillat, J.-P. Fleurial, A. Borshchevsky, J. Vandersande, B. Chen, and C. Uher, Phys. Rev. B bf 51, 9622 (1995).

[9] D. Mandrus, A. Migliori, T. W. Darling, M. F. Hundley, E. J. Peterson, and J. D. Thompson, Phys. Rev. B **52**, 4926 (1995).

[10] T. Caillat, A. Borshchevsky, and J.-P. Fleurial, J. Appl. Phys. **80**, 4442 (1996).

[11] E. Arushanov, K. Fess, W. Kaefer, Ch. Kloc, and E. Bucher, Phys. Rev. B **56**, 1911 (1997).

[12] E. Arushanov, H. Rakoto, M. Respaud, J. M. Broto, J. Leotin, Ch. Kloc, E. Bucher, and S. Askenazy, *Shubnikov de Haas ascillations in $CoSb_3$ single crystals*, preprint.

[13] D. J. Singh and W. E. Pickett, Phys. Rev. B **50**, 11235 (1994).

[14] V. P. Zhukov, Phys. Solid State **38**, 90 (1996).

[15] L. Nordström and D. J. Singh, Phys. Rev. B **53**, 1103 (1996).

[16] J. L. Feldman and D. J. Singh, Phys. Rev. B **53**, 6273 (1996).

[17] M. Llunell, P. Alemany, S. Alvarez, V. P. Zhukov, and A. Vernes, Phys. Rev. B **53**, 10605 (1996).

[18] D. J. Singh and I. I. Mazin, Phys. Rev. B **56**, R1650 (1997).

[19] R. W. G. Wyckoff, *Crystal Structures*, (Interscience, New York, 1948), Sec. V,b16.

[20] E. O. Kane, in *Semiconductors and Semimetals*, edited by R. K. Willardson and A. C. Beer (Academic, New York, 1975) Vol. 1, Chap. 3.

[21] P. Blaha, K. Schwarz, and J. Luitz, WIEN97, Vienna University of Technology, 1997. (Improved and updated Unix version of the original copyrighted WIEN-code, which was published by P. Blaha, K. Schwarz, P. Soratin, and S. B. Trickey, in Comput. Phys. Commun. **59**, 399 (1990)).

[22] D. Singh, *Plane Waves, Pseudopotentials, and the LAPW Method* (Kluwer Academic, New York, 1994).

[23] J. P. Perdew and Y. Wang, Phys. Rev. B **45**, 13244 (1992).

[24] J. P. Perdew, S. Burke and M. Ernzerhof, Phys. Rev. Lett. **77**, 3865 (1996).

[25] D. Singh, Phys. Rev. B **43**, 6388 (1991).

[26] D. L. Rode, in *Semiconductors and Semimetals*, edited by R. K. Willardson and A. C. Beer (Academic Press, New York, 1975) Vol. 10.

NICKEL SUBSTITUTED SKUTTERUDITES : SYNTHESIS AND PHYSICAL PROPERTIES

L. CHAPON, D. RAVOT, J. C. TEDENAC
Laboratoire de Physicochimie de la Matière Condensée.
Université Montpellier II, UMR 5617 Place Eugene Bataillon
34095 MONTPELLIER, FRANCE

ABSTRACT

Starting to $CeFe_4Sb_{12}$ and trying to obtain low gap semiconductors with very low thermal conductivity, we have performed in this compound the substitution of Ni for Fe.This substitution induces a reject of cerium from the structure. In this paper we present synthesis and physical properties of $Ce_yFe_{4-x}Ni_xSb_{12}$ in which a relationship is existing between x and y to retain the electronic account giving semiconducting character.

INTRODUCTION

Binary skutterudites as $CoSb_3$ exhibit good thermopower [1] but too large lattice thermal conductivity to be useful in thermoelectric devices. Nevertheless in such a compound, two voids are existing in the unit cell [2] which can be filled with heavy atoms as rare earth (R). The "rattling" of R in the voids produces phonon diffusion which decreases the lattice thermal conductivity by a factor of ten with respect to binary skutterudites[3]. The formula of these ternary compounds can be written RA_4Sb_{12} where A is a metallic atom and B a pnictogen.

$CeFe_4Sb_{12}$ is intensively studied because the voids available for cerium are the largest in the pnictogenide series [4]. Unfortunately, Ce is trivalent and $Ce^{3+}[Fe_4Sb_{12}]^{4-}$ shows a metallic or semi-metallic conductivity [5] with heavy fermion-like characteristics. So, at the present time, most of the works devoted to this compound are concerned with the charge compensation, in order to give it semiconducting character. This can be done by substituting on the metal site [6] or on the pnictogen site [7].

Many authors substitute Co for Fe. To increase the disorder and so the phonon diffusion, we have chosen to substitute Ni to Fe which gives the $CeFe_{3.5}Ni_{0.5}Sb_{12}$ formula if all the voids are assumed to be cerium filled. Synthesizing this compound leads to a Ce deficient phase due to a reject of the cerium from the structure [8]. Combining Ce reject and Ni insertion to obtain semiconducting compounds leads to the generic formula $Ce_yFe_{3.5}Ni_{0.5}Sb_{12}$ with $y=4/3-2/3x$.

EXPERIMENT

Except cerium which is 99.9%, all the starting elements are 99.999% pure. All the handling took place in a glove-box under a continuously purified argon atmosphere. The cerium oxide layer is mechanically removed in the glove-box. Stoichiometric amounts of elements are weighted and place in a carbon coated silica ampoule sealed under vacuum. Thermal treatment consists in heating the ampoule to 1000°C for 2 days, water quenching it, then annealing it at 700°C for several days. Ingot is then removed from the ampoule and the carbon layer is filed down if necessary.

Mat. Res. Soc. Symp. Proc. Vol. 545 © 1999 Materials Research Society

Structural investigations consists of X-ray and neutron diffraction. Rietveld refinement [9] allows us to extract lattice parameters, atomic positions and thermal parameters at room temperature.

SEM checks the single phase character of ingot and microprobe analysis using $CeNi_5$, Fe and Sb as standards gives the composition of the phases.

DTA until 1000°C show the peritectical decomposition point of compounds.

Electrical resistivityy is measured using the Van der Paw technique in DC configuration.

At last, magnetism investigations are done using a VSM system from Oxford instruments in a maximum field of 9 Tesla.

RESULTS

X-Ray powder diffraction experiments (fig .1) show that ingots are almost single phase. Nevertheless, in some compounds, minor extra lines can be detected corresponding to Ce rich phases ($CeSb_2$, according to micro-probe analysis) or Fe-Ni-Sb phases (marked by * in the pattern). The existence of these phases has been previously reported by some

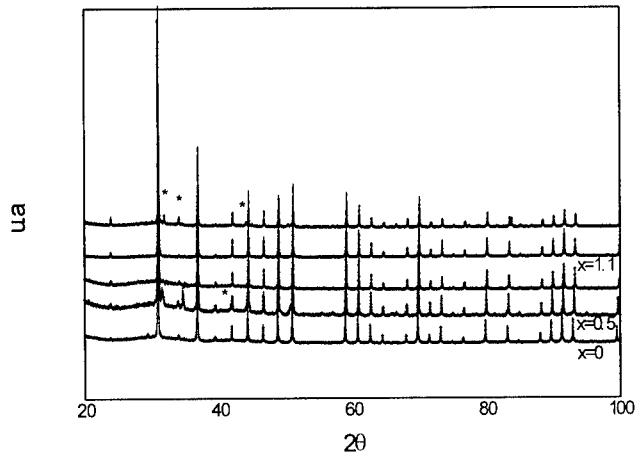

Figure 1 : X ray patterns and Rietveld refinement for different Ni concentrations.

authors. The skutterudite are difficult to synthesize as single phase.

Rietveld refinements totally agree with the Im3 space group with 2(a), 8(c), and 24(g) sites for Ce, Fe-Ni and Sb atoms respectively. The lattice constant is linearly decreasing as the amount of nickel increases [8]. It is worth noticing that compounds $Ce_{0.7}Fe_{3.5}Ni_{0.5}Sb_{12}$ which does not respect the y=4/3-2/3x relationship agrees with this linear dependence. This confirms that cerium is lightly bonded to other atoms and does not influence the "rigid" structure of skutterudite constituted by the metal-pnictogen framework. This variation of the lattice constant is small [8] (0.40%) compared to the one of the ternary compounds in the pnictogen series (15 % between $CeFe_4Sb_{12}$ and $CeFe_4P_{12}$ [4]). The positional parameters of Sb atoms

have been refined and are very close to the Oftedal's line (y+z=1/2) which is the condition for the existence of square rings between Sb atoms. These parameters are listed in table 1 with interatomic distances for each compounds. No major changes exist between the different compositions: (y+z) is close to 0.495 which implies very low quadratic distortion inside the Sb_4 rings.

Nominal composition	$CeFe_4Sb_{12}$	$Ce_{0.7}Fe_{3.05}Ni_{0.95}Sb_{12}$	$Ce_{0.6}Fe_{2.9}Ni_{1.1}Sb_{12}$	$Ce_{0.33}Fe_{2.5}Ni_{1.5}Sb_{12}$
y	0.3361	0.3358	0.3361	0.3355
z	0.1600	0.1585	0.1599	0.1583
y+z	0.4961	0.4943	0.4960	0.4928
Sb-Sb bonds (Å)	2.9945 2.9232	2.9933 2.8892	2.9859 2.9130	2.9942 2.8814
Ce-Sb bonds (Å)	3.4015	3.3843	3.3903	3.3762

Table 1: Atomic positions of antimony and interatomic distances.

Cerium-antimony distances are lower in Ni substituted compounds than in $CeFe_4Sb_{12}$. It's however difficult to correlate this behavior to other parameters. The size of the voids depends on lattice constant and antimony atomic positions (voids become smaller when y and z become equal [10]) which vary simultaneously. However, in all cases the radius of the voids is very large compare to the cerium ionic radius (1.10 Å).

Neutron diffraction experiments performed on $Ce_{0.7}Fe_{3.05}Ni_{0.95}Sb_{12}$ compound (figure 2) allow us to check the "rattling" of atoms as it gives a direct measurement of their average displacement.

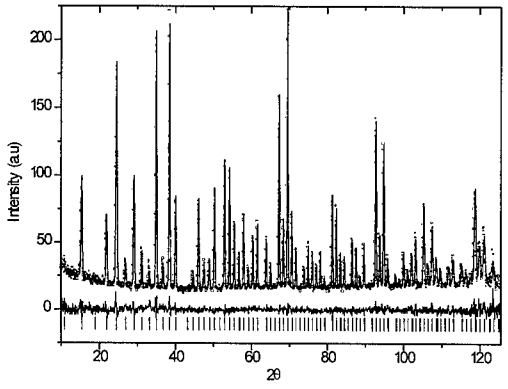

Figure 2 : Neutron diffraction on $Ce_{0.7}Fe_{3.05}Ni_{0.95}Sb_{12}$. Open circles shown experimental data points. The continuous lines represent the refinement and difference curves. Bar represents theoretical diffraction lines positions.

The refinement include 20 free parameters. Occupancy of each sites was directly deduced from microprobe analysis and were not free parameters. Make them free will create no sense results due to the proximity between iron and nickel. Both values R_{Bragg}=0.0439 and $S=R_{wp}/R_{excected}$=1.17 confirm the quality of the fit which is also evident in fig. 2. Antimony, iron and nickel thermal parameters well agree with the values usually founded for these elements on this configuration (B_{Fe}=0.27 Å^2, B_{Ni}=0.27 Å^2, B_{Sb}=0.56 Å^2). The thermal parameter of cerium is instead very large due to "rattling" motion inside the void. Our value, B_{Ce}=1.86 Å^2, can be compared to others in ternary or quaternary compounds. It is five time larger than in ternary phosphorus compounds (B_{Ce}=0.42 for $CeFe_4P_{12}$ [4]). In $CeFe_4P_{12}$ the void's radius is smaller and cerium atoms are less free to "rattle" inside. The value is nevertheless comparable to B_{La}=1.70 Å^2 founded in $La_{0.75}Fe_3CoSb_{12}$ [11]. The lattices parameters are roughly equal in this compound and $Ce_{0.7}Fe_{3.05}Ni_{0.95}Sb_{12}$ and so the larger value of the thermal parameter in the case of cerium could be correlated to its smaller atomic radius.

Thermal incidents in DTA's measurements consists of a well-defined peak near 750°C [8]. Reaching higher temperatures leads to the appearance of the accident corresponding to the antimony melting point. That allows us to define a decomposition temperature and exclude a congruent melting in agreement with the existence of a peritectic decomposition in filled skutterudites [12]. The decomposition temperature decreases with increasing amount of Nickel (figure 3) from 761°C for $CeFe_4Sb_{12}$ to 749 °C for $Fe_{0.5}Ni_{0.5}Sb_3$ [13]. The variation is quite linear with x and the temperature value founded by other authors for x=2 [13] reach the fit line in good agreement with our results. These values must allow the use of these materials in the same temperature range than unsubstituted filled skutterudites.

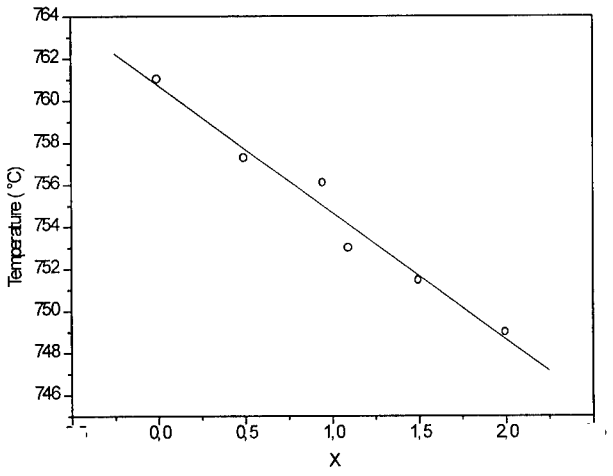

Figure 3 : Temperature of thermal incidents versus the nickel content (x) in $Ce_yFe_{4-x}Ni_xSb_{12}$.

Electrical measurements (conductivity and Seebeck effect) have been already reported [8]. Room temperature electrical resistivity presents a maximum with nickel concentration.

The behavior is metallic or semi-metallic for $CeFe_4Sb_{12}$ but becomes characteristic of degenerated semiconductors as the nickel amount increases and tend to degenerated semiconductors with the increasing nickel concentration. In the same time, the low Seebeck coefficient for $CeFe_4Sb_{12}$ reaches high values for intermediate compositions before becoming negative for larger amount of nickel. So, the thermopower $S^2\sigma$ reaches a maximum for compositions near x=1 i.e. 25% of nickel.

Magnetic investigations have been made under 3T field between room temperature and 5K. Results are showed on figure 4.

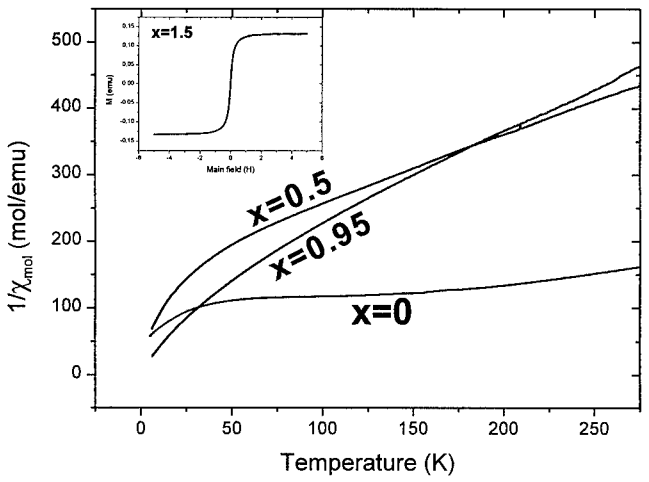

Figure 4 : Thermal dependence of the inverse molar succeptibility. Insert shows the hysteresis cycle for x=0.5 at room temperature.

In agreement with previously published results, $CeFe_4Sb_{12}$ shows a paramagnetic behavior with a positive curvature around 50K. This evolution does not indicate any evolution of the cerium valence under temperature but is rather due to the existence of a large crystal field which splits the $^2F_{5/2}$ ground state of the trivalent cerium into a doublet Γ_7 and a quadruplet Γ_8. Comparing the shape of this thermal evolution to theoretical calculations[14] and experimental data reported on cerium compounds like CeTe-CeSb [15] allows us to assign Γ_7 as the ground level (positive crystal field). This large crystal field precludes the determination of an accurate effective magnetic moment. No magnetic order is evidenced specially no anomaly was observed around 15 K which, following Morelli and Meissner [5], seems to confirm that our compound is free of CeSb impurity.

When the amount of nickel increases the crystal field effect decreases.

The paramagnetic Curie temperatures are large and negative. This could be an artifact due to the crystal field effect or an indication of the existence of a large antiferromagnetic interaction. In this last case it would be surprising not to observe a magnetic ordering at low

temperature. This behavior has previously been encountered in cerium heavy fermions compounds [16].

The compound $Ce_{0.5}Fe_{2.75}Ni_{1.25}Sb_{12}$ (not displayed into fig. 4 for clarity) does not show any crystal field effect. Its paramagnetic Curie temperature is roughly zero and its effective magnetic moment $\mu_{eff}=2.37\mu_B$ is very closed to the theoretical value expected for trivalent cerium ion ($2.54\mu_B$).

For $Ce_{0.33}Fe_{2.5}Ni_{1.5}Sb_{12}$, a ferromagnetic ordering is observed at room temperature (insert in fig. 4) directly correlated to the large amount of nickel. So let us notice that the transition from non ordered compounds to ferromagnetic ones takes place for a nickel concentration between x=1.25 and x=1.5.

CONCLUSION

In conclusion, in this paper we have presented some results we have obtained in the study of new substituted filled cerium skutterudites. Theses preliminary results indicate that these compounds are of great interest either as potentially good thermoelectric materials easy to obtain in n and p form or support for the fundamental study of the correlation between transport properties, composition and ferromagnetic ordering appearance.

ACKNOWLEDGMENTS

We wish to thank Mrs. F. Bouree-Vigneron and her team from the llb, CEA-Saclay (France) for the neutron diffraction experiments she has done in the llb laboratory and for helpful discussions during refinements.

REFERENCES

[1] J.W. Sharp, E.C. Jones, R.K. Williams,P.M. Martin, B.C. Sales, *J. Appl. Phys.* 78,1013 (1995).
[2] N. N. Zhuravlev, G. S. Zhdanov, *Kristallogr.* 1 (1956) 509.
[3] B. C. Sales, D. Mandrus, R. K. Williams, *Science* 272 (1996) 1325.
[4] F. Grandjean, A. Gérard, D. J. Braun, W. Jeitschko, *J. Phys. Chem. Solids* 45 (1984) 877.
[5] D. T. Morelli, G. P. Meisner, *J. Appl. Phys.* 77 (1995) 3777.
[6] G. P. Meisner, D. T. Morelli, S. Hu, J. Yang, C. Uher, *Phys. Rev. Letters* 80 (1998) 3551.
[7] G. S. Nolas, G. A. Slack, D. T. Morelli, T. M. Tritt, A. C. Erlich, *J. Appl. Phys.* 79 (1996) 4002.
[8] L. Chapon, D. Ravot, J. C. Tedenac, J. All. Comp. (accepted and to be published).
[9] Fullprof software freely distributed by J. Rodriguez-Carjaval (llb CEA-Saclay, France)
[10] D. J. Braun, W. Jeitschko, *J. Less. Com. Metals* 51 (1980) 148.
[11] B. C. Sales, D. Mandrus, B. C. Chakoumakos, V. Keppens, J. R. Thompson, *Phys. Rev. B* 56 (1997) 15081.
[12] T. Caillat, J.P. Fleurial, A. Borshchevsky, *J. Cryst. Growth* 166 (1996) 722.
[13] K. W. Richter, H. Ipser, *Journal of Phase Equilibria* 18 (1997) 1476
[14] E. D. Jones, *Phys. Letters* 22 (1956) 266
[15] D. Ravot, A. Mauger, J. C. Achard, M. Bartholin, J. Rossat-Mignod, *Phys. Rev. B* 28(2) (1983) 4558
[16] G. J. Nieuwenhuys in "Handbook of Magnetic Materials", K. H. J. Buschow ed, Elsevier Science B. V. (1995).

PHYSICAL PROPERTIES OF SINGLE-PHASE SKUTTERUDITE THIN-FILMS ($CoSb_3$ and $IrSb_3$)

J.C. CAYLOR *, A.M. STACY *, T. SANDS **, R. GRONSKY **
* Department of Chemistry, University of California, Berkeley, CA 94720
** Department of Materials Science and Mineral Engineering, University of California, Berkeley, CA 94720

ABSTRACT

Bulk skutterudite phases based on the $CoAs_3$ structure have yielded compositions with a high thermoelectric figure-of-merit ("ZT") through the use of doping and substitutional alloying. It is postulated that further enhancements in ZT may be attained in artificially structured skutterudites by engineering the microstructure to enhance carrier mobility while suppressing the phonon component of the thermal conductivity. In this work the growth and properties of single-phase $CoSb_3$ and $IrSb_3$ skutterudite thin films are reported. The films are synthesized by pulsed laser deposition (PLD) where the crystallinity can be controlled by the deposition temperature. Powder X-ray diffraction (PXRD), Transmission electron microscopy (TEM) and Rutherford-Back Scattering (RBS) were used to probe phase, structure, morphology and stoichiometry of the films as functions of growth parameters and substrate type. A substrate temperature of 250°C was found to be optimal for the deposition of the skutterudites from stoichiometric targets. Above this temperature the film is depleted of antimony due to its high vapor pressure eventually reaching a composition where the skutterudite structure is no longer stable. However, when films are grown from antimony-rich targets the substrate temperature can be increased to at least 350°C while maintaining the skutterudite phase. In addition, adhesion properties of the films are explored in terms of the growth mode and substrate interaction. Finally, preliminary room temperature electrical and thermal measurements are reported.

INTRODUCTION

Filled skutterudite phases, based on the $CoAs_3$ structure, have recently become candidate high-temperature thermoelectric materials [1]. This work is part of an initiative to increase the thermoelectric efficiency of skutterudites. To understand how to go about this, the concept of the figure-of-merit (FOM) must be introduced. Written as ZT, the FOM is a dimensionless number that is associated with the performance of a material in a thermoelectric device [2]. The mathematical expression of ZT is given in equation (1),

$$ZT = S^2T/\kappa\rho \qquad (1)$$

where S is the Seebeck coefficient in V/K, κ is the thermal conductivity in W/cm-K, ρ is the electrical resistivity in Ω-cm, and T is the absolute temperature of operation in K. From this expression, many strategies for increasing the FOM can be imagined. The approach being pursued in this research is to increase the FOM by lowering the thermal conductivity of a proven thermoelectric material by using thin film superlattices. Recent work has shown the theoretical and experimental basis for a decrease in the thermal conductivity relative to the bulk value for a material by scattering of phonons off superlattice interfaces [3]. Although there are studies that

Mat. Res. Soc. Symp. Proc. Vol. 545 © 1999 Materials Research Society

show superlattices enhance electrical properties [4], this research is based on the assumption that superlattices will, at least, not have negative effects on the electrical properties of the material. With this aim, skutterudites were chosen as a material on which to test this hypothesis.

With the limited work in the area of preparing thin films and superlattices of these materials, it was decided to begin with binary compounds and compare their thermoelectric properties as thin films to bulk properties. PLD was chosen as the film growth method due to its ability to accurately deposit complex stoichiometries, which will be important when depositing the filled skutterudite phases in the future. In these particular experiments, $CoSb_3$ and $IrSb_3$ were selected as good starting materials in view of their known bulk properties. Earlier work on skutterudites show preferred orientation of thin films, but with no epitaxial growth regardless of substrate [5-7]. This research will endeavor to understand the growth parameters needed to deposit high-quality films for thermoelectric applications.

EXPERIMENT

Two types of targets will be discussed for use in the PLD system. A target with a near-stoichiometric ratio of Co to Sb (1:3) was fabricated by mixing high-purity Co and Sb (75.5 mol% Sb) in a quartz tube, which was evacuated to less than 10^{-4} Torr and sealed. The tube containing the stoichiometric mixture was heated to 850°C for 60 hours and quenched. The product was characterized by PXRD (Siemens D5000, CuKα) and RBS (1.95 MeV $^4He^+$) after being cold pressed to a 0.5" diameter target. J.P. Fleurial and T. Calliat provided a stoichiometric $IrSb_3$ target from the Jet Propulsion Laboratory (JPL). The target was characterized by PXRD and RBS.

Films from these targets were grown on low-stress Si_XN_Y coated Si (100) wafers as well as other substrates. In the PLD system used in these experiments, the substrate was about 5cm from the target and mounted with silver paste to a temperature controlled heater block. A KrF excimer laser (248 nm) was used to ablate material from the target onto the substrate. The optimal growth conditions were found to be a pressure of $<10^{-6}$ Torr, substrate temperature of 250°C, and laser power of 550 mJ/pulse ($\approx$ 2-3 J/cm^2). Film structure, stoichiometry and morphology were probed by PXRD, RBS and TEM (JEOL 200CX).

A non-stoichiometric target was prepared from high-purity Co with excess Sb (90.1 mol% Sb). The material was sealed in an evacuated quartz tube as before and heated to 600°C for 25 hours. The material was hydraulically pressed to the 0.5" diameter size, then pressed in an isostatic cold press to 180,000 psi, and finally pressed in an isostatic hot press for 2 hours at 15,000 psi and 550°C. PXRD was used to characterize the pressed target. Films from this target were grown with the same conditions mentioned above, except the temperature was systematically increased to 350°C. Again, PXRD and RBS were used to probe film structure and stoichiometry.

RESULTS

The diffraction patterns for films grown from the stoichiometric $CoSb_3$ target as well as the target itself are shown in **Figure 1a**. The patterns show that under these growth conditions, polycrystalline films are produced. The resulting intensities do not match those for the powder, which could indicate preferred orientation. However, the fact that all powder reflections are present leads one to believe that texturing is minimal. As the substrate temperature increases above 250°C the abundance of the impurity phase $CoSb_2$ increases until only $CoSb_2$ is observed

above 300°C. Diffraction patterns for films grown from the $IrSb_3$ target and the target itself are shown in **Figure 1b**. As with $CoSb_3$, the $IrSb_3$ film loses Sb when deposited above 250°C. However, these films show less evidence of preferred orientation. To further characterize the films, TEM was performed on 300nm thick films grown at 250°C on Si_XN_Y /Si substrates. These micrographs, **Figure 2(a, b),** show grain sizes in the films to be on the order of 200 nm.

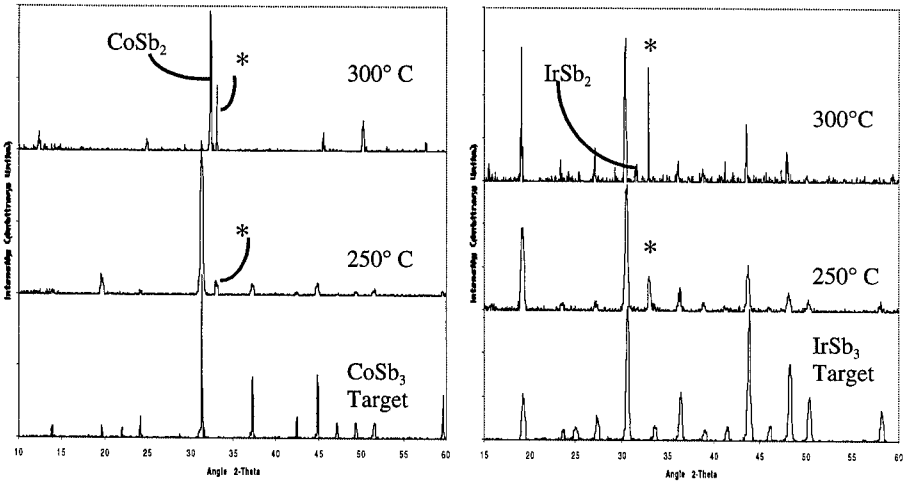

Figure 1:
a) (left) PXRD patterns of $CoSb_3$ target (bottom), 300 nm film grown at 250° C (middle) and 300 nm film grown at 300°C (top) (on Si_XN_Y /Si)
b) (right) PXRD patterns of $IrSb_3$ target (bottom), 300 nm film grown at 250° C (middle) and 300nm film grown at 300°C (top) (on Si_XN_Y /Si)
(*-denotes substrate peak)

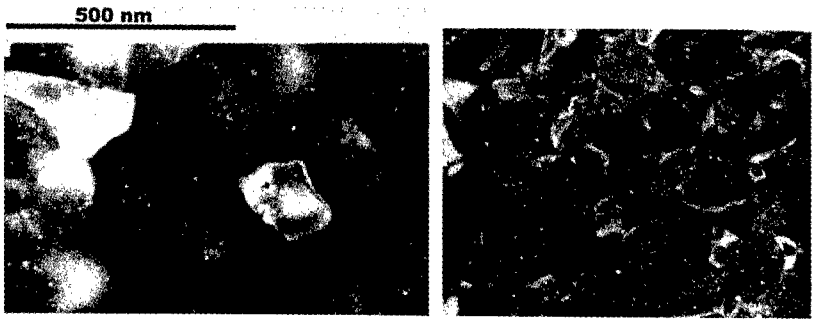

Figure 2:
a) (left) TEM micrograph of 300 nm thick $CoSb_3$ film grown on Si_XN_Y/Si at 250°C
b) (right) TEM micrograph of 300 nm thick $IrSb_3$ film grown on Si_XN_Y/Si at 250°C

To test the properties of the deposited films, preliminary room temperature electrical and thermal data was collected from a 300 nm thick $IrSb_3$ film grown on Si_XN_Y/Si from a stoichiometric target. The data is presented in **Table I** (bulk data taken from Slack *et al* [8]).

Table I: Room temperature electrical and thermal data for 300nm thick $IrSb_3$ film grown at 250° C from stoichiometric target on SiN

	Film	Bulk
S (μV/K)	60	72
σ $(\Omega*cm)^{-1}$	1488	2330
κ(mW/cmK)	45	160
n ($10^{19}cm^{-3}$)	260	1.1
Grain (μm)	0.2	6
ZT	0.035	0.023

Although PXRD showed the targets to be single-phase skutterudite, RBS gave a stoichiometry of $CoSb_{2.6}$ for the Co/Sb target and the film grown from it. RBS gave a stoichiometry of $IrSb_{3.3}$ for the Ir/Sb target; however, the film grown from this target had a stoichiometry of 1:3. This gives evidence that the excess Sb in the JPL target evaporated during the deposition process, leaving a stoichiometric film. As a result of this observation, an Sb-rich $CoSb_3$ target was designed, as described earlier, to deposit films at a higher temperature while providing the excess Sb needed to sustain the skutterudite phase. Diffraction patterns from this series of experiments are shown in **Figure 3**. The results show that single-phase films can be grown up to at least 350°C. RBS data shows that the films grown at 300°C have a stoichiometry of $CoSb_{3.1}$ while the

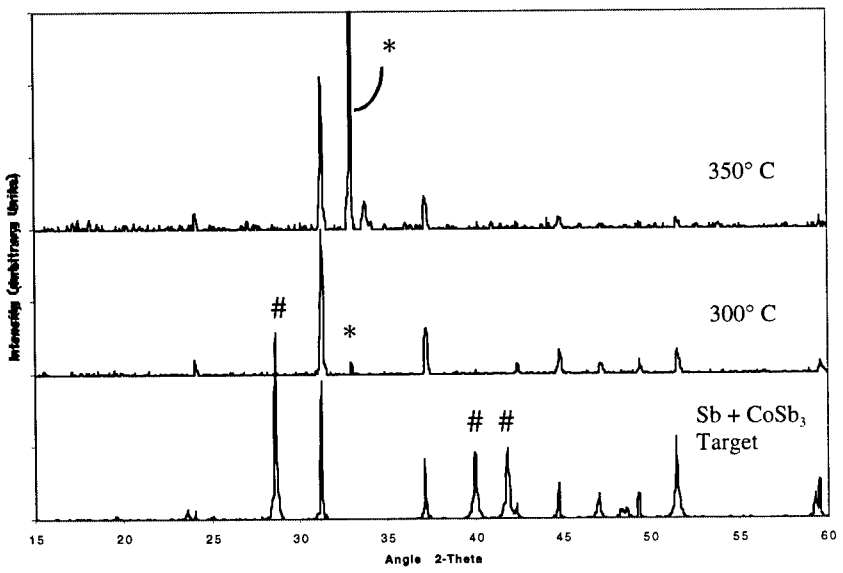

Figure 3: PXRD data for Sb-rich $CoSb_3$ target (bottom), film grown at 300°C (middle) and film grown at 350°C (top)
(Films grown on Si_XN_Y/Si) (*-denotes substrate peak, #-denotes antimony peak)

film grown at 350°C exhibits the ideal 1:3 stoichiometry. As before, the intensity of the diffraction peaks could lead one to suggest some preferred orientation, but most of the powder peaks are visible in all patterns.

CONCLUSIONS

This research has shown that single-phase skutterudite films ($CoSb_3$ and $IrSb_3$) can be grown from stoichiometric targets with a substrate temperature up to 250°C. The room temperature electrical properties of the 300 nm thick $IrSb_3$ film show that it behaves like that of a bulk polycrystalline sample, which is what one would expect for a thick film. Although these measurements are preliminary, they give a baseline to compare later films and multilayers where properties are expected to change. In addition, films from non-stoichiometric, Sb-rich, targets remain single-phase up to at least 350°C. However, achieving higher growth temperatures while controlling film stoichiometry necessitates the ability to limit the volatility of antimony by introducing a continuous flux of antimony vapor to maintain a high vapor pressure of antimony over the film. A deposition technique that may be conducive to this scenario is electron-beam deposition. Experiments using this technique are planned for the near future.

Another issue in the growth of skutterudite films is their adhesion characteristics. Films are easily removed from all substrates deposited on by tape or cotton swabs. The TEM results also show the spherical nature of the crystal grains, which would imply a three-dimensional growth mode and the non-wetting property of the films on all experimental substrates. There are two avenues to improve adhesion. One is to deposit a thin reactive wetting layer like chromium or titanium to improve film wetting of the substrate. The more attractive alternative, however, is to find a chemically compatible lattice matched substrate. Calculations show InSb is a close lattice match and possesses similar chemical bonding. Experiments are planed to grow on InSb wafers in the near future. With the possibility of access to higher growth temperatures and better adhering films, hopes are high for quality films of the binary skutterudites. This would in turn lead to the deposition of multilayers and more complex skutterudite phases for study.

ACKNOWLEDGMENTS

Funding was provided by the Department of Defense (MURI - ONR) #N00014-97-1-0516.

This work benefited from the use of the U.C. Berkeley Integrated Materials Laboratory that is supported by the National Science Foundation (award number: DMR9214370). RBS data was collected with Dr. Kinman Yu at the Lawrence Berkeley National Laboratory. Measurements were performed in conjunction with Dr. Wendy Fuller-Mora at the Naval Research Laboratory and Dr. Gang Chen at UCLA, Department of Mechanical and Aerospace Engineering. I would also like to thank H.M. Christen (Neocera, Inc.) for discussions on PLD and Dr. Fleurial and Dr. Calliat for discussions on skutterudites.

REFERENCES

1. G.S. Nolas, G.A. Slack, D.T. Morelli, T.M. Tritt, A.C. Ehrlich, J. Appl. Phys. **79** (8), 4002 (1996).

2. H.J. Goldsmid, Thermoelectric Refrigeration, Plenum Press, 1964.

3. G. Chen, ASME DSC-Vol. 59, 13 (1996).

4. L.D. Hicks, M.S. Dresselhaus, Phys. Rev. B, **47**, 12727 (1993).
5. H. Anno, K. Matsubara, Y. Notohara, T. Sakakibara, K. Kishimoto, and T. Koyanagi, Proc. XV Int. Conf. on Thermoelectrics, Pasadena, CA, March 26-29, 1996.

6. H-M. Christen, D.G. Mandrus, D.P. Norton, L.A. Boatner, B.C. Sales, presented at the 1997 MRS Spring Meeting, San Francisco, CA, 1997 (proceedings publication unknown).

7. B. Chen, J-H. Xu, S. Hu, C. Uher, Mat. Res. Soc. Symp. Proc. Vol. 452, 1037 (1997).

8. G. A. Slack, G. T. Tsoukala, J. Appl. Phys. **76** (3), 1665 (1994).

THERMOELECTRIC PROPERTIES OF Cr_3S_4-TYPE SELENIDES

G. Jeffrey Snyder*, T. Caillat, and J. -P. Fleurial
Jet Propulsion Laboratory/California Institute of Technology
4800, Oak Grove Drive, MS 277-207, Pasadena, CA 91109
*jeff.snyder@jpl.nasa.gov

ABSTRACT

Several compounds with the Cr_3S_4 structure type have been studied for their thermoelectric properties. All exhibit low lattice thermal conductivity of about 15 mW/cmK, independent of temperature. Many of the compounds, such as Co_3Se_4, Ni_3Se_4, Fe_3Se_4, Ti_3Se_4, $FeNi_2Se_4$, and $FeCo_2Se_4$, are metals with relatively low electrical resistivity and Seebeck coefficient. The Cr containing compounds, such as Cr_3Se_4, $NiCr_2Se_4$, $CoCr_2Se_4$, and $FeCr_2Se_4$, have the largest Seebeck coefficients and highest resistivity. The most promising of these materials for thermoelectric applications is $FeCr_2Se_4$.

INTRODUCTION

The growth of commercial applications of thermoelectric devices depends primarily on increasing the figure of merit, ZT, for thermoelectric materials. The figure of merit is defined as $ZT = \alpha^2\sigma T/\lambda$, where α is the Seebeck coefficient, σ the electrical conductivity, λ the thermal conductivity, and T is the absolute temperature. Materials with a large $\alpha^2\sigma$ value, or power factor, are usually heavily doped semiconductors, such as Bi_2Te_3. The thermal conductivity of semiconductors is usually dominated by phonon or lattice thermal conductivity. Thus, one method for finding new, advanced thermoelectric materials is to search for semiconductors with low lattice thermal conductivity.

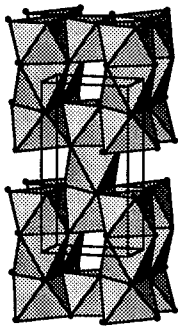

Figure 1. Illustration of the Cr_3S_4 unit cell showing S atoms as spheres and Cr atoms (not shown) at the center of the shaded octahedra. The vertical chain of face sharing octahedra is cut into segments of three units by a vacancy. The monoclinic unit cell is indicated.

In this paper we evaluate compounds based on the defect-NiAs structure, Cr_3S_4, with general composition $A_xB_{3-x}X_4$ where A and B are transition metals and X is a chalcogen, primarily Se. Previous work on such compounds [1] have shown that a range of metals and insulators exist with this structure type, and that they may have extremely low thermal conductivity [2, 3]. For instance, the magnetic semiconductor $FeCr_2Se_4$ has been reported [2-4] to have room temperature thermal conductivity of 1.1 mW/cm K which is an order of magnitude lower than the state-of-the-art thermoelectric material, Bi_2Te_3 alloys.

The structure of Cr_3S_4 (Figure 1) consists of hexagonally close packed S atoms with metal atoms in the octahedral holes as in NiAs. The metal atoms have 6 anion near neighbors (forming

Mat. Res. Soc. Symp. Proc. Vol. 545 © 1999 Materials Research Society

an octahedron) plus two nearby metal atoms along the *c*-axis. As suggested by Spitzer [5] the relatively high coordination number of the atoms in this structure may favor low lattice thermal conductivity. Due to the stoichiometry (three metal atoms for every 4 non-metal atoms), 1/4 of the octahedral holes must be vacant. The scattering of phonons by these vacancies should help reduce the lattice thermal conductivity.

In many defect-NiAs compounds, the defects order, increasing the unit cell size and lowering the symmetry (*e.g.* from hexagonal $P6_3mc$ in NiAs to monoclinic $C2/m$ for Cr_3S_4). The vacancies cut the chains of metal atoms along the NiAs *c*-axis into units of 3 (Figure 1). Since there are two equivalent end members of the three atom chain for every central atom, one may expect that for the composition AB_2X_4 the B atoms would occupy the end positions and the A atom the central position of the chain. However, since these two metal atom sites are nearly identical (the central site is slightly larger, due to the greater number of vacancies nearby), there can be significant mixing of different atoms on these two sites. Indeed, a full solid solution is found for many of these $A_xB_{3-x}X_4$ compounds.

There are approximately 90 known $A_xB_{3-x}X_4$ compounds with the Cr_3S_4 structure type. Many of these compounds have X = Se compounds with 3-d transition metals for A and B atoms (Figure 2), and constitute most of the samples in this investigation. Several of the known AB_2S_4 sulfides with the Cr_3S_4-type structure are high temperature/pressure polymorphs of compounds with the Spinel structure at room temperature and pressure. Known compounds with X = Te are metals with low thermopower (α) (Table 1).

The Cr_3S_4-type selenides are attractive for thermoelectric applications not only because they may have low thermal conductivity as suggested above, but they also exhibit a range of electronic properties – from metals to semiconductors. Precise, heavy doping of the semiconductor is critical to obtain optimal power factor for both n- and p-type materials. Proven thermoelectric materials such as filled Skutterudites and Zn_4Sb_3 are often difficult to dope to the optimal n- or p-type carrier concentration. An advantage of the $A_xB_{3-x}X_4$ compounds is the chemical versatility of the structure, allowing continuous doping from metal to n- and p- type semiconductor.

Experimental

The thermoelectric properties of many Cr_3S_4 compounds reported in the literature [1] were used to narrow the search. Compounds with thermopower or thermal conductivity data are summarized in Table 1.

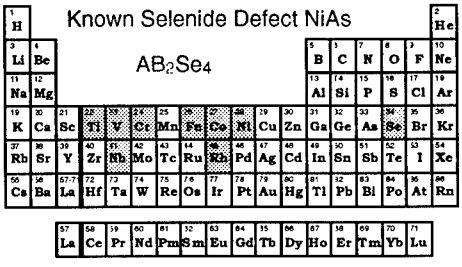

Figure 2. Elements known to make $A_xB_{3-x}Se_4$ compounds with the Cr_3S_4 structure type, where A and B are metals shaded in the figure.

Polycrystalline samples were prepared by mixing and reacting elemental powders in evacuated silica ampoules for several days at 700° - 800° C. The samples were analyzed by x-ray diffractometry to confirm the crystalline structure. The powders were then hot-pressed in graphite dies into dense samples, 3 mm long and 12 mm in diameter. The hot-pressing was conducted at a pressure of 1400 kg/cm^2 and 700° - 800° C for about 2 hours under argon atmosphere. The density of the samples was calculated from the measured weight and

dimensions and was found to be greater than 95% of the theoretical density for all samples except those containing Ti. Pellets containing Ti or rich in Fe had many cracks and often broke apart.

The samples were also characterized by microprobe analysis which was performed using a JEOL JXA-733 electron superprobe operating at 20 kV and 15 nA. All samples not containing Ti or V were found to have less than 1% of impurity phases. The elemental concentrations determined from microprobe analysis were within experimental uncertainty (about 1% atomic) of the expected values.

Table 1. Thermoelectric properties of Cr_3S_4-type compounds found in the literature [1-4, 6-12].

Composition	ρ_{300} m Ω.cm	S_{300} μV/K	λ_{300} mW/cmK	$\lambda_{lattice}$ mW/cmK	Ref
Fe_3Se_4	2	-15			9
$TiFe_2Se_4$	0.3	40			6
VFe_2Se_4	3	40			6
	1	-15	21	16	7
$NiFe_2Se_4$	0.2	-10	29	2	7
$CrFe_2Se_4$	5	-18	7.5	6	7
NiV_2Se_4	1	-5			8
VCr_2Se_4	45		4.4		3
	50	4	7		2
$NiCr_2Se_4$	20	-21			8
	30	3.5	9	9	2
	27		5.5	5	3
$FeCr_2Se_4$	100	48	1.1	1	2
	10	60			4
	125	25	1.1	1	3
Rh_3Se_4	2.6	-15			10
$NiRh_2Se_4$	0.3	5			12
Cr_3Te_4	1	-12			1
$FeCr_2Te_4$	1	2			4
$CoCr_2Te_4$	5	-10			11

Samples in the form of disks (typically a 1.0 mm thick, 12 mm diameter slice) were cut from the cylinders using a diamond saw for electrical and thermal transport property measurements. Temperature dependence of electrical resistivity, Hall effect, Seebeck coefficient, thermal diffusivity and heat capacity measurements were conducted on selected samples between 80 and 800K. The resistivity and Hall effect were measured using the method of Van der Pauw [13]. The carrier density was calculated from the Hall coefficient, assuming a scattering factor of 1.0 in a single carrier scheme, by $n = 1/R_H e$, where n is the density of holes or electrons, and e is the electron charge. The Hall mobility (μ_H) was calculated from the Hall coefficient and the resistivity values by $\mu_H = R_H/\rho$. Normally, the uncertainty is estimated to be ± 0.5% and ± 0.2 cm^2/Vs for the resistivity and mobility data, respectively. The Hall effect, however, is very small and compounded by the anomalous Hall effect because of the magnetism. Therefore it is difficult to estimate the Hall mobility or carrier concentration. The Hall mobilities shown in Table 2 equate to carrier concentrations in excess of $10^{20}/cm^3$. The Seebeck coefficient (α) was measured with a high temperature light pulse technique [14]. The error of the Seebeck measurement was estimated to be less than ± 3%. Room temperature thermal conductivity was measured using the comparison method [15]. High temperature heat capacity and thermal diffusivity were measured using a flash diffusivity technique [16]. The thermal conductivity (λ) was calculated from the experimental density, heat capacity, and

Table 2. Room temperature thermoelectric properties from this study. A Lorenz value of 1.8×10^{-8} J^2/K^2C^2 was used to calculate the electronic contribution to the thermal conductivity.

Composition	Metal/ Semic.	ρ_{300} m Ω.cm	S_{300} μV/K	μ_{H300} cm^2/Vs	λ_{300} mW/cmK	$\lambda_{lattice}$ mW/cmK
Ni_3Se_4	M	0.1	-6	0	88	11
$FeNi_2Se_4$	M	0.2	-12	0	34	7
Co_3Se_4	M	0.3	-12	0	35	13
$FeCo_2Se_4$	M	0.3	-15	0	32	15
Ti_3Se_4	M	0.4	1	0.3	31	17
Fe_3Se_4	M	0.7	-5	0	14	6
Cr_3Se_4	M	1.1	-30	-0.9	17	12
$TiFe_2Se_4$	S	2.0	-10	0	12	9
$FeCr_2Te_4$	S	0.6	5	2	18	8
$NiCr_2Se_4$	S	1.0	-28	-0.2	19	14
$CoCr_2Se_4$	S	3.0	-32	-0.1	17	15
$FeCr_2Se_4$	S	10.0	128	0.1	13	12

thermal diffusivity values. The overall error in the thermal conductivity measurements was estimated to be about ± 10%.

Results and Discussion

The Cr_3S_4-type selenides exhibit a wide variety of electronic properties (Table 2). Many are metals (resistivity increases with temperature) having room temperature resistivity (ρ) from about 10^{-4} to 10^{-3} Ωcm. The non-linearities and hysteresis in the resistivity as a function of temperature may be due to magnetic or structural changes, or even loss of Se at high temperatures (Figure 6). Sample cracking at high temperature may cause some of the observed hysteresis. Neither the high power factor of $TiFe_2Se_4$ nor the very low thermal conductivity values reported in the literature (Table 1) could be confirmed.

The room temperature thermopower of the metals tend to be negative and have a somewhat larger magnitude than elemental metals. The Seebeck coefficient is linear with temperature, T, as expected from the diffusion thermopower. For an electron gas the diffusion thermopower is given by $\frac{\pi^2 k_B^2 T}{3e}\left(\frac{\partial \ln(\sigma(E))}{\partial E}\right)_{E_F}$ [17]. The linear extrapolation of the thermopower to a non-zero value may be due to the phonon drag component to the thermopower [18].

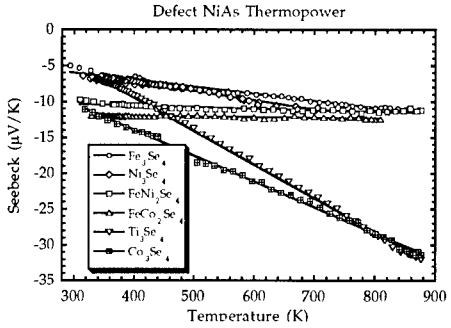

Figure 3. Thermopower of some Cr_3S_4-type metals.

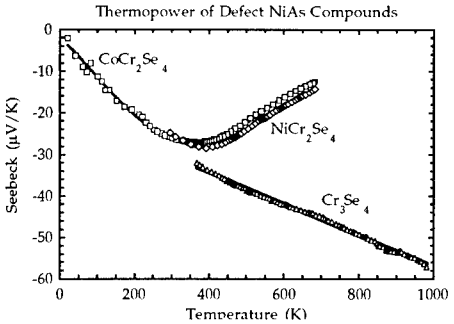

Figure 4. Thermopower of some Cr containing Cr_3S_4-type compounds.

Other Cr_3S_4-type selenides, typically samples with Cr^{+3} are semiconductors where the resistivity decreases with temperature. Many of these semiconductors have low activation energies and low room temperature resistivity. This translates into a small bandgap and high carrier concentration. $CoCr_2Se_4$ and $NiCr_2Se_4$ are low band gap semiconductors (0.02 eV) with maximum Seebeck at about 350K. $FeCr_2Se_4$ is more semiconducting (0.04 eV activation energy at room temperature) with maximum Seebeck at 440K.

Exchange split Cr^{+3} in octahedral coordination will have 3 electrons to completely fill the majority spin T_{2g} orbital (or subsequent band); thus Cr^{+3} may not provide metallic carriers. However, Co^{+2} which has 7 d electrons must have a partially filled orbital. Thus $CoCr_2Se_4$ should be a metal. If these electrons are localized on the Co atoms, which are relatively distant from one another, electron conduction may not be metallic but proceed by a (small polaron) hopping mechanism. Such a compound can also be considered a Mott insulator. If $CoCr_2Se_4$ is a Mott insulator, then $NiCr_2Se_4$ and $FeCr_2Se_4$ are likely Mott insulators for similar reasons.

The resistivity due to small polaron hopping conduction has only a slightly different

temperature dependence ($T\exp(E_a/kT)$) than that expected of a semiconductor ($\mu^{-1}\exp(E_a/kT)$ where the mobility μ is proportional to $T^{3/2}$ for many semiconductors). Both forms are dominated by an exponential with characteristic energy E_a. For the materials described here the resistivity data is not sufficiently well described by either of the exact forms to determine the transport mechanism. Nevertheless, band semiconductor transport characteristically has carriers with high mobility and low concentration while small polarons have high concentration and low mobility. Thus, the data suggests that these materials have polaron conductivity.

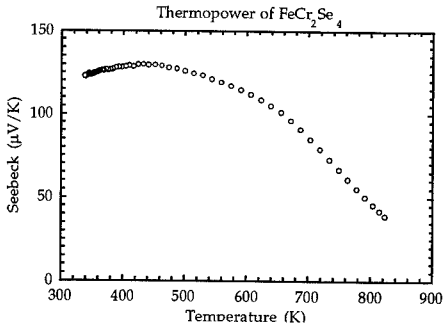

Figure 5. Thermopower of $FeCr_2Se_4$.

The thermal conductivity λ is given by the sum of the electronic λ_E and lattice contributions λ_L. λ_E is directly related to the electronic conductivity: $\lambda_E = L\sigma T$, where L is the Lorenz factor. A Lorenz factor of 1.8×10^{-8} J^2/K^2C^2 gives consistent room temperature lattice thermal conductivity values for the compounds listed in Table 2. If the Lorenz factor typical for metals (2.4×10^{-8} J^2/K^2C^2; see Figure 7) were used, the calculated electronic contribution would be greater than the measured total thermal conductivity. The anomalously low lattice thermal conductivity calculated for $FeCr_2Te_4$ at high temperatures further indicates a lower than expected Lorenz factor (Figure 7). The low Lorenz factor may indicate significant electron-electron scattering ([19] p109).

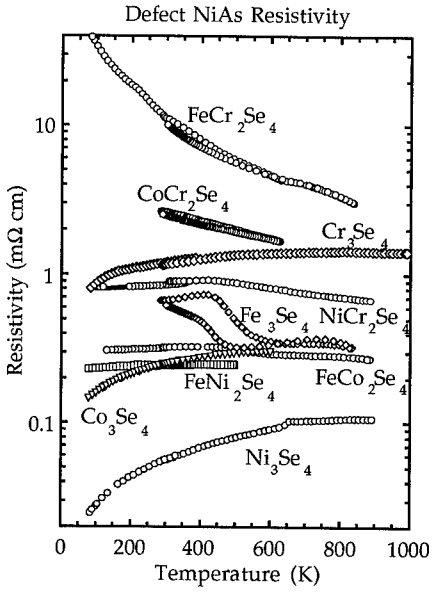

Figure 6. Electrical resistivity of Cr_3S_4-type selenides.

The lattice thermal conductivity is relatively independent of temperature (Figure 7) indicating multiple scattering processes. Low, temperature independent thermal conductivity is found in complex structures such as glasses. Common crystalline materials have large lattice thermal conductivity that is proportional to $1/T$. The ternary Cr_3S_4-type compounds have lower lattice thermal conductivity as is often observed for such alloying.

The power factor and therefore figure of merit is very low for most of these compounds. This may be traced to the very low Hall mobilities. Typical thermoelectric materials have Hall mobilities greater than 10 cm^2/Vs, whereas the materials in Table 2 have mobilities at least 10

times less. This may be due to the hopping method of transport, the increased electron scattering from the transition metal magnetic moments (magnon scattering) or due to the lower covalency of these materials as compared to conventional thermoelectric semiconductors.

The best thermoelectric compounds studied here contain chromium and selenium. Chromium selenide, Cr_3Se_4, has the highest power factor of the metals and the largest apparent Hall mobility. The semiconductor with highest Seebeck coefficient is $FeCr_2Se_4$. The solid solution $Fe_xCr_{3-x}Se_4$ was therefore chosen for further study to determine the optimal thermoelectric properties.

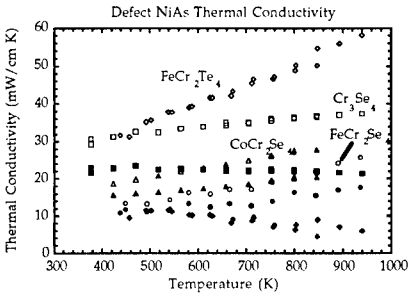

Figure 7. Thermal conductivity (open symbols) and lattice contribution, calculated using the Lorenz factor typical for metals, of Cr_3S_4-type compounds (filled symbols).

Summary

A variety of Cr_3S_4-type compounds were examined for high thermoelectric figure of merit. Reported thermoelectric properties and the existence of known compounds helped guide the selection of materials to reexamine. All showed low, glass-like thermal conductivities. The tellurium containing compounds were eliminated due to their low Seebeck coefficients. The selenides show a variety of electronic properties from metals to small polaron semiconductors, all with very low mobilities. The most promising compound studied is $Fe_xCr_{3-x}Se_4$ since it is the most semiconducting and can easily be doped by changingx.

We would like to thank A. Zoltan, L. D. Zoltan, S. Chung, and A. Borshchevsky for their help on this project. This work was carried out at the Jet Propulsion Laboratory-California Institute of Technology, under contract with NASA and supported by the U. S. Defense Advanced Research Projects Agency, Grant No. E407.

References

[1]*Landolt-Börnstein* (Springer-Verlag, Berlin, Vols. NS III/17h;NS III/12b;NS III/4b.
[2]V. A. Ivanova, D. S. Abdinov, and G. M. Aliev, Phys. Stat. Sol. **24**, K23 (1967).
[3]G. B. Abdullaev, G. M. Aliev, V. A. Ivanova, *et al.*, Heat Transfer-Soviet Research **5**, 30 (1973).
[4]L. M. Valiev, I. G. Kerimov, S. K. Babaev, *et al.*, Inorg. Mater. , 176 (1975).
[5]D. P. Spitzer, J. Phys. Chem. Solids **31**, 19 (1970).
[6]D. A. Guseinov, R. Z. Sadykhov, and A. D. Namazov, Inorg. Mater. **26**, 1511 (1991).
[7]N. R. Akhmedov, N. Z. Dzhalilov, G. M. Aliev, *et al.*, Inorg. Mater. **10**, 711 (1974).
[8]R. J. Bouchard and A. Wold, J. Phys. Chem. Solids **27**, 591 (1966).
[9]D. A. Guseinov, M. A. Aldzhanov, R. Z. Sadykhov, *et al.*, Inorg. Mater. **25**, 1018 (1989).
[10]S. Anzai, M. Ohji, S. Ohta, *et al.*, Jpn. J. Appl. Phys. **32**, 311 (1993).
[11]L. M. Valiev, I. G. Kerimov, A. A. Abdurragimov, *et al.*, Inorg. Mater. , 613 (1977).
[12]R. J. Bouchard, Inorg. Chem. **8**, 850 (1969).
[13]L. J. van der Pauw, Philips Res. Repts. **13**, 1 (1958).
[14]C. Wood, L. D. Zoltan, and G. Stapfer, Rev. Sci Instrum. **56**, 719 (1985).
[15]D. M. Rowe, *Thermoelectric Handbook* (CRC, Boca Raton, 1995).
[16]J. W. Vandersande, C. Wood, A. Zoltan, *et al.*, in *Thermal Conductivity* (Plenum, New York, 1988), p. 445.
[17]R. D. Barnard, *Thermoelectricity in Metals and Alloys* (Wiley, New York, 1972).
[18]H. J. Trodahl, Phys. Rev. B **51**, 6175 (1995).
[19]R. R. Heikes and R. W. Ure, *Thermoelectricity: Science and Engineering* (Interscience, New York, 1961).

THERMAL CONDUCTIVITY OF Fe-DOPED $CoSb_3$ SKUTTERUDITES

Kevin L. Stokes,[1] A.C. Ehrlich [2] and G. S. Nolas[3]

[1] *Advanced Materials Research Institute, University of New Orleans, New Orleans, LA*
[2] *Materials Physics Branch, Naval Research Laboratory, Washington, DC*
[3] *Research and Development Division, Marlow Industries, Inc., Dallas TX*

ABSTRACT

We investigate the effect of Fe substitution for Co on the lattice thermal conductivity of $CoSb_3$ skutterudites. The polycrystalline materials are formed from uniaxially hot-pressed powders. Three alloys were prepared with 0, 3% and 10% Fe, respectively. Thermal conductivity measurements were made between 80 K to 450 K. The lattice thermal conductivity of 10%Fe:$CoSb_3$ is approximately two times smaller than the lattice thermal conductivity of $CoSb_3$ over the entire temperature range. This effect cannot be accounted for by the phenomenlogical theory considering only the mass difference and strain field due to the alloying (Fe) atom. Other phonon scattering mechanisms are discussed. Comparison is made with the partially-filled skutterudite alloy, $La_{0.65}Fe_{2.8}Co_{1.1}Sb_{12}$.

INTRODUCTION

Semiconductors with the skutterudite structure have proven to be a promising class of materials for high temperature thermoelectric applications. Typically, the natural voids in the skutterudite crystal structure are filled with a rare-earth atom in an attempt to increase phonon scattering. Slack[1] first proposed that such an arrangement could cause a significant decrease in the lattice component of the thermal conductivity while possibly having a much smaller effect on the favorable electronic properties (high mobility, large Seebeck coefficient). The basic idea is that the rare earth atom, loosely bound inside the void, introduces a broad spectrum of vibrational modes which interact with the lattice phonons. However, along with the rare earth atom, a neighboring transition metal atom must also be included in the alloy to electronically compensate. Examples of these compounds are the partially-filled $LaFe_xCo_{4-x}Sb_{12}$[2,3] or the fully-filled $CeFe_4Sb_{12}$.[4] Indeed, large decreases in the lattice thermal conductivity have been reported for a variety of rare-earth doped, electronically compensated skutterudites.[2-7]

In order to quantify the effect of void filling on the lattice thermal conductivity, we must first determine the effect of substituting a compensating atom on the metal site. Consequently, we have prepared and studied unfilled, Fe-doped $CoSb_3$ alloys as a function of Fe concentration. Three alloys were prepared for this study with Fe concentrations of 0, 3 and 10 atomic %. Additionally, one partially-filled alloy, $La_{0.65}Fe_{2.8}Co_{1.1}Sb_{12}$, is included for comparison. Thermal conductivity measurements were made between 80 K to 450 K. Obviously, since Fe has one less electron than Co, this substitution results in an excess of holes which also conduct heat. We subtract this carrier contribution from the total measured thermal conductivity so that we can compare only the lattice components of thermal conductivity. We find that the lattice conductivity of 10%Fe substituted $CoSb_3$ is a factor of two smaller than $CoSb_3$ over our entire temperature range. By comparison, the partially rare-earth filled skutterudite, $La_{0.65}Fe_{2.8}Co_{1.1}Sb_{12}$, has thermal conductivity roughly a factor of three smaller than $CoSb_3$. Clearly, the Fe substitution is playing a role in reducing the lattice conductivity. We discuss

Mat. Res. Soc. Symp. Proc. Vol. 545 © 1999 Materials Research Society

these results in terms of the phonon relaxation time approximation and suggest possible scattering mechanisms introduced by the Fe substitution.

EXPERIMENT

The polycrystalline samples were prepared by standard ceramic methods. Stoichiometric amounts of high-purity, powdered elemental constituents were mixed and reacted for many hours at high temperatures (700 °C ~ 1000 °C). The samples were ground to a fine powder using a ball mill and compacted with a uniaxial hot press. Details of this procedure are given in Refs. [4] and [7]. Powder x-ray diffraction measurements verified the skutterudite crystal structure determined the lattice parameters. The stoichiometries were obtained from electron-beam microprobe analysis. Densities were determined by weighing a precisely cut cube of material. Grain sizes were estimated from electron-beam backscatter images and checked with an optical microscope.

Electrical transport properties (resistivity and Hall effect) were measured using a four-probe geometry on an approximately 2 mm × 1 mm × 5 mm parallelepiped of material. Magnetic field and current were reversed, and the appropriate averages taken, to eliminate misalignment and thermal voltages. Measurements were made with the sample in a variable-temperature, liquid nitrogen cryostat.

Thermal conductivity was measured using the 3ω method.[8] In this method, a metal line is vacuum-deposited onto the sample surface and patterned using standard photolithographic techniques. This metal line serves as both heater and thermometer. Sinusoidal current with frequency ω is applied to the heater line causing periodic heat flow ($\propto I^2$) into the sample at frequency 2ω. The temperature dependence of the resistivity of the metal strip causes a periodic change in the resistance at frequency 2ω. The absolute temperature rise on the sample surface is obtained by measuring the small periodic change in the sensor line voltage at frequency 3ω. Recovery of this small signal is made with a lock-in amplifier.

Since it is necessary to isolate the heater/thermometer metal line from our electrically conducting samples, we first deposited approximately 0.7 μm of SiN onto the polished sample surface using plasma-enhanced chemical vapor deposition (PECVD). A 10 μm × 1.5 mm gold strip was then patterned on top of the SiN. The thickness of the insulating SiN layer is much smaller than both the width of the metal strip and the diffusion length of the thermal wave and can be neglected.[8] The sample was surrounded by a radiation shield and placed in a variable-temperature liquid nitrogen cryostat. The sample vessel was evacuated to a pressure of less than 10^{-5} Torr. Typically, the rms magnitude of the applied current was 30 mA which gave an rms heater power of about 10 mW. The measured thermal conductivity was corrected for porosity[9] so that the results correspond to fully dense materials.

RESULTS

Electrical resistivity data are shown in Fig. 1. These results are necessary in order to separate the lattice contribution and electronic contribution to the total thermal conductivity and to determine the role of phonon-electron scattering in the lattice thermal conductivity. The electronic contribution to the thermal conductivity, κ_e, was estimated from the Wiedemann-Franz law, $\kappa_e = LT/\rho$, where L is the Lorenz number, T is the absolute temperature and ρ is the electrical resistivity.

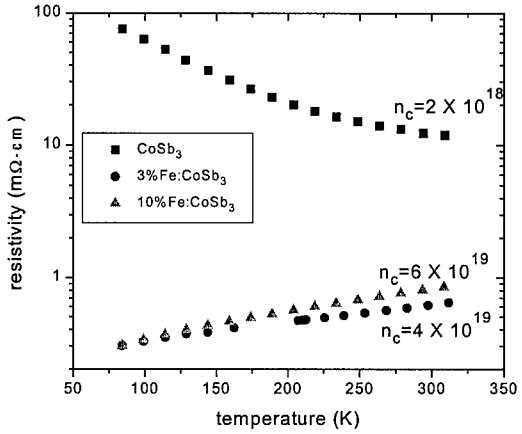

Figure 1. Resistivity for the Fe-doped skutterudites. The Hall carrier concentration at room temperature is given above the curves in units of cm^{-3}.

We use a temperature-independent Lorentz number of 2.44×10^{-8} V^2/K^2 taken from Ref. [7]. The lattice thermal conductivity, κ_g, was obtained by subtracting the calculated κ_e from the measured total thermal conductivity. The κ_g component of the thermal conductivity was about 99% of the total κ for CoSb; that is, $\kappa_g/(\kappa_g+\kappa_e) = 0.99$. The κ_g contribution was about 86% of the total thermal conductivity for both the 3% Fe- and 10% Fe-doped samples.

The inverse of κ_g, the lattice thermal resistivity, is plotted in Fig. 2. The lattice thermal resistivity of the three unfilled skutterudite samples is roughly linear with temperature with a slope of 3.6×10^{-4} m/W. The lattice thermal resistivity of the rare-earth filled skutterudite sample has a noticeably different temperature dependence. Comparing the magnitudes of the thermal resistivities, we find that 3%Fe:$CoSb_3$ is roughly 1.5 times greater than "pure" $CoSb_3$ over the entire temperature range and that 10%Fe:$CoSb_3$ has a thermal resistivity roughly a factor of two larger than $CoSb_3$ over this temperature range. It appears that the addition of Fe into the alloy produces a significant temperature-independent increase in lattice thermal resistivity.

DISCUSSION

An estimate of the thermal resistivity, *W*, for complex crystals with a large number of atoms per unit cell, valid for temperatures near the Debye temperature is given by Slack[1]

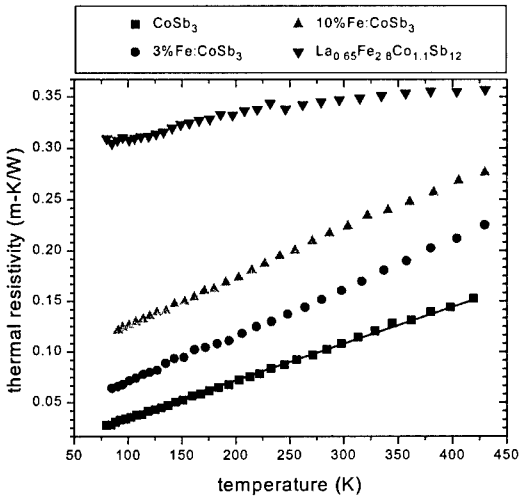

Figure 2. Lattice thermal resistivity as a function of temperature for the three Fe-doped, unfilled $CoSb_3$ skutterudites. Total thermal resistivity for a partially filled skutterudite, $La_{0.65}Fe_{2.8}Co_{1.1}Sb_{12}$, is shown for comparison. The solid line is a fit to Eq. (1).

$$W = \frac{n^{2/3} T \gamma^2}{b_0 M \delta \theta^3} \tag{1}$$

where n is the number of atoms per unit cell, γ is the Grüneisen constant, M is the average mass of an atom in the crystal, δ^3 is the average volume per atom, θ is the Debye temperature and b_0 is a constant equal to 3.04×10^7 s^{-3} K^{-3}. We use the following parameters obtained for single crystal $CoSb_3$ [10]: M=0.106 kg, $\delta=2.845\times10^{-10}$ m, θ=307 K. For the skutterudite crystal structure, n=16 [1]. We then use γ as an adjustable parameter; the best fit to the data is γ=1.23, and is shown as a solid line in Fig. 2. This is between the value of 1.42 obtained for $IrSb_3$[1] and 0.95 obtained for single crystal $CoSb_3$.[10] We note that a value of n=32 was used in the calculations of Ref. [10].

We extend this simple analysis to estimate the change in thermal resistivity due to various phonon scattering mechanisms. Calculation of the lattice thermal conductivity in the Debye theory takes the form[11]

$$\kappa_g = \frac{k_B}{2\pi^2 v}\left(\frac{k_B T}{\hbar}\right)^3 \int_0^{\theta/T} \tau(x) \frac{x^4 e^x}{\left(e^x - 1\right)^2} dx \tag{2}$$

where $x=\hbar\omega/k_B T$, ω is the phonon frequency, k_B is the Boltzmann constant, T is the absolute temperature, v is the sound speed, and τ is the phonon relaxation time. In the limit that the redistribution of phonon modes due to normal (N) processes can be ignored, the total phonon scattering can be described by a relaxation time

$$\tau^{-1} = \sum_i \tau_i^{-1} \tag{3}$$

where τ_i is the relaxation time for each individual scattering mechanism. Using this formalism, we examine the order of magnitude contribution to the thermal resistivity from intrinsic *U*-processes, alloy scattering, boundary scattering and phonon-electron scattering. Assuming that the lattice thermal conductivity of undoped $CoSb_3$ is dominated by *U*-processes, τ_U should be given by

$$\frac{1}{\tau_U} = \frac{1}{b_0}\frac{\pi}{4}\left(\frac{k_B}{2\pi^2 v}\right)\frac{k_B^3 T^3}{\hbar^3 \theta^2}\frac{n^{2/3}\gamma^2}{M\delta}x^2. \tag{4}$$

This is similar to the form of τ_U used by White and Klemens[12] and Vining[13] for the Si-Ge systems, but includes the crystal complexity factor $n^{2/3}$. Using Eq. (4) in Eq. (2), Eq. (1) is recovered for temperatures near the Debye temperature. This allows us to estimate an effective intrinsic relaxation rate of $1/\tau_U \sim 3\times10^{12}$ s^{-1} for temperatures near θ.

First, we consider grain boundaries as a source of extrinsic scattering in our alloys. The relaxation rate is estimated as[12]

$$\frac{1}{\tau_b} = \frac{v}{l} \tag{5}$$

where *l* is the average grain size. We determined the grain size in our samples to be between 4 and 7 μm. The average sound speed from Ref. [10] is 2.934×10^3 m/s. This shows that $1/\tau_b < 10^9$ and is negligible compared to U-process near θ. Also, we note that the room temperature thermal resistivity of our polycrystalline $CoSb_3$ sample (0.108 m-K/W) is very close to the value obtained for a single crystal specimen (0.095 m-K/W)[10], indicating that grain boundary scattering is not important at these temperatures.

Next, we consider alloy scattering. Previously, Nolas, et al.[7] calculated the effect of alloy scattering on the lattice thermal conductivity in La-doped $CoSb_3$ based skutterudite alloys. They employed the point-defect scattering theory of Abeles[14] and found that alloy scattering could not account for the increase in thermal resistivity upon incorporation of La into $CoSb_3$. In this theory, a disorder parameter, Γ, accounts for the different mass and atomic volume of the impurity atom and is given by[14]

$$\Gamma = \chi(1-\chi)\left[\left(\frac{\Delta M}{M}\right)^2 + \varepsilon\left(\frac{\Delta\delta}{\delta}\right)^2\right] \tag{6}$$

where χ is the atomic fraction of impurity atoms, ΔM is the mass difference between the two atoms, $\Delta\delta$ is the difference in average interatomic spacing and ε is an adjustable parameter used to represent the contribution from bond strength. Obviously, the mass difference between Fe and Co is small (5%) and contributes little to this scattering term. The important term in our case is the second term in brackets in Eq. (6). We cannot know for certain the difference in volume between a Co atom in a nominal $CoSb_3$ crystal and an Fe atom on a Co site. However, by comparing lattice parameters of $CoSb_3$ and 10%Fe:$CoSb_3$, we can assume that the difference is less than 0.1% and contributes little to the thermal resistivity. Using any reasonable value of ε (40 - 400, from Refs. [14] and [1]) and the formulae of Abeles[14], Eqs.(22)-(24), we also find that alloy scattering can contribute at most only a few percent to the thermal resistivity. This certainly cannot account for the 100% increase we measured for 10%Fe:$CoSb_3$ alloy.

Finally, we consider phonon-electron scattering. An estimate of the relaxation rate due to this process is given in Ref. [12] as (for $T=\theta$),

$$\frac{1}{\tau_{p-e}} = \frac{n_c^2 e^2 v^2 \rho}{N k_B \theta \alpha} \tag{8}$$

where n_c is the carrier concentration, e is the electronic charge, ρ is the electrical resistivity, N is the number density of atoms $\alpha=16/(3^{1/2}\pi)(vm^*\delta/\hbar)^{3/2}$ and m^* is the carrier effective mass. Using our measured values of $n_c=6\times10^{19}$ cm^{-3} and $\rho=0.8$ mΩ-cm (for sample 10%Fe:$CoSb_3$) and a value of $m^*=0.25m_0$ from Ref. [10] we get a phonon-electron relaxation rate of $\sim10^{12}$ s^{-1}. This is comparable to the intrinsic relaxation rate estimated above and may be the source of the increased thermal resistivity.

A rigorous analysis should include all possible phonon scattering sources and include *N*-processes as well. What we have not considered here is scattering from dislocations and scattering from magnetic ions. More experimental information is necessary before we can estimate the magnitude of these effects.

SUMMARY

We have measured the lattice component of the thermal conductivity of three unfilled, Fe-doped, $CoSb_3$ skutterudite alloys over the temperature range from 80 K to 450 K. We find that the lattice conductivity of 10%Fe substituted $CoSb_3$ is a factor of two smaller than $CoSb_3$ over our entire temperature range. By comparison, the partially rare-earth filled skutterudite, $La_{0.65}Fe_{2.8}Co_{1.1}Sb_{12}$, has thermal conductivity roughly a factor of three smaller than $CoSb_3$. Clearly, the Fe substitution is playing a role in reducing the lattice conductivity. Our estimates indicate that electron-phonon scattering is contributing to the decrease in thermal conductivity, but grain boundary scattering or alloy scattering is not significant. More information is needed especially in quantifying the effect of electron-phonon scattering and investigating the possible magnetic ion scattering.

REFERENCES

1. G.A. Slack and V.G. Tsoukala, J. Appl. Phys. **76:**1665 (1994).
2. B.C. Sales, D. Mandrus and R.K. Williams, Science **272:**1325 (1996).
3. D.T. Morelli, G.P. Meisner, B. Chen, S. Hu and C.Uher, Phys. Rev. B **56:**7376 (1997).
4. D.T. Morelli and G.P. Meisner, J. Appl. Phys. **77:**3777 (1995).
5. G.S. Nolas, G.A. Slack, D.T. Morelli, T.M. Tritt and A.C. Ehrlich, J. Appl. Phys. **79:**4002 (1996).
6. J.W. Sharp, E.C. Jones, R.K. Williams, P.M. Martin and B.C. Sales, J. Appl. Phys. **78:**1013 (1995).
7. G.S. Nolas, J.L. Cohn and G.A. Slack, Phys. Rev. B **58:**164 (1998).
8. D.G. Cahill, Rev. Sci. Instrum. **61:**802 (1990).
9. A. Bjorneklett, L. Haukeland, J. Wigren, H. Kristiansen and S. Si, J. Mater. Sci. **29:**4043 (1994).
10. T. Caillat, A. Borshchevsky and J.-P. Fleurial, J. Appl. Phys. **80:**4442 (1996).
11. R. Berman, *Thermal Conduction in Solids* (Claredon Press, Oxford, 1976).
12. D.P. White and P.G. Klemens, J. Appl. Phys. **71:**4258 (1992).
13. C.B. Vining, J. Appl. Phys. **69:**331 (1991).
14. B. Abeles, Phys. Rev. **131:**1906 (1963).

IMAGING OF THE CARRIER DENSITY OF STATES IN LOW DIMENSIONAL STRUCTURES USING ELECTROSTATIC FORCE MICROSCOPY

D. GEKHTMAN[1], Z.B. ZHANG[1], D. ADDERTON[2], M.S. DRESSELHAUS[1,3], AND G. DRESSELHAUS[4]

[1]Department of Physics, Massachusetts Institute of Technology, Cambridge, MA 02139

[2]Digital Instruments, Santa Barbara, CA 93117

[3]Department of Electrical Engineering and Computer Science, Massachusetts Institute of Technology, Cambridge, MA 02139

[4]Francis Bitter Magnet Lab, Massachusetts Institute of Technology, Cambridge, MA 02139

ABSTRACT

In this work we show that scanning probe electrostatic force microscopy (EFM) can be applied to low dimensional electronic nanostructures for imaging the density of states of quantum confined carriers. The results on EFM studies are presented for quasi-one-dimensional (1D) Bi quantum wire arrays and quasi-two-dimensional (2D) $GaAs/Al_xGa_{1-x}As$ multiple quantum well structures.

INTRODUCTION

Scanning Probe Microscopy (SPM) has been recognized as a powerful tool for studying various materials properties under high spatial resolution. Scanning Tunneling Microscopy[1] (STM) can be applied to a highly conducting continuous surface for examining its electronic structure by measuring the tunneling current between a small biased conducting probe and the adjacent local surface region. The surface topography of either conducting or dielectric materials can be studied by Atomic Force Microscopy[2] (AFM), which utilizes optically detected cantilever deflections resulting from the probe-surface atomic interaction. The second generation Electrostatic Force Microscope[3] (EFM) measures the electrostatic force gradient acting on a small charged probe as a result of the long-range Coulomb interaction between the probe and the near-surface charges. This technique, in contrast with STM and AFM, allows us to study the electronic properties of surfaces containing both conducting and dielectric regions with a lateral resolution of less than 5nm. Therefore, EFM can be applied to study nanoscale quantum heterostructures. The main advantage of EFM over the scanning capacitance method[4], which is widely used in the semiconductor industry, is due to the directly measured spatial second-order derivative of the local probe-sample capacitance that dramatically increases the signal-to-noise ratio at small probe-sample distances. So far, EFM has been successfully applied to detecting surface trapped charges[5], profiling the dopant concentration[6] in micro-devices and measuring the work functions[7] of various materials.

Here we use the EFM technique to study the electronic states of a near-surface electron gas confined to the quantum wire and the quantum well structures, which are, respectively, examples of 1D- and 2D-electronic systems.

Mat. Res. Soc. Symp. Proc. Vol. 545 ©1999 Materials Research Society

EXPERIMENT

Structures

We study the melt-injection grown[8] single-crystalline Bi quantum wire arrays embedded in anodic alumina (Al_2O_3) templates and the MBE-grown GaAs/$Al_xGa_{1-x}As$ multiple quantum wells. Both structures were electrically grounded by evaporation of a conducting Au-alloy layer from one side of the structure and scanned from the other side in the cross-sectional surface plane. A bias voltage (V_b) is applied between the structure and the probe in the range $-2<V_b<2V$. The surface of the Bi wire arrays was Ar^+-milled prior to the scanning, in order to remove the oxide layer from the wire surface. In the case of the quantum wells, the freshly cleaved surface was scanned.

SPM procedure

The SPM measurements[9] are made in two consecutive passes[10] along each scan-line. On the first pass, topography data are acquired in the conventional AFM tapping mode near the resonant frequency (≅80kHz) of the Au-coated etched silicon probe. On the second EFM pass, the probe is lifted to a given lift-height (z) and, then, it is scanned along the path of height variations acquired on the first pass (which are used instead of the standard AFM feedback loop), while the probe resonant frequency shift is monitored. This frequency shift, within the harmonic approximation, provides a measure of an external electrostatic force axial gradient (F') acting on the biased charged probe at a constant distance from the local surface regions. In order to control the probe-sample distance (h, which is, in general, unknown), we vary the lift-height values in the range $-9\leq z\leq 30$nm with respect to a fixed set point, which is maintained constant throughout the whole measurement. In the range of parameters used for these measurements, we found that h remains large enough (>5nm) for both the short range Van der Vaals[11] force and the tunneling (dc) current[12] to be below a detectable level. However, h is comparable with the electron screening length λ (~10nm) for the above structures. Thus, the measured F' is sensitive to the near-surface electronic density of states distribution governed by the geometry of the structures.

RESULTS

Bi quantum wires

Figure 1a shows the height (upper graph) and the F' (lower graph) line-scans acquired for the R=30±3nm Bi wire array along the same path connecting the centers of two neighboring wires, as indicated by arrows on the topography image in the inset of Fig.1a. The observed lower height and very flat (within ±2nm) wire surface topography are produced by the Ar^+-beam as a result of the faster ion-milling rate of conducting Bi relative to that of insulating Al_2O_3. We observe that, while scanning over the Bi wire surface regions at a nearly constant height, the measured attractive F' is increased and shows maxima near the wire boundaries. These maxima appear to follow the circular boundary cross-section of an individual wire, as seen from the F'-image shown in Fig. 1b.

There are two reasons why the observed increase of F′ near the wire boundaries cannot be assigned to the probe interaction with the Al_2O_3 surface charges induced by the template

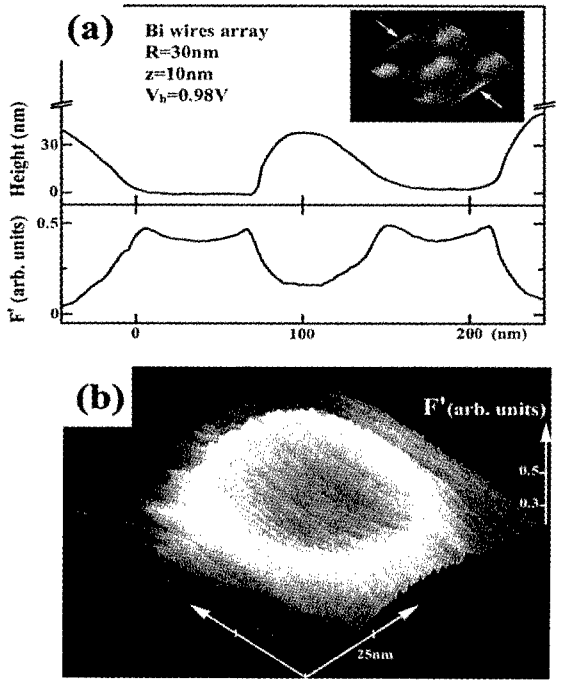

Figure. 1 : **(a)** Consecutive height (upper graph) and electrostatic force gradient (F′, lower graph) line-scans acquired for the lift-height value of z=10nm and under the bias voltage of V_b=0.98V. The scan direction is shown by arrows on the topography image of the Bi wire array with an average radius of R=30±3nm. **(b)** F′-image of the surface of an individual Bi wire measured for the same parameters as in (a).

height variations: 1. Such an interaction with nearly vertical "walls" would result in a **decrease** in the measured electrostatic attraction (that can be seen from the simplest consideration of three image charges induced by the nearby charged probe); 2. The dielectric constant of amorphous Al_2O_3 is very low[13] (≅1.3), which makes this interaction negligible. Therefore, we attribute the observed F′-distribution over the wire surface to the intrinsic electronic properties of the1D Bi-nanocrystal.

GaAs/Al_xGa_{1-x}As quantum wells

Figure 2 describes our results for the quantum well system, where ten 5nm-wide n-doped GaAs wells are sandwiched between $Al_{0.23}Ga_{0.77}As$ barriers, each 50nm in width (Fig.2a).The acquired F′-scan presented in Fig. 2b shows a large intensity for the

measured electrostatic attraction, while scanning over the regions corresponding to the heavily doped GaAs substrate and top layers (left and right edges of the scan, respectively). The scan also shows oscillations at the multiple quantum well regions, yielding maximum F′ intensity near the wells and minimum intensity while scanning over the barriers. The F′-image shown in the inset of Fig. 2b indicates that the intensity maxima indeed follow the geometry of the parallel layers in the quantum wells.

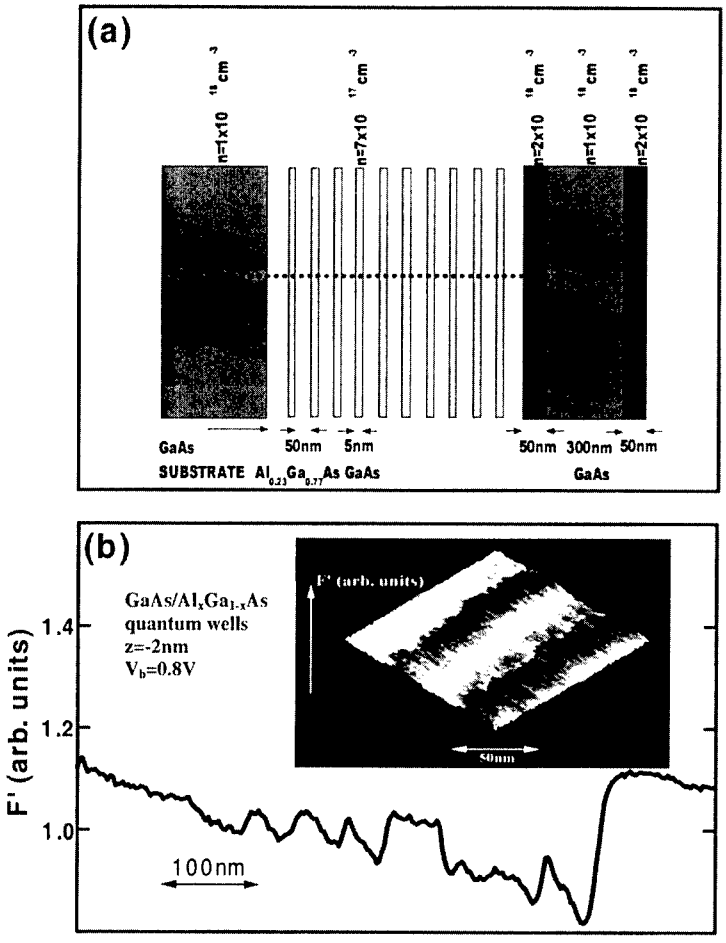

Figure 2 : **(a)** Schematic structure of GaAs/$Al_xGa_{1-x}As$ multiple quantum wells shown in the cross-sectional plane. Si-dopant bulk densities (n) are also indicated. **(b)** Electrostatic force gradient (F′) line-scan acquired along the structure growth axis, as shown schematically by the dashed arrow in (a). The F′- image of the structural area containing two quantum wells is shown in the inset.

DISCUSSION

The simplest picture for interpreting the measured force gradient F' is given by assuming a plane capacitor geometry formed by the scanning probe and a nearby local surface region. This gives[14]:

$$F' = \frac{S V_b^2}{4\pi (h + \lambda)^3}, \qquad (1)$$

where the electron screening length $\lambda=(4\pi e^2 \partial n_e/\partial \mu)^{-1/2}$ is inversely related to $\partial n_e/\partial \mu$, the thermodynamic density of electron states (TDOS, the derivative of the electron density n_e with respect to the electrochemical potential μ), $S \approx 10nm \times 10nm$ is the effective area of the probe tip, and the bias voltage V_b is measured with respect to the work function difference between the structure and the probe. Thus, according to Eq. 1, the measured F' is directly related to the TDOS.

We emphasize that both structures under study are in the quantum regime, in the sense that peaks of the TDOS, which are due to the size quantization, are well-resolved at room temperature, as confirmed by both numerical calculations and spectroscopic observations. Indeed, the F'-variations measured for the quantum well system imply that the electron TDOS is distributed differently from the in-well doping profile, since the electron wave function penetrates strongly into the barriers in accordance with the solution of the Schrödinger equation for the multiple quantum well structure. Furthermore, as seen from Fig. 2, the EFM measurement provides information on the electronic density redistribution between various quantum wells in thermal equilibrium. In the case of Bi quantum wires, however, "hard" wire boundaries as well as the nonparabolic electron dispersion relation of bismuth make the simplest single-particle-in-a-box quantization scheme inappropriate for describing even qualitatively the spatial variation of the TDOS over the wire cross-sectional plane. We believe that the observed increase of the measured F', while scanning towards the wire boundary circumference, results from the self-consistent potential well including inter-carrier Coulomb repulsion[15], which forces the excited carriers to be localized near the wire boundaries.

CONCLUSIONS

A better understanding of the electronic spatial properties of quantum nanostructures, as revealed by EFM, should contribute significantly to the development of novel electronic and thermoelectric low dimensional devices. In the case of Bi quantum wires, as a result of quantum confinement effects, spatial separation of the electron and the hole contributions to the thermoelectric power factor would appreciably increase the figure of merit. As far as GaAs-based devices are concerned, direct EFM imaging of the carrier density of states might lead to a more reliable design of the structural parameters to achieve better device performance.

ACKNOWLEDGEMENTS

We thank Professor Clifton Fonstad for supplying us with the $GaAs/Al_xGa_{1-x}As$ multiple quantum well samples. Support from Navy contract # N00167-98-K-0024 and from MURI/UCLA subcontract 0205-5-7A114-01 are gratefully acknowledged.

REFERENCES

1. G. Binnig, H. Rohrer, Ch. Gerber, and E. Weibel, *Phys. Rev. Lett.* **49**, 57 (1982).

2. G. Binnig, C. Quate, and Ch. Gerber, *Phys. Rev. Lett.* **56**, 930 (1986).

3. Y. Martin, D.W. Abraham, and H. Kumar Wickramasinghe, *Appl. Phys. Lett.* **52**, 1103 (1988); J. E. Stern, B.D. Terris, H. J. Mamin, and R. Rugar, *Appl. Phys. Lett.* **53**, 2717 (1988).

4. *The National Technology Roadmap for Semiconductors*, Semiconductor Industry Association, San Jose, CA (1994).

5. B.D. Terris, J. E. Stern, R. Rugar, and H. J. Mamin, *Phys. Rev. Lett.* **63**, 2669 (1989).

6. A.K. Henning and T. Hochwitz, *Mater. Sci. Eng.* **B42**, 88 (1996).

7. R.M. Nyffenegger, R. Penner, and R. Schierle, *Appl. Phys. Lett.* **71**, 1878 (1997).

8. For details on the Bi wire array fabrication see Z.B. Zhang, J.Y. Ying and M.S. Dresselhaus, *J. Mater. Res.* **13**, 1745 (1998).

9. For example, O. Marti, and J. Colchero, in *"Forces in Scanning Probe Methods"*, ed. by H.J. Güntherodt, D. Anselmetti, and E. Meyer, NATO ASI Series (1995).

10. Lift-mode operation manual, *Digital Instrument Inc.*, Santa Barbara, CA (1996).

11. T.R. Albrecht, and C.F. Quate, *J. Appl. Phys.* **62**, 2599 (1987).

12. U. Dürig, O. Züger, and D.W. Pohl, *Phys. Rev. Lett.* **65**, 349 (1990).

13. For example, *"Handbook of Optical Constants of Solids"*, ed. by E.D. Palik Academic Press, San Diego (1991).

14. For a review of quantum capacitance see M. Büttiker, *J. Phys. Condensed Matter* **5**, 9361 (1993).

15. The classical boundary problem is considered in J.C. Maxwell, *"Treatise on Electricity and Magnetism"*, Oxford (1904)

FABRICATION, CHARACTERIZATION AND ELECTRONIC PROPERTIES OF BISMUTH NANOWIRE SYSTEMS

Zhibo B. Zhang[a], M. S. Dresselhaus[a,b]*, Jackie Y. Ying[c]
[a]Department of Physics, Massachusetts Institute of Technology, Cambridge, MA 02139
[b]Department of Electrical Engineering and Computer Science, Massachusetts Institute of Technology, Cambridge, MA 02139
[c]Department of Chemical Engineering, Massachusetts Institute of Technology, Cambridge, MA 02139

ABSTRACT

We have fabricated ultra-fine Bi nanowire (10-120 nm) arrays with packing densities as high as $7.1 \times 10^{10}/\text{cm}^2$ by pressure injecting its liquid melt into the evacuated nano-channels of an anodic alumina template. Using this fabrication technique, we have also prepared Te-doped n-type Bi nanowires. Free-standing Bi nanowires with an aspect ratio (length/diameter) higher than 500 are obtained by etching away the anodic alumina matrix without attacking the Bi. The resulting Bi nanowires are shown to be single crystals (with the same crystal structure as bulk Bi) and all the wires of a nanowire array are similarly oriented along the wire axis. The small electron effective mass of Bi, the high anisotropy of its Fermi surface, and the large aspect ratio of the Bi nanowires make this a very promising material for low-dimensional thermoelectric applications and an excellent system for studying quantum confinement effects in a quasi-one-dimensional (1D) electron gas. A theoretical model based on the basic band structure of bulk Bi, suitably modified for the 1D situation, is constructed to explore the electrical transport properties of Bi nanowires, which are expected to be very different from those of bulk Bi.

INTRODUCTION

Nanowire systems, especially nanowire arrays embedded in a dielectric matrix, have attracted a great deal of research interest because of their potential applications in electronic devices and promise for studying one-dimensional (1D) quantum-properties. The quantum confinement of carriers in the two dimensions normal to the wire axis will significantly change the electronic energy states of the carriers and make the transport properties of these quasi-1D systems very different from their bulk counterparts. Because of the extremely small electron effective mass of Bi and the high anisotropy of its Fermi surface, Bi nanowires are of special interest for thermoelectric applications.

A promising approach to generate nanowire systems is to fill an array of nano-channels with the medium of interest. In this work, we have successfully fabricated closely packed Bi nanowire arrays with various wire diameters and Te dopant concentrations by pressure injection of liquid Bi melt into the evacuated nano-channels of an anodic alumina template [1]. The individual Bi nanowires are found to be essentially single crystals and all the nanowires in an array have a similar crystal orientation along the wire axis. These excellent materials characteristics make the Bi nanowire arrays very attractive for thermoelectric

*Author to whom correspondence should be addressed.

Mat. Res. Soc. Symp. Proc. Vol. 545 © 1999 Materials Research Society

applications, where high carrier mobility is very desirable. Also importantly, anodic alumina is amorphous Al_2O_3 with a small amount of impurities coming from the anodizing electrolyte [2]. The thermal conductivity of anodic alumina was found to be about 50 times smaller than that of polycrystalline Al_2O_3 [3], which, together with its large bandgap of $\sim$3 eV make it a very desirable barrier layer material for low-dimensional thermoelectric applications. The novel fabrication technique that we developed is highly versatile. The method not only can be easily modified to incorporate dopants into the Bi nano-wires (such as Te as an electron donor or Pb as a hole donor to produce n-type or p-type Bi nano-wires), but also can be applied to other low melting temperature metals, semiconductors (such as Bi_2Te_3), and alloys (such as $Bi_{1-x}Sb_x$).

MATERIALS FABRICATION AND CHARACTERIZATION

The porous anodic alumina template was generated by anodizing a mechanically and electrochemically polished high-purity Al substrate (99.99 + %) using a strong acid solution (such as 20 wt % H_2SO_4 or 4 wt % $H_2C_2O_4$) as the electrolyte [4]. The channel diameter, channel packing density, and channel length of the anodic alumina could be systematically controlled with the processing parameters, such as the anodizing voltage, electrolyte temperature and anodizing time. After a brief thermal treatment, the porous film, which was kept on the Al substrate, was placed inside a high-pressure reactor chamber and surrounded by high-purity (99.999%) Bi pieces. To degas the porous film, the chamber was evacuated to $\approx 10^{-2}$ mbar while heated to a temperature slightly lower than T_m, the melting point of Bi. The temperature of the reactor was then raised above T_m. After the Bi pieces melted, high-pressure Ar gas was introduced to drive the molten Bi into the evacuated channels of the anodic alumina template. The low T_m of Bi and the high thermal stability (up to 800°C)[5] and rigidity of the anodic alumina film make this filling process possible. After the injection process was completed, the reactor was slowly cooled down to room temperature, and the impregnated Bi was solidified and crystallized inside the nano-channels. The pressure was then slowly released. Next, the sample was mechanically retrieved from the surrounding Bi metal, and the Al substrate was etched away by an amalgamation process [1]. We also obtained free-standing Bi nanowires by dissolution of the alumina matrix in a special acid solution without affecting the Bi nanowires [4]. In this work, we have successfully fabricated Bi nanowire arrays with wire diameters between 13 - 110 nm. The highest wire packing density obtained was $\sim 7.1 \times 10^{10}$ wires/cm^2, and the wire lengths are between 20 - 65 μm. We also produced 0.1 at. % Te-doped Bi nanowire arrays by introducing an appropriate amount of Te impurities into the liquid Bi before the pressure injection.

The fabricated Bi nanowire arrays were investigated by various characterization techniques, such as X-ray diffraction (XRD), scanning electron microscopy (SEM), transmission electron microscopy (TEM), and selected area electron diffraction (SAED) [1, 4]. The single crystallinity of the Bi nanowires was confirmed by both high-resolution electron microscopy (HREM) and SAED studies on free-standing Bi nanowires. XRD experiments revealed that all the wires in a nanowire array are highly oriented along the wire axis, with more than 90% of the wires being oriented along a crystal direction normal to the (202) lattice plane of the rhombohedral crystal structure of Bi [4, 6]. In the XRD experiments, we found that all the strong diffraction peaks are close to the peak positions of a polycrystalline Bi standard, indicating that the rhombohedral crystal structure of bulk Bi is also preserved in the small-diameter Bi nanowires [1, 6]. This is also very important for Bi nanowires in thermoelectric

applications, because it implies that the unique properties of bulk Bi, such as the small electron effective masses and the highly anisotropic Fermi surface, are preserved in the small diameter Bi nanowires.

ELECTRONIC PROPERTIES

Since the diameter d_w of the Bi nanowires studied in this work is much smaller than the mean free path l_e of the electrons in Bi, especially at low temperatures, the electrons will experience quantum confinement effects, which is one of the most important factors in determining the electrical transport properties of Bi nanowires. When electrons are confined inside a nanowire, the allowed transverse momenta for the electrons become discrete, and the electronic energy states are split into subbands. Since Bi has very small electron effective mass components, the formation of subbands becomes important for Bi nanowires with diameters on the order of 100 nm, which is much larger than is common for other materials. Because of the high anisotropy of the Fermi surface of Bi, the quantum confinement of carriers will make the electronic subband structure of Bi nanowires very different from that of bulk Bi.

For an ideal 1D Bi quantum wire system, where electrons are confined inside a perfect cylindrical potential well with an infinite potential height, in the lowest approximation where we assume parabolic bands for both the electrons and holes, the energy levels E_{ij} that these quasi-1D electrons can occupy become

$$E_{ij}(k_l) = \frac{\hbar^2 k_l^2}{2m_l^*} + \frac{2\hbar^2 \chi_{ij}^2}{m_c^* d_w^2}, \tag{1}$$

where $2\pi\hbar$ is Planck's constant h, m_c^* is an average effective mass (approximated by the cyclotron effective mass) in the plane normal to the wire axis, m_l^* is the effective mass component along the wire axis, $\hbar k_l$ is the electron momentum along the wire axis, and χ_{ij} are roots of the Bessel function $J_i(\chi_{ij}) = 0$. This dispersion relation represents free-electron-like motion along the wire axis and bounded states in the cross-sectional plane.

Due to the small L-point band gap and the small electron effective masses of Bi, non-parabolic effects are important in describing the electron dispersion relations away from the band edge [7]. Following the Lax model [8], which was derived using two-band perturbation theory (the L-point conduction and valence bands), the dispersion relations for the non-parabolic electron pockets in a Bi quantum wire can be expressed as,

$$E_{ij}(k_l) \approx \sqrt{\frac{E_{gL}^2}{4} + 2E_{gL}\left(\frac{\hbar^2 k_l^2}{2m_l^*} + \frac{2\hbar^2 \chi_{ij}^2}{m_c^* d_w^2}\right)} - \frac{E_{gL}}{2}, \tag{2}$$

where E_{gL} is the 3D band gap at the L-point. Following Eq. (2), we calculate the electronic subband structure for Bi nanowires of different wire diameters. The results for the electronic subband structures of the $[10\bar{1}1]$ wires are shown in Fig. 1, treating the L-point electron and hole bands as mirror bands, following the two-band Lax model. For the $[10\bar{1}1]$ nanowire crystal orientation, the electron pocket denoted by A has a very small electron cyclotron effective mass normal to the wire axis, while the other two electron pockets (denoted by B and C) are equivalent and have a cyclotron effective mass about two times heavier than that of electron pocket A. Thus, the lowest subband edge of electron pockets B and C

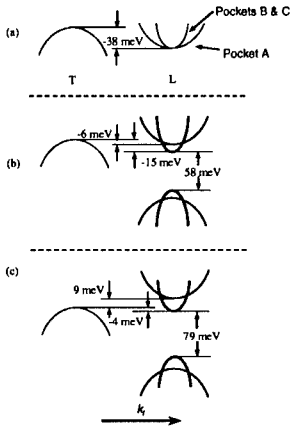

Figure 1: Schematic energy band diagram showing the energies of the lowest subband edges for the three L-point electron pockets and the highest subband edges for T-point and L-point holes for: (a) bulk Bi where the L-point band gap is 15 meV [9], (b) 90 nm-diameter Bi nanowires oriented along the $[10\bar{1}1]$ direction, and (c) 65 nm-diameter Bi nanowires oriented along the $[10\bar{1}1]$ direction. The energy dispersion relation for each subband is for the wave vector along the wire axis k_l, while the band edge energy of each subband is determined by m_c^* (see Eq. 2).

recedes from the 3D band edge more slowly than for electron pocket A, because of the higher m_c^* for carrier pockets B and C relative to pocket A, as shown in Fig. 1. The greater dispersion of the L-point electron subbands for the B and C carrier pockets relative to the A electron pocket is also seen in the figure. Since quantum confinement pushes the conduction subband up and pushes the valence subband down, the Bi nanowires undergo an interesting semimetal-to-semiconductor transition when the wire diameter is reduced.

For bulk Bi, which is a semimetal, both electrons and holes contribute to its electrical transport. Since the Fermi surface of Bi is highly anisotropic, the electrical transport properties of bulk Bi are different along different crystal orientations. In a Bi quantum wire, for instance, the electrical conductivity σ can be expressed as a sum of contributions from each electron and hole subband. For simplicity, we neglect the energy (E) dependence of the effective mass tensor for a given subband as we move away from the subband edge, and include only the non-parabolic effects regarding the determination of the energy of each subband edge. Then, the T dependence of the zero-field conductivity of a Bi quantum wire can be expressed as

$$\sigma(T) = \sum_i \frac{n^{(i)}(T) e^2 \tau(T)}{m_l^{(i)}}, \tag{3}$$

where $1/m_l^{(i)}$ is the component of the reciprocal effective mass tensor $\mathbf{M}^{(i)}$ along the wire direction for the T-point holes (all T-point hole subbands have the same effective mass tensor) and for the L-point electrons at the edge of the i^{th} electron subband for each of the carrier pockets. Since L-point hole carriers can be excited thermally, their dispersion relations are treated similarly to those for the L-point electrons. For each electron subband, $\mathbf{M}^{(i)}$ can be derived from the Lax model and is given by

$$\mathbf{M}^{(i)} = \frac{2E^{(i)} + E_{gL}}{E_{gL}} \mathbf{M}, \tag{4}$$

where $E^{(i)}$ is the onset energy of the i^{th} electron subband measured from the 3D band edge

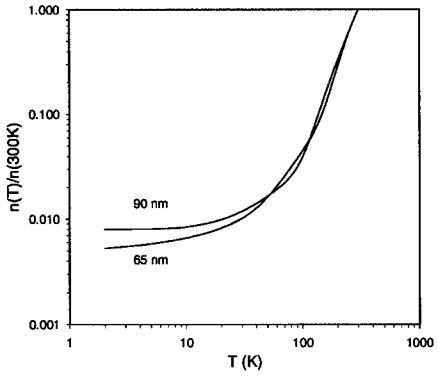

Figure 2: Calculated carrier concentration as a function of temperature for Bi nanowires with wire diameters of 65 nm and 90 nm. The calculations are based on the electronic band structure of Bi nanowires shown in Fig. 1.

of the L-point electron pockets, and M is the effective mass tensor of electrons at the 3D band edge. A similar equation also holds for L-point holes. In modeling the T dependence of the zero-field conductivity of a Bi quantum wire, we can conveniently write $\mu^{(i)} = e\tau^{(i)}/m_l^{(i)}$ where $\mu^{(i)}$ for electrons denotes the mobility along the wire axis for the i^{th} electron subband, and the effective mass tensor component $m_l^{(i)}$ for electrons is computed at the edge of the i^{th} electron subband along the wire axis. A similar approach is used to handle the T-point holes and the thermally excited L-point holes. The temperature dependence of the carrier densities for electrons (or holes) is shown in Fig. 2 on a log-log plot for Bi nanowires with 90 nm and 65 nm diameters oriented along the $[10\bar{1}1]$ direction. Here we see that the carrier concentration n is similar for the two wire diameters at high T (above 70 K), but becomes increasingly smaller at low T for the 65-nm nanowire.

The theoretical model presented here results in electronic properties for Bi nanowires that are very different from that of bulk Bi and are very sensitive to the wire diameter. For both the 90-nm and 65-nm Bi nanowires oriented along the $[10\bar{1}1]$ direction, the populations of electron pocket A and electron pockets B and C are different and all change in a complicated way with temperature. When the wire diameter is reduced, the Bi nanowires undergo a semimetal-to-semiconductor transition [1, 6]. If we define d_c as the diameter at which the Bi nanowires undergo a semimetal-to-semiconductor transition, then $d_c = 59$ nm, 58 nm, 40 nm and 25 nm for Bi nanowires oriented along the $[10\bar{1}1]$, bisectrix, trigonal and binary directions, respectively, taking non-parabolic effects into account in an approximate way, as discussed above. These values for d_c are smaller than those presented in reference [6], where the non-parabolic effects of the L-point conduction band were ignored. These semiconducting nanowires can be doped with electron donors or acceptors to become either n-type or p-type, and a high thermoelectric figure of merit is expected to be achieved in both n-type and p-type semiconducting Bi nanowires [10].

CONCLUSIONS

In summary, ultra-fine Bi nanowire arrays have been fabricated by a novel vacuum melting and pressure injection process. The excellent materials properties of the fabricated Bi nanowires have been confirmed by various characterization techniques. A detailed theoretical model, which takes into account the non-parabolic effects of the L-point electron bands, has been constructed to calculate the electronic subband structure and the electrical transport properties of the Bi nanowires. As the wire diameter is reduced, the Bi nanowires are expected to undergo a semimetal-to-semiconductor transition. If appropriately doped with electron donors or acceptors, these semiconducting Bi nanowires are expected to show a high thermoelectric figure of merit at very low wire diameters.

We thank Dr. G. Dresselhaus of MIT and Prof. G. Chen of UCLA for valuable discussions. This project is partially funded by the U.S. Navy (Contract No. N00167-98-K0024) and National Science Foundation (Grant No. DMR-98-04734) and MURI (Subcontract No. 0205-6-G-7A114-01).

REFERENCES

[1] Z. B. Zhang, J. Y. Ying, and M. S. Dresselhaus, J. Mater. Res. **13**, 1745 (1998).

[2] G. E. Thompson, R. C. Furneaux, G. C. Wood, J. A. Richardson, and J. S. Goode, Nature **272**, 433 (1978).

[3] G. Chen. In *Thermoelectric Materials–The Next Generation Materials for Small-Scale Refrigeration and Power Generation Applications: MRS Symposium Proceedings, Boston, volume* **544**, edited by T. M. Tritt, H. B. Lyon, Jr., G. Mahan, and M. G. Kanatzidis, Materials Research Society Press, Pittsburgh, PA, 1999.

[4] Z. B. Zhang, D. Gekhtman, M. S. Dresselhaus, and J. Y. Ying, (unpublished).

[5] Z. B. Zhang. *Fabrication, characterization and transport properties of bismuth nanowire systems.* Ph.D. thesis, Massachusetts Institute of Technology, Department of Physics, December 1998.

[6] Z. B. Zhang, X. Z. Sun, M. S. Dresselhaus, J. Y. Ying, and J. P. Heremans, Appl. Phys. Lett. **73**, 1589 (1998).

[7] V. S. Edel'man, Adv. Phys. **25**, 555 (1976).

[8] B. Lax and J. G. Mavroides, in *Advances in Solid State Physics*, (Academic Press, New York, 1960), Vol. 11.

[9] R. T. Isaacson and G. A. Williams, Phys. Rev. **185**, 682 (1969).

[10] X. Sun, M. S. Dresselhaus, Z. Zhang, and G. Chen. In *Thermoelectric Materials–The Next Generation Materials for Small-Scale Refrigeration and Power Generation Applications: MRS Symposium Proceedings, Boston, volume* **544**, edited by T. M. Tritt, H. B. Lyon, Jr., G. Mahan, and M. G. Kanatzidis, Materials Research Society Press, Pittsburgh, PA, 1999.

THERMAL CONDUCTIVITY AND PHONON ENGINEERING IN LOW-DIMENSIONAL STRUCTURES

G. Chen,* S.G. Volz, T. Borca-Tasciuc, T. Zeng, D. Song
Mechanical and Aerospace Engineering Department, University of California, Los Angeles, CA 90095-1597, *Email: gchen@seas.ucla.edu

K.L. Wang
Electrical Engineering Department, University of California, Los Angeles, CA 90095

M.S. Dresselhaus
Department of Electrical Engineering and Computer Science, and Department of Physics, Massachusetts Institute of Technology, Cambridge, MA02139

ABSTRACT

Understanding phonon heat conduction mechanisms in low-dimensional structures is of critical importance for low-dimensional thermoelectricity. In this paper, we discuss heat conduction mechanisms in two-dimensional (2D) and one-dimensional (1D) structures. Models based on both the phonon wave picture and particle picture are developed for heat conduction in 2D superlattices. The phonon wave model, based on the acoustic wave equations, includes the effects of phonon interference and tunneling, while the particle model, based on the Boltzmann transport equation, treats the internal as well interface scattering of phonons. For 1D systems, both the Boltzmann transport equation and molecular dynamics simulation approaches are employed. Comparing the modeling results with experimental data suggest that the interface scattering of phonons plays a crucial role in the thermal conductivity of low-dimensional structures. We also discuss the minimum thermal conductivity of low-dimensional structures based on a generalized thermal conductivity integral, and suggest that the minimum thermal conductivities of low-dimensional systems may differ from those of their corresponding bulk materials. The discussion leads to alternative ways to reduce thermal conductivity based on the propagating phonon modes.

INTRODUCTION

Heat conduction in low-dimensional structures is a central issue for realizing high ZT in low dimensional structures [1-3]. An increasing number of experimental works have recently been reported on the reduced thermal conductivity of superlattices in directions parallel and perpendicular to the superlattice plane [4-12]. Earlier experimental work was geared towards applications in semiconductor lasers where the low thermal conductivity is detrimental [4-6]. More recently, attention has been shifted towards the applications to thermoelectrics where low thermal conductivity may lead to a higher figure of merit [7-12]. Theoretically, several models have been developed to explain the observed thermal conductivity in low-dimensional structures. The first prediction of a reduced thermal conductivity in superlattices considered increased unklampp scattering due to zone folding and mini-phonon gap formation in superlattices [13]. The predicted thermal conductivity reduction due to such increased scattering mechanisms, however, was not enough to account for the orders of magnitude reduction observed experimentally. Based on the Boltzmann transport theory, Chen and Tien [14] predicted a

Mat. Res. Soc. Symp. Proc. Vol. 545 © 1999 Materials Research Society

significant reduction in the thermal conductivity in quantum well structures. Over the last two years, several models have been established to explain the reduced thermal conductivity in superlatttices structures [15-19].

While there are an increasing number of works on heat conduction in two-dimensional (2D) structures, little work has been done for one-dimensional (1D) structures. There have been some discussion on localization vs. ballistic heat conduction in one-dimensional wires [20-22] and a few experimental data have been published on the thermal conductivity of wires at low temperatures [23-25]. In general, the present understanding of heat conduction mechanisms in one-dimensional wires is far from adequate.

In this paper, we present and compare several approaches for modeling the heat conduction in 2D superlattices and we will provide initial results on the direct simulation of the thermal conductivity in 1D wires. The mechanisms of heat conduction in low-dimensional structures will be explored. We also provide a qualitative discussion on the minimum thermal conductivity and point out alternative ways to reduce thermal conductivity in low-dimensional structures as compared to the traditional methods for bulk materials, through engineering the propagating modes of phonon in these structures.

THERMAL CONDUCTIVITY OF TWO-DIMENSIONAL SUPERLATTICES

In this section, we will focus on the discussion of heat conduction mechanisms in two-dimensional superlattices. Two characteristics of superlattices are distinctly different from bulk materials: the existence of many interfaces and the periodicity in the structure. We will start with a discussion of phonon transport at a single interface, followed by examining phonon transport in superlattices from a wave and a particle point of view.

Phonon Reflection and Thermal Boundary Resistance at an Interface

Phonons are the quantized normal modes of lattice vibrations. An example is the sound wave, which consists of low frequency phonons. Most of the wave characteristics of phonons can be obtained from the wave equations established under Newton's second law. Intuitive understanding of heat transfer through an interface can be gained through studying the propagation of acoustic waves at interfaces and by making an analogy to photons [26]. Compared to an electromagnetic wave that is always transverse, a phonon wave can be transverse as well as longitudinal waves. For the long wavelength acoustic waves, the phonon reflection is due to the difference between the acoustic impedances across the interface of two materials. Here the acoustic impedance is defined as the product of the mass density and the speed of sound. In the most general case as illustrated in Fig. 1(a), an incident acoustic wave

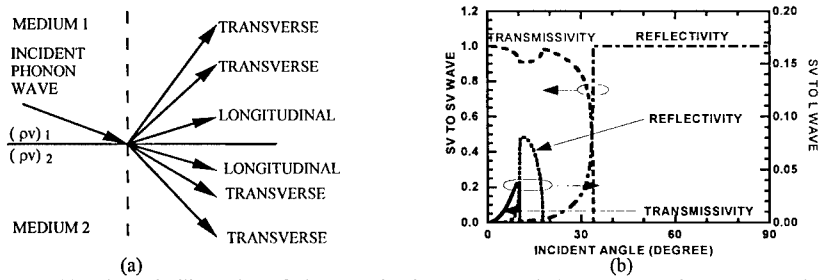

Figure 1 (a) Schematic illustration of phonon reflection and transmission at an interface and (b) calculated reflectivity and transmissivity at an interface similar to Si/Ge for a transverse phonon polarized in the plane of incidence (SV phonon) incident from the Ge side, showing the mode conversion [from SV wave into a longitudinal wave (L)] and the total internal reflection phenomena.

may excite three reflected and three transmitted phonon waves of different polarizations. The phonon reflectivity and transmissivity can be derived from the continuity requirements for the atom displacement and the traction force at the interface. Figure 1(b) shows the calculated phonon reflectivity and transmissivity at an interface similar to that between Si and Ge, albeit with isotropic properties such that the two transverse phonon modes are degenerate. The incident phonon is from the Ge side with a transverse wave polarized in the plane of incidence. This figure shows (1) the mode conversion and (2) the total reflection phenomena. Some of the transverse phonons are converted into longitudinal phonons. For incident angle higher than ~33°, the critical angle, total internal reflection occurs. Beyond the critical angle, an evanescent wave exists in the Si side as illustrated in Fig. 1(b). Such an evanescent wave, however, does not carry net energy flow into the second medium.

In terms of heat transfer, one consequence of the phonon wave reflection is the thermal boundary resistance existing at a perfectly flat solid interface, or the Kapitza resistance for the interface between a solid and the liquid helium. Predictions for the thermal boundary resistance, based on the perfect acoustic-mismatch model, are reasonably good at low temperatures, but fail at high temperatures [27,28]. One possible reason is that at high temperatures, the dominant phonon wavelength is shorter and the interface roughness becomes more important, causing diffuse scattering of phonons. Another possible source of discrepancy lies in the mismatch of the phonon spectra between the two materials. Due to the mismatch in the phonon spectrum, the high frequency phonons must split into lower frequency phonons to transmit into the adjacent materials, or they will be limited inside the original medium, causing total reflection. Past work indicates that inelastic scattering should be taken into account in explaining the experimentally measured thermal boundary resistance at high temperature [29]. In general, the detailed interface phonon scattering mechanisms at room temperature are not clear and models are highly idealized.

Heat Conduction in Superlattices, Treating Phonons as Waves

To the accuracy of the harmonic oscillator approximation, the major differences between heat transfer at one interface and that in multilayer structures such as superlattices are the phonon interference and tunneling phenomena. Two distinct approaches have been developed for investigating phonon behavior in superlattices. One is based on the transfer matrix method for calculating the transmissivity of phonons and the other is to directly calculate the phonon dispersion as has been typically done in solid-state physics [30,31]. The two approaches lead to similar results. The phonon interference phenomenon in superlattices was demonstrated by directly measuring phonon transmissivity across a superlattice [32]. The measurement showed the familiar dip in the phonon transmissivity under certain wavelengths as observed in optical interference filters. In Fig. 2(a), we show the phonon transmissivity in a Ge/n(Si/Ge)/Si/Ge superlattice structure calculated from the transfer matrix method, as a function of the incident phonon frequency. Here the n-period Si/Ge superlattice is sandwiched between two Ge substrates, with an additional Si layer between the superlattice and one Ge-susbtrate. Several stop bands is formed at this particular incident angle. This translates into the formation of mini-gaps in the phonon spectra of superlattices and the corresponding reduced phonon group velocity, as schematically illustrated in Fig. 2(b).

In evaluating the thermal conductivity of superlattices in the cross-plane direction, Mahan and Hyldgaard [17] used a lattice dynamics model for a 2x2 Si/Ge superlattice and calculated the phonon group velocity reduction in such a superlattice. Here we took a different approach to investigate the effects of the phonon group velocity reduction and mini-gap formation on the heat conduction. We use the transfer matrix method [30] to calculate the heat transfer over the Ge/n(Si/Ge)/Si/Ge superlattice structure mentioned before. To calculate the heat flow across the

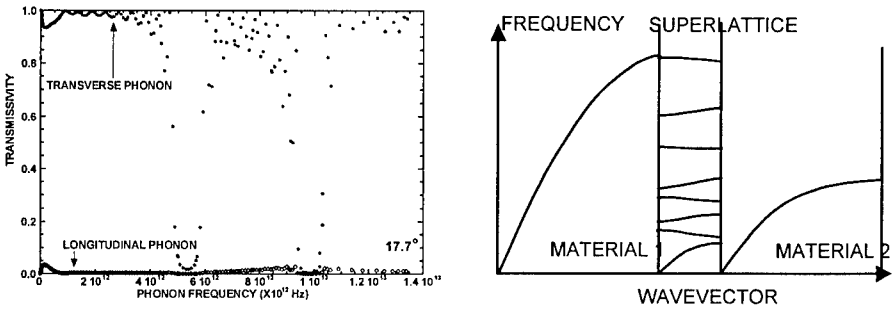

(a) (b)

Figure 2 (a) Phonon transmissivity over a Ge/10(Si/Ge)/Si/Ge superlattice with each layer at 5 Å for a SV wave incident at 17.7°, showing the stop bands caused by the phonon interference. This translates into the formation of mini-gaps in the phonon dispersion relation of superlattices, as schematically illustrated in Fig.. 2(b).

superlattice, we make the following assumptions: (1) each of the two cladding materials is at a uniform temperature, (2) all materials are isotropic, (3) the thermal phonons can be decomposed into plane waves, (4) internal scattering inside each layer is negligible, and (5) phonon scattering at interfaces is specular and elastic. Since the internal scattering is totally neglected, we do not expect the model to capture all the heat conduction mechanisms occurring in superlattices. The emphasis here is on the impact of the phonon group velocity reduction and the mini-gap formation on the thermal conductivity.

For calculating the total heat flux, the phonon dispersion in each of the materials must be known. We make two approximations regarding the phonon dispersion relations. One is a linear dispersion approximation, as has been often used in the study of phonon propagation in superlattice structures [30,31]. We will refer this linear dispersion relation as the Debye model. Since thermal conduction involves all the phonons, the nonlinear phonon dispersion relation close to the Brillouin zone boundary will affect the total heat transmission. In a second model, we approximate the longitudinal and the transverse phonon dispersions by sinc functions and call the latter case the dispersion model. For both models, the contribution of optical phonons is neglected, which is reasonable because of: (1) the small group velocity of the optical phonons and (2) the large mismatch of the optical phonon energies between Si and Ge.

When the temperature difference between the two cladding media is small, the effective thermal conductivity of the superlattice can be calculated from the following relation

$$k_{eff} = (d/2)\sum_{p} \int_0^{\omega_{pm}} \left(\hbar\omega v_p D(\omega) df/dT \int_0^1 \tau_p(\chi,\omega,d)\chi d\chi\right) d\omega \qquad (1)$$

where d is the thickness of the whole superlattice structure, f the Bose-Einstein distribution at temperature T, v_p the phonon group velocity, ω the phonon angular frequency, τ the phonon transmissivity, and $\chi(=\cos\theta)$ the directional cosine. The summation is made over the three phonon polarizations.

Equation (1) indicates that the thermal conductivity will be linearly proportional to the film thickness if the phonon transmissivity is thickness independent. This is because internal scattering is assumed to be negligible. A more appropriate property for heat conduction under this circumstance is the thermal conductance, which is defined as

$$K = q/\Delta T = (1/2)\sum_p \int_0^{\omega_{pm}} \left(\hbar\omega v_p D(\omega) df/dT \int_0^1 \tau_p(\chi,\omega,d)\chi d\chi\right) d\omega \qquad (2)$$

where q is the heat flux and ΔT the temperature difference.

The key in evaluating Eqs. (1) and (2) is to evaluate the phonon transmissivity, which is calculated using a well-established transfer matrix method [26,30]. For the Debye model, such a calculation is straightforward. Considering the continuity requirements on the displacement and the traction forces, we conclude that the integration in frequency should be extended only to the maximum of the transverse phonons in the Ge layer (ω_{pm}). Above this frequency, no phonons can be transmitted through the superlattice. The contribution of the normal incident phonons above the maximum of the transverse phonons is neglected. For the dispersion model, additional complications arise because both the phonon phase and group velocities depend on frequency. To use the continuum acoustic wave results, we use the frequency-dependent phase velocities for the transverse and the longitudinal phonons in the calculation of the transmissivity, and we introduce the frequency-dependent Lamb's constants based on their relations with the phase velocities.

Figure 3(a) shows the thermal conductance of superlattices made of different periods as a function of the layer thickness, calculated from the Debye model. In the same figure, we also give the results for a Ge/Si/Ge double heterojunction structure [33]. Both the wave and the ray-tracing results are shown for this latter structure. The ray-tracing method neglects the interference and tunneling effects of the phonon waves. For the single layer structure (n=0), the tunneling and interference effects become important if the layer thickness is thinner than 10 Å. Tunneling has a more profound impact on K than interference effects, and tunneling increases the thermal conductance as the film becomes thinner. For films thicker than 10 Å, both the wave and the ray tracing methods give the same results. As a comparison, we also calculated the thermal conductance for a transparent interface by assuming that the transmissivity equals one in Eq. (2). The conductance obtained under this circumstance is 0.1027 W/m^2K, which is a factor of 10 higher than that obtained by the ray tracing method after considering the interface reflection due to the acoustic and the frequency mismatches. Out of this factor of 10 reduction of the interface conductance due to the phonon reflection, about a factor of four of which is due to the acoustic mismatch (the difference in the acoustic impedance) and a factor of 2.5 due to the frequency mismatch.

The simulation results in Fig. 3(a) show that for superlattices, the tunneling and interference

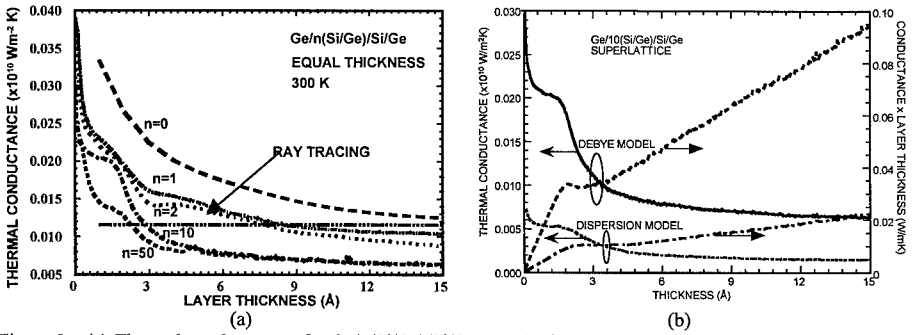

Figure 3 (a) Thermal conductance of a Ge/n(Si/Ge)/Si/Ge superlattice structure calculated by the transfer matrix method, where the layer thickness is the thickness of each individual layer in the superlattice (equal thickness is assumed). The ray tracing results neglect the interference and tunneling effects. (b) Comparison of results obtained from Debye model and the dispersion model for a 10 period superlattice.

effects become stronger for shorter periods. As the number of periods increases, the thermal conductance converges to the same curve for thicker layers. The value of the conductance changes little as the layer becomes thicker. Compared to a single layer, the thermal conductance of superlattices is further reduced by a factor of two due to multiple reflections. The convergence of the conductance at large periods indicates that the superlattice approaches one with an infinite number of repetitions. The thermal conductivity for such an infinite repetition superlattice structure, however, would diverge to infinite because we neglected internal scattering.

From Fig. 3(b), we show the thermal conductance results obtained from the Debye model and from the dispersion model. Due to reduced phonon group velocity in the dispersion model, the thermal conductance is further decreased by about a factor of four. Compared to the thermal conductance value obtained by assuming perfect transmission at the interface, 0.1027 W/m^2K, we estimate that a factor of 20-80 reduction in the thermal conductance is possible due to reflection at interfaces caused by the acoustic mismatch and the frequency mismatch.

We also show in Fig. 3(b) the product of the thermal conductance with the layer thickness, despite the fact that the thickness in Eq. (1) should be the total thickness of the superlattice. As we pointed out before, the thermal conductivity of the whole structure diverges due to the neglect of internal scattering. We use this product to illustrate that it may not be beneficial to reduce the layer thickness to lie within the range where tunneling can significantly increase the thermal conductance (typical one or two monolayers) and thus reduce the effectiveness of the interface in impeding the heat flow. This result also resolves one problematic issue: what happens to the thermal conductivity if a superlattice is made so short that it effective is an alloy (due to interface mixing, for example)? In the latter case, the wave scattering mechanism changes totally.

Heat Conduction in Superlattices, Treating Phonons as Particles

One major difficulty in the wave approach of heat conduction in superlattices lies in the treatment of interface conditions. The wave calculation is most suitable for specular interfaces. Past experimental results on the thermal boundary resistance suggest that at room temperature, diffuse scattering at interfaces is possible and may even be dominant. We have taken an approach based on treating phonons as particles and solving the Boltzmann transport equation (BTE) for phonon transport with heat flow in both the in-plane and the cross-plane directions. The input parameters for these models include the phonon mean free path (MFP), specific heat, mass density, and group velocity in the each bulk material constituent of the superlattices. Previously developed models for interface thermal boundary resistance [27,28] have been extended to include phonon dispersion and the possibility of inelastic scattering. Because the mechanism for phonon scattering at interfaces is not clear, we assumed that the interfaces are partially diffuse and partially specular and used a fitting parameter p to represent the fraction of specularly scattered (reflected and transmitted) phonons at the interface. Interface scattering is treated as a boundary condition in solving the BTE, rather than as a volumetric scattering process. Details of these models have been published [16,18,19]. Here we would like to emphasize several points.

First, the reduction of the thermal conductivity depends on layer thickness relative to the phonon MFP in each layer. Thermoelectric materials typically have low thermal conductivity to start with and thus short phonon MFPs. We should emphasize, however, that the simple kinetic theory, which yields $k=1/3CvL$, underestimates the MFP of those phonons that carry the heat. Here C is the volumetric specific heat, v the speed of sound, and L the phonon MFP. This is because of the following two factors. (1) Phonons are dispersive and their group velocities vary from the speed of sound at the Brilloin zone center to zero at the zone edge. The average phonon group velocity is much smaller than the speed of sound. (2) Optical phonons contribute to the

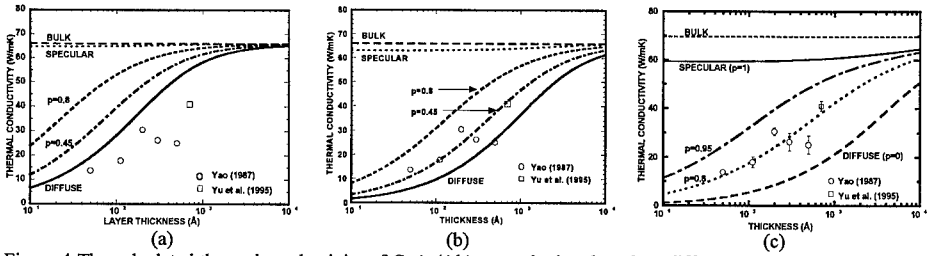

(a) (b) (c)

Figure 4 The calculated thermal conductivity of GaAs/AlAs superlattices based on different ways of estimating the phonon MFP in bulk materials: (a) kinetic theory, (b) average the phonon MFP over the acoustic branches and neglect contributions from optical phonons, and (c) frequency dependent phonon relaxation time.

specific heat but typically contribute little to heat flux due to their low group velocity and their high scattering rates. Hyldgaad and Mahan [15] estimated the phonon mean free path (MFP) based on a spectral averaging method and concluded that the phonon MFP is much longer than the value obtained from the simple kinetic theory. We use Figs. 4(a)-(c) to strengthen this point. These figures compare the modeling results with experimental data of the thermal conductivity for GaAs/AlAs superlattices based on different ways of estimating the phonon MFP. In Fig. 4(a), the MFP is estimated based on the simple kinetic theory, the bulk specific heat and the speed of sound, which leads to a phonon MFP about 209 Å in GaAs and 369 Å in AlAs. The underestimation of phonon MFP is clear from Fig. 4(a), since even worst scenario results, i.e., totally diffuse interfaces, lead to theoretical values much larger than the experimental results. In Fig. 4(b), we estimate the average phonon group velocity and MFP based on a sine-function approximation to the phonon dispersion relation and totally neglecting optical phonon contributions to thermal transport. The phonon MFPs thus obtained are 1058 Å for GaAs and 2248 Å for AlAs. The agreement with experimental data is much better. In Fig. 4(c), we show the calculated thermal conductivity based on the frequency-dependent phonon relaxation time and again good agreement with experimental data is obtained, albeit with a very different interface specularity parameter. Naturally, one would think that the frequency dependent treatment is more accurate. We would like to point out, however, that the frequency dependent relaxation time is obtained from models that fit into the bulk thermal conductivity of those materials, and those models are subject to high uncertainty.

Second, although specular interfaces do not seem to reduce the thermal conductivity of Si/Ge or GaAs/AlAs superlattices, they could produce a large reduction in the thermal conductivity of alloy-based superlattices. Figure 5 shows modeling results for $Si/Si_{0.8}Ge_{0.2}$ superlattices as a function of the Si well thickness for a $Si_{0.8}Ge_{0.2}$ barrier fixed at 300 Å. This is because in GaAs/AlAs and Si/Ge superlattices, each material has a fairly large thermal conductivity and thus a large phonon MFP. When phonons are refracted from one layer into another, their MFP is

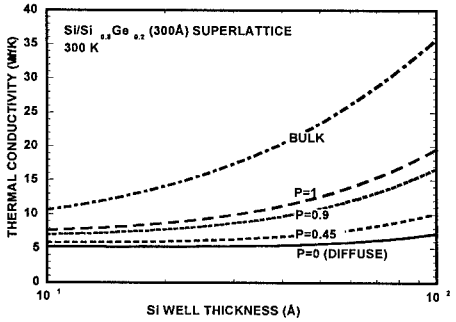

Figure 6 Modeled thermal conductivity of a $Si/Si_{0.8}Ge_{0.2}$ as a function of the Si well thickness for a 300 Å $Si_{0.8}Ge_{0.2}$ barrier.

not altered significantly. For alloy-based superlattices, since the alloy layer has a low thermal conductivity value and thus a short phonon MFP, phonons refracted from the Si layer into the SiGe layer will effectively shorten the phonon MFP within the Si layer.

Third, by comparing the cross-plane thermal conductivity data with the two different models, where one model assumes that interface scattering is totally elastic, while the other model assumes that interface scattering is totally inelastic, we concluded that inelastic scattering must occur at the interface. Otherwise, the predicted thermal conductivity would be too low to agree with experimental results, as shown in Figs. 6(a) and (b). This is also in agreement with our assessment from a wave point of view, as discussed in the previous section. We should point out that phonon zone folding and quantum confinement phenomena have been observed experimentally using for example, Raman spectroscopy [34]. There exist, however, no quantitative assessments presently of the magnitude of the phonon confinement.

Figure 7 shows the temperature drop inside each layer and across the interfaces of one period of a superlattice. This figure shows that most of the temperature drop occurs at the interfaces

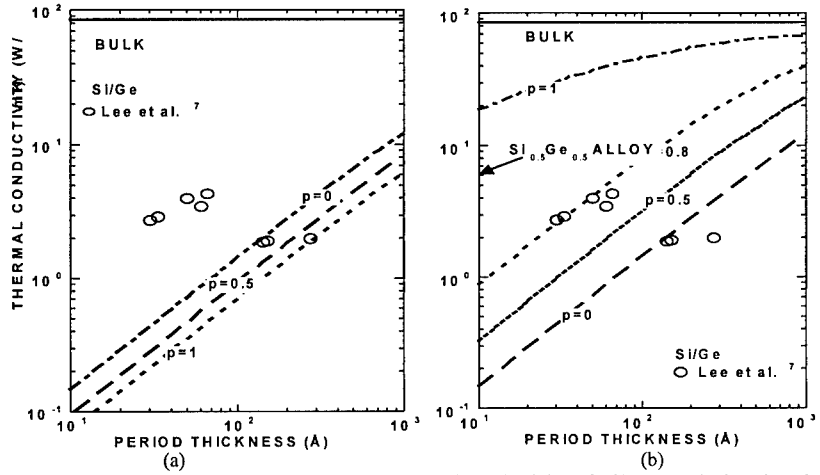

Figure 6 Comparison of models with reported thermal conductivity of Si/Ge superlattices based on the assumption of (a) elastic interface scattering and (b) inelastic interface scattering [19].

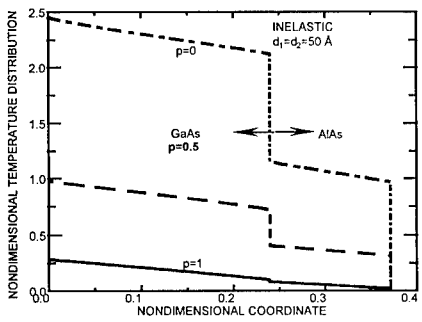

Figure 7 Temperature distribution in one period of a superlattice for heat conduction in the cross-plane direction, demonstrating that most of temperature drop occurs at the interface.

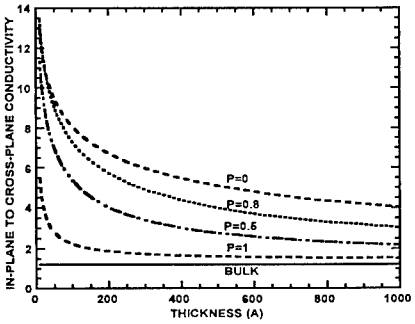

Figure 8 Ratio of the cross-plane thermal conductivity to the in-plane thermal conductivity for Si/Ge superlattices. All phonon MFP estimates are based on the average of the phonon group velocity.

due to the thermal boundary resistance phenomenon we explained before, although for superlattces, the multiple reflection at interfaces alter the expression for calculating this interfacial thermal boundary resistance. When the phonon MFP is larger than the film thickness, it is not the bulk thermal conductivity, but the mismatch of the density, group velocity, phonon spectrum, and the specific heat of the two adjacent materials that controls the thermal conductivity of the superlattice structure.

In Fig. 8, we compare the anisotropy of the thermal conductivity as a function of layer thickness, with the interface specularity as a free parameter to vary, for equal thickness Si/Ge superlattice. Phonon MFPs in Si and Ge are estimated based on an average of the group velocity and the in-plane and cross-plane thermal conductivity is calculated based on the models we developed. This figure shows that the most efficient way to reduce the thermal conductivity is to arrange the transport to be in the cross-plane direction.

Finally, we should emphasize that the above models neglected the impacts of structural defects on the thermal conductivity of superlattices. Existing experimental data [8] and modeling [18] indicate that dislocations and other structural defects can significant reduce the thermal conductivity. Our recent measurements on a Si/Ge superlattice actually indicate a smaller in-plane thermal conductivity in the in-plane direction than the cross-plane direction.

HEAT CONDUCTION IN ONE-DIMENSIONAL STRUCTURES

The above discussion focuses on phonon transport in superlattices. It is not difficult to understand that similar but stronger size effects will occur inside one-dimensional (quantum wires) and zero-dimensional (quantum dots) structures. A few experimental and theoretical works have been reported on the thermal conductivity of wire type materials [20-25], but no conclusive experimental data on semiconductor materials around room temperature have yet been reported.

To estimate size effects on the thermal conductivity of wire type materials, we used a molecular dynamics (MD) method to directly compute the thermal conductivity of Si nanowires [35,36]. The MD techniques trace the time history of individual atoms and calculate the transport properties from atomic trajectories. The classical MD simulation could include phonon wave effects within the accuracy of the harmonic oscillator approximation, but it may not correctly account for the scattering mechanisms due to the differences between the Bose-Einstein and the Boltzmann distribution functions. We anticipate that the MD technique will be valid at high temperatures where the difference between these two statistical distribution functions is small. We have successfully combined the MD technique with a model based extrapolation to calculate the thermal conductivity of bulk Si, as shown in Fig. 9(a) [35]. The calculated thermal conductivity is higher than the experimentally reported thermal conductivity of natural silicon but is comparable to the extrapolated experimental value of isotopically enriched silicon [37]. In Fig. 9(b), we show the MD simulation and the BTE solution of the thermal conductivity of Si nanowires [36], demonstrating a significant reduction of the thermal conductivity of such wires. The limitation of the MD method, however, is the computational power and the accuracy of the interatomic potential. Embedded in the MD results are the physics of the phonon heat conduction processes. It is not a trivial task to understand the physics behind the MD results.

MINIMIUM THERMAL CONDUCTIVITY AND PHONON ENGINEERING

Some of the calculations we have done lead to thermal conductivity values much lower than the minimum bulk thermal conductivity theory [38,39]. We should stress that our previous models did not include any consideration on the minimum phonon MFP. Those results, however, raises the interesting question of whether the low-dimensional structures can have

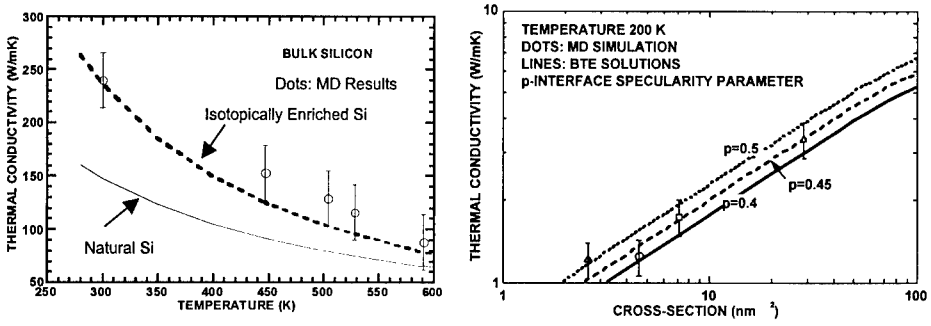

(a) (b)

Figure 10 Molecular dynamics (MD) simulation of the thermal conductivity of (a) bulk silicon and (b) silicon nanowires. Solution of the Boltzmann transport equation (BTE) for the rectangular nanowire is also given, for various values of the interface specularity parameter, p.

minimum thermal conductivity values lower than those the bulk materials. In this section, we provide a qualitative discussion of the minimum thermal conductivity of low-dimensional structures. The discussion also leads to directions for phonon engineering in low-dimensional materials to further reduce the thermal conductivity of those structures.

We start with a brief review of the key ideas behind Slack's minimum thermal conductivity theory [38]. The thermal conductivity of bulk materials can be expressed as

$$K = \frac{1}{3}\int_0^{\omega_{max}} C(\omega)v(\omega)\Lambda(\omega)d\omega \tag{3}$$

Slack argued that the minimum phonon MFP must be of the order of its wavelength and later Cahill et al. [39] further limited it to half the wavelength. For acoustic phonons, the speed of sound is used for estimating the minimum thermal conductivity and for optical phonons, the velocity is replaced with the interatomic spacing multiplied by the phonon frequency.

While the minimum thermal conductivity is very intuitive for bulk materials, it may not be valid for low-dimensional structures because those structures are highly anisotropic. From the previous discussion of phonon wave and particle transport in superlattices, we can easily accept that both the phonon group velocity and the MFP are directional-dependent quantities. We could rewrite the thermal conductivity expression to account for such directional dependences as

$$K = \frac{1}{4\pi}\int_0^{\omega_{max}}\left[\int_0^{2\pi}\sin^2\varphi d\varphi\left\langle\int_0^{\pi}C(\omega)v\ (\omega,\theta,\varphi)\Lambda(\omega,\theta,\varphi)\cos^2\theta\sin\theta d\theta\right\rangle\right]d\omega \tag{4}$$

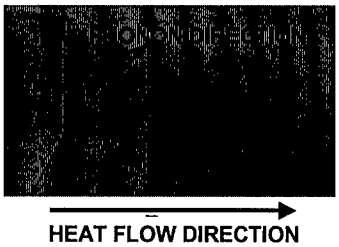

Figure 11 Coordinates used for the thermal conductivity integral, Eq. (4).

where θ and φ are the polar and azimuthal angles formed with the heat flux direction, as shown in Fig. 10. From the above equation, we can see the following alternative approaches to decrease the thermal conductivity value, which is possible through engineered low-dimensional structures.

First, the group velocity can be altered in low-dimensional structures. The formation of standing waves in nanostructures means that the group velocity becomes smaller, thus reducing the thermal conductivity. In superlattices, the bulk acoustic phonons can be changed into optical phonons, drastically reducing their group velocity.

Second, it is possible to induce anisotropic scattering in low-dimensional structures. For example, interface reflection and transmission are highly angular-dependent. As another example, the optical phonons in two materials have totally different energies. It is likely that the scattering of optical phonons at the interface will be highly directional, i.e., the optical phonons will be scattered backwards.

Third, even the specific heat of nanostructures can be changed by changing (a) the density of states and (b) the degrees of freedom in the atomic vibrations. Theoretical studies on superlattices, however, suggest that these changes are not strong except, perhaps at low temperatures [40,41].

Fourth, it is possible to change the limits of the integrals in Eq. (4). For example, in the angular integration, the phonon transmission above the critical angle is zero. Also, for the frequency integration, the phonon confinement effect may lead to a lower integration limit.

Compared to the classical way of reducing the thermal conductivity in bulk materials, the above discussion shows that low-dimensional structures leads to additional flexibility in reducing the thermal conductivity values by other means. An interesting question one could ask is whether it would be beneficial to combine the classical thermal conductivity reduction approach, i.e., through increasing the randomness of the structure, to reduce the thermal conductivity further. This approach, however, may not be the best strategy for low-dimensional thermoelectric structures. This is because most of the alternative ways listed above for reducing the thermal conductivity are based on the propagating wave characteristics of phonons, while the classical phonon-glass concept is based on phonon diffusion model, i.e., localized phonon modes.

Finally, we would like to point out that superlattice may not be the best structure 2D structure to reduce the thermal conductivity. From a wave propagating point of view, it is possible to engineer more complex multilayer structure to lower the phonon transmissivity, similar to optical multilayers.

CONCLUSIONS

In this work, we discuss heat conduction mechanisms 2D and 1D structures. Models based on both the phonon wave picture and particle picture are developed for heat conduction in 2D superlattices. The phonon wave model, based on the acoustic wave equations, includes the effects of phonon interference and tunneling, while the particle model based on the Boltzmann transport equation treats the internal as well interface scattering of phonons. For 1D systems, both the Boltzmann transport equation and molecular dynamic simulation approaches are employed. Comparing modeling results with experimental data suggest that the interface scattering of phonons plays a crucial role in the thermal conductivity of low-dimensional structures. We also discuss the minimum thermal conductivity of low-dimensional systems and suggest that the minimum thermal conductivities of low-dimensional systems differ from those of their corresponding bulk materials. There are more methods in reducing the thermal conductivity values based on low-dimensional structures and probably the best way to reduce thermal conductivity is based on the traveling properties of phonons rather than the localized diffusion modes of phonons.

ACKNOWLEDGMENTS

This work is supported by a DOD MURI program on thermoelectrics and an NSF young investigator award to G.C..

REFERENCES

[1] L. D. Hicks and M.S. Dresselhaus, Phys. Rev. B., **7**, 12727 (1993).
[2] T.C. Harman, D.L. Spears, and M.J. Manfra, J. Electron. Mat., **25**, 1121 (1996).
[3] R. Venkatasubramanian, Nav. Res. News, **XLVIII**, 31, (Four/1996).
[4] T. Yao, Appl. Phys. Lett., **51**, 1798 (1987).
[5] G. Chen, C.L. Tien, X. Wu and S. Smith, J. Heat Transf., **116**, 325 (1994).
[6] X.Y. Yu, G. Chen, A. Verma, and J.S. Smith, Appl. Phys. Lett., **67**, 3553 (1995).
[7] W.S. Capinski and H.J. Maris, Physica B, **219**, 699 (1996).
[8] S.-M. Lee, D. Cahill, and R. Venkatasubramanian, Appl. Phys. Lett., **70**, 2957 (1997).
[9] T. Borca-Tasciuc, et al., presented at this symposium.
[10] R. Venkatasubramanian, E. Siivola, and T. Colpits, ICT'98, 191 (1998).
[11] G. Chen, et al., ICT'98, 202 (1998).
[12] W.S. Capinski et al., Physica, C, in press.
[13] S.Y. Ren and J.D. Dow, Phys. Rev. B, **25**, 3755 (1982).
[14] G. Chen and C.L. Tien, J. Thermophys. & Heat Transf., **7**, 311 (1993).
[15] P. Hyldgaard and G. Mahan, in Thermal Conductivity **23**, 172 (1995).
[16] G. Chen, J. Heat Transf., **119**, 220 (1997).
[17] P. Hyldgaard and G.D. Mahan, Phys. Rev. B., **56**, 10754 (1997).
[18] G. Chen and M. Neagu, Appl. Phys. Lett., **71**, 2761 (1997).
[19] G. Chen, Phys. Rev. B, **57**, 14958 (1998).
[20] J. Jackle, Solid State Comm., **39**, 1261 (1981).
[21] M.J. Kelly, J. Phys. C.: Solid State Phys., **15**, L969 (1982).
[22] A. Greiner et al, Phy. Rev. Lett., **78**, 1114 (1997).
[23] A. Potts, M.J. Kelly et al., Superlattices and Microstructures, **9**, 315 (1991).
[24] T.S. Tighe, J.M. Worlock, and M.L. Roukes, Appl. Phys. Lett., **70**, 2687 (1997).
[25] J. Seyler and M.N. Wybourne, Phys. Rev. Lett., **9**, 1427 (1992).
[26] A.H. Nayfeh, Wave Propagation in Layered Anisotropic Media, (Elsvier, Amsterdam, 1995)
[27] W.A. Little, Can. J. Phys., **37**, 334 (1959).
[28] E.T. Swartz and R.O. Pohl, Rev. Mod. Physs, **61**, 605 (1989).
[29] R.J. Stoner and H.J. Maris, Phys. Rev. B, **48**, 16373 (1993).
[30] S. Tamura, D.C. Hurley, and J.P. Wolfe, Phys. Rev. B, **38**, 1427 (1989).
[31] C. Colvard et al., Phys. Rev. B, **31**, 2080 (1985).
[32] V. Narayanamurti et al., Phys. Rev. Lett., **43**, 2012 (1979).
[33] G. Chen, ASME Proc., HTD-Vol. 357-3, 205 (1998).
[34] B. Jusserand, Phys. Rev. B, **42**, 7256 (1990).
[35] S. Volz and G. Chen, Physica B, in press.
[36] S. Volz and G. Chen, Proc. ASME HTD-361-4, 199 (1998).
[37] W.S. Capinski et al., Appl. Phys. Lett., **71**, 2109 (1997).
[38] G.A. Slack, in Solid State Physics, **34**, 1 (1979).
[39] D.G. Cahill, S.K. Waston and R.O. Pohl, Phys. Rev. B, **46**, 6131 (1992).
[40] H. Grille, K. Karch, F. Bechstedt, Physica B, **220**, 690 (1996).
[41] R.S. Prasher and P.E. Phelan, in ASME Proc. HTD-Vol. 357-3, 195 (1998).

EXPERIMENTAL STUDY OF THE EFFECT OF THE QUANTUM WELL STRUCTURES ON THE THERMOELECTRIC FIGURE OF MERIT IN $Si/Si_{1-x}Ge_x$ SYSTEM

X. Sun[a], J. Liu[b], S. B. Cronin[a], K. L. Wang[b], G. Chen[c], T. Koga[d], M. S. Dresselhaus[e]
[a]Department of Physics, Massachusetts Institute of Technology, Cambridge, MA 02139
[b]Department of Electrical Engineering, University of California, Los Angeles, CA 90024
[c]Department of Mechanical and Aerospace Engineering, University of California, Los Angeles, CA 90024
[d]Division of Engineering and Applied Sciences, Harvard University, Cambridge, MA 02138
[e]Department of Electrical Engineering and Computer Science and Department of Physics, Massachusetts Institute of Technology, Cambridge, MA 02139

ABSTRACT

In bulk form, $Si_{1-x}Ge_x$ is a promising thermoelectric material for high temperature applications. In this paper, we report results from an experimental study as well as theoretical modeling of the quantum confinement effect on the enhancement of the thermoelectric figure of merit. $Si/Si_{1-x}Ge_x$ multiple quantum well structures are fabricated using molecular beam epitaxy (MBE) on SOI (Silicon-on-Insulator) substrates in order to eliminate substrate effects, especially on the Seebeck coefficient. A method to eliminate the influence of the buffer layer on the thermoelectric characterization is presented. An enhancement of the thermoelectric figure of merit within the quantum well over the bulk value is observed.

INTRODUCTION

It has been shown theoretically [1] that it may be possible to increase the thermoelectric figure of merit (Z) of certain materials by preparing them in the form of two-dimensional (2D) quantum-well structures. This has already been demonstrated experimentally [2] using n-type $PbTe/Pb_{1-x}Eu_xTe$ multiple-quantum-well structures grown by molecular-beam epitaxy.

In bulk form, $Si_{1-x}Ge_x$ is a promising thermoelectric material for high temperature applications [3–5], and has been used in radioactive-isotope thermoelectric generators (RTGs) on satellites and spacecraft for compositions of about $Si_{0.7}Ge_{0.3}$ operating at $\sim 1000\,K$ [6]. Because of the large amount of expertise and information available regarding the materials science of fabricating $Si/Si_{1-x}Ge_x$ quantum wells, it is an interesting system for the demonstration of both proof-of-principle and 2D thermoelectric device operation at high temperatures. By carefully designing the $Si/Si_{1-x}Ge_x$ superlattice structures, we expect this system to have sufficiently good thermoelectric performance to be interesting for possible device applications.

TWO-DIMENSIONAL THERMOELECTRICITY OF Si

The effect on Z of using materials in two-dimensional (2D) structures, such as 2D multiple-quantum-well (MQW) structures, has been studied earlier [1], and it was shown theoretically

Mat. Res. Soc. Symp. Proc. Vol. 545 © 1999 Materials Research Society

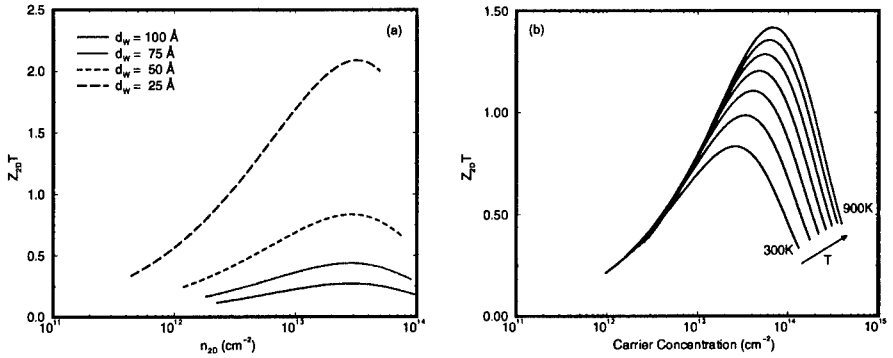

Figure 1: (a) The 2D thermoelectric figure of merit for Si/SiGe superlattices as a function of sheet carrier density for various quantum well widths at $T = 300\,\mathrm{K}$, with the specularity $p = 1$. (b) The calculated $Z_{2D}T(\zeta^*)$ versus carrier density at various temperatures (300 K, 400 K, ..., 900 K) for a 50 Å Si quantum well. The electron mobility is determined empirically as $\mu_n = 2.11 \times 10^5 T^{-1}\mathrm{cm}^2/\mathrm{Vs}$ (T in K) from data for bulk n-type Si with a carrier concentration of $10^{18}\mathrm{cm}^{-3}$, appropriate for thermoelectricity applications.

that this approach could yield a significant increase in Z over the bulk value as the quantum-well width is decreased. The proposed increase in the power factor $S^2\sigma$ arises mainly from the enhancement of the density of electron states per unit volume (near the Fermi level) that occurs for small quantum well widths. Further increase in Z is possible through the reduction of the thermal conductivity, κ, resulting from enhanced phonon scattering at the interfaces between the quantum wells and barriers [7].

Si has six electronic ellipsoids along the [100]-axes of the Brillouin zone in the silicon conduction band. Each ellipsoid is characterized by the transverse ($m_\perp = 0.19m_0$) and longitudinal ($m_\parallel = 0.92m_0$) effective mass components. When quantized along the (100) direction, the mass anisotropy (roughly 4.5:1) causes different shifts of the longitudinal and transverse subbands due to their different effective mass components.

We considered an infinite series of quantum wells and barriers in a superlattice structure with a finite height of the barrier potential. Suppose the quantization is along the z-direction, then the subband minima are determined by

$$\left(\frac{\kappa^2 - k^2}{2\kappa k}\right) \sinh \kappa d_B \sin k d_W + \cosh \kappa d_B \cos k d_W = 1 \tag{1}$$

where d_W is the width of the quantum well, m_x, m_y, and m_z are the diagonal components of the effective mass tensor, d_B is the width of the barrier layer, and $\kappa = (2m_z U/\hbar^2 - k^2)^{1/2}$, in which U is the height of the barrier potential and k is the magnitude of the wave vector. The roots $\hat{k}_n$ of Eq. (1) give the energy band structure as

$$\mathcal{E}_n(k_x, k_y) = \frac{\hbar^2 k_x^2}{2m_x} + \frac{\hbar^2 k_y^2}{2m_y} + \frac{\hbar^2 \hat{k}_n^2}{2m_z}. \tag{2}$$

Multiple band theoretical calculations of the power factor have been carried out as a function of the 2D carrier concentration for n-type Si, assuming that $d_B = 300\,\text{Å}$ and

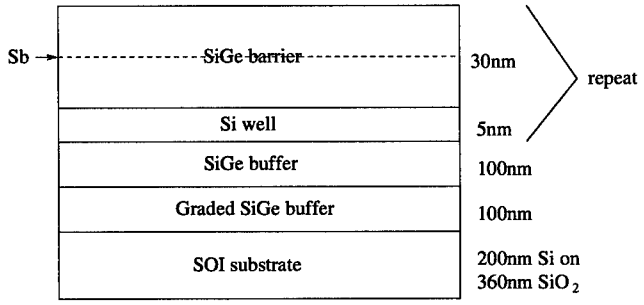

Figure 2: The structure of a set of three samples. Each period consists of a Si well and a SiGe barrier and is 35 nm wide. The three samples have 5, 10 and 15 periods, and are denoted as JL057, JL058 and JL059, respectively.

$U = 100\,\text{meV}$. For a multiple band model, the transport tensor is a linear combination of contributions from each transport subband. The overall electrical conductivity and Seebeck coefficient can then be calculated from

$$\sigma = \sum_n \sigma^{(n)}, \qquad S = \frac{\sum_n \sigma^{(n)} S^{(n)}}{\sum_n \sigma^{(n)}}. \tag{3}$$

In a simple kinetic theory for phonon transport, the lattice thermal conductivity is determined by

$$\kappa = \frac{1}{3} C v l \tag{4}$$

where C is the specific heat, v the sound velocity, and l the mean free path (MFP) for phonons. Such a treatment underestimates the MFP of those phonons that actually carry heat because (1) the optical phonons contribute to the specific heat but not much to the thermal conductivity due to their low group velocity, and (2) acoustic phonons in Si/SiGe materials have a large dispersion, so that their velocities are also smaller than the speed of sound. Therefore, we estimated the average phonon MFP theoretically by including only acoustic phonons and used an averaged phonon group velocity in Eq. (4) [8]. The interface scattering effect is also considered in the modeling of the Si/SiGe thermal conductivity. A parameter p is introduced to characterize the specularity of the interface scattering, where $p = 1$ refers to pure specular scattering, while $p = 0$ refers to pure diffusive scattering [8]. It is shown that the reduction in thermal conductivity is significant even in the case of pure specular interface scattering ($p = 1$) [9].

The calculated two-dimensional thermoelectric figure of merit for Si/SiGe superlattices as a function of sheet carrier density for different quantum well widths at room temperature is shown in Fig. 1(a). Here we see that $Z_{2D}T$ within the quantum well can reach as high as 2.0 at room temperature for a superlattice with a quantum well width of 25 Å. This makes this system very interesting even at room temperature.

Since bulk $Si/Si_{1-x}Ge_x$ is a thermoelectric material that is aimed at high temperature operation (up to 1000 K), it is interesting to investigate the thermoelectric performance of $Si_{1-x}Ge_x$ quantum well systems at elevated temperatures. Since the power factor for $Si_{1-x}Ge_x$ materials generally increases with increasing T above room temperature, the power

Table 1: Hall measurements of samples JL057-JL059 at room temperature.

Sample	JL057	JL058	JL059
# of periods	5	10	15
Mobility (cm^2/Vs)	405.5	689.1	640.8
Sheet carrier density (cm^{-2})	2.5×10^{13}	5.17×10^{13}	1.04×10^{14}
Sheet carrier density per period (cm^{-2})	5.0×10^{12}	5.17×10^{12}	6.9×10^{12}

factor as well as the thermoelectric figure of merit for $Si_{1-x}Ge_x$ quantum wells is expected to increase as T is increased above 300 K. By carefully considering the behavior of the carrier mobility as a function of temperature [7], we calculated the two-dimensional thermoelectric figure of merit as a function of quantum well width at elevated temperatures, as shown in Fig. 1(b). These results indicate that $Z_{2D}T$ for $Si/Si_{1-x}Ge_x$ quantum wells is quite favorable at higher temperatures.

EXPERIMENTAL STUDIES

Si with low electrical conductivity has a very high Seebeck coefficient. It is therefore expected that the Si substrate as well as the buffer layer, which is essential to get the relaxed type-II superlattice, might contribute to the transport measurements, especially to the Seebeck coefficient measurement. Therefore, it is necessary to eliminate the contributions of the substrate and buffer layer to the measured transport coefficients, in order to make reliable measurements on superlattice samples. To eliminate the substrate contribution, we make use of Silicon-on-Insulator (SOI) substrates. In order to characterize the contributions to the measurements from the buffer layer, we grow a series of samples with the same structure, but with different numbers of periods. Three similar superlattice samples with 5 periods, 10 periods and 15 periods, respectively, were fabricated. Their structures are shown in Fig. 2, and are denoted as JL057, JL058 and JL059, respectively.

These samples were grown continuously, one after the other, using a solid source MBE system. Firstly, SOI wafers with 200 nm Si on top of 360 nm SiO_2 were used as substrates. After a standard Shiraki cleaning procedure, the substrates were immediately introduced into the MBE chamber. The protective oxide layer was removed by subsequently heating the substrates at 930 °C for 15 minutes. The growth temperature was kept at 550 °C except that the δn doping layers (Sb) were grown at 350 °C. The growth rate for Si and Ge were monitored and controlled by a Sentinel III Deposition controller. With these conditions, 100 nm of an undoped $Si_{1-x}Ge_x$ layer with x varying from 0 to 0.3 was grown first, on top of which a 100 nm layer of $Si_{0.7}Ge_{0.3}$ was grown, yielding a buffer layer with an overall thickness of 200 nm. Hall measurements (Table 1) show that these samples have a very similar sheet carrier density per period, which is essential to validate Eq. (5) that will be discussed below.

The Seebeck coefficients for samples JL057, JL058 and JL059 are measured with high precision at room temperature, as shown in Fig. 3(a)–(c). Least mean squared linear regressions are performed on the ΔV-ΔT data to get the slopes for the Seebeck coefficients. The small offsets in the measurements suggest that we have achieved high quality electrical and thermal contacts in our measurements.

A simple calculation considering the contribution from both the buffer layer and the

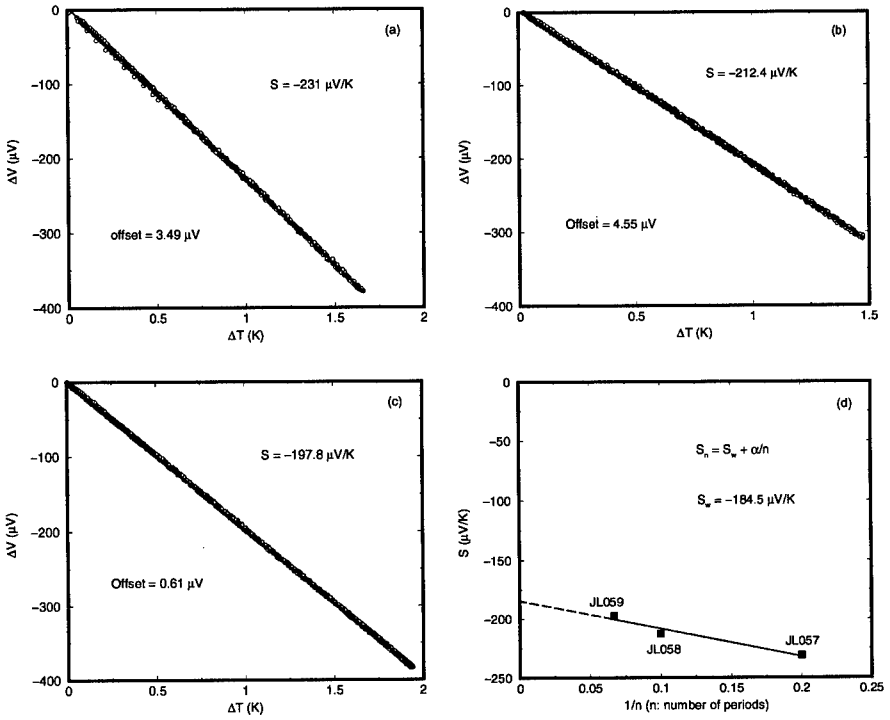

Figure 3: The Seebeck coefficients for samples JL057, JL058 and JL059 are measured with high precision at room temperature, as shown in (a), (b) and (c), respectively. The measured Seebeck coefficient at room temperature as a function of $1/n$, where n is the number of periods in each sample, is shown in (d). The Seebeck coefficient for the quantum well S_w is extrapolated to the limit $1/n \to 0$, or $n \to \infty$.

lattice to the Seebeck coefficient measurement shows that

$$S_n = S_w + \frac{R_w S_b}{R_b}\left(\frac{1}{n}\right), \tag{5}$$

where S_n is the measured Seebeck coefficient for a sample with n periods, S_w and S_b are the Seebeck coefficients for the quantum well and buffer regions, respectively, and R_w and R_b are resistances for the quantum well and buffer regions, respectively. Though R_b is very large compared to R_w, S_b is also very large due the low carrier density in the buffer layer. Therefore, the contribution of the second term could be significant. Figure 3(d) shows the room temperature results for samples JL057-JL059, and the Seebeck coefficient for the quantum well is extrapolated by setting $1/n \to 0$, or $n \to \infty$, whereas successfully eliminated the contribution from the buffer layer.

The power factor $(S^2\sigma)$ at room temperature for this set of samples is found to be $45\,\mu\mathrm{W/cmK^2}$, resulting in a two-dimensional thermoeletric figure of merit at 300 K of value

0.14, using the calculated value for the thermal conductivity, 9.64 W/mK, from our model as described above. Although this is a significant enhancement over the Si bulk value [7], we expect better performance if better carrier mobility (see Table 1) can be achieved by improving the interface quality.

CONCLUSIONS

Theoretical modeling of the thermoelectric figure of merit for $Si/Si_{1-x}Ge_x$ quantum well structures suggests that an increase in the thermoelectric figure of merit over bulk values in the $Si/Si_{1-x}Ge_x$ quantum well system should be possible. Further enhancement in $Z_{2D}T$ for $Si/Si_{1-x}Ge_x$ quantum well structures is expected at elevated temperatures through both quantum confinement and phonon interface scattering effects. $Si/Si_{1-x}Ge_x$ multiple quantum well structures are fabricated using the MBE technique, and the thermoelectric properties are successfully measured for a single period, after eliminating the contributions from the substrate and the buffer layer. An enhancement of the thermoelectric figure of merit in the quantum well over the bulk value in Si at 300 K is observed.

ACKNOWLEDGMENTS

The authors thank Drs. G. Dresselhaus, T. C. Harman and C. B. Vining for valuable discussions. The authors gratefully acknowledge support by the US Navy under Contract No. N00167-98-K-0024 (MIT), by the ONR MURI subcontract #0205-G-7A114-01, and by the Honda Motor Corporation.

REFERENCES

[1] L. D. Hicks and M. S. Dresselhaus, Phys. Rev. B **47**, 12727 (1993).

[2] Lyndon D. Hicks, PhD thesis, Massachusetts Institute of Technology, 1996.

[3] G. A. Slack and M. A. Hussain, J. Appl. Phys. **70**(5), 2694 (1991).

[4] C. B. Vining, in *CRC Handbook of Thermoelectrics*, edited by D. M. Rowe (CRC Press, New York, 1995) p. 329.

[5] G. D. Mahan, in *Solid State Physics*, edited by H. Ehrenreich and F. Spaepen, (Academic Press, 1997) p. 82.

[6] C. Wood, Rep. Prog. Phys. **51**, 459 (1988).

[7] X. Sun, M. S. Dresselhaus, K. L. Wang, and M. O. Tanner, in *Thermoelectric Materials - New Directions and Approaches*, edited by T. M. Tritt, M. G. Kanatzidis, H. B. Lyon, Jr., and G. D. Mahan (Mater. Res. Soc. Proc. **478**, Pittsburgh, PA, 1997) pp. 169–174,

[8] G. Chen, J. Heat Transfer **119**, 220 (1997).

[9] X. Sun, M. S. Dresselhaus, G. Ghen, and K. L. Wang, presented at the APS 1998 March Meeting, Los Angeles, CA, 1998.

CARRIER POCKET ENGINEERING TO DESIGN SUPERIOR THERMOELECTRIC MATERIALS USING GaAs/AlAs SUPERLATTICES

T. Koga*, X. Sun*, S. B. Cronin*, and M. S. Dresselhaus*,**
*Division of Engineering and Applied Sciences, Harvard University, Cambridge, MA 02138
*Department of Physics and **Department of Electrical Engineering and Computer Science, Massachusetts Institute of Technology, Cambridge, MA 02139

ABSTRACT

A large enhancement in the thermoelectric figure of merit for the whole superlattice, $Z_{3D}T$, is predicted for short period GaAs/AlAs superlattices relative to bulk GaAs. Various superlattice parameters (superlattice growth direction, superlattice period and layer thicknesses) are explored to optimize $Z_{3D}T$, including quantum wells formed at various high symmetry points in the Brillouin zone. The highest room temperature $Z_{3D}T$ obtained in the present calculation is 0.41 at the optimum carrier concentration for either (001) or (111) oriented GaAs(20 Å)/AlAs(20 Å) superlattices, which is about 50 times greater than the corresponding ZT for bulk GaAs obtained using the same basic model.

INTRODUCTION

There have been an increasing number of studies on the enhanced thermoelectric figure of merit Z ($= S^2\sigma/\kappa$), where S is the Seebeck coefficient, σ is the electrical conductivity, and κ is the thermal conductivity, for a material in the form of a multiple-quantum-well (MQW) structure or superlattice [1-9]. The most popular approach to enhance the figure of merit within the quantum wells, denoted by Z_{2D} [1-3], is to utilize the quantum confinement effect (to enhance S) and the boundary scattering of phonons at the barrier-well interfaces (to reduce κ_{ph}, where κ_{ph} is the lattice thermal conductivity). Recently, experiments on superlattices which do not explicitly make use of the quantum confinement effect have been carried out and show promise for enhancing ZT for the whole superlattice, denoted by $Z_{3D}T$ [8, 9].

In this report, we consider the case of a superlattice in which both the well and barrier regions contribute to S and the interfaces between the wells and barriers preferentially reduce κ relative to σ. First, we consider the case where only the Γ-point subband is important for the transport properties in GaAs/AlAs. In this case, the extension from the 2D quantum well approach is straightforward. Second, we present the idea of carrier pocket engineering, where both the quantum well and the barrier layers contribute to S. To make this concept work, we need all the Γ, X and L subbands in the GaAs/AlAs superlattices to have about the same energy. This is possible, since the Γ point band has a light mass and the quantum well and barrier widths can each be chosen appropriately. We emphasize that the calculations shown here pertain to the 3D figure of merit of the superlattices, denoted by $Z_{3D}T$, not to the 2D figure of merit $Z_{2D}T$, as was discussed previously [1-3].

CALCULATION

The calculation of the energy dispersion relations along the superlattice axis (z axis) was carried out at each high symmetry point (Γ, X, and L points) in the Brillouin zone

Mat. Res. Soc. Symp. Proc. Vol. 545 ©1999 Materials Research Society

using a plane wave approximation with an appropriate boundary condition (Krönig-Penney model) [11]. Requiring that the particle current be conserved at the GaAs/AlAs interfaces, we have the boundary condition, $\Psi_{\rm GaAs} = \Psi_{\rm AlAs}$ and $m^{-1}_{z({\rm GaAs})}\, d\Psi_{\rm GaAs}/dz = m^{-1}_{z({\rm AlAs})}\, d\Psi_{\rm AlAs}/dz$, where $\Psi_{\rm GaAs}$ and $\Psi_{\rm AlAs}$ denote the electron wavefunction in the GaAs and AlAs layers, respectively, and $m_{z({\rm GaAs})}$ and $m_{z({\rm AlAs})}$ are the z components of the effective mass tensor for GaAs and AlAs, respectively. The conduction band offsets at each symmetry point are calculated using the experimentally determined $\Delta E_c/\Delta E_g = 0.68$, where ΔE_c is the conduction band offset at the Γ point, and ΔE_g is the difference in the direct energy band gap at the Γ point between GaAs and AlAs [12]. The in-plane components of the effective mass tensor are calculated by projecting the 3D constant energy surface for the well material on to the plane of the quantum wells. It is noted that, for the band offsets calculated in this way, the Γ and L point quantum wells are formed within the GaAs layers and the X point quantum wells are formed within the AlAs layers [10] (see Fig. 1), so that we can effectively separate the carriers in different carrier pockets in real space to minimize the inter-valley scattering, which is also favorable for achieving high Z. The band parameters used in the present calculation for GaAs/AlAs superlattices are tabulated in Ref. [4].

The transport coefficients for the whole superlattice are calculated using the following equations [14]:

$$\sigma = \mathbf{L}^{(0)}, \quad \mathbf{S} = -\left(\frac{1}{eT}\right)(\mathbf{L}^{(0)})^{-1}\mathbf{L}^{(1)}, \quad \kappa_e = \left(\frac{1}{e^2T}\right)(\mathbf{L}^{(2)} - \mathbf{L}^{(1)}(\mathbf{L}^{(0)})^{-1}\mathbf{L}^{(1)}) \tag{1}$$

where κ_e is the electronic contribution to the thermal conductivity, and the $\mathbf{L}^{(\alpha)}$s for the case of a 2D quantum well are given by,

$$\mathbf{L}^{(\alpha)}_{\rm 2D}(\zeta) = e^2 \int \frac{d\mathbf{k}}{2\pi^2 d_W}\left(-\frac{\partial f}{\partial \varepsilon}\right)\tau\,(\mathbf{k})\,\mathbf{v}\,(\mathbf{k})\mathbf{v}\,(\mathbf{k})\,(\varepsilon\,(\mathbf{k}) - \zeta)^{\alpha}\,, \tag{2}$$

where d_W is the quantum well thickness and ζ is the chemical potential. Assuming only the lowest subband in the quantum well, the xx components of the $\mathbf{L}^{(\alpha)}_{\rm 2D}$s are evaluated in terms of the Fermi-Dirac related integrals in Ref. [3].

For superlattice samples which have some energy dispersion along the z axis, we use the following equation to calculate the $\mathbf{L}^{(\alpha)}$s

$$\mathbf{L}^{(\alpha)}_{\rm SL}(\zeta) = \rho^{-1}_{\rm 2D} \int \mathbf{L}^{(\alpha)}_{\rm (2D)}(\zeta - \varepsilon)\frac{\partial \rho(\varepsilon)}{\partial \varepsilon} d\varepsilon, \tag{3}$$

where $\rho(\varepsilon)$ is the density of states as a function of energy for the whole superlattice for the pertinent subband and $\rho_{\rm 2D}$ is the density of states for the pertinent quantum well if it had only a single subband and no band broadening ($\rho_{\rm 2D} = (m_{t({\rm 2D})}m_{l({\rm 2D})})^{\frac{1}{2}}/\pi d_W \hbar^2$). The $\mathbf{L}^{(\alpha)}_{\rm SL}$ functions for the whole superlattice are calculated by summing the $\mathbf{L}^{(\alpha)}_{\rm SL}$s over all subbands, evaluated separately.

Γ Point Superlattice

We first show the result of the calculation for the Γ point superlattices. Shown in Fig. 2(a) is the calculated density of states for the Γ point subband for the GaAs/AlAs superlattices with equal thicknesses for the GaAs and AlAs layers. We find that the density of states near the band edge increases appreciably as the superlattice period ($d_{\rm GaAs} + d_{\rm AlAs}$) decreases from 160 Å to 40 Å. It is noted that the broadening of the Γ point subband becomes appreciable

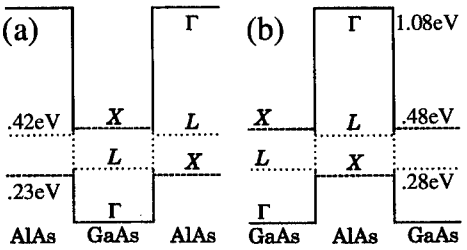

Figure 1: Barriers and wells in GaAs/AlAs, showing the three lowest conduction bands. (a) Γ and L point quantum wells are formed within the GaAs layers. (b) X point quantum wells are formed within the AlAs layers. Pictures are taken from Ref. [10].

below $d_{GaAs} = 20$ Å so that the Seebeck coefficient for a given carrier concentration actually decreases with decreasing d_{GaAs} below $d_{GaAs} = 20$ Å, as shown in the inset of Fig. 2(a) for $n = 10^{18}$ cm^{-3}.

Detailed modeling for the lattice thermal conductivity has been carried out elsewhere for a GaAs/AlAs superlattice, where the thickness of the GaAs layer is equal to that of the AlAs layer [15]. Briefly, we find that the lattice thermal conductivity (κ_{ph}) for superlattices with $d_W = d_B$ is reduced from the value for bulk GaAs (440 mW/cm·K) to a value of 170 mW/cm·K for the (100 Å/100 Å) superlattice (reduction by a factor of 2.6 relative to the value for bulk GaAs), where we express the GaAs and AlAs layer thicknesses d in terms of (d_{GaAs}/d_{AlAs}), and κ_{ph} is further reduced to 73 mW/cm·K for the (20 Å/20 Å) superlattice (factor of 6 reduction relative to bulk GaAs) at room temperature.

With these data for κ_{ph} as a function of d_W, the models for other transport coefficients (Eq. 1) are combined to calculate the ZT for the whole superlattice. Values of $U_0 = 1$ eV and $\mu = 3000$ cm^2/V·s were taken for the band offset energy and the carrier mobility, respectively, for the GaAs/AlAs Γ-point superlattice. The results thus obtained for $Z_{3D}T$ normalized to the bulk $(ZT)_{bulk}$ value are shown in Fig. 2(b) as a function of d_W. It is noted that $(ZT)_{bulk}$ for bulk GaAs is as small as 0.0085 at the optimum carrier concentration, whereas $Z_{3D}T$ for the (20 Å/20 Å) Γ point superlattice is more than 0.1 at the optimum carrier concentration (see Fig. 4), which is more than a ten times enhancement in $Z_{3D}T$ relative to the value for bulk GaAs. It is noted that, although it is not legitimate to assume that only the Γ point subband is occupied in GaAs/AlAs superlattices, since the location of the lowest-lying subband in the GaAs/AlAs superlattice Brillouin zone depends on the GaAs and AlAs layer thicknesses as we discuss below, the assumption that only the Γ point subband is occupied is valid for most GaAs/$Al_{1-x}Ga_xAs$ superlattices that have been fabricated until now with low carrier concentrations ($<10^{18}$ cm^{-3}).

Carrier Pocket Engineering

Shown in Fig. 3 are the calculated subband band edge energies for various subbands in (001) (a) and (111) (b) oriented GaAs/AlAs superlattices for the superlattice period ($d_{GaAs} + d_{AlAs}$) = 40 Å. The orientations of the superlattices are thus chosen, since these are the two orientations where we can minimize the energy splitting of the degenerate subbands. By making a superlattice in the (001) orientation, the three equivalent pockets at the X point in the Brillouin zone have an energy splitting between one longitudinal and two transverse pockets, whereas the four equivalent L pockets in the bulk form remain degenerate in the (001) oriented superlattices (see Fig. 3(a)). We denote the resulting split X subbands in the superlattice as the longitudinal (X_l) and transverse (X_t) subbands, respectively. Similarly, for the (111) oriented superlattices, the four equivalent L pockets in the Brillouin zone have

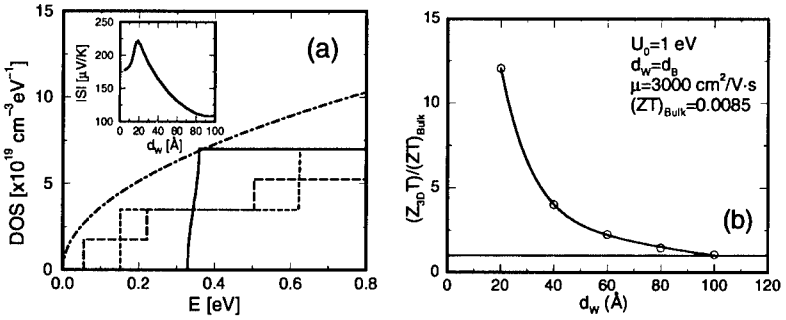

Figure 2: (a) Density of states for equal thickness ($d_W = d_B$) GaAs/AlAs Γ point superlattices as well as for bulk GaAs (dash-dotted line). The quantum well thickness is chosen to be 20 (solid line), 40 (short dashed line), and 80 (long dashed line) Å. In the inset, the calculated Seebeck coefficient is plotted as a function of d_W for a given carrier concentration $n = 10^{18}$ cm^{-3}. (b) Plot of $Z_{3D}T$ for various GaAs/AlAs superlattices with $d_W = d_B$ at optimum doping concentration and at $T = 300$ K, normalized to that of bulk GaAs, using values of $U_0 = 1$ eV and $\mu = 3000$ cm^2/V·s for the band offset and electron mobility, respectively.

an energy splitting between one longitudinal (L_l) and three oblique (L_o) pockets. The X pockets, however, remain degenerate after making a superlattice in the (111) orientation (see Fig. 3(b)).

We find that the Γ, X and L subbands all lie very close in energy for the (20 Å/20 Å) superlattice in either the (001) or (111) orientations. Therefore, the (20 Å/20 Å) superlattices are expected to be close to the optimum structure for thermoelectric applications. Shown in Fig. 4 are the calculated $Z_{3D}T$ as a function of carrier concentration for various superlattice structures and orientations. It is noted that the solid line in the figure denotes the results of the Γ point superlattice discussed in the previous subsection for the (20 Å/20 Å) structure. We find that the highest $Z_{3D}T \sim 0.41$ is obtained for an (001) oriented (20 Å/20 Å) superlattice for a carrier density of $\sim 5\times10^{19}$ cm^{-3}. A similar value of $Z_{3D}T$ is also obtained for a (111) oriented (20 Å/20 Å) superlattice at a similar carrier concentration. The major difference in the calculated $Z_{3D}T$ between the (001) oriented and the (111) oriented (20 Å/20 Å) superlattices is their values at lower carrier concentrations ($<5\times10^{18}$ cm^{-3}). We find larger values of $Z_{3D}T$ for the (111) oriented superlattice than those for the (001) oriented superlattice for these lower carrier concentrations. This is because the lowest lying subband for the (001) oriented superlattice is an X_l subband, which has a very small mobility (180 cm^2/Vs), whereas the lowest lying subband for the (111) oriented superlattice is an L_l subband which has a relatively high mobility (950 cm^2/Vs). In calculating $Z_{3D}T$ we used the same value for κ_{ph} (7.3 Wm^{-1}K^{-1}) for both the (001) and (111) oriented superlattices (20 Å/20 Å). We also plot the calculated $Z_{3D}T$ values for the (001) oriented (30 Å/20 Å) and (20 Å/30 Å) superlattices for comparison, as shown in Fig. 4, to show that the (20 Å/ 20 Å) structures are indeed close to the optimum structures for getting a high $Z_{3D}T$ [4].

CONCLUSIONS

In summary, we have calculated the thermoelectric figure of merit $Z_{3D}T$ for various GaAs/AlAs superlattices. It is found that $Z_{3D}T$ for the Γ-point superlattice could be more

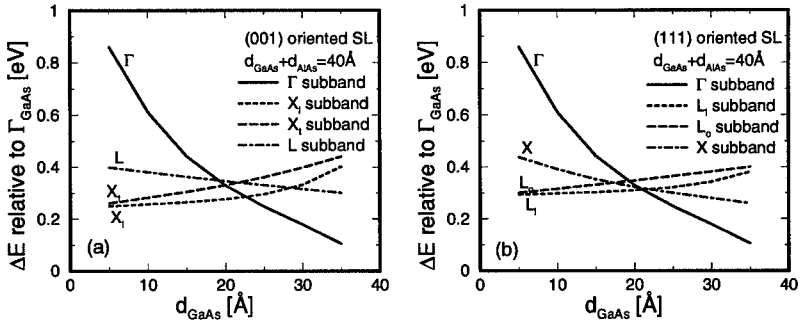

Figure 3: Subband band edge energies measured from the Γ-point energy for bulk GaAs, for (a) (001) and (b) (111) oriented GaAs/AlAs superlattices for the superlattice period ($d_{\mathrm{GaAs}}+d_{\mathrm{AlAs}}$) = 40 Å. It is noted that the X point quantum well is formed within the AlAs layers, whereas the Γ and L point quantum wells are formed within the GaAs layers. In the figure, subscripts l, t and o denote the orientation of the pertinent carrier pockets: *l*ongitudinal, *t*ransverse, and *o*blique orientations, respectively, relative to the superlattice growth direction.

Figure 4: Estimated $Z_{3D}T$ as a function of carrier concentration for a (001) oriented (20 Å/20 Å) superlattice (dotted line), (001) oriented (30 Å/20 Å) superlattice (short dashed line), (001) oriented (20 Å/30 Å) superlattice (long dashed line), and (111) oriented (20 Å/20 Å) superlattice (long dash-short dash line). The solid line denotes $Z_{3D}T$ calculated assuming only carriers in the Γ-point subband for a (20 Å/20 Å) superlattice.

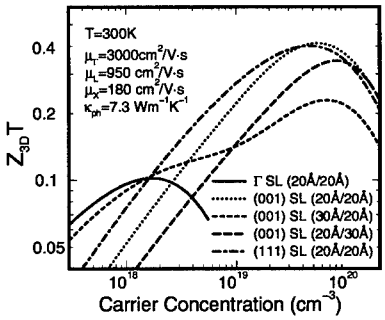

than ten times as high as that for bulk GaAs. We have also studied the contributions from the other quantum wells, formed at the X and L points in the Brillouin zone, to the total transport coefficients. We have explored various superlattice parameters, such as the superlattice period, layer thicknesses and the superlattice growth direction, to optimize the thermoelectric figure of merit. A value of $Z_{3D}T \sim 0.41$ is predicted at room temperature for either (001) or (111) oriented superlattices under heavy doping conditions ($\sim 5 \times 10^{19}$ cm^{-3}), whereas $Z_{3D}T \sim 0.2$ is expected at moderate carrier concentrations ($\sim 5 \times 10^{18}$ cm^{-3}) for a (111) oriented (20 Å/20 Å) superlattice, still much greater than the ZTs for bulk GaAs ($ZT \sim 0.0085$) or for the Γ-point superlattice ($Z_{3D}T \sim 0.1$) at 300 K obtained using the same basic models. The concept of carrier pocket engineering can be extended to other superlattice systems with a possibility of getting even higher $Z_{3D}T$ by finding a better combination of well and barrier materials.

ACKNOWLEDGMENTS

The authors would like to thank Drs. G. Chen and G. Dresselhaus for valuable discussions and inputs. The authors gratefully acknowledge support from the Honda Corporation and from ONR under MURI subcontract #205-G-7A114-01 with UCLA.

REFERENCES

[1] L. D. Hicks and M. S. Dresselhaus, Phys. Rev. B **47**, 12727 (1993); L. D. Hicks and M. S. Dresselhaus, Phys. Rev. B **47**, 16631 (1993);

[2] L. D. Hicks, T. C. Harman, X. Sun, and M. S. Dresselhaus, Phys. Rev. B **53**, R10493 (1996); T. C. Harman, D. L. Spears, and M. J. Manfra, J. Electron. Mater. **25**, 1121 (1996); T. C. Harman, D. L. Spears, D. R. Calawa, S. H. Groves, and M. P. Walsh, Proceedings for 16th International Conference on Thermoelectrics page 416 (1997).

[3] Lyndon D. Hicks. *The effect of quantum-well superlattices on the thermo-electric figure of merit.* PhD thesis, Massachusetts Institute of Technology, June 1996. Department of Physics.

[4] T. Koga, X. Sun, S. B. Cronin and M. S. Dresselhaus, Appl. Phys. Lett. **73**, 2950 (1998), and references therein.

[5] J. O. Sofo and G. D. Mahan, Appl. Phys. Lett. **65**, 2690 (1994).

[6] D. A. Broido and T. L. Reinecke, Appl. Phys. Lett. **67**, 100 (1995); D. A. Broido and T. L. Reinecke, Appl. Phys. Lett. **67**, 1170 (1995); P. J. Lin-Chung and T. L. Reinecke, Phys. Rev. B **51**, 13244 (1995); D. L. Broido and T. L. Reinecke, Phys. Rev. B **51**, 13797 (1995); D. A. Broido and T. L. Reinecke, Appl. Phys. Lett. **70**, 2834 (1997);

[7] D. M. Rowe and G. Min, Proceedings for 13th International Conference on Thermoelectrics page 339 (1994); Y. Nishio and T. Hirano, Jpn. J. Appl. Phys., Part 1 **36**, 170 (1997).

[8] R. Venkatasubramanian, T. Colpitts, E. Watko, M. Lamvik, and N. El-Masry, Journal of Crystal Growth **170**, 817 (1997).

[9] T. C. Harman, D. L.Spears, and M. P. Walsh, Abstract for the 40th Electronic Materials Conf., Charlottesville, J. Electron. Mater. Lett. **27**, No. 7, 44 (1998); T. C. Harman, D. L.Spears, and M. P. Walsh, J. Electron. Mater. Lett. **28**, L1 (1999).

[10] J. H. Davies, *The Physics of Low-Dimensional Semiconductors* (Cambridge University Press, New York, 1998).p.91.

[11] C. Kittel, *Introduction to Solid State Physics 7th edition* (John Wiley & Sons, Inc., New York, 1996).p.180.

[12] S. Adachi, J. Appl. Phys. **58**, R1 (1985).

[13] Landolt-Bornstein. *Numerical Data and Functional Relationships in Science and Technology.* New Series. Vol. 22a (Springer-Verlag, Berlin, 1987).

[14] N. W. Ashcroft and N. D. Mermin, *Solid State Physics* (W. B Saunders Company, Philadelphia, 1976). chapters 12, 13.

[15] Gang Chen, Trans. ASME, J. Heat Trans. **119**, 220 (1997).

SUBSTITUTIONAL EFFECTS ON THE THERMOELECTRIC PROPERTIES OF TRANSITION METAL PENTATELLURIDES

R. T. Littleton IV[1], J. W. Kolis[1,2], C. R. Feger[2], and Terry M. Tritt[1,3]

1 Materials Science and Engineering Department
2 Department of Chemistry
3 Department of Physics and Astronomy
Clemson University, Clemson, SC 29634 USA

Abstract:

The thermoelectric properties (resistivity and thermopower) of single crystals of the low-dimensional pentatelluride materials, $HfTe_5$ and $ZrTe_5$, have been measured as a function of temperature from 10K < T < 320K. Both parent materials exhibit a resistive transition peak, $T_p \approx 80K$ for $HfTe_5$ and $T_p \approx 145K$ for $ZrTe_5$. Each display a large positive (p-type) thermopower ($\alpha \geq +125\mu V/K$) around room temperature, which undergoes a change to a large negative (n-type) thermopower ($\alpha \leq -125\mu V/K$) below the peak temperature. The magnitude of this resistive anomaly is typically 3-7 times the room temperature value of ≈ 1 mΩ•cm. Through isoelectronic substitution of Zr for Hf ($Hf_{1-X}Zr_XTe_5$), a systematic shift is observed in T_p as the Zr concentration increases. Small Ti substitution for Hf and Zr affects the electronic properties strongly, producing a substantial reduction in T_p for either parent compound. However, the large values of thermopower and the magnitude of the resistive peak remain essentially unchanged. Substitutions of Se or Sb on the Te sites greatly affects the electronic behavior of the parent materials. Se doping increases the thermopower values by ≈20% while decreasing the resistivity by as much as 25%. These effects double the power factor, $\alpha^2\sigma T$, of the parent materials. Small Sb substitutions appear to completely suppress the resistive anomaly. These features in the resistivity and thermopower signal a large degree of tunability in the temperature range of operation. The potential of these materials as candidates for low temperature thermoelectric applications will be discussed.

Introduction:

Bi_2Te_3 and $Si_{1-X}Ge_X$ systems have been extensively researched and optimized for their use in thermoelectric refrigeration (where the optimum temperature, T_{OPT}, $T_{OPT} \approx$ 320K for Bi_2Te_3) and power generation applications ($T_{OPT} \approx 1000K$ for $Si_{1-X}Ge_X$)[1-3]. There still remains substantial room for improvement despite the thorough and comprehensive investigation of the traditional thermoelectric, TE, materials. Renewed interests[4] in the investigation of new and significantly more efficient TE materials has been driven by the need for much higher performance as well as new temperature regimes for TE devices in many applications. There are continuously expanding needs for lower temperature (T < 250K) TE materials. Lower temperature thermoelectric cooling packaging for HgCdTe infrared detectors could provide increased sensitivity and faster response than current technology.[5] TE materials operating at lower temperature regimes are also

Mat. Res. Soc. Symp. Proc. Vol. 545 © 1999 Materials Research Society

significant to "cryoelectronics" and "cold computing". Electronic component cooling is the fundamental limit to cold computing system performance.[6] Reliable-low-maintenance cooling and refrigeration technology limit cellular phone communications technology that employ superconducting narrow-band spectrum dividers to increase frequency band utilization.

Thermoelectric materials transfer heat via the Peltier effect when subjected to an electric current which in turn produces a temperature gradient. Heat is absorbed on the cold side and rejected at the sink, thus providing a refrigeration capability. An imposed ΔT will act conversely and result in a voltage or current, i.e. small scale power generation.[7] Potential thermoelectric materials need to possess a high dimensionless figure of merit, ZT, in which $ZT = \alpha^2\sigma T/\lambda$, where α is the Seebeck coefficient, σ is the electrical conductivity, T is the temperature in K, and λ is the total thermal conductivity ($\lambda = \lambda_L + \lambda_E$; the lattice and electronic contributions respectively). Materials of both n-type (negative thermopower) and p-type (positive thermopower) are necessary if a thermoelectric device is to be fabricated with the highest efficiency. The current state of the art materials typically possess a $ZT \approx 1$ at their peak application or operating temperature.

Many new classes of compounds and new synthetic techniques are being investigated as next generation thermoelectrics with some of these showing promising results, however at this time, only at temperatures well above room temperature.[8-15] The most promising materials for thermoelectric applications have been semiconductors with carrier densities, *n*, in the range of 10^{19} carriers/cm^3. In most materials, at temperatures far from a phase transition, the electrical conductivity and thermopower are related to the electron density of states near the Fermi energy $g(E_F)$. The conductivity is proportional to $g(E_F)$ while α is proportional to $(1/g)dg(E)/dE$ at $E=E_F$. Hence, as *n* (or g) is increased, σ typically increases while α decreases. These relationships create a mechanism for optimizing the thermoelectric properties through doping in order to tune the number of carriers. In this scheme, high mobility carries are especially desirable so that σ can be largest at a given carrier density.

In metallic-like systems, the thermopower typically decreases as the temperature decreases, i. e. the Mott diffusion thermopower. Semiconducting materials exhibit a thermopower that is proportional to 1/T (as well as a temperature activated conductivity), with eventually a zero thermopower at the lowest temperatures. One of the important issues relative to low temperature thermoelectric materials is mechanisms which can give high thermopower at low temperatures. A number of systems that are candidates for low temperature thermoelectric materials are heavy fermion materials, Kondo systems, as well as quasi-one-dimensional materials. Low dimensional systems are known to be susceptible to van Hove singularities (or cusps) in their density of states, electronic phase transitions, and exotic transport properties which can add structure in g(E) near E_F. Doping can produce very substantial effects in these types of materials and can drastically change their electronic transport. Quantum well systems take advantage of a low dimensional character through physical confinement in thin film structures to enhance the electronic properties of a given material.[8]

Transition Metal Pentatellurides:

This investigation centers around a very interesting class of quasi-1-D conductors known as transition metal pentatellurides, $HfTe_5$ and $ZrTe_5$. Resistivity and thermopower data are shown in Figure 1, for the undoped $HfTe_5$ and $ZrTe_5$, respectively, as a function of temperature. Several aspects of the electrical transport properties of these materials, specifically in relation to the broad resistive peak, were studied in the early 1980's, albeit not in relation to the materials' properties for applications in thermoelectrics.[16-23] Early data suggested a possible charge density wave (CDW) peak but no evidence of a CDW transition or SDW behavior was found. DiSalvo et. al.[17] performed Zr and Ta substitution for Hf in the $HfTe_5$ material and found the doping and substitutions substantially change the peak temperature, while also affecting the magnitude of the resistivity of these materials. This indicated that the transition appears most likely electronic in origin. The thermopower was not reported in that study. An investigation by Jones et. al.[16] found that the magnitude of the thermopower was highly sample dependent, probably due to small amounts of trace impurities or differences in growth conditions.

Single crystals of both the undoped and doped materials were grown in similar conditions to previously reported methods.[24] A stoichiometric ratio of the materials were sealed in a fused silica tubing with iodine ($\approx$ 5 mg/mL) and placed in a tube furnace. Initial materials were at the center of the furnace and the other end of the reaction vessel near the furnace to provide a temperature gradient. Crystals of the materials were obtained in excess of 1.5 mm long and 100 μm in diameter with the preferred direction of growth along the *a* axis, as determined by face indexing. These are long chain systems with an orthorhombic crystal structure.[25] They exhibit slightly anisotropic transport properties with the high conductivity axis along the growth axis (*a* axis). Electrical contact was made using Au wires bonded to the crystal with Au paint.

As illustrated in Figure 1, the resistivity for $HfTe_5$ gradually decreases and then sharply rises as the temperature is decreased from room temperature, exhibiting a peak at around $T_P \approx 75K$ after which the resistivity falls rapidly as the temperature is further reduced. The resistivity at the peak is approximately six times the resistivity at room temperature. The $ZrTe_5$ material behaves in a similar manner except that the peak occurs at a higher temperature, $T_P \approx 145K$ with a magnitude three times larger than its room temperature resistivity.[26] The room temperature electrical conductivity of these materials is $1.4(m\Omega \cdot cm)^{-1}$ for $HfTe_5$ and $1.5(m\Omega \cdot cm)^{-1}$ for $ZrTe_5$ which is comparable to the best known thermoelectric materials.

The thermopower of these materials also shows behavior indicative of their potential for thermoelectric use (Figure 1). At high temperatures ($T >> T_p$) pentatellurides display a large positive (p-type) thermopower, > +125 μV/K. Near T_p, the thermopower undergoes a dramatic change, passing through zero before reaching a negative (n-type) peak < -125 μV/K. Thus, these materials exhibit thermopower that is relatively large over a broad temperature range and can have either sign: exhibiting n-type ($T < T_p$) and p-type ($T > T_p$). These materials, therefore, show promise for future studies in relation to their low-temperature thermoelectric properties.

Isoelectronic Substitutions on the Transition Metal Site

Resistivity and thermopower measurements performed on single crystals of $Hf_{1-X}Zr_XTe_5$ where x varies from $0 \leq x \leq 1$, are shown in Figure 1. The $HfTe_5$ and $ZrTe_5$ results were consistent with previous studies.[27] As Hf is replaced by Zr, the peak temperature, as determined by the resistivity vs. temperature measurement, is shifted to higher temperature. In each of the samples the resistivity decreases from high temperatures (T ~ 300K) before passing through a shallow minimum. As the temperature decreases further, the resistance rises rapidly, passing through a maximum at T_p. From lower temperatures, $T < T_p$, the resistivity falls steadily, as shown in Figure 1. The thermopower of each sample reveals a systematic shift in temperature as the Zr concentration is increased, similar to the resistivity, as shown in Figure 1. Each concentration exhibits relatively large p-type thermopower at room temperature. As the temperature decreases the thermopower for each sample increases until reaching a maximum. For lower temperatures, the thermopower drops sharply, passes through zero, at T_0, and continues to decrease until reaching a maximum n-type thermopower. From even lower temperatures, the thermopower begins to rise again going towards zero thermopower as the temperature approaches absolute zero in a relatively linear fashion, characteristic of diffusion type thermopower. As noted in the introduction, the resistance peak was first thought to be evidence of a charge density wave phenomenon, but no supporting evidence such as satellite spots in X-ray diffraction patterns or non-linear conductive behavior was found. The origin of the transition in these pentatellurides, as discussed by DiSalvo et. al.[17], appears to be an electronic phase transition as opposed to a structural phase transition. Therefore, the electronic properties of this system should be susceptible to doping which is evident with these results. The uncertainty in the concentrations of Hf or Zr does not allow for

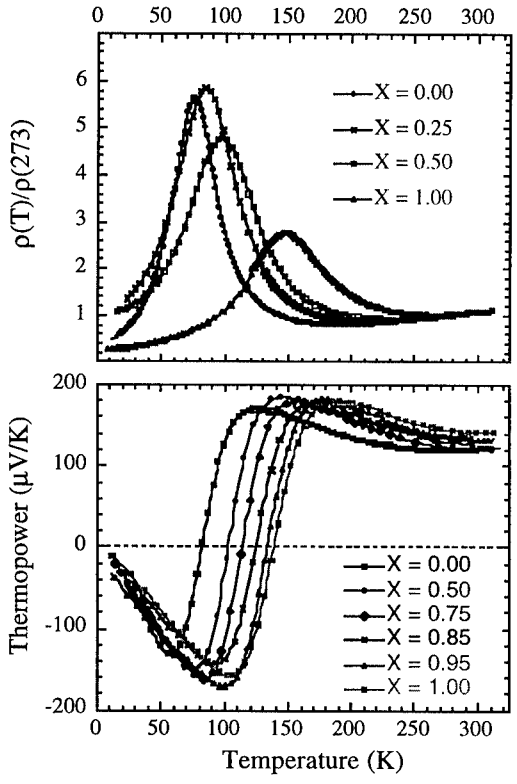

Figure 1. Normalized resistivity, ρ(T)/ρ(273), and absolute thermopower as a function on temperature for the isoelectronic series: $Hf_{1-X}Zr_XTe5$, where $0 \leq X \leq 1$.

the prediction of an obvious dependency with regards to the zero thermopowers or resistive peaks. However, the correlation between the zero thermopower and the resistivity peak at each concentration is quite evident.

Titanium Substitution

The thermopower of pentatelluride materials has been shown to be substantially affected by pressure. The n-type thermopower, below the peak, changes 150% or more to values of approximately -240 μV/K in $ZrTe_5$ at T = 120K and P = 12 kbar while the resistivity decreases by a factor of 4.[18] These trends enhanced the power factor ($\alpha^2\sigma T$) by an order of magnitude. Smaller changes are observed in $HfTe_5$ under similar conditions. Uniaxial stress measurements exhibit substantial effects in both parent materials.[23] These results favor the idea of an electronic phase transition.

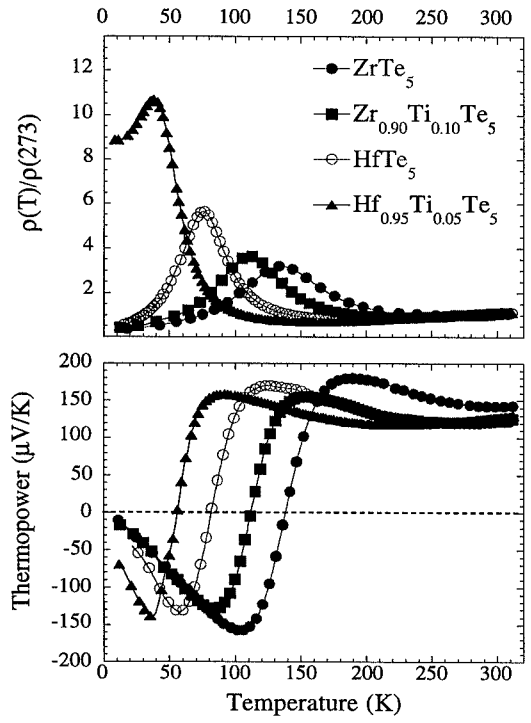

Figure 2. The normalized resistivity, ρ(T)/ρ(273), and the absolute thermopower, α, as a function of temperature for single crystals of $ZrTe_5$, $Zr_{0.90}Ti_{0.10}Te_5$, $HfTe_5$, and $Hf_{0.95}Ti_{0.05}Te_5$.

Ti atoms, r = 2.00Å, are substantially smaller than either Hf or Zr, both with r = 2.16Å, and therefore should produce some slight compression of the lattice, possibly in correlation to the applied external pressure. The Ti substitution is also isoelectronic (3d electrons instead of 4d or 5d) and hence should not directly alter the carrier concentration of the compounds. The resistivity and thermopower, respectively, are shown for the $HfTe_5$ and $Hf_{0.95}Ti_{0.05}Te_5$ materials in Figure 2. This small amount of Ti substitution (≈ 5%) shifts the peak temperature substantially from 80K for $HfTe_5$ to T_p = 38K for $Hf_{0.95}Ti_{0.05}Te_5$, but in contrast to previous results the zero crossing of the thermopower occurs at a much higher temperature (T_0 ≈ 50K) than T_p.[28] The relative resistive peak of the Ti doped sample is nearly

doubled that of the undoped resistive peak magnitude. A high resistance state appears to exist below the peak in comparison to all other pentatelluride materials studied. This is in contrast to the metallic behavior evident in other samples. The low temperature-high resistive state is similar to that observed in $HfTe_5$ under strain.[23] Since the origin of the transition is still unknown, it would be impractical to speculate on this high resistance state. Figure 2 also shows similar resistivity and thermopower data for $ZrTe_5$ and $Zr_{0.90}Ti_{0.10}Te_5$ which is consistent with previous results. A nominal Ti substitution of 10% for Zr shifts the peak temperature from 145K for $ZrTe_5$ to T_p = 110K for $Zr_{0.90}Ti_{0.10}Te_5$, with T_0 coincident with T_p. The relative resistance peak is slightly larger than that of the parent material, $ZrTe_5$. The strong metallic behavior is again evident below T_p, with a positive resistivity slope ($d\rho/dT > 0$). Substitutional doping of Ti for either Hf or Zr leads to a systematic variation of the peak temperature from 38 to 145K, while maintaining the relatively large values of thermopower at low temperature.

Se Substitutions

Substitutional studies are important in order to find the desired combination of elements in a compound to produce certain desirable characteristics. Such studies were performed on the Bi_2Te_3 compound which led to a series of related alloys and pseudo-ternary compounds that have resulted in effectively optimized thermoelectric materials.[29] This optimizing process found that certain stoichiometric amounts of Se aided in the enhancement of the BiTe compounds. Results from Se substitutions on Te sites of both parent pentatelluride materials are quite promising as well. As seen in Figure 3, a 5% nominal substitution of Se for Te reduces the temperature dependency of T_p and T_0. T_p and T_0 are reduced nearly 20K from $HfTe_5$ to $HfTe_{4.75}Se_{0.25}$, while reduction is only a few Kelvin for $ZrTe_5$ to $ZrTe_{4.75}Se_{0.25}$. The magnitudes of the absolute thermopower for both Se doped materials are increased approximately 20% from their parent materials. Thermopower values exceeding 200μV/K were measured for both $HfTe_{4.75}Se_{0.25}$ and $ZrTe_{4.75}Se_{0.25}$ at temperatures of ≈ 95K and ≈ 185K respectively. Another favorable effect of the Se substitution is the reduction in the resistivity. The resistivity of the parent pentatellurides decreases approximately 25% with the nominal addition of 5% Se for Te. The increase in the thermopower, combined with the decrease in the resistivity, results in an enhancement of the power factor, α^2T/ρ, by a factor of two.

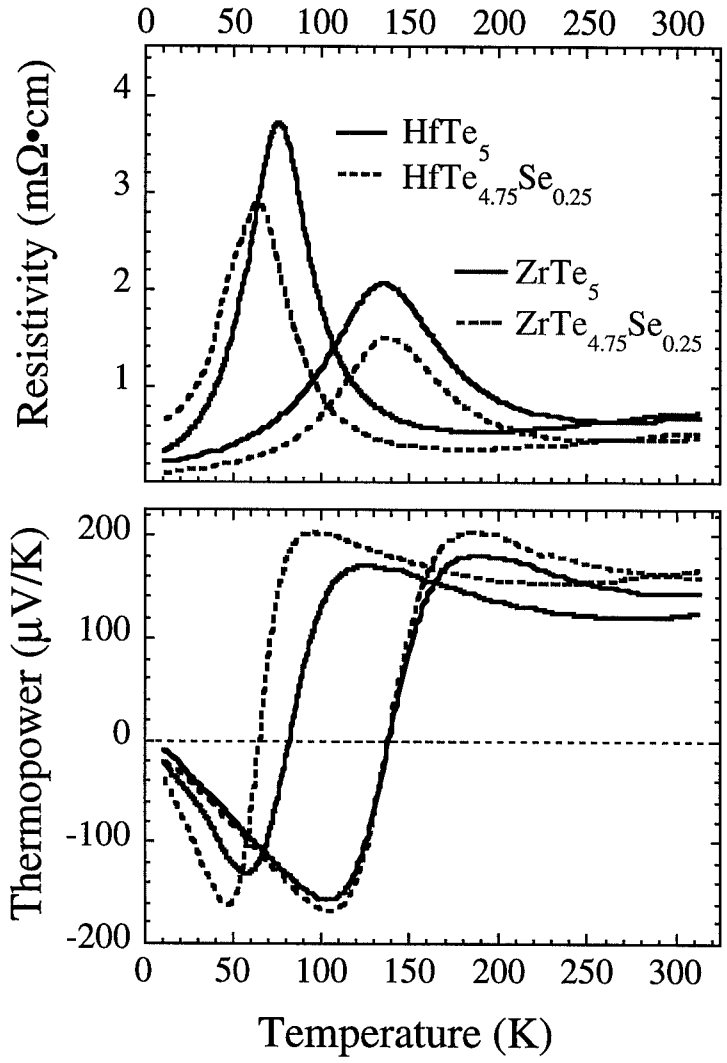

Figure 3. Resistivity, ρ, and thermopower, α, for 5% Se doped and undoped $HfTe_5$ and $ZrTe_5$. A nominal addition of 5% Se decreases ρ nearly 25%, while increasing $\alpha \approx 20\%$.

Sb Substitutions

Antimony is also an element in many thermoelectric materials including BiTe[29] and of course BiSb[30] compounds. Similar to Se, Sb was added to Bi_2Te_3 to enhance thermoelectric properties. Bismuth antimony alloys have extremely large magneto-thermoelectric figure of merit values below room temperature. Small amounts of antimony doped pentatellurides, shown in Figure 4, did not seem to increase the thermoelectric properties at lower temperatures. Instead, the Sb appears to completely alter the temperature dependency of both the thermopower and the electrical resistivity. The 5% nominally doped pentatellurides, $HfTe_{4.75}Sb_{0.25}$ and $ZrTe_{4.75}Sb_{0.25}$, both exhibit thermopower and resistivity values which increase with temperature. The samples measured had relatively low room temperature resistivity values of 0.48 and 0.36 mΩ•cm for $HfTe_{4.75}Sb_{0.25}$ and $ZrTe_{4.75}Sb_{0.25}$ respectively. The $HfTe_{4.75}Sb_{0.25}$ samples have temperature dependent values which are larger in thermopower and lower in resistivity than those of $ZrTe_{4.75}Sb_{0.25}$. The autonomous transition which occurs in the parent materials, apparently, no longer exists. The possibility of a dissimilar structural phase was eliminated by X-ray analysis which reconfirmed the pentatelluride structure.

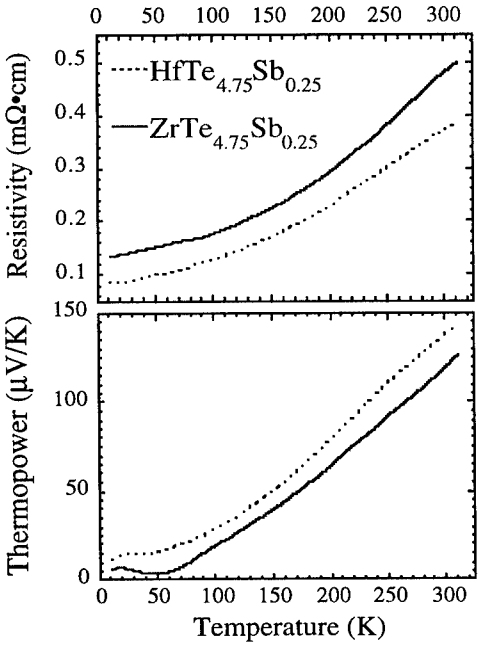

Figure 4. Resistivity, ρ, and thermopower, α, as a function of temperature for $HfTe_{4.75}Sb_{0.25}$ and $ZrTe_{4.75}Sb_{0.25}$.

Summary:

A low-dimensional pentatelluride system has been investigated for its potential as a low temperature (T < 250K) material. The parent compounds, $HfTe_5$ and $ZrTe_5$, exhibit exotic electrical transport due to an undetermined transition. A broad resistive anomaly occurs at a temperature $T_p \approx 80K$ for $HfTe_5$ and $T_p \approx 145K$ for $ZrTe_5$. These pentatellurides also display large thermopower values ($\alpha > +125\mu V/K$) around room temperature. These large p-type thermopower values decrease sharply passing through zero, at $T=T_0$, until reaching a relatively large n-type thermopower values ($\alpha < -125\mu V/K$). A solid solution of the parent pentatellurides, $Hf_{1-x}Zr_xTe_5$ ($0 \le x \le 1$), reveals that T_0 and T_p are systematically changed depending on the Hf-Zr concentration.

Substitutional studies have determined that small amounts of Ti for either parent transition metal greatly reduces T_p and T_0. Ti doping also increases the magnitude of the resistive anomaly. The Te sites of the pentatelluride system have also been partially substituted for as well. A 5% nominal substitution of Se for Te results in an increase in α as well as a reduction in ρ from the parent compound. These result in a power factor that is nearly doubled that of the parent compound. Power factors of Se doped pentatellurides range from:

$$P.F. = \alpha^2\sigma T \geq 1.25 \text{Watts/mK} \ @ \ 150K \leq T \leq 320K \text{for } HfTe_{4.75}Se_{0.25},$$

$$\geq 1.50 \text{Watts/mK} \ @ \ 225K \leq T \leq 320K \text{ for } ZrTe_{4.75}Se_{0.25}.$$

Antimony substitutions on the Te sites appear to completely eliminate the resistive peak exhibited by the parent compounds. Lower resistive values also make these substitutions desirable for further studies. The room temperature power factors of Sb doped pentatelluride samples are $\approx$ 1.50W/mK and $\approx$ 0.85W/mK for $HfTe_{4.75}Sb_{0.25}$ and $ZrTe_{4.75}Sb_{0.25}$ respectively. Through substitutional doping, the electronic properties of these pentatelluride materials may be tuned. These effects greatly enhance the TE possibilities of the pentatelluride system, especially at lower temperatures where efficient materials are scarce.

Acknowledgments:

The authors wish to acknowledge support from an ARO/DARPA (grant #DAAG55-97-1-0267), as well as, ONR (PPMS grant #N00014-98-1-0271), and from the research funds provided (TMT) from Clemson University. Sample contributions were made by Dr. Doug Ketchum and Dr. Michael Korzenski from the Chemistry Department at Clemson University, and Dr. F. Levy from the Institut De Physique in Laussanne, Switzerland.

References:

1. H. J. Goldsmid, Electronic Refrigeration, Pion Limited Publishing, London, (1986).
2. CRC Handbook of Thermoelectrics, edited by D.M. Rowe, CRC Press, Boca Raton (1995).
3. C. W. Wood, Rep. Prog. Phys. 51, 459-539 (1988)
4. G. Mahan, Brian Sales and Jeff Sharp, Physics Today, March 1997.
5. Andrew W. Allen, Detector Handbook, Laser FocusWorld, March issue 1997
6. J. Sloan, Superconductor Industry, Fall 1996, p30 (1996)
7. Terry M. Tritt, Science, **272**, 1276 (1996)
8. L. D. Hicks and M. S. Dresselhaus, Phys. Rev. B., **47**, 12727 (1993)
9. J. P. Fleuriel, T. Calliet and A. Borshchevsky, Proc. of the XIII International Conference on Thermoelectrics, AIP, p 40-44 (1995)
10. B. C. Sales, D. Mandrus and R. K. Williams, Science, **272**, 1325 (1996)
11. D. T. Morelli et. al., Phys. Rev. B, **51**, 9622 (1995)
12. Glen A. Slack and V. G. Toukala , Jour. Appl. Phys., **76**, 1635 (1994)
13. G. Nolas, G. Slack, D. T. Morelli, T. M. Tritt and A.C. Ehrlich, Jour. Appl. Phys., **79**, 4002(1996)
14. T. M. Tritt et. al., Jour. Appl. Phys., **79**, 8412 (1996)
15. G. Nolas, G. Slack, V. G. Harris and T. M. Tritt, Jour. Appl. Phys., **80**, 6304 (1996)
16. T. E. Jones et. al., Solid St. Comm., **42**, 793 (1982)
17. F. J. DiSalvo, R. M. Fleming and J. V. Waszczak, Phys. Rev. B., **24**, 2935 (1981)
18. W. W. Fuller et. al., Journal de Physique, **C3,** 1709 (1983)
19. M. Isumi, et. al., Solid State Comm., **42**, 773 (1982)
20. D. W. Bullett, Solid State Comm., **42**, 691 (1982)
21. G. N. Kamm et. al., Phys. Rev. B., **35**, 1223 (1987)
22. G. N. Kamm et. al., Phys. Rev. B., **31**, 7617 (1985)
23. E. P. Stillwell, A. C. Ehrlich, G. N. Kamm and D. J. Gillespie, Phys. Rev. B., **39**, 1626 (1989)
24. F. Levy and H. Berger, J. Cryst. Growth, **61**, 61 (1983)
25. L. Brattas and A. Kjekshus, Acta Chem. Scand., **27**, 2367 (1973)
26. T. M. Tritt et. al., M.R.S. Proc., Thermoelectric Materials: New Directions and Approaches, Spring 97, edited by T. M. Tritt et. al., **478**, 249-54 (1997)
27. R. T. Littleton IV, M.L. Wilson, C. R. Feger, M. J. Marone, J. Kolis, and T. M. Tritt, Proceedings of the XVI International Conference on Thermoelectrics, ed. by A. Heinrich (1997)
28. R. T. Littleton IV, T. M. Tritt, C. R. Feger, J. Kolis, M. L. Wilson, M. Marone, J. Payne, D. Verebeli, and F. Levy, Appl. Phys. L., **72**, 2056-8 (1998)
29. W. M. Yim and F. D. Rosi, Solid-State Electronics, **15**, 1121-40, (1972)
30. W. M. Yim and F. D. Rosi, Solid-State Electronics, **15**, 1141-65, (1972)

Thermoelectric Properties of Two Ternary Tellurides

Jeff W. Sharp*, Brian C. Sales†, David G. Mandrus† and Bryan C. Chakoumakos†
*Research and Development Division, Marlow Industries, Dallas, Texas 75238
†Solid State Division, Oak Ridge National Lab, Oak Ridge, TN, 37831

ABSTRACT

We present initial assessments of the thermoelectric properties of two ternary tellurides with known crystal structures, Tl_2GeTe_5 and Tl_2SnTe_5. Tl_2SnTe_5 appears to have a p-type figure of merit about the same as that of Bi_2Te_3, the best thermoelectric material among binary compounds. A good figure of merit is possible because the lattice thermal conductivity is very low. Based on neutron diffraction data, we have calculated atomic displacement parameters and thermal expansion coefficients. The atomic displacement parameters give some understanding of the low lattice thermal conductivity.

INTRODUCTION

The utility of the Peltier effect for most cooling applications is sensitive to the performance of the thermoelectric material. In the important temperature range of 250 to 350 K, the best materials known are solid solutions found in the Bi_2Te_3-Sb_2Te_3-Bi_2Se_3 system. Much work has gone into finding better thermoelectric materials, and the thermoelectric potential of plausible binary candidates has been evaluated, with a few exceptions [1, 2]. Many ternary compounds have been investigated also [3], but until recently [4, 5] these have been mainly variations on binary structures. The great diversity of ternary and quaternary structures [6] is largely unexplored with regard to thermoelectric properties. We are focussing particularly on ternary tellurides and antimonides. The solid state chemistry of these systems leads to many unusual crystal structures, including semiconductors that approximate the ideal "phonon glass" [7]. In this paper we report the properties of two such compounds, one of which seems to have a thermoelectric figure of merit at room temperature comparable to that of *p*-type Bi_2Te_3.

CRYSTAL STRUCTURES

Tl_2SnTe_5 (TST, Fig. 1) and Tl_2GeTe_5 (TGT) are two among numerous compounds in the Tl-Sn-Te [8] and Tl-Ge-Te [9] systems. Table I lists some crystal structure data for these tetragonal compounds. Both TST and TGT have columns of Tl ions along the crystallographic *c* axis. Low lattice thermal conductivity (κ_L) is expected for these compounds due to the large interatomic distances of the 8-fold coordinated Tl ions (Fig. 2). Transverse to the *c* axis the Tl columns alternate with an anion substructure that is also one-dimensional. In TST (Fig. 1), we find $SnTe_4$ tetrahedra linked by Te atoms that have square-planar coordination. The details of the bonding in the $GeTe_5$ chains of TGT are rather different. Paying due attention to Te-Te bond lengths, these chains are composed of alternating Te_4 square rings and edge-sharing pairs of $GeTe_4$ tetrahedra (composition of each pair of tetrahedra = Ge_2Te_6). Despite these differences,

Mat. Res. Soc. Symp. Proc. Vol. 545 © 1999 Materials Research Society

Table I. Crystal data for Tl_2SnTe_5 and Tl_2GeTe_5. For Tl_2GeTe_5, the ADP values are from a structure refinement using an orthorhombic cell (ref. b), but the atomic coordinates changed little in the preferred tetragonal cell (ref. c).

Tl_2SnTe_5[a]	**Tl_2GeTe_5**[b,c]
Tetragonal	Tetragonal
a = 8.306 Å c = 15.161 Å	a = 8.243 Å c = 14.918 Å
Space group I4/mcm	Space group P4/mbm
32 atoms/cell	32 atoms/cell
x-ray density = 7.40 g/cm^3	x-ray density = 7.34 g/cm^3

a) V. Agafanov, B. Legendre, N. Rodier, J. M. Cense, E. Dichi and G. Kra, *Acta Cryst.* C **47** (1991) p. 850.

b) A. Abba-Touré, G. Kra, R. Eholié, J. Olivier-Fourcade, J.-C. Jumas and M. Maurin, *J. Sol. St. Chem.* **84** (1990) p. 245.

c) R. E. Marsh, *J. Sol. St. Chem.* **87** (1990) p. 467.

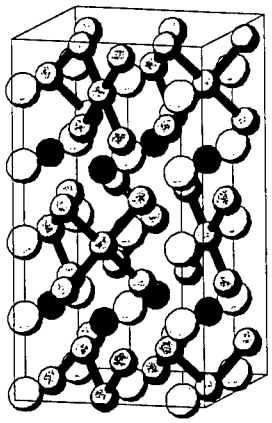

Figure 1. Crystal structure of Tl_2SnTe_5. The larger spheres represent Tl, and the darker small spheres represent Sn. There are no Tl-Tl bonds, but the Tl atoms have been connected by thin lines to show their arrangement along the (vertical) *c*-axis. $TeTe_4$ square planar units have been emphasized. For clarity, the Sn-Te (tetrahedral Sn) and Tl-Te bonds are not shown. There are two eight-fold sites for Tl: cubic and square anti-prism.

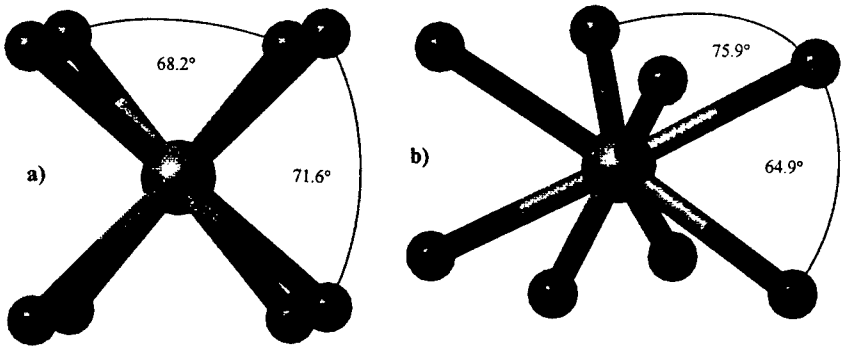

Figure 2. Cubic (a) and square anti-prismatic (b) environments of Tl in Tl_2SnTe_5. The Tl-Te distances are 3.66 Å and 3.49 Å respectively.

TST and TGT can be viewed as polytypes of one another, with different stacking sequences of (Ge/Sn)Te_4 tetrahedra and $TeTe_4$ square planar units linked into chains by edge sharing [10].

SYNTHESIS AND CHARACTERIZATION

For polycrystalline sample synthesis, stoichiometric or nearly stoichiometric mixtures of Tl (5 9's), Sn (5 9's), Ge (intrinsic, ultrahigh purity) and Te (5 9's, excluding traces of Se) were sealed in silica tubes that were coated with pyrolytic carbon, evacuated and back-filled with argon (approximately one-third atmosphere). All purities are on a metals basis. The Tl comes as ½" diameter rod that has a black, heavily oxidized surface. This surface layer is removed in a glovebox, and only shiny gray material from the interior is used. Mixing the elements at 750 °C, quenching the melt and annealing for a few days at temperatures just below the melting points yields single phase samples of TST and TGT. TST and TGT melt incongruently at approximately 285-290 °C and 265-270 °C respectively. For TST a second melting event occurs within 15 °C of the first. For TGT we see a second melting at approximately 322 °C, the same temperature at which congruent melting was reported for this compound [11]. The synthesis procedure was validated by excellent agreement between the x-ray diffraction patterns of our polycrystalline samples and powder patterns calculated from the reported crystal structures.

We have also made some solid solutions based on TST and TGT, which seem to show full mutual solubility. It appears that the TGT structure is found except when the Ge fraction is less than 10%, but the TST and TGT powder patterns are quite similar, making this a non-trivial distinction. A sample with 10% Se substitution for Te was multiphase.

We used powder neutron diffraction down to liquid helium temperatures (performed at the High Flux Isotope Reactor of Oak Ridge National Lab) to refine the crystal structures and calculate atomic displacement parameters (ADP's). ADP's measure the mean-square displacement amplitude of an atom about its average position in a crystal. A large ADP value can mean that an atom is weakly bound about a single equilibrium position, or that there are multiple equilibrium positions for that atom in the structure. Either type of behavior will lead to a low κ_L, and so ADP data can be useful in the search for new thermoelectric materials [12]. In both TST and TGT there are large ADP's for the Tl ions and some of the Te atoms. The largest ADP's are for a portion of the Tl atoms, and are equivalent to a root-mean-square displacement of about 0.22 Å. The temperature dependence of the ADP's indicates that the disorder is thermal rather than static. That is, both crystallographically distinct Tl ions have a single equilibrium position.

We have also used neutron diffraction to measure the lattice parameters of TST and TGT as a function of temperature, in order to determine the linear thermal expansion coefficients (α). Large and anisotropic α's, which is what we have found, could be the reason that some of our samples, especially TST samples, crack when subjected to rapid thermal cycling. Our results are that along the *c* axis $\alpha = 13$ for TST and $\alpha = 20$ for TGT (in units of 10^{-6}/°C). For the equivalent *a* and *b* axes, $\alpha = 29$ for both TST and TGT. For comparison, the thermal expansion coefficients for hexagonal Bi_2Te_3 are $\alpha = 13$ and $\alpha = 22$ along the *a* and *c* axes respectively [13].

The process described above for single phase synthesis also can yield samples suitable for transport measurements. Alternatively, the annealed mass can be powdered (hand ground in ~ 100 ppm O_2 nitrogen glovebox) and hot pressed to give a higher density sample. It is relatively easy to achieve high density hot pressed compacts. Greater than 95% of x-ray density is reached in one hour at a temperature of 250 °C and pressure of 23.5 Kpsi. However, ejection stresses may be responsible for some of the macro-cracks that we have observed. A composition near the eutectic of the Tl-Te system ($\simeq TlTe_2$) seems to make a good flux for growth of small single crystals. The crystals were platelet shaped, ~ 2.5 x 2.5 x <1 mm^3, and were used for electrical measurements in the *ab* plane.

Representative transport properties are shown in Fig. 3. For the polycrystalline samples, the data shown here were collected by using a small heater to create the temperature gradient, with thermocouples and voltage leads epoxied onto a lateral face of the sample. Current is injected via a conductive epoxy coating the ends of the sample. No heat loss corrections are made, so measured thermal conductivity values (κ) are expected to be higher than the true values. Concurring transport measurements have been made in two additional systems. In one of these, the heat from a resistor flows through two standards and the sample, located symmetrically between the standards (Pyrex 7740, 3ω method [14]). In the third measurement system the temperature gradient is created by the Peltier effect, and heat loss corrections are applied.

The Seebeck coefficient (S) (Fig. 3a) is positive for all our samples, and in the range 150 to 300 μV/K at room temperature. Hall measurements on a TST sample with S= 210 μV/K at room temperature yielded a carrier concentration and mobility of p = 2.8 x 10^{19} cm^{-3} and μ = 55 cm^2/V-s. Similarly, for a TGT sample with S = 270 μV/K at 300 K, we found p = 2.0 x 10^{19} cm^{-3} and μ = 26 cm^2/V-s. In solid solutions, S increases in going from TST to TGT. The thermal band gap (E_g) of a semiconductor can be estimated from S(T) curves according to $E_g \simeq 2eS_{max}T_{max}$, where S_{max} and T_{max} are the peak of S and the temperature at which the peak occurs [15]. Our estimates are $E_g \simeq 0.25$ eV for TST and $E_g \simeq 0.17$ eV for TGT.

Figure 3b shows some examples of the dependence of resistivity (ρ) on temperature. Generally the variation of ρ with temperature is less strong than the theoretical relationship based on acoustic phonon scattering, $\rho \propto T^{1.5}$. In the case of single crystals and some quenched/annealed samples, ρ is approximately linearly proportional to T from 150 to 300 K. However, ρ for many quenched/annealed or hot pressed samples reaches a minimum between 200 and 250 K. The increase of ρ at lower temperatures may be an indication of a contribution from cracking, grain boundary resistance, or both. Because we suspect that grain boundary resistance is a problem, we have hot pressed some samples without first powdering them. The compacts so formed do in general have better electrical properties.

The total measured κ is very low for both TST and TGT (Fig. 3c). The lattice portion is not more than 5 mW/cm-K, which is less than 1/3 of κ_L of pure Bi_2Te_3. The measured increase in κ for TGT above 200 K probably is a radiation effect that is more or less significant depending on sample geometry. Because no corrections have been applied to the κ data, we expect that the curves in Fig. 3c are slightly higher than reality at all temperatures, except for cases in which the effective thermocouple separation is underestimated. At room temperature the electronic contribution to κ is estimated to be

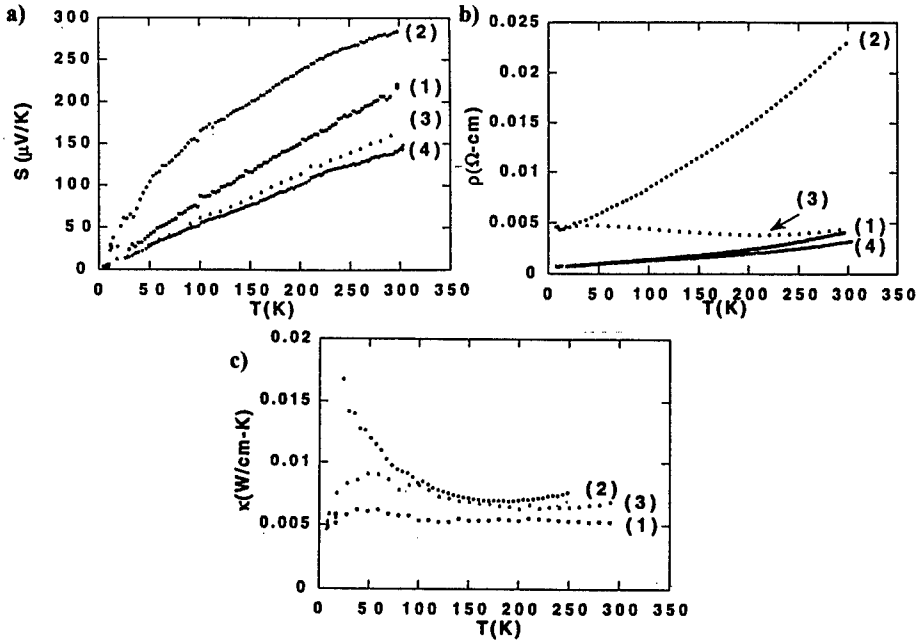

Figure 3. Seebeck coefficient (a), electrical resistivity (b) and thermal conductivity (c) data for three polycrystalline samples and one single crystal sample: 1) TST, 2) TGT, 3) hot pressed TST, 4) TST single crystal. Samples 1 and 2 were melted, quenched and annealed. Electrical properties were measured in the *ab* plane of the platelet-shaped single crystal. For the polycrystalline samples, the geometry (length-to-area ratio) uncertainty is ±15%.

about 20% for TST, but less than 10% for TGT due to the higher resistivity. Because κ_L is dominant relative to the electronic portion, we can say from Fig. 3c that κ_L is rather flat from 100 to 300 K. This is atypical for good thermal conductors, but typical for crystalline compounds in which κ approaches the glass-like limit [16].

For sample 1 (Fig. 3) we project a maximum thermoelectric figure of merit, $ZT = S^2T/\rho\kappa$, of 0.85 at 400 K. Because we do not have reliable thermal conductivity values at that temperature, we have used the room temperature value to estimate ZT. ZT at 300 K is about 0.6, as is the case for *p*-type Bi_2Te_3.

SUMMARY

In summary, we have reported the initial studies of two ternary tellurides that have very low values of the lattice thermal conductivity. In each case, the low lattice thermal conductivity is associated with a large degree of thermal disorder on the part of highly coordinated Tl atoms. For the compound that appears better at the moment, Tl_2SnTe_5,

the best power factor (S^2/ρ) obtained to date is approximately 10 $\mu W/cm\text{-}K^2$, yielding a dimensionless figure of merit comparable with that of *p*-type Bi_2Te_3. The main area for possible improvement seems to be in the electrical resistivity, if in fact grain boundaries are contributing to the measured resistivity of the present samples. Also, since K_2SnTe_5 and Rb_2SnTe_5 have structures [17, 18] equivalent to that of TST, there is unexplored solid solution chemistry that might yield *n*-type samples.

Our results (largely outside the scope of this paper) lead us to believe that the selected search field contains many crystalline compounds with κ_L low enough for advanced thermoelectric performance. The main scientific hurdle is to find ones that also have good electrical properties. Aside from a general preference for covalent bonding, there is an absence of theoretical guidance for obtaining high power factors, leaving us still with a high degree of empiricism in the quest for new thermoelectric materials.

REFERENCES

1. T. M. Tritt, M. L. Wilson, R. L. Littleton, Jr., C. Feger, J. Kolis, A. Johnson, D. T. Verebelyi, S. J. Hwu, M. Fakhruddin and F. Levy, in Mat. Res. Soc. Symp. Proc. Vol. 478 Ed. T. Tritt, M. Kanatzidis, H. Lyon Jr. and G. Mahan, (Materials Research Society, Pittsburgh, 1997), p. 249.
2. Ch. Kloc, K. Fess, W. Kaefer, K. Friemelt, H. Riazi-Nejad, M. Wendl and E. Bucher, in 15th Internatl. Conf. On Thermoelectrics Proc., (IEEE, Piscataway, NJ, 1996), p. 155.
3. D. P. Spitzer, *J. Phys. Chem. Solids* **31** (1970), p. 19.
4. J. W. Sharp, G. S. Nolas and E. H. Volckmann, in Mat. Res. Soc. Symp. Proc. Vol. 478, Ed. T. Tritt, M. Kanatzidis, H. Lyon Jr. and G. Mahan, (Materials Research Society, Pittsburgh, 1997), p. 91.
5. J. L. Schindler, T. P. Hogan, P. W. Brazis, C. R. Kannewurf, D.-Y. Chung and M. G. Kanatzidis, Mat. Res. Soc. Symp. Proc. Vol. 478, Ed. T. Tritt, M. Kanatzidis, H. Lyon Jr. and G. Mahan, (Materials Research Society, Pittsburgh, 1997), p. 327.
6. J. L. C. Daams, J. H. N. van Vucht and P. Villars, *J. All. Comp.* **182** (1992), p. 1; J. L. C. Daams and P. Villars, *J. All. Comp.* **197** (1993), p. 243; J. L. C. Daams and P. Villars, *J. All. Comp.* **215** (1994), p. 1.
7. G. A. Slack, in CRC Handbook of Thermoelectrics, Ed. D. M. Rowe (CRC Press, Boca Raton, FL, 1995), pp. 407-440.
8. E. Dichi, G. Kra, R. Eholié and B. Legendre, *J. All. Comp.* **194** (1993) p. 147; **194** (1993) p. 155; **199** (1993) p. 7; **199** (1993) p. 21.
9. A. Abba-Touré, G. Kra and R. Eholié, *J. Less Comm. Met.* **170** (1991) p. 199. R. E. Marsh, *J. Sol. St. Chem.* **87** (1990) p. 467.
10. V. Agafanov, B. Legendre, N. Rodier, J. M. Cense, E. Dichi and G. Kra, *Acta Cryst.* C **47** (1991) p. 850.
11. A. Abba-Touré, G. Kra, R. Eholié, J. Olivier-Fourcade, J.-C. Jumas and M. Maurin, *J. Sol. St. Chem.* **84** (1990) p. 245.
12. B. C. Sales, B. C. Chakoumakos, D. Mandrus, J. W. Sharp, N. R. Dilley and M. B. Maple, submitted to *Phys. Rev. Lett.*
13. M. H. Francombe, *Brit. J. Appl. Phys.* **9** (1958), p. 415.
14. D. G. Cahill, *Rev. Sci. Instrum.* **61** (1990) p. 802.
15. H. J. Goldsmid and J. W. Sharp, Submitted *to J. Elec. Matl.*
16. D. G. Cahill, S. K. Watson and R. O. Pohl, *Phys. Rev. B* **46** (1992), p. 6131.
17. B. Eisenmann, H. Schwerer and H. Schäfer, *Mat. Res. Bull.* **18** (1983), p. 383.
18. C. Brinkmann, B. Eisenmann and H. Schäfer, *Mat. Res. Bull.* **20** (1985), p. 299.

APPROACHES TOWARD CHEMICALLY PREPARED MULTIPLE QUANTUM WELL STRUCTURES

S.B. Cronin[a], T. Koga[b], X. Sun[a], Z. Ding[c], S.-C. Huang[c*], R.B. Kaner[c], M. S. Dresselhaus[a,d]

[a]Department of Physics, Massachusetts Institute of Technology, Cambridge, MA 02139
[b]Division of Engineering and Applied Sciences, Harvard University, Cambridge, MA 02139
[c]Department of Chemistry and Biochemistry, University of California, Los Angeles, Los Angeles, CA 90095
[d]Department of Electrical Engineering and Computer Science, Massachusetts Institute of Technology, Cambridge, MA 02139

ABSTRACT

An enhanced thermoelectric figure of merit, ZT, has been predicted for Bi_2Te_3 in the form of 2-dimensional quantum wells. A new approach to making multiple quantum well (MQW) structures for thermoelectric applications utilizing a chemical intercalation technique is proposed and investigated. It is proposed that by starting from Li intercalated Bi_2Te_3 and Bi_2Se_3, the layers of these materials can be separated by chemical means. The layers of Bi_2Te_3 or Bi_2Se_3 can then be restacked, by self-assembly, forming a non-periodic array of quantum wells. These chemically prepared MQWs are characterized by X-ray diffraction, SEM (scanning electron microscopy) and TEM (transmission electron microscopy) at various stages in the sample preparation to assess the degree to which the actual samples match the proposal. Experimental measurements of the Seebeck coefficient (S) and the electrical conductivity (σ) were performed over a range of temperatures for the initial bulk materials. It is found that some of the steps in the proposed fabrication have been achieved but still much improvement is needed before any practical thermoelectric 2D-system can be provided.

INTRODUCTION

Bi_2Te_3 and Bi_2Te_3 alloys have the highest room temperature ZT of any conventional thermoelectric material ($ZT \approx 0.6$ for Bi_2Te_3 and $ZT \approx 1$ for Bi_2Te_3 alloys) [1]. Because of their high ZTs, these materials have become the industrial standard for thermoelectric elements. Any improvement over presently available materials would have great practical impact. An enhancement in ZT has been predicted for Bi_2Te_3 in the form of a two-dimensional quantum well [2]. This enhancement is brought about by the increased density of states of a 2D electron gas over its 3D counterpart, which results in a higher value of the Seebeck coefficient (S) for a given value of the electrical conductivity (σ). It has been shown that for a Bi_2Te_3 quantum well of 10Å, the smallest basic structural unit thickness for Bi_2Te_3, a $Z_{2D}T$ of ≈ 2.0 within the quantum well is theoretically possible at room temperature [2]. This enhancement within the quantum well is almost a factor of 4 greater than that of bulk Bi_2Te_3. For two basic structural units, 20Å, it is predicted that $Z_{2D}T \approx 1.0$ is possible. In addition to the enhancement of ZT due to electronic transport, we also expect enhancement due to a decrease in the thermal conductivity caused by the increased scattering of phonons at the interfaces. However, in any real quantum well sample there must be barrier layers

*Shu-Chuan Huang is currently affiliated with the Department of Chemistry, National Dong Hwa University Shoufeng, Hualien 974 Taiwan

Mat. Res. Soc. Symp. Proc. Vol. 545 © 1999 Materials Research Society

which contribute strongly to the thermal conductivity but only weakly to the electronic transport. The barrier effectively reduces the temperature gradient across the sample without contributing much to the Seebeck coefficient (S), and thus the presence of the barriers decreases the ZT of the overall sample. Considering all of these competing factors, we expect to see an enhancement in the thermoelectric properties of Bi_2Te_3 quantum wells of 1 basic structural unit thickness, 10Å, if such a system can be synthesized experimentally.

Recently a new approach for making Bi_2Te_3 and Bi_2Se_3 in the form of quantum wells (described below) has been developed by Richard Kaner and his group at UCLA. This fabrication technique may provide an inexpensive method for fabricating quantum well systems, in that samples could be prepared without the use of expensive fabrication equipment, such as molecular beam epitaxy (MBE) or molecular chemical vapor deposition (MOCVD).

In this report, we first give a description of the fabrication concept. We then present the results of our structural analysis of materials during various stages of the fabrication process. We next report our results of preliminary measurements on the electronic transport properties. Finally we discuss the achievements made so far and problems that need to be addressed in the future.

FABRICATION CONCEPT

Bi_2Te_3 is a layered material in which the stacking ordering occurs within the "quintuple layer" basic structural unit (BSU) Te-Bi-Te-Bi-Te, which is 10.15Å thick. The layers within a BSU are tightly bound by electrical forces, while binding between adjacent BSUs is by weak van der Waals forces. Hence a quantum well of Bi_2Te_3 can only have discrete possible thicknesses which are integer multiples of 10.15Å. It should be mentioned that in Bi_2Te_3 the in-plane transport, that is in the plane of the BSUs, possesses the potential for high values of ZT.

A schematic diagram of the fabrication concept developed by the Kaner group at UCLA is shown in Fig. 1. Beginning with bulk Bi_2Te_3, or bulk Bi_2Se_3, Li ions can be intercalated between the BSU layers, as shown in the figure. The next step in the process is exfoliation, whereby the Li ions are solvated causing the layers of Bi_2Te_3 to be stripped off from the bulk sample. The solvated Li ions are much larger than the bare Li ions, and it is the separation of the layers provided by the solvated Li ions that allows exfoliation to take place. At this stage, ideally, we have plates that are long in the in-plane directions and very thin, perhaps 1 or 2 BSUs, in the perpendicular direction (the c-axis direction). Once the material has been reduced to thin plates, the sample can either be in the form of particles in a solution or in a powder sample. To make a macroscopic film sample, it is proposed that the plates are restacked by depositing the solution on a substrate and letting the particles settle out. The self-assembly of films will only be successful if the particles are indeed long thin plates, in which case we expect they will lie down with their c-axes pointing upward, thus regaining a common c-axis orientation. It is important for the platelets to regain a common c-axis orientation, since it is the in-plane transport that exhibits the desirable thermoelectric properties.

There are various types of restacking that can be performed. The simplest case of restacking, denoted as *reassembly* in the figure, is where the plates of one type of material (*e.g.*, Bi_2Te_3 or Bi_2Se_3) are restacked alone. Ideally these plates will restack turbostratically with a common c-axis orientation, but with random in-plane orientations. The scattering of electrons and phonons in the *reassembled* films should differ significantly from the bulk. However, in the absence of a barrier material, we don't expect any quantum confinement

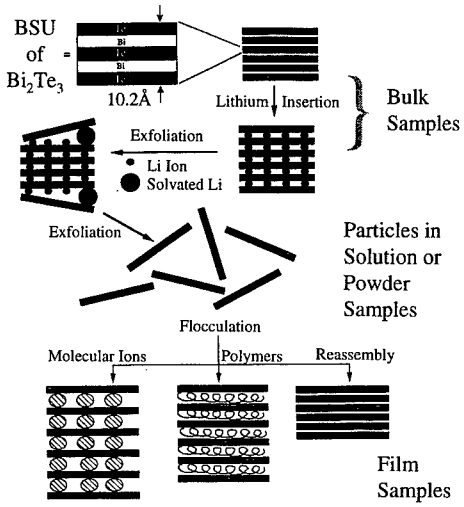

Figure 1: Schematic diagram of the self-assembly fabrication concept of 2D MQW structures of Bi_2Te_3 based on intercalation.

of carriers. In this case, an enhancement in ZT would occur through preferential scattering of phonons at the interfaces relative to electron scattering. The other two depictions in the schematic show films with insulating barrier layers inserted between the conducting layers which would provide adequate confinement to achieve two-dimensional electron transport within the Bi_2Te_3 or Bi_2Se_3 layers. We are now working on inserting a monolayer of a wide band gap semiconductor between the layers, for example MoS_2 or $MoSe_2$, which have band gaps of 1.9 and 1.6 eV, respectively [3]. Compared to Bi_2Te_3 which has a much smaller band gap of 130 meV, these wide band gap semiconductors should provide very high barriers for the confinement of electrons. We also consider inserting ionic or polymeric materials between the conducting layers, as depicted in the figure as the left and middle film samples. The good electrical insulating properties of ions or polymers can provide quantum confinement of carriers, while the low thermal conductivity of the polymer barriers will not increase the overall thermal conductivity of the sample by as much as for a crystalline material. In the present paper we have only investigated simple *reassembled* Bi_2Te_3 films and Bi_2Se_3 films with no barrier layers.

STRUCTURAL INVESTIGATION

The self-assembly fabrication concept described in the previous section is highly idealized. We investigate the materials at various stages of fabrication to determine the structure that is achieved experimentally and to identify the steps in the processing that need further improvement. In this section we describe our structural investigation of materials using the TEM (transmission electron microscopy), SEM (scanning electron microscopy) and X-ray

diffraction techniques.

Bi_2Te_3 and Bi_2Se_3 are quite similar in physical structure. However, Bi_2Te_3 is far superior in terms of thermoelectric properties. Because of their similarity in structure, both of these materials were processed into MQWs using the fabrication procedure described above in hopes of gaining more insight into the processing technique. The differences between Bi_2Te_3 and Bi_2Se_3 samples were quite striking. Both Bi_2Te_3 and Bi_2Se_3 samples were intercalated with Li, as indicated by X-ray and transport measurements as discussed below. The Li intercalation step was able to exfoliate the samples to form exfoliated particles or platelets (see Fig. 1).

For the preparation of TEM specimens we deposit a dilute solution of exfoliated particles on a TEM grid and study the size, shape and crystal quality and orientation of the individual particles. With TEM we can measure the electron diffraction of small areas of the sample, on the order of $1\mu m^2$. This allows us to look at the crystal quality and orientation of individual particles as well as to see how the crystalline structure varies from one end of an exfoliated particle to the other.

For the Bi_2Se_3 samples, the particles were typically on the order of $1\mu m^2$ in size and typically showed clear hexagonal electron diffraction patterns. Approximately 75 percent of the particles in the Bi_2Se_3 TEM sample showed clear hexagonal electron diffraction patterns, which indicates that the c-axes of the particles are pointing normal to the substrate, and as we had hoped the particles are long thin plates that are lying down. Though no method for measuring the exact thickness of the platelets has been developed, it is expected, from the strength and clarity of the electron diffraction patterns, that these platelets are much thicker than 1 BSU. The Bi_2Te_3 sample, on the other hand, contained particles typically 100 times smaller in area than those of the Bi_2Se_3 sample, approximately 100 nm^2 in area, and again the thickness was not known. From the electron diffraction measurements, the Bi_2Te_3 particles showed no c-axis preferred orientation, but instead appeared to be randomly oriented. At the present time we have not been able to achieve a preferred orientation in a Bi_2Te_3 film sample. We expect that this can be corrected, at least in part, by varying the reaction conditions.

Films on the order of $1\mu m$ in thickness were prepared by depositing a solution of particles on Si substrates. It should be stated that electron transport measurements of deposited films were attempted early on in our investigation of this system but due to infinite resistances (open circuits) no meaningful data could be taken. We studied the surfaces of the deposited films of Bi_2Te_3 and Bi_2Se_3 using SEM. At 2000X the Bi_2Te_3 film appeared highly cracked with large voids, approximately 100nm wide. This clearly accounts for the infinite electrical resistances measured for these films. The Bi_2Se_3 film at 2000X appears highly porous, instead of cracked. However, at 8000X smaller cracks are clear, again explaining the infinite resistances that were measured. The continuity of the films must be improved before any meaningful transport data can be taken.

The X-ray diffraction 2θ scans of Bi_2Te_3 and Bi_2Se_3 films are shown in Fig. 2. Again we see striking differences between the two types of films. The Bi_2Se_3 film shows strong c-axis $(0,0,l)$ peaks, which indicates that the constituent platelets in the film are lying down with their c-axes pointing normal to the substrate. The diffraction spectrum for the Bi_2Te_3 film, on the other hand, shows no preference for c-axis peaks, but shows all (h,k,l) peaks with roughly the relative intensities that are typical of a powder sample. For example, in a typical Bi_2Te_3 powder sample, it is the (0,1,5) peak that is dominant in intensity [4], and this peak also has a high intensity for the film sample.

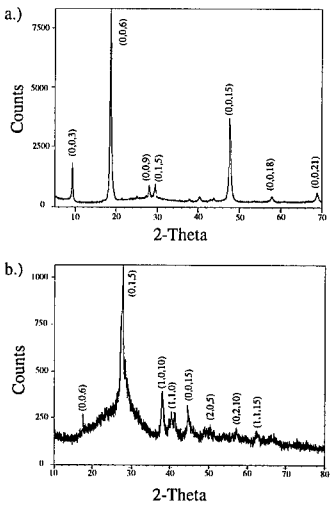

Figure 2: XRD intensity versus 2θ for a) an annealed Bi_2Se_3 film and b) a Bi_2Te_3 film.

Our results from X-ray measurements indicate that the Bi_2Se_3 films have a preferred c-axis orientation, which is what we want for thermoelectric applications, but the thickness of the exfoliated particles is likely to be greater than one or two basic structural units (see Fig. 1). The Bi_2Te_3 film, however, seems to consist of randomly oriented particles, which is not good for thermoelectricity, but the particle thickness may be much thinner, and perhaps close to being a few BSUs. These XRD results are consistent with those from our electron diffraction study using TEM. As previously stated, future effort will seek progress in making exfoliated particles as thin as a single BSU, and in aligning the deposited particles with their c-axes normal to the surface, an has been done for Bi_2Se_3.

TRANSPORT INVESTIGATION

As was mentioned above, the electrical conductivity (σ) and the Seebeck coefficient (S) of the Bi_2Te_3 and Bi_2Se_3 films could not be measured because the extremely high resistances. The physical continuity of the films must be improved before any meaningful data can be taken. As a preliminary measurement, we have measured S and σ as a function of temperature for the initial bulk materials. These measurements show evidence for the successful intercalation of Li (see Fig. 1). In addition, these measurements will serve as a basis for comparison of the films to the precursor materials once the film continuity is improved.

Shown in Fig. 3 is the power factor ($S^2\sigma$) measured below room temperature for three initial bulk samples: Bi_2Se_3, Bi_2Te_3 and Li intercalated Bi_2Te_3. The Bi_2Se_3 sample has high σ and low S, which indicates that the carrier density is very high and beyond that which is desirable for thermoelectrics. For bulk Bi_2Te_3 doped for optimum ZT, literature values indicate $\sigma \approx 1000\Omega^{-1}\text{cm}^{-1}$ and $S \approx 200\mu\text{V/K}$ at room temperature, which yields a power factor of approximately $40\mu\text{W/K}^2\text{cm}$ [1]. From our data we find a power factor of about $8\mu\text{W/K}^2$ cm for Bi_2Te_3 at 300 K, which is significantly lower than the optimum value. We also find that both σ and S are lower than those of the literature values mentioned above. In the previous section on structural investigation it is stated that the exfoliated Bi_2Te_3 layers

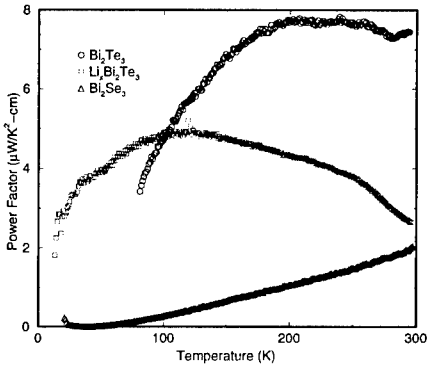

Figure 3: The measured temperature dependence of the power factor for Bi_2Se_3, Bi_2Te_3 and Li intercalated Bi_2Te_3 bulk samples.

were not *plate-like*. Possible explanations for the low power factor in these samples are poor crystal quality of the initial bulk materials, *i.e.*, grain boundaries, as well as being far from optimum carrier concentration. Future efforts will be directed toward improving the quality and purity of the materials produced.

CONCLUSIONS

A new method for fabricating quantum well structures utilizing intercalation chemistry and self-assembly has been proposed. Some steps in the fabrication have been demonstrated, but still much improvement is needed in realizing the fabrication concept experimentally. The lack of success in the Bi_2Te_3 system can be attributed to exfoliated particles not being *plate-like* enough to restack appropriately. Despite these inadequacies in the present samples, significant insight has been gained into the specific fabrication processes that need further improvement. It has been shown that Li intercalation can cause exfoliation of a bulk Bi_2Se_3 sample into thin layers and then restacked into a film regaining a common c-axis orientation. Though the thickness of the exfoliated layers is unknown (i.e., how many BSUs comprise these platelets), the concept of restacking of Bi_2Se_3 layers has been demonstrated in principle.

ACKNOWLEDGMENTS

The authors gratefully acknowledge support by ONR MURI under subcontract with UCLA Grant No. 0205-6-G-7A114-01.

REFERENCES

[1] H. J. Goldsmid, *Thermoelectric Refrigeration* (Plenum Press, New York, 1964).

[2] T. Koga, X. Sun, S. Cronin, M.S. Dresselhaus, K. Wang, and G. Chen, *Journal of Computer-Aided Materials Design*, **4** (1997) 175-182.

[3] K.-H. Hellwege, O. Madelung, *Landolt-Bornstein, Numerical Data and Functional Relationships in Science and Technology*, Group III, Volume 17, subvolumes f,g Springer-Verlag, New York 1983.

[4] National Bureau of Standards (U.S.) Monograph 25, 3 16 (1964).

THERMOELECTRIC PROPERTIES OF THE HALF-HEUSLER COMPOUND (Zr,Hf)(Ni,Pd)Sn

V. M. Browning [a], S. J. Poon [b], T. M. Tritt[c], A.L Pope[c], S. Bhattacharya[c],
P. Volkov[b], J. G. Song[b], V. Ponnambalam[b], A. C. Ehrlich[a]
[a] Naval Research Laboratory, Washington, DC 20375
[b] University of Virginia, Charlottesville, VA 22904
[c] Clemson University, Clemson, SC 29634

ABSTRACT

Recent measurements of the thermoelectric transport properties of a series of the half-Heusler compound ZrNiSn are presented. These materials are known to be bandgap intermetallic compounds with relatively large Seebeck coefficients and semimetallic to semiconducting transport properties. This makes them attractive for study as potential candidates for thermoelectric applications. In this study, trends in the thermoelectric power, electrical conductivity and thermal conductivity are examined as a function of chemical substitution on the various fcc sub-lattices that comprise the half-Heusler crystal structure. These results suggest that the lattice contribution to the thermal conductivity may be reduced by increasing the phonon scattering via chemical substitution. The effects of these substitutions on the overall power factor and figure-of-merit will also be discussed.

INTRODUCTION

In recent years there has been a renewed interest in the development of novel thermoelectric materials with improved properties for applications such as thermoelectric cooling and power generation. In general, those materials which look most promising exhibit a large Seebeck effect, S, good electrical conductivity, σ, and poor thermal conductivity, κ. Together, these quantities are used to determine the dimensionless figure-of-merit, $ZT = S^2\sigma T/\kappa$, which provides a measure for performance of a given material in a thermoelectric device application. Due to their relatively large Seebeck coefficients, narrow band semiconductors and semi-metals are one of the most widely studied classes of materials for thermoelectrics. The ability to chemically dope these materials means that it is often possible to achieve reduced κ values in polycrystalline samples while preserving the overall power-factor, $S^2\sigma$, thereby increasing ZT.

One class of materials which is being investigated for use in thermoelectric power generation applications at intermediate temperatures are the half-Heusler compounds (MNiSn, M=Zr,Hf,Ti). These intermetallic compounds are known to exhibit Seebeck coefficients on the order of 100-300 μV/K at room temperature and exhibit semi-conducting electrical transport [1,2,3]. High temperature resistivity measurements suggest the presence of a gap in the density of states at the Fermi surface on the order of 0.1 to 0.2 eV [2]. Evidence suggesting that the thermopower continues to increase above room temperature in these materials makes them potentially attractive for use in thermoelectric applications above room temperature. However, the thermal conductivity of these materials has been found to be prohibitively large in well-ordered samples. Therefore, recent studies of this system for thermoelectric applications have focussed on reducing the thermal conductivity by introducing additional phonon scattering mechanisms.

Mat. Res. Soc. Symp. Proc. Vol. 545 © 1999 Materials Research Society

The structure of the half-Heuslers is that of MgAgAs [4,5,6] which consists of three filled and one vacant interpenetrating fcc sublattices. The vacancy sub-lattice separates the half-Heusler compounds from the Heusler compounds, MNi_2Sn, which contain an additional Ni fcc sublattice. The ability to substitute isoelectronic atoms with differing masses on the various sub-lattices has been suggested as a possible approach to reducing the lattice contribution to the thermal conductivity [7]. In particular, C. Uher *et al.* [8,9] have reported on the effects of substitution on the Zr sublattice in ZrNiSn and have demonstrated significant reductions in κ at low temperatures. Unfortunately, the effects on the room temperature values of κ have been minimal. Uher *et al.*'s studies have also demonstrated an unusual dependence of the transport properties on annealing conditions. Their results showed that high temperature anneals resulted in a substantial increase in thermal conductivity accompanied by a corresponding decrease in the electrical conductivity. The effects of annealing on the electrical transport are in agreement with earlier studies which showed that increasing disorder resulted in an overall decrease in resistivity and an onset of a metal-insulator transition at low temperature [2]. While the increase in thermal conductivity can be understood in terms of increased ordering of the crystal structure, the decrease in electrical conductivity is not so well understood. These results underscore the need for further study of the effects of processing conditions on the thermoelectric transport properties of these materials.

In the present study, the effects of differential mass scattering are further explored via chemical substitutions on both the Zr and Ni sub-lattices in ZrNiSn.. Early measurements of samples made under non-optimum processing conditions exhibited thermal conductivity values as low as 25- 30 mW/cm-K [10]. Unfortunately, these early results have not been reproduced in samples made under improved conditions. However, the weight loss in the ingots from which both sets of samples were obtained was found to be less than 1% of the nominal weight. That is, the different results seen are not attributable to compositional variation. In an effort to determine whether the thermal conductivity can systematically be reduced to the values observed in the early samples, it is necessary to understand the effects of chemical disorder in the observed transport properties. Due to their similar size, the Zr and Sn atoms are known to substitute for each other on their respective lattice sites [11]. The substitution of more massive, isoelectronic atoms in this system may, therefore, affect the transport properties both by modulating the degree of Zr/Sn site substitution and by directly affecting the band structure and the electron and phonon scattering mechanisms. The results reported here look specifically at the effects on the thermoelectric transport properties of simultaneous substitutions of Hf and Pd for Zr and Ni, respectively. In addition, the effects of varying Sn composition are studied as well as the effects of the addition of boron which, due to its small size, is expected to substitute interstitially. Trends in the thermal conductivity, resistivity, and thermopower values are examined as a function of chemical composition. These results suggest that this system has not yet been optimized in terms of its potential for thermoelectric applications. Preliminary results on a similar study of chemically disordered TiNiSn samples will also be presented.

EXPERIMENT

Sample Preparation

Ingots of nominal composition were prepared by melting together elements (>99.9% purity) in an arc furnace. Phase purity was assessed via x-ray diffraction studies performed on a Scintag X-ray diffractometer using Cu K_{α} radiation. The observed peaks in the diffraction spectra were indexed successfully to the MgAgAs structure. Of concern is whether the samples

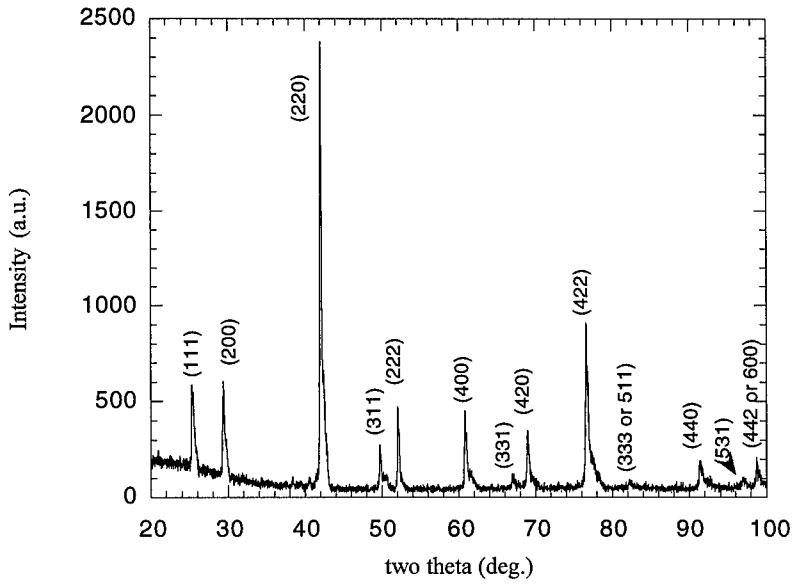

Figure 1: X-ray diffraction scan of $Ti_{0.5}Hf_{0.5}Ni_{0.85}Pt0_{.15}Sn_{0.95}$ alloy indexed to the MgAgAs structure.

remain single phase with chemical substitution. It was found that in all samples, the observed peaks were consistent with a single phase material. A sample scan demonstrating that phase purity is maintained even in chemically substituted samples is shown for $Ti_{0.5}Hf_{0.5}Ni_{0.85}Pt_{0.15}Sn$ is shown in Figure 1. These results are consistent with those reported for pure ZrNiSn [11] and TiNiSn [3].

In addition to x-ray diffraction measurements, thermal analysis studies using a Perkin Elmer DTA7 indicated thermal stability of the compounds up to 1250° C. Thermal stability at high temperatures is essential in these materials if they are going to be of use in thermoelectric devices at moderate to high temperatures. Although the thermal analysis results suggest that these materials retain structural stability up to temperatures > 1200° C, annealing studies suggest that the transport properties may drastically change at temperatures above 800° C, thus restricting their use to temperatures below this value.

Experimental Procedures

Characterization of the thermoelectric transport properties of the samples was carried out in collaboration between facilities at the Naval Research Laboratory and Clemson University. Measurements taken at the Naval Research Laboratory were accomplished using a transient voltage ZT-meter technique. In this technique, the Peltier effect is used to generate a temperature gradient across the sample. The resulting Seebeck component of the sample voltage is monitored

as a function of the Peltier induced ΔT, and the Seebeck coefficient, S, is determined by the linear slope of the $S(\Delta T)$ curve. This experimental configuration also allows measurement of the thermal conductivity which is determined by the relation: $\kappa = (S*T*I/\Delta T)*C$, where S is the thermopower, T is the sample temperature, I is the applied current and ΔT is the resulting Peltier induced temperature gradient. The quantity C is a correction factor which accounts for losses due to radiation and thermal conductance of the leads. Complete details of this technique can be found elsewhere [12].

Thermopower measurements taken at Clemson University were accomplished by applying a temperature gradient on the order of 1% of the sample temperature via a small chip heater attached to the sample and monitoring the induced Seebeck voltage. Thermal conductivity measurements were taken using an absolute technique in which heat is introduced to the sample via a resistive heater. The temperature gradient of the sample is monitored as a function of input power to the heater to determine κ. Both the NRL and Clemson resistivity measurements were taken using a standard 4-probe technique.

RESULTS AND DISCUSSION

In order to determine the feasability of differential mass scattering as a means of optimizing the thermoelectric performance of the ZrNiSn compound, the various thermoelectric transport properties of a series of samples with varying compositions were measured. Specifically, this study focussed on the following compositions: ZrNiSn, $ZrNi_{0.97}Sn$, $Zr_{0.7}Hf_{0.3}Ni_{0.7}Pd_{0.3}Sn$, $Zr_{0.8}Hf_{0.2}Ni_{0.7}Pd_{0.3}Sn_{0.97}$, $Zr_{0.5}Hf_{0.5}Ni_{0.7}Pd_{0.3}Sn_{0.95}$, and ZrNiSn with 10% boron. Measurements reported for the ZrNiSn and ZrNiSn with 10% boron were taken on as-cast samples. The remaining samples were subjected to a 12 hour anneal at 900° C prior to measurement. Figure 2 shows the temperature dependent resistivities measured for these samples. In general, with increasing chemical disorder the resistivity decreases in magnitude. In addition, the overall temperature dependence of the resistivity varies widely from apparently activated behavior in the pure ZrNiSn sample to a crossover between non-metallic to metallic behavior in a boron substituted sample. In the sense that increased disorder enhances the electrical conductivity, our results are in agreement with previous annealing and substitutional studies.

The general form for the resistivity in systems exhibiting activated behavior is: $\rho = \rho_0(T)\exp(\Delta_\rho/k_BT)$. In the simplest case, where carriers are thermally excited over an energy gap, Δ_ρ, at the Fermi surface, $\rho_0(T)$ is taken as a constant, and Δ_ρ is determined from the slope of the $\ln \rho$ versus $1/T$ curve. In disordered systems, localization effects become significant and $\rho(T)$ exhibits a power law behavior which is dependent on the mechanism of localization. Disorder can localize carriers either through Anderson localization or, in the presence of strong electron-phonon coupling, through the formation of polarization induced lattice distortions known as polarons. Figure 3 shows the resistivity plotted as $\ln\rho$ versus $1/T$. Clearly over this temperature range, the data cannot be explained by simple thermal activation over an energy gap, suggesting that localization of carriers is a contributing factor in the observed transport properties. Evidence for a metal-insulator transition in some of the samples further supports the presence of a localization potential in this system.

Although the trends in the resistivity data with increasing disorder are not completely understood, earlier theoretical work provides some insight to two possible mechanisms which may be responsible for the observed trends in the transport properties. Band structure

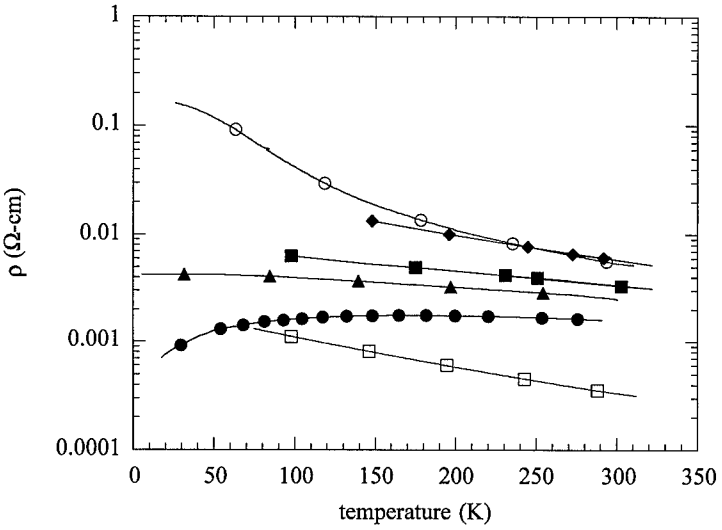

Figure 2: Resistivity versus temperature for a series of chemically substituted ZrNiSn samples: ZrNiSn (○), $ZrNi_{0.97}Sn$ (□), $Zr_{0.7}Hf_{0.3}Ni_{0.7}Pd_{0.3}Sn$ (◆), $Zr_{0.8}Hf_{0.2}Ni_{0.7}Pd_{0.3}Sn_{0.97}$ (■), $Zr_{0.5}Hf_{0.5}Ni_{0.7}Pd_{0.3}Sn_{0.95}$ (▲), and ZrNiSn with 10% boron (●).

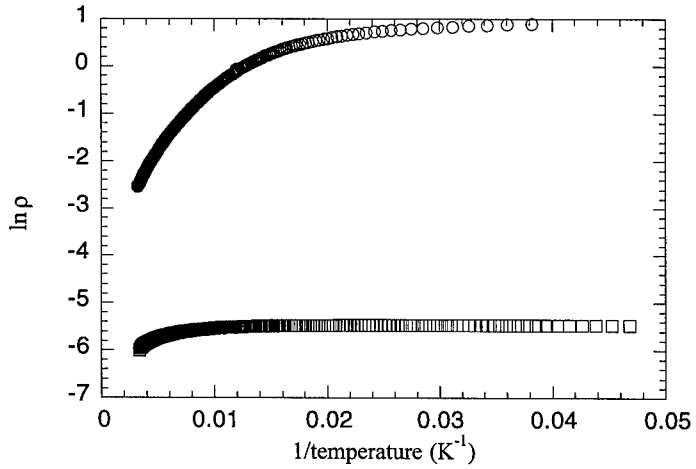

Figure 3: Temperature dependent resistivity plotted as ln (ρ) versus 1/T for ZrNiSn(○) and $Zr_{0.5}Hf_{0.5}Ni_{0.7}Pd_{0.3}Sn_{0.95}$ (□).

calculations of these materials are in agreement with experiment in that they predict semiconducting transport properties for well ordered samples. Using the pseudopotential total-energy method, S. Ogut and K.Rabe [13] have predicted the existence of an indirect semiconducting gap near the Fermi level of approximately 0.5 eV. The existence of this gap is attributed to a hybridization of the Sn *p* and Zr *d* -levels which is mediated by the Ni sub-lattice. The magnitude of the calculated gap is several times larger than that observed in ZrNiSn at high temperatures. However, they are able to account for this discrepancy by allowing for inter-site substitution between the Zr and Sn sub-lattices in their calculations. It is interesting to note that by allowing for this inter-site substitution, their calculations also predict that with approximately 15% site substitution, the gap closes, thereby forming a semi-metal. This result is in quite good agreement with experiments showing the existence of a metal-insulator transition in ZrNiSn samples with inter-site substitutions on the order of 20% as evidenced by x-ray diffraction studies [11].

It has also been suggested that the vacant Ni sub-lattice may serve as a localization potential for charge carriers [2]. In this scenario, it is argued that a narrow band, associated with the ordered Ni vacancy sublattice, exists near the Fermi level and beneath the conduction band. It is postulated that this vacancy band localizes charge carriers within the gap. Positron annihilation experiments in NiMnSb which reveal the presence of localization centers at vacancy sites [14] are cited as experimental evidence for this model. Presumably, any increase in disorder would have a deleterious effect on the ability of the fcc vacancy sub-lattice to serve as a localization potential for charge carriers.

The trends in the resistivity may be explained within the framework of either model and it is likely that both mechanisms are, to some degree, contributing to the experimental observations. The electrical resistivity is sensitive to both carrier concentration and mobility and, therefore, it is difficult to determine the degree to which carriers are localized based on electrical transport measurements alone. In principal, thermopower measurements may help to determine whether carrier concentration or carrier mobility is dominating the electronic transport. In a thermally activated system, the thermopower is expected to exhibit a temperature dependence of the form: $S(T) = k_B/e[(\Delta_S/k_BT) + B]$. Since thermopower is predominantly sensitive to carrier concentration while resistivity is equally sensitive to carrier concentration and mobility, one can distinguish localized "hopping" transport from thermal activation of carriers over an energy gap by comparing the relative magnitude of Δ_S and Δ_ρ. If $\Delta_\rho >> \Delta_s$, then carrier mobility is dominating the transport properties. Figure 4 plots the temperature dependent thermopower for the various ZrNiSn compounds. None of the samples exhibited a strictly 1/T temperature dependence over the entire range suggesting, in agreement with the resistivity measurements, that the observed transport properties cannot be explained by assuming either strictly thermal activation over an energy gap or localization of charge carriers as the dominant mechanism. While the significant decrease in the thermopower with disorder suggests an increase in the states available for electric transport, the temperature dependence does not support thermal activation of carriers over the measured temperature range. Clearly further study of the transport properties is needed to fully understand this system.

In order to determine whether this system is likely to prove useful for thermoelectric applications, one also needs to know the thermal conductivity. The effect of chemical disorder on the thermal conductivity is shown in Figure 5. The multinary compounds $Zr_{0.8}Hf_{0.2}Ni_{0.7}Pd_{0.3}Sn_{0.97}$ and $Zr_{0.7}Hf_{0.3}Ni_{0.7}Pd_{0.3}Sn$ exhibited a significant reduction in the thermal conductivity values compared to the pure ZrNiSn sample. Interestingly, the addition of 10% boron did not significantly change the room temperature value of the thermal conductivity. One possible explanation for this result is that any decrease in lattice thermal conductivity may be

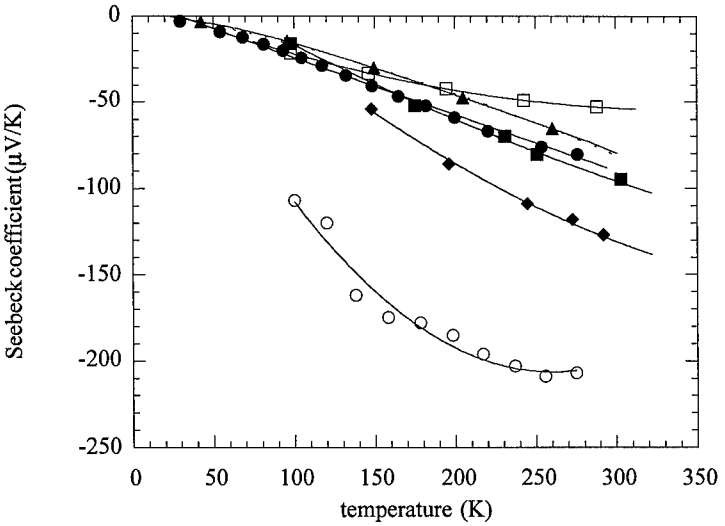

Figure 4: Thermopower versus temperature for chemically substituted ZrNiSn: ZrNiSn (○), $ZrNi_{0.97}Sn$ (□), $Zr_{0.7}Hf_{0.3}Ni_{0.7}Pd_{0.3}Sn$ (◆), $Zr_{0.8}Hf_{0.2}Ni_{0.7}Pd_{0.3}Sn_{0.97}$ (■), $Zr_{0.5}Hf_{0.5}Ni_{0.7}Pd_{0.3}Sn_{0.95}$ (▲), and ZrNiSn with 10% boron (●).

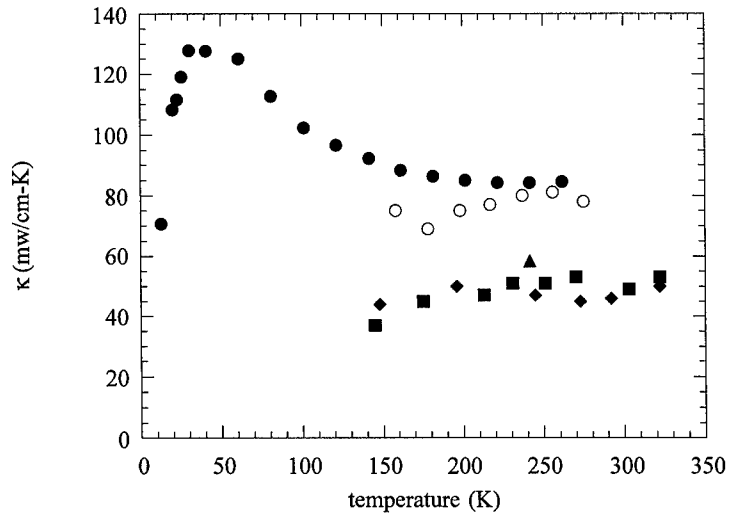

Figure 5: Thermal conductivity versus temperature for chemically substituted ZrNiSn: ZrNiSn (○),$Zr_{0.7}Hf_{0.3}Ni_{0.7}Pd_{0.3}Sn$ (◆), $Zr_{0.8}Hf_{0.2}Ni_{0.7}Pd_{0.3}Sn_{0.97}$ (■), $Zr_{0.5}Hf_{0.5}Ni_{0.7}Pd_{0.3}Sn_{0.95}$ (▲), and ZrNiSn with 10% boron (●).

offset by an increase in the electronic contribution as evidenced by the order of magnitude decrease in resistivity shown in Figure 2. Figure 6 shows the overall net effect of the chemical substitution on the power factor, S^2/ρ. These results show that all of the substitutions lead to a net decrease in the power factor. When one takes into account the thermal conductivities, one sees that the figure-of-merit, ZT, is also decreased by these substitutions as shown in Figure 7. The small values of ZT at room temperature together with the trends in the data are not encouraging in terms of prospective thermoelectric applications. With this in mind, recent studies have focussed on another of the half-Heusler compounds TiNiSn. Figure 8 shows the power factor for this system for several compositions. In contrast to the ZrNiSn study, these results show a net increase in power factor with chemical complexity. Further clarification of whether this system may prove useful for thermoelectric applications awaits further study including measurement of the thermal conductivity properties.

CONCLUSION

In summary, we have studied the thermoelectric properties of a series of ZrNiSn samples with various chemical substitutions in an effort to assess the feasability of optimizing these properties for potential thermoelectric applications. Although, the properties varied greatly with composition, no net increase in the figure-of-merit, ZT, was achieved. However, recent results obtained by Uher *et al.* [8] suggest that substition with indium may enhance ZT. In addition preliminary measurements of chemically substituted TiNiSn suggest that this system may hold promise for enhanced ZT values in chemically disordered materials.

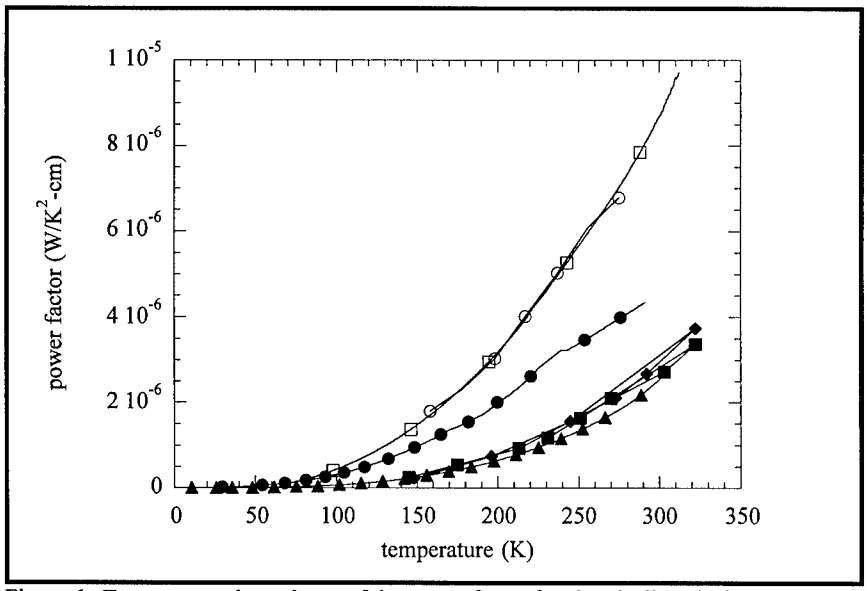

Figure 6: Temperature dependence of the power factor for chemically substituted ZrNiSn: ZrNiSn (○), $ZrNi_{0.97}Sn$ (□), $Zr_{0.7}Hf_{0.3}Ni_{0.7}Pd_{0.3}Sn$ (◆), $Zr_{0.8}Hf_{0.2}Ni_{0.7}Pd_{0.3}Sn_{0.97}$ (■), $Zr_{0.5}Hf_{0.5}Ni_{0.7}Pd_{0.3}Sn_{0.95}$ (▲), and ZrNiSn with 10% boron (●).

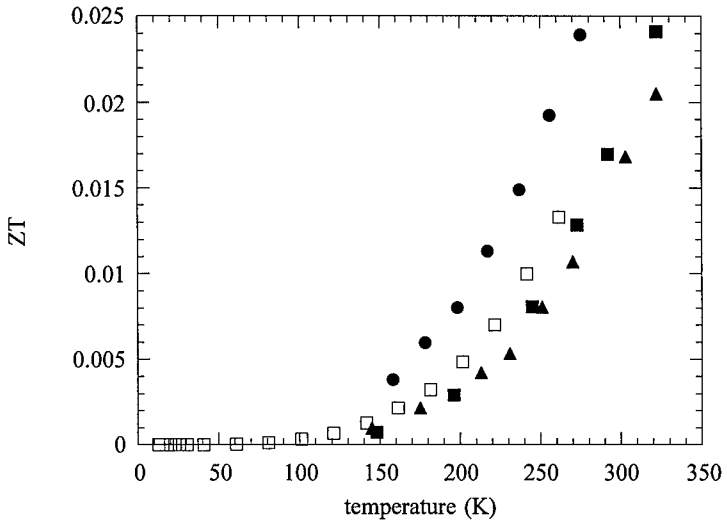

Figure 7: Figure-of-merit, ZT, versus temperature for chemically substituted ZrNiSn: ZrNiSn (●), ZrNiSn w/10% boron (□), $Zr_{0.8}Hf_{0.2}Ni_{0.7}Pd_{0.2}Sn_{0.97}$ (▲), $Zr_{0.7}Hf_{0.3}Ni_{0.7}Pd_{0.3}Sn$ (■).

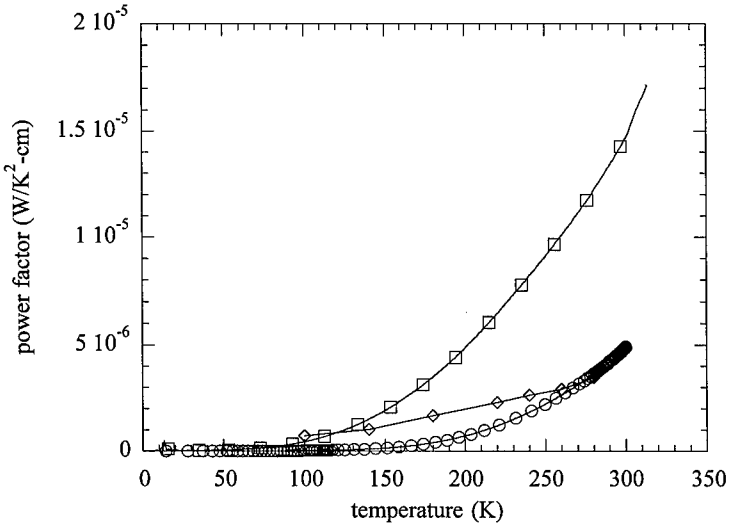

Figure 8: Power factor as a function of temperature for chemically substituted TiNiSn: TiNiSn (○), $TiNi_{1.03}Sn$ (□), $Ti_{0.5}Hf_{0.5}Ni_{0.85}Pt_{0.15}Sn_{0.95}$ (◊).

ACKNOWLEDGEMENTS

V. M. Browning gratefully acknowledges the financial support of both DARPA and ONR. S. J. Poon acknowledges support from NSF #DMR 97-00504. In addition, T. M. Tritt acknowledges financial support from DARPA/ARO #DAA G55-97-1-0-267, ONR #N00014-98-1-0271 and ONR #N00014-98-1-004. One of us (A.L. Pope) acknowledges Clemson University for partial finanical support through the *Dean's Scholars Award Program.*

REFERENCES

1. F. G. Aliev, N. B. Brandt, V. V. Moshchalkov, V. V. Kozyrkov,R. V. Skolozdra, and A. I Belogorokhov, Z. Phys. B **75**, 167 (1989).

2. F. G. Aliev, Physica B **171**, 199 (1991).

3. B. A.Cook, J. L. Harringa, Z. S. Tan, and W. A. Jesser in *Proceedings XV International Conference on Thermoelectrics* , (IEEE Cat. No. 96TH8169, New York, 1996), p. 122.

4. W. Jeitschko, Metall. Trans. **1**, 3159 (1970).

5. T. T. M. Palstra, G. J. Nieuwenhus, R. M. F. Vlastuin, J. A.Mydosh, J. van den Berg and K. H. J. Bushow, J. Magn. & Magn. Mater. **67**, 331 (1987).

6. F. G. Aliev, N. B. Brandt, V. V. Kozyrkov, V. V. Moshchalkov, R. V. Scolozdra and Yu. V. Stadnik, Fiz. Nizk. Temp. **12**, 498 (1987).

7. P. G. Klemens in *Proc. Phys. Soc. (London) A* **68**, 1113 (1955).

8. C. Uher, J. Yang, S. Hu, D. T. Morelli, and G. P. Meisner, (submitted to Phys. Rev. B).

9. C. Uher, S. Hu, J. Yang, G. P. Meisner, and D. T. Morelli, in *Proc. XVI Int. Conf. On Thermoelectrics* (in press).

10. V.M. Browning (unpublished results).

11. F. G. Aliev, N. B. Brandt, V. V. Kozyrkov, V. V. Moshchalkov. R. V. Scolozdra, Yu. V. Stadnyk, and V. V. Pecharskii, Pis'ma v Zh. Eksp. Teor. Fiz. **45**, 535 (1987).

12. R. J. Buist in *CRC Handbook of Thermoelectrics* , edited by D. M. Rowe (CRC Press, Boca Raton, 1995) p. 143.

13. S. Ögut and K. M. Rabe, Phys. Rev. B **51**, 10443 (1995).

14. K. E. H. M. Hannssen and P. E. Mijnarends, Phys. Rev. B **34**, 5009 (1986).

Thermoelectric Properties of the AlPdMn Quasicrystalline System

A. L. POPE[1], T. M. TRITT[1,2], M. CHERNIKOV[3], M. FEUERBACHER[3], S. LEGAULT[4], R. GAGNON[4], J. STROM-OLSEN[4]
1. Department of Physics and Astronomy, Clemson University, Clemson, SC 29634 USA
2. Materials Science and Engineering Department, Clemson University, Clemson, SC
3. Institut fuer Mikrostrukturforschung, Forschungszentrum Juelich GMBH, D-52425 Juelich, Germany
4. McGill University

ABSTRACT

We have begun a systematic investigation the electrical transport properties of the AlPdMn quasicrystalline system. Resistivity and thermopower measurements have been performed over a temperature range between 5K and 320K. In the pure, single phase $Al_{70}Pd_{20}Mn_{10}$ we have observed thermopowers as high as +80 μV/K around room temperature with resistivities of 1.5 mΩ-cm. Thermal conductivity measurements have been performed yielding values less than 2 W/m-K for all the samples investigated to date. We will discuss how the thermopower and resistivity vary as a result of differing sample composition as well as different processing and annealing conditions. Several different preparation techniques have been employed to further understand how various factors affect the thermal and electrical properties of this quasicrystalline system and how these may be adjusted to optimize these materials for possible thermoelectric applications.

INTRODUCTION

Renewed interest in thermoelectrics for refrigeration and power generation applications demand that new and novel materials be investigated in order to find materials that have higher efficiency and/or operate over a specific temperature range. For a material to be a good candidate for a thermoelectric, it must posses a high figure of merit, Z, where $ZT=S^2\sigma T/\lambda$. Here S is the Seebeck coefficient or thermopower, σ is the electrical conductivity, λ is the thermal conductivity, and T is temperature. The thermal conductivity consists of two parts, the electronic and lattice thermal conductivity, λ_E and λ_L respectively. In order to optimize a given system of materials, the thermal conductivity must be minimized while maximizing the thermopower and electrical conductivity.

The most promising materials for thermoelectric applications are typically semiconductors with carrier concentrations around 10^{19} carriers/cm^3. High mobility carriers are desirable to maximize the electrical conductivity for a given carrier concentration. Thermal conductivity is directly proportional to the electrical conductivity through the Wiederman-Franz law ($\lambda_E/\sigma=L_oT$, L_o=Lorentz number ($L_o \approx 2.45 \times 10^{-8}$ V^2/K^2)), making one parameter difficult to optimize without affecting the other. In order to optimize both properties, the phonon or lattice contribution of the thermal conductivity needs to be minimized. This can be facilitated by having complex unit cells that are large in size, with heavy atoms, thus enhancing the phonon scattering. Slack suggested that the best thermoelectric material would behave as a "phonon-glass, electron-crystal."[1] This material would have thermal properties of a glass and electrical properties of a crystal.

Mat. Res. Soc. Symp. Proc. Vol. 545 © 1999 Materials Research Society

We have identified a somewhat non-traditional system of materials that is of interest for thermoelectric applications; quasicrystals. Discovered in 1984 by Shechtman, Blech, Gratias, and Cahn, these materials display a forbidden 5, 8, 10, or 12-fold symmetry.[2] Quasicrystals have long range positional order but do not exhibit long range translational or rotational order. The long range positional order is evident from the sharp Bragg diffraction peaks in these quasicrystalline materials. Quasicrystals are argued to be grown by local matching rules. Even with their forbidden symmetry, many quasicrystals are able to exist as stable compounds. Quasicrystals possess properties of both amorphous materials as well as crystals[3]. Multidomain quasicrystals exhibit the low thermal conductivity that is observed in amorphous materials.[4]

The icosahedral phase is the largest stable group of quasicrystals, having about 60 members. Of these members, 12 can be grown into single phase crystals large enough to be able to perform extensive transport measurements. With their atypical symmetry and structure, quasicrystals have been a "crystallographer's dream" with much work being done to structurally characterize these materials and consequently, not much work has been done on the electrical and transport properties of these materials. Temperature dependence on resistivity appears to be governed by weak localization and electron interaction effects. The electrical resistivity in these systems is observed to increase as the quasicrystalline perfection increases, completely contrary to Matthiessen's rule (electrical resistivity increases as impurities increase)[5]. It is also interesting to note that the electrical conductivity in these systems increases to the highest temperatures of measurement ($T \approx 1000K$)[6].

Quasicrystals are also observed to be very sensitive to composition. Small changes in quality or preparation of samples can greatly affect the thermal and electrical properties of these materials. One of the most promising properties of the quasicrystals for thermoelectrics is the fact that they have intrinsically low thermal conductivities which are essentially sample independent. Quasicrystals have been observed to have structural coherence up to 8000 angstroms, giving AlPdMn the large until cell desirable for low thermal conductivity.[7] In many ways, quasicrystals can be viewed as Slack's "phonon-glass, electron-crystal."

Several stable quasicrystalline systems were examined and the AlPdMn system was determined to be the most promising system. Thermal conductivity in the AlPdMn system has been observed to be low for all samples observed.[8] In the pure, single phase $Al_{70.8}Pd_{20.9}Mn_{8.3}$ system we have observed thermopowers as high as +80 μV/K at room temperature with resistivities of 1.5 mΩ-cm. The corresponding thermal conductivity was approximately 1.8 W/m-K at room temperature.

RESULTS AND DISCUSSION

Quasicrystal samples measured have typical sizes of 10 x 2 x 3 mm^3. Resistance, thermopower, heat capacity and hall measurements have been made on these samples. Experimental procedures for these measurements can be found in a paper by Tritt et. al.[9]

We have measured additional quasicrystalline systems[10,11] and have determined that the properties of the AlPdMn system indicate it to be the most promising system at this time. Thus, with the determination of AlPdMn as a promising system for thermoelectric investigation, we have set out to characterize the thermal and electrical transport properties in this system in a very thorough and systematic manner.

Quasicrystals are made using high purity elements to prepare samples, the elements are melted under a high vacuum using clean RF heating techniques. The samples are then treated and annealed under vacuum. In order to make conclusive arguments, only samples from the same batch should be used. It has been observed that in quasicrystalline systems, samples may differ in resistivity and conductivity significantly from batch to batch as shown in Figure 1. It is important to note that these two samples were prepared at the same facility, by the same person, with the same preparation technique, yet thermopower and electrical conductivity vary substantially. Therefore, it is imperative that measurements be made consistently on the same sample and that only samples from the same batch or ingot are compared in absolute terms. Trends may be considered from batch to batch, however.

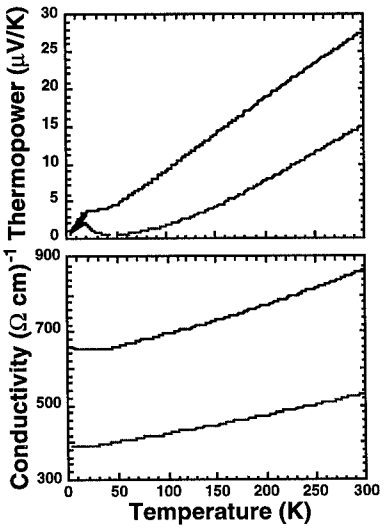

Figure 1: Differences in resistivity and thermopower of as grown $Al_{70}Pd_{22.5}Mn_{7.5}$ samples from different batches.

The electrical properties of the $Al_{70}Pd_{22.5}Mn_{7.5}$ quasicrystals are shown in Figure 1. This is the most well formed quasicrystalline material in the AlPdMn system[12]. Thermopower in the $Al_{70}Pd_{22.5}Mn_{7.5}$ samples range between 15 and 30 μV/K. Electrical conductivity in both samples QC-A and QC-B decreases slightly as temperature increases from 10K to approximately 20 K where the electrical conductivity begins to increase again. The electrical conductivity continues to increase monotonically with temperature to the highest temperatures that we have measured (≈ 320K). These quasicrystals have resistivity or electrical conductivity values typical of a dirty metal. The thermopower of sample QC-A is a diffusion type thermopower that has a small phonon drag peak at 30K. QC-B, although grown under identical conditions, does not display the same type of behavior. Thermopower decreases with temperature and looks as if it will cross zero when a phonon drag peak pushes the thermopower again above zero. It must also be noted that, counterintuitively, the highest thermopower corresponds to the highest electrical conductivity.

Possible reasons for the large variation in transport properties from sample to sample might be due to the presence of small cracks and voids in the samples. This would explain a difference in conductivity, but should not have such a dramatic effect on the thermopower. Another possible reason for variations in thermopower and conductivity might be due to the melting of the synthesizing elements. Each time a reaction is run a certain percentage of the elements are lost. We could be looking at samples with slightly

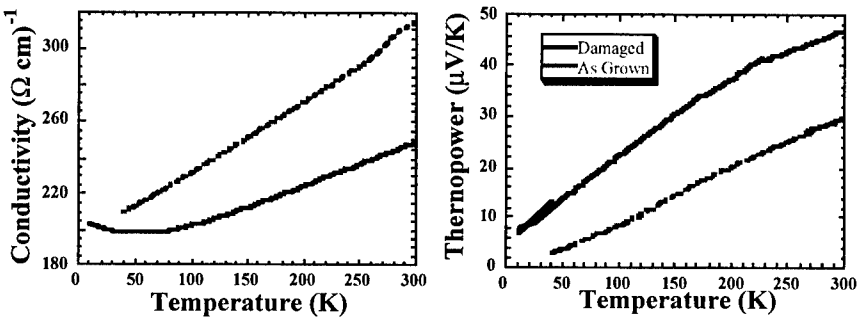

Figure 2: Electrical conductivity and thermopower as a function of temperature for two AlPdMn samples with different growth conditions.

differing composition. It is seen in the literature that small changes in composition can lead to large changes in the transport properties[5]. Elemental analysis and SEM micrograph studies are planned for the near future to investigate and quantify these possibilities.

Due to the variability in samples resulting solely from sample preparation, we have investigated samples with changes in the mechanical processing as well as changes in preparation technique. In the first batch of samples, an AlPdMn ingot was grown and two samples were cut from this ingot. The samples are approximately 1 x 2 x 10 mm^3. The first was left as grown while the second was mechanically damaged. SEM measurements have not yet been performed, therefore we can not quantify the damage on this sample. In Figure 2, we show the electrical conductivity and thermopower of these materials as a function of temperature.

In these samples it is seen that the thermopower and electrical conductivity correspond to each other in the more traditional manner, i. e., the thermopower increases as the sample is damaged while the electrical conductivity decreases, as one would normally expect. This is typical of what one would observe in a material, a high thermopower corresponding to a low electrical conductivity or vice versa. Once mechanically damaged, samples tend to behave like traditional materials. Electrical conductivity is seen to decrease with increasing damage.

The sensitivity of quasicrystals to growth conditions is also seen in the annealing conditions induced on a sample. Another ingot was grown and from this ingot three samples were cut. These samples had dimensions of 2 x3 x 12 m^{m3}. The first sample was annealed for 3 hours in an 800K furnace and then quenched, causing many defects and possible multiple phases to be frozen in. The second sample was annealed for 12 hours at 800K and then furnace cooled, resulting in a high quality crystal with few defects. The final sample was annealed for three hours at 800K and then furnace cooled, resulting in a good quality sample. It is apparent in Figure 3, that as temperature increases the electrical conductivity falls until approximately 40K where it begins to increase linearly with temperature as was seen before. The electrical conductivity versus temperature curves have

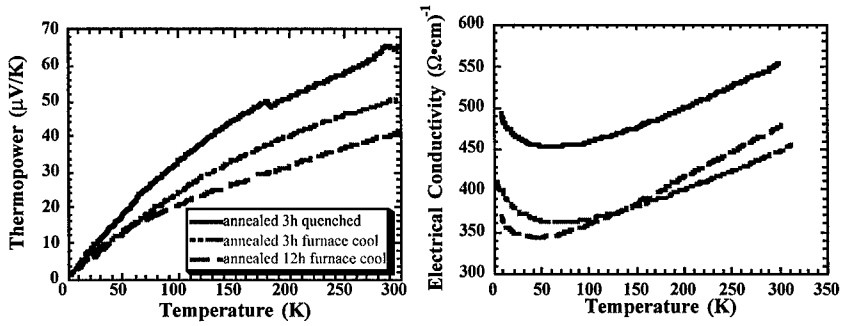

Figure 3: Electrical conductivity and thermopower as a function of temperature for three $Al_{70}Pd_{20}Mn_{10}$ samples (cut from the same ingot) prepared under different annealing conditions.

basically the same shape. Thermopower in this system is observed to monotonically decrease ($S \approx 30 - 60$ μV/K at 300 K) as the temperature decreases from 300 K to $S \approx 0$ at the lowest temperatures.

The electrical conductivity values in the furnace cooled samples are comparable to each other, never deviating from one another by more than 10%. There is a 20% increase in thermopower from the sample that was furnace cooled 12 hours, to the sample that was furnace cooled 3 hours. The sample cooled for three hours corresponds to the sample with the greatest number of defects. The electrical conductivity of the quenched AlPdMn sample overall increases by 15%. This is in direct contradiction to what one would expect from Matthiessen's rule, which predicts that with the addition of impurities or defects the conductivity in a material will decrease. Interestingly enough, we again observe that the highest electrical conductivity once again corresponds to the highest thermopower, which of course is very favorable result relative to the potential of these materials for thermoelectric applications.

With systematic changes in the electrical conductivity the question naturally arises: what happens to the thermal conductivity in these materials? Our measurements show, as seen in Figure 4, that the thermal conductivity in these systems is relatively independent of sample processing. Thermal conductivity in these systems is seen to decrease with decreasing temperature until a shallow minimum and then a peak is seen at 30K. This shallow minimum or plateau is typical of the thermal conductivity of glass-like materials. Thermal conductivity values in the $Al_{70}Pd_{20}Mn_{10}$ system are observed to be between 1 to 3 W/m-K for all the different types of annealing we have currently investigated. A very interesting aspect of the thermal conductivity of these quasicrystals is the continued increase of the thermal conductivity with increasing temperature to our highest measure values. This has been observed by others.[8,13]

Hall measurements and heat capacity measurements are in progress for these quasicrytalline materials. Initial Hall data shows that these quasicrystals are a two carrier system, containing both electrons and holes. Debye temperatures obtained from low

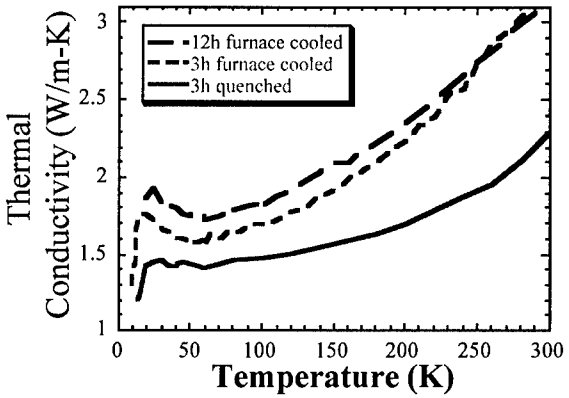

Figure 4: Thermal conductivity in the $Al_{70}Pd_{20}Mn_{10}$ system is observed to be between 1 to 3 W/m-K.

temperature heat capacity data measured on small portions of the ingots with different annealing conditions for these materials (as shown in Table 1) are all around 455K. Thermal conductivity is related to the Debye temperature by

$$\lambda = \frac{k_B{}^3 \Theta_D{}^2}{\pi \hbar^2 v_s}.$$

where θ_D is the Debye temperature, k_B is the Boltzmann constant, h= Planck constant and v_S is the velocity of sound in the material. The Debye temperatures around 455K are somewhat unexpected since these Debye temperatures would indicate a rather high thermal conductivity which is not observed in these materials.

Table 1: Gamma and Debye Temperatures for AlPdMn quasicrystalline samples with different annealing conditions.

Sample	Gamma(mJ/mol-K^2)	Debye Temperature (K)
annealed 12 hours furnace cool	1.68	453.7
annealed 3 hours furnace cool	1.51	449.5
annealed 3 hours quenched	1.59	464.5

SUMMARY

The AlPdMn quasicrystalline system is of interest to thermoelectrics. Counterintuitively, electrical conductivity and thermopower appear to increase together in most of these materials. Interestingly, they appear to increase as disorder increases. Thermal conductivity in these systems remains between 1 to 3 W/m-K despite compositional or annealing changes. Quasicrystalline materials are not well characterized

in terms of electrical and thermal transport , but results indicate that they have untraditional relations between electrical conductivity and thermopower. With the coupling of increase in conductivity and thermopower, the numerator of ZT increases while the denominator (thermal conductivity) remains essentially unchanged. These materials closely match the idea that a good thermoelectric should be a glass-like material in relation to the phonons and a metal in relation to the electronic transport. AlPdMn quasicrystals have thermal conductivity that closely resembles that of an amorphous solid. The tunability in the electrical conductivity and thermopower allows for many compositional, impurity, damage, and additional element studies to be performed in an effort to better understand the transport in this system and optimize the figure of merit for potential thermoelectric application. Obviously, much more work needs to be done to really address the feasibility of these materials for thermoelectric applications. However, along the way much information related to the interplay of many of the parameters to the electrical and thermal transport in these systems will be gained. Thus, a more fundamental understanding of the electrical and thermal transport mechanisms related to the quasicrystalline materials may become evident.

ACKNOWLEDGMENTS

We acknowledge support for this work from the Office of Naval Research, the Army Research Office and DARPA: (ONR #N00014-98-0271 and ONR/DARPA #N00014-98-0444 and from ARO/DARPA #DAAG55-97-0-0267). One of us (AJP) acknowledges Clemson University for partial financial support through the Dean's Scholars Award Program. We would also like to acknowledge Matt Marone his contribution to the thermal conductivity apparatus.

REFERENCES:

[1] G. A. Slack, in CRC Handbook of Thermoelectrics, Rowe ed (1995), ref.2,p 407
[2] D. Shechtman, I. Blech, D. Gratias and J.W. Cahn: Phys. Rev. Lett. **53** (1984) 1951.
[3] C. Janot, *Quasicrystals*, Claredon Press, Oxford (1994).
[4] A. Perrot, J.M. Duboise, M. Cassart and J.P. Issi, Proceesings of the 5th International Conference on Quasicrystals, World Scientific, (1995) 588.
[5] S. J. Poon, Adv. Phys. **41** (1992) 303.
[6] D. Mayou, C. Berger, F. Cyrot-Lackmann, T. Klein, and P. Lanco Phys. Rev. Lett. **25** (1993) 3915.
[7] P. A. Bancel, Quasicrystals: The State of Art World Scientific, Singapore (1991)
[8] M. A. Chernikov, A. Bianchi, H. R. Ott, Phys. Rev. B **51** (1995) 153.
[9] T. M. Tritt, A. L. Pope, M. Chernikov, M. Feuerbacher, S. Legault, R. Gagnon, J. Strom-Olsen, Quasicrystals, 1998 MRS proceedings
[10] T. M. Tritt, A.L. Pope in progress
[11] M. L. Wilson, S. Legault, R. M. Stroud and T. M. Tritt, *Thermoelectric Materials, New Directions and Appraoches*, MRS Volume **478**, edited by T. M. Tritt, M. Kanatzidis, H. B. Lyon and G. Mahan, p321(1997)
[12] Terry M. Tritt, M. L. Wilson, A. L. Johnson (Pope), S. Legault and R. M. Stroud Proceedings of ICT-16, IEEE Press, p455 (1997)
[13] Private Communication: Joe Poon, University of Virginia
[14] S. LeGault, B. Ellman, J.O. Strom-Olsen, L. Taillefer, S. Kycia, T. Lograsso, D. Delaney, New Horizons in Quasicrystals, World Scientific Press, p 224, edited by A. I. Goldman (1997).

OBSERVED PROPERTIES AND ELECTRONIC STRUCTURE OF RNiSb COMPOUNDS (R = Ho, Er, Tm, Yb and Y). POTENTIAL THERMOELECTRIC MATERIALS

S. Sportouch*, P. Larson+, M. Bastea#, P. Brazis†, J. Ireland†, C.R. Kannewurf†, S. D. Mahanti+, C. Uher# and M. G. Kanatzidis*

*Department of Chemistry, Michigan State University, East Lansing, MI 48824

+ Department of Physics and Astronomy, Michigan State University, MI 48824

† Department of Electrical Engineering and Computer Science, Northwestern University, Evanston, IL 60208

Department of Physics, University of Michigan, Ann Arbor, MI 48190-1120

ABSTRACT

The RNiSb compounds (R=Ho, Er, Tm, Yb and Y) and some selected solid solution members such as $(Zr_{1-x}Er_x)Ni(Sn_{1-x}Sb_x)$ and $ErNiSb_{1-x}Pn_x$ (Pn=As, Sb, Bi) have been studied. They all crystallize in the MgAgAs structure type, which can be considered as a NaCl structure type in which half of the interstitial tetrahedral sites are occupied by Ni atoms. The measured values of the Seebeck coefficients, at room temperature, are positive for RNiSb (R=Ho, Er, Yb and Y) compounds and $ErNiSb_{1-x}Pn_x$ (Pn=As, Sb, Bi) solid solutions, but for $(Zr_{1-x}Er_x)Ni(Sn_{1-x}Sb_x)$ members vary from negative to positive values when $0 < x < 1$. Some of these compounds show metallic conductivity while others exhibit thermally activated charge transport. Solid solutions of these materials have lower thermal conductivities than the pure members, RNiSb (R=Ho, Er, Yb and Y) and ZrNiSn. The electronic structures of RNiSb compounds, where R is Y, La, Lu, and Yb, have been studied with density functional theory. The results of the calculations for these systems, except for the Yb compound, indicate narrow gap semiconductors with large effective masses near the conduction band extrema. The Yb system is expected to show heavy fermion characteristics.

INTRODUCTION

In the last several years, a revival to improve thermoelectric materials has occurred which is motivated by the latest technological needs. One of the classes of compounds which has attracted a great deal of attention adopts the MgAgAs structure type. A few years ago the ternary intermetallic compounds MNiSn (M= Ti, Zr, Hf, U, Th) were reported to exhibit unusual transport properties for semiconductors. Indeed, they were later established to be narrow gap semiconductors.[1-3] A remarkable feature of these materials is that, despite the fact that they are composed of only metallic elements, they are semiconductors. Another particularly interesting class of compounds is that of RNiPn compounds, where R is a trivalent electropositive element and Pn is a pnictogen element, and various derivatives thereof, such as RNiSb (R=Y, Gd, Yb, Lu)[4-6]; and YbPtBi.[7,8] These compounds are isostructural and isoelectronic to the MNiSn[1-3] and, in this respect, the study of these materials represents a logical new direction for thermoelectric investigations. Some of these systems show heavy fermion characteristics[7,8], while others are reported as promising candidates for high performance thermoelectric materials. In this paper we will use the electronic structure calculations as a discriminating guide for experiments in order to better identify potential candidates for thermoelectric applications.

Mat. Res. Soc. Symp. Proc. Vol. 545 © 1999 Materials Research Society

CRYSTAL STRUCTURE

RNiPn compounds formed with light rare earth elements (R) crystallize with a hexagonal ZrBeSi structure type[10] (Space group: P 6_3/mmc) whereas those with yttrium and heavy rare earths crystallize in the cubic MgAgAs structure type (Space group: F $\bar{4}$3m), see Figure 1.

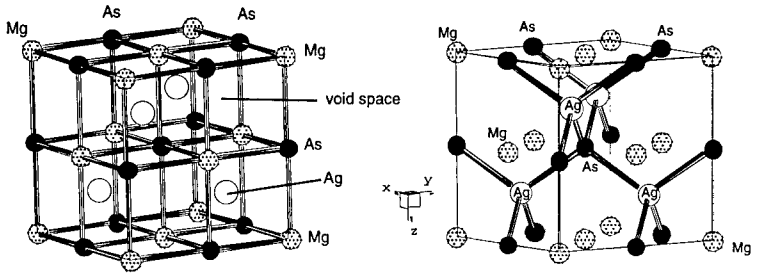

Figure 1 : Two different views of the same cubic structure of MgAgAs. Left : Ag atoms inserted in a MgAs NaCl-type lattice. Right : Mg atoms inserted in a AgAs ZnS-type lattice.

The electropositive metals (R) occupy the Mg sites while the Pn occupies the As site and the tetrahedral Ag site is occupied by Ni. This structure can be described as a filled MgAs, NaCl structure-type, in which Ag atoms are inserted in half of the tetrahedral holes in the lattice. In this description, the compounds can be viewed as complexes of guest Ni atoms in the host $R^{3+}Pn^{3-}$ lattice. The Ni atoms occupy the centers of cubes formed by four R and four Pn atoms. Actually, there are two such cube-center positions that the Ni atoms can occupy, but in the RNiPn compounds, the Ni atoms occupy only one of the cube-center positions. In these systems each Ni atom bonds with four R and four Pn nearest neighbor atoms. Therefore, such a structure allows much flexibility, giving to the chemist a large field of investigation involving substitutions of atoms, non-stoichiometric compounds, solid solutions and doped compounds in order to optimize their properties for high thermoelectric performance.

SYNTHESIS, CHARACTERIZATION AND PROPERTIES

In this work, RNiSb members where R=Ho, Er, Tm, Yb, Y and selected solid solutions $(Zr_{1-x}Er_x)$ Ni $(Sn_{1-x}Sb_x)$ with x=0, 0.25 and 0.75, and $ErNiSb_{1-x}Pn_x$ with (Pn=As, Bi ; x=0.2, 0.6) have been synthesized. The synthesis of these compounds[10-12] was accomplished by direct combination of the elements or by insertion of Ni atoms into the binary RSb using the arc melting method and then annealing at 900°C under static vacuum for one week. Out of all the methods that were attempted, the arc melting technique proved the most successful in synthesizing these materials. The main drawback of the arc welding method, however, is the loss of volatile elements during the process. This could lead to non-stoichiometry which could greatly affect the electrical properties of these materials. The use of binaries minimizes these losses to about 6% of the total weight.

(a) RNiSb (R=Ho, Er, Tm, Yb, Y).

The cubic cell parameters of the RNiSb compounds, reported in Table I, were refined[13] using the experimental X-ray diffraction powder patterns (Figure 2) and are in good agreement with the literature.[10-12] The differential thermal analysis of the pure members of this family of compounds shows that they do not melt below 950°C and indicate no phase transition.

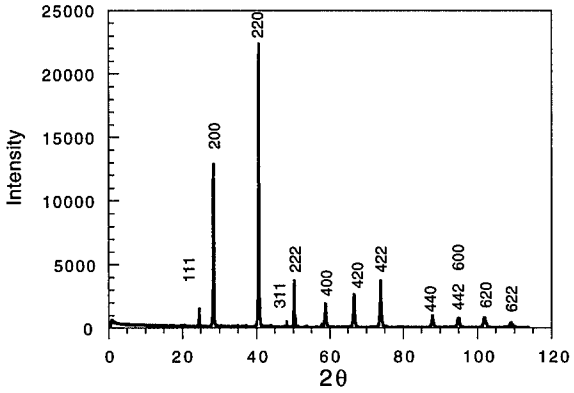

Figure 2 : Experimental X-ray powder diffraction pattern of the ErNiSb compound.

Table I. Cell parameters observed in RNiSb compounds and their corresponding observed band gaps. (RT: room temperature)

Compounds	Cell Parameters (Å)	Observed Band Gaps (eV)	Power factors at RT (mW/K^2m)
HoNiSb	6.2655 (9)	~ 0.09	0.231
ErNiSb	6.2730 (9)	~ 0.08	0.896
TmNiSb	6.2524 (7)	-------	0.095
YbNiSb	6.2337 (5)	~ 0.08	0.097
YNiSb	6.2480 (6)	~ 0.09	0.201
ZrNiSn	6.1199 (9)	~ 0.20	3.150
$(ZrEr)_{0.75}Ni(SbSn)_{0.25}$	6.1612 (9)	------	0.300
$(ZrEr)_{0.25}Ni(SbSn)_{0.75}$	6.2551 (9)	~ 0.10	0.011
$ErNiSb_{0.8}Bi_{0.2}$	6.2650 (9)	~ 0.10	0.090
$ErNiSb_{0.4}Bi_{0.6}$	6.2987 (5)	~ 0.10	0.005
$ErNiSb_{0.8}As_{0.2}$	6.2436 (9)	-------	0.002

The electrical conductivity (σ) data, shown in Figure 3, exhibit, for all the samples, semimetallic or metallic behavior and the room temperature (RT) values of σ are higher than what is seen in Bi_2Te_3 (~ 890 S/cm at RT). The observed values for the Ho, Yb and Y compounds are in a range of 1390 to 2200 S/cm (at RT), much closer to that of a metallic compound. These observations, except for the YNiSb compound, are in disagreement with band gap measurements and with the electronic band structure which predict semiconductor behavior. On the contrary, for the Tm and Er samples, the σ values are 10 times lower, 265 and 350 S/cm (at RT) respectively. The band gaps for the Ho, Er, Yb and Y compounds are less than 0.1 eV (see Table I), while for the Tm compound we were unable to observe a band gap in the mid-IR range. This may be due to

the fact that this band gap is smaller than the limit of our instrument, or the compound is grossly non-stoichiometric.

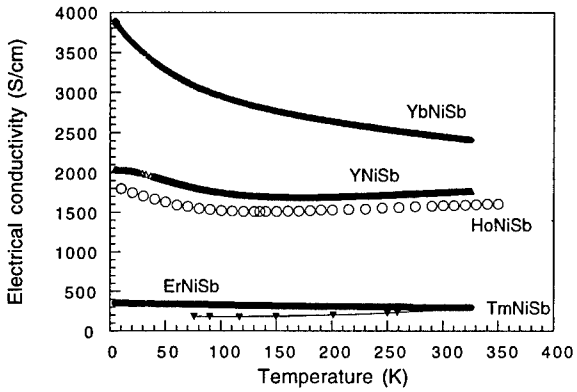

Figure 3 : Electrical conductivity as a function of the temperature for ingot samples HoNiSb, ErNiSb, TmNiSb, YbNiSb and YNiSb compounds.

Thermopower (S) was measured as a function of temperature on the same samples used for electrical measurements. Most of the p-type thermoelectric behaviors show weak Seebeck coefficients. The RT values are 38 μV/K, 60 μV/K, 21 μV/K and 38 μV/K for Ho, Tm, Yb, and Y compounds respectively, whereas the value for the ErNiSb compound is 160 μV/K, see Figure 4. As explained later in this paper, these low values for S are consistent with the low calculated effective masses of the p-doped RNiSb samples[14]; we expect higher thermopower values for the n-doped samples. In addition, the YbNiSb compound is predicted to be a heavy-fermion system with the Fermi energy pinned near the Yb f-levels.

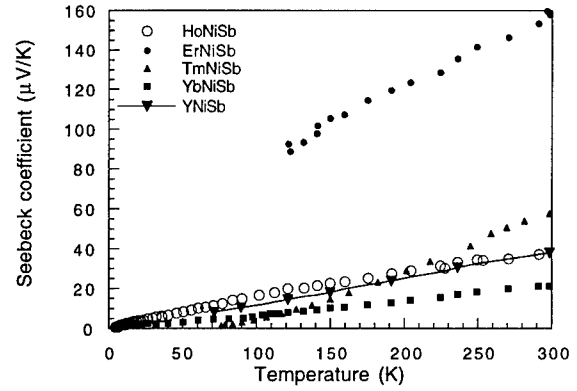

Figure 4 : Thermopower versus temperature for ingot samples of HoNiSb, ErNiSb, TmNiSb, YbNiSb and YNiSb compounds.

The temperature dependence of the thermal conductivity (κ) is shown in Figure 5. They are in the range of 3-8 W/mK (5.6 W/mK, 7.5 W/mK, 2.8 W/mK, 4.4 W/mK and 6.1 W/mK for the Ho, Er, Tm, Yb and Y compounds respectively, at RT). It is encouraging that this range of thermal conductivities is rather low for such a simple structure type, although they are still higher than Bi_2Te_3 (1.4-1.6 W/mK, at RT). We expect to be able to decrease further the total κ by alloying two or more isostructural ternary compounds which will reduce the phonon mean free path.

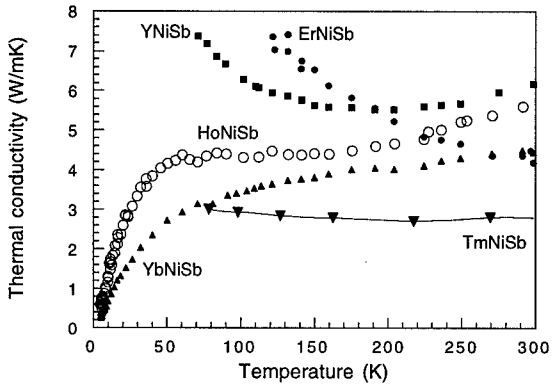

Figure 5 : Thermal conductivity of ingot samples of HoNiSb, ErNiSb, TmNiSb, YbNiSb and YNiSb.

The carrier densities for some of these samples were determined from Hall effect measurements[15], see Figure 6. For the Ho, Er and Tm members the density of carriers at RT is $2.60x10^{20}$ cm^{-3}, $2.25x10^{19}$ cm^{-3} and $1.90x10^{20}$ cm^{-3} respectively. In this magnitude range, the

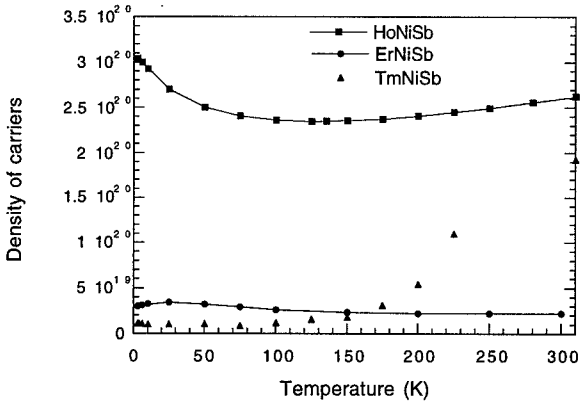

Figure 6 : Carrier density as a function of the temperature as determined from Hall measurements for ingot samples of HoNiSb, ErNiSb, TmNiSb compounds.

contribution of the phonons to κ is usually much lower than the contribution due to the carriers. The very high number of carriers (about $2x10^{20}$ cm^{-3}) could be due to the presence of a considerable degree of non-stoichiometry arising from a still unoptimized synthetic technique. Improvements in the syntheses of these compounds are expected to yield materials with a more controlled carrier density.

The power factor $S^2\sigma$ was calculated for RT values and reported in Table I. Comparison of these values to the room temperature power factor for Bi_2Te_3 (3.92 mW/K^2m) shows that the RNiSb compounds have not yet been optimized for thermoelectric applications. The power factor for the Er compound (0.896 mW/K^2m) is the largest among the systems studied. However, the values for the HoNiSb and the YNiSb systems are reasonable, 0.231 mW/K^2m and 0.201 mW/K^2m respectively, and it may be possible to improve them. Indeed, we expect that reducing the number of carriers in the Ho sample, which possesses a high σ and a low κ, will improve the power factor.

In order to improve their transport properties, we investigated some derivatives, such as ErNiAs, ErNiBi and their solid solutions, as well as solid solutions of ErNiSb with ZrNiSn.

(b) Solid solutions $(Zr_{1-x}Er_x)$ Ni $(Sn_{1-x}Sb_x)$

One of the more promising new thermoelectric compounds possessing the same structure type as RNiSb is ZrNiSn. [1d, 16, 17] Thus, we decided to study solid solutions of the type ErNiSb/ZrNiSn. We prepared ErNiSb; $(Zr_{0.75}Er_{0.25})Ni(Sn_{0.75}Sb_{0.25})$; $(Zr_{0.25}Er_{0.75})Ni(Sn_{0.25}Sb_{0.75})$; and ZrNiSn. Their corresponding cell parameters are reported in Table I. The dependence of the cell parameters as a function of the composition x follows Vegard's law, indicating that indeed we have prepared solid solution compounds.

The band gap of the ZrNiSn determined from the IR diffuse reflectance spectrum is about 0.2 eV, which agrees well with the literature data[17]. The solid solution members possess a band gap in between the end-members (i.e.: ~0.08-0.2 eV), see Table I.

The σ, Figure 7, shows that the solid solutions exhibit electrical conductivities in the range of 1000 - 2050 S/cm at room temperature. Electrical conductivity versus temperature, however, follows a weak temperature dependence and in some samples is slightly thermally activated.

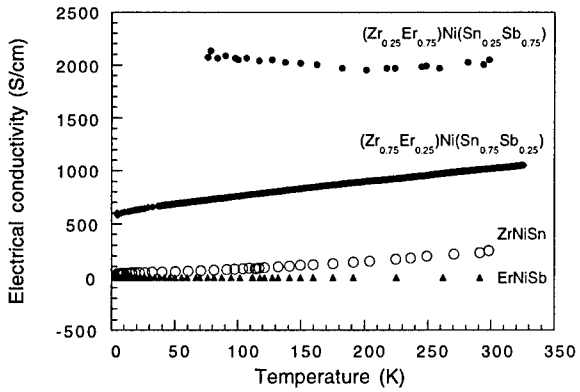

Figure 7 : Electrical conductivity for the solid solutions $(Zr_{1-x}Er_x)Ni(Sn_{1-x}Sb_x)$, where x=0, 0.25, 0.75 and 1. Samples are polycrystalline ingots.

As shown in Figure 8, some samples exhibit negative thermopower values while others possess positive values. The value of S varies from -355 μV/K to +160 μV/K. In fact, the $(Zr_{0.75}Er_{0.25})Ni(Sn_{0.75}Sb_{0.25})$ compound, which has a composition close to ZrNiSn, exhibits a negative thermopower while $(Zr_{0.25}Er_{0.75})Ni(Sn_{0.25}Sb_{0.75})$, which is closer to ErNiSb, shows a positive thermopower. In addition, it is interesting to point out that the low values of thermopower observed (-50 μV/K for $(Zr_{0.75}Er_{0.25})Ni(Sn_{0.75}Sb_{0.25})$ and 7.5 μV/K for $(Zr_{0.25}Er_{0.75})Ni\ (Sn_{0.25}Sb_{0.75})$, at RT) for the solid solutions are almost a stoichiometric average of the values obtained for the extreme end-members.

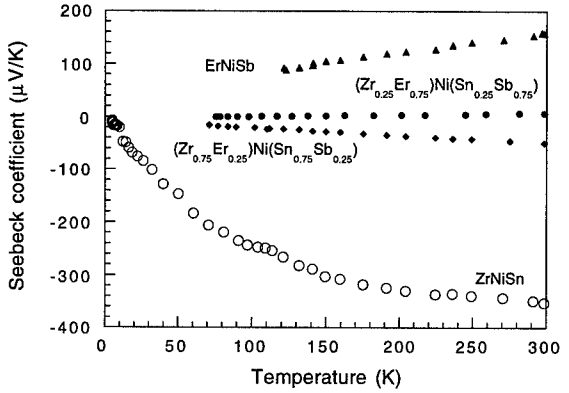

Figure 8 : Variations of the Seebeck coefficient for polycrystalline ingots of $(Zr_{1-x}Er_x)Ni(Sn_{1-x}Sb_x)$ solid solution members.

The κ values for the solid solution members, Figure 9, are 5.7 W/Km and 3.1 W/Km (at RT) for $(Zr_{0.75}Er_{0.25})Ni(Sn_{0.75}Sb_{0.25})$ and $(Zr_{0.25}Er_{0.75})Ni(Sn_{0.25}Sb_{0.75})$ respectively, which is lower

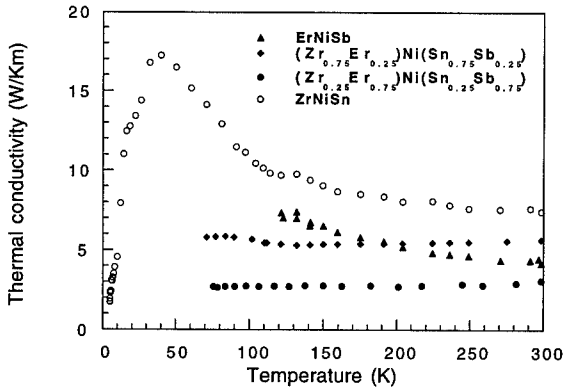

Figure 9 : Thermal conductivity of $(Zr_{1-x}Er_x)Ni(Sn_{1-x}Sb_x)$ solid solution members.

than that for the pure members, about 7.5 W/Km. Thus, alloying decreases κ as expected by increasing the disorder in the structure with decreases in the range from 24% to 59% compared to the end-members.

It appears that in these materials, when n-type and p-type conductors are combined, the solid solutions possess the average properties of their end-members. Therefore, we will aim to combine semiconductors of the same type. This is a primary reason for synthesizing n-doped RNiSb compounds.

(c) Solid solutions $ErNiSb_{1-x}Pn_x$ (Pn=As, Bi)

The partial substitution of Sb atoms by Bi and As atoms was examined for x = 0.2 and 0.6. Preliminary results are displayed in Figures 10, 11 and 12. The electrical conductivity

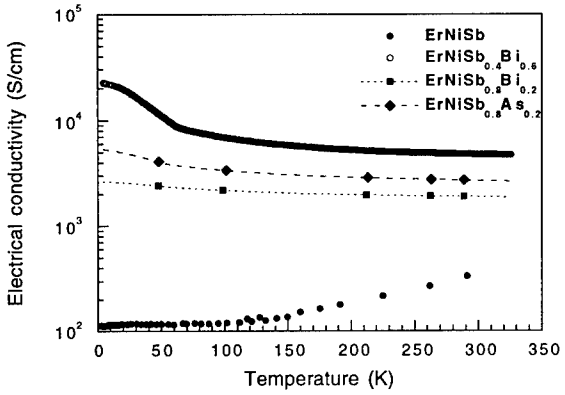

Figure 10 : Electrical conductivity for $ErNiSb_{1-x}Pn_x$ solid solution.

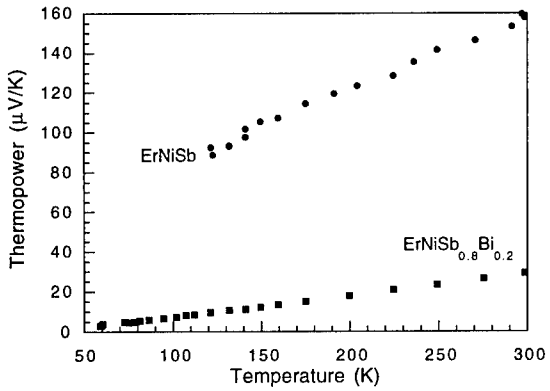

Figure 11 : Thermopower as a function of the temperature. Comparison between ErNiSb and $ErNiSb_{0.8}Bi_{0.2}$.

measurements showed that the solid solution members possess a room temperature σ in the metal range (2100 S/cm, 5130 S/cm and 3700 S/cm for $ErNiSb_{0.8}Bi_{0.2}$, $ErNiSb_{0.4}Bi_{0.6}$ and $ErNiSb_{0.8}As_{0.2}$ respectively, Figure 10). The electrical conductivity values of the substituted members are 10 times higher than that of the pure compound ErNiSb, suggesting a drastic increase of the number of carriers. Nevertheless, the temperature dependence is still of the semiconductor type. The fact, that the solid solution samples $ErNiSb_{1-x}Pn_x$ are nearly metallic is disappointing. Especially for $ErNiSb_{0.8}As_{0.2}$ since the end-member ErNiAs is predicted by theory to have a larger indirect band gap than ErNiSb. We believe that we are probably dealing with highly defected samples with considerable deviations from the 1:1:1 stoichiometry. We expect that improved synthetic procedures will lead to ameliorated samples whose properties will be closer to those expected from semiconductors.

On the other hand, the Seebeck coefficient is lower by a factor of 10 to 100. The room temperature values of Seebeck coefficient are very low, 30 μV/K, 3.3 μV/K, and 2.1 μV/K for $ErNiSb_{0.8}Bi_{0.2}$ (Figure 11), $ErNiSb_{0.8}Bi_{0.6}$ and $ErNiSb_{0.8}As_{0.2}$ respectively.

The κ values for the $ErNiSb_{0.8}Bi_{0.2}$ are reported in Figure 12, in the temperature range between 50 and 300K. κ has been reduced by 57% compared to the pure end-members and never exceeds 3.4 W/mK. Thus, the alloying method has substantially droped the contribution of the phonons to κ.

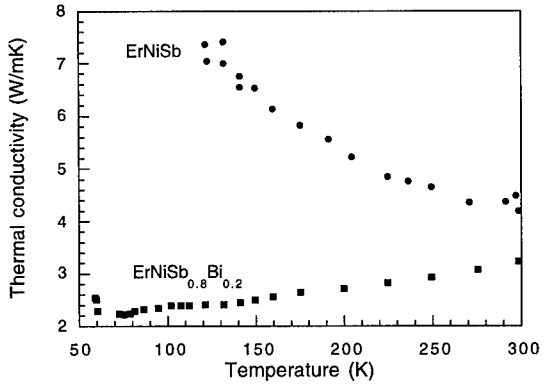

Figure 12 : Thermal conductivity versus temperature. Comparison between ErNiSb and $ErNiSb_{0.8}Bi_{0.2}$.

The metallic behavior of these solid solutions is really surprising especially because their electronic band structure calculations suggest that they have a larger indirect band gaps than ErNiSb. This may be due to the non-stoichiometric nature of the samples. For example, pnictogen or nickel vacancies in the lattice could drastically change the electronic distribution around the Fermi level, giving rise to very high carrier densities. According to the 6% weight lost during the arc melting process, there is a strong probability that the samples are far from the 1:1:1 stoichiometry. We plan to perform detailed characterization studies to address the issue of non-stoichiometry and to improve the synthetic method.

ELECTRONIC STRUCTURE CALCULATIONS

In order to understand the transport properties of the systems discussed above, we performed electronic structure calculations in several pure systems.[14] Electronic structure

calculations were performed using self-consistent full-potential linearized augmented plane-wave (LAPW) method[18] within density functional theory (DFT)[19] using the generalized gradient approximation (GGA) of Perdew, Burke, and Ernzerhof[20] for the exchange and correlation potential. The calculations were performed using the WIEN97 package.[21, 22] All the results reported in this paper include SO interaction and in Table II are given the lattice constants used in the calculations.

Table II. Lattice constants used in the calculations and estimated band gaps taken from the calculations.

System	Lattice Constant (a.u.)	Calculated Band Gap (eV)
YNiSb	11.928	0.28
LaNiSb (cubic)	12.603	0.44
LuNiSb	11.752	0.19
YbNiSb	11.788	metal (heavy fermion)
YNiAs	11.662	0.53
YNiBi	12.115	0.13

(a) YNiSb, LaNiSb (cubic), LuNiSb: Semiconductors

The band structures for YNiSb, LuNiSb and LaNiSb (hypothetical cubic) are given in Figures 13(a,b,c) respectively. As can be seen in all three cases, most of the Ni d-bands lie below

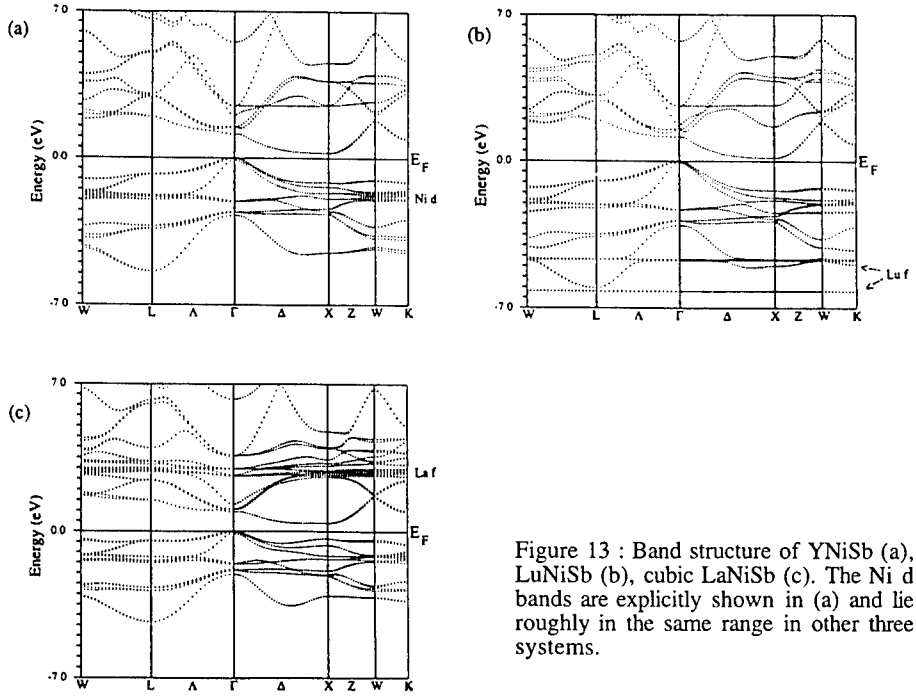

Figure 13 : Band structure of YNiSb (a), LuNiSb (b), cubic LaNiSb (c). The Ni d bands are explicitly shown in (a) and lie roughly in the same range in other three systems.

the Fermi level (about 1 to 3 eV below). However, the lowest conduction band along Γ-X-W has appreciable Ni d-character. The Ni 4s bands are found considerably above the Fermi level, making Ni an almost d^{10} system. In the absence of Ni, such as in YSb, the bottom of the Y-d band at the X point lies below the top of the Sb p-band at the Γ point, making it a metal. The Ni d-orbitals, however, strongly perturb with the R d-orbitals. This band at the X point in YSb, gets pushed sufficiently up and now lies above the Fermi energy.[14] This opens up an energy gap and makes these systems indirect narrow gap semiconductors. A similar situation also occurs in the La and Lu systems. This opening of a gap was also seen in RNiSn systems, which contain no f electrons[2]. Since the f-levels in the La and Lu systems lie more than 3 eV above and about 5 eV below the Fermi level respectively, the f-p hybridization does not significantly affect the band structure in the neighborhood of the Fermi level. Thus, the origin of the gap formation in RNiSb (R ≠ Yb) compounds is the insertion of Ni d-orbitals, as in the case of RNiSn, although the particular details differ somewhat from compound to compound.

(b) YbNiSb: Heavy Fermion Compound

The Yb atom has one hole in the f-shell and the compound is most likely a mixed-valence heavy-fermion system.[5] We are curious to see how well one could apply standard *ab initio* band-structure calculations based on density functional theory to obtain a realistic description of the electronic structure near the Fermi energy in this heavy fermion system. Similar attempts have been made successfully for the mixed-valence systems $CeRu_2Si_2$.[24] Of course, one has to be careful in comparing the results of band calculations (within DFT) with experiments for systems where the f-levels lie at the Fermi energy.

The only published electronic structure calculation for YbNiSb[4] of which we are aware was carried out at the scalar relativistic level within LDA using LMTO-ASA. However, their calculated band structure differs considerably from that of the closely related system, YbPtBi.[7] In Figures 14(a,b) we give the total density of states (TDOS) and band structure for the YbNiSb compound. The SO splitting between $f_{5/2}$ and $f_{7/2}$ levels is about 1.25 eV, in agreement with the calculations on YbPtBi.[7] Insertion of Ni in the YbSb lattice (to form YbNiSb) places the Ni d-bands below the f-levels, which get pushed up in energy. As a result, there is a partial charge flow from the Yb f-levels into the Sb p-bands. Yb f-levels become partially occupied and YbNiSb acquires a heavy fermion character much like YbPtBi. The TDOS at the Fermi Level, $N(E_F)$, is 12.6 states/eV of which 77% is of Yb f-character. The electronic structure suggests that the Yb may have a high thermopower due to the large derivative in the DOS near the Fermi level.[25]

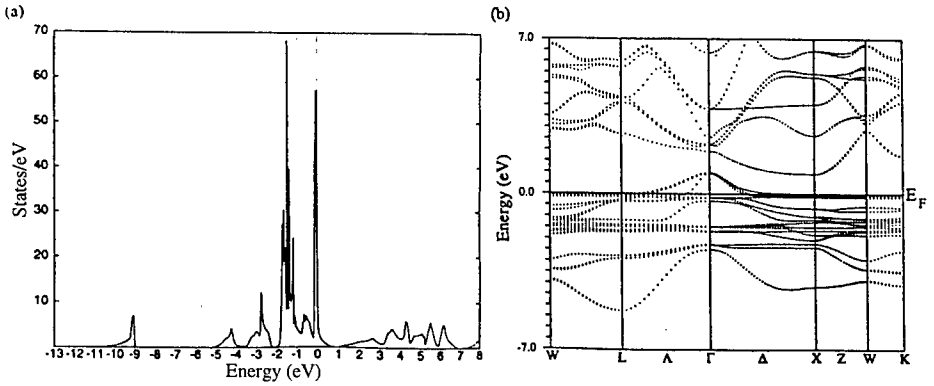

Figure 14 : Total density of states (a) and band structure (b) of YbNiSb.

(c) Effective Masses

Recently Uher et al.[26] have studied the transport properties of ZrNiSn and related compounds. They have estimated the effective mass of the states near the bottom of the conduction band of ZrNiSn and found that it is about 2-3 times m_e, the free electron mass. We have calculated the effective masses associated in ZrNiSn and YNiSb with the conduction band minimum (at the X point) and found it to be highly anisotropic. In ZrNiSn, we find that along the XΓ direction the effective mass is about $10m_e$, where as along the other two orthogonal directions, it is nearly m_e. Thus, the average transport mass will be about $(10)^{1/3}m_e$, which is consistent with Uher et.al.'s findings. This might explain why the observed room temperature electron-like thermoelectric coefficient in ZrNiSn is large.[24] A similar situation also occurs in YNiSb in which the heavy electron mass along the XΓ direction is a factor of two larger than ZrNiSn. If the YNiSb can be doped n-type, it should also show a large negative thermopower at room temperature. We find that the effective hole masses in ZrNiSn are also large which suggests that p-doped ZrNiSn should show large positive thermopower at room temperature. In constrast, the hole effective masses in YNiSb are less (about $1m_e$) and, therefore, p-doped YNiSb should not show as large a thermopower at room temperature as its n-doped analog.

CONCLUSION

The charge transport properties of the RNiSb compounds as well as the solid solutions, $(Zr_{1-x}Er_x)Ni(Sn_{1-x}Sb_x)$ and $ErNiSb_{1-x}Pn_x$, studied vary widely as a function of R and as a function of the composition x. The properties of RNiSb compounds range from semiconducting, for R=Er and Tm, to semimetallic or metallic for R=Ho, Yb, Y. These large variations could be due to defects or non-stoichiometry, both of which need to be investigated further. [27] Their thermopower values range from 21 μV/K to 160 μV/K, while the thermal conductivity is in a reasonable range from 3 W/mK to 7.5 W/mK. One member of the RNiSb system stands out as a promising candidate for thermoelectric applications. ErNiSb possesses a Seebeck coefficient of 160 μV/K, an electrical conductivity of 340 S/cm, a thermal conductivity of 7.5 W/Km and a carrier density of $2.25x10^{19}$ cm^{-3}. Therefore, by reducing the phonon mean free path we may obtain substantial improvements in the final figure of merit (ZT) of this compound. To improve further the charge transport properties of ErNiSb we have tested the solid solution approach to decrease the lattice thermal conductivity. We have shown that some of the selected solid solutions improve drastically, with κ decreasing by 24% to 59%.

It is important to synthesize solid solutions between semiconductors possessing the same type of carriers in order to avoid averaging the properties of the end-member materials. For this purpose we are working on synthesizing n-type RNiSb compounds and investigating different doping levels. As a consequence of this study, we believe that some promising thermoelectric compounds may be obtained by suitable n-type doping of the ErNiSb, HoNiSb and ZrNiSn compounds.

The FP-LAPW calculations within DFT and generalized gradient corrections predict that this class of materials are narrow indirect gap semiconductors, when R is Y, La, and Lu, or when the f-levels lie far away from the Fermi energy. The formation of the band gap can be identified primarily with the introduction of Ni into the host binary RSb compound. The conduction band is quite flat in RNiSb near the band bottom and the effective masses of this band are predicted to be highly anisotropic with values of $10m_e$ or more in certain directions.

ACKNOWLEDGMENTS

The work was partially supported by DARPA Grant # DAAG55-97-1-0184.
Work at NU made use of the Central Facilities supported by the National Science Foundation through the NU Materials Research Center (DMR-9632472).

REFERENCES

1. (a) F. G. Aliev, N. B. Brandt, V. V. Moschalkov, V. V. Kozyrkov, R. V. Skolozdra, A. I. Belogorokhov, *Z. Phys. B: Conden. Matter* **80**, 353 (1990) ; (b) F. G. Aliev, *Physica B* **171**, 199 (1991); (c) R. Kuentzler, R. Clad, G. Schmerber, Y. Dossmann, *J. Magn. Mater.* **104-107**, 1976 (1992); (d) H. Hohl, A. P. Ramirez, W. Käfer, K. Fess, Ch. Thurner, Ch. Kloc, E. Bucher, *Mater. Res. Soc. Symp. Proc.* **478**, 109 (1997).
2. S. Ogut, K. M. Rabe, *Phys. Rev. B* **51**, 10443 (1995).
3. K. Takegahara, T. Kasuya, *Solid State Commun.* **74**, 243 (1990).
4. A. K. Solanki, A. Kashyap, S. Auluck, M.S.S. Brooks, *J. Appl. Phys.* **75**, 6301 (1994).
5. S. K. Dhar, S. Ramakrishnan, R. Vijayarghavan, G. Chandra, K. Satoh, J. Itoh, Y. Onuko, K. A. Gschneider Jr., *Phys. Rev. B* **49**, 641 (1994).
6. I. Karla, J. Pierre, R. V. Skolozdra, *J. Alloys Compd.* **265**, 42 (1998).
7. G. J. McMullen, M. P. Roy, *J. Phys.: Conden Matter* **4**, 7095 (1992).
8. P. M. Oppener, V. N. Antonov, A. N. Yaresco, A. Ya Perlov, H. Eschrig, *Phys. Rev. Lett.* **78**, 4079 (1997).
9. P. Villars, L. D. Calvert, *Pearson's Handbook of Crystallographic Data for Intermetallic Phases* (American Society of Metals, Metals Park, OH, 1985).
10. K. Hartjes, W. Jeitschko, *J. Alloys Compd.* **226**, 81, (1995).
11. A.E. Dwight, *Proceedings of the Rare Earth Research Conference*, (11th, Michigan, 1974), **2**, 642 (1974).
12. Z. Lingmin, Y. Jialin, O. Xiangli, H. Wei, Z. Yinghong, *Trans. Nonferrous Met. Soc. China* **8**, 1, 18 (1998).
13. M. Evain, U-fit : "A cell parameter refinement program", Institut des matériaux de Nantes, France 1992.
14. P. Larson, S.D. Mahanti, S. Sportouch, M.G. Kanatzidis, submitted to *Phys. Rev. B.*
15. S. Sportouch, M. Bastea, C. Uher, M. G. Kanatzidis, manuscript in preparation.
16. W. Käfer, K. Fess, Ch. Kloc, K. Friemelt, E. Bucher, *Inst. Phys. Conf. Ser.* **152A**, 185 (1997).
17. F. G. Aliev, N. B. Brandt, V. V. Moschalkov, V. V. Kozyrkov, R. V. Skolozdra, A. I. Belogorokhov, *Z. Phys B: Conden. Matter* **75**, 167 (1989).
18. D. Singh, *Plane waves, pseudopotentials and the LAPW method*, (Kluwer Academic Press, Boston, 1994).
19. (a) P. Hohenberg, W. Kohn, *Phys. Rev.* **136**, B864 (1964); (b) W. Kohn, L. Sham, *Phys. Rev. A* **140**, 1133 (1965).
20. J. P. Perdew, Burke, Ernzerhof, *Phys. Rev. Lett* . **77**, 3865 (1996).
21. P. Blaha, K. Schwarz, J. Luitz, WIEN97, Vienna University of Technology 1997.
22. The values of atomic radii[23] were taken as 2.18 a.u. for Ni and as 2.36 a.u. for As, Sb, and Bi. The atomic radii for the rare earths were kept constant at 2.46 a.u., close to the value for Y. Adjustment of these radii within a reasonable range showed little dependence of the final band structure on these variations. Convergence of the self-consistent iterations was performed with 22 k-points in the reduced Brillouin zone to within 0.0001 Ry with a cutoff between valence and core states of -6.0 Ry. Scalar relativistic corrections and spin-orbit (SO) interactions were included in the calculation. The latter is particularly significant for f-electrons and for heavy atoms such as Bi.
23. L. Pauling, *J. Am. Chem. Soc.* **69**, 542 (1947).
24. E.K.R. Runge, R. C. Albers, N. E. Christensen, G. E. Zwicknagl, *Phys. Rev. B* **51**, 10375 (1995).
25. There has been some suggestion (see G. Mahan and J. O. Sofo, *Proc. Natl. Acad. Sci. USA* **93**, 7436 (1996)) that if f-levels lie close to the Fermi energy, the systems can exhibit large thermoelectric response.
26. C. Uher, J. Yang, S. Hu, D. T. Morelli, G. P. Meisner, submitted to *Phys. Rev. B.*
27. Band calculations indicate all these compounds to be narrow gap semiconductors except YbNiSb, which is predicted to be a heavy fermion metal.

SEMICONDUCTOR CLATHRATES: A PGEC SYSTEM WITH POTENTIAL FOR THERMOELECTRIC APPLICATIONS

G.S. NOLAS
R & D Division, Marlow Industries, Inc., 10451 Vista Park Rd., Dallas, Texas 75238

Abstract

An investigation into the structural, chemical, electronic, and thermal properties of polycrystalline semiconductor clathrate compounds with different "guest" ions in the voids of these structures is presently underway by the author and his colleges. Despite the well-defined crystalline structure of these semiconductor materials, the thermal conductivity shows a magnitude and temperature dependence more typical of amorphous materials than crystalline materials. The localized low frequency vibrations of these "guest" ions is believed to interact with the acoustic phonons of the host lattice resulting in a very low thermal conductivity. Indeed in the case of Ge-clathrates a "glass-like" thermal conductivity was observed. The markedly low thermal conductivity displayed by these semiconductor materials, along with the high power factors, demonstrates the potential of this material system for thermoelectric applications.

Introduction

It is well known that glasses and other amorphous materials display thermal properties that are markedly different from that of crystalline materials.[1] There are however examples of crystalline dielectric materials that possess thermal properties similar to those of amorphous materials.[2,3] In these disordered crystals the lattice vibrations are essentially similar to those of amorphous solids. In particular, the thermal conductivity, κ, of these systems approaches that of their theoretical minimum.[4] These systems are therefore considered to be "glass-like" and have been used as models for the study of disorder in solids.[2]

The search for *semiconductors* that exhibit "glass-like" thermal properties was initiated by Slack[5] with his "phonon-glass electron single crystal" (PGEC) approach to obtaining excellent thermoelectric materials. PGEC systems would possess electronic properties normally associated with good semiconductor single crystals and κ values normally associated with amorphous materials. The importance of this approach can be most easily understood from the definition of the figure of merit, $Z=S^2\sigma/\kappa$, where S is the Seebeck coefficient and σ the electrical conductivity. The magnitude of Z defines a "good" thermoelectric material. It was first proposed by Slack that the group IV elements forming clathrate-structured compounds are potential PGEC compounds and therefore are of interest for thermoelectric applications.[3] Most recently this was shown to be the case for compounds with nominal composition $Sr_8Ga_{16}Ge_{30}$.[6] The measured transport properties of a series of such compounds indicate this is indeed a PGEC-type system with relatively high Z values.[6] The magnitude and temperature dependence of κ was similar to that of amorphous SiO_2 (a-SiO_2) while the power factor ($S^2\sigma$) for these compounds was relatively high. Low temperature (< 1 K) thermal conductivity measurements on $Sr_8Ga_{16}Ge_{30}$ indicated a T^2 temperature dependence.[7] This is not the normal crystalline T^3 dependence associated with boundary scattering but is similar to the T^α temperature dependence (with $\alpha \sim 2$) for amorphous compounds[2] and to the T^2-dependence calculated for the theoretical minimum κ at low temperatures.[4] This T^2-dependence indicates that indeed these crystalline materials have glass-like heat conducting properties.

Mat. Res. Soc. Symp. Proc. Vol. 545 © 1999 Materials Research Society

In this report an overview of work currently underway by the author and his collaborators on this material system is presented. Data on representative samples of different Si, Ge and Sn-clathrate compounds are discussed. An overview of the salient features and concepts underlying the basic properties of interest with an emphasis on demonstrating the potential this material system possesses for thermoelectric applications is presented.

Synthesis Approach

There are a few different techniques that have been successfully employed to synthesize clathrate compounds.[8,9] The approach that has been employed in the synthesis of the samples described in this report involves the mixing and subsequent reacting of stoichiometric amounts of the constituent elements at a temperature above the melting point of the constituents. In the case of the alkaline earth and rare earth containing clathrates the elements were placed in a pyrolitic boron nitride crucibles which were sealed in quartz ampules that contained an argon atmosphere. For the case of the alkali metal containing clathrates the constituent elements were mixed in tungsten crucibles which were sealed in welded stainless steal canisters also containing an argon atmosphere. The subsequent clathrate compounds had a metallic luster. The Ge and Si-clathrates were unreactive in air and moisture but could be etched in aqua regia. The Sn-clathrates developed some discoloration on the surface with time. For subsequent transport measurements the samples were densified in a hot press employing a graphite die. Metallographic, x-ray diffraction (XRD) and electron-beam microprobe analyses indicated the structural and chemical properties of each sample.

Structural and Chemical Properties

The polycrystalline Si, Ge and Sn-clathrates that form the type-I hydrate crystal structure have been synthesized with alkali metal, alkaline earth and rare earth ions in their voids. The type-I clathrate hydrate crystal structure crystallizes in a cubic crystal lattice comprised of tetrahedral networks with periodic fullerene-like voids or "cages" of 20 and 24 coordinated (CN) polyhedra comprised of group IV elements in a 1:3 ratio, respectively. The ions enter the lattice interstitially, residing inside these large cages. XRD spectra from powdered pieces of the samples presented in this report revealed sharp lines with no phases other than that of the type-I clathrate-hydrate ($Pm3n$). Electron beam microprobe analysis of a polished surface of each sample confirmed the XRD results and produced exact stoichiometric percentages of each sample. In the case of the Ge-clathrates scanning tunneling microscopy was employed and showed a defect free structure within the grains. Figure 1 is an x-ray spectrum of $Sr_8Ga_{16}Ge_{30}$. This spectrum is typical of that obtained for other compounds that have the type-I clathrate hydrate structure. Table I lists some of the physical and electronic properties of the dense polycrystalline samples. All samples were phase-pure with the exception of the Si-clathrate were trace amounts of Si were also observed. The compounds listed in Table I possess the type-I clathate hydrate crystal structure with the exception of $Ba_8Ga_{16}Sn_{30}$ which has a unique structure with the Ba inside 20 CN cages.[9] The Ga was used in order to charge compensate for the encapsulated ions. This means that two Ga atoms act as "acceptors" for the two "donated" electrons from each Sr^{2+}, Eu^{2+} or Ba^{2+} ion or the one "donated" electrons from each Rb^{+} or Cs^{+} ion. It is presumed that the Ga is randomly substituted for the group IV elements in these compounds. The two vacancies in the Cs_8Sn_{44} compound are required to provide the necessary charge neutrality (i.e. 184 electrons per unit cell in the case of the type-I clathrate hydrate structure). This "defect" type-I clathrate compound therefore is also a semiconductor,

as shown in Table I. Hall coefficient measurements using the van der Pauw technique were conducted at room temperature. For the compounds shown in Table I the room temperature electron carrier concentrations varied from over 10^{20} cm^{-3} for the Si-clathrate to 10^{17} cm^{-3} for Cs_8Sn_{44}. The $Sr_8Ga_{16}Ge_{30}$ sample had a carrier concentration of 10^{19} cm^{-3}.

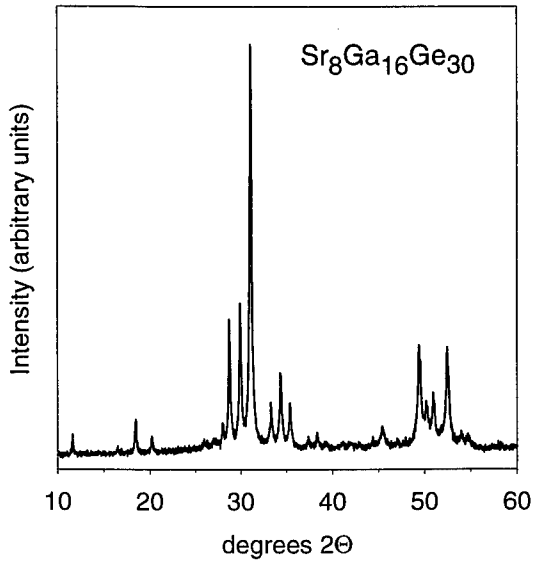

Figure 1. XRD spectrum of the type-I clathrate structure of $Sr_8Ga_{16}Ge_{30}$.

Table I. Representative clathate compounds indicating the atomic percentages from electron-beam microprobe analysis, the lattice parameters, a_0, the average grain size, the measured density, D, absolute Seebeck coefficient, S, and resistivity, ρ, at room temperature.

compound	Elemental atomic %	a_0 (Å)	grain size (μm)	D g/cm^3	S (μV/K)	ρ (mΩ-cm)
$Ba_8Ga_{16}Sn_{30}$	14.4Ba/29.7Ga/54.9Sn	11.594	9.0	5.73	-145	14.9
Cs_8Sn_{44}	15.6Cs/84.4Sn	12.113	13	5.39	-304	59.4
$Rb_8Ga_8Sn_{38}$	14.6Rb/14.9Ga/70.4Sn	11.981	21	4.62	-153	0.767
$Ba_8Ga_{16}Si_{30}$	15.2Ba/27.5Ga/57.0Si	10.554	9.6	3.90	-66.3	2.05
$Sr_8Ga_{16}Ge_{30}$	14.8Sr/30.2Ga/55.3Ge	10.731	9.6	4.65	-320	12.9
$Eu_8Ga_{16}Ge_{30}$	14.2Eu/28.3Ga/57.6Ge	10.711	5.4	5.39	-152	2.56
$Sr_4Eu_4Ga_{16}Ge_{30}$	8.2Sr/6.9Eu/28.6Ga/56.4Ge	10.726	12	5.57	-88.1	1.02

Transport Properties

Thermal transport and thermopower (S) measurements were carried out by the two-thermocouple, steady state heat-flow technique. Due to the very low κ of these samples, the losses due to radiation and conduction through the wires was measured and corrected for. These corrections were 15% near room temperature and < 5% for temperatures below 120 K. The samples were cut into parallel faced parallelepipeds. The heat flow was measured along the longest axis. Since the clathrate compounds are cubic, κ_g is isotropic. Figure 2 shows the lattice thermal conductivity, κ_g, in the temperature range from 300 to 6 K for five representative clathrate samples from Table I. Also shown is κ for amorphous germanium (a-Ge),[10] a-SiO_2[2] and the calculated minimum thermal conductivity for Ge, κ_{min}. From the measured values of the electrical resistivity, measured using the standard four-probe technique, and the Wiedemann-Franz law we have estimated and subtracted the electronic contribution to κ in Figure 2.

As seen in Figure 2 the Ge-clathrates exhibit a κ_g that is typical of amorphous solids. The values are well below that of a-SiO_2 and close to a-Ge near room temperature. In addition, the temperature dependence of the Ge-clathrates is much like that of a-SiO_2. In the $Sr_4Eu_4Ga_{16}Ge_{30}$ sample there are two atoms in the voids of the crystal structure which introduces an even greater disorder. This compound exhibits the lowest κ_g values in the teperature range shown and the most "glass-like" temperature dependence of κ_g. The $Ba_8Ga_{16}Si_{30}$ sample has a rather low κ_g (lower than κ_{min} = 1.2 W/mK at room temperature for Si[10])however it's temperature dependence is more typical of a crystalline solid. In the case of Cs_8Sn_{44}, κ_g has a temperature dependence typical of crystalline materials (a T^{-1} temperature

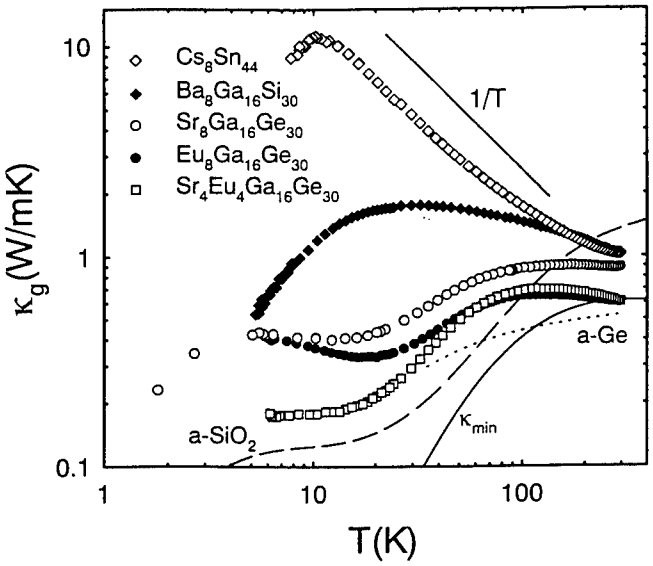

Figure 2. Lattice thermal conductiviy measured from 5 K to 300 K for five representative clathrate compounds along with data for a-SiO_2, a-Ge and κ_{min} for Ge.

dependence as shown in Figure 2) although the magnitude of κ_g is also rather low. This temperature dependence may be because the Cs^+ ion is not as free to "rattle" in the cages of this compound as in the case of the other clathrates. This may be due to the fact that there are two Sn vacancies in the Sn-matrix with a resulting effect on the size and shape of the cages encapsulating the Cs^+ ions. The exact nature of this phenomena is presently under investigation.

The radii of the Ba^{2+}, Eu^{2+} and Sr^{2+} ions are 2.07, 1.91 and 1.90 Å, respectively, from x-ray crystallographic data of the respective telluride compounds with the NaCl-type structure.[11] These ion dimensions may not be accurate for these ions in the Si or Ge-clathrates where they are in large 20 and 24 CN polyhedra however the trend in the sizes should be similar. The diameter of Ba^{2+} is most likely slightly larger in size than the radius of the smaller Si_{20} cage and approximately to that of the Si_{24} cage. The Si_{20} and Si_{24} cage radii are estimated to be 2.05 and 2.23 Å, respectively, from XRD data on alkali metal filled Si-clathrates.[8] Although Ba is much more massive than the elements that make up the host matrix (i.e. Ga or Si), a prerequisite for glass-like κ_g,[5] the temperature dependence of κ_g is not similar to that of the Ge-clathrates. This is due to the fact that Ba^{2+} is similar in size to Si_{20} and Si_{24} cages. From x-ray diffraction data, it does not appear that Ga increases the average size of the cages very much, if at all.

From Riedvelt analysis of the XRD data (see Figure 1) on $Sr_8Ga_{16}Ge_{30}$ samples the Ge_{20} and Ge_{24} cages are 2.16 and 2.32 Å in radius, respectively. These values are slightly higher than those obtained for alkali metal Ge-clathrates.[8] Assuming these cage sizes do not change substantially for Eu filling, the Sr^{2+} and Eu^{2+} ions have much more room to "rattle" in the voids of the Ge-clathrate than Ba^{2+} in the Si-clathrate. The result is a much larger disorder in the Ge-clathrates, even though Ba^{2+} is the more massive ion. The interaction between the guest ions and the host lattice forming the relatively large cages creates disorder due to the fact that the guest ions are entrapped in oversized cages. In our model these ions resonantly scatter phonons via localized low-frequency vibrations.[7] This "rattling" of the trapped atoms in their oversized cages creates a marked reduction in κ_g. In addition, to this dynamic disorder, a static disorder may also result from a possible random displacement of these ions from the center of the 20 and 24 CN polyhedra. In both cases the smaller and more massive ion in a particular cage, the larger the reduction in κ_g. This effect is similar to that observed in the skutterudite system where κ_g decreases as the size (mass) of the trivalent lanthanide ions interstitially placed in the cage of this crystal structure decreases (increases).[12] In the present case however the disorder results in a glass-like κ_g. Note Eu^{2+} is almost twice the mass of Sr^{2+} although they are approximately equal in radius. The $Eu_8Ga_{16}Ge_{30}$ compound therefore has a lower thermal conductivity than that of the $Sr_8Ga_{16}Ge_{30}$ sample. The largest disorder results from placing both Sr^{2+} and Eu^{2+} in the voids of the Ge-clathrate.

Figure 3 shows κ_g as a function of temperature for two Sn-clathrates plus the Cs_8Sn_{44} compound shown in Figure 2. The $Rb_8Ga_8Sn_{38}$ compound has a very low κ_g in the temperature range shown. In addition its temperature dependence is atypical of a crystalline material. The Rb^+ ion is smaller than the Cs^+ ion[13] and therefore may "rattle" more inside it's cage of Sn atoms. The $Ba_8Ga_{16}Sn_{30}$ forms a clathrate-type structure which contains only one type of cage,[9] as opposed to the two different cages in the type-I and II clathrate hydrates. This compound also has a relatively low κ_g however its temperature dependence indicates that some characteristics of a crystalline solid remain.

The S and ρ of four representative clathrates with the type-I hydrate structure are shown in Figure 4. The thermopower decreases with increasing temperature, typical of semiconductor

behavior, with the amplitude dependent on the carrier concentration. The ρ of $Ba_8Ga_{16}Si_{30}$ and $Eu_8Ga_{16}Ge_{30}$ decreases slightly with decreasing temperature, typical of semiconductors with high dopant concentrations. For the case of $Sr_8Ga_{16}Ge_{30}$ and $Rb_8Ga_8Sn_{38}$ a semiconducting temperature dependence is observed. From the low temperature data on these two samples a straight line fit of the data to the equation $\rho=\rho_0\exp(\Delta/T)$ can be used to to obtain the activation energy ($E_a=2\Delta$) for the donors. From such an analysis E_a = 15 meV and 55 meV for the $Sr_8Ga_{16}Ge_{30}$ and $Rb_8Ga_8Sn_{38}$ samples, respectively. The value for the Ge-clathrate is comparable to 14.17 meV for shallow donors such as As in Ge. For the Sn-clathrate the activation energy is higher. High temperature data, which may provide band gap information, is presently underway.

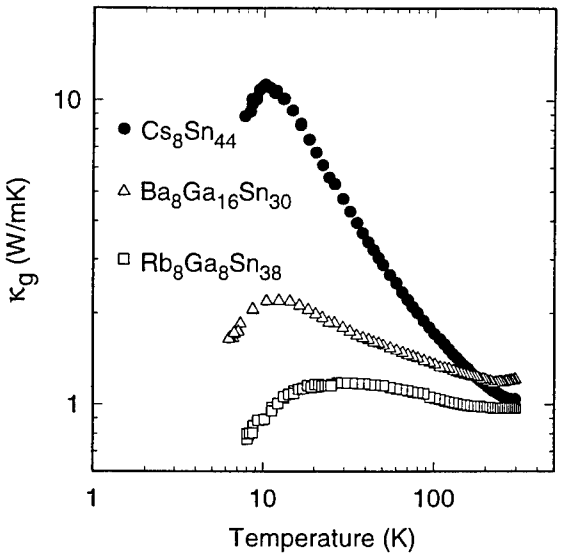

Figure 3. Lattice thermal conductivity vs. temperature for three representative Sn-clathrates.

Conclusion

From the results presented in this report it is clear that the semiconductor clathrates possess a unique crystal structure with the required properties resulting in a PGEC material system. These compounds are therefore of interest for thermoelectric applications. The key to this however is the fact that these compounds have a very low κ, similar to that of amorphous compounds. They indeed can be synthesized to possess glass-like κ. Future work hinges on synthesizing compounds with even lower κ. Only then will a 'new' thermoelectric material for cooling applications emerge.

Acknowledgements

The author greatfully appreciates and would like to thank Dr. G.A. Slack for helpful discussions and Dr. J.L. Cohn for transport properties measurements. This work was funded by Marlow Industries, Inc.

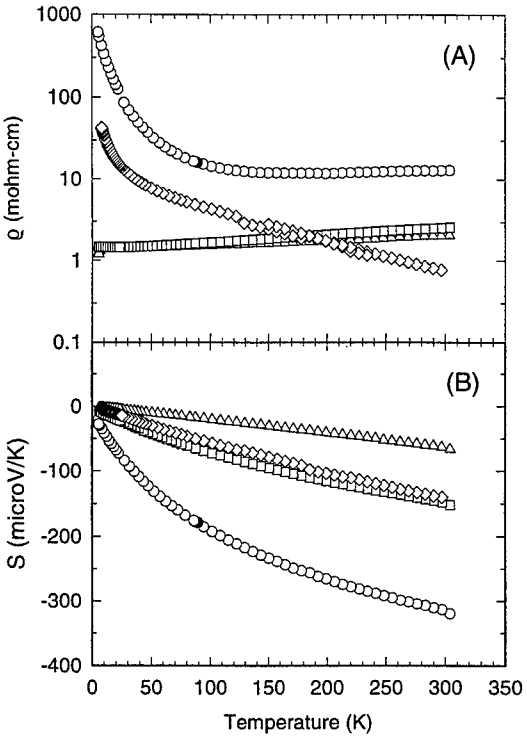

Figure 4. Resistivity (A) and Seebeck coefficient (B) as a function of temperature for N-type clathrate samples $Sr_8Ga_{16}Ge_{30}$ (○), $Rb_8Ga_{16}Sn_{30}$ (◇), $Eu_8Ga_{16}Ge_{30}$ (□) and $Ba_8Ga_{16}Si_{30}$ (△).

References

1. see for example D.G. Cahill and R.O. Pohl, Ann. Rev. Phy. Chem. **39**, 93 (1988) and references therein.
2. D.G. Cahill, S.K. Watson and R.O. Pohl, Phys. Rev. B **46**, 6131 (1992) and references therein.
3. G.A. Slack, in *Thermoelectric Materials -- New Directions and Approaches*, edited by T.M. Tritt, M.G. Kanatzidis, H.B. Lyon, Jr., and G.D. Mahan (Mat. Res. Soc. Symp. Proc. Vol. 478, Pittsburgh, PA, 1997) p. 47.
4. G.A. Slack, in Solid State Physics, Vol. 34, edited by H. Ehrenreich, F. Seitz, and D. Turnbull (Academic Press, New York, 1979) p. 1.
5. G.A. Slack, in *CRC Handbook of Thermoelectrics*, edited by M. Rowe (CRC Press, Boca Raton, FL, 1995) p. 407.
6. G.S. Nolas, J.L. Cohn, G.A. Slack and S.B. Schujman, Appl. Phys. Lett. **73**, 178 (1998)
7. G.S. Nolas, to appear in the Proceedings of the Eighteenth International Conference on Thermoelectrics (IEEE, Piscataway, New Jersey, 1999); J.L. Cohn, G.S. Nolas, V. Fessatidis, T.H. Metcalf and G.A. Slack, to appear in Phys. Rev. Lett.

8. C. Cross, M. Pouchard and P. Hagenmuller, J. Solid State Chem. **2**, 570 (1970).
9. B. Eisenmann, H. Schafer and R. Zagler, J. Less-Comm Metals **118**, 43 (1986).
10. D.G. Cahill, H.E. Fischer, T. Klitsner, E.T. Swartz and R.O. Pohl, J. Vac. Sci. Technol. A **7**, 1259 (1989).
11. R.W.G. Wycoff, Crystal Structures, Vol. I, 2nd edition (Wiley, New York, 1963).
12. G.S. Nolas, G.A. Slack, D.T. Morelli, T.M. Tritt and A.C. Ehrlich, J. Appl. Phys. **79**, 4002 (1996).
13. R.D. Shannon and C.T. Prewitt, Acta Cryst. B **25**, 925 (1969).

Theoretical calculation of the vibrational modes in Ge_{46} clathrate and related $M_xGa_yGe_{46-y}$ type clathrates

Jianjun Dong[a], Otto F. Sankey[a], A.A. Demkov[c], Ganesh K. Ramachandran[b], Jan Gryko[b,d], Paul McMillan[b], and Wolfgang Windl[e]

(a) Department of Physics and Astronomy and Materials Research Center, Arizona State University, Tempe, Arizona 85287, (b) Department of Chemistry and Materials Research Center, Arizona State University, (c) Motorola Inc., Mesa AZ, (d) Jacksonville State University (e) Motorola Inc, Los Alamos National Laboratory, Los Alamos, NM 87545.

We have calculated theoretically the vibrational modes of the type-I Ge_{46} clathrate and some related Zintl phase structures $M_xGa_yGe_{46-y}$ using *ab initio* density functional theory. The vibrational modes of pure Ge_{46} (without guest species) are compared to the $M_xGa_yGe_{46-y}$ structures, and it is found that small metal atoms (e.g. Na) have vanishing restoring force in the large cage, while the larger alkali-earth metal Ba has a restoring force constant less than 10% of that of the a framework atom. This makes them ideal "rattler" systems.

I. INTRODUCTION

Ge clathrates are an expanded phase of Ge, where each Ge atom is 4-coordinated as it is in diamond phase. The structure contains cages which typically are fractionally occupied by "guest" alkali or alkali-earth metal atoms. Stereo pictures of the clathrate structures can be found in Ref. [1,2]. In thermoelectrics, one requires *high* Seebeck coefficient and electrical conductivity, and *low* thermal conductivity. Since clathrates are semiconductors, they exhibit desirable Seebeck and electrical conductivities, and in fact these quantities are tunable by altering the guest species.

One of the new "design concepts" in thermoelectrics is to reduce the thermal conductivity by introducing "rattling" vibrational modes into the structure as has been achieved with the skutterudites [3]. The goal is to achieve a "crystal-like" electrical conductivity and a "glass-like" thermal conductivity [4]. Semiconducting clathrates (Ge_{46} is one example) offer similar possibilities, and recently Nolas *et al.* have synthesized $Sr_8Ga_{16}Ge_{30}$ which showed a remarkably low thermal conductivity [5].

In the present study, we will theoretically investigate the vibrational modes of three systems. The first is the pure Ge_{46} clathrate-I phase, which is the ideal framework and is the standard for comparison. We report here the frequencies for the IR and Raman modes, which have not yet been determined experimentally. The second and third systems are $Na_6Ga_6Ge_{40}$ (Model I), and $Na_2Ba_6Ga_{14}Ge_{32}$ (Model II). As described below, these two models cover two extremes – the Na is smaller in size than its encapsulating cage, while the Ba is larger. These models are two particular choices from the general category of Zintl phase $M_xGa_yGe_{46-y}$ solids, where M is guest alkali or alkali-earth metal located inside the cages. The structure of the framework in this type of solid is that of Ge_{46} because the Ga atom becomes "Ge-like" by accepting the extra electrons donated by the M metal atoms.

II. STRUCTURE AND VIBRATIONAL PROPERTIES OF TYPE-I GE CLATHRATE

Ge_{46} is in the type-I clathrate structure, which has a simple cubic primitive cell of 46 atoms. All the Ge atoms have four tetrahedrally bonded nearest neighbors. Although Ge_{46} has similar *local* bonding environment with that of diamond phase, its medium and long-range topology is distinctly different and produces an open, cage-like framework. In the primitive unit cell, there are six Ge_{24} (big) cages and two Ge_{20} (small) cages. These cages

Mat. Res. Soc. Symp. Proc. Vol. 545 © 1999 Materials Research Society

will encapsulate the metal guest species, and these guests are capable of rattling in these cages. First we determine the vibrational mode of the pure Ge_{46} structure with no metal atoms.

Our calculations is based on *ab initio* density functional theory within the local density approximation (LDA) and pseudopotential approximation. We use a planewave ultra-soft pseudopotential implementation of this theory using the VASP code [6]. Computations for Si clathrate can be found in Ref. [7].

The calculated optimized lattice constant of Ge_{46} is 10.5 Å. The band-structure shows that the band-gap of Ge_{46} has dramatically increased by 1.1 eV compared to diamond phase Ge. A similar effect of band-gap-opening has also been found in Si clathrates [1,7]

The vibrational modes of Ge_{46} are computed from the force constant matrix within harmonic approximation using finite displacements of the atoms. An *ab initio* force constant matrix calculation is computationally expensive and symmetry must be exploited.

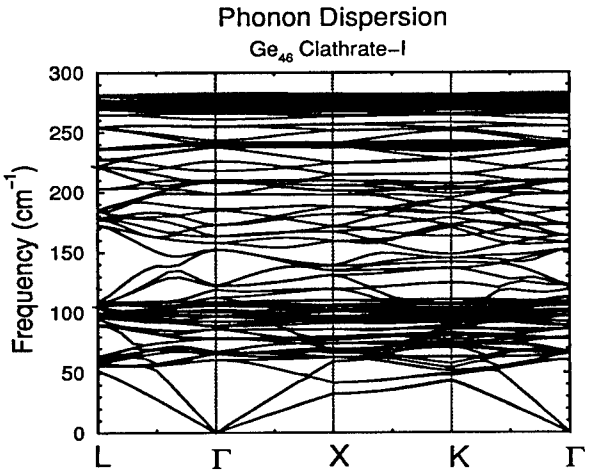

FIG. 1. Phonon dispersion relation of pure Ge_{46}.

The phonon dispersion curve is shown in Figure 1. Because our calculation is done only with *primitive* unit cell, the phonon frequencies are exact only at Γ point and frequencies at other k points are approximate. Approximately, the optical modes are located from 60 cm^{-1} to 285 cm^{-1} in frequency domain, with relative high state densities in both 60 cm^{-1} - 110 cm^{-1} and 265 cm^{-1} - 285 cm^{-1} frequency bands. The acoustic modes, which are important to thermal transport, are located from 0 cm^{-1} to 60 cm^{-1}.

The phonon modes at the Γ point ($\vec{k}$ = (000)) are of special interest in optical spectroscopy experiments. Because of degeneracy, the 138 phonon eigen-modes have only 57 ($8T_{1g} + 10T_{1u} + 8T_{2g} + 9T_{2u} + 7E_g + 4E_u + 3A_{1g} + 2A_{1u} + 4A_{2g} + 2A_{2u}$) distinct frequencies. Among them, eight T_{2g} modes(61.5, 77.3, 89.0, 175.7, 235.2, 272.2, 276.3, and 278.2 cm^{-1}), seven E_g modes (67.1, 131.5, 169.8, 238.2, 268.3, 275.5, and 278.7 cm^{-1}), and three A_{1g} modes (189.1, 247.4, and 282.4 cm^{-1}) are Raman active. Ten T_{1u} modes (0.0, 68.7, 88.9, 92.8, 172.3, 215.1, 234.9, 263.4, 272.5, 274.6 cm^{-1}) are infrared active. We have not computed the relative intensities of these modes.

III. STRUCTURE AND VIBRATIONAL PROPERTIES OF $M_XGA_YGE_{46-Y}$ TYPE CLATHRATES

When the cages inside clathrates are 100% filled with a single type of guest metal atom, there is no ambiguity about guest location in the $M_xGa_yGe_{46-y}$ type structures. However, the the distribution of Ga atoms in the framework is not clear. We find that the distribution of Ga amongst the framework sites leads to very different electronic structure. Briefly, this initial study seems to indicate that if two Ga atoms are near neighbors, then the material becomes metallic. Presumably the energy of such a situation is higher in energy, and during growth the Ga atoms will seek sites distant from one another. This is very similar to the Lowenstein rule in zeolites in which Al (substituting for Si) is not near another Al.

We have examined four models of $M_xGa_yGe_{46-y}$, which are listed in Table I. 6c, 16i, 24k are atom sites in the clathrate-I framework, and 2a and 6d are atom sites in the center of small and large cages respectively. The number N_{Ga-Ga} is the number of Ga-Ga bonds per unit cell, σ indicates the electrical conductivity. Models I and II are those we use to investigate guest vibrational modes. In the second and third rows, we list two identical compositions for $Ba_8Ga_{16}Ge_{30}$. In one composition the 16 Ga atoms are distributed amongst the 16i sites. This maintains perfect $Pm\bar{3}n$ symmetry. However this structure has 8 Ga-Ga bonds, and an evaluation of its band-structure shows it to have no band-gap; i.e. it is a metal. We then redistributed the Ga atoms over the 16i-sites and 24k-sites (third row of Table I) so that there were no Ga-Ga bonds. Indeed the material reverts back to a semiconductor. Unfortunately, this structure has very low symmetry, and is not an ideal candidate to study vibrations in this initial investigation.

There exist many possible geometries for $M_xGa_yGe_{46-y}$, and we consider two of them which have high symmetry, are semiconducting, and have no Ga-Ga bonds. They are model I ($Na_6Ga_6Ge_{40}$) and model II ($Na_2Ba_6Ga_{14}Ge_{32}$) (See Table I). Within the LDA, the band-gap is about 0.5 eV for model I and 0.1 eV for model II. In both cases the band gap has dropped dramatically compared to the pure Ge_{46} clathrates. We now investigate their vibrational modes.

First we consider model I ($Na_6Ga_6Ge_{40}$) which maintains the $Pm\bar{3}n$ space group, and the Na atoms reside in the large cages. The diameter of the big cage is approximately 4.7Å, while the atomic diameter of Na is approximately 3.7Å. (The ionic diameter is much smaller.) Thus the Na atom fits very "loosely" inside the cage. The (discrete) Γ point phonon spectra of model I are shown in Figure 2, along with that of pure Ge_{46} for comparison. Each vertical bar represents a phonon mode (degeneracy not included), and its location designates it frequency. The dotted line is the (broadened) vibrational state density at the Γ point.

TABLE I. Properties of some Zintl phase Ge clathrates with different Ga atom distribution.

Composition	2a site	6d site	6c site	16i site	24k site	Symmetry	N_{Ga-Ga}	σ
Ge_{46}			6Ge	16Ge	24Ge	$Pm\bar{3}n$		semicond.
$Ba_8Ga_{16}Ge_{30}$	2Ba	6Ba	6Ge	16Ga	24Ge	$Pm\bar{3}n$	8	metal
$Ba_8Ga_{16}Ge_{30}$	2Ba	6Ba	6Ge	4Ga+12Ge	12Ga+12Ge	low	0	semicond.
(I)$Na_6Ga_6Ge_{40}$		6Na	6Ga	16Ge	24Ge	$Pm\bar{3}n$	0	semicond.
(II)$Na_2Ba_6Ga_{14}Ge_{32}$	2Na	6Ba	6Ga	8Ga+8Ge	24Ge	high	0	semicond.

The significant new feature for $Na_6Ga_6Ge_{40}$ is the appearance of low frequency modes between 25 cm^{-1} to 28 cm^{-1} and "negative" frequency modes between about -45 cm^{-1} and -34 cm^{-1}. The appearance of negative frequencies is a mathematical artifact which alerts us to the fact that the system is either very an-harmonic or dynamically unstable. The eigen-vectors for the 18 modes that are low frequency or negative reveal that all eighteen modes are strongly *localized* on the guest Na atoms in the center of the big cages.

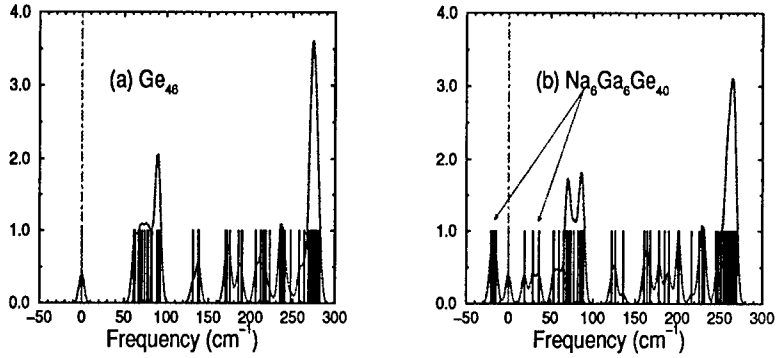

FIG. 2. Γ point phonon modes of Ge_{46} and model I ($Na_6Ga_6Ge_{40}$).

To better understand this behavior, we compute the potential energy curve when we displace a single Na atom in one of the large cages and keep the framework rigid. The large cage contains 12 pentagons and 2 hexagons, and thus appears "squashed" along the axis of the two directly opposed hexagons. We determine the potential energy for displacements parallel to motion along this squashed direction, and perpendicular to this direction. The potential energy curves for these two Na displacements are shown in Fig. 3b, and for comparison we show the energy curve for an analogous displacement of an atom on the framework using a typical spring constant of a bulk semiconductor (10eV/Å^2) such as Ge. We see a stunning difference between the framework potential (Fig 3a), and the Na guest potential (Fig 3b). The potential for the loose fitting Na is extremely weak and an-harmonic, presumably because the cage is "oversized". This is an ideal situation to obtain "rattling" behavior, and large framework phonon scattering from the an-harmonicity. We fit these potentials to a harmonic and an-harmonic potential, $E_x = 1/2Kx^2 + 1/4K'x^4$, and the parameters are given in Table II. We see the spring K for parallel displacements is approximately 1% that of the framework (10 *vs.* 0.135), and the perpendicular displacement shows an unstable system (negative K, K=-0.16eV/Å^2). The negative spring constant for perpendicular displacements is however very small in magnitude and the system is better described simply as an an-harmonic ($1/4K'x^4$) potential. Next we consider the vibrational modes of model II, $Na_2Ba_6Ge_{14}Ge_{32}$. In this case the Na is in the small cage and the Ba is in the large cage. The small cage contains 12 pentagons and no hexagons, and has a diameter of approximately 4.3Å. The Na (diameter 3.7Å) is not so oversized in this case. The large cage containing Ba is 4.7Å, but the Ba atomic diameter is about 4.4Å. Thus both atoms fit comfortably in these cages. (In the Nolas *et al.* experiments with Sr [5], the Sr atomic diameter is just slightly smaller than Ba)

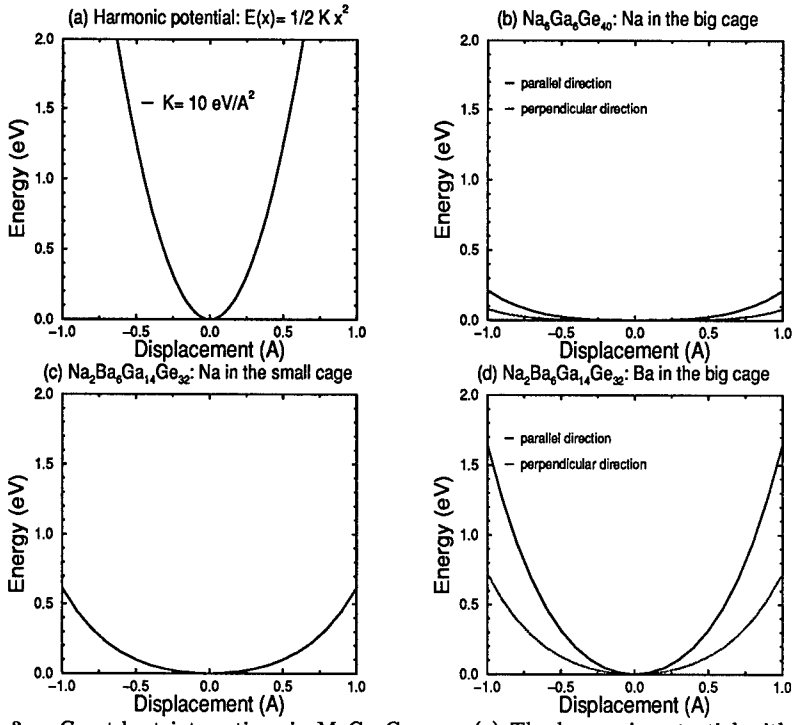

FIG. 3. Guest-host interactions in $M_xGa_yGe_{46-y}$. (a) The harmonic potential with spring constant typical in Ge semiconductors (K $\approx$ 10 eV/Å^2). (b) The Na-host interaction energy curve in $Na_6Ga_6Ge_{40}$, where Na is in the center of big cage. The solid line is the interaction energy along six-fold axis ($\parallel$ direction), and the dotted line is along the direction normal to the six-fold axis ($\perp$ direction).

TABLE II. The guest-host interaction energy curves: using $E(x)= 1/2\ K\ x^2 + 1/4\ K'\ x^4$ model.

	K (eV/Å^2)	harmonic ω (cm^{-1})	K$'$ (eV/Å^4)
harmonic potential	10	$\approx$ 200	
Na ($\parallel$) in $Na_6Ga_6Ge_{40}$	0.135	40	0.5824
Na ($\perp$) in $Na_6Ga_6Ge_{40}$	-0.016	-14	0.3156
Na in $Na_2Ba_6Ga_{14}Ge_{32}$	0.60	84	1.24
Ba ($\parallel$) in $Na_2Ba_6Ga_{14}Ge_{32}$	2.31	67	1.69
Ba ($\perp$) in $Na_2Ba_6Ga_{14}Ge_{32}$	0.82	40	1.25

Figure 3c and 3d shows the potential energy for atomic displacement of Na and Ba respectively, and the analytic fits are given in Table II. Na is now found to be harmonic in this small cage but its spring constant is still only approximately 6% of that for Ge. An estimate of the vibrational frequency using only this potential is $84cm^{-1}$. This represents an upper bound since the mode will involve the cooperative motion of other atoms which will reduce the frequency.

Ba in the large cage has an anisotropic environment, and the ratio of spring constants parallel and perpendicular to the cage axis is 2.8 (2.31/0.82), with the perpendicular direction being the softer of the two. Estimates of the frequencies for perpendicular and parallel displacement are $40cm^{-1}$ and $67cm^{-1}$ respectively. These frequencies are again upper bounds, and the cooperative mode patterns will reduce these estimates. Rough estimates from the full force constant matrix suggest they will be reduced by approximately 2/3 their value. This would yield frequencies in the 27-$45cm^{-1}$ range. These results are quite in line with the results of Nolas *et al.* for caged Sr, where their findings suggest a scattering mode near $55cm^{-1}$. Scaling our results by the appropriate mass factor to convert from Ba to Sr ($\sqrt{\frac{137}{88}}$= 1.25), we estimate Sr frequencies in the 34-$56cm^{-1}$ range.

IV. CONCLUSIONS

Using first-principles electronic structure methods, we study the vibrational properties of the pure Ge type-I clathrate (Ge_{46}) and two Zintl phase clathrates ($Na_6Ga_6Ge_{40}$ and $Na_2Ba_6Ga_{14}Ge_{32}$). We find Ga-Ga near neighbors lead to metallic systems. Caged metal atoms are found to have effective spring constants that are 6-23% of those for the framework (Ge-Ge bonds), and oversize cages are completely an-harmonic. Finally we report the Raman and IR mode frequencies of the ideal Ge type I clathrate.

V. ACKNOWLEDGEMENTS

We thank the NSF (DMR-95-26274) and the NSF-ASU MRSEC (DMR-96-32635) for support. It is our pleasure to thank for George Nolas for insightful discussions.

[1] G.B. Adams, M. O'Keeffe, A.A. Demkov, O.F. Sankey and Y. Huang, Phys. Rev. B **49**, 8048 (1994).

[2] G.K. Ramachandran, J. Dong, J. Diefenbacher, J. Gryko, O.F. Sankey, R.F. Marzke, M. O'Keeffe, and P.F. McMillan, J. Solid State Chem., submitted.

[3] L. Mihaly, Nature **395**, 839 (1998); V. Keppens, *et al.*, ibid., **395**, 876 (1998).

[4] G. A. Slack, "Thermoelectric Materials – New directions and Applications", Materials Research Society, Symposium Proceedings 478 (Pittsburgh, PA, 1997) p. 47.

[5] G.S. Nolas, J.L. Cohen, G.A. Slack and S.B. Schujman, Appl. Phys. Lett. **73**, 178 (1998).

[6] G. Kresse and J. Furthmüller, Comput. Mat. Sci. **6**, 15 (1996).

[7] J. Dong and O.F. Sankey, submitted.

[8] J. Dong and O.F. Sankey, unpublished.

Enhanced Thermionic Emission Cooling in High Barrier Superlattice Heterostructures

Ali Shakouri*, Chris LaBounty**, Patrick Abraham**, Joachim Piprek**, and John E. Bowers**

*Jack Baskin School of Engineering, University of California, Santa Cruz, CA 95046
**Electrical and Computer Engineering, University of California, Santa Barbara, CA 93106
ali@cse.ucsc.edu

ABSTRACT

Thermionic emission current in heterostructures can be used to enhance thermoelectric properties beyond what can be achieved with conventional bulk materials. The Bandgap discontinuity at the junction between two materials is used to selectively emit hot electrons over a barrier layer from cathode to anode. This evaporative cooling can be optimized at various temperatures by adjusting the barrier height and thickness. Theoretical and experimental results for nonisothermal thermionic emission in heterostructures are presented. Single stage InGaAsP-based heterostructure integrated thermionic (HIT) coolers are fabricated and characterized. Cooling on the order of a degree over one micron thick barriers has been observed. Nonisothermal transport in highly doped tall barrier superlattices is also investigated. An order of magnitude improvement in cooling efficiency is predicted for InAlAs/InP superlattices.

INTRODUCTION

Current state-of-the-art thermoelectric material for cooling and energy conversion at room temperature is based on BiTe. This material was discovered in 1950's. Its thermoelectric figure-of-merit ZT ($=S^2\sigma T/\beta$) is about 0.7-0.9. This corresponds to efficiencies on the order of 7-10% of Carnot efficiency [1-3]. This is much smaller than the efficiency of compressor based refrigerators that is more than 40-50%. Hence, conventional thermoelectrics have had limited applications for low cooling powers (< 50W) [4]. Various factors contribute to the low efficiency of thermoelectric refrigerators. Vining in a recent article [5] gave a lucid description of the thermoelectric process and pointed out a major difference with gas-cycle engines, i.e. the absence of phase transition near operating temperatures. A recent and important application of thermoelectric coolers is for temperature stabilization of optoelectronic components (lasers, filters, switches, etc.) used in high speed and wavelength division multiplexed fiber optics communication systems. In this case, the important factors are cost, reliability, and size [6]. Efficiency is not the major issue.

Thermionic emission in heterostructures was recently proposed as a mean to increase the *cooling power* of conventional semiconductor materials such as AlGaAs, InGaAsP, HgCdTe or SiGe beyond what can be achieved with bulk thermoelectrics [7-8]. In thermionic emission process, hot electrons from a cathode layer are selectively emitted over a barrier to the anode junction. Since the energy distribution of emitted electrons is almost exclusively on one side of Fermi energy, upon the current flow, strong carrier-carrier and carrier-lattice scatterings tend to restore the quasi-equilibrium Fermi distribution in the cathode by absorbing energy form the lattice, and thus cooling the emitter junction. The performance of the device can be optimized at

Mat. Res. Soc. Symp. Proc. Vol. 545 © 1999 Materials Research Society

various temperatures and for different cooling powers by changing the height and thickness of the barrier layer.

In the following we will review the initial theoretical predictions and experimental results for single barrier heterostructure integrated thermionic (HIT) coolers. After discussing some of the practical difficulties to achieve optimum performance of these thin film devices, we extend our analysis to highly doped structures. We will first describe the conventional trade off between electrical conductivity and Seebeck coefficient in bulk materials. Tall barrier HIT coolers are then proposed as a mean to overcome this trade off. It is shown that with proper doping one can increase the *efficiency* of InGaAs/InAlAs HIT coolers by as much as an order of magnitude with respect to the bulk material.

SMALL BARRIER HIT COOLERS

A schematic diagram of a single barrier HIT cooler as proposed in Ref. [7] is shown in Fig. 1. Thermionic emission is well understood in semiconductors, and is used in many devices. The hottest electrons are emitted over a barrier and collected on the other side. The coolest electrons remain behind. Vacuum thermionic generators were intensively studied in the 1950's and 60's [11,12]. They convert the heat energy into electricity by extracting electrons from hot metal plates onto another cold plate. The same device could work as a cooler by reversing the direction of current, but this cooler can only work at very high temperatures (>700°C) due to the availability of low work function metals and because the current flow is limited by space charge between the plates [13]. Thinner gaps work better, but there are limits to how close two plates can be placed to each other. Uneven gaps result in highly nonuniform current flow and hot spots develop.

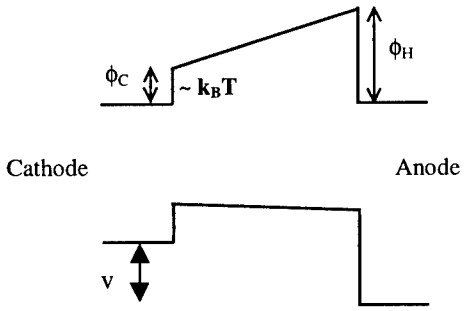

Fig. 1 Small barrier heterostructure integrated thermionic emission for high cooling power densities at room temperature.

The precise control of layer thickness and composition using techniques of molecular beam epitaxy (MBE) or metalorganic chemical vapor deposition (MOCVD), in conjunction with bandgap engineering allow the design of *semiconductor* thermionic emission devices with improved cooling capacities. One can easily design different barrier heights in the anode and in the cathode (typically 0 to 0.4eV). This is determined by the bandedge discontinuity between heterolayers. Depending on the growth constraints and lattice mismatch between materials, one can grade the barrier composition to produce internal fields and to enhance electron transport

properties (see Fig. 1). Close and uniform spacing of cathode and anode is not a problem anymore and is achieved with atomic resolution.

Theoretical predictions

The overall cooling capacity of a single barrier HIT cooler, with cathode side barrier height of ϕ_C, barrier thickness d and its thermal conductivity β, can be expressed as

$$Q_{TI} = \left[\Phi_C + 2\frac{k_B T_C}{e}\right]\cdot I - IV\left[\left(\frac{1}{2} - \frac{\lambda_E}{d}\right) - \frac{\lambda_E^2}{d^2}\left(e^{-d/\lambda_E} - 1\right)\right] - \frac{\beta}{d}\Delta T$$

where k_B is the Boltzmann constant, e the electric charge, T_C the cold side (cathode) temperature, and $\Delta T = T_H - T_C$. λ_E is the energy relaxation length for carriers [8]. The dependence on electrical conductivity of the barrier (carrier mobility) is hidden in the I(V) relationship [8]. This energy balance equation has three terms that describe thermionic cooling at the cathode, "Joule" heating in the barrier and heat conduction from the hot to the cold side. Thermionic cooling is equal to average energy of emitted electrons time the current. Assuming Boltzmann distribution for carriers, which is valid for barrier heights > $2k_BT$, this average energy is $(\phi_C + 2k_BT_C/e)$. The Joule heating term is IV times a coefficient, which takes into account the finite electronic energy relaxation length λ_E. In the limit of very thick devices, this coefficient reduces to 1/2 which is the result for pure diffusive transport. In the other limit of very short devices, the Joule heating term vanishes. In this case of ballistic transport, all of the electron's energy is deposited at the anode side.

In order to optimize HIT cooling devices, it is important to minimize Joule heating in the barrier. It is thus necessary to understand what are the main mechanisms that determine electronic energy relaxation length (λ_E) in semiconductors. For this purpose we will use Monte Carlo simulations of electron transport in GaAs. Other III-V semiconductors such as InP have similar characteristics. Ternary and quartenary compounds have in addition alloy scattering, but this is not expected to change energy relaxation considerably.

Fig. 2 displays the Joule heating as a function of distance for 5000 electrons injected over a 0.1 eV barrier into a 3 μm thick GaAs layer under an electric field of 5 kV/cm. It can be seen that, it will take about 1 μm before electrons reach equilibrium and lose energy equal to what they gain at steady state from the external electric field. Fig. 2 displays also the contribution of major scattering processes to electron energy relaxation as a function of distance. It can be seen that major scattering events responsible for energy relaxation at short distances (< 0.5μm) are polar optical phonon emission and absorption in the Gamma valley. At longer distances, there is a substantial population in the L valley. In this case, L-valley polar optical phonon emission and absorption and inter L-valley scatterings will start to contribute to the electronic energy loss mechanisms.

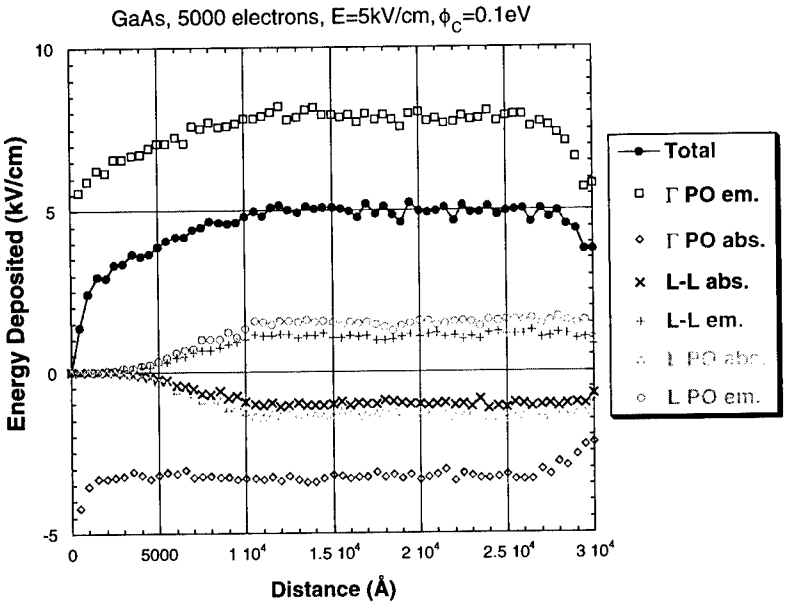

Fig. 2 Monte Carlo simulation of Joule heating as a function of distance for 5000 electrons injected over a 0.1 eV barrier into a 3-micron thick GaAs layer. Various curves show different energy loss mechanisms in a thin barrier heterostructure device. The important processes are Γ-valley polar optical phonon (PO) emission and absorption, L-valley PO phonon scattering and inter L-valley scattering (L-L).

Using various material parameters of InGaAs, and taking 0.4 μm for energy relaxation length, we can calculate the net cooling power at the cold side as a function of the thickness of the barrier for different cathode barrier heights (Fig. 3). The anode barrier height does not enter directly in the calculation of maximum cooling power. It is assumed to be high enough to suppress the reverse current form the hot to the cold side. It can be seen that at room temperature, thermionic cooling can maintain a temperature gradient of 10 degrees over a distance of 2 microns and provide a net cooling power of couple of 100 W/cm^2. The currents required for this cooling are on the order of 50 kA/cm^2.

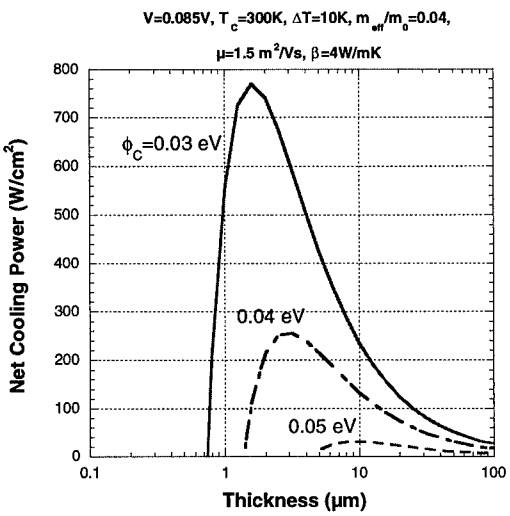

Fig. 3 Calculated net cooling power as a function of barrier thickness for small barrier InGaAs HIT cooler. Different curves correspond to different cathode side barrier heights.

Experimental results

In order to investigate experimentally thermionic emission cooling in heterostructures, a single InGaAsP (λ_{gap}=1.3 μm) barrier surrounded by n^+ InGaAs cathode and anode layers was grown using metal organic vapor phase epitaxy (MOCVD). Cathode and anode layer thicknesses were 0.3 and 0.5 μm and they were doped to $3x10^{18}$ cm^{-3}. The barrier layer had an n-doping of $2x10^{17}$ cm^{-3} and was one micron thick. Mesas with an area of 90x180 μm^2 were etched down using dry etching techniques. Ni/AuGe/Ni/Au was used for top and bottom contact metallization. Fig. 4a displays the temperature on top and on the bottom of the device as well as the substrate temperature far away from the device as a function of current. All temperatures are relative to the value at zero current. The rise in substrate temperature is an indication of the relatively high thermal resistance of ceramic package and the soldering layer used to mount the sample. Despite the poor performance of the heat sink on the anode side, a net cooling of 0.5°C is observed on top of the device. This cooling over 1 μm thick barrier corresponds to cooling capacities on the order of 200-300 W/cm^2. To understand these results a two dimensional finite difference heat equation solver (ANSYS) was used to simulate the performance of the device. Joule heating in the layers, substrate, and gold wire bonds were included as well as thermionic emission cooling (heating) at the cathode (anode) junction and the thermoelectric effect at the metal/semiconductor junctions. The Peltier effect at the junction InGaAs(n^+)/Au was studied by applying current between two bottom contacts. A cooling 2-3 times smaller than the thermionic cooling was measured.

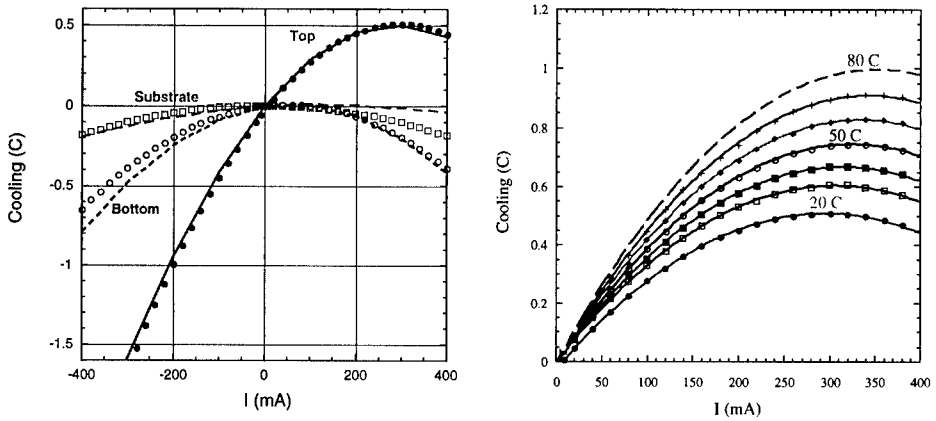

Fig. 4 (a) Measured temperature on top and on the bottom of the HIT cooler, as well as the substrate temperature far away form the device as a function of current. All temperatures are relative to the value at zero current. The heat sink temperature is 20°C. The simulation results are solid curve for top temperature, short-dashed curve for bottom temperature and dashed curve for the substrate. (b) Measured cooling at various substrate (heat sink) temperatures.

Assuming the thermal conductivity of InGaAsP to be 2 W/mK (i.e. 50% of textbook value [17]) and a solder layer and package with total thermal resistance of 2.5×10^3 K/W, the overall cooling and the temperature distribution in the device fit reasonably well the measured values in Fig. 4a. The simulation results are solid curve for top temperature, short-dashed curve for bottom temperature and dashed curve for the substrate. In order to minimize the effect of series and contact resistances, a number of p- and n-type HIT coolers connected electrically in series and thermally in parallel should be used (similar to conventional thermoelectric cooling modules). By improving the packaging, 10°C cooling for single stage InGaAsP HIT coolers is expected.

Fig. 4b displays the measured cooling at various substrate temperatures. The device cools much better at higher temperatures. A net cooling of about 1°C is measured at 80°C. The reason for the improved performance is two fold. First, the thermal conductivity of the barrier decreases at higher temperatures, and second, thermionic emission cooling increases due to the larger thermal spread of carriers near the Fermi energy.

The above theoretical and experimental results indicate the potential of HIT devices to achieve high cooling power densities. These devices have, however, a low efficiency (a few % of the Carnot value). The main problem is that the high cooling power at the cathode should fight the large heat flux that is coming from the hot junction only 1 or 2 μm away. As it can be seen in Fig. 3, the device can not achieve net cooling when the barrier is thick. For the case of thick

barriers, electron transport is not any more determined by the "supply" of electrons at the cathode. One thus loses the advantages of thermionic emission cooling. Recently Mahan et al. [15-16] have proposed to use multi barrier thermionic coolers to achieve ZT's a factor of 2-3 better than the bulk values. Their design is based on small barrier heights (~ k_BT), and uses the ballistic transport of electrons in very thin superlattice barriers.

Based on a different approach, in the following we first briefly reexamine the trade off between high electrical conductivity and large Seebeck coefficient in bulk semiconductors. We will then introduce tall barrier HIT coolers, as a mean to overcome this trade off. Preliminary theoretical analysis of InGaAs/InP and InGaAs/InAlAs superlattices HIT coolers show that an improvement in efficiency by an order of magnitude with respect to the bulk material can be achieved.

ELECTRICAL CONDUCTIVITY AND POWER FACTOR TRADE OFF IN BULK THERMOELECTRICS

In the conventional thermoelectric effect, electrons flow from a material in which they have an average transport energy smaller than the Fermi energy to another material in which their average transport energy is higher. They thus absorb thermal energy from the lattice and this will cool down the junction between two materials. In Fig. 5(a) we can see that at high doping densities there are many more carriers that contribute to the conduction process. Despite the reduction in electron mobility due to charged impurity scattering, the net electrical conductivity continues to rise with doping concentration.

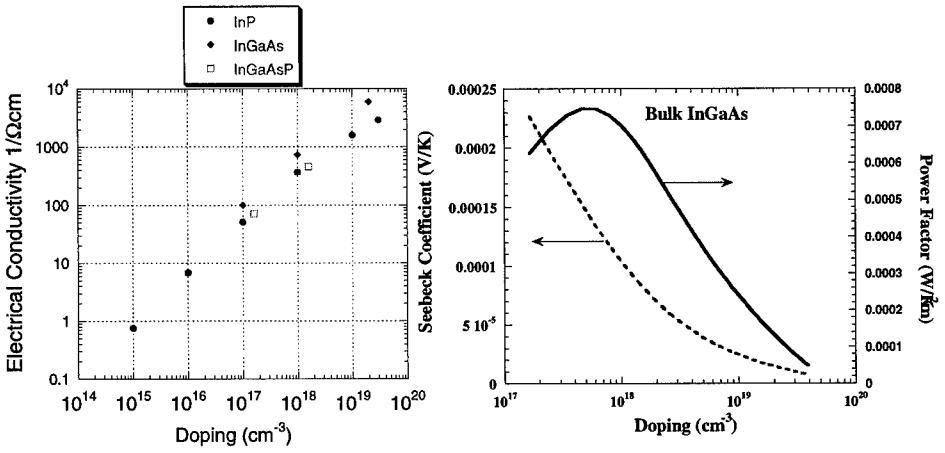

Fig. 5 (a) Experimental electrical conductivity of InP, InGaAs, InGaAsP (λ_{gap}=1.3 μm) as a function of doping. (b) Substantial decrease in Seebeck coefficient at high dopings is the cause of low power factor and thus poor ZT.

Fig. 5(b) shows that the poor power factor (electrical conductivity times square of Seebeck coefficient) is a result of significant decrease in Seebeck coefficient when Fermi energy is deep inside the conduction band. At high doping densities, the situation is similar to the metals. Since the Fermi energy is deep inside the band, there are almost as many electrons above the Fermi energy as the ones below, so the average energy of moving electron gas under an electric field is very close to the Fermi level. This gives a small thermopower (Seebeck coefficient), and thus poor thermoelectric cooling properties.

High barrier heterostructure integrated thermionic coolers

Tall barriers in a highly degenerate semiconductor can be used to selectively emit hot electrons, and to achieve thermionic emission cooling similar to the original small barrier HIT coolers. Because of the large number of electrons involved in the conduction process, small electric fields can be applied to achieve substantial cooling. In this near ohmic conduction regime, electrical conductivity, Seebeck coefficient and the Z parameter can be defined similar to bulk material.

Fig. 6 displays the thermoelectric figure-of-merit for bulk InGaAs as a function of doping. The experimental doping dependence of electron mobility is included in the calculations. This figure shows also the expected ZT for multibarrier structures with tall InP (ΔEc=0.24 eV) or InAlAs (ΔEc=0.51 eV) barriers. The order of magnitude improvement in ZT is due to large increase in Seebeck coefficient at high doping densities in multibarrier devices. The thermal conductivity of the composite material is taken to be 5 W/mK, i.e. identical to the bulk InGaAs. Several recent studies [18-20] have shown that superlattice thermal conductivity is also reduced comparing to bulk value, so further improvement in ZT is expected.

In the above analysis quasi diffusive transport of electrons above the barriers is assumed. We do not expect significant changes in the device performance due to the finite electron energy relaxation length. In fact, corrections due to ballistic transport will tend to improve the cooling characteristics even more.

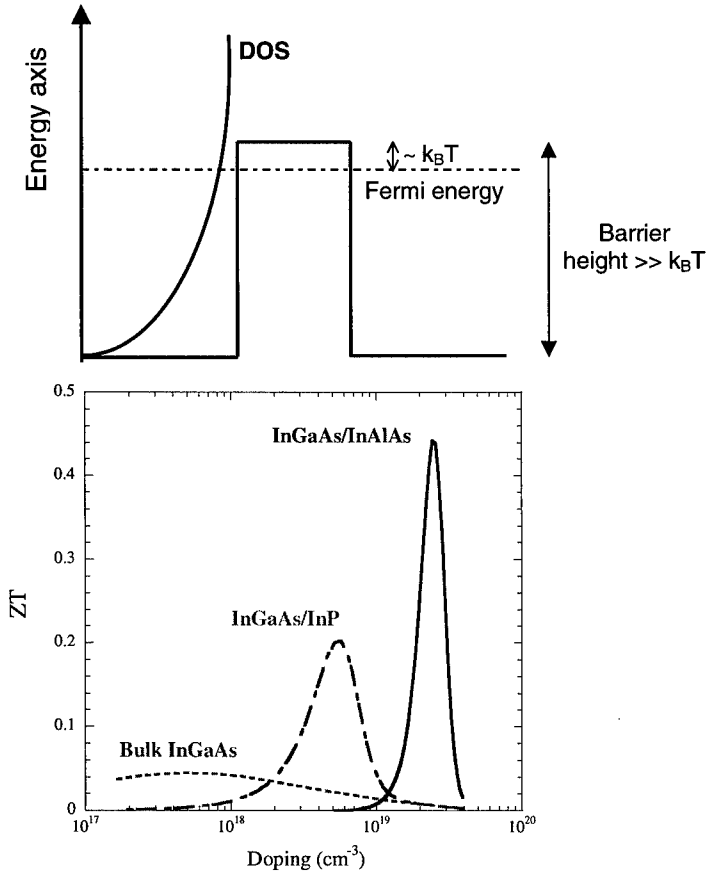

Fig. 6 Theoretical thermoelectric figure-of-merit (ZT) for bulk InGaAs and for high barrier heterostructure thermionic coolers based on InGaAs/InP (ΔE_c=0.24eV) and InGaAs/AlGaAs (ΔE_c=0.51eV) at various doping densities. The thermal conductivity of the composite material is taken to be 5 W/mK, i.e. identical to the bulk value. The order-of-magnitude improvement in ZT is purely due to thermionic emission of hot carriers above the barrier.

ACKNOWLEDGMENTS

The authors would like to acknowledge many stimulating discussions with Profs. Herb Kroemer, Venky Narayanamurti, and Dr. D. L. Smith. This work was supported by DARPA and the Office of Naval Research under the contract 442530-25845.

REFERENCES

1. H. J. Goldsmit, *Electronic Refrigeration* (Pion, London, 1986).

2. D. M. Rowe, *CRC Handbook of Thermoelectrics* (CRC Press, New York, 1995).

3. C. B. Vining, Thermoelectric materials of the future, in Twelfth International Conference on Thermoelectrics, Yokohama, 1993, P. 126.

4. H. B. Lyon Jr., Overview of industrial interest in new thermoelectric materials, in *Thermoelectric Materials - New Directions and Approaches*, Materials Research Society, Symposium Proceedings vol. 478, Ed. T. M. Tritt et al., P. 285-296, 1997.

5. C. B. Vining, The thermoelectric process, in *Thermoelectric Materials - New Directions and Approaches*, Materials Research Society, Proc. vol. 478, Ed. T. M. Tritt et al., P. 3-13, 1997.

6. L. Rushing, A. Shakouri, P. Abraham, and J. E. Bowers, Micro thermoelectric coolers for integrated applications, in the proceedings of Sixteen International Conference on Thermoelectrics, Dresden, Germany, August 1997.

7. A. Shakouri, J. E. Bowers, Heterostructure integrated thermionic coolers, Appl. Phys. Lett. 71, 1234 (1997).

8. A. Shakouri, E. Y. Lee, D. L. Smith, V. Narayanamurti, J. E. Bowers, Thermoelectric effects in submicron heterostructure barriers, Microscale Thermophysical Engineering 2, 37 (1998).

9. D. M. Rowe, and G. Min, Multiple potential barriers as a possible mechanism to increase the Seebeck coefficient and electrical power factor, in Thirteen International Conference on Thermoelectrics, Kansas City, pp. 339-342, 1994.

10. L. W. Whitlow, and T. Hirano, Superlattice applications to thermoelectricity, Journal of Applied Physics, vol.78, pp. 5460-5466, 1995.

11. B. Moyzhes, Possible ways for efficiency improvement of thermoelectric materials, in Fifteenth International Conference on Thermoelectrics, Pasadena, 1996, P. 183.

12. G. N. Hatsopoulos, E. P. Gyftopoulos, *Thermionic energy conversion* (Vol. I, II) (Cambridge, MIT Press 1973-79).

13. G. D. Mahan, Thermionic refrigeration, J. of Appl. Phys., 1 Oct. 1994, vol.76, (7), P. 4362.

14. A. Shakouri, C. LaBounty, J. Piprek, P. Abraham, J. E. Bowers, Thermionic emission cooling in single barrier heterostructures, Appl. Phys. Lett. (to be published January 1999).

15. G. D. Mahan, L. M. Woods, Multilayer thermionic refrigeration, Phys. Rev. Lett. 80, 4016 (1998).

16. G. D. Mahan, J. O. Sofo, M. Bartkowiak, Multilayer thermionic refrigerator and generator, J. Appl. Phys. 83, 4683 (1998).

17. S. Adachi, *Properties of InP* (INSPEC, UK, 1993).

18. D. G. Cahill, Heat transport in dielectric thin films and at solid-solid interfaces, Microscale Thermophysical Engineering, vol.1, pp. 85-110, 1997.

19. G. Chen, Thermal conductivity and ballistic-phonon transport in the cross-plane direction of superlattices. Phys. Rev. B (Condensed Matter), vol.57, pp.14958-73, 1998.

20. R. Venkatasubramanian, E. Siivola, T. S. Colpitts, In-plane thermoelectric properties of freesstanding Si/Ge superlattice structures, in Seventeenth International Conference on Thermoelectrics, Nagoya, Japan, 1998.

Thermionic Refrigeration

G.D. MAHAN
Department of Physics and Astronomy, University of Tennessee, Knoxville, TN 37996, and Solid State Division, Oak Ridge National Laboratory, Oak Ridge, TN 37831, gmahan@utk.edu

ABSTRACT

The principles of thermionic refrigeration are explained. The simplest device is composed of two metal plates separated by a vacuum gap. This device is efficient at room temperature only for plates with small work functions ($e\phi$ <0.3 eV). Small barriers are available in semiconductor-semiconductor interfaces (band off-sets) and in metal-semiconductor interfaces(Schottky barriers). An efficient refrigerator is modeled for these systems. Possible realizations are discussed.

INTRODUCTION

Thermionic refrigeration is a solid state refrigerator based upon evaporative cooling. A barrier is imposed to the flow of electrons. Those electrons with sufficient kinetic energy to surmount the barrier are swept away by a small voltage. A system cools if its most energetic particles are systematically removed.

We invented this device[1] in 1994 for a simple system of two conducting plates separated by a vacuum gap. The device has a very high efficiency if the conducting plates have a small work function, on the order of $e\phi < 0.3$ eV. This number is obtained by a simple argument. The flow of current (J) over a barrier is governed by Richardson's equation, and the flow of energy (J_Q) is obtained by a similar formula

$$J_R(T) = AT^2 e^{-e\phi/k_B T} \quad (1)$$

$$eJ_Q(T) = (e\phi + 2k_B T)J_R(T) \quad (2)$$

where $A \approx 120$ A/(cm K)^2. Setting J_Q= 10 W/cm^2 at $T = 300$ gives a solution that $e\phi = 0.3$ eV. This value of heat flow is needed to overcome

Mat. Res. Soc. Symp. Proc. Vol. 545 © 1999 Materials Research Society

unavoidable losses such as radiation transfer. Unfortunately, this small value of work function is unobtainable in any electrode, so the device is impractical.

SUPERLATTICES

Small barriers to the motion of electrons and holes are readily available at solid state interfaces. In semiconductor superlattices, which are alternate layers of two different semiconductors, band off-sets serve as energy barriers. Similarly, at the interface between a metal and a semiconductor there are Schottky barriers between the chemical potential of the metal and the conduction and valence bands of the semiconductor. Such barriers can be used to provide thermionic refrigeration[2, 3, 4, 5].

In an all-solid state refrigerator, the thermal conductivity plays a crucial role. This parameter controls the flow of heat from the hot to the cold electrodes, which is contrary to the flow provided by evaporative cooling. Efficient solid-state refrigeration requires that the thermal conductivity be as low as possible[6, 7, 8, 9]. Thermionic devices only provide efficient refrigeration if the thermal conductivity has a low value such as typical of a glass or disordered material: 0.2-0.3 W/(m K). These low values are found in a superlattice when the heat flow is measured perpendicular to the plane of the layers. This astounding result has been measured in several semiconductor superlattices[10, 11, 12, 13], and these low values are predicted by theoretical calculations[14, 15]. The reduction can be a factor of ten for materials with high thermal conductivity such as silicon or gallium arsenide. A reduction of a factor of 3-4 has been reported[13] in Bi_2Te_3 which has a low thermal conductivity. The low values of thermal conductivity are caused by thermal boundary resistance. A superlattice has lots of boundaries. Similar reduction is expected in metal-semiconductor superlattices but there is neither data nor theory for this type of system.

Multilayer thermionic refrigeration was invented to take advantage of these two properties of multilayers: low thermal conductivity and periodic barriers. For current and heat flow perpendicular to the plane of the layers, the heat flow from phonons is small due to thermal boundary resistance. The periodic barriers, from band off-sets or Schottky barriers, can be used for evaporative cooling. We developed a computer model to predict the optimal properties of such a device. An important idea is that a multilayer device is

more efficient than a single layer device. This assertion is quite important to the understanding of attaining relatively high efficiencies. The equations for the flow of current (J) and heat ($\dot{Q}$) in a device of a single barrier are based upon the definitions in eqns. (1) and (2)

$$J = J_R(T_c) - J_R(T_h)e^{-eV/k_BT_h} \tag{3}$$

$$\dot{Q} = J_Q(T_c) - J_Q(T_h)e^{-eV/k_BT_h} - \frac{(T_h - T_c)}{R_1} \tag{4}$$

$$\eta = \frac{\dot{Q}}{JV} \tag{5}$$

where (T_c, T_h) are the cold and hot temperatures, V is the applied voltage acrossed the barrier, and R_1 is the thermal resistance of a single barrier device. Typical values are $R_1 \sim 10^{-7}$ m^2 K/W. The voltage is applied to suppress the current from the hot side $eV > 0$. The last equation is the Carnot definition of efficiency, which is the heat removed from the cold side divided by the input power JV. The device parameters such as V are varied to have the largest value of efficiency. The maximum efficiency is governed by the second law of thermodynamics to be $\eta_C = T_c/(T_h - T_c)$ which is a large number for a typical refrigerator with $T_c = 260$ K, $\Delta T = 40$ K. A useful quantity is the relative efficiency $\eta_{\rm rel}$

$$\eta = \eta_{\rm rel}\left(\frac{T_c}{T_h - T_c}\right) \tag{6}$$

Whenever we use (5) to calculate an efficiency, then we convert it to a relative efficiency using (6). An example is provided in figure 1, where we show the relative efficiency of a thermionic refrigerator for a single barrier with $e\phi =$ 30,50, and 70 meV, $T_c = 290$ K, and $R_1 = 10^{-7}$m^2 K/W. For each value of T_h the computer finds the value of voltage V with the largest efficiency, and then computes the relative efficiency. Note that the relative efficiency declines with increasing temperature difference $\Delta T = T_h - T_c$. A one barrier device with $\Delta T = 40$ K is relatively inefficient. A thermoelectric device with ZT=1 has a value of $\eta_{\rm rel} = 0.1$ while a freon compressor has $\eta_{\rm rel}$= 0.2. The thermionic device only has a high relative efficiency for a small temperature difference. This observation is the basis for having multiple layers. Each barrier has a small $\Delta T \approx 1$ K, and macroscopic cooling is achieved with many such barriers. The entire multilayer device has an overall efficiency similar to the

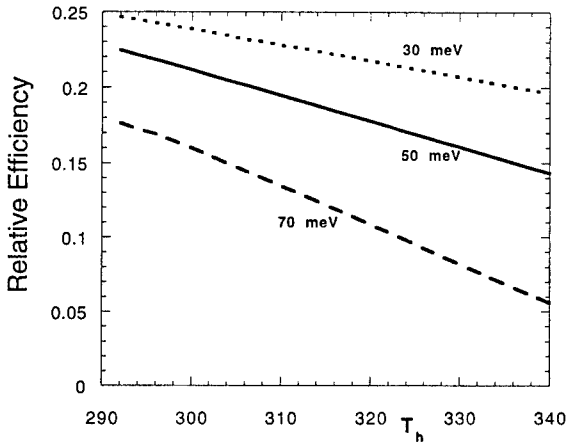

Figure 1: Relative efficiency of a thermionic refrigerator with a single barrier. The cold temperature is $T_c = 290$ K and the hot temperature is the axis. Results are presented for three values of barrier height $e\phi = 30$, 50, and 70 meV. The resistance is $R_1 = 10^{-7}$ m^2 K/W. The voltage V is varied to give the maximum efficiency.

high values shown in the figure. The reader is cautioned that the heat flow in such a device must be calculated self-consistently, since each barrier creates a small amount of Joule heat which must flow out of the device. These details are discussed in ref. [2-3].

In summary, the multilayer thermionic refrigerator attains a relatively high efficiency, compared to thermoelectric devices with $ZT = 1$, by combining two factors: (1) the very low thermal conductivity of superlattices parallel to the c-axis, and the relatively high efficiency of evaporative cooling for a small temperature gradient in each barrier. However, a thermoelectric device with the same low value of thermal conductivity would also have a high figure of merit. The latter case could be achieved by making a superlattice which has no barriers, so that it is isotropic in its electrical properties, yet did have a low thermal conductivity due to thermal boundary resistance.

The realization of this idea into a practical device depends upon finding materials with the correct properties. Since many other research groups are making semiconductor superlattices, our own efforts have been devoted to the metal-semiconductor superlattice. The modeling shows that the optimal

Crystal	Gap	K
Bi_2Te_3	0.15	1.3
Bi_2Se_3	0.16	2.4
Sb_2Te_3	0.21	2.4
GeTe	0.10	1.3
SnTe	0.20	1.5
PbSe	0.27	1.7
PbTe	0.31	2.0

Table 1: Energy gaps (in eV) and thermal conductivity [in W/(m K)] at T =300 K for several materials.

Schottky barrier must be in the range of $e\phi \sim 1 - 3k_BT$ which comes to 30-70 meV. After spending a great deal of time in the library, I discovered that Schottky barrier measurements do not exist for most narrow gap semiconductors. For type IV and III-V semiconductors the Schottky barrier is determined by surface states in the band gap. Small Schottky barriers come from materials with small energy gaps. However, for IV-VI semiconductors, and materials similar to bismuth telluride, Schottky barrier information does not exist. We are presently measuring such materials to identify those with small Schottky barriers for common metals. As always, one also desires a small thermal conductivity. In table 1 we present a short list of narrow band gap materials with low thermal conductivities. Not surprisingly, the list contains most of the good thermoelectric materials, since they also desire the same characteristics of small energy gap and low thermal conductivity.

DISCUSSION

What is the difference between a thermionic and a thermoelectric device? A thermoelectric device has the current flow as drift in an electric field, which is a type of forced diffusion. The electrons scatter repeatedly during their conduction, and the current is described by average relaxation times. In a thermionic process, the intent is to have the electrons transverse the barrier ballistically. Efficient evaporative cooling is achieved when all of the energy of the electron is carried from one electrode to the other, without scattering in a barrier. In a device with multiple barriers, the electron must go across

one barrier ballistically, and then thermally equilibrate in the next electrode. Each of the multiple barriers acts as in independent evaporative cooler.

The constraint that the electron undergo ballistic transport means that the barrier thickness L must be thinner than the mean-free-path λ of the electron. There are several different mean-free-paths in semiconductors. Here we mean the mfp for energy loss. Impurity scattering, which is mostly elastic scattering, does not rob the electron of energy so is not a limiting factor. Scattering processes which cost the electron energy are mostly due to scattering by phonons, and it is this process which dominates the mfp in the present problem. The metal electrodes have plasmon modes but these are generally too energetic to provide scattering to the thermal electrons of the present case.

Research support is acknowledged from ONR, DARPA, the University of Tennessee, and Oak Ridge National Laboratory which is managed by Lockheed Martin Energy Research Corp. for the U.S. Department of Energy under contract DE-AC05-96OR22464.

References

[1] G.D. Mahan, J. Appl. Phys. **76**, 4362 (1994)

[2] G.D. Mahan and L.M. Woods, Phys. Rev. Lett. **80**, 4016 (1998)

[3] G.D. Mahan, J.O. Sofo and M. Bartkowiak, J. Appl. Phys. **83**, 4683 (1998)

[4] A. Shakouri and J.E. Bowers, Appl. Phys. Lett. **71**, 1234 (1997)

[5] A. Shakouri, E. Y. Lee, D. L. Smith, V. Narayanamurti and J. E. Bowers, *Microscale Thermophysical Engineering* **2**, 37 (1998)

[6] H.J. Goldsmid, *Electronic Refrigeration* (Pion Limited, London, 1986)

[7] G.D. Mahan, J. Appl. Phys. **65**, 1578 (1989)

[8] G.D. Mahan, B.C. Sales, and J. Sharp, *Physics Today* (March, 1996)

[9] G.D. Mahan, in *Solid State Physics*, vol. 51, ed. H. Ehrenreich and F. Spaefen (Academic Press, 1998) pg 81

[10] G. Chen, C.L. Tien, X. Wu and J.S. Smith, J. Heat transfer **116**, 325 (1994)

[11] W.S. Capinski and H.J. Maris, Physica B **219 & 220**, 699 (1996)

[12] S.M. Lee, D.G. Cahill and R. Venkatasubramanian, Appl. Phys. Lett. **70**, 2957 (1997)

[13] R. Venkatasubramanian and T. Colpitts, in *Thermoelectric Materials–New Directions and Approaches*, ed. T.M. Hicks, M.G. Kanatzidis, H.B. Lyons Jr, and G.D. Mahan (MRS, Vol. 478, 1997) pg 73

[14] P. Hyldgaard and G.D. Mahan, Phys. Rev. B **56**, 10 754 (1997)

[15] G. Chen and M. Neagu, Appl. Phys. Lett. **71**, 2761 (1997)

Hot Electron Effects on Thermionic Emission Cooling in Heterostructures

Taofang Zeng and Gang Chen†
Mechanical and Aerospace Engineering Department, University of California, Los Angles, CA 90095, †gchen@seas.ucla.edu

Abstract

The energy conversion between electrons and phonons in a heterostructure is studied for thermionic cooling by using the hot electron approximation. Calculations show that the energy exchange rate between electrons and phonons should be small for a net cooling power, and the layer length should be in the range of submicron for effective cooling.

Introduction

Solid-state thermionic emission cooling has gained attention recently because of its potential high cooling power [1-5]. Semiconductor thermionic devices utilize the band edge offset at heterojunction as the thermionic emission potential barrier and bulk layer to separate the hot and cold sides [2]. The basic phenomena used in these semiconductor thermionic devices is similar to the conventional vacuum-based thermionic engine [2,6]: A fraction of electrons possessing a sufficiently high value of kinetic energy overcomes the retarding potential barrier at the cathode junction, sweep through the bulk layer and finally releases their kinetic energy to the anode. As energy is carried out of the cathode, the cathode is cooled down. To achieve a high efficiency of cooling, electrons should ideally pass through ballistically the bulk layer between the cathode and anode. This requires that the layer thickness is less than the mean free path of the electrons in the bulk layer [2,3].

Since the length of a practical device is typically larger than the electron mean free path, the electrons will experience collision in the bulk layer. Many studies have been reported in the past on the thermionic current flow over the Schottky barriers and heterojunctions [eg. 7-11]. Most of these studies were based on the combined thermionic emission / drift-diffusion theory. It deals with the current in two separate parts in series: a thermionic emission current across the heterojunction interface, and a drift-diffusion current in the layer. Other approaches including the electrohydrodynamic equations and Monte Carlo simulations have also been reported.

Though the transport of electrons as current has been well studied, little attention has been paid to the energy conversion. Monte Carlo simulation by Shakouri et al. [5] Shows that the heating mechanism inside the layer deviates from pure(conventional) Joule heating. In this study we investigate the energy exchange between electrons and phonons within a heterojunction based on the hot electron approach. An analytical solution for the energy conversion is obtained that includes the nonequilibrium energy exchange between electrons and phonons.

Hot Electrons over Heterojunctions

Figure 1 shows the configuration of the heterostructure being considered in this work. At the cathode, we assume that the conduction band edge is higher and a built-in potential is formed due to space charge. The bulk layer band bending is neglected, which could be realized by heavy doping. At the anode, we assume there is no potential barrier but there exists a interface for thermal boundary resistance. Such a configuration is essentially similar to that of a

Mat. Res. Soc. Symp. Proc. Vol. 545 © 1999 Materials Research Society

metal/semiconductor interface. The advantage of this modeling configuration is that it allows controlling the current level though external bias, rather than though varying the layer height. Although this modeling configuration is rather restrictive, we believe it could be extended to more complicated situations. In medium 1, the electrons and lattice (phonons) are at equilibrium with the same temperature T_0. Under an applied external potential, the electrons with energy higher than the barrier height can go over the barrier and transmit into the bulk layer. Those electrons passing over the barrier height have an average energy higher than the local phonons in the layer. In addition, those electrons also gain energy from the electric field. Such kinds of electrons are not in equilibrium with the local phonons and are called "hot" electrons [13, 14]. A definite distribution function does not exist for these carriers at nonequilibrium states. The scattering among electrons, however, can be very fast such that a quasi-equilibrium among the electrons can be established. One generally defines an electron temperature (T_e) independent of the actual form of the nonequilibrium distribution by [15]:

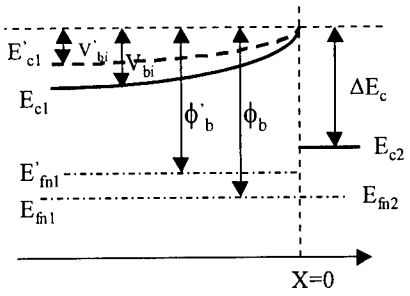

Fig. 1 Schematic band diagram of an abrupt heterojunction with built-in potential. $E_{fn1,2}$ represents the electron quasi-Fermi level in each semiconductor. V_{bi} is built-in potential.

$$\langle E \rangle = \frac{3}{2} k_B T_e \tag{1}$$

where <E> is the average kinetic energy of an electron.

The average kinetic energy of electrons, flowing over the barrier is approximately 3/2 $k_B T_0$ with reference to the peak of the barrier. Once electrons go into the bulk layer, the kinetic energy of those electrons relative to the bottom of the conduction band is:

$$< E >_2 = \Delta E_c + \frac{3}{2} k_B T_0 \tag{2}$$

Combining Eqs. (1) and (2) gives the temperature of electrons in the bulk layer at the junction:

$$T_e(0) = \frac{2}{3} \frac{\Delta E_c}{k_B} + T_0 \tag{3}$$

$T_e(0)$ is the initial temperature of electrons just passing over the barrier. As carriers travel within the layer, their motion is often interrupted by collisions with impurity atoms, phonons, crystal defects, or other carriers. The interaction between electrons and phonons is considered in this study, and the interaction rate can be expressed as [16]:

$$\frac{\partial < E >}{\partial t} = \frac{3}{2} \frac{k_B (T_e - T_l)}{\tau_E} \tag{4}$$

where T_l is the phonon temperature, and τ_E is the energy relaxation time, which can be expressed as [15]:

$$\tau_E = \frac{3k_B\mu_0}{2qv^2}\frac{T_eT_l}{T_e+T_l} + \frac{m^*\mu_0}{2q}\frac{T_l}{T_e} \tag{5}$$

where μ_0 is the mobility of electrons at equilibrium, v the drift velocity, q the electron charge, and m^* the effective mass. Now the cooling power can be expressed as:

$$W_{cool} = J/q \bullet \left(V_{bi}' + \frac{3}{2}k_BT_0\right) \tag{6}$$

J-V characteristics

In heterostructure device, electrons consecutively go over the barrier height and sweep through the bulk layer. At the heterojunction, the current density can be calculated as:

$$J = A^* \exp(-\frac{q\phi_b}{k_BT_0})\left(\exp(\frac{qV}{k_BT_0}) - 1\right) \tag{7}$$

where V is the voltage drop at the interface, A^* the Richardson's coefficient. In the bulk layer,

$$J = n\mu E = n\mu\frac{V_{barrier}}{L} \tag{8}$$

where n is the number of electrons per unit volume, E the electric field, $V_{barrier}$ the voltage drop in the bulk layer, and L the length of the layer. We used an average mobility $\overline{\mu} = \mu_0(\overline{T_l}/\overline{T_e})^{1/2}$ to account for the effect of electron and phonon temperatures. The total applied voltage is used to overcome the barrier height and the resistance in the bulk layer:

$$V_{applied} = V + V_{barrier} \tag{9}$$

Solving Eqs. (7)-(9) provides the J-$V_{applied}$ characteristics (Fig.2). Compared to the standard thermionic emission-drift-diffusion model [9], which treats the thermionic emission at the interface as a boundary condition, the approximation we use here is simpler.

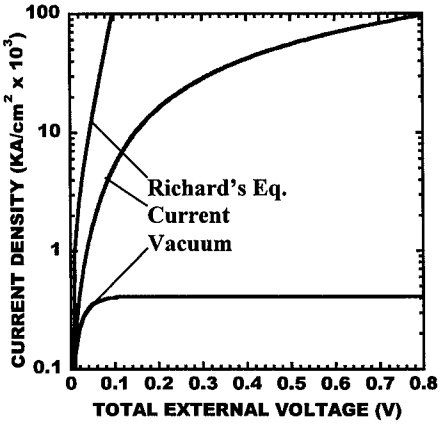

Fig. 2 J-V characteristic curves.
L=3 micron, layer height=0.08eV

Governing Equations

The electrons flowing in the layer were taken as an electron gas. When this hot electron gas flow through the bulk layer, it loses energy to the phonons. Meanwhile it also gains energy from the externally applied voltage. Transport equations have been established to deal with nonequilibrium electron-phonon interaction during laser material interaction [17,18], and we modify it to include the energy gain under the external field as:

$$-K_e \frac{d^2 T_e}{dx^2} + nG(T_e - T_l) = J \frac{V_{barrier}}{L} \tag{10}$$

$$-K_l \frac{d^2 T_l}{dx^2} + nG(T_l - T_e) = 0 \tag{11}$$

where K_e is the thermal conductivity of electrons, K_l the thermal conductivity of phonons, $G = 3/2k_B/\tau$, the electron-phonon coupling factor. The four boundary conditions for electron and phonons are

$$T_e(0) = \frac{2}{3}\frac{\Delta E_c}{k_B} + T_0, \qquad \frac{dT_e}{dx}\Big|_{x=L} = 0$$

$$K_l \frac{dT_l}{dx}\Big|_{x=0} = \frac{T_l(0) - T_0}{R_{b1}}, \qquad K_l \frac{dT_l}{dx}\Big|_{x=L} = \frac{T_l(L) - T_L}{R_{b2}} \tag{12}$$

where R_{b1} and R_{b2} are thermal boundary resistances at the two ends of layer (x = 0 and x = L). The above equations and boundary conditions are normalized with following dimensionless parameters:

$$\theta_e = \frac{T_e - T_0}{T_L - T_0} \qquad \theta_l = \frac{T_l - T_0}{T_L - T_0} \qquad \bar{x} = \frac{x}{L} \qquad \alpha = \frac{L^2 nG}{K_e} \qquad \beta = \frac{L^2 nG}{K_l}$$

$$\gamma = \frac{JV_{barrier}L}{K_e(T_L - T_0)} \qquad \overline{R_{b1}} = \frac{L/K_l}{R_{b1}} \qquad \overline{R_{b2}} = \frac{L/K_l}{R_{b2}}$$

Results Analysis and Discussion

Analytical expressions for $\overline{\theta_e}(\bar{x})$ and $\overline{\theta_l}(\bar{x})$ were obtained. As the expressions are very lengthy, they are not provided here. Instead, the results for two typical situations are depicted in Fig. 3. Figure 3a shows a case for the semiconductors with small electron mobility. As small mobility implies strong interaction between electrons and phonons, they become equilibrium after some distance. In this case, no net cooling was obtained. Electrons convert all their energies, gained from the electric field and the kinetic energy from the difference of the two potential energies (ΔE_c) of two faces at the junction, to the phonons. And phonons conduct energy back to the cold side. In Fig. 3b, the mobility of electrons is large, and the interaction

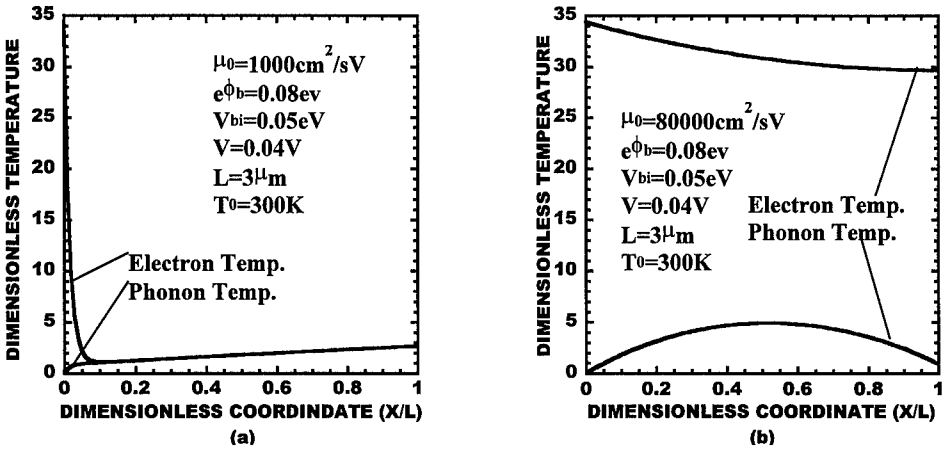

Fig. 3 Temperature profiles for different systems. In Fig.(a) the mobility of electrons is small, where there is no net cooling. In Fig.(b) the mobility of electrons is large, where there exists net cooling.

between electrons and phonons is weak, so that electrons and phonons do not become equilibrium. Nevertheless, the temperatures of phonons change as a parabolic curve, indicating a nearly uniform internal heat source from the electrons. In this case, net cooling power is available, because only part of the electrons' energy is conducted back to the cold side by phonons. The net cooling power is calculated as:

$$Q_{net} = J/q \bullet (V_{bi}^{'} + \frac{3}{2} k_B T_0) - K_l \frac{dT_l}{dx}|_{x=0} \tag{13}$$

Q_{net} as a function of layer length is presented in Fig. 4. From the figure, it can be seen that if the layer length is too small, there will be no net cooling power, because the heat conduction by phonons is too large. On the other hand, if the layer length is too large, hot electrons can impart their energy to the phonons, which in turn conduct the heat back to the cold side producing no net cooling power. The results for the coefficient of performance, COP ($=Q_{net}/JV_{applied}$), as a function of layer length are depicted in Fig. 5.

Conclusions

A simple analytical model that includes the nonequilibrium electron-phonon interactions and thermal boundary resistance for energy conversion in a heterostructure is developed. Calculations show that when the bulk layer length is too short, the heat conducted back to the cold side will be larger than the cooling power of the electrons thus generating no net cooling power. On the other hand, if the bulk layer length is too large, the energy carrier on by the electrons will impart to the phonons, which in turn conduct the energy back to the cold side and yielding no net cooling power either. The semiconductors with high electron mobility should be used as the bulk layer.

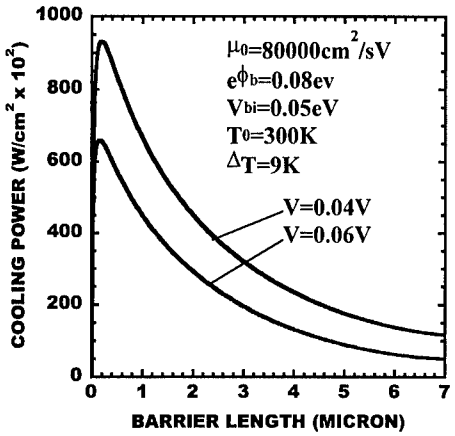

Fig. 4 Net cooling power as a function Of layer length with different voltages

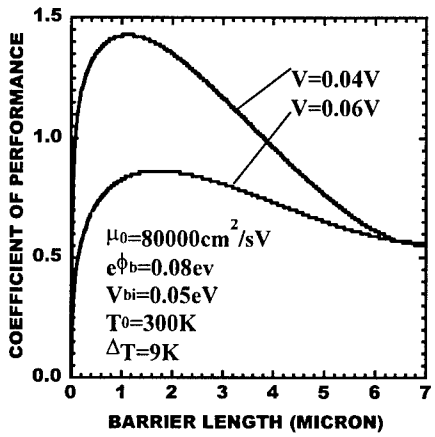

Fig.5 Coefficient of Performance(COP) as a function of layer length with different voltages

References

1. Mahan, G. D., J. Applied Physics, v. 76, p. 4362 (1994)
2. Shakouri, A., and Bowers, J. E., Applied Physics Letters, v. 71, p. 1234 (1997)
3. Mahan, G. D., and Woods, L. M, Physical Review Letters, v. 80, p. 4016 (1998)
4. Mahan, G. D., Sofo, J. O., and Bartkowiak, M., J. Applied Physics, v. 83, p. 4683 (1998)
5. Shakouri, A., Lee, E. Y., Smith, D. L., Narayanamurti, V., and Bowers, J. E., Microscale Thermophysical Engineering, v. 2, p.37 (1998)
6. Hatsopoulous, G. N., and Kaye, J. J., Applied Physics, v.29, p. 1124 (1958)
7. Rhoderick, E. H., and Williams, R. H., Metal-Semiconductor Contacts, 2nd Ed., Clarendon Press, Oxford (1988)
8. Tait, G. B., and Westgate, C. R., IEEE Trans. Electron Devices, v. 38, p.1262 (1991)
9. Hario, K., and Yanai, H., IEEE Trans. Electron Devices, v. 37, p. 1093 (1990)
10. Yang, K., East, J. R., and Haddad, G. I, Solid-State Electronics, v. 3, 00. p. 321 (1993)
11. Hjelmgren, H., and Tang, T. W, Solid-State Electronics, v. 9, p. 1649 (1994)
12. Sze, S. M., Physics of Semiconductor Devices, 2nd Ed., John Wiley & Sons, New York, 1981
13. Reggiani, L. (Ed.), Hot-Electron Transport in Semiconductors, Springer-Verlag, 1985
14. Stratton, R., Physical Review, v. 126, p.2002 (1962)
15. Hess, K., Advanced Theory of Semiconductor Devices, Prentice Hall, New Jersey, 1988
16. Lundstrom, M., Fundamentals of Carrier Transport, Addison-Wesley, Reading, MA, 1990
17. Qiu, T.Q., and Tien, C. L., J. Heat Transfer, v.115, p.835 (1993)
18. Kaganov, M.I., Lifshitz, I.M., and Tanatarov, L.V., Sov. Phys. JETP, v. 4, p.173 (1957)

ANISOTROPIC THERMAL CONDUCTIVITY OF A Si/Ge SUPERLATTICE

T. Borca-Tasciuc[1], D. Song[1], J. L. Liu[2], G. Chen[1,*], and K. L. Wang[2]
[1]Mechanical and Aerospace Engineering Department, [2]Department of Electrical Engineering
University of California, Los Angeles, CA 90095-1597, *Email: gchen@seas.ucla.edu

X. Sun[3] and M. S. Dresselhaus[3,4]
[3]Department of Physics, [4]Department of Electrical Engineering and Computer Science
Massachusetts Institute of Technology, Cambridge, MA 02139

T. Radetic and R. Gronsky
Department of Materials Science and Mineral Engineering
University of California, Berkeley, CA 94720

ABSTRACT

Experimental evidence for a significant thermal conductivity reduction have been reported in recent years for GaAs/AlAs, Si/Ge, and Bi_2Te_3/Sb_2Te_3 superlattices. In this work, we present preliminary experimental results on the reduction of the in-plane and cross-plane thermal conductivity for a symmetric Si/Ge superlattice. A differential 2-wire 3ω method is developed to perform the anisotropic thermal conductivity measurements. In this technique, a patterned heater with a width much larger than the film thickness yields the cross-plane thermal conductivity of the film. The in-plane thin film thermal conductivity is inferred from the temperature rise of a narrow width heater that can create more heat spreading in the in-plane direction of the thin film. A differential method to measure the temperature drop across the film is employed in order to increase the accuracy of the measurement.

INTRODUCTION

Experimental results on the thermal conductivity of superlattices were reported in recent years for several material systems, including GaAs/AlAs [1-3], GaAs/AlGaAs [4], Si/SiGe [5], Si/Ge [6-8] and Bi_2Te_3/Sb_2Te_3 [9, 10]. These studies demonstrated that the thermal conductivity of a superlattice could be much lower than that estimated from the bulk values of its constituent materials [1] and even smaller than the thermal conductivity value of the equivalent composition alloys. Several models have been developed for both the in-plane and the cross-plane direction. For the in-plane direction, models based on the Boltzmann transport equation explain well the measured thermal conductivity of GaAs/AlAs superlattices [11,12]. For the cross-plane direction, models have been established based on the phonon group velocity reduction [13] and the Boltzmann transport equation [14,15]. The latter approach leads to the conclusion that the phonon transport in Si/Ge and GaAs/AlAs superlattices is ballistic [14,15]. Consequently, the thermal conductivity of these superlattices is strongly influenced by the mismatch between the specific heat, phonon group velocity, and density, of the two materials forming the superlattice. Moreover, these studies suggest the possibility of controlling the thermal conductivity of superlattice structures through phonon engineering.

In this work, we provide new experimental evidence for a thermal conductivity reduction for a Si/Ge superlattice structure. A differential 2-wire 3ω method is developed to perform simultaneous in-plane and cross-plane thermal conductivity measurements on a symmetric Si/Ge superlattice. With this technique, the cross-plane thermal conductivity is obtained by measuring the temperature of a patterned heater with a width much larger than the film thickness. The in-plane thin-film thermal conductivity is determined using a small width heater which can create more heat spreading in the in-plane direction of the thin film. A differential method is employed to measure the temperature drop across the thin film experimentally in order to increase the accuracy of the thermal conductivity determination. A similar method had been used to measure the anisotropic thermal conductivity of Si/SiGe [5] and polymer films [16].

The experimental data show that the cross-plane and the in-plane thermal conductivities of this structure are smaller than the corresponding $Si_{0.5}Ge_{0.5}$ alloys. The result reinforces the idea of

Mat. Res. Soc. Symp. Proc. Vol. 545 © 1999 Materials Research Society

controlling the thermophysical properties of low dimensional structures through phonon engineering.

SAMPLE AND MEASUREMENT TECHNIQUE

The configuration of the MBE grown sample measured in this report is shown in Fig. 1. A graded buffer film, composed of 11 layers of Si_xGe_{1-x}, is initially grown on an n-type (~ 20 Ωcm) Si substrate. The concentration of silicon (x) in the layers varies from one (pure Si) near the substrate to zero (pure Ge) near the buffer/superlattice interface. The buffer film is not intentionally doped. We intended to grow a symmetric 66Å period Si/Ge superlattice with 33Å for each layer. X-ray diffraction shows that the period thickness is actually ~ 73 Å. A total of 150 periods are grown, yielding a total thickness of the superlattice as 1.1 μm. The buffer thickness was re-scaled to 1.2 μm by assuming the same relative error between the intended (1.1 μm) and the true thickness value. The superlattice film is uniformly doped with As during the growth. In order to perform the thermal conductivity measurements, metallic wires with different widths are patterned onto the sample. Since the superlattice film is semiconducting, the metallic wire must be insulated from the film to avoid current leakage. The electrical insulation is provided by a 3600 Å SiO_2 film deposited by plasma enhanced chemical vapor deposition at 300 ° C onto the sample.

The sample described above has a complex multilayers configuration and we approximate it as an effective 3-layer structure. Taking the buffer as one effective-layer, there are two thermally anisotropic films (buffer and superlattice) and one isotropic film (SiO_2 insulation) deposited onto the substrate. In a previous work [5], simultaneous in-plane and cross-plane thermal conductivity characterization was performed on a two-film-on-substrate system composed of only one anisotropic film and one isotropic film. In this work, the previously developed 2-wire 3ω method [5] will be extended to accommodate thermal characterization of samples with the current 3-layer configuration.

The starting point in developing the thermal conductivity measurement technique is the 2-wire 3ω method [5]. This method is based on extending the 3ω method developed originally by Cahill and co-workers [17, 18]. In the 3ω method, a metal wire is deposited onto the film to act as both a heater and a temperature sensor, as shown in Fig.1. The 3ω method has been traditionally used in the measurement of the cross-plane thermal conductivity of thin films. The 2-wire 3ω method [5] extends the 3ω method for both the in-plane and the cross-plane thermal conductivity of thin films. The idea is to measure the temperature of heaters having two different wire widths with respect to the film thickness. A wide wire will be more sensitive to the cross-plane thermal conductivity of the film. This is because heat will spread less in the in plane direction, and heat conduction across the film will be essentially one-dimensional. The narrow wire will be relatively more sensitive to the in-plane thermal conductivity. The theoretical model of the 2-wire 3ω method [5] is developed to calculate the heater temperature rise for a two-layer-

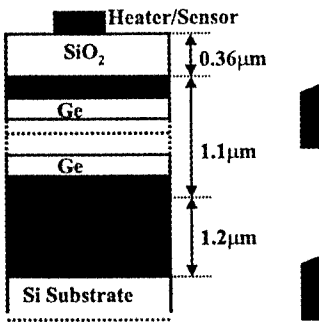

Fig. 1 Sample configuration.

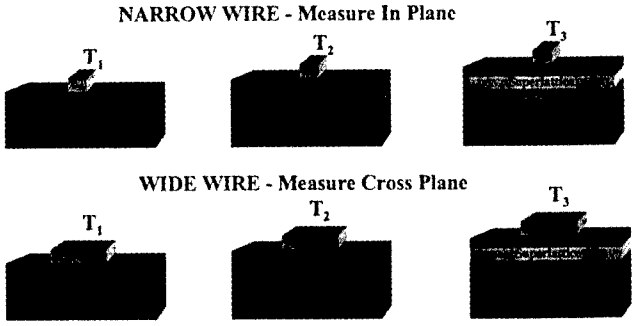

Fig. 2 Differential 2-wire 3ω method.

-film-on-substrate system composed of one isotropic film and one anisotropic film. To determine the in-plane and cross-plane thermal conductivity of the anisotropic film, the theoretically estimated temperature rise is compared to the experimentally measured temperature rise for two different wire widths. The method relies on thermal conductivity values of the isotropic insulating film and the substrate, which are necessary to calculate the theoretical temperature rise of the heater. The thermal conductivity of the substrate and isotropic film are measured by the 3ω method on a separate sample. However, the slope method [17, 18] employed by the 3ω technique to measure the substrate thermal conductivity can generate significant errors. Furthermore, the error in the substrate thermal conductivity can generate inaccuracy in the determination of the isotropic film thermal conductivity. The errors could accumulate and increase the uncertainty of the measured in-plane and cross-plane thermal conductivity of the anisotropic film. This problem will become even more important for the case of multi-layered thin films on substrate systems.

A differential 2-wire 3ω method is used in this work to increase the accuracy of the anisotropic thermal conductivity measurements for multilayered films on substrate systems. The idea is to use the experimentally measured temperature drop across one layer to back-up the thermal conductivity of the layer. This temperature drop is measured based on a series of samples as illustrated in Fig.2. The differential 2-wire 3ω thermal conductivity characterization of the 3-layer-film-on-substrate-system requires deposition of wires with different widths on three different samples, including a substrate, a buffer grown on the substrate, and a superlattice with the buffer. All three samples have the same insulation layer. Metallic heaters/temperature sensors with wire widths between 2 - 30 μm are processed at the same time on all the three samples. For a given wire width, the same power is passed through the heaters and the temperature rise at a given frequency is recorded for all three samples. The measured temperature difference between the buffer sample and the substrate sample, for two different wire widths, will be used to determine the in-plane and cross-plane thermal conductivity of the effective buffer layer. The same technique can be applied for the superlattice sample and the substrate sample to determine the thermal properties of the effective anisotropic film composed of the buffer and the superlattice layers. By subtracting the buffer contribution from the effective buffer / superlattice film, the in-plane and cross-plane thermal conductivity of the Si/Ge superlattice can be determined.

The above-presented measurement approach is based on the approximation that a multilayered structure is equivalent from the heat-transfer point of view to an effective anisotropic film. This assumption allows the calculation of the heater temperature rise by using the expressions previously derived in the theoretical framework of the 2-wire 3ω method [5] for a two-layer-film-on-substrate formed by one isotropic film and one anisotropic film.

EXPERIMENTAL RESULTS AND DISCUSSION

The expression for the frequency dependent temperature rise of a heater situated on the surface of a two-layer-on-a-substrate system, composed of one isotropic and one anisotropic film, was derived elsewhere [5]. One example of the calculated temperature rise is shown in Fig. 3. The solid line represents the temperature rise of the heater situated on a two-layer-film-on-substrate-system composed of one isotropic film and one anisotropic film. The dashed line

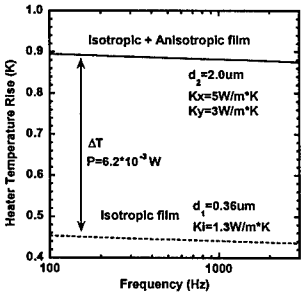

Fig. 3 Example of the theoretically calculated temperature rise for a 2 μm heater on a two-layer-on-substrate system composed of one anisotropic and one isotropic film (solid line). The dashed line represents the calculated temperature rise when the heater is on the surface of the one-layer isotropic film.

describes the temperature rise of the heater when situated on the isotropic film-on-substrate system under the same conditions. The substrate is assumed to be semi-infinite. The difference in the temperature rise between the two curves is constant over a wide frequency range (f) and is equal to the DC temperature difference (for f=0). This behavior allows an accurate determination of the temperature drop across the anisotropic film. Starting from the expression for the frequency dependent ac temperature rise of the heater situated on a two-layer-film-on-substrate system composed of one isotropic and one anisotropic film [5], the expression for the frequency independent DC temperature difference can be easily derived. Normalizing this DC temperature difference ($\Delta\theta_{DC}$) to the heat flux (q) through the heater, leads to,

$$\frac{\Delta\theta_{DC}}{q} = f\left(K_x, K_y, K_s, K_i, d_1, d_2, b\right) \qquad (1)$$

where b is the half-width of the wire and f is a complicated integral function that depends on the in-plane (K_x) and cross-plane (K_y) thermal conductivities of the anisotropic film, the substrate thermal conductivity (K_s), the insulation (isotropic) film thermal conductivity (K_i), isotropic film thickness (d_1) and thickness of the anisotropic film (d_2). This normalized temperature difference can be experimentally determined for two different wire widths and will be use to back out the thermal conductivities of the anisotropic film.

The differential 2-wire 3ω method is first applied to determine the anisotropic thermal conductivity of the buffer film. Figure 4a shows the experimental temperature rise for 3 μm and 30 μm heaters deposited on the buffer and substrate samples. The temperature difference measured between the buffer sample and the substrate sample is constant over a wide frequency range. Therefore, the experimental temperature difference normalized by the heat flux can be determined for each heater width. Equation (1) is then employed to calculate the contours of the constant normalized temperature difference for the given wire width. These curves are plotted with solid lines in Fig. 4b. The narrow wire is sensitive to both the in-plane and the cross-plane components of the thermal conductivity of the buffer film. The wide wire is almost insensitive to the in-plane component of the thermal conductivity. This behavior is explained by the different relative spreading experienced by the thermal wave for the two different wire widths. For the measured buffer sample, the two curves intersect with each other for a 7.8 W/m K in-plane thermal conductivity and for an 11.5 W/m K cross-plane thermal conductivity of the buffer layer. The smaller in-plane value is unexpected but may be due to a high density of threading dislocations in the growth direction. Another possibility is the experimental error. The dashed-lines in Fig. 5 represent the curves of constant normalized temperature difference of the two

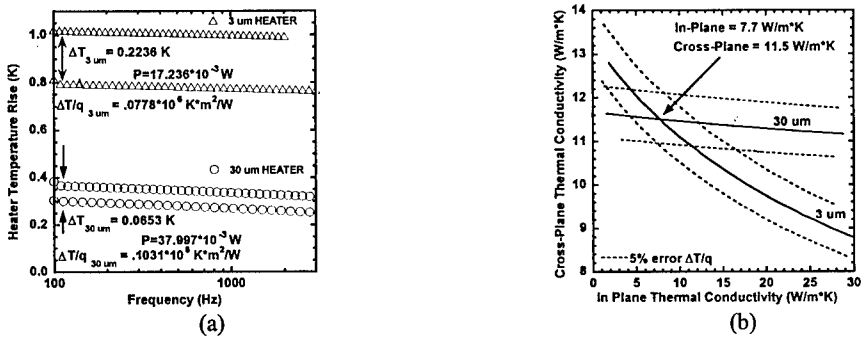

Fig. 4 (a) Experimentally measured temperature difference across the buffer layer for two wire widths. (b) Contours of constant normalized temperature difference across the buffer layer for two wire widths. The intersects lead to the in-plane and cross-plane thermal conductivities of the anisotropic film.

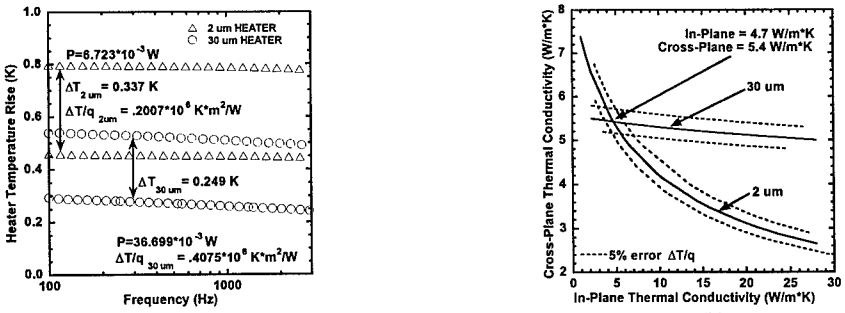

Fig. 5 (a) Experimentally measured temperature difference across the buffer/superlattice effective layer for two wire widths. (b) Contours of constant normalized temperature difference across the buffer/superlattice effective layer for two wire widths. From the effective thermal conductivity of the buffer/superlattice effective layer, the thermal conductivity of the superlattice is determined as 1.4 W/m K in the in-plane direction and 3.4 W/m K in the cross-plane direction.

heaters, for a ± 5% error in the determination of the experimental normalized temperature drop. An error in the normalized temperature difference will generate a relatively much larger inaccuracy in determination of the in-plane thermal conductivity. The cross-plane measurement is less affected by the error.

In order to determine the anisotropic thermal conductivity of the Si/Ge superlattice, the differential 2-wire 3ω method is applied to measure the effective anisotropic thermal properties of the buffer/superlattice film. Figure 5a shows the experimental temperature rise for the 2 μm and 30 μm heaters deposited on the superlattice and substrate samples. Figure 5b shows the curves of constant normalized temperature difference, calculated for the experimental values of the normalized temperature difference for the 2 μm and 30 μm heaters. The intersection of the curves yields an effective in-plane thermal conductivity of 4.7 W/m K and an effective cross-plane thermal conductivity of 5.4 W/ m K for the composite layers. The dashed-lines in Fig. 5b represent the curves of constant normalized temperature difference of the two heaters, for a ± 5% error in the determination of the experimental normalized temperature drop.

The anisotropic thermal conductivity of the Si/Ge superlattice can be determined by eliminating the buffer contribution. The measured thermal conductivity of the Si/Ge superlattice is 1.4 W/ m K in the in-plane direction, and 3.4 W/m K for the cross-plane direction. The experimental data show that the anisotropic thermal conductivity of the Si/Ge superlattice structure is about two to three times smaller than that for the corresponding $Si_{0.5}Ge_{0.5}$ alloys. The measured thermal conductivity in the in-plane direction is smaller than in the cross-plane direction, which is unexpected. TEM analysis of the sample showed a high density of dislocations although high magnification micrographs clearly show the periodic Si-Ge superlattice structure. The high dislocation density may arise from the fact that the grown buffer is not totally relaxed. The threading dislocations could be the reason causing the smaller in-plane thermal conductivity. Yet one other possible explanation could be the relatively large uncertainty in the determination of the in-plane thermal conductivity in the present set-up, as shown by the dashed-lines in Fig. 4b and Fig. 5b. However, the sensitivity of the measurement in the in-plane direction could be improved if the width of the narrow wire is reduced, or the thickness of the superlattice is increased. Furthermore, the measurement inaccuracy could be reduced if more than two wires are used to determine the intersection of the constant normalized temperature difference curves. Improvements in both the sample quality and measurement accuracy will be pursued in our future work.

CONCLUSION

A differential 2-wire 3ω method was developed to measure simultaneously the in-plane and cross-plane thermal conductivity of anisotropic films. Preliminary results are reported for an MBE grown Si/Ge superlattice. The measured value for the cross-plane thermal conductivity, 3.4 W/m K, is smaller than the thermal conductivity of the $Si_{0.5}Ge_{0.5}$ alloy. A smaller than cross-plane thermal conductivity, 1.4 W/m K, was measured in the in-plane direction. This could be due to the high density of threading dislocations in the superlattice or to measurement inaccuracy. The accuracy of the method can be improved by using multiple and narrower wires or increasing the superlattice thickness.

ACKNOWLEDGEMENTS

This work is supported by a DOD MURI program on thermoelectrics. We would like to thank Prof. M. S. Goorsky and Dr. C. Moore for the X-ray diffraction measurements of the superlattice period.

REFERENCES

1. T. Yao, Appl. Phys. Let. **51**, p. 1798 (1987).
2. X. Y. Yu, G. Chen, A. Verma, and J. S. Smith, Appl. Phys. Let. **67**, p. 3554-3556, **68**, p. 1303 (1995).
3. W. S. Capinski, and H. J. Maris, H.J., Physica B **219**, p. 699-701 (1996).
4. G. Chen, C. L. Tien, X. Wu, and J. S. Smith, J. Heat.Trans. **116**, p. 325-331 (1994).
5. G. Chen et al., Proc. 17th Int. Thermoelectrics Conf. ICT98, p. 202-205 (1998).
6. S. M. Lee, D. G. Cahill, and R. Venkatasubramanian, Appl. Phys. Let. **70**, p. 2957-2959 (1997).
7. R. Venkatasubramanian and T. Colpits, in Mater. Res. Soc. Symp. Proc. **478**, p. 73 (1997).
8. R. Venkatasubramanian, E. Siivola, and T. Colpits, Proc. 17th Int. Thermoelectrics Conf. ICT98, p. 191-196 (1998).
9. R. Venkatasubramanian, Naval Research Reviews **58**, p. 44 (1998).
10. I. Yamasaki, R. Yamanaka, M. Mikami, H. Sonobe, Y. Mori and T, Sasaki, Proc. 17th Int. Thermoelectrics Conf. ICT98, p. 210-213 (1998).
11. G. Chen, J. Heat Trans.**119**, p. 220-229 (1997).
12. P. Hyldgaard and G. D. Mahan, in *Thermal Conductivity* **23**, (Technomic, Lancaster, 1995). p. 172-182.
13. P. Hyldgaard and G. D. Mahan, G.D., Phys. Rew. B. **56**, p. 10754-10757 (1997).
14. G. Chen and M. Neagu, Appl. Phys. Let. **71**, p. 2761-2763 (1997).
15. G. Chen, G., 1998, Phys. Rew. B. **57**, p. 14958-14973 (1998).
16. K. Kurabayashi, M. Touzelbaev, M. Ashegi, Y. S. Ju, and K. E. Goodson, Proc. 7th AIAA/ASME Joint Thermophysics and Heat Transfer Conf. ASME, HTD **357-3**, p. 187 (1998).
17. D. G. Cahill, 1990, Rev. Sci. Instrum. **61**, p. 802-808 (1990).
18. S. M. Lee, and D. G. Cahill, J. Appl. Phys. **81**, p. 2590-2595 (1997).

INVESTIGATION OF THE MECHANISM OF THE ENHANCED $Z_{3D}T$ IN PbTe BASED SUPERLATTICES

T. Koga*, T. C. Harman**, X. Sun*, S. B. Cronin*, and M. S. Dresselhaus*,**
*Division of Engineering and Applied Sciences, Harvard University, Cambridge, MA 02138
**Lincoln Laboratory, Massachusetts Institute of Technology, Lexington, MA 02420
*Department of Physics and **Department of Electrical Engineering and Computer Science, Massachusetts Institute of Technology, Cambridge, MA 02139

ABSTRACT

Various possible mechanisms for the recently discovered enhanced Seebeck coefficient S in PbTe/Te superlattices relative to the corresponding PbTe bulk are investigated. Among the various mechanisms which can account for the enhanced S, the energy dependent τ model ($\tau \sim \varepsilon^r$) seems the most plausible. Here the effective scattering parameter r is preferably increased due to the extra scattering by the periodic Te layers introduced in the superlattice. Other transport properties including the longitudinal magnetoresistance are also discussed.

INTRODUCTION

There has been an increasing interest in the enhanced thermoelectric figure of merit Z ($= S^2\sigma/\kappa$), where S is the Seebeck coefficient, σ is the electrical conductivity, and κ is the thermal conductivity, for a material in the form of a superlattice or multiple-quantum-well (MQW) structure [1-8]. In the early stage of this research area, most work was focused on the enhanced Z within the quantum well region due to the quantum confinement of electrons, denoted by Z_{2D} (quantum well approach). Another advantage of having a superlattice structure is the reduced lattice thermal conductivity κ_{ph} due to the boundary scattering of phonons at the barrier-well interfaces, which contributes to the enhancement of both $Z_{2D}T$ and $Z_{3D}T$, where $Z_{3D}T$ denotes the figure of merit for the whole superlattice. Recently, the idea of the quantum well approach has been extended to predict an enhanced $Z_{3D}T$ for the GaAs/AlAs superlattices [4], which shows that this extended approach is promising for future thermoelectric applications.

Another approach to design a good thermoelectric material using a superlattice structure is the so-called potential barrier model [6, 7] (potential barrier approach). It is suggested that the potential barriers introduced in a superlattice would contribute to a moderate increase in S and a moderate decrease in σ. Then, the overall consequence is a moderately increased $S^2\sigma$ for optimized conditions. The merit of having a reduced κ_{ph} in a superlattice structure should be preserved in the potential barrier approach as well.

Recently, novel Pb-chalcogenide-based MBE-grown superlattices, i.e. PbTe/Te superlattices, have been experimentally discovered to have enhanced thermoelectric properties [3]. It is found that this class of materials has a Seebeck coefficient larger by 35–58 μV/K (enhancement of S by 42 % on average) than that for the corresponding MBE-grown bulk PbTe at the same carrier concentration. The observed Hall carrier mobility is almost the same or slightly smaller than those for the corresponding bulk PbTe. The resulting $S^2\sigma$ and $Z_{3D}T$, estimated using the bulk value for κ_{ph} from the literature, are therefore enhanced by 23 and 25 %, respectively. It is noted that the optimum $S^2\sigma$ and $Z_{3D}T$ occur at relatively higher carrier concentrations for the PbTe/Te superlattices ($n_{opt}\sim 1\times10^{19}$ cm^{-3}) than for the cor-

Mat. Res. Soc. Symp. Proc. Vol. 545 © 1999 Materials Research Society

Sample No.	S [μV/K]	n [cm^{-3}]	μ [cm^2/Vs]	d_{PbTe} [nm]	# of periods
T184	-149	7.3×10^{18}	1200	bulk PbTe	bulk PbTe
T442	-80	4.0×10^{19}	650	21.6	189
T444	-163	1.3×10^{19}	785	26.7	189
T446	-193	8.2×10^{18}	880	29.9	190
T447	-203	5.8×10^{18}	1015	14.8	314

Table 1: Summary of the superlattice parameters and 300 K properties for the MBE-grown PbTe and PbTe/Te superlattice samples used in the present study. Data are taken from Ref. [3].

responding bulk PbTe ($n_{\mathrm{opt}}\sim6\times10^{18}$ cm^{-3}). In this report, we first consider the possible mechanisms which may account for the observed enhancement in S and then discuss other transport measurements such as the longitudinal magnetoresistance to get further insight into the mechanism for the observed enhanced thermoelectric properties in PbTe/Te superlattices.

EXPERIMENTS AND MODELS

The details of the sample preparation are given elsewhere [3]. Briefly, the PbTe/Te multilayer structures were grown by molecular beam epitaxy where the thickness of the PbTe layer was varied from 14.8 to 29.9 nm as shown in Table 1. The thickness of the Te layer is believed to be 2 to 3 monolayers (ML), since we find that the Te layers are only adsorbed layers on the PbTe surface. The Bi dopants were introduced into the PbTe layers homogeneously to make the material n-type. A summary of the samples used in the present study is given in Table 1 from Ref. [3].

Shown in Fig. 1 is a plot of the experimental Seebeck coefficient as a function of Hall carrier concentration [3] together with the theoretical curves calculated using an (a) energy-dependent τ model and (b) potential barrier model, which are described in more detail in the following subsections. First we discuss the possibility of having an enhanced effective mass, which is relevant to having a quantum confinement of electrons.

In the constant relaxation time approximation, the Seebeck coefficient S and the carrier concentration n for a material with parabolic energy bands are expressed as

$$S = -\frac{k_B}{e}\left(\frac{5F_{3/2}(\zeta^*)}{3F_{1/2}(\zeta^*)} - \zeta^*\right) \quad \text{and} \quad n = \frac{1}{2\pi^2}\left(\frac{2k_BT}{\hbar^2}\right)^{\frac{3}{2}}(m^*)^{\frac{3}{2}}F_{1/2}(\zeta^*), \tag{1}$$

respectively, where $F_i(\zeta^*)$ denotes the Fermi-Dirac related integrals defined elsewhere [1]. We find that S is a function of only the reduced chemical potential ζ^* ($\zeta^* = \zeta/k_BT$), whereas the carrier concentration is proportional to the power 3/2 of the density-of-states mass m^* ($m^* = N^{2/3}(m_t^2m_l)^{1/3}$), where N is the number of equivalent carrier pockets in the Brillouin zone. This implies that the increased effective mass along the superlattice growth direction due to the quantum confinement could account for the observed enhanced S. However, we exclude this possibility because: 1) we did not observe any difference in the optical band gap between the PbTe/Te superlattices and MBE-grown PbTe, implying that no quantum confinement is taking place in the samples, 2) the periodically-introduced Te layers in the PbTe/Te superlattices are so thin (0.8–1.5nm) that it is hardly believed that the Te layers behave as either quantum wells or barrier layers.

Energy Dependent τ model

Another possibility which may explain the observed enhancement in S is the preferably modified energy dependence of τ. Assuming $\tau \sim \varepsilon^r$, where ε is the energy for an electron and r denotes a scattering parameter, S for a bulk semiconductor is expressed as

$$S = -\frac{k_B}{e}\left(\frac{(r+5/2)F_{r+3/2}(\zeta^*)}{(r+3/2)F_{r+1/2}(\zeta^*)} - \zeta^*\right). \tag{2}$$

It is known that the scattering parameter r is $-1/2$ for deformation potential scattering due to the acoustic phonons, $1/2$ for the piezoelectric scattering due to the acoustic phonons, and $3/2$ for the ionized impurity scattering. Shown in Fig. 1(a) is the theoretical fitting of the experimental data using various values for r. It is found that $r = 1$ to 1.5 would explain the observed enhancement in S, which is well within the range of values for the conventional scattering mechanisms. Therefore, our future work should be focused on investigation of the scattering mechanism associated with the extra Te layers in the PbTe/Te superlattices, since they may modify the details of the scattering mechanism for electrons and give the same effect as increasing r (the higher the r, the higher the S for a given ζ^*). Thus, we need to investigate other transport properties such as the longitudinal magnetoresistance of the PbTe/Te superlattices (discussed below) to get further information on the scattering mechanism that enhances S.

Potential Barrier Model

We also considered whether the so-called potential barrier model (PBM), proposed by Rowe *et al.* [6] and Nishio *et al.* [7], could explain the observed enhancement in S for the PbTe/Te superlattice samples. In this model, S is calculated by solving the Boltzmann equation with the assumption that the scattering time τ is zero if the energy of the electron ε is smaller than some value for the potential barriers E_0, and $\tau = \tau_0$ if ε is larger than E_0, where τ_0 is assumed to be independent of ε for simplicity. Shown in Fig. 1(b) are the results of the theoretical fitting to the experimental data using the PBM with various values for E_0. We find: 1) the PBM with reasonable values for E_0 (typically $E_0 \simeq 50$ meV) predicts a large enhancement in S only at relatively low carrier concentrations n (typically $<5\times10^{18}$ cm^{-3}) and negligible enhancement at high n (typically $>10^{19}$ cm^{-3}), 2) the experimentally observed enhancement in S persists at moderate to high n values ($>5\times10^{18}$ cm^{-3}), whereas the calculated enhancement in S does not, as mentioned above, and 3) although the difference in the experimental S between the PbTe/Te superlattice and bulk PbTe at a given n is almost constant as a function of n, the PBM predicts that the difference in S between the samples with and without the potential barriers should decrease with increasing n. Because of these discrepancies, we also have to exclude the possibility of the PBM in its present form as the possible mechanism for the observed enhancement in S in PbTe/Te superlattices.

Longitudinal Magnetoresistance, Magneto-Mobility and Hall Mobility

Our analysis in the previous subsections suggests a more detailed study is needed of the transport properties in PbTe/Te superlattices to collect more information on the details of the scattering mechanism due to the extra Te layers. Here, we chose to study the longitudinal magnetoresistance for this purpose. Both the magnetic field and the electric current are applied parallel to the plane of the superlattice, i.e. in the $(1\bar{1}0)$ direction. Considering

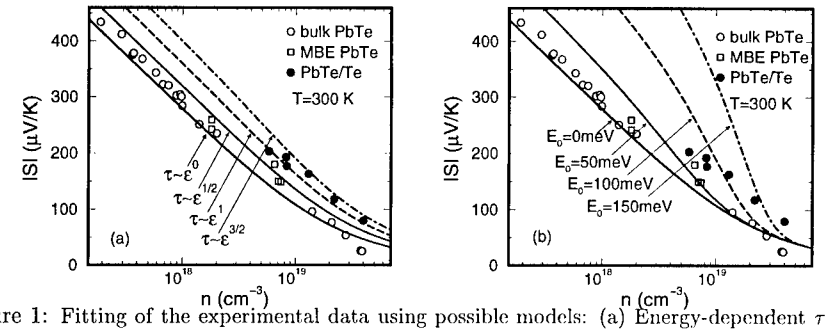

Figure 1: Fitting of the experimental data using possible models: (a) Energy-dependent τ with various scattering parameters r. (b) Potential barrier model with various values for the potential barrier E_0. The experimental data are taken from Refs. [2] and [3].

the L point carriers in this configuration, we can calculate the magneto-conductivity tensor $\sigma(B)$, using an equation of motion for an electron, $e\,(\mathbf{E} + \mathbf{v} \times \mathbf{B}) = m\mathbf{v}/\tau$, from which we can calculate the longitudinal magnetoresistance ($\Delta R/R_0$). This formulation suggests that the coefficient for the B^2 term in the magnetoresistance is related to the carrier mobility $\mu_{\rm M}$ by:

$$\left.\frac{\Delta\rho}{\rho B^2}\right|_{\rm longit.} = \mu_{\rm M}^2 \frac{3K(K-1)^2}{(2K+1)^3}, \quad \text{where } \mu_{\rm M} = \frac{|e|}{3}\left(\frac{2}{m_t}+\frac{1}{m_l}\right)\left(\frac{\langle\tau_m^3\rangle}{\langle\tau_m\rangle}\right)^{\frac{1}{2}} \text{ and } K = \frac{m_l}{m_t}, \quad (3)$$

where $(\langle\tau_m^3\rangle/\langle\tau_m\rangle)^{1/2} = \tau$ for the constant τ approximation.

Shown in Fig. 2(a) are the results of the calculation using the experimentally obtained magneto-mobilities for MBE-grown bulk PbTe (see Fig. 3a) $\mu_{\rm M}$ = 5100, 13100, 38000, and 53000 cm^2/Vs for T = 150, 77, 30, and 4.5 K, respectively, under the constant τ approximation. The generic features shown in this figure are: 1) $\sim B^2$ dependence of $\Delta R/R_0$ at small magnetic field B, 2) a saturation behavior of $\Delta R/R_0$ at large magnetic field, and 3) the saturation level for $\Delta R/R_0$ is just above 0.2.

Shown in Fig. 2(b) are the experimental results for MBE-grown bulk PbTe (T184). We find the above three generic features in Fig. 2(b) for T = 150, 77 and 30 K. However, we also see a non-saturation effect for $\Delta R/R_0$ at high magnetic field and low temperature (T = 4.5 K). This discrepancy may be due to entering the quantizing field regime, consistent with the appearance of oscillations in $\Delta R/R_0$ at high B for the T = 4.5 K data. Our semi-classical model is not strictly valid in this regime. Shown in Figs. 2(c) and (d) are two typical experimental behaviors observed for PbTe/Te superlattices (T446 and T447), in addition to the observed behaviors that are consistent with the model calculation (Fig. 2a). One (c) shows a linearly increasing $\Delta R/R_0$ with magnetic field below T = 30 K, whereas the other (d) shows a sharp peak in $\Delta R/R_0$ around 0.3 T which becomes pronounced below T = 30 K. All PbTe/Te samples that have been investigated show one or the other of these typical behaviors. At the present time, we do not know the exact origin for these unexpected behaviors in the longitudinal magnetoresistance for PbTe/Te superlattices. However there might be some relation between the observed anomalies in the longitudinal magnetoresistace and the observed enhanced S in PbTe/Te superlattices.

Despite the anomalous behaviors discussed above, the behavior of the observed magnetoresistance in the low field regime (typically <0.1 T) is consistent with the transport

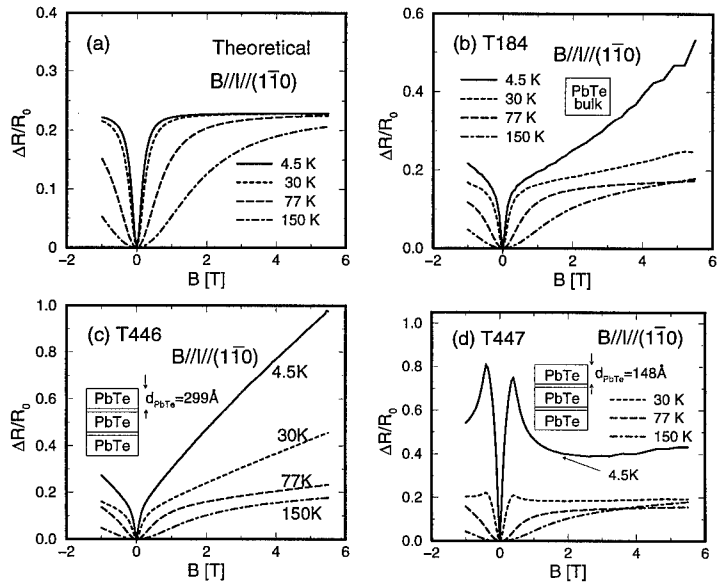

Figure 2: The calculated (a) and the experimental (b, c and d) results for the longitudinal magnetoresistance for bulk PbTe (a and b) and for PbTe/Te superlattices (c and d) at various temperatures. See Table 1 for the properties of the various samples.

properties in zero field. Shown in Fig. 3(a) is the mobility deduced from the longitudinal magnetoresistance via Eq. 3, while the carrier mobility obtained from the Hall measurement (shown in Fig. 3b) is in qualitative agreement with the mobility obtained from the longitudinal magnetoresistance.

CONCLUSIONS

Various possible mechanisms are investigated to explain the recently discovered enhanced Seebeck coefficient in PbTe/Te. The energy dependent τ model ($\tau \sim \varepsilon^r$) is found to be the most reasonable among the various theoretical models considered. Thus our future research should focus on investigation of the effective scattering parameter r for the scattering due to the extra Te layers. The longitudinal magnetoresistance (LMR) of PbTe/Te superlattices has been investigated for this purpose. The low field LMR is found to be consistent with the transport mobility at zero field. Some anomalies are found in the LMR at low temperatures and in moderate to high magnetic fields. The relation between these anomalies and the observed enhanced Seebeck coefficient should be investigated in more detail in the future, especially with regard to possible energy dependent relaxation processes.

ACKNOWLEDGMENTS

The authors would like to thank Dr. G. Dresselhaus for valuable discussions and inputs. Support from the US Navy (N00167-98-K-0024) for this work is also gratefully acknowledged. The Lincoln Laboratory portion of this work was sponsored by the Department of the Navy,

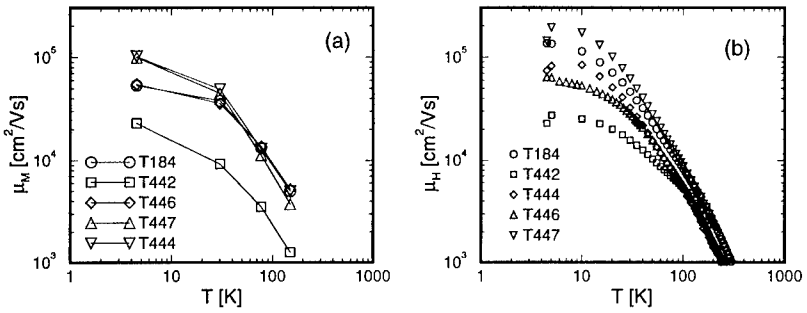

Figure 3: (a) Magneto mobility calculated from the longitudinal magnetoresistance measurements via Eq. 3 and (b) Hall carrier mobility for MBE-grown bulk PbTe (T184) as well as PbTe/Te superlattices as a function of temperature.

The Army Research Office, and the Defense Advanced Research Projects Agency (DARPA) under AF Contract No. F19628-95-0002. The opinions, interpretations, conclusions and recommendations are those of the authors and are not necessarily endorsed by the United States Air Force.

REFERENCES

[1] L. D. Hicks and M. S. Dresselhaus, Phys. Rev. B **47**, 12727 (1993); L. D. Hicks and M. S. Dresselhaus, Phys. Rev. B **47**, 16631 (1993);

[2] T. C. Harman, D. L. Spears, and M. J. Manfra, J. Electron. Mater. **25**, 1121 (1996); L. D. Hicks, T. C. Harman, X. Sun, and M. S. Dresselhaus, Phys. Rev. B **53**, R10493 (1996); T. C. Harman, D. L. Spears, D. R. Calawa, S. H. Groves, and M. P. Walsh, Proceedings for 16th International Conference on Thermoelectrics page 416 (1997).

[3] T. C. Harman, D. L.Spears, and M. P. Walsh, Abstract for the 40th Electronic Materials Conf., Charlottesville, J. Electron. Mater. **27**, No. 7, 44 (1998); T. C. Harman, D. L. Spears, and M. P. Walsh, J. Electron. Mater. Lett. **28**, L1 (1999).

[4] T. Koga, X. Sun, S. B. Cronin and M. S. Dresselhaus, Appl. Phys. Lett. **73**, 2950 (1998).

[5] J. O. Sofo and G. D. Mahan, Appl. Phys. Lett. **65**, 2690 (1994); D. A. Broido and T. L. Reinecke, Appl. Phys. Lett. **67**, 100 (1995); D. A. Broido and T. L. Reinecke, Appl. Phys. Lett. **67**, 1170 (1995); P. J. Lin-Chung and T. L. Reinecke, Phys. Rev. B **51**, 13244 (1995); D. L. Broido and T. L. Reinecke, Phys. Rev. B **51**, 13797 (1995); D. A. Broido and T. L. Reinecke, Appl. Phys. Lett. **70**, 2834 (1997);

[6] D. M. Rowe and G. Min, Proceedings for 13th International Conference on Thermoelectrics page 339 (1994).

[7] Y. Nishio and T. Hirano, Jpn. J. Appl. Phys., Part 1 **36**, 170 (1997).

[8] R. Venkatasubramanian, T. Colpitts, E. Watko, M. Lamvik, and N. El-Masry, Journal of Crystal Growth **170**, 817 (1997).

THERMOELECTRIC TRANSPORT IN SUPERLATTICES

D. A. Broido* and T. L. Reinecke**
*Department of Physics, Boston College, Chestnut Hill, MA 02167, broido@bc.edu
**Naval Research Laboratory, Washington DC 20375, reinecke@estd.nrl.navy.mil

ABSTRACT

A quantitative description of the power factor for thermoelectric transport in quantum well and quantum wire superlattices has been developed. The size dependence of the carrier scattering rates as well as carrier tunneling between layers are included, and results are obtained for full three-dimensional superlattice systems. In addition, model calculations of the lattice thermal conductivity of free standing wells and wires have been obtained, and their implications for the thermoelectric figure of merit are discussed. Illustrative results are given for GaAs and PbTe systems.

INTRODUCTION

Recently, there has been considerable interest in understanding thermoelectric transport properties of quantum wire and quantum well superlattices[1-10]. The desirability of a material for applications is characterized by the dimensionless "figure of merit"[11] :

$$ZT = \frac{PT}{\kappa} \qquad (1)$$

Here, T is the temperature, P is the power factor, $P = \sigma S^2$ where σ is the electrical conductivity, S is the Seebeck Coefficient. κ is the thermal conductivity, $\kappa=\kappa_e+\kappa_L$, which consists of two components, κ_e and κ_L, corresponding to the carrier and lattice contributions, respectively. Thus, the power factor gives a measure of the electronic contribution to the figure of merit. In many systems of interest the thermal conductivity is dominated by the lattice contribution, which then strongly influences the figure of merit.

We have investigated theoretically thermoelectric transport in quantum well and quantum wire superlattice systems. We use a multi-subband treatment of the Boltzmann equation that includes carrier scattering by optic and acoustic phonons and by impurities. This treatment includes the well and wire width dependence of the scattering rates. The effects of carrier tunneling through the barriers is included, and results are given for full three-dimensional superlattice systems. Calculations for GaAs illustrate the behavior of single valley systems and those for PbTe illustrate multi-valley systems. In addition, the lattice thermal conductivity of free standing well and wire systems has been investigated employing a simple model that includes the effects of phonon scattering at interfaces, and its effects on the figure of merit are illustrated.

POWER FACTOR IN QUANTUM WELL SUPERLATTICES

We consider first thermoelectric transport in quantum well superlattices with transport in the plane of the quantum well layers. We take a (b) to be the thickness of the quantum well (barrier). We begin with systems having a single isotropic conduction valley in the bulk, and later we will discuss the extension to anisotropic multi-valley systems. The state of the electron is specified by the superlattice state $\alpha=(n, \mathbf{k})$, where n is the subband index and $\mathbf{k}$ the wave vector with $k_{\|}$ along the plane.

The electric and heat currents in the superlattice are given by:

Mat. Res. Soc. Symp. Proc. Vol. 545 © 1999 Materials Research Society

$$\mathbf{J}_e = -e \sum_{\alpha} \mathbf{v}_\alpha df_\alpha = -e \sum_{n} \int \frac{dk}{4\pi^3} \mathbf{v}_n \delta f_n \tag{2}$$

$$\mathbf{J}_Q = \sum_{\alpha} \mathbf{v}_\alpha (\varepsilon - \mu) \delta f_\alpha = \sum_{n} \int \frac{dk}{4\pi^3} \mathbf{v}_n (\varepsilon - \mu) \delta f_n \tag{3}$$

Here, δf_α is the deviation from the equilibrium distribution function for the α^{th} carrier subband state.

Previous results suggest that strong confinement within the quantum well layers produces large *ZT's*. For the moment, we consider the strong confinement limit, in which the potential barrier height, $V_0 \rightarrow \infty$ and the barrier width, $b \rightarrow 0$. In this case, tunneling through the barrier layers does not occur, and the dispersion along the superlattice direction is flat. For weak electric fields and thermal gradients, the distribution function for a quantum well subband can be expressed as $f_\alpha = f_0 + \delta f_\alpha$, with f_0 being the equilibrium distribution and:

$$\delta f_\alpha = \left(-\frac{\partial f_0}{\partial \varepsilon} \right) \mathbf{v}_n \cdot \left[-e\mathbf{E}\, \tau_{1n}(k_{||}) - \frac{\nabla T}{T} \tau_{2n}(k_{||}) \right] \tag{4}$$

Here, the scattering functions, τ_{1n} and τ_{2n}, are isotropic in the quantum well plane because we have taken the in-plane band structure to be isotropic. The electric and heat currents are related to the transport coefficients by

$$\mathbf{J}_e = \sigma\mathbf{E} - \sigma S \nabla T \qquad \mathbf{J}_Q = \sigma S T \mathbf{E} - \gamma_e \nabla T \tag{5}$$

where $\gamma_e = \kappa_e + \sigma S^2 T$, and κ_e is the electronic contribution to the thermal conductivity. Combining Eqs. 2-5, we obtain expressions for the transport coefficients, σ, S and κ_e. These quantities are evaluated using the scattering functions given by the solution of the Boltzmann equation for the well superlattice for steady state electron transport [12]:

$$-\frac{e\mathbf{E}}{\hbar} \cdot \nabla_{\mathbf{k}} f_\alpha + \frac{\nabla_{\mathbf{k}} \varepsilon_\alpha}{\hbar} \cdot \nabla_{\mathbf{r}} f_\alpha = \frac{\partial f_c}{\partial t} \tag{6}$$

$$\frac{\partial f_c}{\partial t} = \sum_{\alpha'} \left[W_{\alpha'\alpha} f_{\alpha'} (1 - f_\alpha) - W_{\alpha\alpha'} f_\alpha (1 - f_{\alpha'}) \right] \tag{7}$$

$W_{\alpha\alpha'}$ is the scattering rate taking electrons from state α to state α', and the collision operator, $\frac{\partial f_c}{\partial t}$, accounts for intra- and inter-subband scattering into and out of the state α. Substituting Eq. 4 into the Boltzmann equation we obtain to two sets of coupled equations for the scattering functions:

$$L_c(\{\tau_{1n}\}) = 1 \tag{8}$$

$$L_c(\{\tau_{2n}\}) = \varepsilon - \mu \tag{9}$$

where the collision operator is:

$$L_c(\{\tau_{in}\}) = \frac{A}{2\pi^2}\sum_{n'}\int d\mathbf{k}_{\|}' W_{nn'}(\mathbf{k}_{\|},\mathbf{k}_{\|}')\left(\frac{1-f_{0n'}(k_{\|}')}{1-f_{0n}(k_{\|})}\right)\left(\tau_{in}(k_{\|}) - \frac{\mathbf{k}_{\|}\cdot\mathbf{k}_{\|}'}{k_{\|}^2}\tau_{in}(k_{\|}')\right) \qquad (10)$$

with i=1,2, from Eqs. 8 and 9. Here, $W_{nn'}(\mathbf{k}_{\|},\mathbf{k}_{\|}')$ is obtained by integrating $W_{nn'}(\mathbf{k},\mathbf{k}')$ over k_z.

The two sets of coupled equations, Eqs. 8 and 9, are analogous to those obtained for bulk material [13, 14]. In our treatment of well and wire superlattices we include carrier scattering by: 1) acoustic phonon scattering via the deformation potential interaction, and 2) polar optical phonon scattering via the Fröhlich interaction, and 3) ionized impurity scattering. We expect these to be the dominant scattering mechanisms at room temperature. Note that the inelastic carrier-optic phonon scattering is treated fully rather than assuming a constant relaxation time. We consider first carrier-phonon scattering and return to carrier-impurity scattering and screening later. We take the phonons to be unaffected by the superlattice structure and take the electrons to have modified superlattice wave functions. The scattering rates by optic phonons have been shown to be given to a good approximation by bulk plane waves for the phonons [15, 16] and the superlattice periodicity has only small effects on the acoustic phonons. In the strong confinement limit, the scattering rates to due phonons and impurities are found to be the same as the result obtained for single quantum wells, and we use the corresponding expressions in our solution of the Boltzmann equation .

The preceeding description applies to semiconductor materials with a single conduction band valley. Most of the interesting thermoelectric materials, such as Bi_2Te_3 and PbTe, are multi-valley semiconductors. We will consider below PbTe, which has 4 equivalent ellipsoidal conduction band valleys along the [111] directions. We represent each of the several valleys in the bulk by anisotropic parabolic bands, giving for the j^{th} valley,

$$\varepsilon_j(\mathbf{k}) = \frac{\hbar^2}{2}\left(\frac{k_z^2}{m_{jz}} + \frac{k_{\|}^2}{m_{j\|}}\right) \qquad (11)$$

Then, the in-plane band structure is again isotropic, and the preceeding results can be extended to the multi-valley case simply by including the appropriate masses, m_{jz} and $m_{j\|}$, and a summation over valleys in the appropriate equations above.

In realistic quantum well systems, the barrier heights are finite, and as a result the spatial extent of the electron wave functions is increased. To incorporate this effect we use the confinement energies for the finite barrier quantum wells and wave functions for infinite barrier wells which gave the same confinement energies. An important consequence of the finite barrier heights is that electrons can tunnel through the barrier region. The finite dispersion $\varepsilon_n(k_z)$ the superlattice direction reduces the 3D density of states, which in turn alters the expressions for the transport coefficients. For finite barrier systems, we evaluate these expressions numerically employing a Kronig-Penney model for the superlattice dispersion [5, 6].

POWER FACTOR IN QUANTUM WIRE SUPERLATTICES

In a quantum wire superlattices transport is taken along the quantum wire axes, which is taken as the x-direction. For systems with a single conduction valley in the bulk, the state of the electron is specified by $\alpha=(n_1, n_2, \mathbf{k})$, where n_1, n_2 are the quantum numbers associated with the two confinement directions, which we take to be the y and z directions. In the strong confinement limit ($V_0\rightarrow\infty$ and the barrier width, $b\rightarrow 0$) for quantum wires, the dispersion along the superlattice direction is flat. The deviation, δf_α, is then:

$$\delta f_\alpha = \left(-\frac{\partial f_0}{d\varepsilon}\right)\frac{\hbar k_x}{m^*}\left[\, -eE_x\,\tau_{1\alpha} - \frac{1}{T}\frac{dT}{dx}\tau_{2\alpha}\right] \qquad (12)$$

where α now specifies the quantum numbers (n_1, n_2, k_x), and the scattering functions, $\tau_{1\alpha}$ and $\tau_{2\alpha}$, are determined by solving the Boltzmann equation. Substituting Eq. 12 into the Boltzmann equation leads to two sets of coupled equations for the scattering functions as in Eqs 8 and 9 where the collision operator is:

$$Lc(\{\tau_{i\alpha}\}) = \frac{L}{(2\pi)}\sum_{\alpha'} W_{\alpha\alpha'}\frac{(1-f_{0\alpha'})}{(1-f_{0\alpha})}\left[\,\tau_{i\alpha} - \frac{k_x'}{k_x}\,\tau_{i\alpha'}\right] \qquad (13)$$

$W_{\alpha\alpha'}$ is the 1D scattering rate integrated over k_y and k_z. In the strong confinement limit, the optic and acoustic phonon scattering rates for quantum wire superlattices become the same as for isolated wires [17], and we evaluate these expressions numerically in calculating the transport coefficients[18]. Treatment of multi-valley systems, tunneling and impurities is done in the same way as for quantum well superlattices. The subband dispersions and transport coefficients are obtained numerically using a 2D Kronig-Penney model.

RESULTS AND DISCUSSION

Figures 1 and 2 show the room temperature power factor for GaAs and PbTe as functions of the size of the quantum well and quantum wire thicknesses. For each well or wire thickness, P and ZT exhibit maxima as functions of the density. The values of P that maximize ZT (evaluated using the bulk value of the lattice thermal conductivity) are plotted. In all cases, P is scaled to the value of P that maximizes ZT for the corresponding bulk system.

Figure 1a shows P for GaAs quantum well superlattices with different barrier heights and barrier widths. It is evident that in the strong confinement limit, $V_0=\infty$ and b=0, P increases monotonically with decreasing well thickness and rises well above the bulk value for narrow wells. When barriers with finite thickness are introduced (dotted curve), P decreases substantially. This occurs because electric current is confined to the well layer only so that current now flows in only half of the structure. For finite barrier heights, P first increases and then decreases with decreasing well thickness. For large well thicknesses, little current penetrates the barrier layers, and so the results approach those for $V_0=\infty$ and b=a. As the well thickness decreases, P first increases because of the enhancement in the density of states produced by the confinement. For narrow wells, tunneling through the barrier layers occurs, which causes a decrease in the density of states and a corresponding decrease in P. The added confinement for V_0=1eV compared with V_0 =200 meV produces a slightly higher maximum value of P.

Figure 1b shows P for PbTe quantum well superlattices with growth axis along the [111] direction for the same cases as considered in Figure 1a. Here, the curves exhibit different behavior. The curve for $V_0=\infty$ and b=0 first decreases and then increases with decreasing well thickness. This behavior is caused by the lifting of the valley degeneracy produced by the confinement. For this superlattice system, the mass for the [111]-oriented "longitudinal" valley along the confinement direction is considerably heavier than that for the other three "oblique" valleys. The light confinement masses for oblique valleys cause the corresponding subbands to have higher energies than those associated with the longitudinal valley. As a consequence, the oblique subbands depopulate with decreasing well thickness and so do not contribute to conduction. This causes P to remain below the bulk value even for very narrow wells. With a further decrease in well thickness, P begins to increase because of the confinement induced enhancement in the density of states for the longitudinal subbands. Note that the curve for

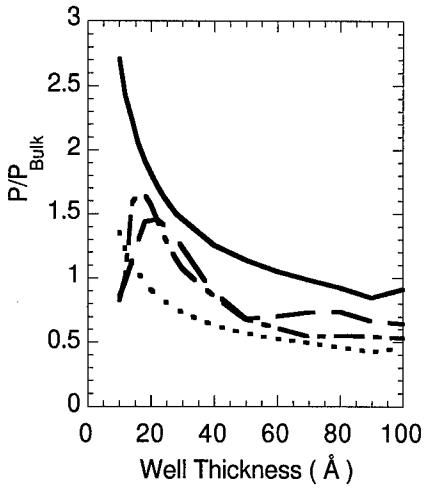

Fig. 1a. The power factor for GaAs quantum well superlattices for different barrier heights and widths . Solid line: $V_0 = \infty$, b=0; Dotted line: $V_0 = \infty$, b=a; Dashed line: V_0 =200 meV, b=a; Dash-dotted line: V_0 =1eV, b=a.

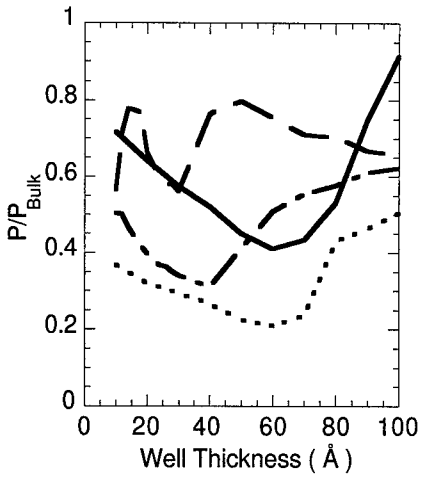

Fig. 1b. The power factor for PbTe quantum well superlattices for different barrier heights and widths . Solid line: $V_0 = \infty$, b=0; Dotted line: $V_0 = \infty$, b=a; Dashed line: V_0 =200 meV, b=a; Dash-dotted line: V_0 =1eV, b=a.

V_0=200 meV and b=a lies above that for $V_0=\infty$ and b=0 for a wide range of well thicknesses. The larger power factor in this case is a result of the increased contribution from the oblique subbands due to the reduced confinement. The added confinement for V_0=1 eV, b=a and $V_0=\infty$, b=a further lifts the valley degeneracy and so again depopulates the oblique valleys and leads to a corresponding reduction in P.

Figures 2a and 2b compare P for quantum well and quantum wire superlattices in the strong confinement limit. Figure 2a shows P for GaAs quantum well (dashed curve) and square quantum wire (solid curve) superlattices with $V_0=\infty$ and b=0. For large well and wire thicknesses, the values of P for both wells and wires approach the bulk value, an indication of the accuracy of the numerical approach. With decreasing thickness, P for wires exhibits a stronger increase than is the case for wells. This occurs because of the larger confinement induced enhancement of the density of states in wires compared to wells [4].

Figure 2b shows P for PbTe quantum well and quantum wire superlattices. Here, the wire confinement directions are taken to be the [111] and [$1\bar{1}2$] directions, while the transport direction is [$1\bar{1}0$]. The solid and dashed curves are for $V_0=\infty$ and b=0, as in fig. 2a. Note that while P for wells remains below the bulk value, that for wires lies well above the bulk value. This occurs in part because of the enhanced density of states in wires compared to wells. In addition, the two confinement directions for wires combined with the strong valley anisotropy in PbTe causes the longitudinal and oblique subbands to stay energetically close thereby allowing the oblique valleys to contribute to conduction. The reduction in P for wires with finite barriers occurs primarily because the barrier volume is three times larger than the wire volume for b=a, while for well systems they have the same volume. It should be noted that confinement directions other than those chosen here that would reduce the lifting of the valley degeneracy and thereby enhance the thermoelectric properties are possible. For example, PbTe quantum wells grown along the [001] direction the valley degeneracy would not be lifted because the confinement masses for all four

valleys are identical. A larger power factor is found for this case than for [111]-oriented PbTe quantum well systems [19].

The effect of ionized impurity scattering and free carrier screening on the power factor of quantum well superlattices is modeled by taking the ionized impurities to be randomly distributed throughout the structure. The carrier density is taken to match the impurity density. We calculate the quasi-2D scattering rate from the singly charged Coulomb centers, and we take the free carrier screening to be described by a 3D Thomas-Fermi dielectric function. The free carrier screening is also included for the scattering rates due to polar optic phonons and acoustic phonons. In general, with increasing density, the increased impurity scattering reduces the conductivity and P, while the free carrier screening moderates this reduction according to the magnitude of the static dielectric constant. The inclusion of ionized impurity scattering and free carrier screening for GaAs quantum

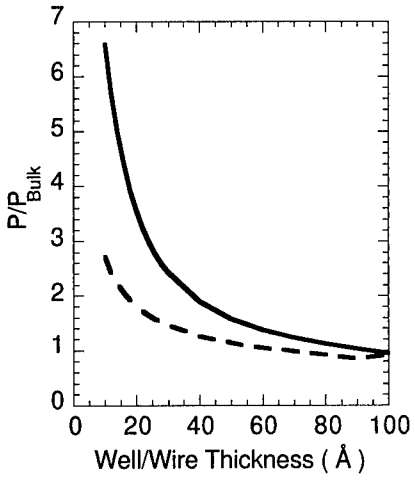

Fig. 2a. The power factor for GaAs quantum well (dashed line) and quantum wire (solid line) superlattices with $V_0=\infty$ and b=0.

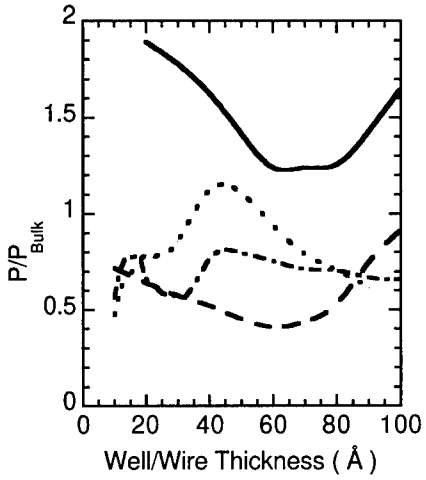

Fig. 2b. The power factor for PbTe well and wire superlattices. Solid line: wire with $V_0=\infty$, b=0; Dashed line: well with $V_0=\infty$, b=0; Dotted line: wire with V_0=200meV, b=a; Dash-dotted line: well with V_0=200meV, b=a.

well systems leads to a reduction in P that increases with carrier density. In turn, for given chemical potential, the carrier density increases with decreasing well thickness. Thus, for narrow wells P can be much less than indicated in fig. 1a. For example, for $V_0=\infty$, b=0, and a=10Å, P is increases by only a 25% over the bulk value as compared with almost a factor of 3 increase seen in Fig. 1a. Modulation doping would partially eliminate this reduction in P. When impurity scattering and free carrier screening are included for bulk PbTe quantum well superlattices, the calculated values of P remain essentially unchanged. This results because of the large dielectric constant, in PbTe, which strongly reduces the impurity scattering rate and leads to efficient screening. Thus, the results given in Fig. 1b are also appropriate when impurity scattering and free carrier screening are included. We note that for materials with high static dielectric constants such as PbTe, modulation doping as compared to uniform doping is not expected to enhance the room temperature transport coefficients for quantum wells because impurity scattering is small. The effect of impurities in quantum wire superlattices is found to be stronger than for quantum well systems. In strictly 1D systems carrier screening is not possible and the interaction of carriers with ionized impurities can lead to carrier localization. This behavior should manifest itself in very narrow wires with strong confinement such that only a single wire subband is occupied. Methods

for removing impurities from the narrow wires, such as modulation doping, would be important in order to achieve high values for P.

LATTICE THERMAL CONDUCTIVITY AND ZT OF WELLS AND WIRES

The room temperature lattice thermal conductivity of bulk semiconductors plays an important role in determining the figure of merit. It is a difficult quantity to calculate microscopically because the dominant scattering mechanism, anharmonic phonon-phonon scattering [12], has a complicated form and the coupling coefficients are not known from experiment. In quantum well and wire superlattices, further complications arise due to interface scattering and changes in the dispersion of acoustic phonons. Studies of the thermal conductivity of quantum well systems have been made previously both theoretically [20-23] and experimentally [24-27] and substantial

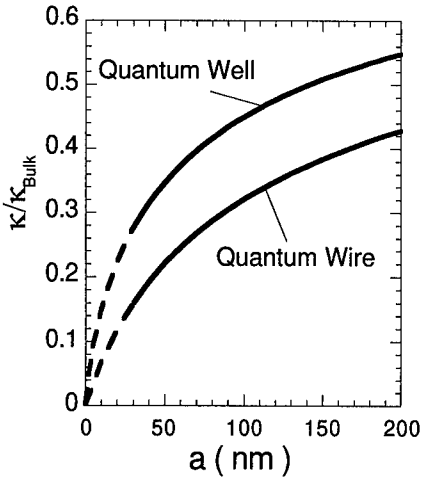

Fig. 3. Lattice thermal conductivity, κ_L, of free-standing GaAs quantum well layers and quantum wires as a function of well/wire thickness, d.

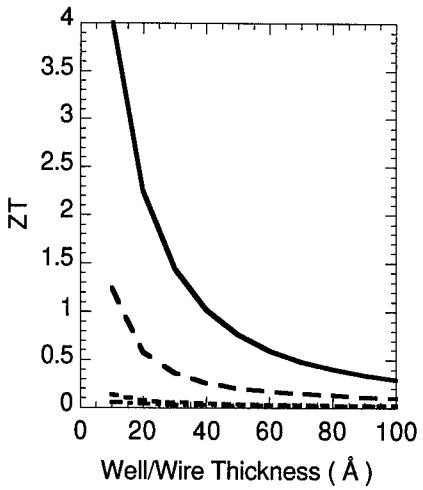

Fig. 4. Figure of merit, ZT for free-standing GaAs quantum wells and wires. Solid line: ZT for wire with wire κ_L. Dashed line: ZT for well with well κ_L; Dotted and dash-dotted curves are for wires and wells with bulk κ_L.

decreases in κ_L have been found compared with the bulk value. We have developed a simple model for free-standing quantum wells and wires [28]. In this model, κ_L is calculated by solving the phonon Boltzmann equation in the relaxation time approximation for bulk phonon-phonon scattering and employing appropriate boundary conditions for phonon scattering at the interfaces. The interface scattering of phonons is taken to be either diffusive or specular [12].

Figure 3 shows the calculated κ_L for free standing GaAs quantum wells and quantum wires as a function of the well/wire size. Results are scaled to the bulk room temperature value of κ_L for GaAs. It is found that κ_L decreases well below the bulk value for decreasing well and wire size. This decrease is a consequence of the increased phonon scattering at the interfaces as the well and wire dimensions decrease below the bulk phonon mean free path. The reduction is larger in wires because of the increased surface to volume ratio as compared to wells. These results are obtained using a frequency-dependent relaxation time to model the bulk anharmonic phonon scattering and taking phonons to scatter only diffusively at the interfaces [28].

To illustrate the possible effect of such large changes in the lattice thermal conductivity, we plot in figure 4 ZT at room temperature for fully confined ($V_0=\infty$, b=0) free standing GaAs quantum wells and wires as a function of well and wire size. The dotted and dash-dotted curves, which barely rise above 0.1, are for wires and wells obtained using the bulk κ_L. Solid and dashed curves are for free standing wires and wells, respectively, obtained using the calculated κ_L shown in Fig. 3. The large values of ZT observed for small well and wire widths is a consequence of the large reduction in κ_L due mostly to the interface scattering and the enhancement of the power factor illustrated in fig. 2a. The strong increase in ZT for the quantum well and wire systems shown here compared to bulk material suggests that the such systems may show promise for applications.

ACKNOWLEDGEMENTS

This work was supported in part by the US Office of Naval Research.

REFERENCES

1. Gerald Mahan, Brian Sales and Jeff Sharp, Physics Today **50** (No. 3), 42 (1997) .
2. L. D. Hicks and M. S. Dresselhaus, Phys. Rev. **B 47**, 12727 (1993).
3. L. D. Hicks, T. C. Harman and M. S. Dresselhaus, Appl. Phys. Lett. **63**, 3230 (1993).
4. L. D. Hicks and M. S. Dresselhaus, Phys. Rev. **B 47**, 16631 (1993).
5. J. O. Sofo and G. D. Mahan, Appl .Phys. Lett. **65**, 2690 (1994).
6. D. A. Broido and T. L. Reinecke, Phys. Rev. B **51**, 13797 (1995).
7. D. A. Broido and T. L. Reinecke, Appl. Phys. Lett. **67**, 100 (1995).
8. D. A. Broido and T. L. Reinecke, Appl. Phys. Lett. **67**, 1170 (1995).
9. P. J. Lin-Chung and T. L. Reinecke, Phys. Rev. B **51**, 13224 (1995).
10. D. A. Broido and T. L. Reinecke, Appl .Phys. Lett. **70**, 2834 (1997).
11. Goldsmid, H. J., in *Thermoelectric Refrigeration*, Plenum Press, NY (1964).
12. J. M. Ziman, Electrons and Phonons (Oxford University Press, Oxford, 1960).
13. See, for example, B. R. Nag, *Electron Transport in Compound Semiconductors* (Springer-Verlag, Berlin, 1980).
14. J. O. Sofo and G. D. Mahan, Phys. Rev. B **49**, 4565 (1994).
15. H. Rücker, E. Molinari and P. Lugli, Phys. Rev. B**45**, 6747 (1992).
16. P. A. Knipp and T. L. Reinecke, Phys. Rev. B 48, 18037 (1993).
17. J. P. LeBurton, J. Appl. Phys. 56, 2850 (1984).
18. D. A. Broido and T. L. Reinecke, to be published.
19. T. Koga, S. B. Cronin, T. C. Harman, X. Sun and M. S. Dresselhaus, MRS Symposium Proceedings Series, Vol. 490, pg. 263 (1997).
20. C. L. Tien and G. Chen, Journal of Heat Transfer **116**, 799 (1994), and references therein.
21. P. Hyldgaard and G. D. Mahan, Thermal Conductivity 23 (Technomic Publishing Co. Inc., Lancaster, Pennsylvania) pg. 172, (1996).
22. G. Chen, National Heat Transfer Conference, HTD-Vol. 323, 121 (1996).
23. Per. Hyldgaard and G. D. Mahan, Phys. Rev. **B56**, 10754 (1997).
24. T. Yao, Appl. Phys. Lett. **51**, 1798 (1987).
25. X. Y. Yu, G. Chen, A. Verman, and J. S. Smith, Appl. Phys. Lett. **67**, 3554 (1995).
26. W. S. Capinski and H. Maris, Physica B **219&220**, 699 (1996).
27. S. M. Lee, D. G. Cahill, and R. Venkatasubramanian, Appl. Phys. Lett. **70**, 2957 (1997).
28. D. A. Broido and T. L. Reinecke, to be published.

DEVELOPMENT OF THICK-FILM THERMOELECTRIC MICROCOOLERS USING ELECTROCHEMICAL DEPOSITION

J.-P. Fleurial*, A. Borshchevsky*, M. A. Ryan*, W. M. Phillips*, J. G. Snyder*, T. Caillat*, E. A. Kolawa*, J. A. Herman*, P. Mueller**, M. Nicolet**
*Jet Propulsion Laboratory, Pasadena, CA 91109, jean-pierre.fleurial@jpl.nasa.gov
**Electrical Engineering Department, California Institute of Technology, Pasadena, CA.

ABSTRACT

Advanced thermoelectric microdevices integrated into thermal management packages and low power, electrical source systems are of interest for a variety of space and terrestrial applications. By shrinking the size of the thermoelements, or legs, of these devices, it becomes possible to handle much higher heat fluxes, as well as operate at much lower currents and higher voltages that are more compatible with electronic components. The miniaturization of state-of-the-art thermoelectric module technology based on Bi_2Te_3 alloys is limited due to mechanical and manufacturing constraints for both leg dimensions (100-200 μm thick minimum) and the number of legs (100-200 legs maximum). We are investigating the development of novel microdevices combining high thermal conductivity substrate materials such as diamond, thin film metallization and patterning technology, and electrochemical deposition of thick thermoelectric films. It is anticipated that thermoelectric microcoolers with thousands of thermocouples and capable of pumping more than 200 W/cm^2 over a 30 to 60 K temperature diffrence can be fabricated. In this paper, we report on our progress in developing an electrochemical deposition process for obtaining 10-50 μm thick films of Bi_2Te_3 and its solid solutions. Results presented here indicate that good quality n-type Bi_2Te_3, n-type $Bi_2Te_{2.95}Se_{0.05}$ and p-type $Bi_{0.5}Sb_{1.5}Te_3$ thick films can be deposited by this technique. Some details about the fabrication of the miniature thermoelements are also described.

INTRODUCTION

The drive for increased performance and miniaturization of a wide range of electronic systems requires higher power levels and higher packaging densities. However, thermal management problems are rapidly becoming a major issue for this technological process because they limit the degree of integration of devices and components [1]. In addition to reliability issues, significant performance improvement can be obtained by operating the active junction of semiconductor chips at temperatures near or lower than ambient, as well as by maintaining precise temperature control. This is especially true of several electronic and photonic devices such as microprocessors, power amplifiers and infrared lasers [2, 3]. For example, next generation SiC/GaN solid state power amplifiers used for microwave applications will have much higher power levels, with thermal power dissipation requirements increasing from 5 W to over 20 W within the same spatial region. That increase will multiply the heat flux that has to be removed from the back of the die from approximately 30 W/cm^2 to several hundreds W/cm^2. This major thermal management problem must be addressed using novel cooling techniques and designs fully integrated with electronic components [4]. The very high heat flux densities in the immediate vicinity of the GaN active layers lead to an estimated 75-110°C temperature difference with respect to the back of the SiC substrate. It is thus imperative to offset this large temperature gradient between active layer and heat sink by using active cooling techniques.

Mat. Res. Soc. Symp. Proc. Vol. 545 © 1999 Materials Research Society

The specific problem of spot cooling of electronic devices can be very effectively solved by using thermoelectric cooling combined with a complementary thermal management technique. For small thermal loads, high thermal conductivity materials can be used for conducting heat away to the heat sink, while for large thermal loads (high heat flux density), highly efficient heat removal techniques such as heat pipes, microchannels or spray cooling would be incorporated into the package [5-7]. Miniaturization of thermoelectric coolers offers several distinct advantages over current state-of-the-art technology that is established on bulk semiconducting materials. One obvious advantage is that for a given module configuration, the cooling power per unit area of thermoelectric coolers is inversely proportional to the thickness of its thermoelements, or legs. "Bulk" coolers are ill suited to further integration with electronic devices and components since they are typically much larger than the active region of the devices, both in cross-sectional area (typically over 1 cm^2) and thickness (thermoelements usually 1mm thick or higher). In addition, even the smallest coolers now commercially available [8-10] are limited in number of legs, (usually less than 200 legs) due to both thermo-mechanical restrictions and the often painstaking semi-manual assembly techniques, severely curbing the range of operating current and voltage. On the other hand, microcoolers could be manufactured using thin film deposition and integrated circuit techniques compatible with electronic device fabrication, and could literally have thousands of miniature legs interconnected in a variety of ways to provide operating voltage and current flexibility. Moreover, the response time of such microcoolers would be dramatically shortened and could prove to be compatible with transient operation of selected electronics [11]. In this paper, we report on progress made in studying critical issues and developing techniques associated with the fabrication of microcoolers.

ELECTRODEPOSITION OF THICK THERMOELECTRIC FILMS

Electrodeposition From Aqueous Solutions

Thick films (10-100μm) can be difficult and time consuming to make using vacuum techniques such as sputtering or evaporation. In addition, some of these deposition techniques require quite elevated temperature that may not be easily compatible with microdevice fabrication processes [12]. An attractive route is a room temperature electrochemical process from aqueous solution. This is a very well known technique for the deposition of many metals and metallic alloys [13] but its application to semiconductors has been much more limited. However, there is an abundant literature on electrochemical deposition (ECD) of II-VI semiconductors such as CdSe, CdTe $CdSe_{0.5}Te_{0.5}$ and $CdSe_{0.65}Te_{0.35}$ [14,15]. In this technique the elements are deposited on an electrode using an aqueous solution of anions or anionic compounds. ECD constitutes an inexpensive way to synthesize semiconducting films and, depending on the current density used in deposition, the deposition rate can be varied widely, up to several tens of microns per hour. In addition, slight variations in the deposition potential or solution concentration may possibly be used to induce off-stoichiometric films, thus providing p- or n-type doping through stoichiometric deviation. The electrodeposition of thermoelectric materials has not been widely investigated [16, 17] and new experimental methods must be developed to obtain p-type and n-type $Bi_{2-x}Sb_xTe_{3-y}Se_y$ compositions which are optimal for thermoelectric cooling applications near room temperature. An additional advantage of ECD is that some of the interconnect layers necessary to the fabrication of these devices, such as Cu for the electrical path or Ni or Pt for the Cu diffusion barrier can also be deposited by using different aqueous solutions.

All experiments were run at room temperature using standard electrochemistry techniques: a three electrode cell with open beaker configuration but with separate vessels for the reference

electrode (saturated calomel electrode, SCE) and the counter/working electrodes. A salt bridge was used to electrically connect the two beakers. The counter electrode consisted of a fine Pt mesh while metallic foils or metallized high thermal conductivity substrates such as diamond, AlN or Si/SiO_2 were used for a working electrode. Solutions contained dissolved high purity elements (Bi, Sb, Te, Se) into an acidic aqueous medium, typically HNO_3 and deionized water (pH ~ 0). Concentration of the elements in the electrolyte was varied between 0.0001 and 0.01 M. In the case of Sb, a chelating agent must be added to prevent the spontaneous precipitation of an insoluble oxide compound and raise its maximum solubility (about 0.0008 M in 1 M HNO_3 aqueous solution). Both the electrodeposition and cyclic voltammetry measurements were carried out using mechanical solution stirring and a computer-controlled EG&G Princeton Potentiostat/Galvanostat 273A. The thickness of the films was measured using a Dektak profilometer and in some cases a scanning electron microscope. The atomic composition and the crystallographic orientation of the films were obtained using a Siemens D-500 x-ray diffractometer and a JEOL JXA-733 electron superprobe, respectively. Measurements of the electrical transport properties have been conducted in a 100-400K temperature range on some films. Van der Pauw electrical resistivity and Hall effect were measured in the plane of the deposited films (after removal from the metallized substrates), and the Seebeck coefficient was measured in a cross-plane direction using a simple differential thermocouple setup

Electrodeposition of Bi_2Te_3 Alloy Films

Bismuth and tellurium metals dissolve in HNO_3 to make the oxide cations BiO^+ and $HTeO_2^+$. Bi_2Te_3 is insoluble in dilute HNO_3, so reduction of $HTeO_2^+$ to Te^{2-} at an electrode will result in the precipitation of Bi_2Te_3 on the electrode surface. The overall reaction for the process is:

$$13H^+ + 18e^- + 2BiO^+ + 3HTeO_2^+ \rightarrow Bi_2Te_3\downarrow + 8H_2O \qquad (1)$$

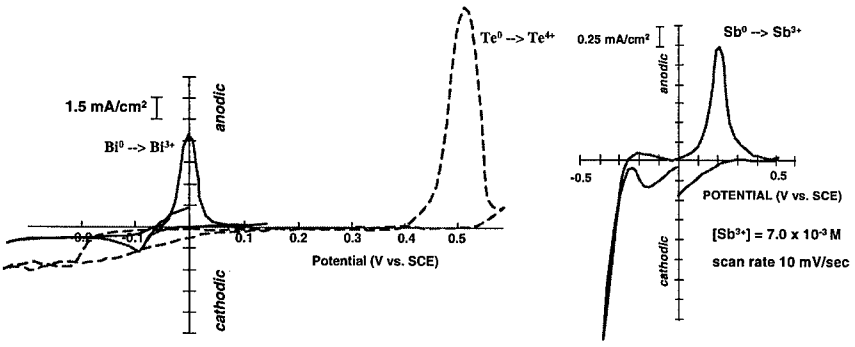

(a) (b)

Figure 1: Current-Voltage graph for the electrochemical deposition of Bi, Te (a) and Sb (b) on a Pt substrate using a nitrate aqueous solution. The oxidation waves for Bi, Te and Sb can be seen for voltages of 0, 0.5 and 0.2 V respectively.

The combined current-voltage behavior of aqueous solutions of $7x10^{-3}$ M BiO^+ and $1.0x10^{-2}$ M $HTeO_2^+$ in 1 M HNO_3 is plotted in figure 1(a) and shows that the reduction regions for each of these compounds overlie each other in the range -50 to -200 mV versus SCE. BiO^+ is reduced to

Bi^0 around –100 mV (not the operative mechanism for Bi and Te co-deposition). It is possible to obtain Bi_2Te_3 within this voltage range, probably most effectively in the range -5 to –75 mV than within the region of the reduction wave for BiO^+. Ternary $Bi_2Te_{3-x}Se_x$ alloy films can also be obtained by adding Se to the dilute HNO_3 solution and by controlling the [Te]/[Se] molar concentration ratio. Figure 1(b) plots the voltammogram for Sb ([Sb] = $0.7x10^{-3}$ M) in a pH = 0 aqueous solution. It can be seen that low cathodic current densities are obtained even at relatively large negative voltages (-100mV and higher). It also shows that there is a rapid increase in current as voltage becomes more negative from 0 to -150mV, indicating that it will be quite difficult to deposit Sb-rich $Bi_{2-x}Sb_xTe_3$ films at lower voltages typically used for Bi_2Te_3 or $Bi_2Te_{3-x}Se_x$ films (-10 to -25 mV).

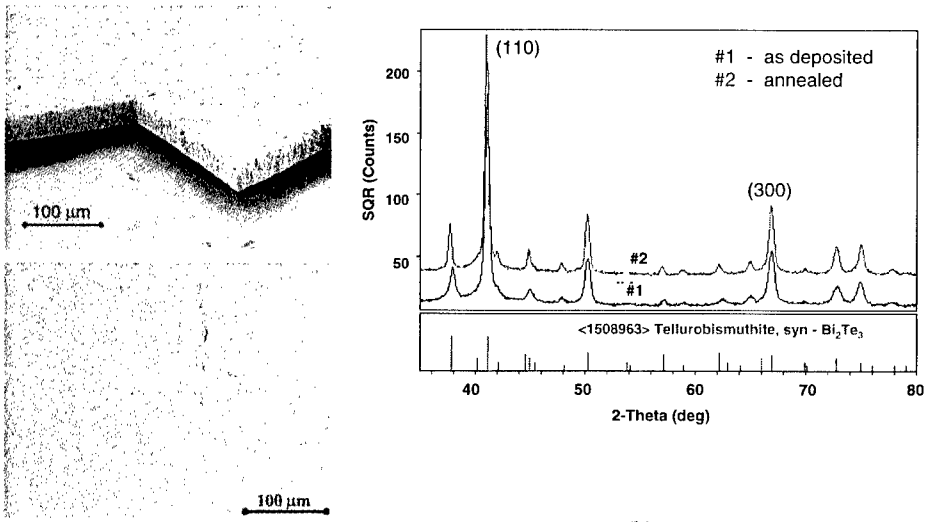

(a) (b)

Figure 2: (a) Micrographs of 40 µm thick Bi_2Te_3 thick films: film lifted off its metallized silicon substrate (top, notice vertical cleavage planes) and film grown by pulsed deposition (bottom); (b) X-ray diffraction pattern for Bi_2Te_3 films, as-deposited and after a 200°C/4hours anneal.

In addition to the deposition voltage, other parameters controlling the quality, composition and properties of the Bi_2Te_3 alloy films grown by ECD are: bath temperature, Bi , Te and Se molar concentrations in the HNO_3 solution, deposition time, substrate surface finish and geometry, convective diffusion in the bath (stirring), depletion rate of [Bi] and [Te] in the bath (volume), and current distribution between counter and deposition electrodes (distance and symmetry). Electrodeposition on Pt-coated substrates have shown that thick near-stoichiometric Bi_2Te_3 films could be grown from a 0.008 M [Bi] and 0.01 M [Te] solution. The thickness of the films ranged from 10 to 60 µm and the composition of the films was very close to the 40/60 at% ratio. In addition, back-scattering and secondary electron analysis indicated that films grown at low deposition voltages had relatively smooth top surfaces (about 1 µm of roughness). Even better results can be obtained through pulse deposition alternating growth and etch sequences (roughness of less than 100nm). These results are illustrated in Figure 2(a). The growth rates ranged from 10 to 20 µm/hour depending on the deposition voltage. The crystal orientation of

the films is very reproducible regardless of the substrate used, and x-ray diffraction data (Figure 2(b)) show that the c axis of the Bi_2Te_3 hexagonal unit cell is located in the plane of the film. This is a particularly important result, similar to previous reports for deposition on stainless steel substrates [17], since it means that the Bi_2Te_3 cleavage planes are perpendicular to the film surface. This is precisely the desired orientation considering the well-known transport property anisotropy of bulk Bi_2Te_3 and our vertically integrated module configuration.

Sb_2Te_3-rich $Bi_{2-x}Sb_xTe_3$ compositions are best for p-type thermoelements. Such alloys can also be obtained in electrodeposited films by controlling the [Sb]/[Bi] ratio in the electrolyte while maintaining a constant [Te]/([Bi]+[Sb]) ratio, as shown in Figure 3(a). However, if no chelating agent is used, only low [Sb] concentrations (up to 0.0008 M) and relatively high voltages (-120 mV and more negative values) can be used. This is illustrated in Figure 3(b) for such low [Sb] concentrations where the atomic film composition (1.5 is stoichiometric) is plotted as a function of the deposition voltage for a constant [Te]/([Bi]+[Sb]) ratio in the electrolyte. At less negative voltages, Bi and especially Te deposition tend to dominate the process and off-stoichiometric films are obtained. Negative deposition voltages in excess of -100mV result in stoichiometric film compositions ($Bi_{0.4}Sb_{1.6}Te_3$) but with high porosity, dendritic-like structure. In addition growth rates are much smaller than achieved for Bi_2Te_3, typically on the order of 1 μm/hour. Less negative voltages (-80mV or less) result in much improved morphology and higher deposition rates but require substantially increased [Sb] electrolyte concentrations.

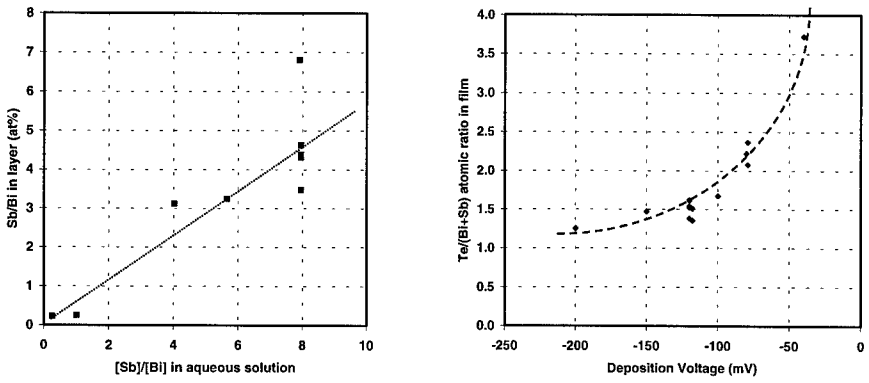

(a) (b)

Figure 3: (a) Change in composition in stoichiometric $Bi_{2-x}Sb_xTe_3$ films as a function of the aqueous [Sb]/[Bi] ratio and (b) increase in Te content for film composition when depositing at less negative voltages (vs. SCE) but using same starting aqueous concentrations.

Transport property measurements on as-deposited Bi_2Te_3 films show heavily doped n-type behavior, similarly to results obtained previously [16] except for lower electron concentrations (~ $1x10^{20}$ cm^{-3}) and higher Hall mobility values (~ 26 cm^2/Vs). Seebeck coefficient values range from -40 μV/K to over -60 μV/K near room temperature. However, one needs to take into account the anisotropy of the transport properties since a typical value of 10^{-5} Ωm for the electrical resistivity is obtained for the in-plane direction. Values in the out-of-plane direction (through the film thickness) are expected to be about four times lower, based on data reported for bulk Bi_2Te_3. Heat-treatments carried out under inert atmosphere at 200 to300°C for a few hours result in much improved electrical properties due to an anneal of structural defects and reduction

in doping levels to the 10^{19} cm^{-3} range. This can be seen in Figure 4(a) plotting the temperature dependence of the in-plane electrical resistivity and Hall mobility for as-deposited and annealed samples. Seebeck values increase up to -200 μV/K at 300K, indicating that the film properties become quite similar to those of optimized n-type Bi_2Te_3 bulk samples. For p-type films, the only transport property measured so far is the Seebeck coefficient in a direction perpendicular to the plane of the film. For near stoichiometric $Bi_{2-x}Sb_xTe_3$ films, values range from +40 to +300 μV/K depending on the Bi/Sb atomic ratio and a slight excess in Te content. The largest values are obtained for compositions that are slightly Te-rich. Some of our results are presented in Figure 4(b) for films grown from three different electrolytes with a constant [Bi]/[Sb] ratio but increasing [Te] concentration, and as a function of the deposition voltage. It has also been found that n-type stoichiometric ternary $Bi_{2-x}Sb_xTe_3$ films could be prepared for x<1.0.

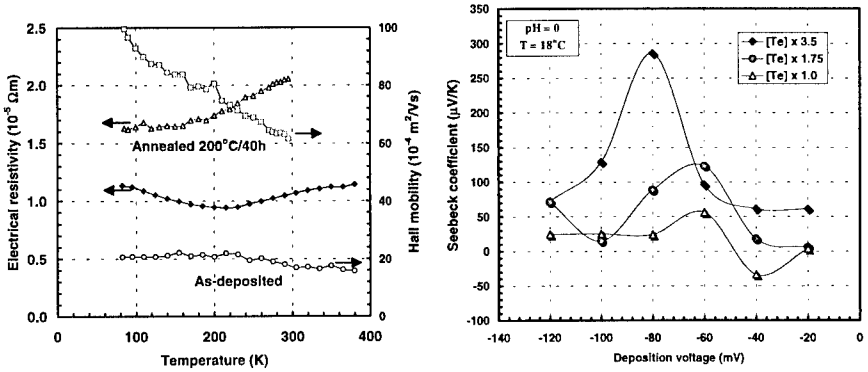

Figure 4: (a) In-plane electrical resistivity, Hall mobility as a function of temperature measured for a 30 μm thick Bi_2Te_3 film, as-deposited and after a 200°C/40h anneal in an inert atmosphere; (b) Seebeck coefficient as a function of deposition voltage for $Bi_{2-x}Sb_xTe_3$ films using electrolytes with high Sb concentrations.

THERMOELECTRIC MICRODEVICE FABRICATION

Special Considerations for Heat Transfer and Electrical interconnects

By selecting a vertically integrated thermoelectric module configuration compared to a planar thin film configuration, device performance is not degraded significantly due to heat losses through the supporting substrate [11, 18]. However, with short legs and high heat flux values, the performance of microcoolers is much more sensitive to electrical and thermal contact resistances than that of bulk devices. For resolving the thermal issues, the use of substrates such as AlN or diamond (thermal conductivity respectively one and two orders of magnitude higher than alumina) is necessary so that as small a ΔT as possible is dropped across the substrate due to its thickness and cross-sectional area (heat spreading). For miniaturized devices comprised of thousands of legs, electrical contact resistances can become a very large fraction of the total internal resistance. Low contact resistances (10^{-6} $\Omega.cm^2$ or lower) can relatively easily be obtained using thin film processing techniques developed for integrated circuit technology [19]. The development of thermally stable metallizations for high thermal conductivity substrates such as diamond, AlN or thermally oxidized Si [19] as well as effective diffusion barrier materials

based on amorphous transition metal-silicon nitride layers [20] was recently completed. In addition to thermal and electrical contact resistances, other issues such as heat losses, mechanical strength and stress analysis must be considered. These issues will be developed in a later report.

Fabrication of Thermoelectric Legs

It has been determined that to be able to "shape" the thick legs, electrodeposition should be conducted in an equally thick template. Experiments demonstrated that electrodeposits would rapidly cover the entire surface of the template once they grew out of their patterned "hole". This template is prepared by depositing a thick photoresist layer and then, using conventional UV photolithography equipment, by etching square or round shaped patterns into it for leg deposition. Cylindrically shaped patterns etched into photoresist up to 65 μm thick deposited on top of a metallized silicon substrate have been successfully obtained. Micrographs in Figure 5 show part of arrays composed of thousands of Bi_2Te_3 legs covering a few mm^2 area that were electrodeposited using such a photoresist template.

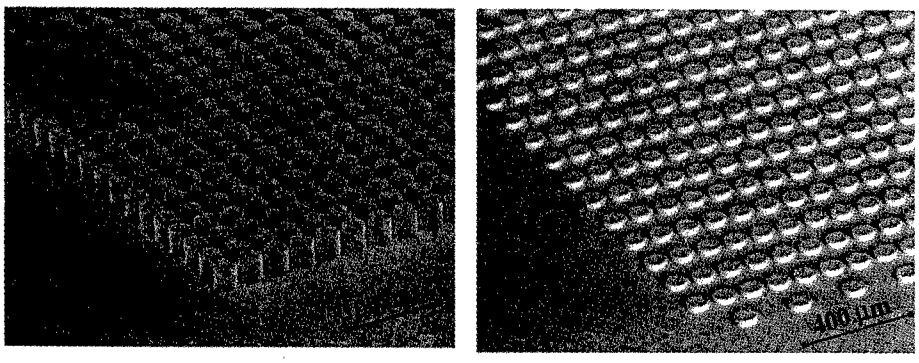

Figure 5: Micrographs showing Bi_2Te_3 legs obtained using electrochemical deposition techniques into thick photoresist templates on fully metallized Si substrates. Micrograph (a) is illustrative of a typical device configuration for power generation applications with an array of 10,000 legs with dimensions of 20 μm in diameter and 50 μm tall; the 70 μm in diameter and 20 μm tall 2500 leg array in micrograph (b) is based on specific cooling applications

CONCLUSION

Thermoelectric microdevices can contribute to solving thermal management issues related to the rapid development of high power, high density electronic components and devices. Low power electrical sources for remote or unattended electronics also offer attractive possibilities. To fabricate such microdevices in a "classic" vertically integrated module configuration, a combination of electrochemical deposition techniques and integrated circuit technology is now under development. It has been shown that both n-type and p-type thick Bi_2Te_3 alloy films (10-60 μm thick) could be synthesized with transport properties similar to that of bulk materials. We are currently focusing on improving the deposition conditions of thick p-type $Bi_{2-x}Sb_xTe_3$ films. We have developed thermally stable metallizations to high thermal conductivity substrates and effective diffusion barriers for fabricating the electrical interconnects between the n- and p-type legs. Thick photoresist templates up to 65 μm have been successfully developed and patterned using conventional UV photolithography, resulting in the reproducible fabrication of closely

packed arrays of thousands of legs as small as 12 μm in diameter. We are now focusing on establishing and completing all of the processing steps for depositing both n-type and p-type legs on fully metallized and patterned substrates in order to achieve the fabrication of several device prototypes. We expect that this effort can also be extended to even smaller configurations that could include recent advances in novel thermoelectric materials and low dimensional structures.

ACKNOWLEDGEMENTS

The work described in this paper was performed at the Jet Propulsion Laboratory/California Institute of Technology under contract with the National Aeronautics and Space Administration. Part of this work was supported by the Office of Naval Research, award No. N0001496F0043.

REFERENCES

1. DARPA Workshop on Microelectronic Thermal Management, *Proceedings*, December 1997.
2. L. S. Mok, *Proc. Tenth Annual IEEE Semiconductor Thermal Measurement and Management Symposium*, New York, IEEE, 59-63 (1994).
3. F. Capasso, J. Faist, C. Sirtori and A.Y. Cho, Solid State Communications, **102**, 231 (1997).
4. J.-P. Fleurial, A. Borshchevsky, M.A. Ryan, W. Phillips, E. Kolawa, T. Kacisch and R. Ewell, *Proc. XVI Int. Conf. Thermoelectrics*, Dresden, Germany, August 26-29, IEEE Catalog No. 97TH8291, 641 (1997).
5. M.T. North, D.B. Sarraf, J.H. Rosenfeld, Y.F. Maidanik and S. Vershinin, Proc. Space Technology and Applications International Forum, AIP 387, 2, 561-566 (1997).
6. M.M. Sherman and G.O. Campbell, Proc. Spacecraft Thermal Control Symposium, Albuquerque, Nov. 1994
7. Isothermal Systems Research Inc.(private communication).
8. V. A. Semeniouk, T. V. Pilipenko, G. C. Albright, L. A. Ioffe, W. H. Rolls, *Proc. XIIIth Int. Conf. on Thermoelectrics*, Kansas City MO, USA, 1994, AIP Conf. Proc. 316, 150 (1995).
9. L. Rushing, A. Shakouri, P. Abraham and J. Bowers, *Proc. XVI Int. Conf. Thermoelectrics*, Dresden, Germany, August 26-29, IEEE Catalog No. 97TH8291, 646 (1997).
10. M. Kishi, Y. Yoshida, H. Okano, H. Nemoto, Y. Funanami, Y. Yamamoto and H. Kanazawa, *Proc. XVI Int. Conf. Thermoelectrics*, Dresden, Germany, August 26-29, IEEE Catalog No. 97TH8291, 653 (1997).
11. V.A. Semeniouk and J.-P. Fleurial, *Proc. XVI Int. Conf. Thermoelectrics*, Dresden, Germany, August 26-29, IEEE Catalog No. 97TH8291, 683 (1997).
12. Yu. A. Boikov, O.S. Gribanova, V.A. Danilov, V.A. Kutasov, Sov. Phys. Solid State **32** (12), 2056 (1990).
13. A.R. Despic and V.D. Jovic in *Modern Aspects of Electrochemistry*, No. 27, edited by R.E. White, J.O'M. Bockris and B.E. Conway, (Plenum Press, New York, 1995), p. 143.
14. K. Rajeshwar, Adv. Mater., 4, 23 (1992) and references therein.
15. Y. Mirovsky, R. Tenne, G. Hodes and D. Cahen, Thin Solid Films, 91, 49 (1982).
16. M. Takahashi, Y. Katou, K. Nagata and S. Furuta, Thin Solid Films, 240 (1-2), 70 (1994).
17. P. Magri, C. Boulanger and J.M. Lecuire, J. Mater. Chem., **6** (5) 773-779 (1996).
18. L.I. Anatychuk and O.J. Luste, *Proc. XV Int. Conf. Thermoelectrics*, Pasadena, USA, March 26-29, IEEE Catalog No. 96TH8169, 279 (1996).
19. E. Kolawa, J.S. Chen, J.S. Reid, P.J. Pokela, M-A. Nicolet, J. Appl. Phys. **70**, 1369 (1991).
20. T. Kacsich, E. Kolawa, J.-P. Fleurial, T. Caillat and M.-A. Nicolet, J. Phys. D, **31**, 1 (1998).

RELIABILITY OF THERMAL CONDUCTIVITY MEASURED BY HARMAN METHOD

Y.SHINOHARA*, Y.IMAI, Y.ISODA and I.A.NISHIDA
The 4th Research Group, National Research Institute for Metals, 1-2-1, Sengen, Tsukuba-shi 305-0047, Japan; *shinohara@nrim.go.jp

ABSTRACT

The Harman method was applied to measure thermal conductivity κ of thermoelectric materials, and the reliability of the measured κ was investigated. The quantitative κ requires a highly sensitive technique to measure minute Peltier heat. Temperature difference by Peltier heat pumping was successfully measured by developing the DC method of resistance measurement. κ of *n*-type Bi_2Te_3 sintered compact and *n*-type PbTe boules was measured at 295K by the Harman method. Static comparative method was also applied to obtain the standard value of κ. In the case of Bi_2Te_3, the κ by the Harman method agreed well with the standard value. In the case of PbTe in the electron concentration n_e range $<5\times10^{24}/m^3$, the κ almost agreed with the standard value. However, PbTe in the n_e range $\geqq1\times10^{25}/m^3$ showed a larger κ than the standard value. The Harman method has an error to give the larger κ for the material with a large carrier component κ_e of κ. This error is due to the fast conduction of Peltier heat by the carrier. The reliable κ can be measured for the material with a small κ_e.

INTRODUCTION

There are several methods to measure thermal conductivity, κ, of thermoelectric materials; static comparative method, laser flash method, Harman method, and so on. The Harman method is characterized by the direct measurement of κ from Peltier heat[1]. The Harman method has been modified to be more practical and more quantitative[2]. The Harman method is attractive to measure the temperature dependence of κ, because the heat source to provide the constant heat flow for a specimen is unnecessary. However, it has not been applied generally for the following reasons:

1) The applicable thermoelectric materials are unknown.
2) The highly sensitive technique to measure minute Peltier heat is necessary for the quantitative and reproducible value.
3) The electrode in good contact with a specimen is essential.
4) The accurate values of Seebeck coefficient α for a specimen and an electrode are essential.

In this paper, the highly sensitive technique to measure Peltier heat has been developed and κ of *n*-type Bi_2Te_3 and *n*-type PbTe has been measured by The Harman method to investigate the reliability of the measured values.

EXPERIMENT

The *n*-type Bi_2Te_3 sintered compact for practical applications and the *n*-type PbTe boules with a different electron concentration n_e were specimens. The measured value of κ by static comparative method was used for the standard value. The specimen size was $4.2\times4.2\times4.3$mm. The standard material was quarts[3].

The DC method with high speed and high resolution to measure the accurate value of electrical resistivity ρ was applied to measure minute temperature difference by Peltier heat pumping. The specimens are set as shown in Fig.1 (a) and (b). In the case of (a), the temperature

Mat. Res. Soc. Symp. Proc. Vol. 545 © 1999 Materials Research Society

difference ΔT is measured directly by type-R thermocouples 76μmϕ. κ can be obtained by the following equation[1]:

$$\pi I = \frac{A}{\ell} \kappa \Delta T \qquad (1)$$

π : Peltier coefficient $[(\alpha_{material} - \alpha_{electrode}) \times T]$
I : Current
A : Cross sectional area
ℓ : Distance between thermocouples

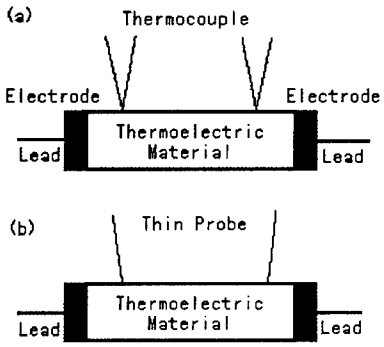

Fig. 1 Specimens for Harman method

In the case of (b), ΔT is calculated from the thermoelectromotive force ΔE between Pt probes 50μmϕ:

$$\Delta T = \frac{\Delta E}{\alpha_{material}} \qquad (2)$$

The electrodes were Pb-Bi solder(α=2.8μV/K at 295K) for Bi_2Te_3 and Pb-Sn-In (α=0.4μV/K) for PbTe. The leads were Pt wires 0.2mmϕ. The length of specimen was 10mm.

Both the measurements of Harman method and static comparative method were performed at 295K in a vacuum of less than 1×10^{-3}Pa.

RESULTS

Measurement of Minute Peltier Heat

When the current running through the specimen was 50mA(current density: 2mA/mm^2) or more, the specimen temperature was increased by Joule's heat during measurement. The current of less than 50mA were applied for this study.

The probe voltage change with measurement time for Bi_2Te_3 is shown in Fig.2. The current was 10mA, and the probes were spot-welded at the points 3 and 4.5mm distant from the one electrode. The electrical resistance of the specimen generates the voltage of 7.8μV immediately after the current runs through the specimen. The voltage is increased with time to a constant value. The voltage increase is by Peltier effect[4]. The plateau of approximately 1s is detected at the beginning of the voltage increase.

The voltage change was evaluated in relation to the probe position with keeping the distance between the probes 1.5mm. When the probes were very close to the electrode, the plateau was not detected. When the probes were almost at the center of the specimen, the plateau was approximately 2s. The plateau was directly affected by the probe position.

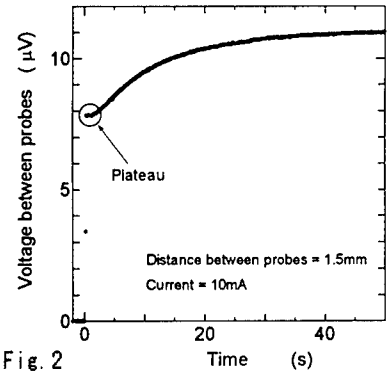

Fig. 2 Voltage change between probes as a function of time in n-Bi_2Te_3 specimen 10mm long

The temperature change in the specimen with time is shown in Fig.3. The measured points in the specimen were 0.45, 2.52 and 5.00mm distant from the electrode. The point of 5.00mm was just at the center of the specimen 10mm long. When the point is closer to the electrode, the increasing rate of temperature is higher. At the center of the specimen, the temperature is not changed because pumping up of Peltier heat from one electrode side and pumping down from the other side are balanced. A plateau of temperature is detected at the position of 2.52mm. It is clarified that the plateau is the duration without Peltier effect.

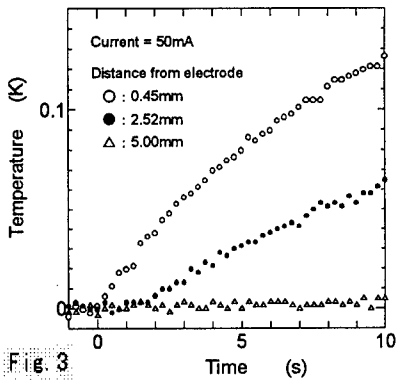

Fig. 3
Temperature change by Peltier heat in n–Bi_2Te_3 specimen 10mm long

The value of κ measured by static comparative method was 1.53W/(Km) for Bi_2Te_3. κ is mainly the sum of electronic thermal conductivity κ_e and lattice thermal conductivity κ_L:

$$\kappa = \kappa_e + \kappa_L \tag{3}$$

κ_e is obtained by the Wiedemann-Franz relation:

$$\kappa_e = \frac{LT}{\rho} \tag{4}$$

,where L, T and ρ are Lorenz number, temperature and resistivity, respectively. L for n-Bi_2Te_3 is $1.53 \times 10^{-8} V^2/K^2$ at 300K[5] and the ρ is $11.7 \mu\Omega m$ from Fig.2. From Eqs.3 and 4, the κ_e and the κ_L are 0.39 and 1.14W/(Km).

The heat diffusion constant by the carrier D_e is calculated from Einstein's relation:

$$\frac{D_e}{kT} = \frac{\mu}{e} \tag{5}$$

,where k, μ and e are Boltzmann constant, mobility and electric charge, respectively. The μ is $200 cm^2/(Vs)$ at 300K. From Eq.5, the D_e is $5 cm^2/s$. The specific heat of carrier C_e is 0.005J/(mol K).

The specific heat of lattice C_L for n-Bi_2Te_3 is 120J/(molK) at 300K[6]. The heat diffusion constant by lattice D_L is $0.01 cm^2/s$.

The Peltier heat pumping has a heating effect on the specimen from one electrode side and also a cooling effect from the other side. The heat deviation $\Delta H(x,t)$ in a specimen can be expressed by applying the diffusion equation:

$$\Delta H(x,t) = Q' t(1 - erf(\frac{x}{2\sqrt{Dt}})) - Q' t(1 - erf(\frac{1-x}{2\sqrt{Dt}})) \tag{6}$$

$$Q' = Q - Q(1 - erf(\frac{1}{2\sqrt{Dt}})) \tag{7}$$

,where x, t and Q are the position, the time and the charged Peltier heat, respectively. By using

Eqs.6 and 7, the heat deviation by Peltier heat pumping was calculated for the point 3mm distant from the electrode, assuming the carrier and the lattice had no interaction of heat. The result is shown in Fig.4. The plateau of approximately 1s is simulated at the beginning of Peltier heat pumping.

The heat conducted by the carrier is very fast, while that by lattice is slow. The carrier and the lattice have a large difference in the conducting behavior of heat. The fast conduction of Peltier heat causes that the heat to pass quickly though the specimen and that the heat is not accumulated at a specific point in the specimen. The carrier should provide some of its heat for the lattice by the heat interaction. Heat deviation in the specimen originates mainly in the slow heat conduction by the lattice. This explains the appearance of the plateau in Fig.2. The plateau of probe voltage is the time for the lattice to conduct Peltier heat to the probe.

The calculated heat deviation by the carrier and lattice was increased with time to reach a constant value. This constant value corresponds to thermoelectric voltage in Fig.5; ΔE is equal to thermoelectric voltage. When the plateau of probe voltage is detected, the accurate measurement of ΔE can be achieved; the accurate ΔT can be calculated from Eq.2.

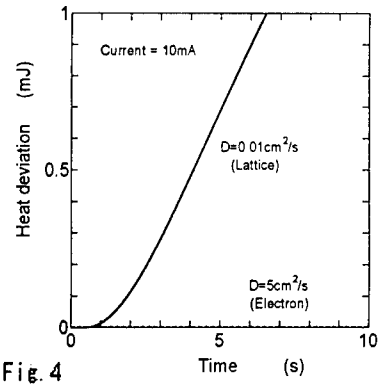

Fig. 4

Calculated heat deviations at a point 3mm distant from electrode in n-Bi_2Te_3 specimen 10mm long

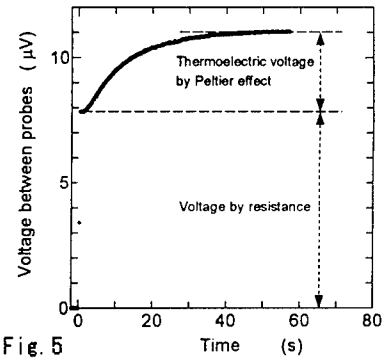

Fig. 5

Voltage change between probes as a function of time showing thermoelectric voltage

Quantitative Harman Method

The value of ΔT by the thermocouples(Fig.1 (a)) was more than 30% smaller than that by the thin Pt probes(Fig.1 (b)). Some of Peltier heat is lost through the thermocouples. The thin probes are better to prevent the heat loss. The thin probes were used for the measurement of ΔT.

If the heat transfer through the Pt current leads 0.2mmϕ is negligibly small, the accuracy of ΔT is high. In the case of the current of 30mA or more, the Joule's heat of the Pt leads affected ΔT. The current of 20mA or less was applied for the measurement of ΔT.

When the temperature is not linearly distributed in a steady state of Peltier heat pumping, the measured value of thermoelectric voltage is changed by the probe position. The absolute values of thermoelectric voltage in relation to the current direction are shown in Fig.6. The probe positions **A** and **B** are also schematically described. The slope of

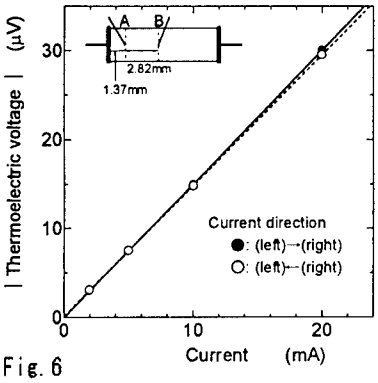

Fig. 6

Thermoelectric voltage as a function of current

the solid line is the same as that of the broken line. The absolute value of thermoelectric voltage is independent of the current direction. The temperature distribution is symmetrical in the specimen.

Only the probe position **A** was moved, and the change of thermoelectric voltage was evaluated. The thermoelectric voltage was proportional to the distance between **A** and **B**. The temperature distribution in the half of the specimen was linear.

From these results, the temperature is linearly distributed through the whole specimen in a steady state of Peltier heat pumping.

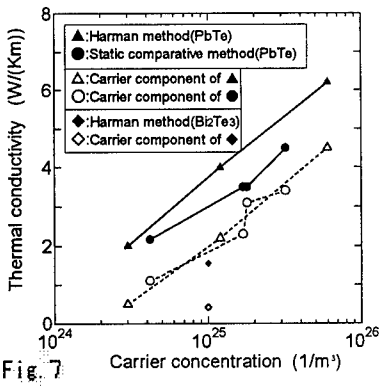

Fig. 7 Thermal conductivity of PbTe and Bi 2Te3 by Harman and static comparative methods

κ of Bi_2Te_3 was measured by The Harman method. The value of κ was 1.56W/(Km), which agreed with the value of 1.53W/(Km) by static comparative method. This result suggests the heat loss through the Pt probes 50μmϕ and the Pt leads 0.2mmϕ are negligibly small. The quantitative κ was obtained by developing the DC method of resistance measurement.

κ of PbTe was measured by the Harman method. The result is shown in Fig.7. κ_e was calculated from Eq.4. The κ by the Harman method almost agrees with that by static comparative method in the carrier concentration n_e range $< 5\times10^{24}/m^3$, while the former is larger than the latter in the n_e range $\geqq 1\times10^{25}/m^3$. The Harman method is applicable only to PbTe with a low n_e, of which κ_e is small, less than 1W/(Km). It is shown Bi_2Te_3 has also the small κ_e of 0.39W/(Km).

The Harman method has an error to give the larger κ than the true value for the material with a large κ_e.

As is mentioned above, the heat deviation in the specimen is mainly contributed by the slow heat conduction by the lattice. The measured ΔT is smaller than the true value contributed by both the carrier and the lattice, resulting in the larger κ. Eq.1 can not be simply applied to the material with a large κ_e.

It is concluded that the Harman method can give the quantitative κ for the material with a small κ_e and that the application of this method is limited in the material with a small κ_e.

CONCLUSIONS

The Harman method was applied to measure thermal conductivity κ of thermoelectric materials, and the reliability of the measured values was investigated. The conclusions are as follows:

1) Temperature difference by Peltier heat pumping was successfully measured by developing the DC method of resistance measurement.
2) In the case of Bi_2Te_3, the κ by the Harman method agreed well with that by static comparative method.
3) In the case of PbTe in the n_e range $< 5\times10^{24}/m^3$, the κ by the Harman method almost agreed with that by static comparative method.
4) In the case of PbTe in the n_e range $\geqq 1\times10^{25}/m^3$, the Harman method had an error to give the larger κ than the true κ. This error is due to a large difference in the Peltier heat conducting behavior between the carrier and the lattice.
5) The application of the Harman method is limited in the material with a small κ_e.

ACKNOWLEDGMENT

This work was partly supported by the Special Coordination Funds for Promoting Science and Technology from the Science and Technology Agency (STA) of Japan.

REFERENCES

1. T.C.Harman, Semiconductor Products, Sep., p.13(1963).
2. R.J.Buist in *CRC Handbook of THERMOELECTRICS,* edited by D.M.Rowe, CRC Press Inc., New York, 1994, pp.189-209.
3. K.Uemura and I.A.Nishida, *TERMOELECTRIC MATERIALS and APPLICATIONS* (in Japanese), Nikkan Kogyo Shinbunsha, Tokyo,1988, pp.195.
4. I.A.Nishida in *CRC Handbook of THERMOELECTRICS,* edited by D.M.Rowe, CRC Press Inc., New York, 1994, pp.157-164.
5. H.Kaibe, Y.Tanaka, M.Sakata and I.A.Nishida, J.Phys.Chem.Solid, 50, p.945(1989).
6. K.C.Mills, *Thermodynamic DATA for Inorganic Sulphides, Selenides and Tellurides,* Butterworth, London,1974.

MICROSTRUCTURE AND THERMOELECTRIC PROPERTIES OF THIN FOILS OF BISMUTH TELLURIDE ALLOYS

E. KOUKHARENKO*,**, N. FRETY**, V.G. SHEPELEVICH*, J.C. TEDENAC**
* Physics Department, Belarussian State University, Minsk, 220080 Belarus
** LPMC-UMR 5617, Université de Montpellier II, case 003, Place E. Bataillon, 34095 Montpellier cedex 5, France

ABSTRACT

Ultrarapid quenching processes have been extensively studied during the past few years, particularly for glasses. In the case of polycrystalline materials, the problem is slightly different. In this case, the microstructures obtained by this process are very different from those obtained by normal cooling and they induce new physical properties.

This synthesis process has been used for bismuth telluride and its alloys with antimony telluride in order to study their thermoelectric properties. The ultrarapid quenched material is obtained in the shape of foils, the thickness of which varies in the range of 20 to 60 μm, which corresponds to a cooling rate of about 10^6K/s. These foils are textured and this texture induces specific material properties. The aim of this work is to correlate microstructure and thermoelectric properties in relation with the fabrication process. In the first step of this study, we will present the results of the correlation of the microstructure with the process conditions. The effects of quenching temperature and post quenching thermal treatment have been studied. Materials were characterized using X-ray diffraction and Scanning Electron Microscopy. We then will discuss the thermoelectric properties of these textured materials.

This study evidences feasibility and reproducibility of ultrarapid quenching process and shows that this process method is very interesting for this kind of materials.

INTRODUCTION

Bismuth telluride based materials are well known for their thermoelectric applications at room temperature [1-3]. They are used in the fabrication of thermopiles [2], thermal sensors, cooling laser diodes [4] and thermoelectric refrigeration [5].

Bismuth telluride and its alloys are commonly obtained using conventional materials fabrication techniques. The major drawback of these techniques is that it often appears difficult to get materials of chemical homogeneity [2]. This is an important point as thermoelectric properties are greatly correlated with chemical homogeneity.

Ultrarapid quenching process route could appear to be a new way to get bismuth telluride based materials with chemical homogeneity. But the high cooling rate (about 10^6-10^7K/s) leads to the formation of non thermodynamically stable alloys [6, 7]. It is then necessary to study the materials microstructure and the related thermoelectric properties. The purpose of this paper is to present our first results on materials in the Bi-Sb-Te ternary system obtained by this way.

EXPERIMENT

Fabrication of bismuth telluride alloy foils

Bismuth telluride alloy materials have been obtained from ultrarapid quenching method. Polycristalline ingots have been previously prepared by the conventional melting route. A

Mat. Res. Soc. Symp. Proc. Vol. 545 © 1999 Materials Research Society

mass of about 0.2 g was then cut off from this ingot and introduced into a quartz tube. After being melted at a temperature of 600, 630 or 675°C, this material was quenched on the polished section of a rotating copper cylinder with a cylinder diameter of about 20 cm and a rotation speed of 25 revolutions per second. The 600, 630 and 675°C temperatures will be hereafter called quenching temperatures. The ultrarapid quenched material is obtained in the shape of foils, the length of which is of about 5 cm and the width of about 1 cm. The thickness of the studied foils varied in the range of 20 to 60 μm. According to calculations, this thickness range corresponds to a cooling rate of about 10^6K/s [8].

Some of the foils have been heat treated under an air atmosphere to study the influence of the heat-treatment on microstructure and thermoelectric properties.

Characterization techniques

The ultrarapid quenched foils microstructure has been observed by Scanning Electron Microscopy (SEM) (Cambridge S360) equiped with Energy Dispersive Spectrometry (EDS) (Link and EDAX) to evaluate chemical composition. The phase analysis has been performed using X-ray diffraction (XRD) (Philips PW1380 with a copper anticathode). The structure has been studied using a diffractometer DRON-3 with a Cobalt anticathode.

The foils texture has been determined using the inverse pole figure. The polar density, P_{hkl}, of the diffraction lines (0 0 0 6, 1 0 $\bar{1}$ 5, 1 0 $\bar{1}$ 8, 0 1 $\bar{1}$ 0, 1 1 $\bar{2}$ 0, 0 1 $\bar{1}$ 4, 0 2 $\bar{2}$ 5, 1 0 1. $\bar{2}$ 0, 2 1 $\bar{3}$ 5, 0 3 $\bar{3}$ 0) was calculated from the Harris method [9].

Thermoelectric properties have been determined by measuring Seebeck coefficient, electrical resistivity and Hall coefficient.

RESULTS

Microstructural study

The obtained foils show macroscopically two types of surface: a bright one, corresponding to the material in contact with the polished copper cylinder, and an unpolished one, corresponding to the material being solidified in air. These two types of surface have been observed using SEM. The bright surface is made of lamellae preferentially oriented according to the cylinder rotation direction. On the unpolished surface, it can be observed a needles network, corresponding to the columnar growth observed on the foil cross section (figure 1).

The chemical composition has been studied performing EDS analysis on different sample points and shows the chemical homogeneity of the raw and heat treated samples. It appears that the chosen composition has been obtained after heat-treatment for each material. Microprobe analysis will be performed in order to confirm the chemical composition and homogeneity.

Concerning Bi_2Te_3 material, X-ray diffraction phase analysis confirmed that foils are made of crystalline Bi_2Te_3 whatever the quenching temperature (600°C, 630°C, 675°C).

It then appears that Bi_2Te_3, $Bi_{0.4}Sb_{1.6}Te_3$ and $Bi_{1.6}Sb_{0.4}Te_3$ compounds can be obtained in a reproducible way, using ultrarapid quenching fabrication method.

Texture study

The texture has been studied for raw samples of different thickness (ranging from 20 to 35 μm). $Bi_{2-x}Sb_xTe_3$ texture has been determined, the x value varying from 0 to 2 by steps of 0.2. The polar density P_{hkl} has been calculated in each case. The results are reported in figure

2. A preferentially orientation is obvious for Bi_2Te_3. It can be observed the formation of a well defined (0 2 $\bar{2}$ 5) texture during the ultrarapid quenching process for Bi_2Te_3 foils. This crystallographic orientation corresponds to 87% of the alloy global volume. A misorientation appears when Sb quantity increases. The (0 2 $\bar{2}$ 5) texture decrease seems to be associated with the appearance of the (1 1 $\bar{2}$ 0) texture.

Figure 1 : Columnar growth observed on Bi_2Te_3 foil cross section

The texture formation of the studied Bi_2Te_3 foils is due to the particular Bi_2Te_3 cristallographic structure and to the covalent bonds orientation. The Bi_2Te_3 - type structure can be represented as a set of quintets normal to the threefold axis of the unit cell. These quintets are bonded with Van der Waals interactions. Each quintet consists of five layers in which the atoms form a plane hexagonal net. The sequence of layers can be described as - Te(1)-Bi-Te(2)-Bi-Te(1)-. The Te atoms lying in the Te(2) layer are surrounded by the six nearest neighbours (three Bi atoms from each adjacent layer). The Te atoms from the Te(1) layer are bonded to three Bi atoms and three Te atoms from the Te(1) layer belonging to the neighbouring quintet. The Bi-Te(1) and Bi-Te(2) bonds are mainly covalent. Crystallographic analyses show that two covalent bonds, Bi-Te(1) and Bi-Te(2), are located in the {1 1 $\bar{2}$ 0} planes, whereas four other bonds, two Bi-Te(1) and two Bi-Te(2), are formed between the atoms lying in the neighbouring planes of the same type. In the {2 0 $\bar{2}$ 5} planes, each Bi atom forms either two Bi-Te(1) bonds or two Bi-Te(2) bonds, whereas the remaining bonds are formed by the atoms from the neighbouring planes of this type. Such an orientation of the covalent bonds promotes fast growth of crystallites forming the solid-liquid interface coinciding with the planes {1 1 $\bar{2}$ 0} and {2 0 $\bar{2}$ 5} of the structure.

During the growth, the alloys surface consists of dangling bonds forming active centers of nucleation. Steps of atomic dimensions are readily formed with a high density on the solid phase surface. The atoms lying at the step edge form dangling covalent bonds oriented along the interface and promote the attachment of atoms, thus giving rise to the side step motion and growth of crystallites with the orientations indicated above. At the same time, the existence of weak Te(1)-Te(1) bonds between the quintets hinders the formation of atomic steps at the end planes of the quintets, which decelerates growth of the {0001} oriented crystallites and results in a low pole density of the (0006) diffraction reflection. In the {1 0 $\bar{1}$ 0}-type planes, the Bi-Te(1) and Bi-Te(2) bonds are not formed at all. Such bonds are formed only between the atoms located in the neighbouring planes of this type. At the interface coinciding with such planes, the formation of dangling covalent bonds is energetically advantageous : these bonds

promote the attachment of atoms from the liquid phase and the formation of the steps of atomic dimensions on the crystallite surface. However, such steps can hardly participate in the side motion, because there are no covalent bonds oriented in the $\{1\ 0\ \bar{1}\ 0\}$ planes. Therefore, the crystallites whose interface lies in the $\{1\ 0\ \bar{1}\ 0\}$ plane cannot grow at high rates, which explanes the low pole density of the $\{1\ 0\ \bar{1}\ 0\}$ diffraction reflection [10].

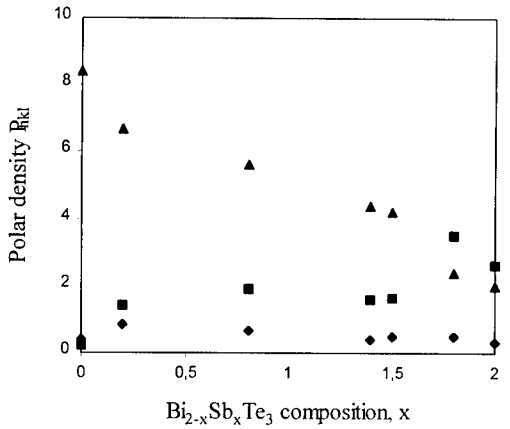

Figure 2 : Variation of polar density, P_{hkl}, with ($Bi_{2-x}Sb_xTe_3$) x value for (0006) ♦, (1 1 $\bar{2}$ 0) ■ and (0 2 $\bar{2}$ 5) ▲ diffraction lines

Thermoelectric properties

Seebeck coefficient evolution with heat treatment temperature

Successive measurements of the Seebeck coefficient have been performed on heat treated materials. Materials have been heat treated under air for 10 minutes from room temperature to 420°C, the temperature step being 20°C.

For the three studied materials, it appears that the S value remains constant from room temperature to a temperature of about 160°C. Then it can be observed an S absolute value increase (figure 3), each curve being the mean result of the measurements performed on three different samples. This evolution is due to the metastable state of the foils structure induced by the ultrarapid quenching method. This could be explained by the annihilation of antisite defects as it was previously observed on other kind of materials [11, 12].

Seebeck coefficient, Hall coefficient and electrical resistivity evolution with temperature

The evolution of Seebeck coefficient, Hall coefficient and electrical resistivity with temperature have been measured for the three studied materials.

For the three studied materials, the Hall coefficient, R_H, remains constant with temperature with mean values of $-0.4\ 10^{-2}cm^3/C$, $8\ 10^{-2}cm^3/C$ and $-12\ 10^{-2}cm^3/C$ respectively

for Bi_2Te_3, $Bi_{0.4}Sb_{1.6}Te_3$ and $Bi_{1.6}Sb_{0.4}Te_3$. Concerning the electrical resistivity, the value slightly increases with temperature, from 2.6 10^{-4} to 4.7 10^{-4} Ω.cm, 3.3 10^{-4} to 6.7 10^{-4} Ω.cm and 13.6 10^{-4} to 28 10^{-4} Ω.cm, respectively for Bi_2Te_3, $Bi_{0.4}Sb_{1.6}Te_3$ and $Bi_{1.6}Sb_{0.4}Te_3$.

The carrier concentrations are respectively 1.4 10^{21} cm^{-3}, 7.5 10^{19} cm^{-3} and 3.4 $10^{19}cm^{-3}$ for Bi_2Te_3, $Bi_{0.4}Sb_{1.6}Te_3$ and $Bi_{1.6}Sb_{0.4}Te_3$ at room temperature. This indicates that the materials are degenerate semiconductors. Simultaneously it can be observed that there is an increase of the S absolute value. Bi_2Te_3 and $Bi_{1.6}Sb_{0.4}Te_3$ are n type materials, with a $|S|$ value respectively of 19μV/K and 71 μV/K at room temperature. These values are very low compared to that obtained from other processing routes [13, 14]. The Bi_2Te_3 n-type is associated to a Te excess in this material as it was confirmed by differential scanning calorimetry. $Bi_{0.4}Sb_{1.6}Te_3$ material shows a S value of 110 μV/K at room temperature, which is similar from the value obtained from other processing routes [14, 15].

These results point out the feasibility of the ultrarapid quenching method to produce Sb-rich $Bi_{2-x}Sb_xTe_3$ materials. It is now necessary to optimize the melt composition to get near Bi_2Te_3 compositions and well-doped materials with better thermoelectric properties.

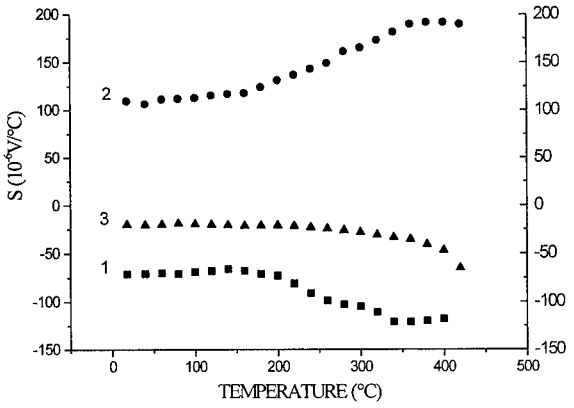

Figure 3 : Evolution of Seebeck coefficient with temperature for Bi_2Te_3 (3), $Bi_{0.4}Sb_{1.6}Te_3$ (2) and $Bi_{1.6}Sb_{0.4}Te_3$ (1) materials

Heat-treatment influence on $Bi_{0.4}Sb_{1.6}Te_3$ thermoelectric properties

$Bi_{0.4}Sb_{1.6}Te_3$ material has been successively heat treated under air for 2 hours at 100°C and then 160°C. Other foils have been heat treated for 2 hours at 300°C. Then Hall coefficient, R_H, and electrical resistivity, ρ, were measured and mobility, μ, and carriers concentration, p, have been calculated from these values. It can be observed that there is a slight increase of R_H with temperature from 8.10^{-2} cm^3/C at 25°C to 20.10^{-2} cm^3/C at 300°C and a slight increase of ρ with temperature from 6.7.10^{-4} at 25°C to 13.3.10^{-4} Ω.cm at 300°C. The carrier concentration value remains nearly constant with temperature and is of the order of 10^{19} cm^{-3}. Concerning the mobility, the value increases from 125 $cm^2/V.s$ at 25°C to 150 cm^2/V at 300°C.

CONCLUSION

This study showed the feasibility and the reproducibility of the ultrarapid quenching process route to get a single phase Bi_2Te_3 material as well as bismuth telluride alloys.

After ultrarapid quenching, foil samples show a (0 2 $\bar{2}$ 5) texture which is correlated to the orientation and the dangling nature of the Bi-Te covalent bonds in this plane. When the alloys are Sb richer, the (0 2 $\bar{2}$ 5) texture is less obvious and the (1 1 $\bar{2}$ 0) texture appears.

Ultrarapid quenched foil samples are in a metastable state, which leads to an increase in the magnitude of the Seebeck coefficient above 160°C.

It appears that the ultrarapid quenching method leads to materials with good thermoelectric properties for rich-Sb alloys as thermoelectric properties of poor-Sb alloys need to be improved by melt composition optimization and doping.

REFERENCES

[1] D.R. Benson and C.E. Tracy, Proceedings of the Fourth International Conference on Thermoelectric Energy Conversion, University of Texas, Arlington, March, 1982. (IEEE, N° 82ch 1763-2, 1982) p.11.

[2] B.M. Goltsman, V.A. Kudinov and I.A.Smirnov, Semiconducting Thermoelectric Materials Based on Bi_2Te_3, Moskow:Nauka, 1972, p.320.

[3] M. Ferhat, B. Liautard, G. Brun, J.C. Tedenac, M. Nouaoura and L. Lassabatere, Comparative studies between the growth characteristics of Bi_2Te_3 thin films deposited on SiO_2, Si(100) and Si(111), Journal of Crystal Growth, 167, 1996, p.122-128.

[4] D.W. Rowe and C.M. Bhandari, Modern Thermoelectrics, Holt, Rinehart and Winston, London, 1983, p.103.

[5] Goldsmid H J, Thermoelectric Refrigeration , New York, Plenum, 1964.

[6] V.M. Glazov and Yu.V.Yatmanov, Metastable Solid Solutions Obtained by Ultrarapid Liquid Quenching in AV-BVI Systems, DAN USSR, 1984, Vol.227, 2, p.391-394.

[7] V.M. Glazov and Yu.V.Yatmanov, Decomposition of Metastable Semiconductor Solid Solutions Prepared by Liquid Quenching, Izv. Akad. Nauk SSSR Neorg.Mater., 1990, Vol.26, 11, p.2291-2294.

[8] I.S. Miroshnichenko, Quenching from the Liquid State, Moskow: Metallurgiya, 1982, p.162.

[9] G.Vasserman and I.Greven, Textures of Metallic Materials, M: Metallurgiya, 1969, p.654.

[10] V.G. Shepelevitch, Semimetal Chalcogenide Foils Texture Produced by Ultrarapid Liquid Quenching, Kristallografiya, 1997, Vol. 42, 3, p. 538-540.

[11] J. Horak, K.Cermak and L.Koudella, Energy Formation of Antisite Defects in Doped Sb_2Te_3 and Bi_2Te_3 Crystals, J. Phys. Chem. Solids, 1986, Vol.47, 8, p. 805-809.

[12] Z. Stary, J. Horak, M. Stordeur and M. Storlzer, Antisite defects in $Sb_{2-x}BixTe_3$ Mixed Crystals J. Phys. chem. Solids, 1988, Vol.49, 1, p. 29-34.

[13] Yu. A. Boikov, O.S. Gribanova, V.A. Danilov and V.A. Kutasov, Hole Mobility in p-Bi_2Te_3 Polycristalline Films, FTT, 1991, Vol.32, 12, p. 3440-3544.

[14] Z.M. Dashevskii, E.A. Zhemchuzhina, Ya.A.Kaller, N.V. Kolomoec, Yu.G. Polistanskii and L.A. Nikolashin, Elaboration and Properties Study of Monocristalline Films of Bi_2Te_3-Sb_2Te_3 System, Electronnay Technika, Ser. Materiali, 1974, Vol.8, pp. 74-78.

[15] Yu. A. Boikov, O.S. Gribanova, V.A. Danilov and V.A. Kutasov, P-$Bi_{0.5}Sb_{1.5}Te_3$ Thin Films Obtaine by Hot-Wall Method, Inorganic Materials, 1990, Vol.26, 8, p.1628-1631.

THE EFFECT OF A GRADED In PROFILE ON THE FIGURE OF MERIT OF PbTe

Z. DASHEVSKY, S. SHUSTERMAN, A. HOROWITZ, AND M. P. DARIEL
Department of Materials Engineering, Ben-Gurion University of the Negev,
P.O.B. 653, Beer-Sheva 84105, Israel. E-mail: zdashev@bgumail.bgu.ac.il

ABSTRACT

The present study was aimed at demonstrating the possibility of producing a graded charge carrier concentration in a PbTe crystal by taking advantage of the concentration profile that is set up by the diffusion of In from an external source. Doping by indium generates deep impurity levels lying close to the edge of the conduction band. The Fermi level pinning effect and the electron population of the In impurity levels, which reduces the minority carrier concentration at elevated temperature, significantly improve the thermoelectric behavior of the resulting material. The penetration profiles of In, originating from an external gaseous or liquid source, were determined using Seebeck coefficient measurements in *p*- and *n*-type PbTe crystals. In the *p*-type crystal, the Seebeck coefficient changed sign as the In concentration induced a change from *p*-type to *n*-type character. The thermovoltage of a PbTe crystal in which an In concentration profile, generated by In diffusing from a gaseous source had been established, was determined in the 50 to 430 °C temperature range. The constant Seebeck coefficient that was observed over the whole temperature range provides the experimental support for the underlying premises of this study.

INTRODUCTION

In order for thermoelectricity to be an attractive energy conversion alternative, to be able to challenge successfully competing conversion systems and to promote new applications, the dimensionless figure of merit ZT must attain an average minimum value of 1.5. This rationale stands behind the systematic search for advanced thermoelectric materials that display a potential for maximum ZT values. The figure of merit ZT, is a function of two dimensionless parameters $ZT = F(B, \beta)$ [1]. The first dimensionless constant is

$$B = \xi \mu T k_b^2 / q K_l, \qquad (1)$$

where ξ is the density of states in the conduction band, μ, the carrier mobility, K_l, stands for the phonon part of the thermal conductivity, k_b is Boltzmann's constant, q, the electron charge and T, the absolute temperature. It is apparent from eq.(1) that a promising thermoelectric material is associated with a high value of electrical properties (mobility) and low heat conductivity. Such materials, most likely semiconductors, should display a high density of states (four or more equivalent band minima, N_C, are necessary [1]). In accordance with these principles, the type IV-VI semiconductor compound PbTe is one of the best thermoelectric materials. The room-temperature mobility in heavily doped PbTe is higher than for Si and Ge ($\mu \approx 2000$ $cm^2/Vsec$), the phonon part of the thermal conductivity is uniquely low ($K_l \cong 2 \times 10^{-2}$ W/cmK) and the density of states is high ($N_C = 4$).

The second dimensionless constant, β, is a parameter that stands for the effect of the minority carriers. In the presence of two types of charge carriers (electrons and holes), $\beta = E_g/k_B T$, where E_g is the width of the band gap and determines the bipolar term in the Seebeck coefficient, S, and in the thermal conductivity, K.

Mat. Res. Soc. Symp. Proc. Vol. 545 ©1999 Materials Research Society

The contribution of the minority carriers to the Seebeck coefficient and the thermal conductivity can be expressed in terms of a second dimensionless parameter:

$$-\Delta S \sim e^{-\beta} \text{ and } \Delta K \sim e^{-\beta}(4+\beta)^2, \text{ respectively.} \qquad (2)$$

The thermal excitation of minority carriers plays an adverse role in determining the figure of merit. At the operating temperature, the presence of an operating mechanism able to reduce or suppress this process by lowering the density of minority carrier is highly desirable. In monolithic thermoelectric materials that are usually considered, the various material parameters along the operating temperature gradient do not display the optimal properties. A higher efficiency than for traditional thermoelectric materials can be expected, if appropriate property profiles are fitted to the temperature gradient. Three approaches can be taken to achieve this goal: (a) by varying the carrier concentration (doping with shallow level impurities), (b) by varying the width of the band-gap (changing of composition), (c) by producing a concentration gradient of impurities that have deep lying levels. Thermoelectric materials built according any of these approaches are so-called FGM (Functionally Graded Materials) and are the focus of much current interest [2]. In the present work we consider a graded material in which the third of these approaches was applied.

The strong influence that impurities exert on the electron properties of PbTe is connected with the deep-lying states that appear as a result of In doping. An indium impurity in PbTe displays donor-like properties, yet in spite of the high solubility of In in PbTe (20 mol % In), the original NaCl-type rock-salt structure is retained and the electron concentration does not exceed n $\cong$ (3-5)$\times 10^{18}$ cm^{-3}. In contrast to shallow lying states, deep lying ones consist of wave functions that belong to several bands. Consequently, their energy levels are not connected to any particular band edge E_C and E_V, they may lie in a band as well as in a band-gap. The behavior of In in PbTe was subject to several investigations [3,4]. It was established that:

- At low temperature the In energy level is close to E_C. Its position doesn't depend on the In concentration up to $N_{In} \approx 3$ at %.
- Each In atom occupying a Pb lattice site contributes one free electron and two states. Thus, the impurity level is half- filled.
- At low temperature, the Fermi level practically coincides with the impurity level (pinning of the Fermi level).
- The position of the impurity level with respect to E_C can be varied by changing the alloy composition e.g. in $Pb_{1-x}Sn_xTe$ or the temperature.
- Additional doping of PbTe<In> with I (one charged donor) or Na (one charged acceptor) practically doesn't affect the electron concentration until the additional impurity concentration reaches the concentration of In.

EXPERIMENTAL TECHNIQUES

Single n-type (doping impurity - I, using PbI_2 compound) and *p*- type (doping impurity - Na) PbTe crystals were grown by the Czochralski technique. The large, 25-30 mm diameter crystals were grown at 2 cm/h growth rate and δ = 0.5 1/s rotation speed. Structural characterization was performed using a Rigaku D/MAX-2000 computer controlled diffractometer. Small 4×4×4 mm^3 samples were cut from the single crystals and subjected to diffusion doping with In.

The indium diffused into the PbTe lattice originated either from a liquid or a gaseous phase. According to the first approach, a relatively thick In metal coating was deposited by vacuum evaporation onto one of the PbTe crystal surfaces and subsequently diffused into the crystal from the molten state. According to the second approach, indium atoms were transported unto the

PbTe crystal surface from an In_4Te_3 vapor source, as described below [5]. Using this approach, a constant level of surface In concentration was maintained during the entire diffusion anneal. These anneals were carried out in the 600 to 750 °C temperature range, for 25 to 200 hour long durations. At the completion of the diffusion anneals, the samples were rapidly quenched to room temperature.

During the diffusion anneal the sample was kept in sealed and evacuated 10-12 mm inside diameter and 6-8 cm long quartz ampoules. The ampoule was built at its end with a round reservoir that contained the In_4Te_3 powder, used as a source for the gaseous In. The reservoir was connected by a thin neck (~ 2mm diameter) to the rest of the ampoule and contained also some PbTe powder, from the same source as the sample, to maintain the crystal stoichiometry. The evacuated and sealed ampoules were inserted into a horizontal oven that had a zone of uniform temperature longer than the full length of the ampoule.

After doping anneal the samples were examined by optical microscopy for signs of surface damages. The room temperature Seebeck coefficient along the sample was measured at 10 μm. intervals using a 5 μm diameter "hot" probe. The temperature of probe was kept constant within $\pm 0.1^0$C. The transport parameters (Seebeck coefficient, electrical and thermal conductivity) were measured over the 50 to 500 ^{0}C temperature range.

RESULTS AND DISCUSSION

The variation of the Seebeck coefficients, measured in a direction parallel to the penetration of In by diffusion in a *p*-type PbTe, crystal is shown in Fig.1. The Seebeck coefficient for the crystal in which no In penetration took place has, as expected, a constant positive value (line 1). The S values for all crystals in which In had diffused (curves 2 to 5) drop at the front-end of the crystal to a large negative value reflecting the effect of the large In addition that over-compensates the presence of the initial Na acceptors and transforms the initial *p*-type PbTe into a *n*-type PbTe. The values of S as one proceeds into the crystal, increase according to the penetration profile of In, change sign and revert to the positive value, characteristic of In-free PbTe. Clearly, the ability of In, that originates from a gaseous source is significantly more effective than In diffusing from the liquid state, in penetrating the PbTe lattice. The large In concentration gradient that prevails at the interface between the In surface-layer and the PbTe crystal, for samples in which In diffused from the liquid phase, leads possibly to the formation of intermetallic compounds that act as diffusion barriers impeding the penetration of In in the PbTe lattice. Above a certain In concentration, the value of S stays at a constant value. According to ref. [6]:

$$S = \frac{E_F - E_C}{qT} - \frac{2k_b}{q} \quad , \qquad (3)$$

where E_C is the edge of conduction band and E_F is the Fermi level. The constant value of the Seebeck coefficient, S, in samples having reached a certain In concentration indicates that (E_F - E_C) remains constant and doesn't depend on the indium concentration This effect is related to the pinning of the Fermi level by the presence In level with respect to the edge of the conduction band, E_C.

The variation of the Seebeck coefficient in parallel to the penetration in *n*-type PbTe crystals is shown in Fig.2. Straight line (1) stands for the measured low value of S in the original crystal doped with shallow level impurities (from the PbI_2 a source) and in which no In had yet been introduced. The large In concentration at the front-end of the crystals in which In has diffused decreases S to large negative values (curves 2 to 5). From the front-end on, the S values increase

according to the penetration profiles of In, from the large negative towards the initial low negative value of In-free *n*-type PbTe. As for p-type PbTe crystals, the origin of the In diffusing into the crystals affected to a significant extent its penetration profile. It is also noteworthy that the initial large negative *S* value in the *n*-type PbTe crystal (~ -120 mV/K) is less negative than for the *p*-type crystal (~ - 200 μV/K). This observation can be accounted for in terms of the energy level

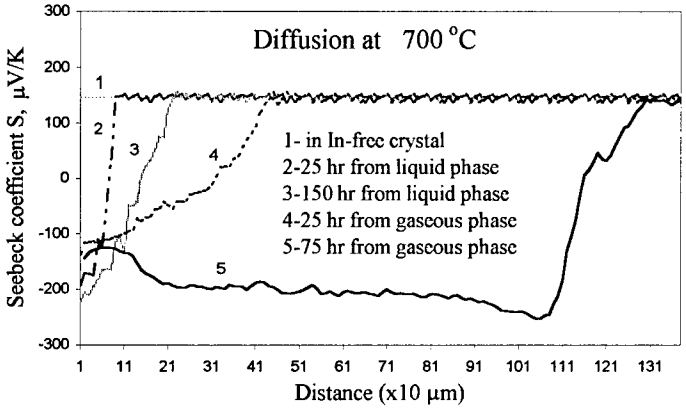

Fig. 1. The variation of the Seebeck coefficient, measured at room temperature along the penetration profile of In into a *p*-type PbTe crystal.

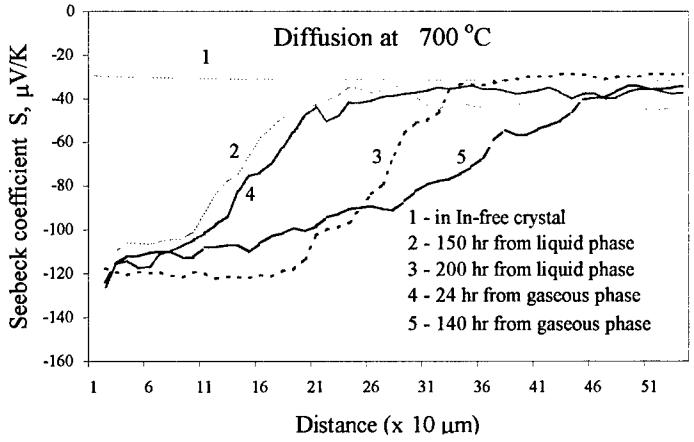

Fig. 2. The variation of the Seebeck coefficient, measured at room temperature along the penetration profile of In into a *n*-type PbTe crystal.

schemes of initially n and p-type PbTe, respectively, in which In has diffused, shown in Fig. 3. The left-side figure shows the energy scheme in an originally p-type crystal into which In had diffused.

The presence of In generates a narrow impurity band (E_{In}) at room temperature. Some of electrons from the band E_{In} annihilate the holes that initially were present in the valence band of p-type PbTe. The Fermi level (E_F) in the In-containing p-type PbTe crystal is located slightly below the In band. In n-type PbTe, even though some of the original electrons of the conduction band dropped into the In-band, the Fermi level is still located in the conduction band. According to Fig.3, clearly ($E_F - E_C$) has a negative value in formerly p-type PbTe (Fig.3a), while in initially heavily doped n-type PbTe, it has a positive value. Thus, according to eq.3, the absolute value of S in the formerly p-type will be higher than in the formerly n-type crystal.

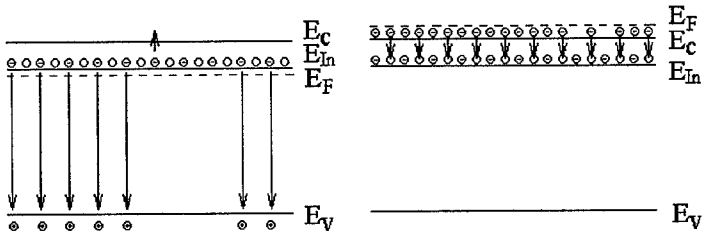

a) b)

Fig. 3. Schematic band diagram for In-doped PbTe.
a) - in an originally p-type PbTe crystal.
b) - in an originally heavily doped n-type PbTe crystal.

A 2 mm thick slice was cut from the p-type PbTe sample that had been doped with In originating from the gaseous phase. The portion that was cut coincided with the region in which a In .gradient was set up as determined by the Seebeck coefficient measurements.

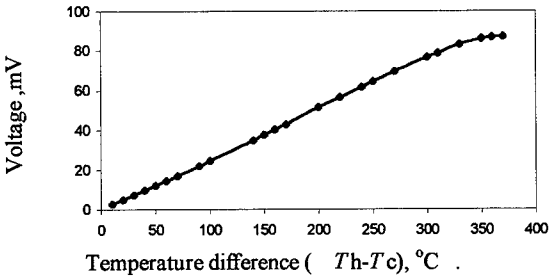

Fig. 4. The thermovoltage of a graded PbTe<In> crystal as a function of the temperature difference

The two end-surfaces of the graded crystal were polished and positioned between two flat surfaces. The lower surface was kept at constant 50 °C and the temperature of the upper surface increased up to 430 °C. The measured thermovoltage, V, of the graded n-doped PbTe<In> is shown in Fig.4. It is noteworthy that the dependence $V(\Delta T)$ is linear within a close approximation. Thus, the Seebeck coefficient $S = V/\Delta T$ is practically constant ($S \approx$ - 250 μV/K) over a wide temperature range. That behavior of $S(T)$ is very different from that in homogeneous n-type PbTe (doped only by iodine). The electrons present in the In-generated band annihilate the minority hole carriers whose influence is significant ordinarily at high temperature. Thus, the term ΔS (Eq.2) can be neglected and S does not decrease at elevated temperature.

CONCLUSIONS

- In the course of a diffusion anneal at 700 ^{0}C during 75 hours, indium solutes from an external vapor phase generate in PbTe crystals a penetration profile that extends over a depth of ≈1mm.
- The presence of the deep, In-generated, impurity level (narrow band), lying close to the edge of the conduction band and the annihilation of minority carriers at elevated temperature by the electrons originating in that band allow to reach an optimal carrier concentration over the 100 to 430 ^{0}C operating temperature range. The Seebeck coefficient stays at a practically constant value over that range.
- The performance of n-type PbTe crystals with a graded structure is improved as compared to that of homogeneous materials. The measured Seebeck coefficient values suggest that the figure of merit in such crystals will attain ZT ≥ 1 over a temperature range up to 600 ^{0}C.

ACKNOWLEDGMENTS

The support of The Israel Science Foundation for the present study, part of program 319/97, is gratefully acknowledged.

REFERENCES

1. G.D. Mahan, Solid State Physics **51**, p. 81 (1997).

2. T. Kajikawa, in Functionally Graded Material 1996, edited by I. Shiota and Y. Miyamoto, (Elsevier Science Publishers, Amsterdam 1997), pp. 475-482.

3. V.I. Kaidanov, Yu. I. Ravich, Soviet Physics Uspekhi **28**, p. 31 (1985).

4. T.V. Bocharova, A.N. Veis, Z. M. Dashevsky, V. A. Kotelnikov and R. Yu. Krupitskya, Sov. Phys. Semicond. **15**, p. 103 (1981).

5. V. Lyahovitskaya, L. Kaplan, J. Goswami and D. Cahen, Proceedings of the 12-th International Conference on Crystal Growth, Israel, p. 302 (1998).

6. F.J. Hyde, Semiconductors, (Macdonald, London,1965), p. 265.

AUTHOR INDEX

Abraham, P., 449
Adderton, D., 345

Badding, J.V., 259
Balandin, A., 111
Barcena, H., 203
Barkyoumb, J.H., 209
Bartkowiak, M., 265
Bastea, M., 123, 421
Baxter, D., 143
Behr, G., 165
Bhattacharya, S., 403
Borca-Tasciuc, T., 111, 357, 473
Borshchevsky, A., 493
Bowers, J.E., 449
Brazis, P.W., 65, 75, 117, 123, 189, 233, 421
Broido, D.A., 485
Browning, V.M., 403

Cai, K-F., 131
Caillat, T., 333, 493
Casian, A., 99
Casperson, J., 37
Cava, R.J., 59
Caylor, J.C., 327
Chakoumakos, B.C., 13, 391
Chapon, L., 321
Charar, S., 93
Chen, G., 87, 111, 215, 273, 357, 369, 467, 473
Chernikov, M., 413
Cho, S., 177, 183, 283
Choi, K-S., 65, 117, 233
Chrissafis, K., 149
Chung, D-Y., 23, 65, 75, 117, 233
Cronin, S.B., 369, 375, 397, 479

Dal Corso, S., 93
Dariel, M.P., 513
Darling, T.W., 295
Dashevsky, Z., 99, 513
Demkov, A.A., 443
Demske, D.L., 209
Dilley, N.R., 13
Ding, Z., 397
DiSalvo, F.J., 171, 259
DiVenere, A., 177, 183, 283
Dong, J., 443
Dresselhaus, G., 87, 215, 345
Dresselhaus, M.S., 87, 215, 345, 351, 357, 369, 375, 397, 473, 479
Dunn, B., 273

Ehrlich, A.C., 273, 339, 403
Eklund, P.C., 303

Fedorov, M.I., 155
Feger, C.R., 381
Feldman, J.L., 3
Feuerbacher, M., 413
Fleurial, J-P., 333, 493
Fornari, M., 3
Foss, C.A., 227
Freeman, A.J., 283
Freibert, F., 295
Frety, N., 507
Fuller-Mora, W.W., 273

Gagnon, R., 413
Gekhtman, D., 345
Gillespie, D.J., 273
Goorsky, M.S., 273
Graf, M.J., 227
Griessmann, H., 165
Grigorian, L., 303
Gronsky, R., 273, 327, 473
Gryko, J., 443
Guardala, N.A., 209

Ha, L., 143
Haidoux, A., 93
Harman, T.C., 479
Hatzikraniotis, E., 149
Heinrich, A., 165
Heising, J., 117
Henningsen, D., 203
Heremans, J., 215
Herman, J.A., 493
Hoffman, C.A., 283
Hofmann, D., 165
Hogan, T., 233
Horowitz, A., 513
Hu, S., 247
Huang, S-C., 397
Huber, T.E., 227

Imai, Y., 501
Imoto, T., 105
Iordanidis, L., 189, 233
Ireland, J., 123, 421
Isoda, Y., 501
Ivanenko, L., 165
Ivanov, Yu.V., 155

Jeffries, J., 137
Jenny, A., 81
Johnson, D.C., 37, 53
Jones, C.D.W., 259

Kaeser, M.A., 137
Kanatzidis, M.G., 23, 65, 75, 117, 123, 189, 233, 421
Kaner, R.B., 397
Kang, H.H., 209
Kannewurf, C.R., 65, 75, 117, 123, 189, 233, 421

Kantser, V., 99
Ketterson, J.B., 177, 183, 283
Khalifah, P., 59
Kido, H., 161
Kilibarda Dalafave, S., 197, 203
Kim, Y., 177, 183, 283
Kleint, C.A., 165
Koga, T., 369, 375, 397, 479
Kolawa, E.A., 493
Kolis, J.W., 381
Koukharenko, E., 507
Kurosawa, K., 105
Kyratsi, Th., 149

LaBounty, C., 449
Larson, P., 23, 421
Legault, S., 413
Liautard, B., 93
Lindsey, N., 209
Littleton IV, R.T., 137, 381
Liu, J.L., 111, 369, 473
Long, M., 137

Mahan, G.D., 265, 315, 459
Mahanti, S.D., 23, 421
Mandrus, D.G., 13, 391
Maple, M.B., 13
Mastronardi, K., 59
Matijasevic, G., 143
Maxwell, S.P., 53
Mazin, I.I., 3
McAllister, H., 197
McMillan, P., 443
Meng, J.F., 259
Meyer, J.R., 177, 183, 283
Migliori, A., 295
Min, X-M., 131
Mohammed, F., 47
Moore, C.D., 273
Mueller, P., 493

Nan, C-W., 131
Nguyen, H.C., 47
Nicolet, M., 493
Nishida, I.A., 501
Nolas, G.S., 37, 47, 339, 435

Paraskevopoulos, K.M., 149
Pecheur, P., 81
Phillips, W.M., 493
Piprek, J., 449
Polvani, D.A., 259
Ponnambalam, V., 403
Poon, S.J., 403
Pope, A.L., 403, 413
Price, J.L., 209
Proctor, K.J., 171

Radetic, T., 473
Ragot, F., 273
Ramachandran, G.K., 443
Ramirez, A.P., 59

Ravot, D., 321
Reinecke, T.L., 485
Riffel, M., 81
Rocci, M., 75, 233
Roche, C., 81
Ryan, M.A., 493

Sakakibara, T., 105
Salamanca-Riba, L., 209
Sales, B.C., 13, 391
Sands, T., 327
Sandu, A., 99
Sankey, O.F., 443
Scherrer, H., 81, 99
Scherrer, S., 81
Schlaefer, D., 165
Schujman, S.B., 47
Schumann, J., 165
Sellinschegg, H., 37, 53
Shakouri, A., 449
Sharma, J., 209
Sharp, J.W., 13, 391
Shen, W-N., 273
Shepelevich, V.G., 507
Shick, A.B., 283
Shinohara, Y., 501
Shusterman, S., 513
Sillars, D., 53
Singh, D.J., 3
Slack, G.A., 47
Snyder, G.J., 333, 493
Sofo, J.O., 315
Song, D., 357, 473
Song, J.G., 403
Sportouch, S., 23, 123, 421
Stacy, A.M., 327
Stokes, K.L., 339
Strom-Olsen, J., 413
Sumanasekera, G., 303
Sun, X., 87, 215, 369, 375, 397, 473, 479
Sur, I., 99

Takigawa, Y., 105
Tang, Y.S., 111
Tani, J-I., 161
Tedenac, J.C., 93, 321, 507
Tritt, T.M., 47, 137, 381, 403, 413
Trugman, S.A., 295

Uher, C., 123, 247, 421

Vedernikov, M.V., 155
Vinzelberg, H., 165
Volkov, P., 403
Volz, S.G., 357
Vurgaftman, I., 283

Wang, C-C., 59
Wang, K.L., 111, 357, 369, 473
Williams, J.R., 37, 53
Windl, W., 443
Wong, G.K.L., 177, 183, 283

Xi, X., 143

Yang, J., 247
Ying, J.Y., 87, 215, 351
Youn, S.J., 283
Young, D., 59
Young, R.A., 47

Zaitsev, V.K., 155
Zeng, T., 357, 467
Zhang, Z.B., 87, 215, 345, 351
Ziegler, J., 197

SUBJECT INDEX

additive process, 143
$AgBiTe_2$, 105
$AgPbBiQ_3$, 123
Ag_2Te, 105
alkali metal, 65
AlPdMn, 413
anodic alumina, 227
apparatus, 137
atomic displacement parameter, 13, 391

band structure, 3
  LnPdSb, 59
bandgap, 315
barrier, 449
Bi, 87, 227
BiSb, 283
Bi_2Te_3, 183, 397
bismuth, 209, 215, 227, 233, 273, 295, 351
  chalcogenide, 117
  selenides, 189
  telluride, 93, 507
BiTe, 177
boron carbide, 131
boundary effects, 265

carbon, 303
ceramic, 131
cerium intermetallic, 171
chalcogenides, 123, 197, 203, 233
charge compensation, 47
Chevrel phases, 81
clathrate(s), 247, 435
  like, 13
cobalt triantimonide, 339
complex bismuth chalcogenides, 23
composite, 209
$CoSb_3$, 315
Cr_3S_4-type compound, 333
crystal structure(s), 117, 189
$Cs_3Bi_4Te_6$, 75

DC method, 501
density
  functional, 3
    theory, 23, 443
  of states, 85, 345
DFT-band structure calculations, 421
doping, 75, 161

effective mass, 315
Einstein oscillator, 13
electrical, 303
  resistivity, 161, 197
  transport, 413
electrochemical deposition, 493
electron transport, 149
electronic
  structure, 23
    model, 351
electrostatic force microscopy, 345
epitaxial thin films, 165
Ettinghausen, 295
experimental, 369

facing target sputtering, 165
films, 493
flux synthesis, 65
folded phonons, 111

GaAs/AlAs, 375
Ge clathrates, 443
glass-like, 435
graded concentration, 513

half-Heusler alloys, 59, 247, 403
Hall effect, 161
Harman method, 501
heat conduction, 501
heterostructure, 449, 467
high temperature, 137
$Ho_3Au_3Sb_4$, 59
HoPdSb, 59
hot wall epitaxy, 93

In diffusion, 513
insertion, 149
iron disilicide/$FeSi_2$, 155, 161

Kane model, 149
Kondo, 303

lead telluride, 99
LnPdSb, 59
low(-)
  dimensional structure, 99
  dimensionality, 397

magnetoresistance, 479
materials, 259
MBE, 183
measurements, 295
metastable, 37
mica, 209
microdevice, 493
microstructure, 131
mixed-valence, 47
modeling, 87
multilayers, 53
multinary bismuth chalcogenide, 65

nanostructures, 345
nanotubes, 303
nanowire(s), 87, 209, 215, 351
narrow-gap semiconductors, 23, 421

optical phonon drag effect, 155

PbTe, 479, 513
Peltier heat, 501
pentatellurides, 381
phonon(s), 3
  engineering, 357
  scattering, 339
porosity, 273
power
  factor, 75
  generation, 403
pressure, 259
pulsed laser deposition/ablation, 327

quantum
  size effect, 227
  well(s), 99, 369, 397, 485
  wires, 485
quasicrystals, 413

Raman spectra, 111
rare earth nickel antimonides, 421
rattlers, 443
refrigeration, 459
resistivity, 137, 381
rhenium silicide, 165
Rh-Sb-Sn ternary system, 47

scanning probe, 345
Seebeck, 333, 381
  coefficient, 513
semiconductors, 81
Si/Ge, 111, 473
silicides, 155
silicon, 131
$Si/Si_{1-x}Ge_x$, 369
skutterudite(s), 3, 13, 37, 47, 53, 233, 315, 321, 327, 339
solid-state synthesis, 117, 123, 233, 421
structural properties, 177
superlattice(s), 111, 283, 327, 357, 375, 449, 459, 473, 479
synthesis, 37, 321
  and characterization, 215

ternary, 37
  telluride, 391
theory, 485
thermal conductivity, 13, 81, 105, 111, 233, 333, 339, 357, 473, 501
thermoconductivity, 123
thermoelectric(s), 3, 23, 53, 75, 81, 105, 137, 155, 171, 177, 183, 209, 215, 259, 273, 295, 315, 327, 333, 351, 357, 397, 403, 413, 459, 493
  cooler, 143
  figure of merit, 369, 375
  materials, 143, 233, 381
  modules, 143
  paste, 143
  power, 197, 203
  properties, 65, 131, 149, 165, 189, 421
  refrigeration, 467
  transport, 485
thermoelectricity, 87, 93, 117, 123, 197, 247, 265, 321, 507
thermoionic, 459
  emission, 449
  refrigeration, 467
thermomagnetic, 295
thermopower, 99, 137, 171, 333, 381, 413
thin film, 53, 93, 265, 273, 288, 327, 507
Ti_2GeTe_5, 391
Ti_2SnTe_5, 391
transport, 283, 303
  data, 75
  properties, 177, 203, 215, 351
tuning, 259

ultrarapid quenching, 507

vibrational modes, 443

Wiedemann-Franz law, 265
wire array, 227

ZrNiSn, 403
ZT, 375, 479